31st Annual Meeting of the German Crystallographic Society (DGK) e. V.

Abstractbook

Table of content

Oral presentations

Organic molecules and coordination compounds 4
Crystallography in Materials Sciences I 11
Crystal physics 21
Bio-Crystallography II: Signaling, macromolecular interactions and new structures 28
Bio-Crystallography I: Hit finding and design of small molecule inhibitors 33
Instrumentation and technological development 38
Micro- and nano-crystalline materials (Powder diffraction, Disordered material) 44
Bio-Crystallography III: New structures and mechanisms 48
Extreme/non-ambient and high-pressure conditions I 55
Crystallography in art and heritage + Teaching 61
Young Crystallographers: Lightning talks 66
Bio-Crystallography IV: Structure-based design 84
Complex, aperiodic and disordered structures 88
Extreme/non-ambient and high-pressure conditions II 95
Computational methods 102
Bio-Crystallography V: Synchrotrons and new technologies 108
Inorganic crystal structures I 116
Theoretical crystallography 123
Micro- and nano-crystalline materials (Powder diffraction, Disordered material) II 130
Electron crystallography and microscopy 135
Crystallography in Materials Sciences II 142

Plenary lectures 148

Table of content

Poster presentations - Poster session I

Minerals 156
Spectroscopy 158
Bio-Crystallography I: Signaling, macromolecular interactions and new structures 159
Bio-Crystallography II: Other technologies (Neutron diffraction, small angle scattering) 170
Crystallography in art and heritage 171
Instrumentation and technological development 201
Micro- and nano-crystalline materials (Powder diffraction, Disordered material) 207
Neutron scattering 215
Organic molecules and coordination compounds 216
Young crystallographers 225
Bio-Crystallography III: Structure-based design 231
Bio-Crystallography IV: Synchrotrons and high throughput methods 235

Poster presentations - Poster session II

Complex, aperiodic and disordered structures 237
Computational methods 244
Electron crystallography and microscopy 246
Extreme/non-ambient and high-pressure conditions 251
Solid state physics in crystallography 263
Crystallography in Materials Sciences 266
Inorganic crystal structures 285
Late Poster 309

State: 21.03.2023

Microsymposium 1 | Organic molecules and coordination compounds

OP-001

Structure determination from unindexed powder data? The challenging case of leuko-pterine

M. U. Schmidt (Frankfurt am Main/DE), F. Bravetti (Frankfurt am Main/DE, Turin/IT), L. Tapmeyer (Frankfurt am Main/DE), K. Skorodumov (Frankfurt am Main/DE), E. Alig (Frankfurt am Main/DE), S. Habermehl (Frankfurt am Main/DE), R. Hühn (Frankfurt am Main/DE), S. Bordignon (Turin/IT), A. Galli (Turin/IT), C. Nervi (Turin/IT), M. R. Chierotti (Turin/IT)

Leuko-pterine, $C_6H_5N_5O_3$, is a natural product, which occurs in butterflies. Its X-ray powder pattern consists of ~16 peaks and several broad humps. Indexing led to different unit cells with various space groups. All attempts at structure determination by the usual direct-space approach failed. Hence, we tried to solve the crystal structure by a global fit to the powder pattern using our FIDEL ("Fit with deviating lattice parameters") method [1]. In this approach, a huge number of random structures is generated, with random values for lattice parameters, molecular positions and orientations, in the statistically most frequent space groups ($P2_1/c$, P-1, $P2_1$ etc). These structures are fitted to the experimental powder pattern using cross-correlation functions, followed by an automated Rietveld refinement. However, the correct crystal structure could not be found. Additionally, we tried to solve the structure by a global fit to the pair-distribution function (PDF) [2]. This PDF global fit starts from a large number of random structures, which are compared to the PDF using cross-correlation functions [3,4], followed by a fit of all promising structures to the PDF data by TOPAS-6 [5]. This approach also failed. Finally, we obtained a tiny single crystal, which allowed a coarse crystal structure determination, which revealed why both global fits failed: leuko-pterin crystallises in the rare space group $P2/c$, which was not included in the global fits. The crystal structure was confirmed by Rietveld refinement, DFT-D, and multinuclear solid-state NMR investigations.

(1) S. Habermehl, C. Schlesinger, M.U. Schmidt, *Acta Cryst.*, **2022**, *B78*, 195–213.
(2) C. Schlesinger, S. Habermehl, D. Prill, *J. Appl. Cryst.* **2021**, *54*, 776–786.
(3) S. Habermehl, C. Schlesinger, D. Prill, *J. Appl. Cryst.* **2021**, *54*, 612–623.
(4) S. Habermehl, C. Schlesinger, M.U. Schmidt, D. Prill, *German Patent Application DE 10 2020 004 292 A1* (2022).
(5) A.A. Coelho, *J. Appl. Cryst.* **2018**, *51*, 210–218.

OP-002

High-quality X-ray powder diffraction data for structure determination

M. Grzywa (Neu-Isenburg/DE)

The determination of the crystal structure is a key element in the characterisation of any new compound and the first step towards tailoring its properties. In most cases, crystal structures are solved using monocrystalline methods. However, not all compounds crystallise in the form of monocrystals of sufficient size and quality. An alternative is to use the powder diffraction methods.

For powder diffraction a very important point in structural analysis is the acquisition of high-quality diffraction data. High-quality data is obtained by using Rigaku instruments equipped with a rotating anode, Johansson monochromator and high-end detectors.

In this presentation, examples of data collected with the SmarLab XE diffractometer will be shown, and examples of structural analysis in SmartLab Studio II will be demonstrated, including steps such as indexing, space group determination, crystal model search and Rietveld refinement.

OP-003

The link between structure and properties for future targeted design of Luminescent complexes

L. C. Folkers (Darmstadt/DE), C. Feldmann (Karlsruhe/DE)

Luminescence originating from the center-coordinated metal in a crown ether complex has rarely been studied, yet a recent investigation found high quantum yields in two Mn^{2+}/18-crown-6 compounds [1]. These findings sparked a more systematic study of such complexes to foster future rational design of luminescent materials.

MnI_2(15-crown-5) (**1**), $MnCl_2$(15-crown-5) (**2**), $[Mn(12\text{-crown-}4)_2]_2[N(Tf)_2]_2$(12-crown-4) (**3**), Sn_3I_6(15-crown-5)$_2$ (**4**) and SnI_2(18-crown-6) (**5**) were prepared by crystallization from ionic liquids (**ILs**) [2]. Larger crystals were measured on a STOE IPDS II diffractometer with a Mo source, while smaller ones were measured on a STOE STADIVARI with an Excillum MetalJet (Ga Kα) and a Dectris EIGER 4M detector.

Syntheses in **ILs** are ideal to prevent the coordination of high energy vibronic ligands, while the spacious crown ethers inhibit concentration quenching. The crystal structures of (**1**) and (**2**) show the so far unseen Mn^{2+}/15-crown-5/I^- coordination and (**3**) and (**4**) even form sandwich complexes, indicating that the size match of M^{2+}/crown ether determines the structural arrangement. Moreover (**5**) shows visible emission, which has not yet been reported for Sn^{2+}/crown ether systems.

Finally, five points matter for the design of luminescent complexes: Structurally, heavier halogens bind more rigidly to the metal than light halogens, a good size match makes the metal – ether bonds more rigid and large ligands (like crown ethers) are preferred to minimize concentration quenching. Furthermore, ligands with high-energy vibronic states should be avoided and d-orbital coupling is preferred over s/p-orbital coupling.

(1) M. Merzlyakova, et al., *J. Am. Chem. Soc.*, **2021**, *143*, 798−804.
(2) M. A. Bonnin, et al., *Inorg. Chem.*, **2021**, *60*, 14645-14654.

OP-004

Irradiation by X-Rays heals and kills the crystal of giant supramolecule

E. Peresypkina (Regensburg/DE), B. Stöger (Vienna/AT), A. Virovets (Frankfurt am Main/DE)

The radiation damage of a single crystal during the X-ray diffraction experiment is an experimental hindrance that seriously reduces data quality. However, during the diffraction studies of an organometallic giant peanut-like supramolecule $[\{Cp''Ta(CO)_2(\eta^4\text{-}P_4)\}_{10}\{CuI\}_{14}]$ (**1**) (Ø 2.8 nm) was found to meet a rather rare exception [1-3]. During the exposure the diffraction pattern was gradually becoming less populated without loss of high-angle data while the crystal color changed from orange to dark brown. Further experiments from various crystals at varied conditions revealed that the diffraction pattern from the irradiated crystal can be indexed in the monoclinic *C*-centered unit cell that is about two times smaller than the initially found one, with new Bravais vectors of $\mathbf{a}' = -\mathbf{a}$, $\mathbf{b}' = -\mathbf{b}$, $\mathbf{c}' = 1/2(\mathbf{a} + \mathbf{c})$. Moreover, in the irradiated crystal the supramolecule lies in the special position $2/m$ of $C2/m$ space group, while originally it was positionally disordered over two positions at a 0.86/0.14 ratio, lying on the 2-fold axis of $C2/c$ group. Thus, counterintuitively the structure becomes more symmetric before the eventual loss of crystallinity.

These observations can be explained in terms of the order-disorder (OD) theory. The supramolecules form layers (001) with idealized $c12/m1$ symmetry. Before the irradiation, the crystal suffers from stacking faults caused by layer misfit, which manifests itself in the positional disorder. The corresponding "stripes" of the diffuse scattering can be found on the reciprocal space reconstruction. Irradiation results in the mutual shift of the planes towards each other. Finally, the $c12/m1$ layer symmetry finds its place in the $C2/m$ space group and positional disorder disappears.

E.P. is grateful for a Postdoc research scholarship for Female Early Career Researchers within the framework of the Free State of Bavaria"s "Program to Realize Equal Opportunities for Women in Research and Teaching" at the University of Regensburg.

(1) E. Peresypkina, A. V. Virovets, M. Scheer. (2021) *Coord. Chem. Rev.* **446**: 213995.
(2) F. Dielmann, E. V. Peresypkina, B. Kraemer, et al (2016) *Angew. Chem. Int. Ed*. **55**, 14833.
(3) E. Peresypkina, B. Stöger, A. V. Virovets, (2022) CrystEngComm **24**, 7118.

Fig. 1

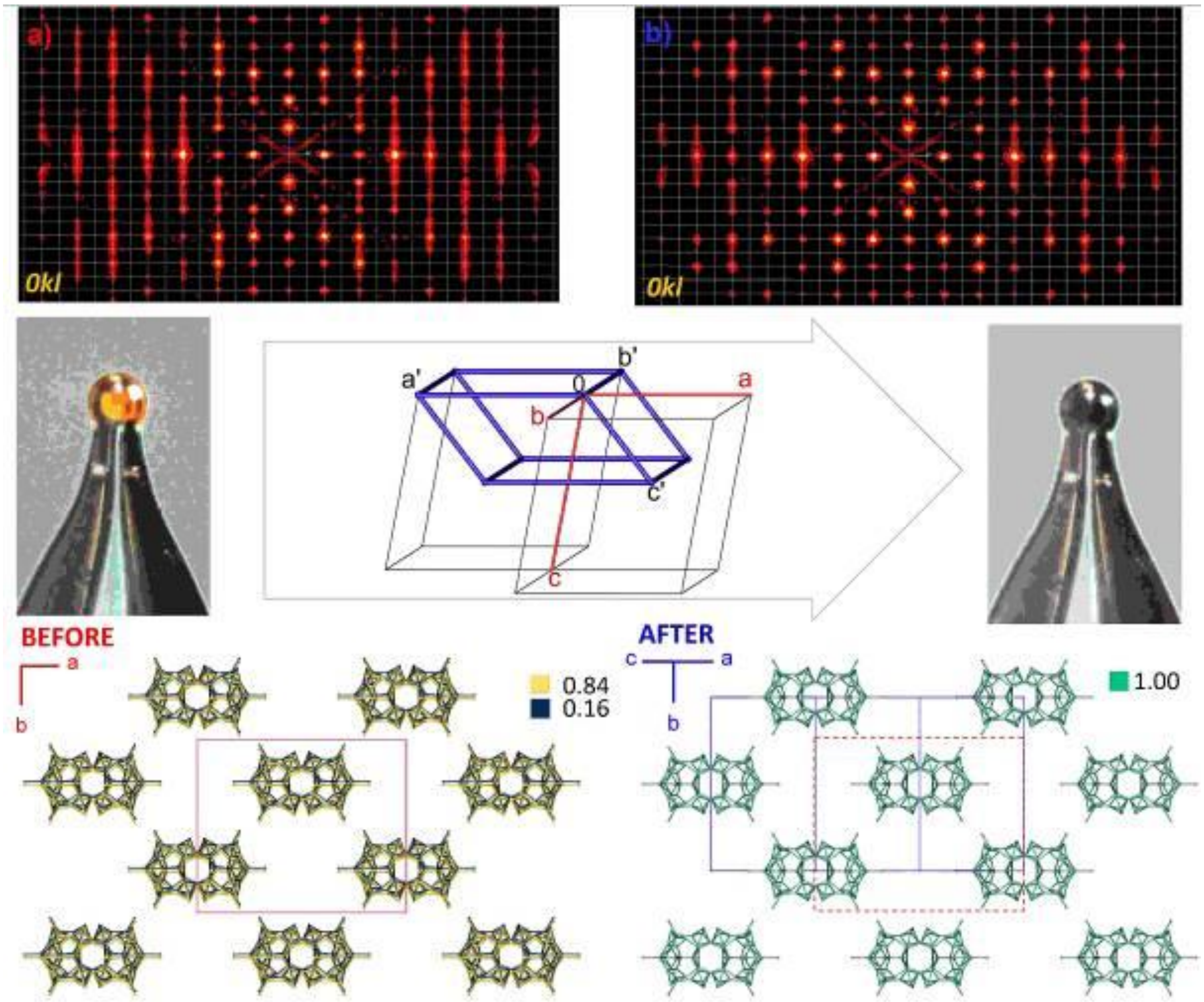

OP-005

Heterobimetallic Coordination Polymers with Dithiocarbamatocarboxylate (DTCC) Ligands

P. Liebing (Jena/DE)

Dithiocarbamate-functionalized carboxylates (DTCCs) can potentially coordinate to a hard (oxophilic) metal and to a soft (thiophilic) metal simultaneously (Figure 1, a). They are therefore attractive for the construction of heterobimetallic coordination polymers, potentially able to form highly porous three-dimensional structures (MOFs). The CSS^- group is selectively complexed by late transition metals such as platinum,[1] and the resulting carboxylate metalloligands are accessible to complex formation with e.g. zinc.[1,2] The resulting products are thermally stable up to 240–400 °C and exhibit different one-, two-, or three-dimensional polymeric structures in the solid state (Figure 1, b)

Figure 1: a) General structure of DTCC ligands and their potential ability to coordinate hard and soft metal centers selectively, b) The porous layer structure of $Zn_2[Pt\{SSCN(CH_2COO)_2\}_2] \cdot 14\ H_2O$ in the crystal (non-coordinated crystal water omitted for clarity).

References:

(1) P. Liebing, J. Witzorke, F. Oehler, M. Schmeide, *Inorg. Chem.* **2020**, *59*, 2825–2832.
(2) P. Liebing, F. Oehler, J. Witzorke, M. Schmeide, *Cryst. Eng. Comm.* **2020**, *22*, 7838–7846.

Fig. 1

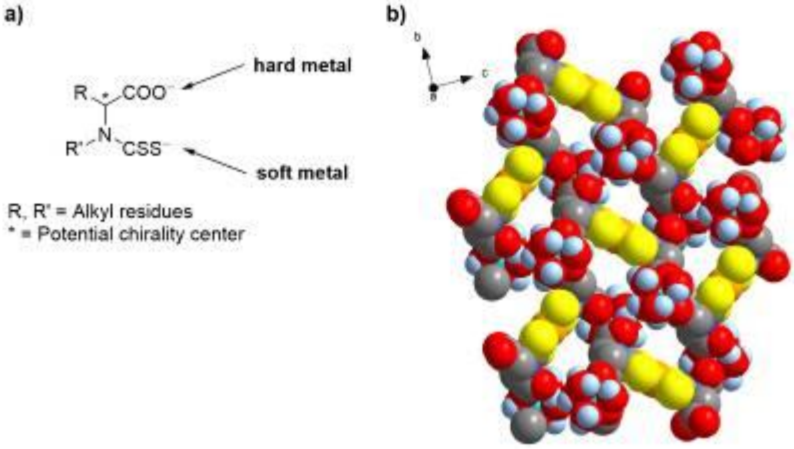

OP-006

How can robots help to crystallize small molecules?

B. Spingler (Zurich/CH)

In past years, our group has reported about "classical" crystallization of molecular compounds.[1, 2] The term "classical" is used for manual, individual setup of every single crystallization experiment. Subsequently, we have applied the commonly used robotic approach for the growth of protein crystals [3] to the single crystal growth of small molecules. We developed a novel anion screen for this purpose, which allowed the crystallization of organic cations [4, 5] and metal complexes [6, 7].

During the presentation, we will discuss the advantages and disadvantages of our novel method.

Acknowledgements:

We thank the University of Zurich and the Swiss National Science Foundation for financial support.

References:

(1) B. Spingler, S. Schnidrig, T. Todorova, F. Wild, *CrystEngComm* 2012, *14*, 751.
(2) P. P. Nievergelt, B. Spingler, *CrystEngComm* 2017, *19*, 142.
(3) P. Shaw Stewart, J. Mueller-Dieckmann, *Acta Cryst.* 2014, *F70,* 686.
(4) P. P. Nievergelt, M. Babor, J. Čejka, B. Spingler, *Chem. Sci.* 2018, *9*, 3716.
(5) M. Babor, P. P. Nievergelt, J. Čejka, V. Zvoníček, B. Spingler, *IUCrJ* 2019, *6*, 145.
(6) R. Bolliger, A. Frei, H. Braband, G. Meola, B. Spingler, R. Alberto, *Chem. Eur. J.* 2019, *25*, 7101.
(7) R. Alvarez, P. P. Nievergelt, E. Slyshkina, P. Müller, R. Alberto, B. Spingler, *Dalton Trans.* 2020, *49*, 9632.

Fig. 1

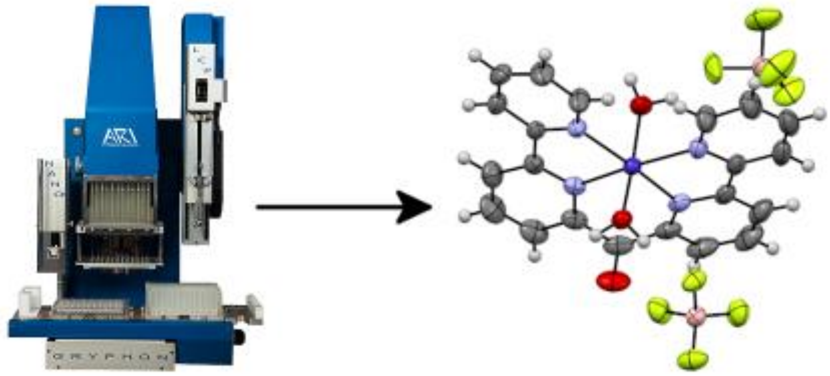

Microsymposium 2 | Crystallography in Materials Sciences I

OP-007

From stannite- to wurtz-stannite-type structure in the $Cu_2Mn(Ge_xSn_{1-x})S_4$ solid solution

D. Matzdorff (Berlin/DE, Berlin/DE), M. Avdeev (Sydney/AU), G. Gurieva (Berlin/DE), S. Schorr (Berlin/DE, Berlin/DE)

The research of quaternary Cu-based chalcogenide semiconductors has caught a large interest for photovoltaic applications, as these materials consist of non-toxic and earth abundant elements. While being environmentally friendly and low cost, materials like Cu_2MnGeS_4 or Cu_2MnSnS_4 are very promising candidates for use in tandem solar cells, because they can cover a wide bandgap range of 1.52-1.72 eV [1, 2]. This study presents new insight into the crystal structure of the solid solution $Cu_2Mn(Ge_xSn_{1-x})S_4$ via neutron powder diffraction.

$Cu_2Mn(Ge_xSn_{1-x})S_4$ mixed crystals presented in this study were synthesized by solid state reaction of pure elements in evacuated silica tubes at temperatures of 800 °C. The chemical composition and homogeneity of the synthesized polycrystalline powder materials were investigated by WDX spectroscopy using an electron microprobe system. LeBail refinement of powder X-ray diffraction data was used to determine the lattice parameters of the mixed crystals.

Since Cu^+ and Ge^{4+} are isoelectronic cations and Mn^{2+} is electronic similar to Cu^+ and Ge_{4+}, they cannot be differentiated in a structural analysis based on X-ray powder diffraction data alone. However, their neutron scattering lengths are different, that is why we apply neutron diffraction to analyze the crystal structure of $Cu_2Mn(Ge_xSn_{1-x})S_4$ mixed crystals.

The crystal structure and the cation distribution in the unit cell were determined on the basis of the neutron diffraction data and their evaluation applying the average neutron scattering length analysis method [3]. in this way it was possible to conclude on the crystal structure and structural disorder. The end members of the solid solution series crystallize in different structures: Cu_2MnSnS_4 adopts the stannite type structure (space group *I-42m*) whereas Cu_2MnGeS_4 adopts the wurtz-stannite structure (space group *Pmn21*).

These investigations enabled us to deduce the complex process within the crystal structure transfers from the stannite- to the wurtz-stannite-type structure in dependence on the chemical composition of the $Cu_2Mn(Ge_xSn_{1-x})S_4$ mixed crystals. It will be shown that Sn-rich mixed crystals ($0 \leq x \leq 0.29$) adopt the stannite type structure, whereas Ge-rich mixed crystals ($0.68 \leq x \leq 1$) of this series adopt the wurtz-stannite type structure. Within $0.29 > x > 0.68$ two chemically identical but structurally different quaternary phases coexist, adopting the tetragonal and the orthorhombic structures respectively.

Additionally, the band gap energy of the mixed crystals was determined by UV-Vis spectroscopy showing the correlation between crystal structure and this important optoelectronic material property.

References:

(1) Rudisch et al. (2019) *Physica Status Solidi (b)*, 256(7), 1800743
(2) Beraich et al. (2020) *Journal of Alloys and Compounds*, 845, 156216
(3) Schorr, S. (2011) *Solar Energy Materials and Solar Cells*, *95*, 1482

OP-008

Systematic study of mechanochemically synthesized perovskite materials

T. Rathmann (Mülheim an der Ruhr/DE), S. U. Arisan (Mülheim an der Ruhr/DE), H. Petersen (Mülheim an der Ruhr/DE), M. Etter (Hamburg/DE), C. Weidenthaler (Mülheim an der Ruhr/DE)

Materials with perovskite structure are of interest for a wide range of applications for example gas sensors, mixed ionic-electronic conductive (MIEC) membranes, or catalysts for exhaust gas treatment and electrochemical devices [1,2]. Synthesizing these materials via mechanochemistry, which provides the energy input directly by mechanical means, is in the focus of research since the turn of the millennium [2]. Typically, high-energy ball milling (HEBM) is the mechanical method of choice [2].

For a good performance of the perovskites in the targeted applications, nanocrystalline materials with high specific surface areas are necessary [2,3]. Usually, perovskites from HEBM synthesis are nanosized, but with comparably low surface areas [2,3]. So far, attempts like wet grinding or leaching methods have resulted in either non-competitive products or high energy and disposal costs [2,3]. Thus, further optimization of the HEBM synthesis is required. In this work, we present a systematic investigation of how several adaptations to the HEBM synthesis affect product properties and synthesis progress. $LaAlO_3$ and $LaCoO_3$ serve as example perovskites and powder X-ray diffraction (PXRD) as the primary method for characterization. We will also address the possibilities and challenges of applying *ex situ* and *in situ* characterization. Furthermore, we will present our first results regarding the mechanochemical synthesis of layered La-Co-perovskites.

(1) G. George, S.R. Ede and Z. Luo, Fundamentals of Perovskite Oxides: Synthesis, Structure, Properties and Applications, CRC Press, 273-317 (2021) (ISBN: 978-0-367-55865-9)
(2) P. Granger, V.I. Parvulescu, S.Kaliaguine and W.Prellier (Ed.), Perovskites and Related Mixed Oxides: Concepts and Applications Volume 1, Wiley-VCH, 25-341 (2016) (ISBN: 978-3-527-33763-7)
(3) H. Alamdari, M. Bassir, P. Seegopaul and A. Van Neste, Process for Optimizing the Catalytic Activity of a Perovskite-Based Catalyst, US Patent (2009) (US20090324470A1)

OP-009

NaSICONs: crystal chemistry and properties

M. Avdeev (Lucas Heights/AU)

A very large number of compositions $A_xM_2(TO_4)_3$ crystallize in the NaSICON crystal structure type built of corner-sharing octahedra [MO_6] and tetrahedra [TO_4]. The voids in the framework can be either empty or filled with A cations (Figure 1). Such topology enables very rich crystal chemistry and remarkable flexibility, similar to that of the perovskite family. The NaSICON structure accommodates hundreds of M and T cation combinations, which leads to a wide range of physical properties. As a result, NaSICON-type materials find applications in very different areas, from nuclear waste immobilization to A-conducting solid electrolytes. Depending on composition and temperature, many NaSICONs also undergo displacive and order-disorder phase transitions.

The previous attempts to rationalize crystal chemistry of the NaSICON structure type had limited success, since the structure has eight internal degrees of freedom and thus no simple "tolerance factor" could be established. In this talk, I will demonstrate that the R-3c structure with undistorted [MO6] octahedra and [TO4] tetrahedra can be used as a common reference point for any NaSICON-type material. More than 300 NaSICON-type oxides present in the Inorganic Crystal Structure Database were quantitatively analysed and it is shown that distortion from the ideal structure is primarily driven by the size mismatch between the A cations and $M_2(TO_4)_3$ framework. The establieshed relationships can be used to optimize the geometry of the structure to control properties, such as A-ionic conductivity or thermal expansion.

Fig. 1

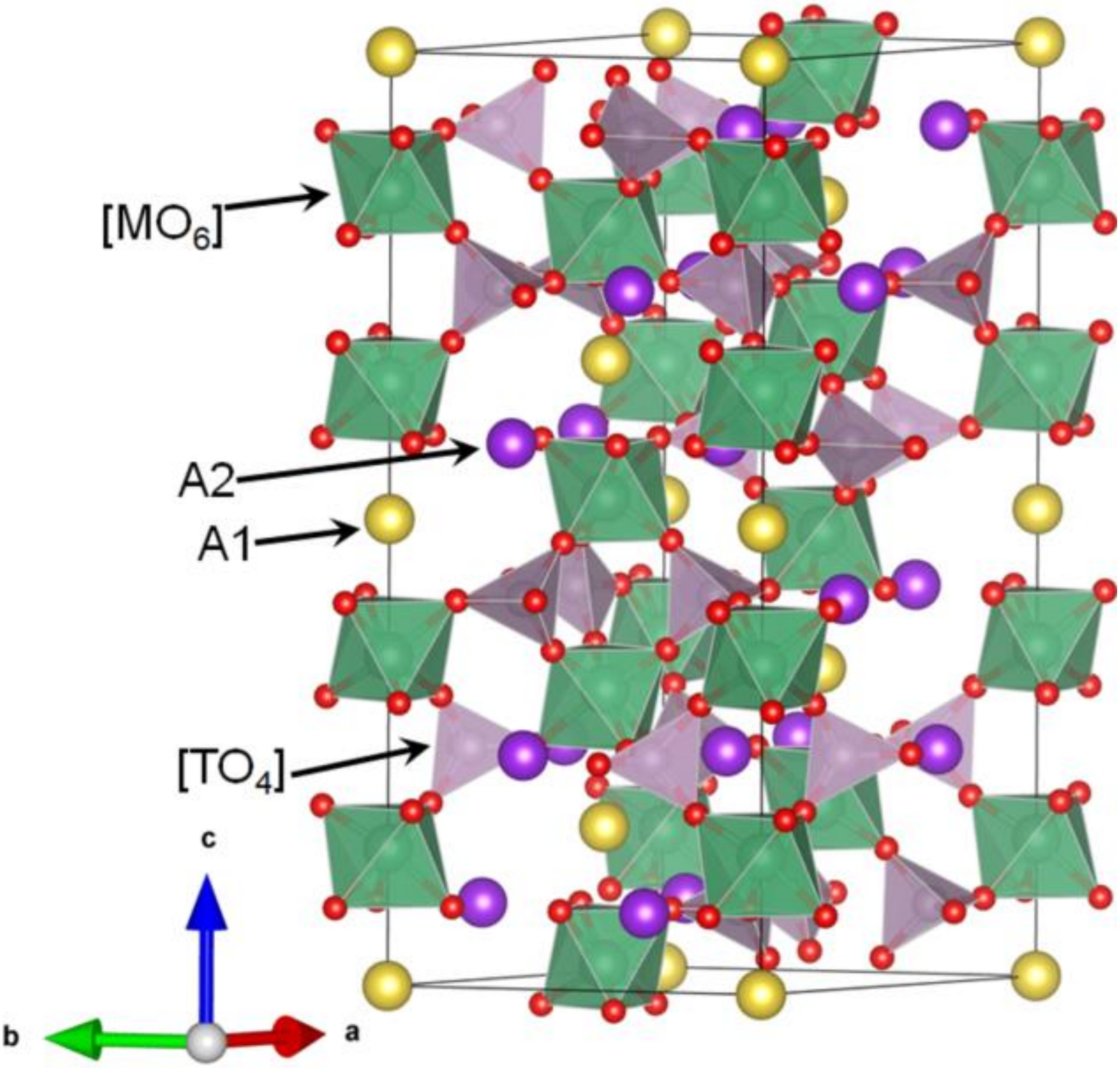

OP-010

Does the Solvent Matter? – Influence of the solvent in hybrid halide perovskites precursor solution

A. Palacios Saura (Berlin/DE), J. Breternitz (Berlin/DE), A. Hoell (Berlin/DE), S. Schorr (Berlin/DE)

Hybrid halide perovskites (HHPs) are highly promising photovoltaic absorbers not only for using low-cost solution-based processing methods but also for the outstanding increase in power conversion efficiency of solar cells up to 25.5% in 2021[1].

Despite the popularity of HHPs, the growth mechanism of HHP crystals in solution is still unknown. With this study, we aim to bring more clarity about the precursor arrangement in solution prior to crystallization and how the solvent affects the atomic arrangement in this early state. For this purpose, we applied small angle synchrotron X-ray scattering (SAXS) to investigate precursor solutions of different HHPs ($MAPbI_3$, $MAPbBr_3$, $MaPbCl_3$, $MAPb(I,Br)_3$ and $FAPbI_3$) in different common solvents used to synthesize HHPs layers, such as γ-butyrolactone (GBL), dimethylformamide (DMF), dimethyl sulfoxide (DMSO) and mixtures thereof. We systematically investigated the influence of the A-cation in the precursor solution using full inorganic formulations based on varying alkaline metal cations as well as the pure precursors in their pristine solutions.

SAXS is a non-destructive characterization technique based on the difference between elastic scattering objects in a solution. With SAXS, it is possible to investigate the size and shape of scattering objects ranging between 1 – 100 nm, determining also the distance between adjacent scattering objects and their interaction with each other[2,3]. We performed SAXS experiments at the HZB synchrotron radiation source BESSYII, at the four-crystal monochromator beamline of the Physikalisch-Technische Bundesanstalt[4] using the ASAXS endstation[5]. Samples have been prepared by dissolving binary precursors (e. g. MAI and PbI_2 to synthesize $MAPbI_3$) in a solvent. The solutions with a concentration of 0.8 M were measured by SAXS 60 minutes after their preparation.

Our measurements show a clear maximum in the scattered intensity at q-values of $\approx 3\ nm^{-1}$, except for $MAPbCl_3$ in DMF:DMSO 1:1, which did not show any peak. The maximum holds two essential pieces of information: it demonstrates the agglomeration of scattering objects and the peak position corresponds to the most abundant distance of scattering objects in a range of 2-3 nm. While all solutions show agglomerations, we were able to demonstrate that the size of those agglomerates changes with the composition of HHP precursors, but also with the solvent. Based on this information, we have developed a core-shell model with $[PbX_6]$ octahedra (X = Cl, Br, I) in the core surrounded by solvent molecules to describe the scattering objects. The size of the solvent molecules as well as the radii of Pb and halides forming $[PbX_6]$ octahedra were derived from a combination of experimental values from diffraction and computationally obtained electron density distributions. We can explain the solvent dependent variation of the experimentally determined distance between the scattering objects by a core size variation realized by a combination of isolated octahedra or corner-sharing octahedra as core, respectively. Since the solvent molecules can be described as an ellipsoid, their orientation must be taken into account. We can explain the variations of the minimal possible distance between the scattering objects (R_{HS}), evaluated from the structure factor determined by analyzing the SAXS data (using SASfit) by a preferred orientation of the solvent molecules in the solvent shell of the scattering objects. Therefore, the choice of the solvent may not only depend on the precursor solubility but also on their chemical and physical behavior.

We will discuss the influences of precursor composition and solvent on the core as well as the solvent shell of the scattering objects, since they have the potential to influence the crystallization process of the HHP and therefore the performance of a device produced from solution processing.

(1) Min et al., Nature, 2021, 598, 444
(2) Schnablegger et al., Anton Paar GmbH, 2013
(3) Flatken et al., J. Mater. Chem. A, 2021, 9, 13477
(4) Krumrey et al., Nucl. Instrum. Methods Phys. Res., Sect. A, 2001, 467, 1175
(5) Hoell et al., DE102006029449, 2007

Figure 1: SAXS pattern of $MAPbI_3$ (black points) and fit (red line) performed with SASfit based on a spherical agglomerate model.

Fig. 1

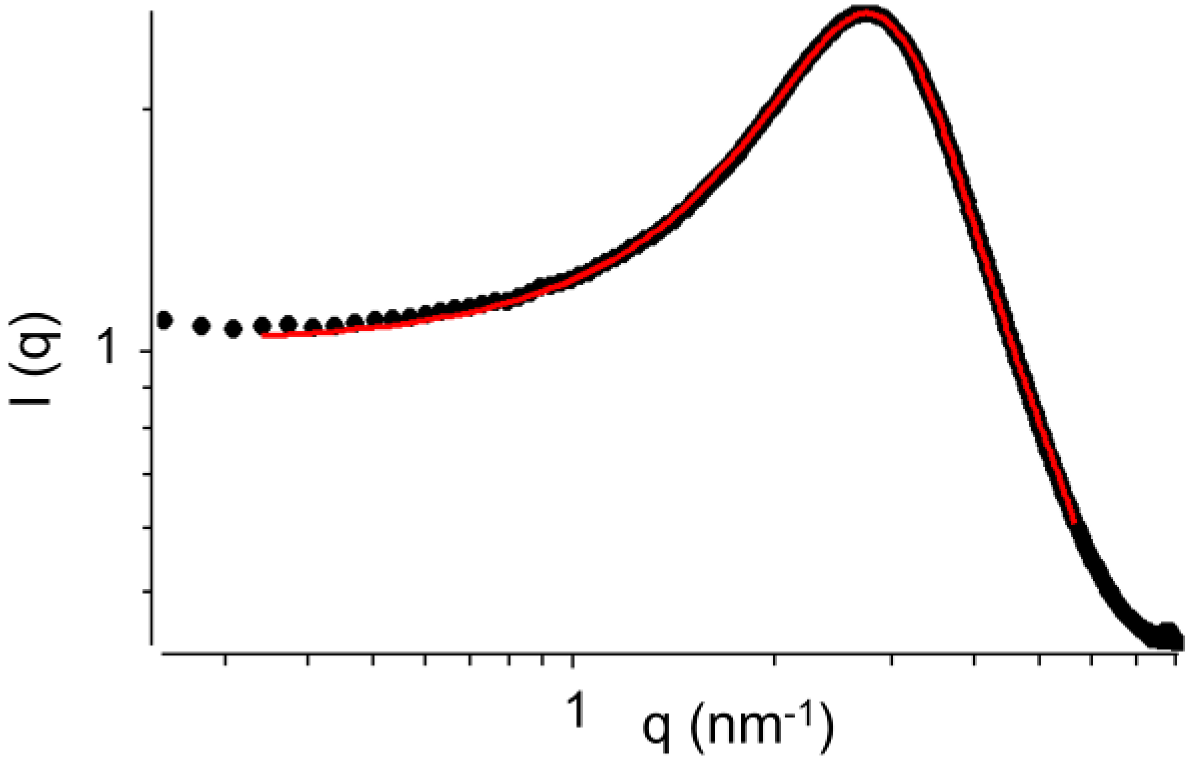

OP-011

Synergic effects of various transition metal cations in cubic anti-perovskites: Structural and electrochemical aspects

M. Gorbunov (Dresden/DE), D. Mikhailova (Dresden/DE)

Nowadays, much efforts are devoted to studies of alternative systems for Li-ion batteries, which still dominate the market of energy storage for portative electronics. One of the research approaches is development of industry-related materials like Li(Ni,Mn,Co)O_2. The other one represents fundamental studies of novel systems, not necessarily applicable in real batteries, but with a rich chemistry, to understand the general trends in structural behavior and charge compensation mechanisms. Such studies are important because the obtained knowledge may be transferred to similar systems, more suitable battery applications.

Cubic anti-perovskites with a general formula of Li_2MSeO (M - Fe, Co, Mn) are perfect model compounds for mentioned fundamental studies due to their electrochemical activity on both cationic and anionic sites combined with a high chemical flexibility of the structure. In this structure, lithium and a transition metal are sharing the same cationic site, and chalcogenides occupy two separate anionic positions (Fig. 1). The materials show drastic difference in electrochemical performance (Fig. 2) and anionic redox activity, depending on their cationic composition. We investigated six compounds using *operando* XRD and XAS methods, perfectly complementing each other, and have proved the possibility to tune the anionic redox activity in Li_2MSeO, the key to which lays in the nature of the M-Se bond, and the preferability of single-phase lithium extraction mechanism in terms of electrochemical kinetics and structural stability.The present study is a continuation of our research works dedicated to sulfur-based anti-perovskites [1-4], and is a part of one of the author's dissertation.

(1) D. Mikhailova, et. al., *ACS Appl. Energy Mater.* 2018, 1, 11, 6593–6599.
(2) Gorbunov, M., et. al., *Inorg. Chem*. 59, 15626–15635.
(3) Gorbunov, M. V., et. al., *Front. En. Res*. 9:657962.
(4) M. A. A. Mohamed, et. al., *J. Mater. Chem. A*, 2021, 9, 23095.

Fig. 1

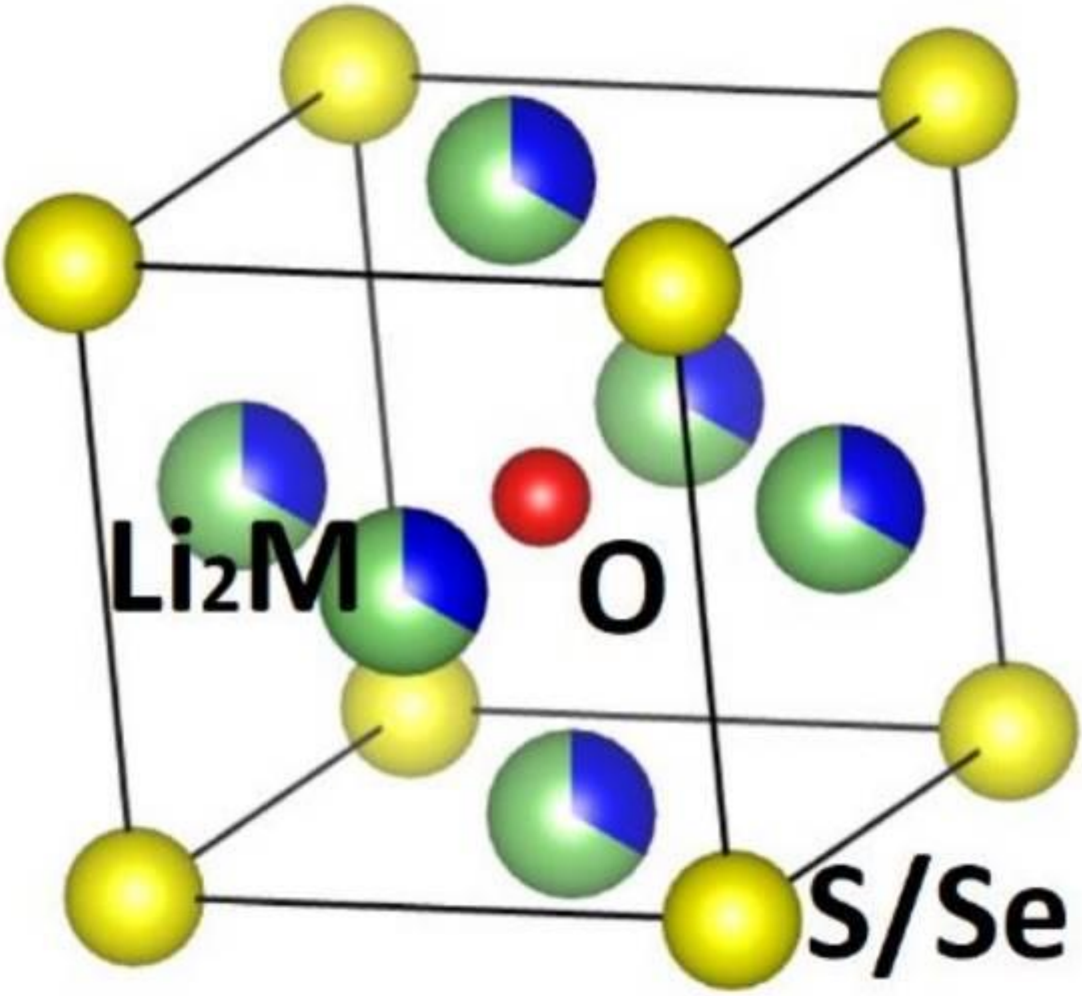

Fig. 2

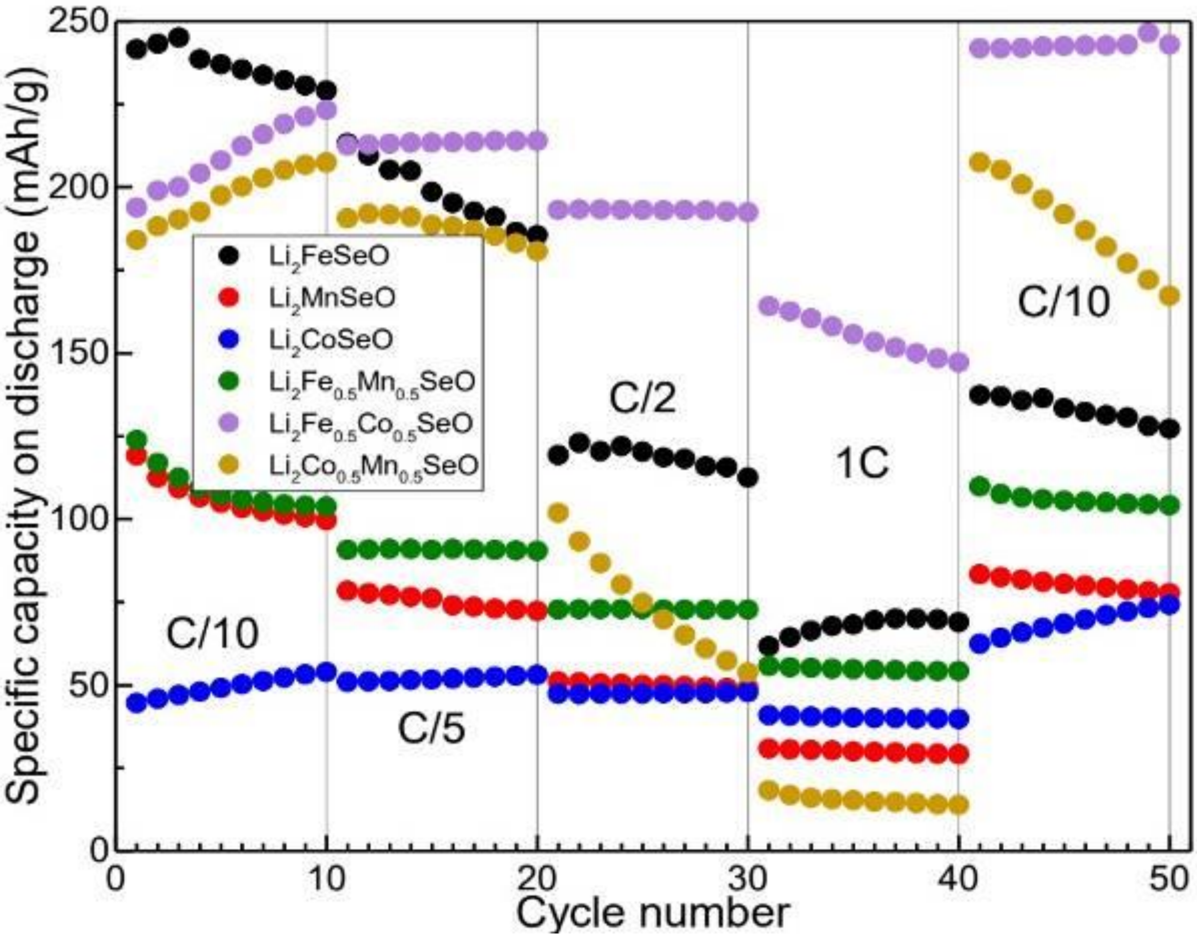
Specific capacity on discharge (mAh/g)
250
200
150
100
50
0
0
10
20
30
40
50
Cycle number
● Li_2FeSeO
● Li_2MnSeO
● Li_2CoSeO
● $Li_2Fe_{0.5}Mn_{0.5}SeO$
● $Li_2Fe_{0.5}Co_{0.5}SeO$
● $Li_2Co_{0.5}Mn_{0.5}SeO$
C/10
C/5
C/2
1C
C/10

OP-012

Structural changes in lanthanide bearing monazite under swift heavy ion irradiation

J. Marquardt (Frankfurt am Main/DE), T. Lender (Aachen/DE), L. Bayarjargal (Frankfurt am Main/DE), E. Haussühl (Frankfurt am Main/DE), C. Trautmann (Darmstadt/DE), L. Peters (Aachen/DE), B. Winkler (Frankfurt am Main/DE)

The safe disposal of nuclear waste is one of the intergenerational issues which needs to be solved. A potential route to effectively immobilize radionuclides could be realized by their incorporation into crystalline solid phases in future radioactive waste repositories. In particular, the immobilization of specific waste streams containing minor actinides (Np, Am, Cm) or Pu in crystalline solid phases may be advantageous compared to glass matrices, which may be less resistant to leaching and disintegration [1-3]. Due to their radiation stability and chemical and structural flexibility, monazite-type compounds are considered suitable matrix materials [4]. To better understand structural changes due to radiation damage, synthetic monazite single crystals with different chemical compositions (La, Nd, Pm, Sm)PO4 were irradiated at the UNILAC beamline of GSI Helmholtzzentrum Darmstadt using 1.7 GeV Au ions and fluences of up to 1e13 ions/cm2. The irradiated single crystals were characterized by Raman spectroscopy, secondary electron microscopy and single crystal X-ray diffraction. The irradiation of monazite with 1.7 GeV Au ions results in an embrittlement of the crystals and the formation of a glassy surface layer of about ~48 µm thickness, which correlates well with the projected range of ~44 µm according to SRIM-2013 calculations [5]. The irradiation results in a significant broadening of the Raman modes and further changes in the lattice dynamics. X-ray diffraction experiments revealed the amorphization of the surface layer.

(1) Donald et al. (1997) J. Mater. Sci. 32;
(2) Ewing (1999) PNAS, 96;
(3) Lumpkin et al. (2006) Elements, 2;
(4) Schlenz et al. (2013) Z. Kristallogr. Cryst. Mater. 228;
(5) Ziegler et al. (2010) Nucl. Instrum. Methods Phys. Res. B 268

J.M & B.W. acknowledge the German Federal Ministry of Education and Research (BMBF) for financial support in the project No. 02NUK060E. T.L. & L.P. acknowledge support by BMBF under project number 02NUK060B.

Microsymposium 3 | Crystal physics

OP-013

Symmetry protected 1D chains in mixed-valence iron oxides

D. Vasiukov (Lund/SE), G. Khanal (Piscataway, NJ/US), I. Kupenko (Münster/DE), G. Aprilis (Grenoble/FR), X. Li (Münster/DE), S. Ovsyannikov (Bayreuth/DE), S. Chariton (Bayreuth/DE), V. Cerantola (Grenoble/FR), V. Potapkin (Bayreuth/DE), A. Chumakov (Grenoble/FR), L. Dubrovinsky (Bayreuth/DE), K. Haule (Piscataway, NJ/US), E. Blackburn (Lund/SE)

Iron oxides are normally Mott insulators with the only notable exception of magnetite (Fe_3O_4), which has good electrical conductivity due to the itinerant mixed-valence state of iron. During the last decade of high-pressure research a whole new series of iron oxides with the same quality was discovered, like Fe_4O_5, Fe_5O_6, Fe_7O_9 etc. [1], featuring closely related structures with arrays of one-dimensional (1D) chains of trigonal prisms embedded between slabs of octahedra. Here, we present a unified approach to the series based on a specific crystallographic generation mechanism (Fig. 1) which predicts the structures of these oxides and naturally classifies them in terms of the slab cycle. When including magnetic interactions, we show that the 1D chains have a symmetry protection against magnetic perturbations from the iron ions in the slabs, and that the slab size determines the type of magnetic order, which is either ferromagnetic or antiferromagnetic. Dynamical mean-field theory calculations reveal the orbitally selective Mott state of the Fe ions and tendency of conductivity to low-dimensional behavior with particular enhancement along the 1D chains. Across the series, the decoupling of the chains increases, and so with the inherent charge ordering of the slabs, these structures have the potential to allow experimental realization of the model system of coupled 1D wires [2]. We point out the possibility to stabilize these compounds in the thin-film form that, together with a wide range of possible ionic substitutions and fact that these compounds are recoverable at ambient pressure, makes them a very promising platform to engineer physical systems with interesting magnetotransport phenomena, as corroborated by the recent discovery of quantum Hall effect in $ZrTe_5$ [3].

Figure 1: The {311} tropochemical cell-twinning in the homologous series of iron oxides as exemplified by the Fe_4O_5 structure. On the left, the rocksalt type FeO structure is projected along [0-11]. Regularly applying a mirror plane parallel to (311) at the oxygen sheet at $5d_{311}$ intervals, we derive a structure with a new unit cell. Upon this operation, pairs of iron atoms, as outlined by the blue triangle, are brought into proximity across twinning planes. The last step is the coalescence of these pairs into a single iron atom that leads to a new crystallographic site at the twinning plane with a trigonal prismatic oxygen environment, as marked by the blue colour in the Fe_4O_5 structure on the right. These trigonal prisms form infinite 1D chains along the *a* axis in the resultant structure. The slab width *N* can be readily determined using either of two equivalent octahedral chains highlighted by the violet and green cages in the Fe_4O_5 structure.

(1) Bykova, E. et al. Structural complexity of simple Fe_2O_3 at high pressures and temperatures. *Nat. Commun.* 7 (2016).
(2) Teo, J. C. & Kane, C. From Luttinger liquid to non-Abelian quantum Hall states. *Phys. Rev. B* 89, 085101 (2014).
(3) Tang, F. et al. Three-dimensional quantum Hall effect and metal–insulator transition in $ZrTe_5$. Nature 569, 537–541 (2019).

Fig. 1

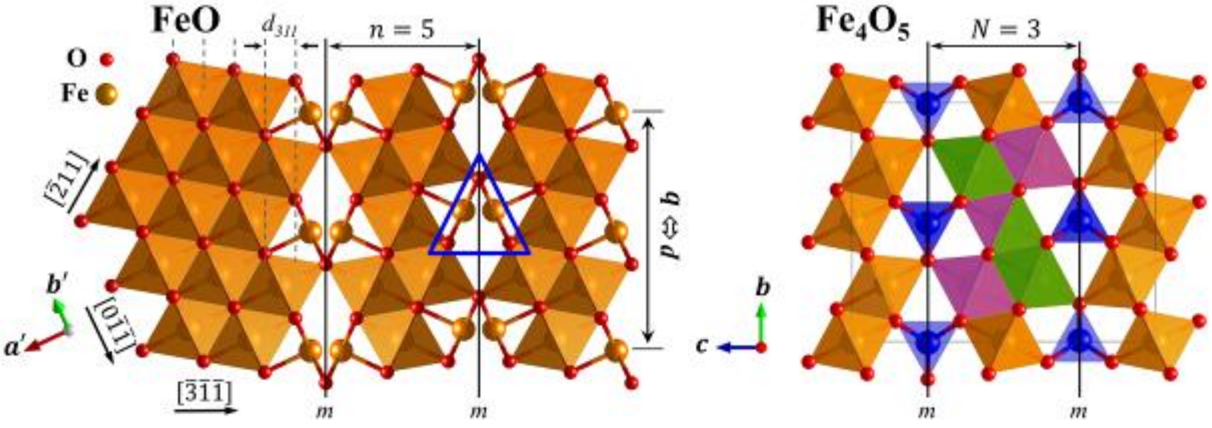
FeO
O
Fe
d_{311}
$n = 5$
$[\bar{2}11]$
b'
a'
$[0\bar{1}\bar{1}]$
$[\bar{3}\bar{1}\bar{1}]$
$p \Leftrightarrow b$
m
m
Fe_4O_5
$N = 3$
b
c
m
m

OP-014

Phase transition and twinning in flexible single crystals of caffeine cocrystal solvate

S. Dey (Aachen/DE), T. Lender (Aachen/DE), C. Paulmann (Hamburg/DE), L. Peters (Aachen/DE)

Discovery of macroscopic elastic flexibility in single crystals of 1:1:1 caffeine, 4-chloro-3-nitrobenzoic acid and methanol (CAF-CNB) about a decade ago[1] sparked off immense interest amongst crystal engineers and material scientists towards design and harnessing of interesting physical and chemical properties coupled with flexibility in molecular crystals.[2 and references therein] However, several contested mechanisms of bending have posed significant hindrance to the advancement of their design from "trial and error" towards rational and predictive strategies.

Although several other crystals of molecular materials have demonstrated elastic flexibility, the system of CAF-CNB remains unique owing to significantly larger unit cell volume [$V_{T\,=\,290\text{ K}}$ = 7491.5(2) Å^3] with significant anisotropy of lattice parameters [a = 33.0350(6) Å, b = 55.3287(9) Å, c = 4.09866(7) Å] compared to other systems. We were successful in synthesizing single crystals of 1:1:1 caffeine, 4-bromo-3-nitrobenzoic acid and methanol (CAF-BNB) that have the same space group symmetry orthorhombic $Fdd2$ with larger but comparable lattice parameters [a = 32.903(2) Å, b = 55.768(1) Å, c = 4.1549(3) Å, V = 7624(1) Å^3]. The crystals were found to possess macroscopic flexibility.

Unlike the CAF-CNB system, where crystal symmetry is preserved at low temperatures, crystals of CAF-BNB undergo reversible phase transition *via* lowering of the space group symmetry to monoclinic (*a*-unique) Fd and significant orthorhombic to monoclinic distortion ($\alpha \sim 90.5°$ at T = 100 K) upon cooling. The symmetry breaking is accompanied by formation of pseudo-merohedral twin domains with twin law described by the high temperature symmetry elements $d \perp \mathbf{b}$ or $2 \parallel \mathbf{c}$. The destruction of the orthorhombic symmetry affects the overall crystal packing with respect to the decoupling of adjacent tapes that act as steric barrier to slippage of molecules aiding in reversible flexibility at ambient conditions. The phase transition has significant implications for the predicted facial bending planes (110)/(1-10) as well as their mechanical properties at low temperatures.

(1) S. Ghosh, C. M. Reddy. Elastic and bendable caffeine cocrystals: Implications for the design of flexible organic crystals. *Angew. Chem. Int. Ed.*, **51**, 10319-10323 (2012).
(2) A. J. Thompson, A. I. C. Orue, A. J. Nair, J. R. Price, J. McMurtrie, J. K. Clegg. *Chem. Soc. Rev.* **50**. 11725-11740 (2021).

S.D. acknowledges fruitful discussion with Prof. C. Malla Reddy and financial support from Alexander von Humboldt Foundation.

OP-015

Li(Nb,Ta)O_3 – phase diagram and Curie temperature of solid solution single crystals

S. Ganschow (Berlin/DE), D. Klimm (Berlin/DE), U. Bashir (Berlin/DE), M. Brützam (Berlin/DE), K. Böttcher (Berlin/DE), F. Bernhardt (Gießen/DE), S. Sanna (Gießen/DE), M. Bickermann (Berlin/DE)

Lithium niobate ($LiNbO_3$, LN) and lithium tantalate ($LiTaO_3$, LT) belong to the most widely used ferroelectric materials, with applications that range from novel electronic and micro-mechanical devices to nonlinear optics. Lithium niobate-tantalate ($LiTa_xNb_{1-x}O_3$, LNT) solid solution single crystals are expected to allow for implementation of unique material"s properties such as tailored birefringence combined with large temperature stability. Knowledge of the relevant phase diagram is a crucial prerequisite for the development of a reproducible crystal growth process. According to current knowledge LN and LT form solid solutions without miscibility gap. A phase diagram calculated based of the assumption of ideal mixing behavior and measured thermophysical data shows, however, a much stronger segregation than was observed in crystal growth experiments. Fig. 1 shows the calculated phase diagram with solid lines. In this figure filled and hollow dots linked by horizontal lines correspond to melt and resulting crystal composition of our growth experiments, respectively.

The objective of this study was to determine the phase diagram of the pseudo-binary system LN—LT by means of differential thermal analysis. To this end, samples prepared from previously grown LNT solid solution single crystals were used. Based on our measurements solution models for both, liquid and solid phases are proposed and a thermodynamically consistent phase diagram was calculated. From measurements of $c_p(T)$ the temperature of the ferro–paraelectric phase transition was determined and a linear dependence of the Curie temperature on composition was ascertained, see Fig. 2 (here the value for pure LN was taken from Carruthers et al. J. Appl. Phys. 42 (1971) 1846).

Implications of the experimental results for important aspects of the crystal growth process, e.g. stability of the interface, possibility of in situ poling, are discussed in greater detail.

Financial support of Deutsche Forschungsgemeinschaft under project number 426703838 in the frame of Research Unit FOR5044 is greatly acknowledged.

Fig. 1

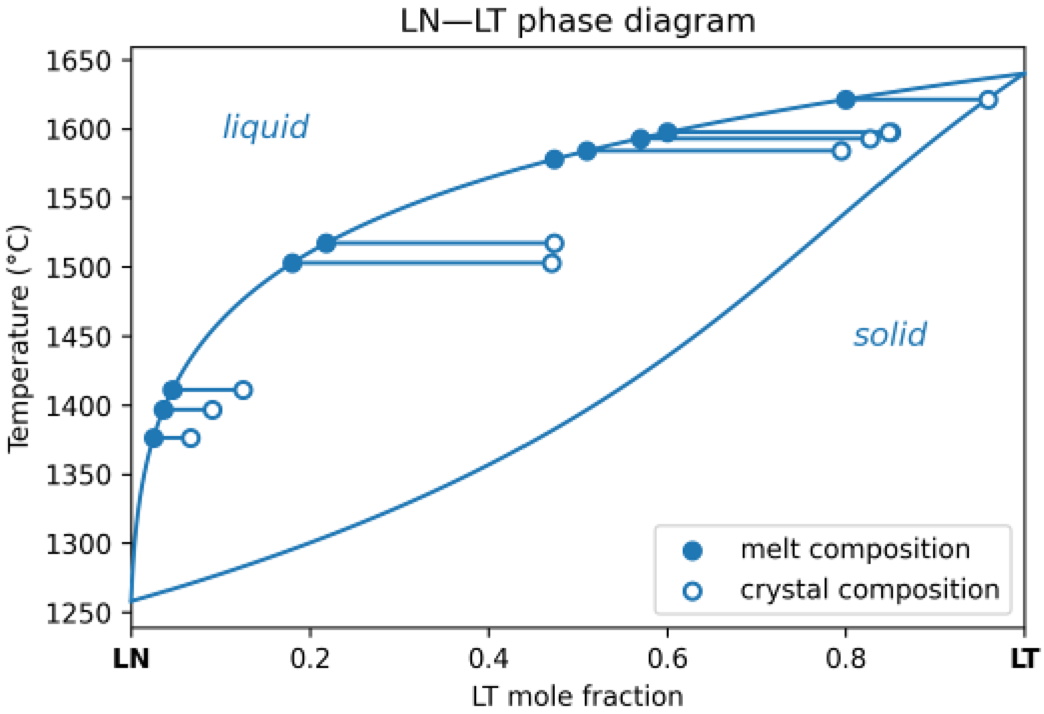

Fig. 2

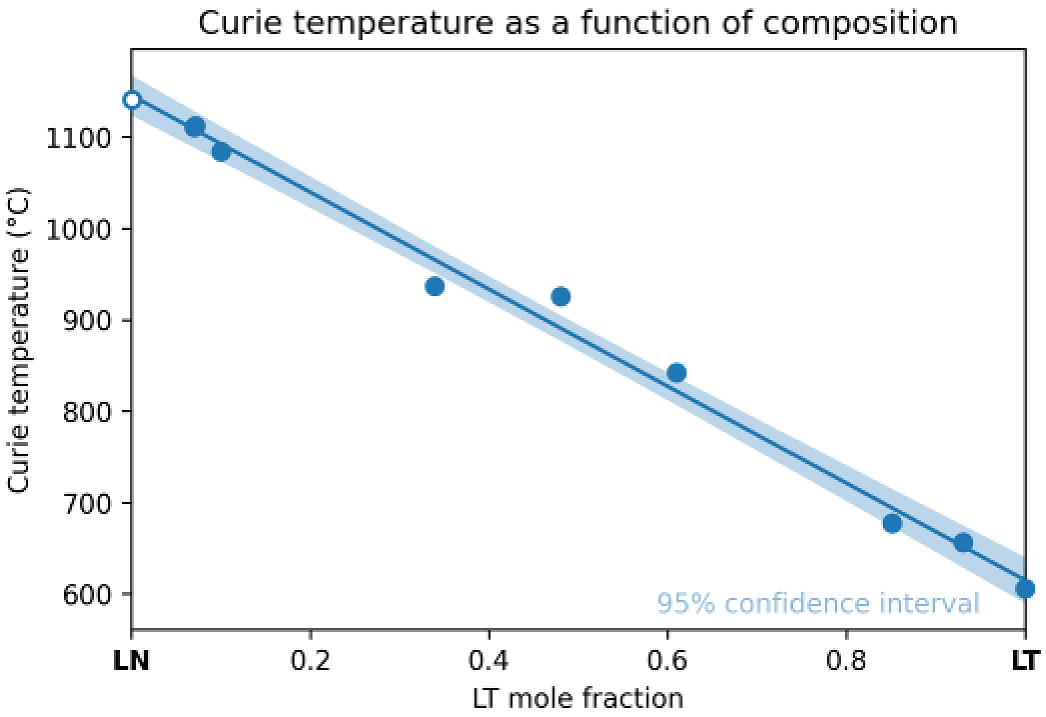
Curie temperature as a function of composition
Curie temperature (°C)
1100
1000
900
800
700
600
LN
0.2
0.4
0.6
0.8
LT
LT mole fraction
95% confidence interval

OP-016

Vibrational circular dichroism of crystals: The interplay of symmetry and chirality

S. Jähnigen (Paris/FR)

Chiroptical spectroscopy provides an increasingly important, cost-effective alternative for the study of chiral substances in the solid state. In recent years, vibrational circular dichroism (VCD) – the chiral form of IR absorption spectroscopy – has come into focus as a very sensitive probe of molecular conformation and environment. It has been applied to a wide range of molecules including natural products, host-guest systems, proteins, nanoparticles, or catalysts, as well as the formation of chiral phases from achiral subunits. VCD differs from electronic circular dichroism in that it relates directly to vibrational transitions in the supramolecular chiral framework, such as functional groups connected by covalent or non-covalent interactions (hydrogen bonds etc.). Therefore, the identification of enantiomorphisms in the crystal structure – at constant IR absorption – is a key feature of solid-state VCD, which can be used to distinguish polymorphic forms.[1,3,4]

Accurate calculations are required to interpret VCD spectra, but unlike conventional IR absorption spectroscopy, they cannot be performed within the Born-Oppenheimer approximation. This is because VCD requires the magnetic response of the electrons bound to the nuclear motion (i.e., the vibrations). Nowadays, these properties are determined using linear quantum response theory and have become a standard feature of many quantum chemical codes.[2] However, the calculation of the VCD of solids has long been considered infeasible due to periodic boundaries imposed by the crystal structure.

In this contribution, we show that it is possible to formulate VCD with an explicit account for periodicity, reconnecting the theoretical model to the (finite) physical system.[1,5] This allows us to distinguish between contributions originating from molecular chirality and from chiral crystal packing. Our calculations of several crystalline systems find that while IR absorption hardly depends on the symmetry of the space group, the situation is different for VCD, where completely new non-local patterns emerge: even for achiral space group, a single proper symmetry operation has a large impact on the VCD spectrum, which reflects the supramolecular chirality of the crystal.[4]

References:

(1) Jähnigen, S. et al. D. Angew. Chem. Int. Ed. 2021, accepted.
(2) Scherrer, A. et al. J. Chem. Phys. 2015 143, 074106
(3) Jähnigen, S. et al. D. Angew. Chem. Int. Ed. 2018 57, 13344-13348.
(4) Jähnigen, S. et al. J. Phys. Chem. Lett. 2021 12, 7213-7220.
(5) Jähnigen, S.; ChirPy; Zenodo 2022 https://doi.org/10.5281/zenodo.4775330.

Figure Legend: Solid-state VCD is closely linked to crystal symmetry and polymorphism: Already an achiral twofold screw axis generates important non-local VCD patterns that appear as two terms: direct coupling (DC) and gauge transport (GT).

Fig. 1

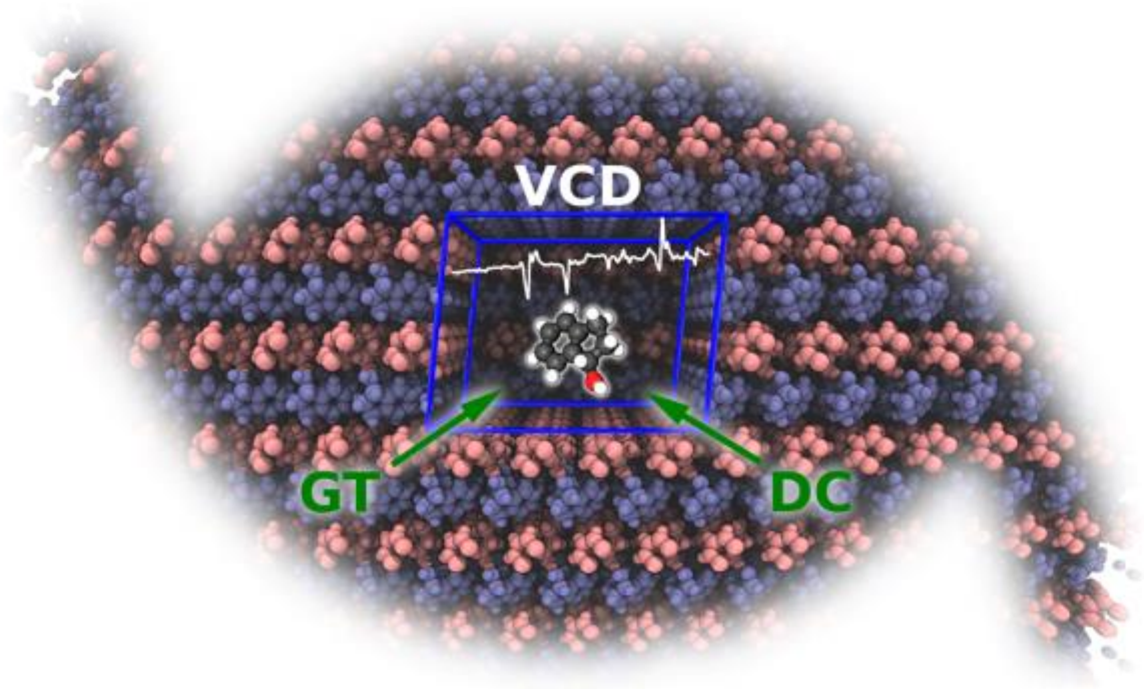

Microsymposium 4 | Bio-Crystallography II: Signaling, macromolecular interactions and new structures

OP-017

Structural and functional characterization of the eukaryotic chaperone trigger factor

Y. Carius (Homburg/DE), F. Ries (Kaiserlautern/DE), F. Willmund (Kaiserlautern/DE), C. R. D. Lancaster (Homburg/DE)

Newly synthesized polypeptides emerging from the ribosomal tunnel require the coordinated action of molecular chaperones in co-translational folding. In prokaryotic cells and chloroplasts of plant cells, the ribosome associated chaperone trigger factor binds nascent polypeptides and promotes their *de novo* folding [1,2]. The structure of bacterial trigger factor is well characterized, resembling a dragon shaped conformation with flexible domains responsible for ribosome binding, peptidyl-prolyl *cis/trans* isomerization (PPIase) and for substrate protein binding. Less is known about eukaryotic trigger factors. We characterized two plastidic trigger factors from *Arabidopsis thaliana* (AtTIG1) and *Chlamydomonas reinhardtii* (CrTIG1) [3] and solved the structure of the CrTIG1 at 2.6 Å resolution [4]. CrTIG1 exhibits a comparable dragon-shaped conformation as its prokaryotic counterparts and shows measurable peptidyl-prolyl *cis/trans* isomerization activity (Fig 1). However, the eukaryotic trigger factor displays distinct charge distributions in the domains, an altered positioning of the helical arms in the C-terminal substrate binding domain, and an uncommon intramolecular domain interaction, thus indicating a specific structural adaptation of eukaryotic trigger factors for their function in chloroplasts.

(1) Hoffmann A, Bukau B & Kramer G (2010) Structure and function of the molecular chaperone Trigger Factor. *Biochim Biophys Acta - Mol Cell Res* **1803**, 650–661.

(2) Rohr M, Ries F, Herkt C, Gotsmann VL, Westrich LD, Gries K, Trösch R, Christmann J, Chaux-Jukic F, Jung M, Zimmer D, Mühlhaus T, Sommer F, Schrod M, Keller S, Möhlmann T & Willmund F (2019) The role of plastidic trigger factor serving protein biogenesis in green algae and land plants. *Plant Physiol* **179**, 1093–1110.

(3) Ries F, Carius Y, Rohr M, Gries K, Keller S, Lancaster CRD & Willmund F (2017) Structural and molecular comparison of bacterial and eukaryotic trigger factors. *Sci Rep* **7**, 10680.

(4) Carius Y, Ries F, Gries K, Trentmann O, Lancaster CRD & Willmund F (2022) Structural features of chloroplast trigger factor determined at 2.6 Å resolution. *Acta Crystallogr Sect D, Struct Biol* **78**, 1259–1272.

Figure 1: Crystal structure of the plastidic trigger factor from *Chlamydomonas reinhardtii* (A) and PPIase activity assay (B).

Fig. 1

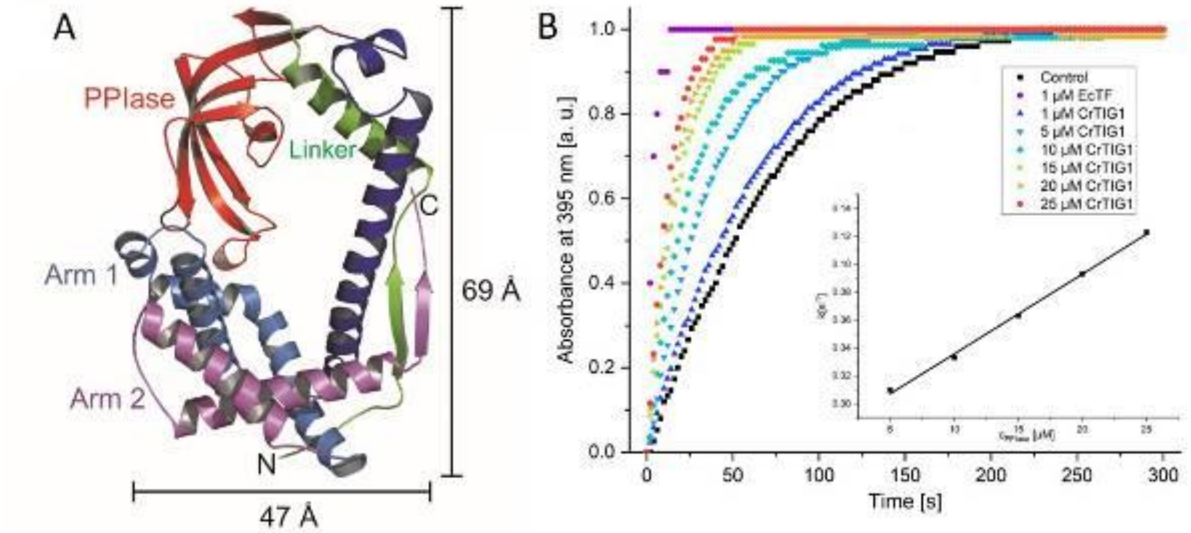

OP-018

Crystal structure of a transient MHC I–tapasin–ERp57 editing complex defines chaperone promiscuity in the endoplasmic reticulum

I. Müller (Frankfurt am Main/DE), C. Winter (Frankfurt am Main/DE), C. Thomas (Frankfurt am Main/DE), R. Spaapen (Amsterdam/NL, Amsterdam/NL), S. Trowitzsch (Frankfurt am Main/DE), R. Tampé (Frankfurt am Main/DE)

Adaptive immunity depends on cell surface presentation of antigenic peptides by major histocompatibility complex class I (MHC I) molecules and on stringent ER quality control in the secretory pathway. The chaperone tapasin in conjunction with the oxidoreductase ERp57 is crucial for MHC I assembly and for shaping the epitope repertoire for high immunogenicity. However, how tapasin–ERp57 heterodimers engage MHC I clients has not yet been determined at atomic detail due to the transient nature of the editing complex. Here, we captured a human MHC I–tapasin–ERp57 complex by a photo-triggered approach for structure determination by X-ray crystallography. Initial crystals of the chaperone-client complex belonging to space group $P2_12_12_1$ diffracted X-rays to 4.0 Å. Utilizing microseed matrix screening[1], we obtained crystals in space group $P22_12_1$ with one complex in the asymmetric unit and an improved resolution of 2.7 Å. Our structural study together with biochemical results unveils molecular details of client recognition by the multichaperone complex and highlights elements indispensable for peptide proofreading. Furthermore, the structure of this transient ER quality control complex provides the mechanistic basis for the selector function of tapasin and showcases how the numerous MHC I allomorphs are chaperoned during peptide loading and editing.

(1) D'Arcy, A., Villard, F. & Marsh, M. An automated microseed matrix-screening method for protein crystallization. *Acta Crystallogr. D. Biol. Crystallogr.* 63, 550–554 (2007).

OP-019

Turning peptides into pyrroloindoline alkaloids: A closer look at crocagin biosynthesis

S. Adam (Saarbrücken/DE), D. Zheng (Glasgow/GB), A. Klein (Saarbrücken/DE), C. Volz (Saarbrücken/DE), W. Mullen (Glasgow/GB), S. Shirran (St Andrews/GB), B. Smith (Glasgow/GB), O. Kalinina (Saarbrücken/DE), R. Müller (Saarbrücken/DE), J. A. Koehnke (Glasgow/GB, Saarbrücken/DE)

The superfamily of ribosomally-synthesized and post-translationally modified peptide (RiPP) natural products has been growing rapidly and features many unusual biochemical transformations[1]. RiPP biosynthesis begins with the expression of a short gene via the ribosomal route to yield a precursor peptide. Precursor peptides usually consist of an N-terminal part named "leader peptide", which is important for substrate recognition by the modifying enzyme(s), and a C-terminal core peptide, which is ultimately converted into the natural product[2].

Crocagins are pyrroloindoline alkaloid RiPPs, and while the responsible biosynthetic gene cluster has been identified[3], their biosynthesis has largely remained a mystery. We set out to elucidate crocagin biosynthesis through a combination of structural biology and *in vitro* biochemical assays.

During these efforts we discovered that two homologous proteins, CgnB and CgnE, bind to the leader peptide and fulfill distinct biochemical functions. Their crystal structures reveal them to be distantly related to aminopeptidases, with the fold repurposed to satisfy the new functions. In addition, CgnB and CgnE appear to be involved in the formation of a larger biosynthetic complex, where they occupy different binding sites. Bioinformatic analyses based on these data led to the discovery of related biosynthetic pathways that may give access to a variety of glycosylated pyrroloindole alkaloids and expand the RiPP superfamily. Together with additional structural and biochemical data we have been able to propose a biosynthetic scheme for crocagins.

(1) Montalban-Lopez, M. *et al.* New developments in RiPP discovery, enzymology and engineering. *Nat Prod Rep*, doi:10.1039/d0np00027b (2020).

(2) Arnison, P. G. *et al.* Ribosomally synthesized and post-translationally modified peptide natural products: overview and recommendations for a universal nomenclature. *Nat Prod Rep* 30, 108-160, doi:10.1039/c2np20085f (2013).

(3) Viehrig, K. *et al.* Structure and Biosynthesis of Crocagins: Polycyclic Posttranslationally Modified Ribosomal Peptides from Chondromyces crocatus. *Angew Chem Int Ed Engl* 56, 7407-7410, doi:10.1002/anie.201612640 (2017).

(4) Adam, S. *et al.* Unusual Peptide-Binding Proteins Guide Pyrroloindoline Alkaloid Formation in Crocagin Biosynthesis. *Under review*.

OP-020

Pharmacological targeting of the LRRK pathway – the kinase domains and beyond

S. Mathea (Frankfurt am Main/DE)

Leucine-rich repeat kinases are involved in the etiology of bone diseases (LRRK1) and Parkinson's disease (LRRK2), respectively. They are regulators of vesicle trafficking by phosphorylating the switch-2 loop of membrane-bound RAB GTPases.

Many type-1 inhibitors of the LRRK2 kinase domain have been developed. Several of them possess superb specificity profiles and in vivo properties, and one of them (DNL151) is currently probed in phase 3 clinical trials. However, the cellular regulation of the LRRK activity, its kinase-substrate recognition, and the downstream signalling are still incompletely understood.

Gaining deeper insights into these processes may allow to identify alternative ways of interfering with the LRRK pathway pharmacologically. Possible avenues include the development of specific inhibitors for LRRK1 and of type-2 inhibitors for LRRK2. Furthermore, the domains flanking the kinase domain can be targeted. And finally, downstream signalling molecules such as the RAB GTPases can be explored as potential therapeutic targets.

OP-021

AI usage in Structural Biology

A. Thorn (Hamburg/DE)

Machine learning methods, in particular convolutional neural networks, have been applied to a variety of problems in cryo-EM and macromolecular crystallographic structure solution, automation and high-throughput the foremost among them [1]. However, they still have limited acceptance by the community, mainly in areas where they replace repetitive work and allow for easy visual checking, such as particle picking, crystal centering or crystal recognition. One big exception is machine learning based protein fold prediction, such as AlphaFold2 [2], which is currently revolutionizing the field.

Whether we will be able to exploit this potential fully, will depend on the manner in which we use machine learning: training data must be well-formulated, methods need to utilize appropriate architectures, and outputs must be critically assessed, which may even require explaining artificial intelligence decisions. In this talk, an overview of current applications of machine learning in structural biology will be given, including examples from our own work, how experimentalist may use fold prediction methods, and how AI could change crystallography in the future.

This work was supported by the German Federal Ministry of Education and Research [grant number 05K19WWA and 05K22GU5], Deutsche Forschungsgemeinschaft [project TH2135/2-1].

(1) Thorn, A.* (2022). Artificial intelligence in the experimental determination and prediction of macromolecular structures, Curr. Opin. Struct. Biol. 74, 102368. https://doi.org/10.1016/j.sbi.2022.102368
(2) Edich, M., Briggs, D.C., Kippes, O., Gao, Y., Thorn, A.* (2022). The impact of AlphaFold on experimental structure solution, Faraday Discussions 240, 184 -195. https://doi.org/10.1039/D2FD00072E

Microsymposium 5 | Bio-Crystallography I: Hit finding and design of small molecule inhibitors

OP-022

Crystallographic fragment screening: Efficient access to new lead in drug discovery

G. Klebe (Marburg/DE)

Fragment-based lead discovery has become increasingly popular to identify first leads for drug discovery. Advantage of using fragments is their low-molecular weight, which leaves sufficient space for subsequent chemical optimization. However, the inherent low-binding affinity of fragments poses major challenge to current biophysical and biochemical screening methods and questions whether such techniques are a reliable pre-screening filter to detect all putative fragments [1]. Usually detected hits from this procedure are crystallized with the target protein [2]. We suggest to invert this process. Data collection at synchrotrons has become fast enough, to perform direct crystallographic fragment screening on protein crystals. Appropriate fragment libraries have been developed and usually hit rates of 10-30 % can be found [3]. From the discovered hits, those binding in promising protein pockets and giving rise to encouraging ideas for follow-up synthesis in the optimization phase are selected for a computational expansion. For this, molecules are retrieved from large compound libraries that embed the original fragments [4]. Alternatively, starting with the crystallographically discoverd binding poses of the selected fragments, established synthesis rules are applied to generate large virtual compound libraries on the computer [5]. Using template-based docking, the expanded ligands are placed into the protein"s binding pocket based on the binding pose of the original fragments. After scoring, the most promising candidates are subjected to synthesis. Since established chemistry is used, the success rate of such syntheses is high. The obtained compounds have a size allowing the reliable application of usual binding assays for testing. Convincing hit rates of micromolar binders are found. Of the most promising hits, a crystal structure with the protein is determined. Alternatively, chemical merging of promising fragment hits can be accomplished. To this end, ligands of comparable size and potency are found as with high throughput screening. However, advantage of this strategy is that the binding mode of discovered hits is crystallographically confirmed and a synthesis route is available which allows fast further optimization steps in the hit-to-lead phase.

(1) Schiebel J. et al., One Question, Multiple Answers: Biochemical and Biophysical Screening Methods Retrieve Deviating Fragment Hit Lists. *ChemMedChem* **2015**, 10: 1511-21.

(2) Schiebel J. et al., Six Biophysical Screening Methods Miss a Large Proportion of Crystallographically Discovered Fragment Hits: A Case Study, *ACS Chem. Biol.* **2016**, 11: 1693-1701.

(3) J. Wollenhaupt, A. Metz, T. Barthel, G. M. A. Lima, A. Heine, U. Mueller, G. Klebe, M. S.Weiss, F2X-Universal and F2X-Entry: Structurally Diverse Compound Libraries for Crystallographic Fragment Screening, Structure, **2020**, 28: 694-706.e5.

(4) A. Metz, J. Wollenhaupt, S. Glöckner, N. Messini, S. Huber, T. Barthel, A. Mehrabet, H.-D. Gerber, A. Heine, G. Klebe, M.S. Weiss

(5) Frag4Lead: growing crystallographic fragment hits by catalog using fragment-guided template docking, Acta Cryst. **2021**, D77: 1168-1182.

(6) J. Müller, R. Klein, O. Tarkhanova, A. Gryniukova, P. Borysko, S. Merkl, M. Ruf, A. Neumann, M. Gastreich, Y. S. Moroz, G. Klebe, S. Glinca, Magnet for the Needle in Haystack: "Crystal Structure First" Fragment Hits Unlock Active Chemical Matter Using Targeted Exploration of Vast Chemical Spaces, J. Med. Chem., **2022**, 65: 10.1021/acs.jmedchem.2c00813.

OP-023

How to successfully conduct crystallographic fragment screening at BESSY II

L. S. Benz (Berlin/DE, Berlin/DE), J. Wollenhaupt (Berlin/DE), T. Barthel (Berlin/DE, Berlin/DE), E. Jagudin (Lund/SE), D. Wallacher (Berlin/DE), T. Hauss (Berlin/DE), T. Crosskey (Berlin/DE), F. Lennartz (Berlin/DE), J. H. W. Scanlan (Berlin/DE), A. Heine (Marburg/DE), T. Krojer (Lund/SE), U. Mueller (Berlin/DE), M. S. Weiss (Berlin/DE)

Drug discovery is shifting from high-throughput screening with drug-sized compounds towards screening smaller low-molecular-weight compounds called fragments. Six drugs have been approved that originated from fragment screening campaigns and over 40 more candidates are in clinical trials[1]. Fragment screening can be performed highly efficiently by crystallography at modern synchrotron beamlines. On top of identifying binders, direct structural information is achieved which fosters structure-based design of follow-up compounds.

The Helmholtz-Zentrum Berlin fragment screening facility provides users with support, know-how, and necessary infrastructure to set up their own fragment screening campaigns[2]. The infrastructure includes a selection of fragment libraries, crystal handling tools such as the EasyAccess Frame[3], two robot operated beamlines, and largely automated data treatment using the FragMAXapp[4].

One of the libraries provided is the shape and pharmaco-diverse F2X-Entry Screen containing 96 compounds[5]. This library is provided as dried-on compounds in 96 well plates and yields consistently high hit rates in user operation, usually in the range 15-25 %. These high hit rates during fragment screening campaigns allow to sample the biological environment of a binding pocket of interest and thereby facilitate evolving fragments by exploring putative additional interactions. Via the Frag4Lead workflow, the affinity of initial hits can be improved by orders of magnitude using catalog compounds, which accelerates projects by avoiding elaborate custom chemistry at the beginning of a project[6]. This is especially attractive for academic groups to initiate tool compound developments or drug discovery.

(1) Erlanson, D. https://practicalfragments.blogspot.com/2021/11/fragments-in-clinic-2021-edition.html (acc. 2022/10/21)
(2) Wollenhaupt, J. et al., J. Vis. Exp. (2021), 169, e62208
(3) Barthel et al., J. Appl. Cryst. (2021). 54, 376–382
(4) Lima, G.M. et al., Acta Crystallogr. (2021), 77, 799–808.
(5) Wollenhaupt, J. et al. Structure (2020). 28, 694-706.e5
(6) Metz, A. et al. Acta Crystallogr. D (2021). 77, 1168–1182.

OP-024

DESY's new High-Throughput screening beamline HiPhaX

W. Ewert (Hamburg/DE), S. Günther (Hamburg/DE), P. Reinke (Hamburg/DE), S. Falke (Hamburg/DE), J. Lieske (Hamburg/DE), L. Gumprecht (Hamburg/DE), J. Meyer (Hamburg/DE), P. Fischer (Hamburg/DE), A. Meents (Hamburg/DE)

The ongoing advances in sample-preparation and synchrotron capacities have pushed high-throughput X-ray crystallography screenings to become a valuable asset in the search for new drug candidates against various diseases. In a recent X-ray screening effort at DESY for the identification of potential drug candidates against SARS-CoV2 more than 6000 compounds from drug repurposing libraries were screened against the virus"s main protease [1].

To further streamline the process of structure-based screenings DESY is - together with collaboration partners - building the new crystallographic endstation HiPhaX at the PETRA-III storage ring, which will be dedicated to high-throughput pharmaceutical screenings. At HiPhaX we combine our expertise on drug-repurposing and fragment-based library screening with our knowledge on beamline design and automation with the goal to develop an extremely reliable and fully automated endstation with the capability of determining more than 1000 protein structures per 24 hours.

In addition to classical cryogenic data collection the new HiPhax beamline offers also a dedicated sample handling flow for fully automatic room temperature data collection with the option to control relative humidity and temperature. First room temperature fragment screening experiments proved the feasibility of this approach, which is expected not only to save efforts on finding the right cryo-conditions but also provides more insights into the dynamical interaction of compounds with the target protein. In future HiPhax will provide dedicated crystal storage and a sample handling robot for fully automated screening experiments also at room temperature.

HiPhaX will further provide fully automatic X-ray based crystal identification and centering and AI supported data collection and analysis and is intended to become a fully autonomously operating beamline for unattended data collection. It is foreseen to open the beamline for both academic and industrial user operation in late 2023 / early 2024.

(1) Günther, S. and Reinke, P. Y. A., et al. (2021). X-ray screening identifies active site and allosteric inhibitors of SARS-CoV-2 main protease. Science 372, 642–646. doi: 10.1126/science.abf7945.

OP-025

Torsion angles to map and visualize the conformational space of a protein

H. Ginn (Didcot/GB)

Present understanding of protein structure dynamics trails behind that of static structures. Representation of protein entities (RoPE), based on torsion angles, derives an interpretable conformational space which correlates with data collection temperature, resolution and reaction coordinate. This is demonstrated with experimental data from trypsin (Fig 1) where each point corresponds to a deposited structure of trypsin. These correlations are so strong, incorrectly deposited collection temperatures can be identified by looking for outliers. This indicates that torsion angles are a more sensitive and biologically relevant descriptor for protein conformation than atomic coordinates. Torsion angles are an optimal parameter space to manipulate protein dynamics in the quest to change protein function.

Fig. 1

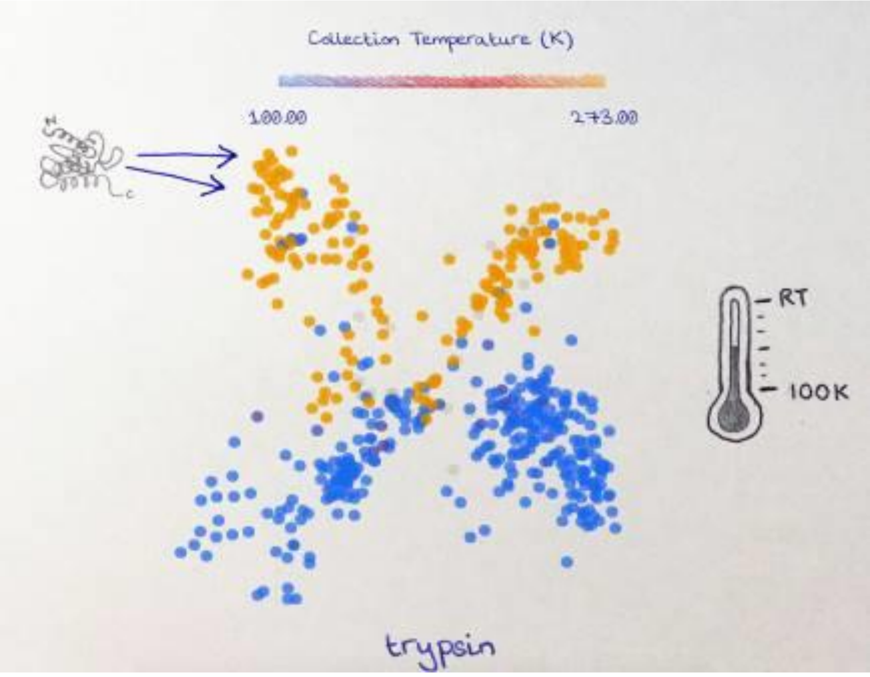

OP-026

Fragment-based design of mycobacterial thioredoxin reductase inhibitors: From a fragment screening to novel inhibitors

F. T. Füsser (Münster/DE, Münster/DE, Münster/DE), P. Otten (Münster/DE), J. Wollenhaupt (Berlin/DE), M. S. Weiss (Berlin/DE), A. Junker (Münster/DE), O. Koch (Münster/DE, Münster/DE), D. Kümmel (Münster/DE)

The resurgence of tuberculosis, caused primarily by Mycobacterium tuberculosis (Mtb), and the appearance of multi-drug and extensively drug-resistant strains leads to an urgent need for new antituberculosis drugs with alternative modes of action. As part of the thioredoxin system, the thioredoxin reductase (TrxR) is essential for thiol redox homeostasis [1]. The mycobacterial TrxR shows a substantial difference in sequence, mechanism and structure to eukaryotic TrxRs leading to the expectation that the mycobacterium tuberculosis TrxR is a selective and promising target for a tuberculosis treatment. The druggability was already shown with a compound class derived from a docking-based virtual screening approach [2,3].

For the identification of new fragment-based starting points and for the investigation of new interaction sites for potential drugs, a crystallographic fragment screening was performed [4]. TrxR crystals that reproducibly showed high-resolution diffraction (~1.7 Å) were soaked with the 96 structurally diverse fragments of the F2X-Entry Screen [5]. The diffraction data were collected at BESSY II [6] processed and refined by a largely automated software pipeline at HZB including the FragMAXapp and hit identification by a multi-dataset analysis approach called PanDDA [7, 8]. 40 fragments were found bound to nine binding sites, of which four sites are positioned at binding pockets or important interaction sites and therefore show high potential for possible inhibition.

After a detailed analysis of all fragments and binding sites, two fragments were chosen to be optimized, based on their unique interaction and potential selectivity for the mycobacterial TrxR. Interesting analogues were analyzed by the SAR-by-catalogue approach using molecular docking. 24 compounds were purchased for further testing. Compounds with an extension of the second fragment were not purchasable due to the needed exit vector that is not synthetically accessible. Therefore, suitable fragment analogues and promising compounds were computational designed, analyzed, and synthesized. After only one round of optimization, a compound with µM inhibitory activity was found, and the binding position was confirmed.

(1) Lin, K.et al.: Mycobacterium tuberculosis Thioredoxin Reductase Is Essential for Thiol Redox Homeostasis but Plays a Minor Role in Antioxidant Defense. PLoS pathogens **2016**, 12, e1005675.
(2) Koch, O. et al.: Identification of M. tuberculosis thioredoxin reductase inhibitors based on high-throughput docking using constraints. Journal of medicinal chemistry **2013**, 56, 4849.
(3) Koch, O., Bering, L. Mycobacterium tuberculosis Thioredoxin Reductase Inhibitor As Antituberculosis Drug, EP 17 179 568.5 filed 04th July **2017** & PCT/EP2018/066768 filed 22th June **2018**
(4) Wollenhaupt, J. et al.: Workflow and Tools for Crystallographic Fragment Screening at the Helmholtz-Zentrum Berlin. Journal of visualized experiments : JoVE [Online] **2021**, No. 169.
(5) Wollenhaupt, J. et al.: F2X-Universal and F2X-Entry: Structurally Diverse Compound Libraries for Crystallographic Fragment Screening. Structure (London, England : 1993) **2020**, 28, 694-706.e5
(6) Mueller, U. et al.: The macromolecular crystallography beamlines at BESSY II of the Helmholtz-Zentrum Berlin: Current status and perspectives. Eur. Phys. J. Plus **2015** ,130, 141-150.
(7) Lima, G. M. A. et al.: FragMAXapp: crystallographic fragment-screening data-analysis and project-management system. Acta crystallographica. Section D, Biological crystallography **2021**, D77, 799-808
(8) Pearce, N., Krojer, T., Bradley, A. et al.: A multi-crystal method for extracting obscured crystallographic states from conventionally uninterpretable electron density. Nat Commun **2017**, 8, 15123.

OP-027

P24 Beamline: A High-Performance beamline for small molecule chemical crystallography at DESY

L. Noohinejad (Hamburg/DE), C. Paulmann (Hamburg/DE), M. Tolkiehn (Hamburg/DE)

P24 is a high-energy diffraction beamline for small molecule chemical crystallography offering scientists powerful tools for structural analysis with PETRA III light source at DESY since 2017. The beamline produces a wide range of tunable energy between 8, 13-44 keV X-ray. A dual- (111)(311) Si-crystal monochromator is cooled with water to produce a very small beam motion with different heat loads. Two experimental hutches are equipped with one heavy load diffractometer (Kappa geometry) for complex sample environments and a Eulerian diffractometer. A new state-of-the-art area detector, LAMBDA 7.5M CdTe, makes it possible resolve individual reflections due to its smaller pixel size and higher angular resolution even at higher energies. This option will bring the new opportunity for solving the complicated structures including aperiodic crystals and twinned crystals. Two Helium gas jet cryostats for temperature ranges of 5K to 100 K and 10-400 K; and the nitrogen gas blower and Anton Paar oven up to 1200 K are available for successful phase transition studies. Installed CRLs can focus the beam and visual alignment cameras together with microscopes allows small crystals to be accurately centered within the x-ray beam. The beamline can be also used for high-pressure DACS, temperature dependent powder diffraction and in-situ electrical field measurements. Some recent crystal structure determinations done at the beamline will be given.

OP-028

Diamond hybrid anodes and high-brightness cathodes: An efficient combination for microfocus X-Ray sealed tubes with very high intensities at low power

J. Graf (Geesthacht/DE), T. Stürzer (Karlsruhe/DE), A. Lübben (Karlsruhe/DE), R. Durst (Karlsruhe/DE), K. Atak (Geesthacht/DE), P. Radcliffe (Geesthacht/DE), C. Michaelsen (Geesthacht/DE)

The structure determination on ever smaller and weakly diffracting crystals is one of the biggest challenges in crystallography, continuously raising the requirements for modern X-ray analytical equipment, including X-ray sources and detectors. Modern low power microfocus sealed tube sources define the state-of-the-art for most in-house X-ray diffraction equipment, as they deliver intensities comparable to microfocus rotating anodes, yet maintaining all the comfort of sealed tube systems. Given today's soaring energy prices, energy efficient microfocus X-ray sealed tubes are more important than ever as, despite of their high performance, they consume less than 5% of the electrical power of a microfocus rotating anode.

On our quest for brighter microfocus X-ray sources, we have continuously explored the physical limitations of impact ionization sources in order to find ways to overcome some of their limitations, such as the heat transfer in the anode. Our innovative hybrid diamond anode technology benefits from an up to 5 times higher thermal conductivity compared to a bulk copper anode. Therefore, using diamond as a heat sink in the anode is an efficient way to increase the power loadability and, hence, the intensity of an X-ray source.

For our diamond hybrid anodes, we found that the cathode brightness became the bottleneck, as the achievable power density on the anode has now largely been limited by the electron emission rate of classical tungsten filament cathodes. Our newly introduced IµS DIAMOND II microfocus source overcomes this limitation by replacing the conventional W filament with a new high-brightness cathode, delivering an electron beam strong enough to fully exploit the potential of the diamond hybrid anode. This results in an impressive twofold gain in intensity compared to the previous generation.

Along a number of selected results from protein and chemical crystallography, we will review the latest innovations in microfocus sealed tube X-ray sources.

OP-029

Instrumentation for time-resolved synchrotron X-ray diffraction studies of adsorption-induced switching in crystalline nanoporous solids

V. Bon (Dresden/DE), A. Khadiev (Hamburg/DE), D. Novikov (Hamburg/DE), S. Kaskel (Dresden/DE)

Switchable porous solids are a sub-class of MOFs with adaptable porosity, which undergo stimuli-induced phase transitions between open porous and contracted or even dense phases, typically triggered by guest molecules, temperature, pressure, or light irradiation.1–3 Such adaptive materials are currently intensively discussed as promising materials for natural gas storage,4 CO2/CH45 and hydrocarbon separation,6 isotopes" separation7 eco-friendly refrigeration technologies,8 design of sensors9 and actuators.10 However, the characterization of these materials requires the development of advanced techniques, which allow monitoring the phase transition during the adsorption and desorption of fluids into the pores. The lack of commercial solutions for in situ PXRD in controlled gas atmospheres, which fulfil the requirements in terms of adsorption temperature, pressure and leakproof at the same time, motivated us to develop four different prototype instrumentations for in situ PXRD in parallel to adsorption of gases and vapours in different pressure and temperature ranges at KMC-2 beamline of HZB.11 plenty of dynamic frameworks possessing unique phenomena such as "breathing", "gate opening" and "Negative Gas Adsorption" have been studied using this setup.

While all these instrumentations work in adsorption equilibrium conditions, recent theoretical and experimental studies on flexible MOFs highlight the importance of *in situ* spatiotemporal monitoring of phase transitions. A deeper understanding of the switching kinetics and activation barriers will open the unique possibility to design "fast" and "slow" switching MOFs, by controlling important real structural factors such as crystallite size, morphology, defects, grain boundaries, surface barriers etc.15

In the current contribution, we report on multipurpose instrumentation for time-resolved PXRD studies of adsorption-induced switching in crystalline nanoporous solids, designed at P23 beamline of PETRA III synchrotron. The first results on crystal size-dependent switching kinetics in MIL-53(Al) will be reported.12

(1) S. Krause, N. Hosono and S. Kitagawa, *Angew. Chem. Int. Ed.*, 2020, **59**, 15325–15341.
(2) A. Schneemann, V. Bon, I. Schwedler, I. Senkovska, S. Kaskel and R. A. Fischer, *Chem. Soc. Rev.*, 2014, **43**, 6062–6096.
(3) S. Horike, S. Shimomura and S. Kitagawa, *Nat. Chem.*, 2009, **1**, 695–704.
(4) J. A. Mason, J. Oktawiec, M. K. Taylor, M. R. Hudson, J. Rodriguez, J. E. Bachman, M. I. Gonzalez, A. Cervellino, A. Guagliardi, C. M. Brown, P. L. Llewellyn, N. Masciocchi and J. R. Long, *Nature*, 2015, **527**, 357–361.
(5) S. Hiraide, Y. Sakanaka, H. Kajiro, S. Kawaguchi, M. T. Miyahara and H. Tanaka, *Nat. Commun.*, 2020, **11**, 3867.
(6) L. Li, R.-B. Lin, R. Krishna, X. Wang, B. Li, H. Wu, J. Li, W. Zhou and B. Chen, *J. Mater. Chem. A*, 2017, **5**, 18984–18988.
(7) L. Bondorf, J. L. Fiorio, V. Bon, L. Zhang, M. Maliuta, S. Ehrling, I. Senkovska, J. D. Evans, J.-O. Joswig, S. Kaskel, T. Heine and M. Hirscher, *Sci. Adv.*, 2022, **8**, eabn7035.
(8) J. García-Ben, J. López-Beceiro, R. Artiaga, J. Salgado-Beceiro, I. Delgado-Ferreiro, Y. V. Kolen"ko, S. Castro-García, M. A. Señarís-Rodríguez, M. Sánchez-Andújar and J. M. Bermúdez-García, *Chem. Mater.*, 2022, **34**, 3323–3332.
(9) P. Freund, L. Mielewczyk, M. Rauche, I. Senkovska, S. Ehrling, E. Brunner and S. Kaskel, *ACS Sustainable Chem. Eng.*, 2019, **7**, 4012–4018.
(10) V. Bon, S. Krause, I. Senkovska, N. Grimm, D. Wallacher, D. M. Többens and S. Kaskel, *Angew. Chem. Int. Ed.*, 2021, **60**, 11735–11739.
(11) N. Klein, C. Herzog, M. Sabo, I. Senkovska, J. Getzschmann, S. Paasch, M. R. Lohe, E. Brunner and S. Kaskel, *Phys. Chem. Chem. Phys.*, 2010, **12**, 11778–11784.
(12) V. Bon, N. Busov, I. Senkovska, N. Bönisch, L. Abylgazina, A. Khadiev, D. Novikov and S. Kaskel, *Chemical communications (Cambridge, England)*, 2022, **58**, 10492–10495.

OP-030

Science case and concepts of a macromolecular diffractometer for the High Brilliance Neutron Source (HBS)

Z. Ma (Jülich/DE), K. Lieutenant (Jülich/DE), J. Voigt (Jülich/DE), T. E. Schrader (Garching/DE), T. Gutberlet (Jülich/DE), T. Brückel (Jülich/DE)

Neutron protein crystallography has lead to the enlightment of many enzymatic processes due to its capability of locating hydrogen atoms. It also provides the possibility to measure data sets on protein crystals at room temperature without noticeable radiation damage. But the technique requires large crystals of more than 0.1 mm^3 volume and instruments with a high neutron flux.

The HBS project for a High Current Accelerator-based Neutron Source (HiCANS) will offer a new powerful neutron sources using a pulsed proton beam of 70 MeV energy and 100 kW of time-averaged power for each of its target stations [1]. In this contribution we compare the performance of two instruments under consideration for protein crystallography based on VITESS Monte Carlo simulations and discuss possible science cases for them. The optimization was aimed at a 1 mm^3 sample with a divergence of 0.38° and 0.8° (FWHM) and a wavelength band of 2 Å starting from 2 Å.

We compare here two different designs: At the HBS target station with 96 Hz frequency a 20 m long instrument has been simulated based on a SELENE neutron guide. With the optimized neutron optics, we can obtain a low background, a very bright, tunable neutron beam spot and beam collimation at the sample with a cross-section as small as 1 mm^2, thus promising a very competitive instrument for the life science community.

At the HBS target station with 24 Hz frequency a 80 m long instrument was simulated with a ballistic neutron guide using elliptic end sections. It has about double the flux at relaxed collimation and a factor of 1.5 better time-of-flight resolution as compared to the 20 m long instrument. But it has the disadvantage that the neutron guide transports a large beam, of which around 1% of the neutrons exiting the guide will actually hit the sample.

So both concepts promise a new powerfull tool to study the diffraction from single crystals below 1 mm^3 volume that will be available to national and international users at the next generation of medium flux sources.

(1) T. Brückel *et al.*, *Conceptual Design Report Jülich High Brilliance Neutron Source (HBS)*, vol. 8. 2020.

OP-031

Growth of good quality bulk size trans-Stilbene single crystal for Neutron and gamma detection applications

R. Paulraj (Chennai/IN), M. A. A. (Chennai/IN), L. Alex (Chennai/IN), M. Tyagi (Mumbai/IN), R. P (Chennai/IN)

In this paper, we have investigated the growth of large-sized trans-stilbene (TSB) single crystal using the vertical Bridgeman technique (VBT). The optimization of the parameters such as furnace setup, ampoule"s cone angle, and material purification were mainly focused during the growth process. The emission wavelength at visible region, the fast scintillation decay and the PSD properties marks its significance in scintillator detector applications.

OP-032

Synchrotron will help you: from subtle diffuse scattering to giant supramolecules

A. Virovets (Frankfurt am Main/DE), E. Peresypkina (Regensburg/DE), B. Stöger (Vienna/AT), M. Scheer (Regensburg/DE)

In this talk we are going to summarize our experience in using DESY beamlines P11 and P24 (Hamburg, Germany) to solve challenging tasks in the single-crystal X-ray diffraction. High flux, ability to perform experiments at Helium temperatures, as well as excellent direct photon counting detectors allowed us advancing in our research.

One class of challenging tasks is related to structural studies of giant up to 4.6 nm in size, organometallic supramolecules based on the organometallic *cyclo*-Pn complexes (n = 4, 5) as building blocks [1]. Their crystals frequently demonstrate weak scattering power due to the severe crystallographic disorder. In many cases, the use the high-flux synchrotron sources become the only remedy. We had to develop special protocols for handling the samples that are prone to oxidation by air, sometimes sensitive to moisture and easily loose solvent being taken out of mother solution. To allow the crystal preparation from Schlenk tubes, within the long-term project II-20180597 with DESY we have installed a vacuum-argon line (Schlenk line) in the sample preparation lab of P24 beamline.

We developed optimal strategies and, in cooperation with Dr. M. Meyer, protocols for the data finalization using *CrysAlisPro* software (Rigaku Oxford Diffraction). It allowed us to not only to obtain high-quality diffraction data even from weakly scattering crystals above *d*min > 1 Å (Fig. a), but also investigate such subtle structural effects as superstructural ordering and order-disorder (OD) phenomenon. Thus, high quality intensity data from the diffuse scattering allowed us to model OD-phenomenon in Cp''Fe(η^5-P_5) (Fig. b) [2, 3].

This work is partly was supported by the DFG within the project Sche 384/44-1. E.P. is grateful for a Postdoc research scholarship for Female Early Career Researchers within the framework of the Free State of Bavaria"s "Program to Realize Equal Opportunities for Women in Research and Teaching" at the University of Regensburg.

(1) E. Peresypkina, A. V. Virovets, M. Scheer (2021) *Coord. Chem. Rev.*, **446**:*213995*
(2) E. Peresypkina, B. Stöger, S. B. Dinauer, A. V. Virovets (2022) *Cryst. Growth Des.* ***22***, 3870
(3) B. Stöger, E. Peresypkina, A. V. Virovets (2022) *Acta Cryst*. **B78**, 734

Fig. 1

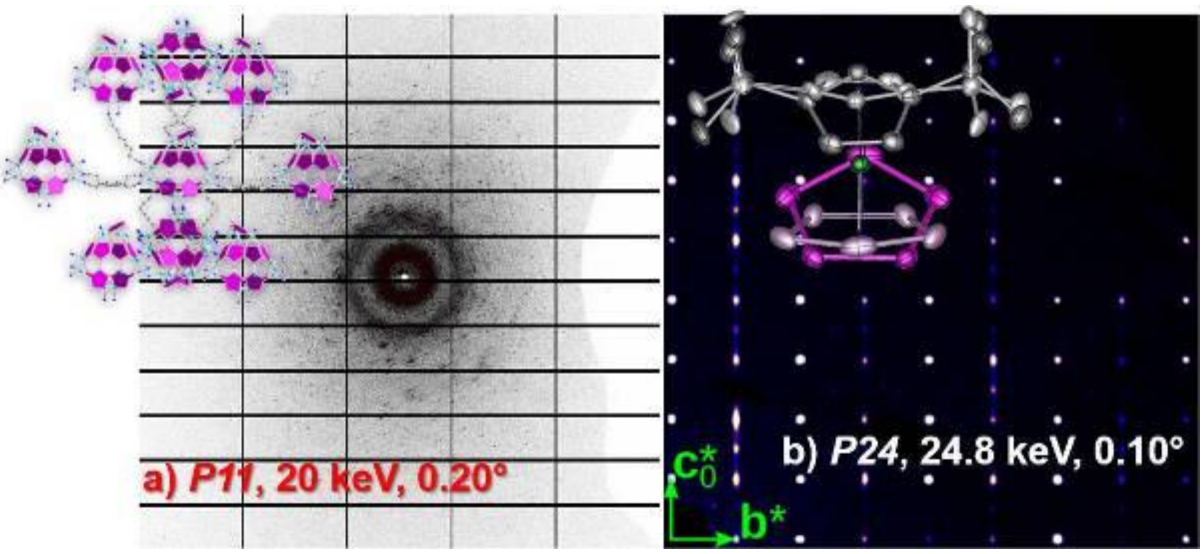

OP-033

Democratizing Quality: High Throughput PXRD & Total Scattering @

B. Hinrichsen (Ludwigshafen/DE)

The extremely brilliant source (EBS) upgrade at the ESRF has enabled phenomenal advances in some fields. The visually most impressive must be the development of the imaging experimental station BM18. The experiment presented here makes equally good use of the brilliant beam for a powder diffraction and total scattering experiment. An extremely high throughput sample changer has been developed. Due to the EBS brilliance, low sample changing dead time and fast detectors data on thousands of samples to be collected per hour. For all samples two datasets are gathered. One total scattering and one for PXRD. Due to the high diffraction space resolution excellent size/strain analyses as well as high quality structure analysis and quantitative analysis ca be performed. The data is virtually noise free due to the extreme brilliance of the source and the efficiency of the large detector. This experiment will increase the availability of high quality scattering data by orders of magnitude, enabling research groups access to this method who have previously shied away from the high cost of a laboratory instrument or the considerable effort involved in the application for beamtime.

OP-034

Microstructural insights into the ordering process of the novel cubic polymorph of low-temperature disordered Cu_2ZnSnS_4

S. Bette (Stuttgart/DE), E. Isotta (Trento/IT), B. Mukharjee (Trento/IT), R. E. Dinnebier (Stuttgart/DE), P. Scardi (Trento/IT)

Cu_2ZnSnS_4 (CZTS) is an attractive material for sustainable photovoltaics and thermaelectrics. Some the material"s properties originates in its pronounced polymorphism. All polytypes exhibit a tetrahedral coordination of the metal cations by sulphide anions and corner sharing $(Cu/Zn/Sn)S_{4/4}$ tetrhedra form a 3D- network. These phases only differ in the degree of ordering of cation substructure materializing in different space group symmetries and unit cell metrics (Fig. 1, a).

A novel, sphalerite-like phase with a completely, occupationally disordered cation substructure was obtained by mechanical alloying[1]. This disordered, cubic polymorph is stable up to 663 K, at which it irreversibly transforms into the tetragonal kesterite phase. The mechanical alloying leads to nanocrystalline (Fig. 1, b) disordered, cubic CZTS, which exhibits stacking faults disorder in shape of deformation or twin faults (Fig. 1, c). *Ab-initio* DFT simulations identified twin faults to occur more likely. Investigation by X-ray powder diffraction (XRPD) revealed the Debye-Waller coefficients of the disordered cubic phase to be considerably larger than in the tetragonal polymorph. A*b initio* calculations confirmed these findings and point to a large contribution of disordered Sn cations.

The slowly occurring, irreversible transition from the disordered cubic into the tetragonal phase was investigated by temperature dependent *in situ* XRPD. Annealing of disordered, cubic CZTS leads to a growth of the domains that is associated with a reduction of strain. After the domains exceed a certain size, the ordering of cation substructure starts. This induces a healing of the stacking faults, which the DFT calculations revealed to be energetically less favourable in a structure with cation ordering. Eventually the reduction of the degree of faulting leads to a decrease of long-range strain (Fig. 1, d).

References:

(1) E. Isotta, B. Mukherjee, S. Bette, R. Dinnebier, P. Scardi, IUCrJ (2022), 9, 277.

Figure 1: (a) The different crystal structures of Cu_2ZnSnS_4 (CZTS), (b) SEAD pattern with indexing for CZTS samples from mechanical alloying, (c) Structural motives considered for the microstructure of cubic CZTS. (d) Evolution of cryst. size, strain and disorder during annealing of cubic CZTS.

Fig. 1

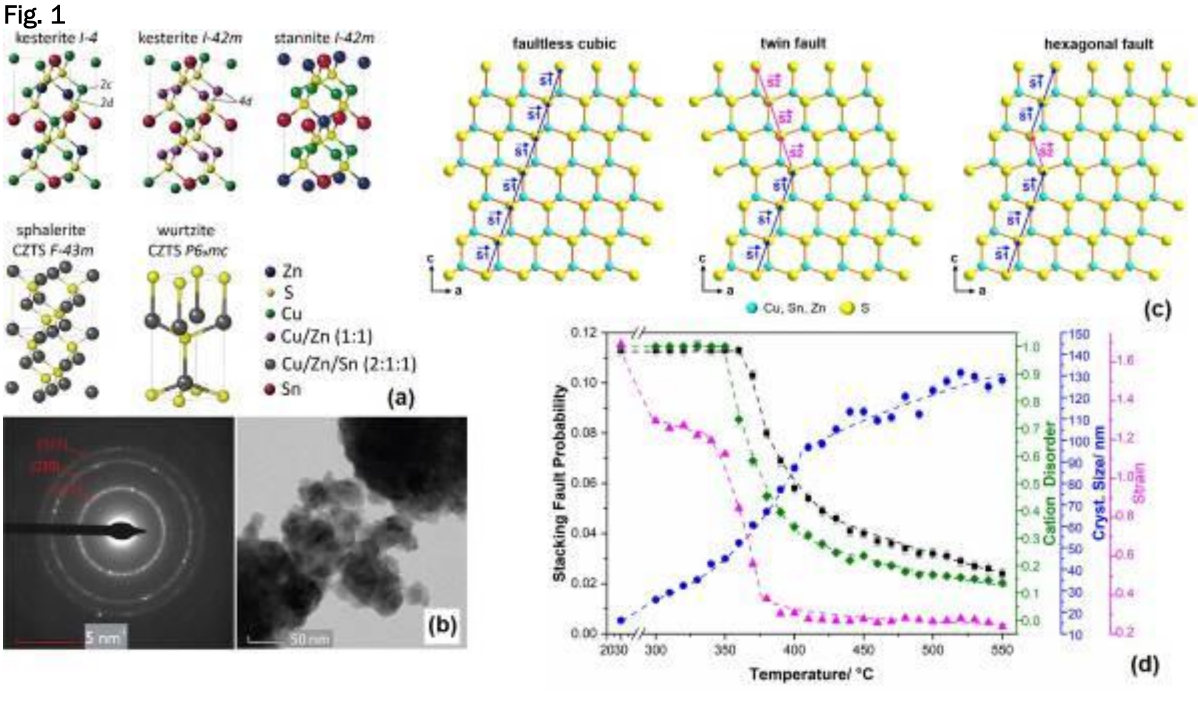

OP-035

Local structure evolution of amorphous sodium tantalate prepared by a sol-gel method investigated by *in situ* crystallization studies

E. Onur Sahin (Mülheim an der Ruhr/DE), S. Zhang (Düsseldorf/DE), C. Scheu (Düsseldorf/DE), C. Weidenthaler (Mülheim an der Ruhr/DE)

The sodium tantalum oxide ($NaTa_xO_y$) system displays a large number of polymorphs in its crystalline form including perovskites with different symmetries, pyrochlore and natrotantite.[1] $NaTa_xO_y$, besides their current applications in electronics, has been shown to act as efficient photocatalysts for water splitting.[2] In this work, the structural evolution of amorphous $NaTa_xO_y$ was examined during crystallization to understand the evolution of the structure at the atomic scale that has a direct effect on the electronic and optical properties. For this purpose, $NaTa_xO_y$ prepared using metal ethoxide precursors was subjected to *in situ* temperature-dependent X-ray total scattering experiments and subsequent pair distribution function (PDF) analysis. The material was examined *ex-situ* by scanning transmission electron microscopy (STEM) and energy dispersive X-ray spectroscopy (EDS) before and after the heat treatment. PDF analysis shows that the material is composed only of short-range ordered clusters in the as-prepared condition. During heating, the PDFs show both natrotantite and perovskite pair correlations, reaching approximately 1:1 ratio (wt%) at 700 °C. The resulting perovskite deviates from the highest symmetry polymorph known to be stable at these temperatures. After heat treatment, a large contribution from the amorphous part is still visible in the XRD pattern as well as in STEM images. Spatially resolved chemical information obtained by STEM and EDS points out the effect of Na distribution on the crystal structure to be formed. While Na-rich regions transform into perovskite, Na-poor regions either transform into natrotantite or stay amorphous. The findings of this work are expected to contribute to the understanding of the structure-performance relationship for this interesting semiconductor material.

References:

(1) T.S. Ercit, F.C. Hawthorne, P. Cerny, *Bull. Minéral.*, 1985, **108**, 541.
(2) T. Grewe, H. Tüysüz, *ACS Appl. Mater. Interfaces*, 2015, **7**, 23153.

OP-036

Finding a measure for the quality of pair distribution functions from in-house total scattering data

K. Krämer (Bremen/DE), T. M. Gesing (Bremen/DE, Bremen/DE), L. Robben (Bremen/DE, Bremen/DE)

Question: Pair distribution function analysis of total scattering data (TS) is a powerful and increasingly popular technique in structure determination of disordered materials. Traditionally these experiments take place at large-scale facilities, providing the necessary radiation intensity and energy. However, since the amount of TS beamlines is limited and the user base is growing, so does the interest in the limits of in-house diffraction data for this purpose.

Currently the main drawback is the low intensity of suitable in-house X-ray sources, which requires measurements to last up to several days. This leads to two questions. 1) What is the minimum measurement time for good quality in-house PDF data? and 2) How reliable are scattering data after a certain measurement period? To approach these issues, we used the statistical error of the total scattering data σI(Q) as a measure for their quality and examined the influence on G(r).

Methods: Assuming a Poisson distribution of detected photons, the error at each angle was determined to be equal to the square root of its respective scattering intensity. This was considered for the sample, the empty sample container and empty instrument. All three errors were propagated to the background corrected sample intensity I(Q). It was necessary to correct the empty container measurement for absorption effects, using the correction proposed by Rouse et al. [1]. Applying the relative error of I(Q) to the total scattering structure function S(Q) we calculated the variance of S(Q) and subsequently the statistical error of the reduced pair distribution function G(r).

Result and Conclusion: Using measurement time as a variable, σG(r) shows a sample specific hyperbolic trend and can be traced during a measurement to assert the statistical certainty of the derived PDF. As such it serves as a quality parameter, suitable for data comparison and optimization of the measurement strategy.

Funding by the DFG within the project RO5995/2-1 is gratefully acknowledged.

References:

(1) K.D. Rouse, et al., Acta Crystallogr. A, 26 (1970), 682-691

Microsymposium 8 | Bio-Crystallography III: New structures and mechanisms

OP-037

Characterization of biohybrid superlattices with single crystal diffraction and small-angle X-ray scattering

T. Beck (Hamburg/DE, Hamburg/DE)

Self-assembly is a key tool for the formation of biomolecular structures, but also for the construction of functional nanomaterials. We have recently established a novel method for the self-organization of biomolecular building blocks and nanoparticles. Here, protein cages, engineered with opposite surface charge, are used as an atomically precise ligand shell for the assembly of inorganic nanoparticles.[1] The assembly of these protein-nanoparticle composites yields highly ordered nanoparticle superlattices with unprecedented precision. The structure of the protein scaffold can be tuned with external stimuli such as metal ion concentration.[2]

Our current work describes the formation of hetero protein structures composed of two different types of protein cages. These two protein cages have different outer diameters and form well-shaped protein crystals. Due to the different cage sizes, nanoparticles and fluorophores as cargo were assembled into novel types of nanoparticle superlattices. We investigated the biohybrid structures with single crystal protein crystallography and single-crystal small-angle X-ray scattering. Functional characterizations are currently carried out, in analogy to recent work with ferritin lattices.[3] Moreover, we used protein crystallography and Rosetta simulations to shed light on the role of individual mutations on the assembly of ferritin lattices.

(1) M. Künzle, T. Eckert, T. Beck, *J. Am. Chem. Soc.* **2016**, *138*, 12731-12734.
(2) M. Künzle, T. Eckert, T. Beck, *Inorg. Chem.* **2018**, *57*, 13431-13436.
(3) M. Lach, C. Strelow, A. Meyer, A. Mews, T. Beck, *ACS Appl. Mater. Interfaces* **2022**, *14*, 10656-10668.

OP-038

Structure and Assembly of the Proline Reductase Complex from *Clostridioides difficile*

C. Behlendorf (Braunschweig/DE), W. Blankenfeldt (Braunschweig/DE)

Introduction: The nosocomial bacterium *Clostridioides difficile* causes thousands of deaths worldwide. Within its highly adaptive metabolism, the so called *Stickland fermentation*, the coupled oxidation and reduction of two amino acids, is to be emphasized. In this context, the reduction of *D*-proline seems to be one of the major ways to obtain energy. There is further evidence for a direct connection between *D*-proline availability and toxin production.

Objectives: The reduction of *D*-proline to 5-aminovalerate is catalyzed by proline reductase Prd, a large ~960 kDa 30-mer-complex composed of three different subunits. These subunits originate from two genes, *prdA* and *prdB*. *prdA* is translated as inactive proprotein. Post-translational processing leads to its cleavage into two subunits with concomitant formation of a pyruvoyl-group that is required for substrate binding. Similar processing is known from many other pyruvoyl-dependent enzymes and generally considered as an autocatalytic reaction. However, pyruvoyl formation and assembly of the proline reductase complex could not be observed *in vitro* until now.

Methods: Heterologous expression of genes associated with proline reductase as well as those potentially involved in the maturation and assembly has been achieved. *In vitro* assays to further investigate the processing reaction have been established. New protein structures could be determined with X-ray crystallography.

Results: A hypothetical protein has been identified as a crucial factor for processing and assembly of proline reductase Prd. Furthermore, the heterologous expression of the complete complex succeeded for the first time. In addition, first crystal structures of accessory proteins with homology to processed PrdA could be determined.

Conclusion: The identification of a novel enzyme involved in the maturation of proline reductase Prd significantly advances our understanding of the enzyme. It also raises doubts about the previously accepted hypothesis of an autocatalytic processing of pyruvoyl-dependent enzymes in general. First crystal structures allow a more detailed view and first statements about the exact mechanism. Furthermore, new possibilities for investigating the enzyme arose through the discovered relationship between maturation and assembly of the complex.

OP-039

Virulence factors of *Pseudomonas aeruginosa* – The Phospholipases

N. Sabharwal (Hamburg/DE), G. Yang (Hamburg/DE), M. Lunelli (Hamburg/DE), U. Sae-Ueng (Hamburg/DE), J. Labhan (Hamburg/DE), M. Kolbe (Hamburg/DE)

Bacterial Phospholipases and sphingomyelinases are enzymes that are involved in the hydrolysis of acyl- and phosphate-esters of phospholipids, generating secondary messengers capable of signal transduction with implications in various cellular processes. Phospholipase C (PLCs) of *Pseudomonas aeruginosa* i.e. PLCH (haemolytic) and PLCN (non-haemolytic) cleave phosphodiester bond in phospholipid backbone; highly homologous with greater than 40% identity and 60% similarity, however differing in terms of substrate specificity. In this project we aimed to characterize the virulent factors i.e. phospholipases using biophysical and structural biology tools. The phospholipases were biophysically characterised using various tools such as mass photometry, circular dichroism, florescence spectrometry, dynamic light scattering and biochemically these were also found active. Furthermore, we were able to solve the structure using X-ray crystallography and Cryo-EM. These phospholipases belong to a novel group of Gram-negative phospholipases. Host specific virulence by PLCs are elicited by including proliferation, differentiation, motility, apoptosis, gene expression, tissue colonization, infection establishment and progression or immune response evasion. However, the exact signalling mechanism for the virulence is still unknown. The biophysical and biochemical characterisation along with the structure solution through this project will provide insights to improve our understating of their mechanism of action.

OP-040

Structural characterization of a cyclic oligonucleotide activated and CRISPR protease triggered antiviral signaling cascade

N. Schneberger (Bonn/DE), H. Chi (St Andrews/GB), K. Blumenstock (Bonn/DE), S. Arau Jakubzik (Bonn/DE), J. Moecking (Bonn/DE), S. Da Vela (Hamburg/DE), J. Schmid-Burgk (Bonn/DE), D. Svergun (Hamburg/DE), M. Geyer (Bonn/DE), M. F. White (St Andrews/GB), C. Rouillon (Bonn/DE), G. Hagelueken (Bonn/DE)

CRISPR antiviral defense systems provide one of the most prominent groups of prokaryotic immune systems and are classified in two classes with a large variety of types and subtypes [1]. In type III CRISPR systems, the use of cyclic oligonucleotides (cOAs) enables a highly complex and versatile immune response upon foreign RNA recognition [2, 3]. These cyclic second messengers normally bind to the CARF domain of special effector proteins and thereby activate them. Numerous effector domains with different functions are known, so far ranging from RNases over transcription regulators to DNases [2]. Computational approaches reported on an unusual effector protein, a membrane-bound "CRISPR associated Lon protease" (CalpL) [4]. Here we present the structural and mechanistical analysis of this first known cOA activated protease and the associated tripartite phage defense system. We were able to solve the structure of CalpL by single-wavelength anomalous diffraction. Unlike predicted, CalpL appears to be a soluble monomeric protein that is activated by a cA4 induced oligomerization which we could show using small-angle X-ray scattering. The activated protease cleaves the CalpT/S complex, consisting of two small proteins that are encoded in the same operon, directly upstream of CalpL. Multiple approaches to investigate the function of CalpT and CalpS finally pointed out striking parallels to bacterial sigma/anti-sigma factor systems. This finding directly connects a type III CRISPR system to the cellular transcription machinery. Our results reveal similarities to the CBASS system [5], recent reports on a CRISPR activated caspase (Craspase) [6] and even to mammalian systems such as the cGAS-STING pathway [7].

(1) Makarova KS, Wolf YI, Koonin EV. **(2018)** Classification and Nomenclature of CRISPR-Cas Systems: Where from Here? *CRISPR J.*
(2) Athukoralage JS, White MF. **(2021)** Cyclic oligoadenylate signalling and regulation by ring nucleases during type III CRISPR defence. *RNA*
(3) Kazlauskiene M, Kostiuk G, Venclovas Č, et al. **(2017)** A cyclic oligonucleotide signaling pathway in type III CRISPR-Cas systems. *Science*
(4) Shmakov SA, Makarova KS, Wolf YI, et al. **(2018)** Systematic prediction of genes functionally linked to CRISPR-Cas systems by gene neighborhood analysis. *Proc Natl Acad Sci.*
(5) Cohen D, Melamed S, Millman A, et al. **(2019)** Cyclic GMP–AMP signalling protects bacteria against viral infection. *Nature*
(6) Hu C, van Beljouw SPB, Nam KH, et al. **(2022)** Craspase is a CRISPR RNA-guided, RNA-activated protease *Science*
(7) Hopfner KP, Hornung V. **(2020)** Molecular mechanisms and cellular functions of cGAS–STING signalling. *Nat Rev Mol Cell Biol*

OP-041

Structure, dynamics and allosteric modulation of the caseinolytic protease P from *Staphylococcus epidermidis*

B. Alves França (Hamburg/DE), V. Srinivasan (Hamburg/DE), H. Rohde (Hamburg/DE), C. Betzel (Hamburg/DE), C. Betzel (Hamburg/DE)

Bacterial Caseinolytic Protease P (ClpP) is a key protein for the development of antimicrobial chemotherapies, as it is involved with different biochemical processes, such as cellular homeostasis and expression of transcriptional factors. To this date, natural and synthetic compounds were identified as modulators of ClpP activity, leading to bacteriostasis by inhibition or causing bacteriocidic self-digestion by a promiscuous intracellular proteolysis reaction [1]. Among the modulators, boronate derivatives play a promising role in the structural and functional studies on ClpP regulation [2]. Despite being known as serine protease inhibitors, when bound to the ClpP catalytic site, they can also enhance peptidolysis and activate proteolysis through an allosteric mechanism [3]. However, since this dual mechanism seems to be organism-dependent [3], further studies with different ClpPs could improve the understanding of how structural aspects can affect the intricate modulation caused by the boronate derivatives.

In this context, the present work proposes an analysis of the interaction between two boronic acid-containing drugs, ixazomib and bortezomib, and ClpP from *Staphylococcus epidermidis*, an opportunistic organism involved in nosocomial infections. *S.epidermidis* ClpP was expressed, purified, crystallized, and complexes of ClpP with the ligands were obtained by both co-crystallization and soaking experiments. Datasets from cryo-cooled crystals of ClpP-ixazomib and ClpP-bortezomib were collected either at P11 or P13 beamlines (PETRAIII/DESY, Hamburg, Germany) to resolutions of 2.4 and 1.7 Å, respectively. Small Angle X-ray scattering (SAXS) data were collected at P12 beamline (EMBL, Hamburg, Germany) to investigate any conformational shift of the ClpP in solution. We also present the results from *in vivo* assays to explore structure-activity relationships, and consequently the relevance of ClpP-boronate complexes for the treatment of microbial infections.

Figure 1: Illustration of ClpP-Ixazomib complex. **A** Front view of the two-stacked heptameric ring conformation. **B** Close-up view of the peptidomimetic ixazomib (backbone in green sticks) covalently bound to the catalytic serine (Ser98) and stabilized by a network of hydrogen bonds.

References:

(1) B. P. Conlon et al., "Activated ClpP kills persisters and eradicates a chronic biofilm infection", Nature, vol. 503, pp. 365-370, 2013.

(2) Y. Ju et al., "Discovery of Novel Peptidomimetic Boronate ClpP Inhibitors with Noncanonical Enzyme Mechanism as Potent Virulence Blockers in Vitro and in Vivo", J. Med. Chem., vol. 63, pp. 3104-3119, 2020.

(3) J. Felix et al. "Mechanism of the allosteric activation of the ClpP protease machinery by substrates and active-site inhibitors", Sci. Adv., vol. 5, pp. 1-18, 2019.

Fig. 1

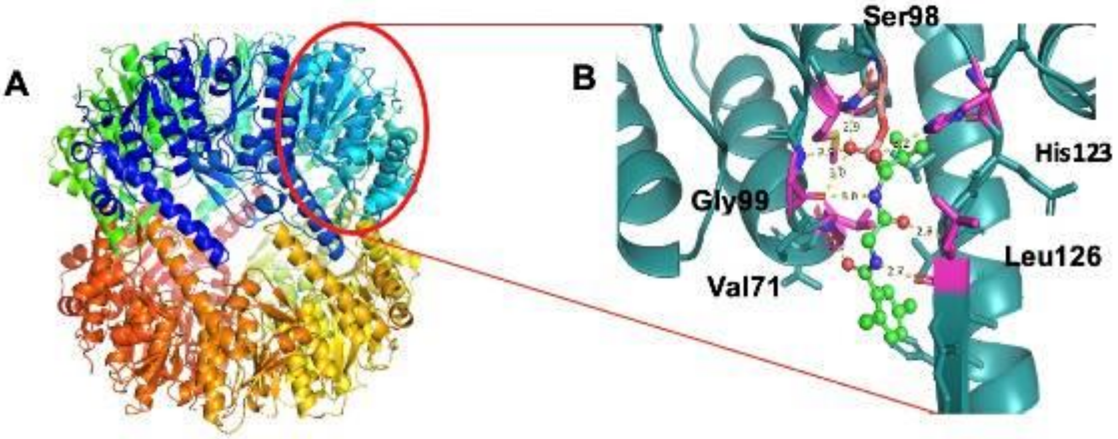

OP-042

Sustainable use of metabolites in glutamine amidotransferases multienzyme complexes

S. Sung (Hamburg/DE), F. Funke (Regensburg/DE), S. Schlee (Regensburg/DE), J. P. Wurm (Regensburg/DE), R. Sprangers (Regensburg/DE), R. Sterner (Regensburg/DE), M. Wilmanns (Hamburg/DE)

Multienzyme systems need to tightly couple their catalytic activities to avoid wasteful consumption of metabolites. A prominent example are glutamine amidotransferases (GATs), comprising 1) a glutaminase for glutamine hydrolysis to produce reactive ammonia and 2) a synthase responsible for the ammonia-mediated incorporation of nitrogen into various metabolites. In all GAT complexes we have investigated so far, glutaminase activity strictly requires the presence of the synthase. Previous findings, which demonstrated contributions of distinct residues of the synthase to complete the glutaminase active site [1] are generally applicable to different GATs, as illustrated by new structures outlined below.

To unravel the mechanism of GAT activation, we have used a combination of static X-ray crystallography, cryo-trapping X-ray crystallography, time-resolved X-ray crystallography, NMR spectroscopy as well as biochemical and biophysical approaches. For the first model enzyme used, the imidazole glycerol phosphate synthase–glutaminase (HisF:HisH) complex, glutaminase activation requires both the presence of glutamine and the synthase substrate. Only once this condition is met, the glutaminase is allosterically activated by a flip of the glutaminase active site oxyanion hole from an inactive to active conformation [2]. In contrast, in the second model GAT system investigated, the aminodeoxychorismate synthase–glutaminase (PabB:PabA) complex, the oxyanion hole is already in an active conformation, irrespective the presence of synthase substrate. Although details on the mechanism of overall activity regulation in aminodeoxychorismate synthase still need to be resolved, our data demonstrate an unexpected level of mechanistic diversity to regulate GAT metabolite consumption by unrelated mechanisms, which is essential for sustainable use of energy-expensive metabolites.

(1) List et al. (2012) Chem. Biol. **19**:1589-99.
(2) Wurm, Sung et al. (2021) Nat. Commun. **12**:2748.

Microsymposium 9 | Extreme/non-ambient and high-pressure conditions I

OP-043

High pressure chemical crystallography: From mineral physics to material sciences

L. Dubrovinsky (Bayreuth/DE), N. Dubrovinskaia (Bayreuth/DE)

The impact of high-pressure studies on fundamental physics and chemistry, and especially on the Earth and planetary sciences, has been enormous. Modern science and technology rely on the fundamental knowledge of matter that is provided by crystallographic studies. Chemical crystallography is a well-established discipline based on single-crystal X-ray diffraction (SCXRD) analysis which enables a structure determination and chemical characterisation. At high pressures, a structure determination based on SCXRD in a diamond anvil cell (DAC) is not that straightforward and until recently was only possible at relatively low pressures up to about 15 GPa. SCXRD analysis was considered inapplicable to materials synthesised at high pressures in a laser-heated (LH) DAC, as the products of chemical reactions are typically multiphase mixtures of microcrystalline solids. About a decade ago, our group pioneered an approach to the SCXRD data collection and analysis for the products of chemical reactions in LHDACS which led to discovery of new materials with unique properties, but it required certain training, crystal-chemical intuition, and experience. Since then we have designed and built new instrumentation to enable sophisticated *in situ* experiments in house and on synchrotron radiation facilities (e.g., single-crystal diffractometer coupled with double-sided laser heating system and sub-micrometer focusing setup for high-pressure crystallography at the Extreme Conditions beamline at PETRAIII, Germany) and created a powerful software (the Domain Auto Finder (DAFi) program) to be used for studies of multiphase polycrystalline and microcrystalline (powder) materials. Our efforts have pushed the range of static pressures achievable in a DAC up to 1 TPa and enabled single-crystal X-ray diffraction experiments at such extreme conditions. Structural studies at simultaneous high pressures of over ~200 GPa and temperatures of several thousand degrees have also become possible. This has led to remarkable findings in mineral physics, solid state physics, and chemistry at extreme conditions: a discovery of numerous, often unpredictable materials and an insight into possible physical phenomena underlying their formation, chemical bonding, and properties. We illustrate application of new methodology for simultaneous high-pressure and high-temperature single crystal diffraction studies using examples of investigations of chemical and phase relations in the carbonates, silicates, nitrides, and hydrides.

OP-044

Lawsonite's phase diagram: *In-situ* HP, HT diffraction study

D. Druzhbin (Grenoble/FR), A. Rosenthal (Grenoble/FR, Canberra/AU), W. Crichton (Grenoble/FR)

The hydrous phase lawsonite ($CaAl_2Si_2O_7(OH)_2{\cdot}H_2O$) is a mineral found in high-pressure metamorphic rocks and formed under high pressure (P) and low temperature (T) conditions, which are common in subduction zones. Its capacity to retain water molecules and hydroxyl groups in its structure at high P-T (up to 12 GPa and 1200 K) is the reason for its heightened interest [Baur, 1978; Schmidt, 1995; Martin et al., 2014]. In this regard, lawsonite plays a unique function in the transport of H_2O from the earth's surface to the mantle in subducting slabs [Pawley, 1994; Schmidt and Poli, 1994].

At ambient conditions, lawsonite is orthorhombic *Cmcm*. At pressures exceeding 9 GPa, the compressibility of lawsonite decreases significantly due to the strengthening of the hydrogen-bonding between hydroxyl groups and framework oxygen atoms. A modest intraframework shift along the AlO_6 - octahedral chains results in the creation of a low-symmetry monoclinic $P2_1/m$ phase [Daniel et al., 2000; Pawley and Allan, 2001; Boffa-Ballaran and Angel, 2003; O"Bannon 2017].

In this current work, we have conducted high-P high-T synchrotron *in-situ* angle dispersive x-ray diffraction in multianvil apparatus experiments at ID06LVP, ESRF, on natural lawsonite at pressures up to ~12.0 GPa and 1000 K to study its polymorphism. We report lawsonite"s HP-HT phase diagram and present evidence of a more complex picture of the phase transitions exhibited by natural lawsonite.

OP-045

The effect of Al on the post-stishovite transition of H_2O-bearing stishovite: Insights from in-situ XRD and ultrasonic interferometry

A. Rosenthal (Grenoble/FR, Canberra/AU), W. Crichton (Grenoble/FR), A. Thomson (London/GB), J. Brodholt (London/GB), D. Druzhbin (Grenoble/FR), R. Myhill (Bristol/GB), R. Huang (London/GB)

Al-bearing stishovite and, later, post-stishovite are among the chief hydrogen-bearing phases in subducted oceanic crust (eclogite) at lower mantle conditions[1], being able to carry up to ~0.3 wt. % of H_2O[1-4]. H_2O-bearing Al-stishovite was recently suggested to cause seismic discontinuities and heterogeneities in the deep Earth's lower mantle at ~1000 km depth[5].

The incorporation of Al into stishovite leads to significant changes to its phase diagram and ability to take up H_2O[5,6]. For instance, it halves the pressure required for its rutile- to $CaCl_2$-type transformation, which exhibits significant elastic softening and may be seismically observable[5,6].

A range of defective stishovite samples were synthesized between 15-32 GPa at ~1200 °C from glasses using 10/5, 10/4 and 7/3 multianvil assemblies. Recovered samples were double-polished (~0.5 mm thick) and quantitatively analysed by EPMA. Combined in-situ X-ray diffraction and ultrasonic interferometry, using 10/4 and 7/3 geometries, were conducted at ID06-LVP of the ESRF to ~ 32 GPa and 1800 K. In highly defective samples the onset of the transition to post-stishovite was accompanied by significant softening of shear wave velocities V_S. Therefore, the effect of Al- and H_2O-defects on the acoustic velocities of stishovite and an estimate of the role of defects in controlling the transformation pressure to the post-stishovite phase were assessed.

This study provides density and sound velocity measurements and thus, enable better experimental constraints of bulk elastic properties and their P and T derivatives of Al-H_2O-bearing stishovite at mantle-relevant P, T. This study extends information essential to the interpretation of the seismic observables and contribute to more complete modelling of eclogitic bodies inside the Earth's deep mantle.

(1) The study is supported by MSCA-IF 898169 "ELASTIC" to AR.
(2) Litasov et al. (2007) *EPSL* **262**, 620-634.
(3) Irifune & Ringwood (1993) *EPSL* **117**, 101-110.
(4) Litasov & Ohtani (2005) *PEPI* **150**, 239-263.
(5) Ono et al. (2001) *EPSL* **190**, 57–63.
(6) Lakshtanov et al. (2007) *PNAS* **104**, 34, 13588-13590.
(7) Lakshtanov et al. (2005) *Phys Chem Miner* **32**, 466–470.

OP-046

Pressure-induced solid-state amorphization of SnI_4 revisited

K. Fuchizaki (Matsuyama/JP)

SnI_4 undergoes solid-state amorphization (SSA) at about 15 GPa upon compression.1) This fact was a starting point for a series of our subsequent studies, which revealed that the pressure-induced SSA is only one side of the polyamorphic nature exhibited by SnI_4. However, we are still unaware of how SnI_4 transforms from the ambient-pressure crystalline phase, CP-I, to the closed-packed crystalline phase, CP-III, via amorphization because the structure of the intermediate-pressure modification, CP-II, has not been solved yet. The metastable state for CP-II could be the amorphous state called Am-I, more strictly, the low-pressure amorphous state of Am-I.2) Revealing the structural relationship between CP-II and Am-I would thus be a critical piece of the jigsaw puzzle.

The purpose of this presentation is twofold. The first one is to promote a technique called Combined Angle- and Energy-dispersive Structural Analysis and Refinement (CAESAR) devised by Wang *et al*.3) to investigate the structure in the pressure region in question utilizing synchrotron x-ray diffraction. The second point is to have an opportunity to discuss how to solve a structure in a partially crystalline state.

A diamond-anvil-cell (DAC) technique has been commonly used to investigate the relevant pressure region. We recently approached the region using the CAESAR technique with a multianvil press of DIA-6 type, thereby overcoming the problems (such as a measurable sample quantity and non-hydrostaticity) associated with DAC measurements. At this moment, MAX80 installed in beamline NE5C, KEK-AR would probably be the only apparatus that could be used for CAESAR measurement in a 6—6 compression mode. The resultant intensity distribution at a fixed photon energy, say 54.8604 keV, gives the typical angle-dispersive diffraction pattern, as depicted in Fig. 1, which could be that for CP-II. Surprisingly, most of the peaks are indexed based on Pa3, the structure of CP-I, except only for a few peaks designated by solid triangles. (Those specified by open triangles were reported in previous studies.4),5)) This situation, reflecting the strong first-order nature of the CP-I-to-CP-II transition, makes it difficult to determine the structure of CP-II. A variation of the peak distribution against pressure changes along the 640 K isotherm revealed the two transition pressures, 5 and 10 GPa, at which the distribution changes qualitatively. In our previous view,4),6) the lower pressure should correspond to the transition point. We speculate at this moment, based on thermodynamic consideration, that it could be the spinodal point of CP-II.

We tried to collect the scattering intensities to investigate the local structure at 533 K and 15.22 GPa, just like measuring a liquid structure.7) Figure 2, exhibiting an aspect of partial crystalline state, is the converted structure factor plotting against wavenumber. We are currently exerting ourselves to simulate the real-space structure with the help of reverse Monte Carlo analysis. We believe that the local structure could be sheared with both amorphous and crystalline states, thereby hinting at how to solve the CP-II structure.

(1) Y. Fujii, M Kowaka and A. Onodera, J. Phys. C **18**, 789 (1985).
(2) K. Fuchizaki, A. Ohmura, H. Naruta, and T. Nishioka, J. Phys.: Condens. Matter **33**, 365401 (2021).
(3) Y. Wang, T. Uchida, R. von Dreele, M. L. Rivers, N. Nishiyama, K. Funakoshi, A. Nozawa, and H. Kaneko, J. Appl. Cryst. **37**, 947 (2004).
(4) N. Hamaya, K. Sato, K. Usui-Watanabe, K. Fuchizaki, Y. Fujii, and Y. Ohishi, Phys. Rev. Lett. **79**, 4597 (1997)
(5) B. Grocholski, S. Speziale, and R. Jeanloz, Phys. Rev. B **81**, 094101 (2010).
(6) K. Fuchizaki, N. Hamaya, T. Hase, and Y. Katayama, J. Chem. Phys. **135**, 091101 (2011).
(7) K. Fuchizaki, T. Hase, A. Yamada, N. Hamaya, Y. Katayama, and K. Funakoshi, J. Chem. Phys. **130**, 121101 (2009).

Fig. 1

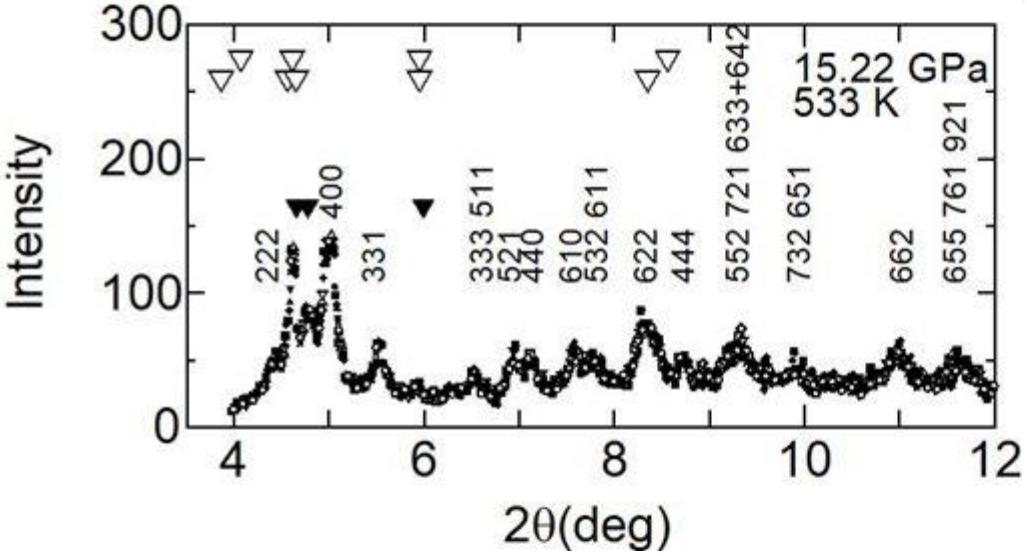
Intensity
2θ(deg)
15.22 GPa
533 K
222
400
331
333 511
521
440
610
532 611
622
444
552 721 633+642
732 651
662
655 761 921
0
100
200
300
4
6
8
10
12

Fig. 2

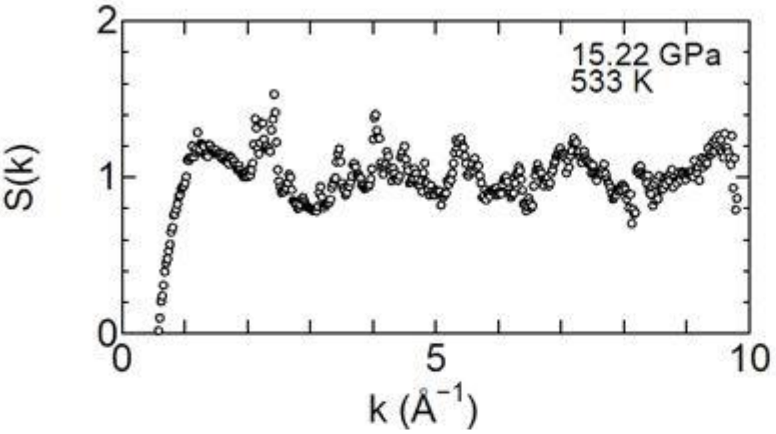
S(k)
k (Å^{-1})
15.22 GPa
533 K
0
1
2
0
5
10

OP-047

Swift heavy ion irradiation of nano-structured bismuth pressurized in diamond anvil cells

C. Schroeck (Frankfurt am Main/DE, Darmstadt/DE), I. Tzifas (Darmstadt/DE), L. Bayarjargal (Frankfurt am Main/DE), K. O. Voss (Darmstadt/DE), I. Schubert (Darmstadt/DE), M. Wagner (Darmstadt/DE), W. Sigle (Stuttgart/DE), I. Armstrong-Cowell (Darmstadt/DE, Darmstadt/DE), M. E. Toimil-Molares (Darmstadt/DE), C. Trautmann (Darmstadt/DE, Darmstadt/DE), B. Winkler (Frankfurt am Main/DE)

The simultaneous exposure of materials to multiple extreme conditions is a field of increasing interest in modern high pressure (HP) research. Concomitantly applying HP using diamond anvil cells (DACs) and irradiation with swift heavy ions (SHI) of GeV energies represents a worldwide unique approach, that has been pioneered at GSI Helmholtz Centre Darmstadt. Ground-breaking experiments revealed new effects such as the generation of new phases far from thermodynamic equilibrium or the stabilization of HP phases at ambient conditions [1,2].

This report presents our activities to exploit intrinsic properties of nanomaterials that are beneficial for manipulating HP phase diagrams in order to establish nano-structuring as an additional tool to explore and promote ion-induced effects. As material of interest we selected bismuth (Bi), due to its complex and well-characterized HP phase diagram [3] (Fig.1) and its sensitivity to SHI irradiation [4]. We fabricated Bi-nanowire networks (Bi-NWNWs) with a diameter of 35 nm by electrodeposition in etched ion-track membranes [5] and irradiated samples at HP using 238-U ions of up to 100 GeV kinetic energy. Ion-induced effects were investigated applying in-situ Raman spectroscopy and offline synchrotron-XRD. Complementarily, HP studies on pristine Bi-NWNWs and ion-irradiation experiments at ambient pressure conditions were performed. Here, we will discuss the impact of ion-irradiation on the HP-behaviour of nano-structured and bulk Bi.

The authors gratefully acknowledge funding and beamtime provided by the GSI Helmholtz Centre, as well as support during the synchrotron beamtime at PETRA-III, DESY (Hamburg, Germany).

(1) Glasmacher, U.A. et al., PHYS REV LETT, 96(19), 200), p. 195701
(2) Lang, M. et al., NAT MAT, 8(10), 2009, p. 793
(3) Ono, S. et al., HIGH PRESSURE RES, 38(4), 2018, p. 414
(4) Dufour, C. et al., J PHYS-CONDENS MAT, 5(26), 1993, p. 4573
(5) Wagner, M.F.P. et al., ADV ELECTRON MATER, 7(3), 2021, p. 2001069

Figure 1: a) Equilibrium phase diagram of bulk-Bi (adapted from [3]), b) pristine Bi-NWNW (own work).

Fig. 1

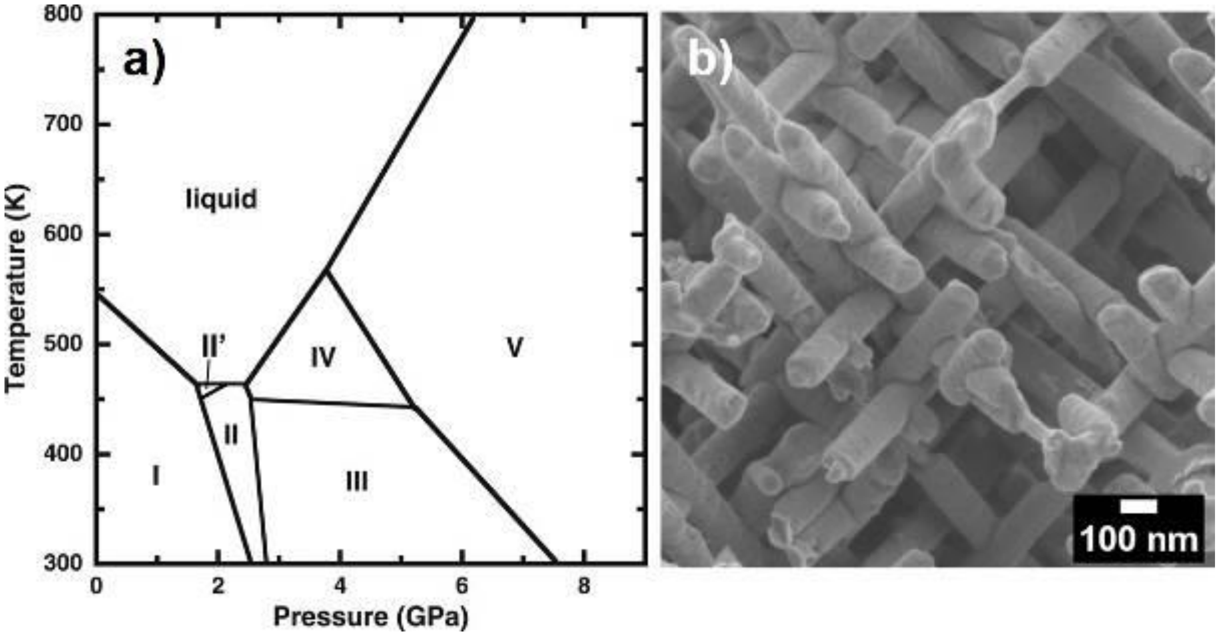

OP-048

Teaching crystallographic symmetry online

M. I. Aroyo (Leioa/ES), E. Kroumova (Bilbao/ES), G. de la Flor (Karlsruhe/DE)

The aim of this contribution is the brief presentation of two websites, namely, the *Symmetry Database* (https://symmdb.iucr.org/) and the *Bilbao Crystallographic Server* (https://www.cryst.ehu.es), and their potential in the online teaching of crystallographic symmetry.

The *Symmetry Database* is included in the online edition of *International Tables for Crystallography*, while the *Bilbao Crystallographic Server* is a website that can be used free of charge from any computer with a web browser via the Internet. Both web sources grant access to the space and point groups crystallographic databases along with more complex programs to facilitate a better understanding of fundamental crystallographic concepts, and the in-depth study of symmetry relations between space groups and their applications in crystal-structure relationships, phase transitions, and domain-structure analysis. The crystallographic databases expand and complement the symmetry information provided in the print editions of *International Tables for Crystallography* Vol. A [1], *Space-group Symmetry*, and Vol. A1, *Symmetry relations between space groups* [2]. Help pages briefly explain the crystallographic data and the functionality of the programs. Interactive programs permit not only the visualization of symmetry elements of crystallographic point and space groups but also the teaching of essential symmetry concepts.

(1) The presentation of the databases and programs offered by the *Symmetry Database* and the *Bilbao Crystallographic Server* will be accompanied by case studies illustrating the capacity and efficiency of the online tools in the teaching of crystallographic symmetry.

(2) [1] *International Tables for Crystallography* (2016). Volume A, *Space-Group Symmetry*, 6th ed., edited by M. I. Aroyo. Chichester: Wiley.
(3) [2] *International Tables for Crystallography* (2010). Volume A1, *Symmetry Relations between Space Groups*, 2nd ed., edited by H. Wondratschek & U. Müller. Chichester: John Wiley & Sons.

OP-049

X-ray powder diffraction in education

R. E. Dinnebier (Stuttgart/DE), P. Scardi (Trento/IT)

A collection of user-friendly, interactive, and freely distributable Mathematica (Wolfram Research, 2022) teaching scripts for visualizing various contributions to the peak profile and peak intensity in a powder diffraction pattern in terms of physical models was developed. In particular, the so-called "Manipulate" command is extensively used to visualize the impact of parameters in an interactive manner. When possible, parameter values from real-life examples are given as the default inputs. The idea is to "learn by doing"; one may gain intuition for how a given mathematical model performs for describing diffraction peaks in an experimental powder pattern and what are the limitations of said model. Every model is an oversimplification of the underlying physics, but different models can be useful for studying various phenomena or increasing the precision of the investigation.

The first collection of scripts deals with the various contributions to the peak profile in a powder diffraction pattern[1] while the second set of scripts visualizes the complex atomic form factor for angular and energy dispersive X-ray diffraction and the displacement factor due to thermal motion, as well as various correction factors for step-scan and integrated intensities (Fig. 1). In addition, the intensity distribution of a powder pattern is demonstrated for a nanocrystalline material, following two alternative approaches based on: (i) structure factor and common volume function (CVF), including the effect of small angle scattering for spherical particles, and (ii) total scattering from a single crystallite, with atomic distances used in the Debye scattering equation (DSE).

Figure 1: Examples of two scripts dealing with the Debye-Waller factor and crystallite size contributions to the peak profile.

(1) *R. Dinnebier and P. Scardi . J. Appl. Cryst. (2021). 54, 1811-1831 (Open Access)*

Fig. 1

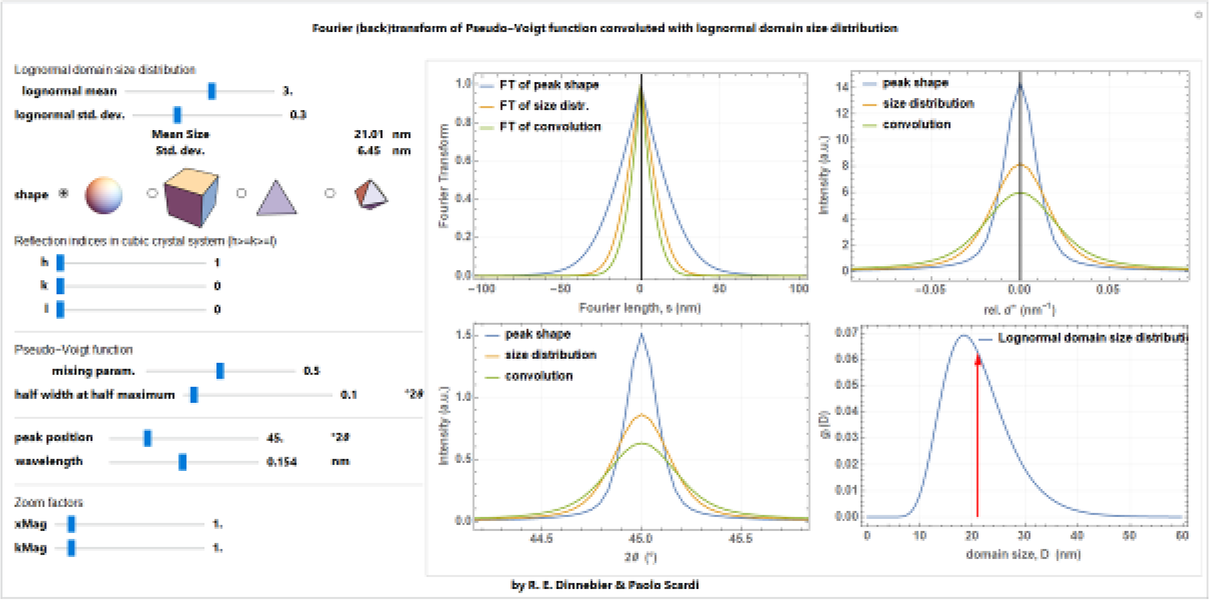

Lognormal domain size distribution
lognormal mean 3.
lognormal std. dev. 0.3
Mean Size 21.01 nm
Std. dev. 6.45 nm
shape ● ○ ○ ○

Reflection indices in cubic crystal system (h>=k>=l)
h 1
k 0
l 0

Pseudo-Voigt function
mixing param. 0.5
half width at half maximum 0.1 °2θ

peak position 45. °2θ
wavelength 0.154 nm

Zoom factors
xMag 1.
kMag 1.

Fig. 2

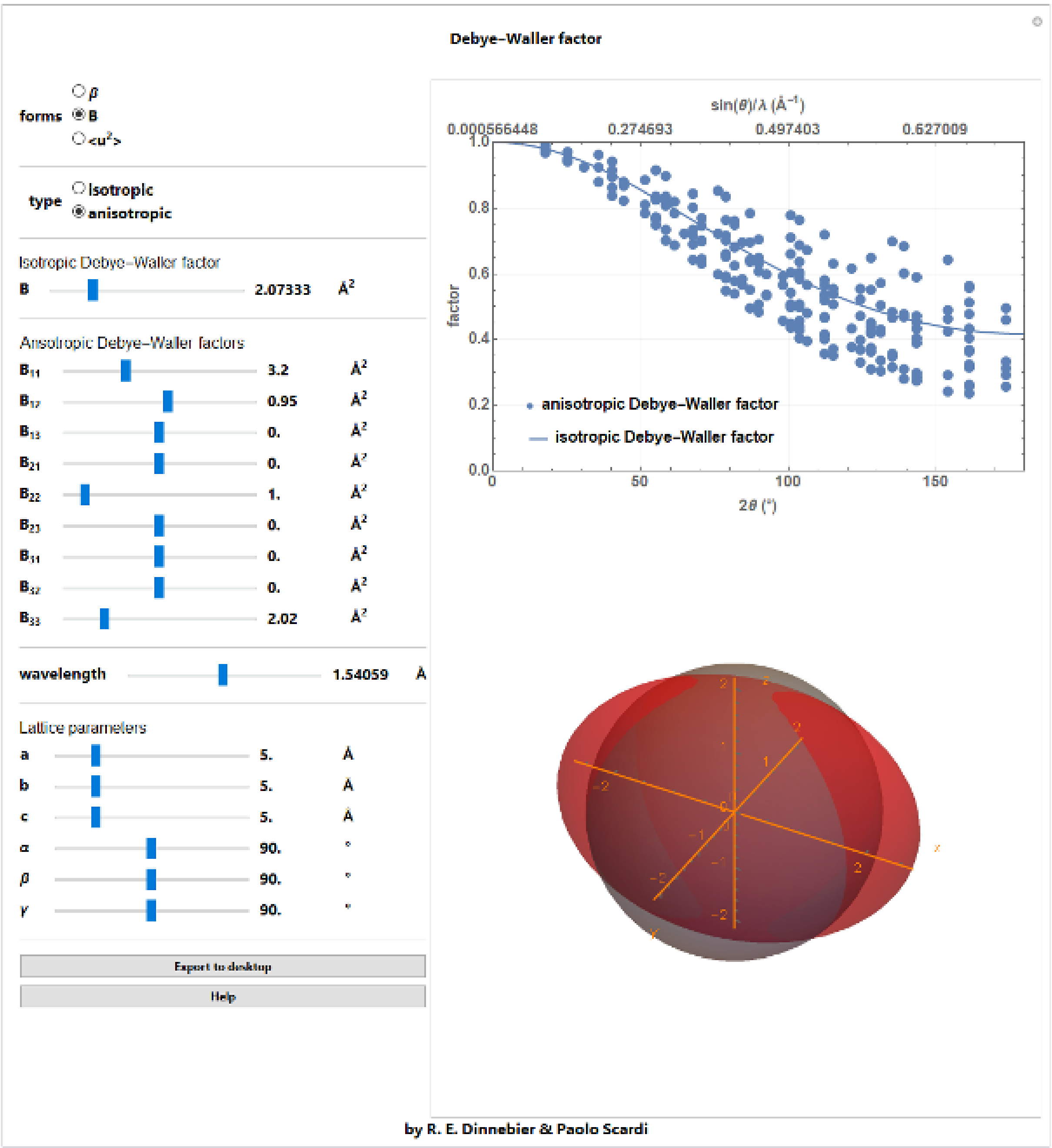

Debye–Waller factor

forms ○ β ● B ○ $\langle u^2 \rangle$

type ○ isotropic ● anisotropic

Isotropic Debye–Waller factor

B 2.07333 Å^2

Anisotropic Debye–Waller factors

B_{11} 3.2 Å^2
B_{12} 0.95 Å^2
B_{13} 0. Å^2
B_{21} 0. Å^2
B_{22} 1. Å^2
B_{23} 0. Å^2
B_{31} 0. Å^2
B_{32} 0. Å^2
B_{33} 2.02 Å^2

wavelength 1.54059 Å

Lattice parameters

a 5. Å
b 5. Å
c 5. Å
α 90. °
β 90. °
γ 90. °

by R. E. Dinnebier & Paolo Scardi

OP-050

Life history reconstruction from tooth enamel of the medieval population in lower Saxony

J. Storsberg (Essen/DE), K. Loza (Essen/DE), I. Heske (Göttingen/DE), M. Epple (Essen/DE)

Introduction: Enamel is the hardest material of the human body. It is arranged in cylindrical bundles of hydroxyapatite crystallites [1]. The Gevensleben burial ground was used as an early Christian cemetery in the 8th-10th century. It represents a source for the life of the ordinary population of the early Middle Ages in Lower Saxony.

Objectives: During the formation of enamel different physiological influences leave an impact on the structure. There are lines that can be analysed representing circadian and weekly rhythms. Moreover, systematic disturbances like malnutrition, metabolic diseases, or fever show an anomalous arrangement of the enamel prisms [2].

Materials & methods: For this purpose, we selected 30 teeth sets from 10 individuals buried in Gevensleben. Each tooth was embedded in epoxy resin for protection and then cut using a low speed saw. The cutting surface was examined using optical microscopy and scanning electron microscopy as well as energy-dispersive X-ray spectroscopy to analyse the chemical composition of the dental enamel and powder diffraction for a structural characterization.

Results: The childhood years of the individuals were reconstructed which confirms the assumption drawn by anthropologists that the children in this population were weaned at around 3 years of age. Furthermore, the chemical composition of the archaeological teeth was compared to modern and it was shown to remain constant.

Conclusion: Since teeth are often one of the few human remains found in archaeological excavation sites. The analysis of these structures can be used to reconstruct life history of individuals. Archaeological and anthropological investigations have already revealed information about the people buried there which matches with these findings.

(2) MC Maas and ER Dumont, Evolutionary Anthropology: Issues, News, and Reviews 8 (4), 133 (1999).
(3) *Ten Cate's Oral Histology (Eighth Edition)*, edited by Antonio Nanci (Mosby, St. Louis (MO), 2013), pp. 122.

OP-051

Structural features of traditional background less ornaments of near East and Central Asia. Modern tessellations by Imamaddin Amiraslan

I. Amiraslanov (Baku/AZ)

In our modern times, there are few people who do not familiar the extremely interesting pictures without a background, which are called tessellation and became famous in the world as the art of M.C.Escher (Fig 1a). We know that dozens of cities in the Middle East and Central Asia, especially in architectural monuments, have mosaic patterns consisting of geometric figures (Fig 1b), as well as thousands of interesting backgroundless ornaments built with the use of Arabic graphics as pattern elements (Fig 1c). Many do not pay attention to the fact that the style of constructing these historical ornaments and Escher's modern tessellation art, made from stylized figures of living objects, are completely identical.

Figure 1: a) Tessellation by Escher, b) Backgraundless geometric ornament, c) Backgraundless colligraphy using arabic inscription.

The preserved architectural monuments and numerous archaeological finds confirm that the creative style based on the absence of background is thousands of years old. The presentation will provide extensive information about the classification, historical evolution and geographical distribution of such ornaments. At the same time, examples of tessellation created by Imameddin Amiraslan (author) will be exhibited. As an example, two of them are shown below (Fig 2).

Figure 2: Tessellation by Imamaddin Amiraslan:

(1) a) 6-fold peagens (P6-plane group),
(2) b) Aperiodic tile with 5-fold symmetry (Penrose tile, Quasicrystal)

Fig. 1

Fig. 2

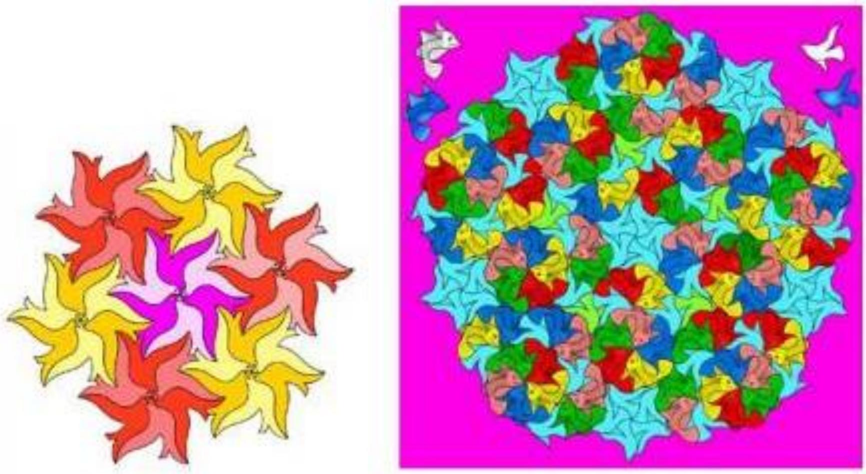

Microsymposium 11 | Young Crystallographers: Lightning talks

LT-01

Towards an understanding of the OAS-Based innate immune signaling: The role of the positively charged residues in the product release channel

P. Kats (Hannover/DE), X. Zhou (Hannover/DE), J. Wiebe (Hannover/DE), O. Zeymer (Hannover/DE), J. Lohöfener (Hannover/DE), N. Steinke (Hannover/DE), P. Baruch (Hannover/DE, Hannover/DE), R. Hartmann (Aarhus/DK), D. J. Manstein (Hannover/DE, Hannover/DE), R. Fedorov (Hannover/DE, Hannover/DE)

The innate immune sensors activate interferon-driven antiviral responses upon recognition of PAMPs and serve as a rheostat for the metabolic activity of the microbiota and its exposure to diet, xenobiotics, and infections. The ability to modulate innate immune sensors opens new ways to novel antiviral and anti-inflammatory drugs and therapies against cancer and aging-associated metabolic, neoplastic, autoimmune, or autoinflammatory disorders. The innate immune sensor 2'-5'-oligoadenylate synthetase (OAS) is among the most promising targets for developing new antivirals. In light of the recent discoveries of the crucial role of OAS in protection against COVID-19 infection [1], the activation of OAS by small-molecule agents is of particular interest for anti-covid therapies. OAS belongs to the large and diverse superfamily of nucleotide triphosphate transferases (NTPTs) which catalyze key cellular processes in all kingdoms of life. A similar mechanism of catalysis in NTPTs is ensured via a highly conserved structure of the active site. Targeting active sites of NTPTs may interfere with other important biological processes through unspecific inhibition (cross-reactivity). At the same time, allosteric mechanisms facilitating activity regulation, and the exchange of reaction components are often specific for each enzyme. Allosteric effects thus can be used to avoid cross-reactivity issues and develop specific activity modulators of the innate immune sensors. An important prerequisite to achieving this goal is a comprehensive structural and mechanistic description of the enzymatic activity cycle.

Towards this end, we established earlier the detailed mechanisms of nucleic acid-induced activation of OAS1, the individual roles of nucleic acid and substrates, and the sources of 2'-specificity of product formation [2]. In our recent kinetic crystallography studies, we observed the series of metastable intermediate states associated with the exchange of reaction components of OAS1. We combined the analysis of these intermediate states with structure analysis, computational studies, and mutagenesis/activity tests to gain new insights into the OAS product release mechanism. Here we report the effect of positively charged residues in the OAS product release channel on the protein *in vitro* activity. With this, we explain the role of those residues for the signaling molecules 2'-5'-oligoadenylates release. Since the product release determines the initial concentration of oligoadenylates that activate the RNase-L immune pathway, our findings shed light on the fundamental mechanism of the rate-limiting steps of the innate immune signaling and provide useful information for the development of OAS allosteric activity modulators.

1. Zhou *et al*. A Neanderthal OAS1 isoform protects individuals of European ancestry against COVID-19 susceptibility and severity. Nat. Medicine. 27:659-667 (2021).
2. Lohöfener *et al*. The Activation Mechanism of 2'-5'-Oligoadenylate Synthetase Gives New Insights Into OAS/cGAS Triggers of Innate Immunity. CELL Structure. 23(5):851-862 (2015).

LT-02

Mono- and heterometallic REE heptafluorobutyrates as single-source precursors for NaLnF$_4$ thin film deposition

A. Shevchenko (Stuttgart/DE), D. Blinnikova (Moscow/RU), S. Bette (Stuttgart/DE), A. Anosov (Moscow/RU), D. Tsymbarenko (Moscow/RU)

The complex fluoride NaYF$_4$ is considered to be one of the most promising inorganic host matrixes for up-conversion luminescence (UL) phenomena. In the last few decades, it has been extensively studied in powdered and nanoparticulate forms [1]. UL could be used to enhance modern photovoltaic cells by converting the near infrared part of the solar spectrum into the visible one, but this would require deposition of the fluorides as thin films. Metal-organic chemical solution deposition (MOCSD) method is a cheap and easily expandable method that would require specific precursors.

In this work, we present structural features and thermal behavior of rare-earth heptafluorobutyrates – potential precursors for the MOCSD method.

The synthesis of individual compounds was carried out by reaction between stoichiometric amounts of heptafluorobutyric acid (Hhfb) and metal oxides or carbonates followed by solvent evaporation. The heterometallic NaY(hfb)$_4$ salt was prepared by co-crystallization of corresponding individual salts from aqueous solution. All metal heptafluorobutyrates were characterized by TG, FTIR, and VT-PXRD, which helped to identify their chemical compositions (incl. hydration states) and thermal behaviors. Yb and Sc compounds were additionally studied by single-crystal XRD, providing an interpretation of the observed VT-PXRD data. All Ln(hfb)$_3$(H$_2$O)$_2$ (Ln = Y, Lu, Yb, Tm, Er, Ho, Tb, Eu) crystallize with space group symmetry $P2_1/c$ forming wiggly chains of Ln^{3+} ions that are straightened out upon dehydration through heating (Fig. 1). Anhydrous Sc salt crystallizes from aqueous solution and is isostructural to the dehydrated REE analogs (Fig. 2). At higher temperatures (>130 °C) all REE heptafluorobutyrates transform into a trigonal modification with disordered trifluoromethyl groups.

In summary, the evolution of an interesting crystal system of REE heptafluorobutyrates with several phase transitions was described over a wide temperature range, which provided an opportunity to control phase purity of the precursors and a deeper understanding of their decomposition process.

Figure 1: Representation of Yb^{3+} chain in the Yb(hfb)$_3$(H$_2$O)$_2$ salt.

Figure 2: A chain of Sc^{3+} ions in an anhydrous Sc(hfb)$_3$ salt.

References:

(1) M. K. Mahata. Luminescence - An Outlook on the Phenomena and their Applications. IntechOpen, 2016. https://doi.org/10.5772/65118

Fig. 1

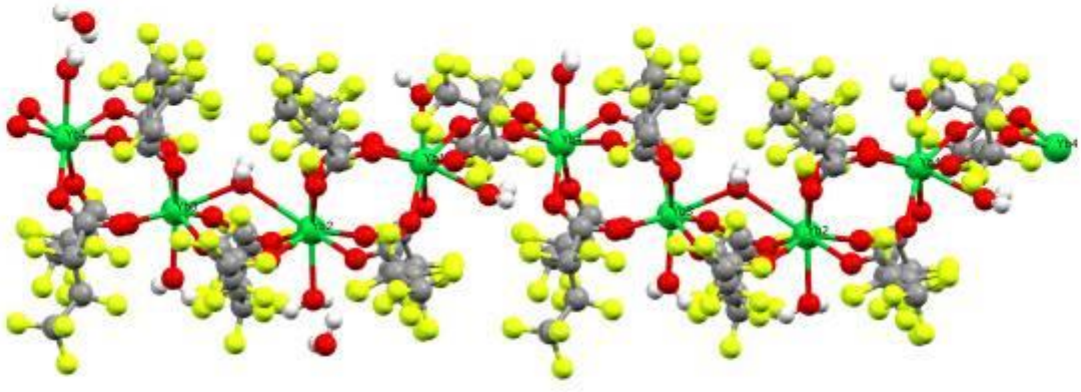

Fig. 2

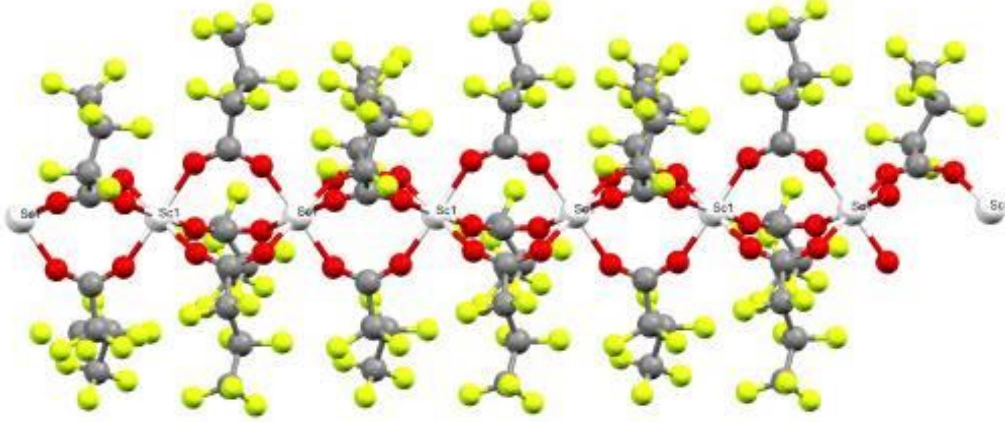
Sc1
Sc1
Sc1
Sc1
Sc1
Sc1
Sc1
Sc1

LT-03

High-pressure synthesis of ternary nitrides in Na-W-N system

N. Martynova (Cologne/DE), E. Bykova (Bayreuth/DE), T. Fedotenko (Hamburg/DE), L. Dubrovinsky (Bayreuth/DE), M. Bykov (Cologne/DE)

Transition metal binary and ternary nitrides are currently attracting attention due to their functional properties. Among transition metal nitrides, tungsten nitrides possess unique high hardness and toughness, high thermal and chemical wear stability and resistance, catalytic activity, high incompressibility, electrochemical stability, high conductivity. These properties of tungsten nitrides allow using them in various technological applications. Despite much promise in the functionality of nitride materials preparation of these nitrides is challenging because the incorporation of nitrogen into tungsten lattice is thermodynamically unfavorable at atmospheric pressure. Application of pressure is an effective approach to overcome the energy barrier and synthesize new nitride phases.

In this work we studied the formation of novel phases in ternary Na-W-N system at high-pressure high-temperature conditions. Sodium azide mixed with the tungsten foil was loaded inside a sample chamber of the BX90 diamond anvil cell equipped with Boehler Almax type diamonds with 200-µm culet size. The novel phases were crystallized after laser heating of the initial mixture at pressures of 5-11 GPa. Products of chemical reaction were studied by single-crystal X-ray diffraction at the beamline P02.2 of Petra III at DESY. The laser heating at 5 GPa resulted in the formation of the novel ternary NaW2N3 nitride with a hexagonal crystal structure with the space group *P*63/*mmc*. The structure of NaW2N3 is built of columns of WN6 prisms connected with each other through edges and forming the hexagonal layers of W2N3 with intercalated Na atoms. NaW2N3 is stable under normal conditions.

At higher pressures we synthesized a novel compound Na6WN4. Na6WN4 crystalizes in a monoclinic crystal structure with the space group *P*21/*n*. The structure is built of isolated WN4 tetrahedra separated through Na atoms. Na6WN4 phase is not stable under normal conditions and was oxidized during decompression to ambient conditions with the formation of sodium tungstate.

The new approach of high-pressure synthesis of larger amount of sample was suggested and tested in this work using a new type of large-volume diamond anvil cell.

LT-04

Low-Temperature Measurement of the Unexpected Hydrate $Cs_2[B_{12}H_{12}] \cdot 2\ H_2O$

R. Aghaei Hakkak (Stuttgart/DE), T. Schleid (Stuttgart/DE)

The *closo*-dodecaborate anion $[B_{12}H_{12}]_2^-$ is one of the most stable structures among all hydroboron clusters and well known since the 1960"s. The crystal structure of the cesium salt has been determined in 2000 be isotypic with $K_2[B_{12}H_{12}]$ [1] adopting the cubic space group *Fm-3 (a* = 1128.12(7) pm, *Z* = 4) [2]. The single crystal was obtained by fast crystallization of a supersaturated aqueous solution of $Cs_2[B_{12}H_{12}]$. The collected crystal from the diluted solution was not stable in air at room temperature, so due to that the single crystal X-ray diffraction of what turned out to be $Cs_2[B_{12}H_{12}] \cdot 2\ H_2O$ was performed at 100 K. This unexpected hydrate crystallizes in the orthorhombic space group *Pbcm* with *a* = 956.31(6) pm, *b* = 1365.72(8) pm and *c* = 1027.68(6) pm for *Z* = 4. The unit-cell volume of $Cs_2[B_{12}H_{12}] \cdot 2\ H_2O$ is almost 7 % smaller than the one of $Cs_2[B_{12}H_{12}]$ (1342 Å^3 versus 1436 Å^3) despite containing more particles. In contrast to the anhydrate $Cs_2[B_{12}H_{12}]$, two crystallographically different Cs^+ cations are present. $(Cs1)^+$ carries three and $(Cs2)^+$ one water molecule at distances of 318 pm and 333 pm, respectively, while ten or twelve hydrogen atoms 306 – 335 pm apart complete both coordination numbers to C.N. = 13. This diverse behavior of cesium and water leads to an endless chain along [001] (see Figure). $Cs_2[B_{12}H_{12}]$ has only one crystallographically unique Cs^+ cation with twelve coordinating hydrogen atoms at a distance of 313.4 pm (12×). The same special crystallographic behavior was observed in a similar network of ammonia and cesium reported in the low-temperature measurement of $Cs_2[B_{12}H_{12}] \cdot 6\ NH_3$ (*Pbca*, *a* = 775.69(8) pm, *b* = 1408.65(14) pm, *c* = 1807.48(17) pm, *Z* = 4) [3] with Cs-N distances of 313, 326 and 378 pm. There is also a chain formation observed, although only two-thirds of the ammonia molecules are involved. With *V* = 1975 Å^3 the unit-cell is larger than in the dihydrate case, since one-third of the NH_3 particles represent interstitials. The reason for the contraction of $Cs_2[B_{12}H_{12}] \cdot 2\ H_2O$ is not only the extra water ligands at the Cs^+ cations but also rather strong classical hydrogen bonds among water molecules and non-classical dihydrogen bonds between the negatively polarized hydrogen atoms of the $[B_{12}H_{12}]^{2-}$ clusters and positively polarized hydrogen atoms of the H_2O molecules.

Literature:

(1) J. A. Wunderlich, W. N. Lipscomb, *J. Am. Chem. Soc.* **1960**, *82*, 4427.
(2) I. Tiritiris, Th. Schleid, K. Müller, W. Preetz, *Z. Anorg. Allg. Chem*. **2000**, *626*, 323.
(3) F. Kraus, M. Panda, T. Müller, B. Albert, *Inorg. Chem*. **2013**, *52*, 4692.

Fig. 1

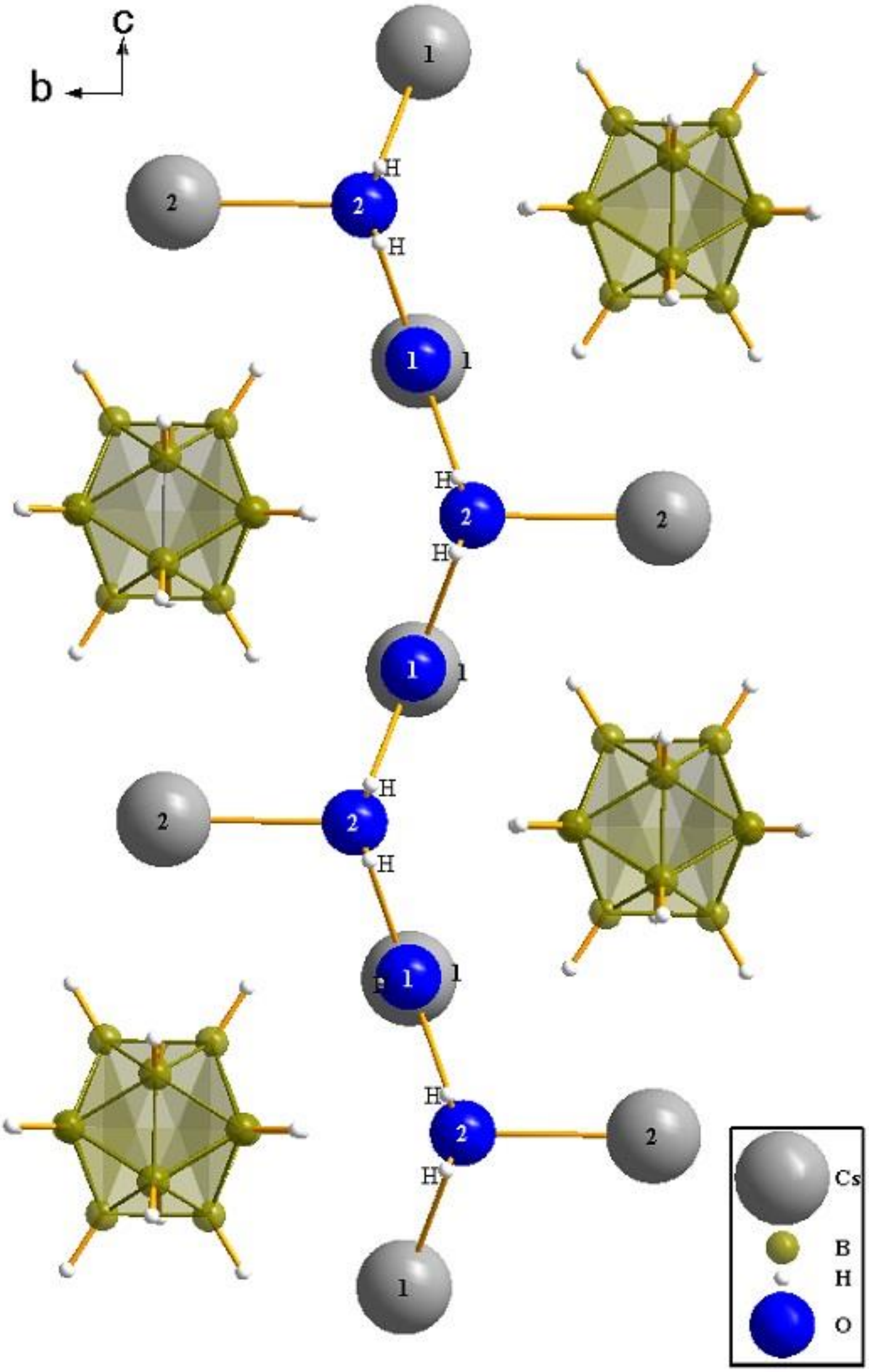

Fig. 2

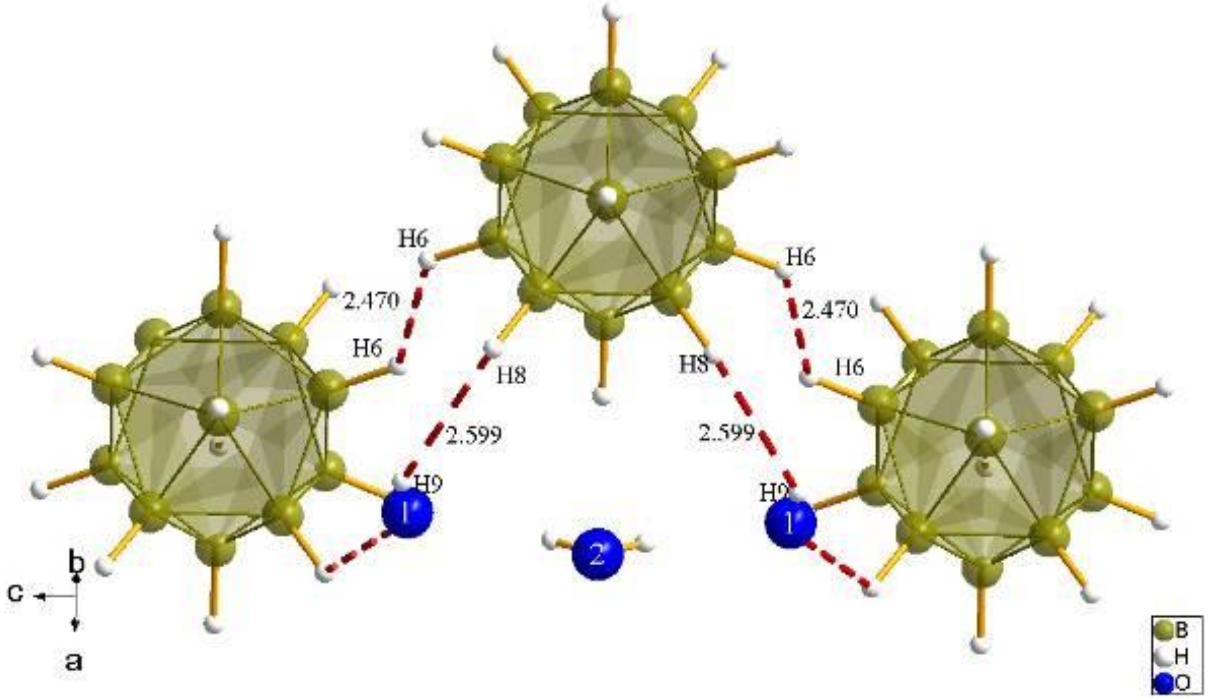

LT-05

The Heaviest Lanthanoid-Containing Silver Thiophosphate: $Ag_3Lu[PS_4]_2$

P. L. Lange (Stuttgart/DE), T. Schleid (Stuttgart/DE)

$Ag_3Lu[PS_4]_2$ was synthesized without any crystalline by-products, as confirmed by powder X-ray diffractometry (PXRD), from lutetium sesquisulfide (Lu_2S_3), diphosphorus pentasulfide (P_2S_5) and silver hemisulfide (Ag_2S) in a stoichiometric ratio of 1:2:3. The title compound, incorporating the heaviest lanthanoid lutetium, crystallizes isotypically with other compounds $Ag_3Ln[PS_4]_2$ (Ln = Y, Dy, Ho, Er)[1] adopting the $Ag_3Y[PS_4]_2$-type structure ($a = 1687.4(3)$ pm, $b = 919.0(2)$ pm, $c = 931.2(2)$ pm and $\beta = 123.17(3)°$ for $Z = 4$)[2] in the monoclinic space group $C2/c$ (no. 15). Following the lanthanoid contraction very well, the lattice parameters for $Ag_3Lu[PS_4]_2$ are $a = 1696.02(9)$ pm, $b = 920.39(5)$ pm, $c = 932.47(5)$ pm and $\beta = 123.278(3)°$ at room temperature (CSD number: 2219575).

Quite common for these types of thiophosphates(V), there are only slightly distorted tetrahedral $[PS_4]^{3-}$ anions (d(P–S) = 202–207 pm) discretely present in the structure. Together with the bicapped trigonal prisms $[LuS_{6+2}]^{13-}$, they form individual strands, connected via common edges, propagating along the c-axis, as can be seen in Figure 1 (d(Lu–S) = 271–280 pm + 305 pm). These strands are separated in [100] direction by the $(Ag2)^+$ cations, which reside in tetrahedral sulfur surrounding in between. The $(Ag1)^+$ cations prevent connecting contact of the strands in the (001) plane. Possible Ag^+-cation diffusion pathways within the structure (d(Ag–S) = 253–272 pm, C.N. = 4 for both) were calculated using bond valence energy landscape calculations based on the single-crystal X-ray diffraction data and hinted at moderate to good silver-ion conductivity (diffusion energy barrier in all three dimensions: $E \approx 0.08$ eV). The optical band gap was determined to be $Eg = 2.47$ eV using UV/Vis diffuse reflectance spectroscopy (DRS).

Ong et al.[3] presented a screening for potentially super-conductive materials and performed theoretical calculations on lithium-ion conductivity for several thiophosphates. As a template, they also took silver thiophosphates into their screening including $Ag_3Y[PS_4]_2$. Their predictions concluded super-ionic Li^+-cation conductivity for $Li_3Y[PS_4]_2$ on the basis of the $Ag_3Y[PS_4]_2$ structure, if silver was substituted with lithium *in silico*[3]. Regarding the structured formula $Ag_3RE[PS_4]_2$, a similarity to the lithium analogue $Li_3La[PS_4]_2$[4] seems obvious, although the two compounds crystallize very differently.

(1) P. L. Lange, Th. Schleid, *Solid State Sci.* **2023**, *in preparation*.
(2) C. Müller, S. Jörgens, A. Mewis, *Z. Anorg. Allg. Chem.* **2007**, *633*, 1633.
(3) Z. Zhu, I.-H. Chu, S. P. Ong, *Chem. Mater.* **2017**, *29*, 2474.
(4) P. L. Lange, Th. Schleid, *Eur. J. Inorg. Chem.* **2021**, *32*, 3247.

The authors are grateful for financial support from the Federal State of Baden-Württemberg (Stuttgart). Furthermore, we thank Dr. Falk Lissner for the single-crystal X-ray diffraction measurement.

Figure 1: Extended unit cell of the $Ag_3Lu[PS_4]_2$ structure with highlighted $[PS_4]^{3-}$ tetrahedra and bicapped trigonal prisms $[LuS_{6+2}]^{13-}$ to emphasize the strands along the c-axis (left). The Ag^+ cations reside in and between these chains, occupying tetrahedral voids (right).

Fig. 1

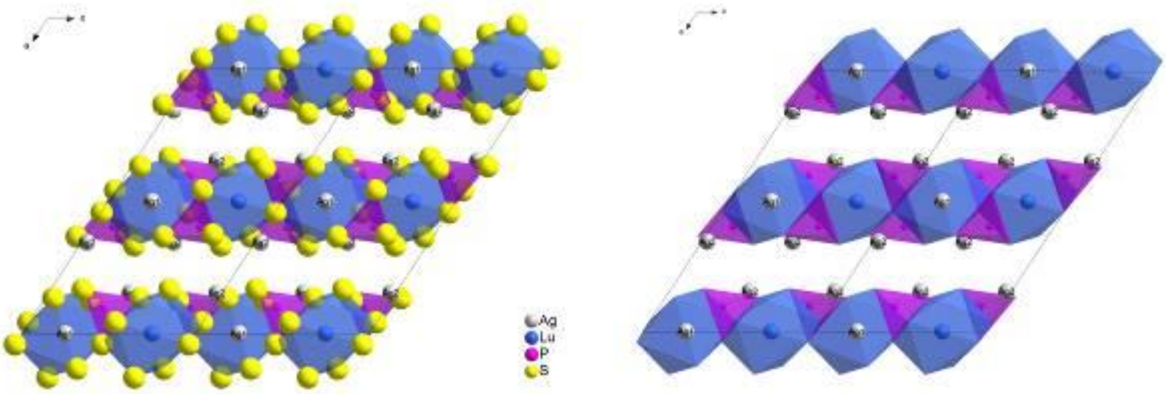

LT-06

Novel binary, ternary and quaternary phases in the Bi-Mn-Pt-I system

M. Herz (Dresden/DE, Dresden-Würzburg/DE), M. Ruck (Dresden/DE, Dresden-Würzburg/DE, Dresden/DE)

Discovered during the search for novel topological insulators[1], we discovered new pseudo one-dimensional compounds. The reaction of Bi with Mn, Pt and BiI_3 above 300 °C yielded shiny, black, air insensitive crystals of the new new subiodides $(Bi_{2x}Mn_{1-3x})[PtBi_6I_{12}]$, with $0 \leq x \leq 1/3$. Through extensive investigations into the synthetic pathways with the help of differential scanning calorimetry, partially and fully substituted versions of the compounds could be isolated and synthesized independently. The rhombohedral crystal structures consist of alternating cuboctahedral $[PtBi_6I_{12}]^{2-}$ cluster anions and Mn^{2+} or Bi^{3+} cations in octahedral coordination between trigonal faces of two cuboctahedra. These concatenate them into either linear chains if all the countercation positions are filled, such as in $Pb[PtBi_6I_{12}]$[2] and $Sn[PtBi_6I_{12}]$[3] or into finite strands when vacant positions remain as in $Bi_2[PtBi_6I_{12}]_3$[4]. Furthermore, novel binary and ternary Mn-based phases were discovered during the in-depth analysis of the synthetic pathway. The strong spin-orbit-coupling of the heavy elements in all of these new phases could potentially exceed the width of the chemical band gap of the compounds, therefore leading to a non-trivial topology being expected.

(1) a) M. Z. Hasan, C. L. Kane, *Rev. Mod. Phy.* **2010**, *82*, 3045; b) Y. Ando, *J. Phys. Soc. Jpn*. **2013**, 82.
(2) M. A. Herz, M. Knies, K. Finzel, M. Ruck, *Z. Anorg. Allg. Chem.* **2020**, *647*, 53.
(3) M. A. Herz, K. Finzel, M. Ruck, *Z. Anorg. Allg. Chem.* **2022**, e202200080.
(4) A. Günther, F. Steden, M. Ruck, *Z. Anorg. Allg. Chem.* **2008**, *634*, 423.

Figure 1: Novel Binary, Ternary and Quaternary Phases in the Bi-Mn-Pt-I System

Fig. 1

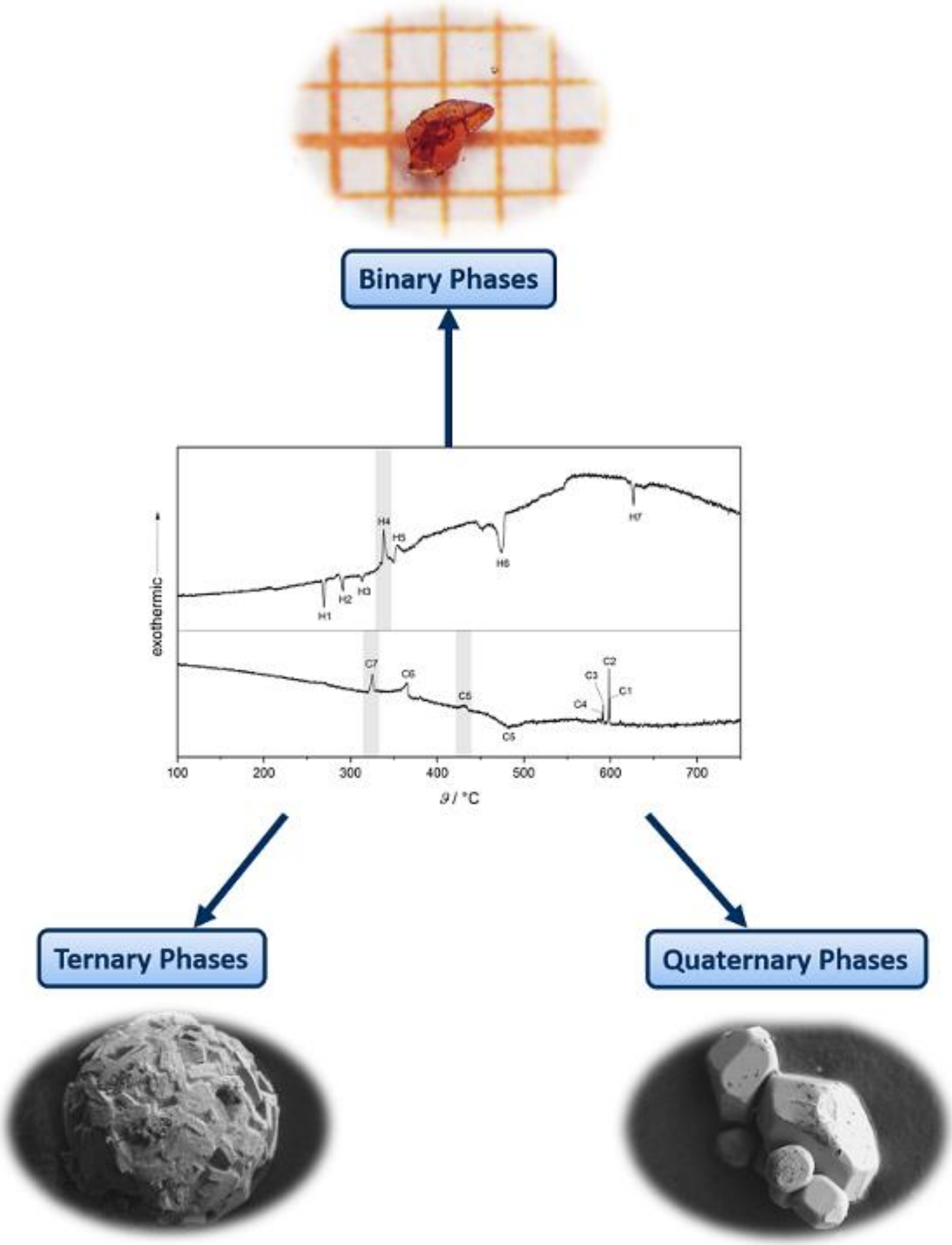
Binary Phases
exothermic
H1
H2
H3
H4
H5
H6
H7
C7
C6
C5
C5
C4
C3
C2
C1
100
200
300
400
500
600
700
ϑ / °C
Ternary Phases
Quaternary Phases

LT-07

Survey of zirconium-containing NaSICON-type solid-state Li+ ion conductors with the aim of increasing reduction stability by partial cation substitution

A. Loutati (Jülich/DE)

Abstract: Various compositions of the series Li1+xM3+xZr2-x(PO4)3 where M3+ = Al3+, Sc3+, Y3+ were prepared by solution-assisted solid-state reaction, since they could have a higher reduction stability as solid electrolytes in lithium batteries than in germanium- or titanium-containing materials. The influence of substitution on crystallographic parameters, density, and ionic conductivity were investigated. The cation substitution of M3+ (M = Al, Sc, Y) for Zr4+ in LiZr2(PO4)3 stabilizes the rhombohedral NaSICON structure (space group) at room temperature and increases the ionic conductivity significantly. Here, at 25 °C and with a consistent relative density of 94-96 %, an ionic conductivity of 2.7 × 10-5 S cm-1, 6.7 × 10-5 S cm-1, and 3.6 × 10-6 S cm-1 was achieved with the compositions Li1.2Sc0.2Zr1.8(PO4)3, Li1.2Y0.2Zr1.8(PO4)3, and Li1.2Al0.2Zr1.8(PO4)3, respectively. In comparison with Li1+xScxZr2-x(PO4)3, the Y3+ substitution in LiZr2(PO4)3 enhanced the ionic conductivity slightly and denoted the maximum Li+ ionic conductivity obtained at room temperature. However, substitution with Al3+ decreased the ionic conductivity.

For the first time, this work provides a complete overview of three series of solid Li-ion conductors in the Li2O-M2O3-ZrO2-P2O5 system where M = Al, Sc, Y. Noticeable differences in the chemistry of resulting compounds were observed, which likely depend on the ionic radius of the cations being substituted. The series with Sc showed complete miscibility from x = 0 to x = 2 with a continuous change of the NaSICON polymorphs. The series with Y showed a solubility limit at about x = 0.3 and higher substitution levels led to the increasing formation of YPO4. The series with Al exhibited continuously decreasing ionic conductivity until x = 1, whereupon the investigation was terminated due to its very low conductivity of about 10-10 S cm-1.

(1) Lonsdale K, Proc. *Phys. Soc.* 54, 314-353(1942).
(2) Wehinger B, et al., *Phys. Rev. Lett.* 118, 035502 (2017).
(3) Mirone, A., Wehinger, B. http://ftp.esrf.fr/scisoft/AB2TDS/index.html (2013); http://ftp.esrf.eu/scisoft/TDS2EL/index.html (2017).
(4) Büscher, et al., *J. Appl. Crystallogr.* 54, 287-294 (2021).
(5) Ramsteiner, I. B., et al. *J. Appl. Crys.* 42.3, 392-400 (2009).

LT-08

Upgrading the High-Energy Beamline P21.1 at PETRA III (DESY)

K. Köhler (Frankfurt am Main/DE), A. C. Dippel (Hamburg/DE), M. von Zimmermann (Hamburg/DE), A. Mirone (Grenoble/FR), B. Winkler (Frankfurt am Main/DE)

The advantages of diffraction experiments with high-energy X-rays (100keV), including the improved access to reciprocal space for a given sample to detector distance, the drastic reduction of radiation-induced damage to crystals, and the possibility to investigate bulk samples containing strongly absorbing elements, have long been recognized[1].

The beamline P21.1 at PETRA III offers ideal conditions for diffraction experiments with high-energy X-rays. An X-ray beam with photon energies of 54 or 100keV, a beam size of about 1mm^2, as well as a hybrid pixel detector (Dectris Pilatus3 X CdTe 2M) are available. In our BMBF-funded project, we plan to further optimize the experimental setup at P21.1. especially with respect to efficiently perform temperature-dependent scattering experiments (diffraction and diffuse scattering) over a wide temperature range, for both small and large crystals.

One set of case studies will focus on the measurement of thermal diffuse scattering (TDS) to extract the complete elastic stiffness tensor (C_{ij}) from small crystals with low symmetry. A theoretical description of TDS was developed early[2], but the experimental requirements became available recently[3-5]. We will improve the data analysis for TDS measurements at P21.1, integrate an open flow cryostreamer to facilitate low temperature measurements down to 30K and aim to introduce CRL-based beam focusing optics to allow the efficient study of small crystals.

We are grateful for funding within the BMBF Project (05K22RF1), further financial support from the DFG and DESY for their excellent cooperation and support.

LT-09

Crystalline sponge method for pharmaceutically active ingredients: A chemical space analysis

C. von Essen (Darmstadt/DE)

In 2013, Makoto Fujita published a new technique commonly known as "crystalline sponge method" (CS-XRD), which enables crystal structure determination without crystallization in nano- to few microgram analyte quantities.[1] Even information on the absolute configuration of chiral centers can be provided.[2] The CS-XRD uses pre-existing single crystals of porous metal-organic frameworks $[(ZnX_2)_3{\cdot}(tpt)_2{\cdot}x(solvent)]_n$ (X=Cl; tpt=2,4,6-*tris*(4-pyridyl)-1,3,5-triazine), which can absorb organic molecules in its pores and make them observable by conventional single crystal X-ray diffraction. Via diffusion, the analyte is absorbed into the porous CS and regularly aligned by non-covalent interactions [3,4]. As a result, the repetitive positioning of the analytes in each pore of the framework serves for structural analysis via X-ray diffraction.

Various literature proves the method"s broad applicability. For example, the combination of CS-XRD with MS or NMR data offers a great opportunity for scientists in drug metabolism and pharmacokinetics to assess the structure of metabolites produced in low amounts from in vitro studies.[5,6]

We will present the chemical space analysis of the analytes successfully used with the crystalline sponge method with respect to active pharmaceutical ingredients stored in ChemBL[8]. To quantitatively describe the physical and chemical information in order to map the chemical space, 208 molecular descriptors, a mathematical representation of molecules" properties, were generated by RDKit[7] and dimensionality reduction by Principal Component Analysis was performed. The analysis provides insight in the method"s broad applicability as well as its boundaries.

References:

(1) Inokuma Y, Yoshioka S, Ariyoshi J, Arai T, Hitora Y, Takada K, Matsunaga S, Rissanen K, and Fujita M (2013) X-ray analysis on the nanogram to microgram scale using porous complexes [published correction appears in Nature (2013) 495:461–466]. *Nature* 501:262.
(2) Zhou H, Han JT, Nöthling N, Lindner MM, Jenniches J, Kühn C, Tsuji N, Zhang L, List B (2022) Organocatalytic Asymmetric Synthesis of Si-Stereogenic Silyl Ethers *J. Am. Chem. Soc.*, 144, 23, 10156–10161.
(3) Inokuma Y, Ukegawa T, Hoshino M, and Fujita M (2016) Structure determination of microbial metabolites by the crystalline sponge method. *Chem Sci (Camb)* 7:3910–3913.
(4) Sakurai F, Khutia A, Kikuchi T, and Fujita M (2017) X-ray structure analysis of n-containing nucleophilic compounds by the crystalline sponge method. *Chemistry* 23:15035–15040.
(5) Rosenberger I, von Essen C, Khutia A, Kühn C, Urbahns K, Georgi K, Hartmann RW, Badolo L (2020) Complete Structural Elucidation of Gemfibrozil Metabolites by Crystalline Sponges. *Drug Metab. Dispos*. 48: 587-593.
(6) Rosenberger I, Jenniches J, von Essen C, Khutia A, Kühn C, Marx A, Georgi K, Hirsch AKH, Hartmann RW, Badolo L (2022) Metabolic Profiling of S-praziquantel: Structure Elucidation Using the Crystalline Sponge Method in Combination with Mass Spectrometry and Nuclear Magnetic Resonance. *Drug Metab. Dispos*. 50(4): 320-326.
(7) https://www.ebi.ac.uk/chembl/
(8) Open-source cheminformatics; http://www.rdkit.org

LT-10

Coordination-Driven insertion of a guest molecule in the pore of a Copper(I)-Based Metallocavitand

T. Pickl (Garching/DE), M. Anneser (Garching/DE), A. Pöthig (Garching/DE)

Pillarplexes are supramolecular organometallic complexes (SOCs) with a tubular pore and a high affinity for the incorporation of linear alkanes.[1] The cavitands consist of two macrocyclic ligands linearly coordinated by a total of eight group 11 metal ions (Ag^I or Au^I). Recently, we reported the first Cu^I-based pillarplex as a landmark example of a metallocavitand, in which the copper ions do not only act as structural elements but their intrinsic reactivity can be harnessed simultaneously.[2] We could also show that the affinity for small molecules to enter the pore of the SOC is also preserved in the Cu^I complex. In this contribution, we report the coordination chemistry of Cu^I pillarplex **Cu$_8$L$_2$(OTf)$_4$** in presence of tetrahydrofuran (THF), investigated in solution by NMR spectroscopy and in the solid state by X-ray diffractometry. ^{1}H NMR showed a distinct shift of the THF resonances in presence of **Cu$_8$L$_2$(OTf)$_4$** in MeCN-*d*$_3$, indicating insertion of the small molecule in the metallocavitand pore. DOSY spectroscopy showed that both molecules move as one associate through solution. Moreover, ^{1}H, ^{1}H NOESY suggested close interactions between THF and the pillarplex. SC-XRD unambiguously confirmed the formation of a host–guest complex by insertion of THF into the pore of **Cu$_8$L$_2$(OTf)$_4$**. In the solid state, the cationic pillarplex fragments align to form channels filled by THF molecules with the triflate (OTf) counter ions bridging the pillarplex cations. Close to the rims of two adjacent pillarplexes, non-classic H-bonds between the THF oxygen and ligand-associated C–bound hydrogen atoms were found. While these cyclic ethers are disordered, one molecule of THF is found in the center of the pore, coordinating the Cu^I ions from the inside. This appears to be energetically favorable enough to enforce a preference of the central THF to remain at this position, accompanied by relatively small ellipsoids that could be modelled anisotropically. Aiming to study the influence and reversibility of THF insertion and its temperature-dependent removal on the solid-state structure, PXRD and thermogravimetry were employed. Eventually, in-depth characterization of the binding properties of THF as a representative example of a coordinating guest molecules inside the pore of metalloavitand **Cu$_8$L$_2$(OTf)$_4$** aides the understanding of future guest molecules as substrates in shape-selective catalysis mediated by our metallocavitand platform.

(1) P. J. Altmann and A. Pöthig, *J. Am. Chem. Soc.* 2016, *138*, 13171–13174.
(2) T. Pickl, M. Anneser, D. P. Halter and A. Pöthig, *manuscript under review,* 2022.

Fig. 1

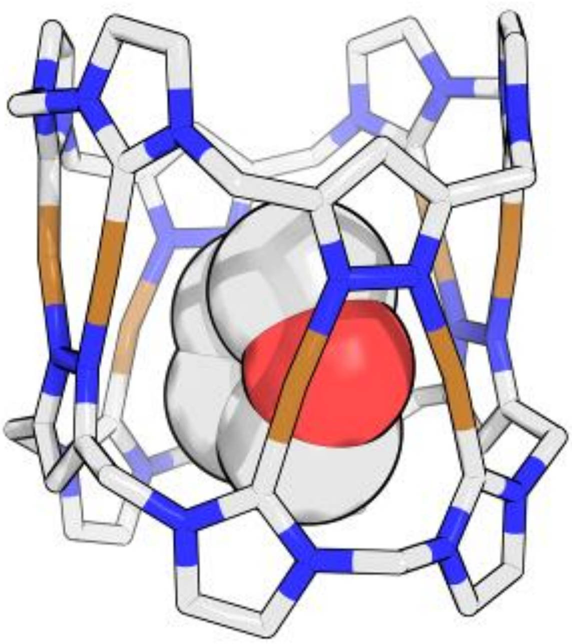

Cu–O coordination inside
the cavity of a **Cu^I pillarplex**

LT-11

Refinement of anomalous dispersion correction parameters in X-ray single-crystal structure determination

F. Meurer, F. Kleemiss (Regensburg/DE), O. Dolomanov, H. Puschmann (Durham/UK), C. Hennig (Grenoble/FR), N. Peyerimhoff (Durham/UK), M. Bodensteiner (Regensburg/DE)

The oldest and most widely used method for the elucidation of atomic structures is the diffraction of X-rays on a single crystal. A structure-specific diffraction pattern is obtained through the interference of the light waves, the positions, and intensities of which are recorded by a detector. Especially the intensities are subsequently used to determine the structure of the compound. To be able to clearly assign the measured intensities to a structural composition, one needs an exact description of the scattering behaviour of the electrons involved. To describe this scattering behaviour as precisely as possible, it is divided into a fully elastic part, in which no photon energy is lost, and an inelastic part, in which part of the photon energy is transferred to the electrons. The inelastic part, the anomalous dispersion, is particularly significant at individual element-specific energies, the absorption edges. In crystallography, especially the more detailed description of the first part has received much attention and is generally treated by the science of quantum crystallography/charge density analysis. However, the second, inelastic part is represented in diffraction experiments by tabulated values, some of which are over 30 years old. These tables differ strongly from one another, especially in the vicinity of absorption edges. This is particularly evident in X-ray absorption spectroscopy. Here, the inelastic fraction is quantified by absorption measurements, and properties such as nuclear charge and the electronic environment of the atom are deduced. Chemically interesting features such as the oxidation state and the influence of a ligand field can be determined. It is important to note that atomic charge and electronic environment are compound-specific and can therefore never be fully represented in tabulated values from elementary calculations in X-ray diffraction.

I want to present the results of my master's thesis, where I aimed to achieve a better description of the inelastic effects experimentally by freely refining the correction parameters in the crystallographic model for small-molecular crystalline compounds. This involved performing diffraction measurements of two different molybdenum compounds at the Rossendorf beamline at the European Synchrotron Radiation Facility in Grenoble at different energies and comparing the models with both refined and tabulated parameters with recorded X-ray absorption spectra of the same compounds. Indeed, the refined dispersion values follow the spectra reliably (Fig. 1) and are thus sensitive parameters for the acquisition of X-ray spectroscopic values in diffraction experiments. Furthermore, the sometimes strong artefacts in the crystal structures with tabulated values are no longer present in the structures with refined values (Fig. 2). Here, the quality of the crystal structures can be explained by the deviation of the tabulated values from the recorded spectra: The greater the deviation, the worse the crystallographic models describe the measured data. The refinement of the dispersion correction for experimental parameters such as the resolution of the data, the choice of the crystallographic model (independent-atom-model, Hirshfeld-atom-refinement, multipolar model), as well as possible correlations of the new parameters to already existing parameters in the model are investigated. A possible application for the method was found for in-house diffractometer data for organometallic compounds in different oxidation states.

(1) F. Meurer, O. V. Dolomanov, C. Hennig, N. Peyerimhoff, F. Kleemiss, H. Puschmann, M. Bodensteiner, IUCrJ **2022** 5, 604–609.

Figure 1: X-ray absorption spectrum (upper half, black line) and its Kramers-Kronig transformation (lower half, black line) compared to the values for f' (upper half, red cross) and f'' (lower half, red cross).

Figure 2: 3D visualisation of the residual electron density maps (red: negative residual density, blue: positive residual density) of Mo(CO)6 at 20,001 eV at various iso-surface levels

Fig. 1

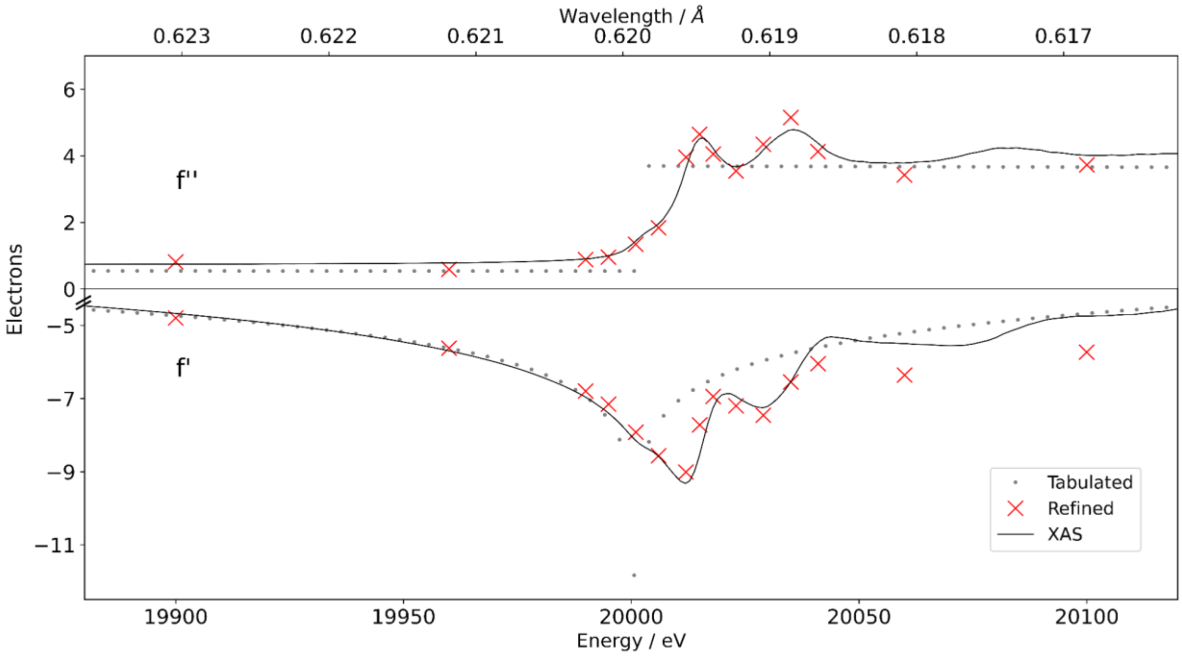
Wavelength / Å
0.623
0.622
0.621
0.620
0.619
0.618
0.617
6
4
2
0
−5
−7
−9
−11
Electrons
f''
f'
Tabulated
Refined
XAS
19900
19950
20000
20050
20100
Energy / eV

Fig. 2

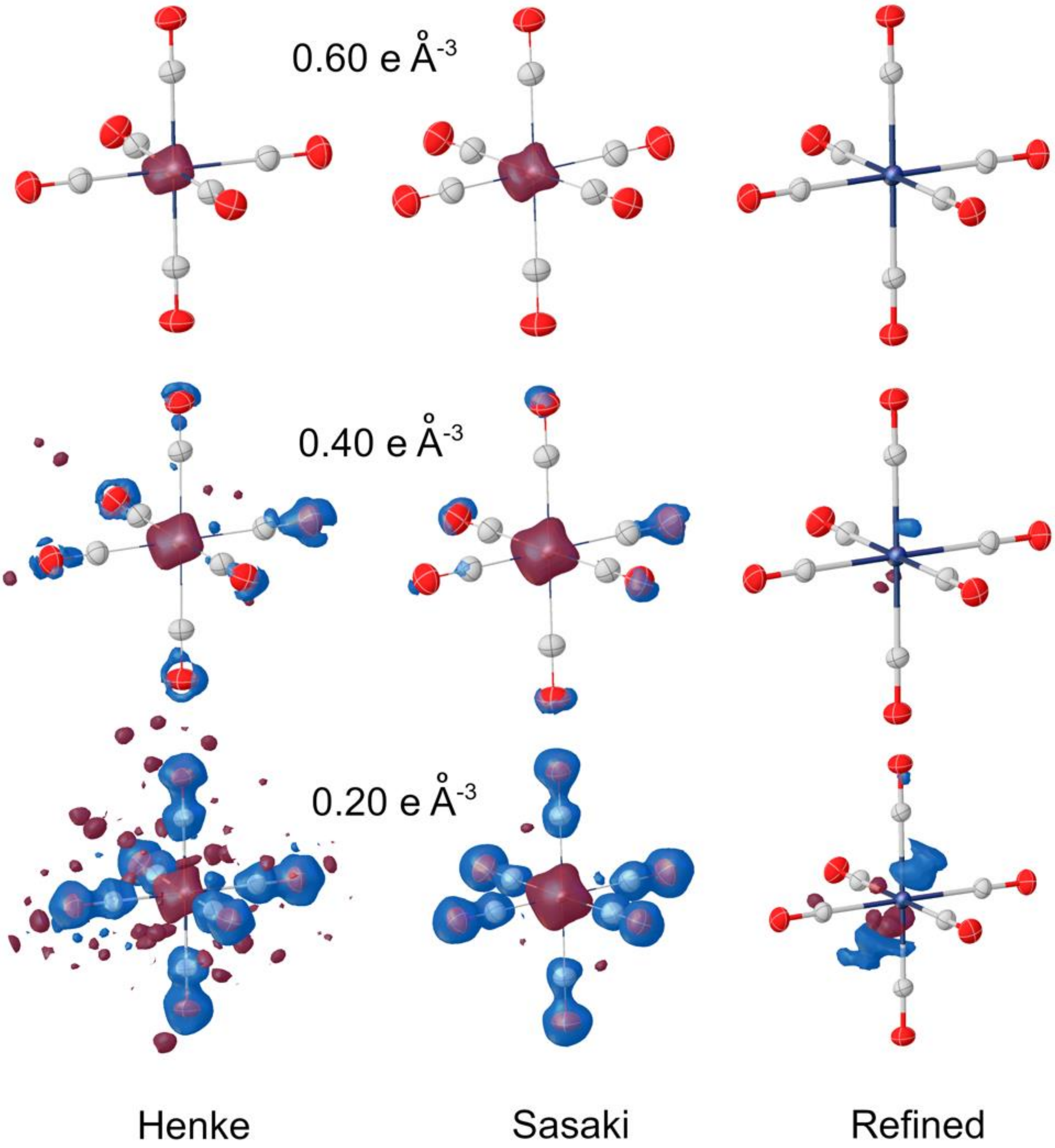

LT-12

Hydrothermal Synthesis of Anisotropic Ferrite Microparticles

Luisa Wartner, E. Fezai, S. Mascotto (Hamburg/DE)

Photocatalysis is a very promising technique to alleviate the global energy crisis and reduce environmental pollution. Tailoring the size, crystal structure, and shape of inorganic materials resulted to be a winning strategy to improve their photocatalytic activity, for example, in CO2 reduction.[1] Orthoferrites of rare earth metals possess great catalytic properties, non-toxicity, and chemical stability, making them very interesting for photocatalytic applications.[2] Due to the strong correlation between surface chemistry and lattice orientation in ternary oxides, it is possible to further improve their catalytic activity by controlling the growth of the crystal facets.[1]

The aim of this work was to prepare different anisotropic Ytterbiumferrite (YbFeO3) microparticles by hydrothermal synthesis. In particular, the effect of the concentrations of the mineralizer (KOH) and additive (urea) on the particle shape was examined by Scanning Electron Microscopy (SEM). Monodisperse, pure microparticles in four distinct anisotropic shapes (cuboids, elongated bipyramids, corner- and edge-truncated cubes, and elongated cuboids (Fig. 1)) have been synthesized. Powder-XRD was revealed to be a useful tool for assessing the anisotropy by comparing the intensities of the six main reflections of the YbFeO3 diffractograms. This method especially enabled the determination of the respective stabilized surfaces, allowing for predictions in crystal growth direction. We found that the stabilization of different crystal facets depends on the concentration of K+-ions and urea.

Finally, anisotropic microparticles with different crystal facets and thus surface chemistry were successfully synthesized. In the future, applications of these materials in photocatalysis will be investigated.

Figure 1: SEM images of (a) cuboids, (b) bipyramids, (c) slightly edge- and corner-truncated cubes and (d) elongated cuboids with unfinished surface areas.

(1) S. Bai, L. Wang, Z. Li, Y. Xiong, Adv. Sci., 2017, 4, 1600216.
(2) Chen. L.; Jiang, T.; Zheng, G.; Yao, G.; Wang, L.; Yang, Y.; Thang, H.; Jiang, Y.; Lu, Y.; Wei, S., Current Chinese Science, 2021, 1, 438-452.

Fig. 1

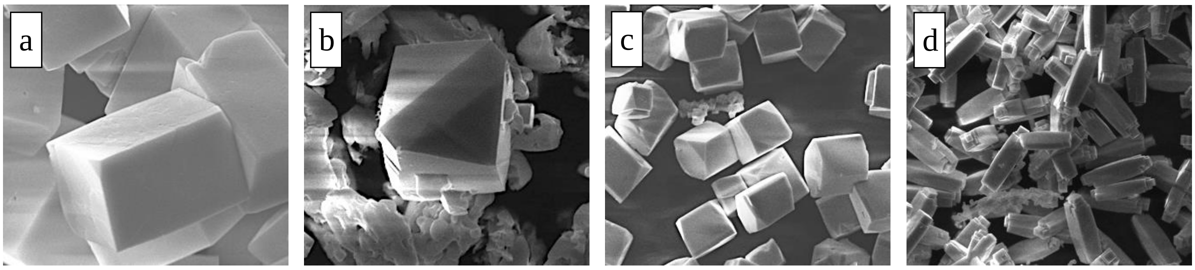

OP-052

Structural characterization of WDR5-degrader interfaces and its implications for optimal PROTAC design

A. Kraemer (Frankfurt am Main/DE)

The chromatin-associated WD40 repeat domain protein 5 (WDR5) serves as a functional subunit of the mixed lineage leukemia (MLL) histone methyltransferase complex and has emerged as a promising drug target in recent years. It is a key determinant for MYC recruitment to chromatin, which acts a main driver of tumorigenesis, and is linked to several cancers. However, published inhibitors that block protein-protein interactions between WDR5 and its binding partners exhibit only modest cancer cell killing effects and lack in vivo efficacy. The development of the PROTAC (proteolysis-targeting chimeras) technology opened up new avenues for tackling this problem, by effectively degrading this scaffolding protein and thereby disrupting any WDR5-mediated interactions. PROTACs are bifunctional molecules that recruit a target protein in proximity to an E3 ubiquitin ligase to trigger protein degradation. Inducing these macromolecular interactions with small molecules is a challenging goal. In many cases, structural elucidation of the key ternary complex between the protein, PROTAC, and ligase, and its impact on degradation selectivity remain elusive. We were able to successfully crystallize several ternary complexes of WDR5 and the E3-ligase Von Hippel-Lindau (VHL) in complex with several PROTAC degraders. These crystal structures provided crucial insights into the binding modes of different linkers and the associated changes in the interaction surface of WDR5 and VHL. Overall, we found a good correlation between an increased interaction surface and selective depletion of WDR5 in cells.

OP-053

Structural elucidation of cathepsin L inhibitors is pushing the concept of dual-target anti-viral drugs

S. Falke (Hamburg/DE), J. Lieske (Hamburg/DE), P. Reinke (Hamburg/DE), S. Günther (Hamburg/DE), A. Herrmann (Munich/DE), W. Ewert (Hamburg/DE), J. Loboda (Ljubljana/SI), K. Karničar (Ljubljana/SI), A. Usenik (Ljubljana/SI), N. Lindič (Ljubljana/SI), A. Sekirnik (Ljubljana/SI), H. Chapman (Hamburg/DE, Hamburg/DE), W. Hinrichs (Greifswald/DE), G. Ebert (Munich/DE), D. Turk (Ljubljana/SI), A. Meents (Hamburg/DE)

Emerging RNA viruses including coronaviruses continue to be a major health threat globally. Cell entry of SARS-CoV-2 via the endosomal pathway involves the host-cell cysteine protease cathepsin L (CatL). We previously performed an extensive X-ray crystallographic compound screening targeting SARS-CoV-2 main protease [1]. It was found that some main protease inhibitors may qualify for a "dual-protease-targeting" approach by also inhibiting CatL [2].

As CatL and related proteases are attractive drug targets in the context of viral and lysosome-related diseases, discovery of novel inhibitors, its structural elucidation and structure-based optimization towards drugs candidates are of high pharmaceutical interest.

We co-crystallized CatL with more than 20 inhibitors and additionally initiated an X-ray screen of a larger fragment library utilizing the dedicated infrastructure for such experiments at DESY. X-ray crystallographic data was collected at the PETRAIII beamlines P09 (HiPhax) and P11. For efficient data handling and processing a software pipeline and a database were developed. In addition to their structural characterization, CatL inhibitors were further analyzed in biochemical assays for their potential and specificity.

Here we present the structures of cathepsin L in complex with selected inhibitors including calpeptin and calpain Inhibitor XII and further report on our fragment screen. In parallel, we evaluated the reduction of SARS-CoV-2 replication by selected compounds in Vero-E6 cells, revealing IC50 values in the low nM regime for a set of covalent inhibitors. Our results show that calpeptin and structurally related inhibitors with other warheads are promising anti-viral drug candidates.

References:

(1) Günther et al., *Science* (2021), DOI: 10.1126/science.abf7945
(2) Hu et al., *ACS Infectious Diseases* (2021), DOI: 10.1021/acsinfecdis.0c00761

OP-054

The induced-fit binding mechanism of cell-permeable dichlorophenylpyridine-based furin inhibitors

S. O. Dahms (Salzburg/AT), G. Schnapp (Biberach an der Riß/DE), M. Winter (Biberach an der Riß/DE), F. H. Büttner (Biberach an der Riß/DE), C. Gnamm (Biberach an der Riß/DE), A. Pautsch (Biberach an der Riß/DE), H. Brandstetter (Salzburg/AT)

Furin belongs to the proprotein convertases (PCs), a family of subtilisin-like proteases involved in the maturation of many secreted proteins. Furin inhibitors might serve as broad-spectrum antiviral therapeutics. (1) The multi-basic consensus cleavage sequence of furin has been utilized to develop very potent substrate-like inhibitors reaching Ki-values down to the low pM-range. Such peptide-based compounds usually include a number of positively charged amino acids that limit the bioavailability and can result in toxicity in mice. (2)

High cellular potency and antiviral activity against the acute respiratory syndrome coronavirus 2 (SARS-CoV-2) has been reported for 3,5-dichlorophenyl-pyridine-derived small molecule furin inhibitors. (3,4,5) Here we characterized the binding mechanism of this inhibitor class using structural, biophysical and biochemical methods. (6) We established a MALDI-TOF MS-based furin activity assay, determined IC50 values and solved X-ray structures of 3,5-dichlorophenyl-pyridine-derived compounds in complex with furin. The inhibitors induced a substantial conformational rearrangement of the active site cleft by exposing a central buried tryptophan residue. These changes formed an extended hydrophobic surface patch where the 3,5-dichlorophenyl-moiety of the inhibitors inserted in a newly formed binding pocket. Consistent with these structural rearrangements, we observed slow OFF-rate binding kinetics and a strong structural stabilization in surface plasmon resonance (SPR) and differential scanning fluorimetry (DSF) experiments, respectively. The discovered furin conformation offers new opportunities for structure-based drug discovery.

(1) Seidah, N. G. & Prat, A. The biology and therapeutic targeting of the proprotein convertases. Nat Rev Drug Discov 11, 367-383 (2012).
(2) Lam van, T. V. et al. The Basicity Makes the Difference: Improved Canavanine-Derived Inhibitors of the Proprotein Convertase Furin. ACS Med Chem Lett 12, 426-432 (2021).
(3) Essalmani, R. et al. Distinctive Roles of Furin and TMPRSS2 in SARS-CoV-2 Infectivity. J Virol 96, e0012822, doi:10.1128/jvi.00128-22 (2022).
(4) Axten, J. M. et al. Furin Inhibitors. WO 2019/215341 A1 (2019).
(5) Douglas, L. E. J. et al. A highly selective, cell-permeable furin inhibitor BOS-318 rescues key features of cystic fibrosis airway disease. Cell Chem Biol 29, 947-957 e948 (2022).
(6) Dahms, S. O. et al. Dichlorophenylpyridine-Based Molecules Inhibit Furin through an Induced-Fit Mechanism. ACS Chem Biol 17, 816-821 (2022).

OP-055

Allosteric inhibition as a new mode of action: A neutralizing antibody targeting the activated form of coagulation factor XI

M. Schaefer (Berlin/DE)

Factor XI (FXI), the zymogen of activated FXI (FXIa), is an attractive target for novel anticoagulants because FXI inhibition offers the potential to reduce thrombosis risk while minimizing the risk of bleeding. A novel anti-FXIa antibody was generated using phage display technology. Crystal structure analysis of the FXIa-antibody complex demonstrated that the tyrosine-rich complementarity-determining region 3 loop of the heavy chain penetrated deepest into the FXIa binding epitope, forming a network of favorable interactions including a direct hydrogen bond from Tyr102 to theGln451 sidechain (2.9 Å). The newly discovered binding epitope caused a structural rearrangement of the FXIa active site, revealing a novel allosteric mechanism.

OP-056

Comparison of the local stabilisation mechanism in Ca- and Y-stabilized zirconia using 3D-ΔPDF-analysis

E. M. Schmidt (Bremen/DE)

Cubic stabilized zirconia has attracted enormous interest over several decades (Frey et al. (2005)) because of its outstanding technological importance, e.g., as a high-temperature oxygen-ion conductor which can be used as an electrolyte in solid oxide fuel cells. Pure zirconia (ZrO_2) is monoclinic (space group $P2_1/c$) at ambient conditions. Increasing the temperature and/or pressure triggers the transformation first to a tetragonal phase ($P4_2/nmc$) and then to the cubic structure (Fm-3m).

The addition of lower-valence oxides creates oxygen vacancies in the structure and at a certain concentration stabilizes the cubic phase at ambient conditions. The interaction of these oxygen vacancies leads to intense local distortion in the structure and decisively influences the thermal, mechanical and electrical properties of zirconia.

This study investigates the defect structures of Ca-(CaSZ, $Zr_{1-x}Ca_xO_{2-x}$) and Y-stabilized zirconia (YSZ, $Zr_{1-x}Y_xO_{2-x/2}$). While previous experimental studies mainly focused on the analysis of single crystal diffuse scattering in reciprocal space (Frey et al. (2005)), here, we analyse the 3D-ΔPDFs from X-ray and neutron diffraction experiments (Weber & Simonov, 2012). We compare our results to the computational and experimental stabilization mechanisms that are reported in literature and demonstrate how the 3D-ΔPDF analysis allows an accurate description of the disorder model in real-space without the need for computationally expensive large supercell modelling.

(1) Frey, F. et al. (2005). *Z. Krist.,* **220**(12), 1017-1026.
(2) Weber, T. & Simonov, A. (2012). *Z. Krist.* **227**(5), 238-247.

Figure 1: (a) Symmetry averaged diffuse scattering in the *hk*0-layer of CaSZ (top) and YSZ (bottom) obtained from neutron (left) and X-ray (right) diffraction experiments. (b) Corresponding 3D-ΔPDFs in the *ab*0-layer.

Fig. 1

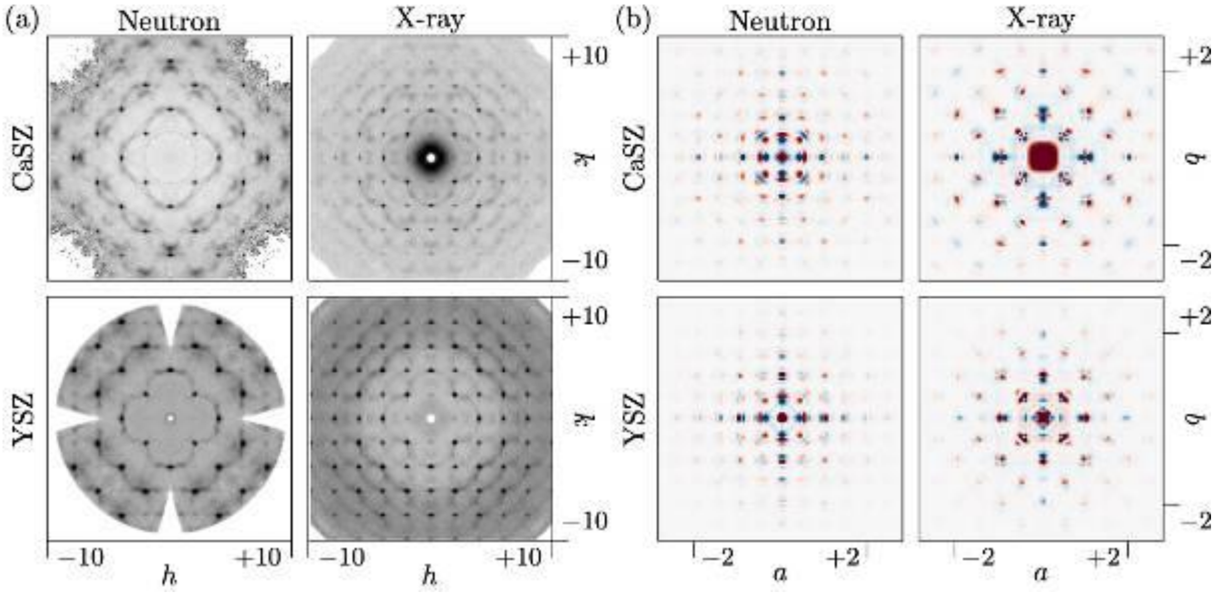

OP-057

Successive modulated phases of Rb_2ZnCl_4

S. R. Kotla (Bayreuth/DE), S. Ramakrishnan (Bayreuth/DE, Higashihiroshima/JP), T. Rekis (Bayreuth/DE, København/DK), A. M. Schaller (Bayreuth/DE), J. K. Bao (Bayreuth/DE, Shanghai/CN), C. Eisele (Bayreuth/DE), L. Noohinejad (Hamburg/DE), M. Tolkiehn (Hamburg/DE), C. Paulmann (Hamburg/DE, Hamburg/DE), G. de Laitre (Saint-Martin-d'Hères, Grenoble/FR), M. de Boissieu (Saint-Martin-d'Hères, Grenoble/FR), S. van Smaalen (Bayreuth/DE)

Rubidium Zinc Chloride (Rb_2ZnCl_4) has the β-K_2SO_4 type crystal structure and belongs to the A_2BX_4 crystal family, which are known to exhibit successive phase transitions. Above room temperature it has an orthorhombic structure with space group *Pmcn* and disorder associated with the $ZnCl_4$ tetrahedra [1]. A structural phase transition at 303 K, driven by the disordered tetrahedra, takes the structure into an incommensurately modulated phase. This modulation is a described with the wavevector $\mathbf{q} = (1/3 - \delta)\,\mathbf{c}^*$, where δ decreases with decreasing temperature. At around T_c = 192 K, δ becomes zero as Rb_2ZnCl_4 undergoes a lock-in transition from an incommensurately modulated structure to a commensurately modulated structure [2]. Lastly, Rb_2ZnCl_4 undergoes an additional phase transition around 75 K [3] with a probable monoclinic lattice distortion.

A detailed structural analysis in each phase, especially in the low temperature phase (T<75 K), is performed using single crystal X-ray diffraction experiments with synchrotron radiation at P24, PETRA III, DESY. The modulation wave function changes from a harmonic sinusoidal function to a highly anharmonic function as it approaches lock-in phase at T_c [4-5] where it is not only described by displacive modulation but also by the modulations of atomic displacement parameters (ADPs) and anharmonic ADPs. In the low temperature phase (T<75 K), additional satellites appear in the **ab** plane with the wavevector $\mathbf{q} = 0.5\mathbf{a}^* + 0.5\mathbf{b}^*$ revealing a second modulation wave, thereby breaking the orthorhombic symmetry. This (3+2)D modulated monoclinic phase, along with the evolution of modulation wave in the (3+1)D modulated phase is the focus of the current work.

(1) Sawada, S., Shiroshi, Y., Yamamoto, A., Takashige, M., & Matsuo, M. (1977). *J. Phys. Soc. Jpn* **43(6)**, 2099-2030.
(2) Gesi, K. & Iizumi, M. (1979). *J. Phys. Soc. Jpn* **46(2)**, 697-698.
(3) Bagautdinov B. Sh., Shekhtman, V. Sh., (1999) *Physics of Solid State*, **41(6)**: 987-993.
(4) Aramburu, I., Friese, K., Perez-Mato, J. M., Morgenroth, W., Aroyo, M., Breczewski, T. & Madariaga, G. (2006). *Phys. Rev. B* **73**, 014112.
(5) Li, L., Wölfel, A., Schönleber, A., Mondal, S., Schreurs, A. M. M., Kroon-Batenburg, L. M. J. & van Smaalen, S. (2011). *Acta. Cryst. B* **67**, 205-217.

OP-058

Modulations in Cu-Pb-Sb-Se andorite-type sulfosalt structures

P. Sicher (Vienna/AT), B. Stöger (Vienna/AT)

Sulfosalts have been catching the eyes of researchers for their potential use as thermoelectric materials because of their low thermal conductivity. Since S-based sulfosalts exhibit low electric conductivity as well, substituting S for Se or Te proved successful in increasing the thermoelectric performance. The aim of our research was to synthesise new selenide compounds in the Cu-Pb-Sb-Se system and to characterise them structurally. We used temperature-dependent single crystal x-ray diffractometry to determine the structure of the sulfosalts and to further characterise their behaviour at higher temperatures. The synthesis was carried out in evacuated quartz ampules using Cu_2Se, PbSe and Sb_2Se_3 at 950 °C and 600 °C.

A family of three modulated structures with one common orthorhombic andorite-type high-temperature structure at 400 °C in *Cmcm* was discovered with cell parameters of about 4, 14 and 20 Å. It consists of one monoclinic two-fold and one orthorhombic three-fold commensurate structures in $P2_1/c$ and $Cmc2_1$ as well as one orthorhombic incommensurate structure with $\mathbf{q} = (0.684, 0, 0)$ in $Cmcm(\alpha00)00s$. The two commensurate structures were found both separately and intergrown in one crystal with common main reflections. Using selected area electron diffraction, diffraction patterns of only one of the two superstructures could be obtained. The satellites of the incommensurate structure disappeared at 340 °C, the satellites of the three-fold commensurate structure at 355 °C and the satellites of the two-fold commensurate structures at 370 °C. After cooling, twinning and changing of two-fold/three-fold ratios is observed. An interesting aspect of these structures is an interstitial Cu-position that only sometimes is exhibited.

This work shows the structures of new compounds that vary only slightly in their elemental composition but show different modulations.

OP-059

Charge density wave phase transition in $EuAl_2Ga_2$ in magnetic phase transition

H. Agarwal (Bayreuth/DE), S. Rohith Kotla (Bayreuth/DE), S. Ramakrishnan (Higashi-Hiroshima/JP), C. Eisele (Bayreuth/DE), L. Noohinejad (Hamburg/DE), M. Tolkiehn (Hamburg/DE), C. Paulmann (Hamburg/DE), B. Bag (Jharkhand/IN), B. Baran Maity (Mumbai/IN), S. Dan (Mumbai/IN), A. Thamizhavel (Mumbai/IN), S. Ramakrishnan (Pune/IN), S. van Smaalen (Bayreuth/DE)

In Eu-based intermetallics, Eu offers two types of valance states of Eu^{2+} (magnetic) and Eu^{3+}(nonmagnetic) due to an unstable *4-f* shell. Eu based intermetallics $Eu(Ga_{1-x}Al_x)_4$ reveal strong correlations between the structural, magnetic, and electronic properties[1]. The compounds remain tetragonal having the $BaAl_4$ type structure with space group *I4/mmm* at room temperature for the whole doping range, with Ga and Al preferentially occupying one or the other of the two transition metal element sites[2]. $EuAl_4$ exhibits both the charge density wave (CDW) at T_{CDW}= 140 K and quadruple antiferromagnetic order below T_N = 15.4 K; however, $EuGa_4$ represents the characteristic of CDW above 1GPa and ordered antiferromagnetically below T_N= 16.4 K[3]. Recent study on $EuAl_4$ shows the tetragonal to incommensurately modulated orthorhombic CDW phase transition.[4] For x = 0.50, the two transition metals fully separate into two sublattices and form an ordered structure $EuGa_2Al_2$ with a minimum unit cell volume in the series. This favours the occurrence of a plausible out-of-plane CDW state at ambient pressure below ~ 51 K. The 3-dimensional CDW compound EuAl2Ga2 have four magnetic transitions temperatures $T_N \approx 19.5$ K, $T_2 \approx 15$ K, and $T_3 \approx 11$ K, $T_4 \approx 7$ K.[5]

The present study reports on the persistence of incommensurately modulated charge density wave in $EuAl_2Ga_2$ at the magnetic transition as well down to 6 K. We have performed the Single-crystal X-ray diffraction (SCXRD) at beamline P24 of PETRA-III at DESY (Hamburg, Germany) in the temperature range of 300 K – 6 K. $EuAl_2Ga_2$ possesses the tetragonal symmetry with space group *I4/mmm* at room temperature. First-order satellite reflections were observed near the transition temperatures within the incommensurate phase of $EuAl_2Ga_2$. These satellites are used to study the incommensurately modulated charge density wave transition in the material at the magnetic transition temperatures as well accompanied by lowering of symmetry. We will present the CDW modulated crystal structure as a function of temperature in $EuAl_2Ga_2$.

References:

(1) Ramarao, S. D., Singh, A. K., Subbarao, U. & Peter, S. C. An overview on the structural diversity of europium based ternary intermetallics. *J. Solid State Chem.* **281**, 121048 (2020).
(2) Stavinoha, M. *et al.* Charge density wave behavior and order-disorder in the antiferromagnetic metallic series $Eu(Ga_{1-x} Al_x)_4$. *Phys. Rev. B* **97**, 195146 (2018).
(3) Nakamura, A. *et al.* Transport and magnetic properties of $EuAl_4$ and $EuGa_4$. *J. Phys. Soc. Japan* **84**, (2015).
(4) Ramakrishnan, S. *et al.* Orthorhombic charge density wave on the tetragonal lattice of $EuAl_4$. *IUCrJ* **9**, 378–385 (2022).
(5) Moya, J. M. *et al.* Incommensurate magnetic orders and topological Hall effect in the square-net centrosymmetric $EuGa_2Al_2$ system. *Phys. Rev. Mater.* **6**, 074201 (2022).

OP-060

Cr-pincer complexes with two disorder modes: One-dimensional diffuse scattering and what we can learn from it

B. Stöger (Vienna/AT), D. Himmelbauer (Vienna/AT)

Order-Disorder (OD) structures [1] are a generalization of crystalline matter accounting for the short range if interatomic interactions. OD structures are built according to strict local rules, but need not possess long-range order. They have been reported for all classes of compounds, from inorganics to proteins and lead to challenging crystallographic problems. We present an interesting case, where two disorder modes lead to a combination of these effects.

The Cr-pincer complexes (POCOP-*t*Bu)CrBr and (POCOP-*t*Bu)$CrBH_4$ crystallize as OD structures and were structurally characterized by single crystal diffraction. Given a layer, the adjacent layer can appear in four orientations, which are related by reflection at either (100) and/or (001). The crystals featured one-dimensional diffuse scattering and additional twinning. The diffuse scattering was simulated using Markov-chain growth models and refined against the experimental data using a global search with the multilevel coordinate search (MCS) algorithm [2].

A simple nearest-neighbor model was inadequate at describing the shape of the diffuse scattering. Therefore, a model using two correlation parameters was implemented. It is shown algebraically that such a model leads to homometry (pairs of stacking arrangements with the same diffraction pattern). Moreover, the influence of desymmetrization of the layers with respect to the ideal symmetry were investigated. It turned out that desymmetrization is a crucial factor for a good fit to the experimental data.

We conclude that an adequate modelling of diffuse scattering may require complex models that take into account desymmetrization, which might only be accessible by theoretical structure optimization.

(1) K. Dornberger-Schiff & H. Grell-Niemann. On the Theory of Order-Disorder (OD) Structures. *Acta Cryst.* **14**, 167–177 (1961)

(2) W. Huyer & A. Neumaier. Global Optimization by Multilevel Coordinate Search. *J. Global Optimization*, **14**, 331–355 (1999)

OP-061

Potassium-iron orthotellurate hydrate H6K3FeTe2O12, an OD structure featuring 1D diffuse scattering

T. Wolflehner (Vienna/AT), B. Stöger (Vienna/AT)

Following the discovery and influx of battery related research of novel $K_2M_2TeO_6$ honeycomb layered tellurates, orthotellurates have garnered interest recently. The closely related novel potassium-iron orthotellurate hydrate $H_6K_3FeTe_2O_{12}$ is likewise built of layers, however not of the honeycomb variety. We describe this novel order-disorder (OD) [1] phase, which shows 1D diffuse scattering owing to stacking faults.

$H_6K_3FeTe_2O_{12}$ was synthesized via a hydrothermal route at 210 °C starting from $FeSO_4.7H_2O$, $Te(OH)_6$ and an excess of KOH. The translucent, pale yellow to colorless plates were analyzed with a four-circle STOE Stadivari single crystal X-ray diffractometer with a high resolution 1M Dectris Eiger CdTe detector and high S/N ratio allowing for a precise quantification of diffuse scattering intensities. A phase transition was observed at 160 °C where dehydration occurs, not impacting the OD nature of the crystals.

The structure is built of two kinds of OD layers. One kind of layers is composed of $[TeO_6]$ and $[FeO_6]$ octahedra (including some OH groups) and possesses $P1(2/n)1$ symmetry, whereby parentheses indicate the stacking direction. The second kind of layers contains the K atoms and water molecules. Owing to the higher symmetry of the latter, the former can appear in two orientations.

The crystals under investigation can be considered as being composed of fragments of two polytypes. The major polytype is monoclinic with $I2/m$ symmetry (a=12.804(7) Å, b=14.9042(8) Å, c=5.9782(3) Å, β=90.085(10)°, R(obs.)=0.0212, wR(all)=0.0491, 2348 observed reflections). The minor polytype has orthorhombic $Pb2b$ symmetry and similar cell parameters. It is evidenced by additional broad reflections owing to a loss of the I-centering. The diffuse scattering was modelled using DIFFaX [2].

We showed that the novel H6K3FeTe2O12 is an OD structure, which can be described with two OD layers and occurs as fragments of two different polytypes, marking the boundary cases of the OD structure.

Figure 1: *1kl* reciprocal plane reconstruction of an initial single crystal XRD measurement of $H_6K_3FeTe_2O_{12}$. Major polytype reflections circled in white, additional reflections belong to the second polytype, which loses the body centering, but shares the same cell parameters. Also visible are streaks of 1D diffuse scattering

(1) K. Dornberger-Schiff and H. Grell-Niemann, "On the theory of order–disorder (OD) struc- tures," Acta Crystallographica, vol. 14, no. 2, pp. 167–177, Feb. 1961. doi: 10.1107/S0365110X61000607. [Online]. Available: https://doi.org/10.1107/S0365110X61000607

(2) M. M. J. Treacy, J. M. Newsam, and M. W. Deem, "A general recursion method for calculating diffracted intensities from crystals containing planar faults," Proceedings: Mathematical and Physical Sciences, vol. 433, no. 1889, pp. 499–520, 1991, issn: 09628444. [Online]. Available: http://www.jstor.org/stable/51916 (visited on 09/13/2022).

Fig. 1

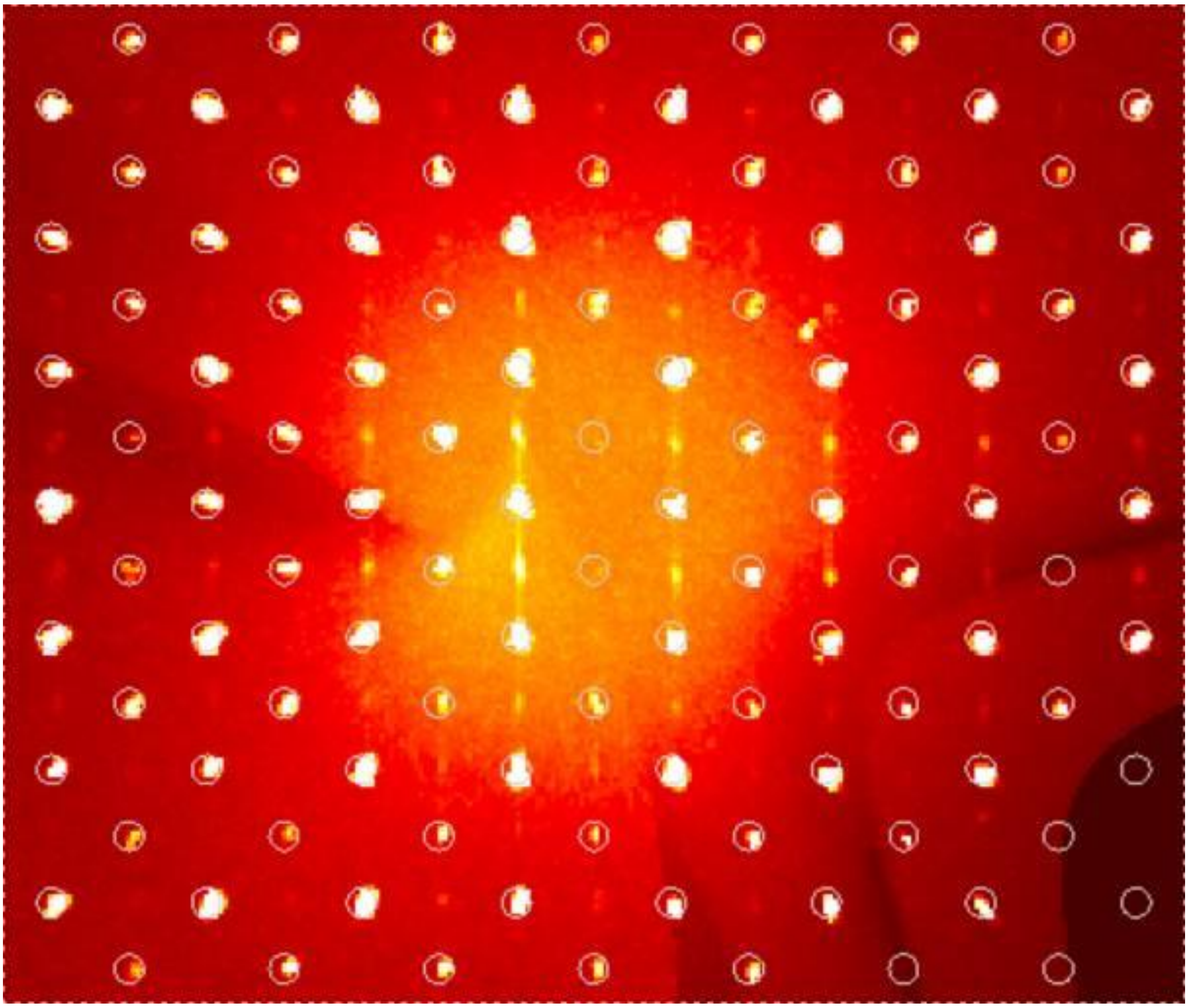

OP-062

Crystal chemical design and high-pressure synthesis of non-dense polynitrides

M. Bykov (Cologne/DE), E. Bykova (Bayreuth/DE), A. Goncharov (Washington, D.C./US), L. Dubrovinsky (Bayreuth/DE)

High-pressure chemistry is known to inspire the creation of unexpected new classes of compounds with exceptional properties. Despite general trends that pressure leads to the formation of dense compounds with elements possessing high coordination numbers, sometimes high-pressure synthesis may counterintuitively lead to the formation of porous or even van der Waals (vdW) bonded layered compounds. Since vdW compounds could potentially be used as precursors to 2D materials, the structural diversity of the accessible high-pressure phases may be used for the design of novel single-layer materials. We have used laser-heated diamond anvil cell technique for the synthesis of two novel compounds: beryllium polynitride BeN_4 and nickel diazenide NiN_2. BeN_4 was synthesized from elements at ~85 GPa and upon decompression to ambient conditions, it transforms into a compound with one-atom-thick BeN_4 layers interconnected via weak van der Waals bonds. Theoretical calculations for a single BeN_4 layer show that its electronic lattice is described by a slightly distorted honeycomb structure reminiscent of the graphene lattice and the presence of Dirac points in the electronic band structure at the Fermi level. The BeN_4 layer, *i.e.*, beryllonitrene, represents a qualitatively new class of 2D materials that can be built of a metal atom and polymeric nitrogen chains and host anisotropic Dirac fermions.High-pressure synthesis from elements leads to a novel nickel diazenide NiN_2 which possesses atom-thick layers comprised of Ni_2N_3 pentagons forming Cairo-type tessellation. The layers of NiN_2 are weakly bonded with the calculated exfoliation energy of 0.72 J/m^2, which is just slightly larger than that of graphene. The compound crystallizes in the space group of the ideal Cairo tiling (*P4/mbm*) and possesses significant anisotropy of elastic properties. The single-layer NiN_2 is a direct-band-gap semiconductor, while the bulk material is metallic. This indicates the promise of NiN_2 to be a precursor of a pentagonal 2D material with a tunable direct band gap.

References:

(1) Bykov *et al*. Realization of an Ideal Cairo Tessellation in Nickel Diazenide NiN_2: High-Pressure Route to Pentagonal 2D Materials. ACS Nano 15(8), 13539 (2021)
(2) Bykov *et al*. High-Pressure Synthesis of Dirac Materials: Layered van der Waals Bonded BeN_4 Polymorph Physical Review Letters 126, 175501 (2021)

OP-063

Cation-substitution in Pyrocarbonates

D. Spahr (Frankfurt am Main/DE), J. König (Frankfurt am Main/DE), L. Bayarjargal (Frankfurt am Main/DE), E. Haussühl (Frankfurt am Main/DE), V. Milman (Cambridge/GB), H. P. Lierman (Hamburg/DE), B. Winkler (Frankfurt am Main/DE)

It is well established that carbonates are the major reservoir of carbon in the Earth"s crust. Hence, understanding their behavior at different *p,T*-conditions and reactions with other phases is of great interest to understanding the deep carbon cycle. Common s*p*^{2}-carbonate phases such as calcite contain trigonal planar [CO_3]-groups, where C-*sp*^{2} hybrid orbitals are formed between a central carbon atom and each of the three surrounding oxygen atoms. Initially, these carbonates were found to be stable up to high pressures (~70 GPa) and high temperatures, but reactions of $CaCO_3$ with oxides (at ~20 GPa) or CO_2 (at ~40 GPa) demonstrated that new carbonate phases (Ca_2CO_4 and CaC_2O_5) can be obtained at significantly lower pressures [1-3]. In these carbonates, with *sp*^{3}-hybridized carbon, [CO_4]-groups can polymerize by corner-sharing, which was not observed in *sp*^{2}-carbonates.

During experiments exploring reactions of CO_2 with different carbonates (*M*CO_3, *M* = Sr, Ba, Pb) at moderate *p,T*-conditions in a LH-DAC (~30 GPa and ~2000 K), we found a novel type of *sp*^{2}-carbonates called pyrocarbonates [4]. In these pyrocarbonates, two [CO_3]-groups are linked by sharing one oxygen atom forming a [C_2O_5]-group. We solved the crystal structure of Sr[C_2O_5] and Pb[C_2O_5] (Fig. 1) and confirmed cation-substitution in pyrocarbonates by synchrotron single crystal diffraction, DFT calculations and Raman spectroscopy [4,5].

Figure 1: (a) Structure of Pb[C2O5] at 30 GPa and (b) isolated [C2O5]-group [5].

(1) Bayarjargal et al. *Phys. Earth Planet. Inter.,* 281, 31 (2018)
(2) Binck et al. *Am. Mineral.,* 107, 336 (2022)
(3) Binck et al. *ACS Earth Space Chem.,* 6, 73 (2022)
(4) Spahr et al. *J. Am. Chem. Soc.,* 144, 2899 (2022)
(5) Spahr et al. *Inorg. Chem.*, 61, 9855 (2022)

We acknowledge funding from the DFG (BA4020, WI1232, FOR2125/CarboPaT) and acknowledge DESY for the provision of experimental facilities and beam time. B.W. is grateful for support by the BIOVIA Science Ambassador program.

Fig. 1

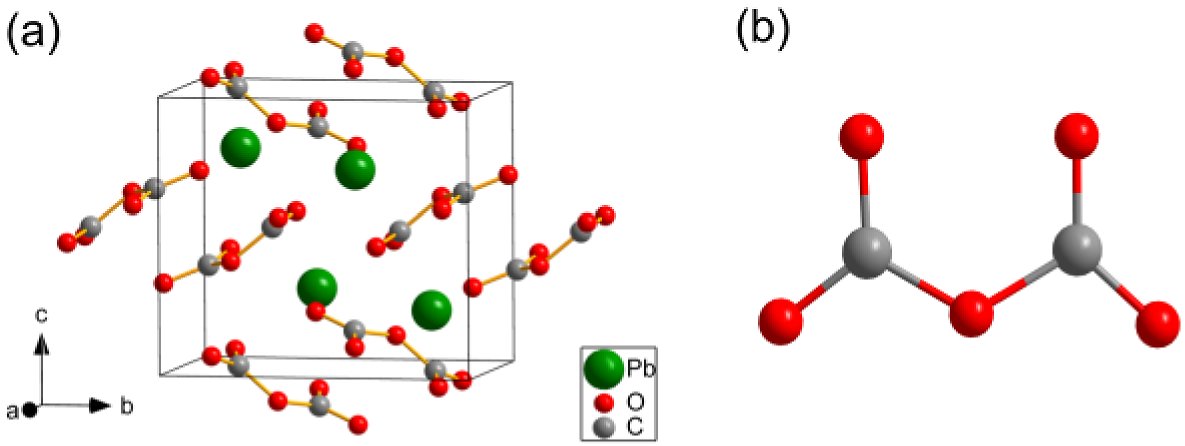

OP-064

Novel dysprosium carbides synthesised at high pressures

F. I. Akbar (Bayreuth/DE), L. Dubrovinsky (Bayreuth/DE), N. Dubrovinskaia (Bayreuth/DE), A. Aslandukova (Bayreuth/DE), A. Aslandukov (Bayreuth/DE), Y. Yin (Bayreuth/DE), T. Fedotenko (Hamburg/DE), D. Laniel (Edinburgh/GB)

Carbides are important compounds in science and technology due to their useful and often unusual properties. Chemical composition, pressure, and temperature are major factors which affect the structure and properties of materials with different types of chemical bonding and crystal chemistry.

In this work, the dysprosium carbides, Dy2C3, Dy4C3, and Dy3C2 were synthesized by laser heating of metallic Dy in diamond anvil cells (DACs). We used the BX90 type DAC equipped with Boehler-Almax type anvils and a rhenium gasket. Flakes of pure Dy were loaded into the pressure chamber along with dried NaCl which served as a thermal insulator. The Dy samples were pressurized to ~19, 55, and 58 GPa and heated up to 2500 K using NIR laser (1070 nm wavelength). The DACs with the samples were transferred to the Extreme Conditions Beamline (PETRA III) and ID11 beamline (ESRF) for *in situ* single-crystal X-ray diffraction studies of products of chemical reactions.

Dy4C3 (space group *I-43d*) was synthesised at 19, 55, and 58 GPa (Fig. 1a). This compound has not been known so far. Its structure belongs to the anti-Th3P4 structure type, which has been described for scandium carbide, but not observed in lanthanides carbides. It consists of single carbon and dysprosium atoms forming dysprosium (III) methanide, Dy(3+)4C(4-)3. According to *ab initio* simulations in the harmonic approximation at 0 K, Dy4C3 is dynamically stable even at ambient pressure.

The cubic Dy2C3 sesquicarbide was synthesized in this work at 19 GPa (lattice parameter *a*=7.9208(5) Å), but it was previously known at ambient conditions (lattice parameter at 1 bar is equal to *a*=8.198(2) Å). This compound is ethylide and contains C=C groups (Fig. 1b). Its structure has the same space group (*I-43d*) as that of Dy4C3. The structures of Dy2C3 and Dy4C3 are closely related: the former can be derived from the latter, as the positions of the centres of dumbbells [C2] in Dy2C3 coincide with the positions of single carbon atoms in Dy4C3, and the coordinates of Dy atoms are the same in the both structures.

Dy3C2 (space group *P4/mbm*) was discovered at 55 GPa (Fig. 1c). This carbide is isostructural to the predicted Ca3C2 calcium carbide. Dy3C2 is ethanide. Its structure contains C-C dumbbells with the C-C distance of 1.51(3) Å which is slightly shorter than the C-C distance in ethane.

Ab initio simulations of the convex hull (Fig. 1d) suggest that at 60 GPa phases we observed in this work (Dy2C3, Dy3C2, and Dy4C3) are thermodynamically stable.

Figure 1: Structures of dysprosium carbides synthesized in a laser-heated diamond anvil cell: a) Dy4C3 (19 GPa, 55 GPa, 58 GPa), b) Dy2C3 (19 GPa), c) Dy3C2 (55 GPa). The blue and brown spheres represent dysprosium and carbon, respectively. d) Calculated convex hull (dashed lines) for the Dy-C binary system; carbides previously reported are given in black, carbides synthesized in this work are given in red (those previously unknown) and in blue (one previously known).

Fig. 1

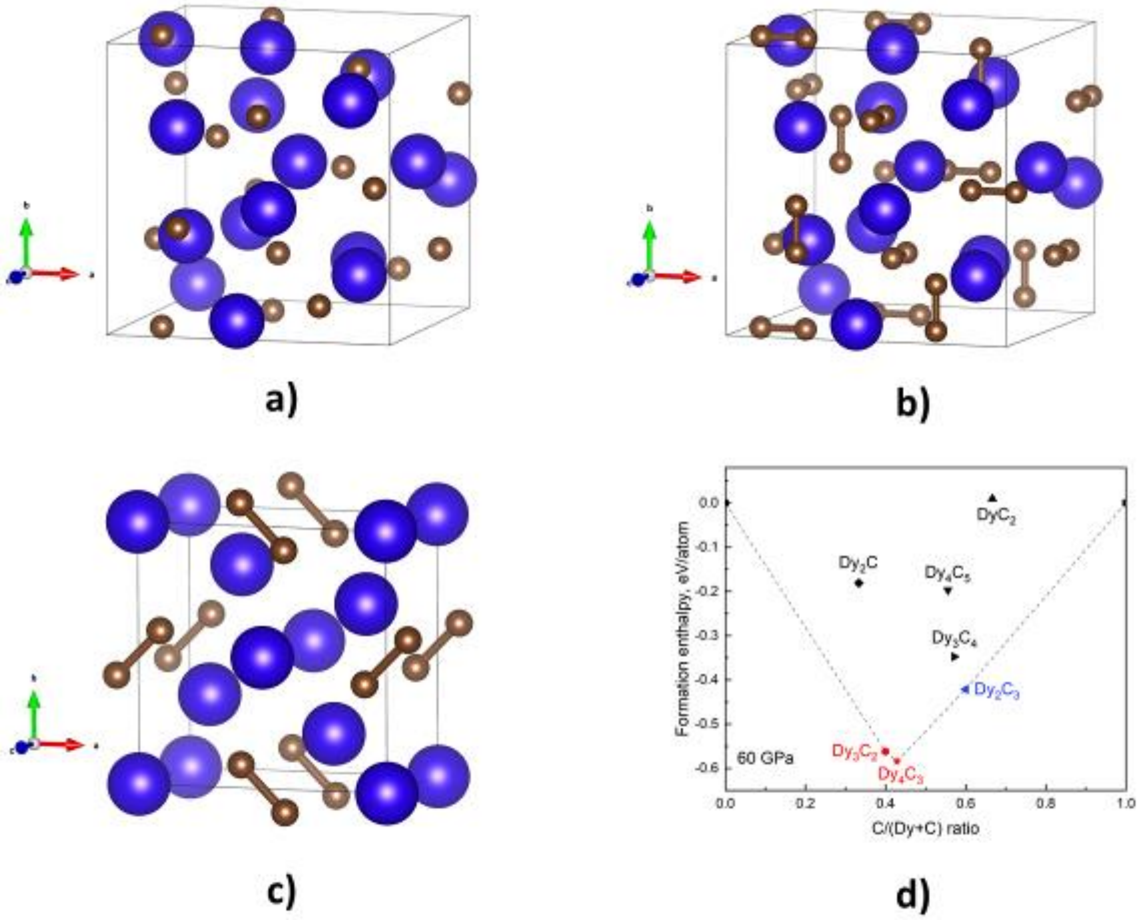
b
a
a)
b
a
b)
b
c
a
c)
Formation enthalpy, eV/atom
0.0
-0.1
-0.2
-0.3
-0.4
-0.5
-0.6
0.0
0.2
0.4
0.6
0.8
1.0
C/(Dy+C) ratio
DyC_2
Dy_2C
Dy_4C_5
Dy_3C_4
Dy_2C_3
60 GPa
Dy_3C_2
Dy_4C_3
d)

OP-065

Columnar hydrofluorocarbons from pressure-induced polymerization of polycyclic arene-perfluoroarene co-crystals

A. Friedrich (Würzburg/DE), I. E. Collings (Grenoble/FR), K. F. Dziubek (Sesto Fiorentino (FI)/IT), S. Fanetti (Sesto Fiorentino (FI)/IT), K. Radacki (Würzburg/DE), J. Ruiz-Fuertes (Santander/ES), J. Pellicer-Porres (Burjassot/ES), M. Hanfland (Grenoble/FR), D. Sieh (Würzburg/DE), R. Bini (Sesto Fiorentino (FI)/IT, Sesto Fiorentino (FI)/IT), S. J. Clark (Durham/GB), T. B. Marder (Würzburg/DE)

Arene-perfluoroarene systems are a robust supramolecular synthon, which is used for the development of highly oriented, stacked π-systems [1]. We found that their crystal structures are very stable at high pressure, which mainly acts to reduce the interplanar π-stacking separations (Fig. 1) [2]. When approaching a critical distance, polymerization along the stacking direction is initiated between the arene and perfluoroarene moieties leading to the formation of highly ordered nanothreads of novel hydrofluorocarbons.

Herein we present, as an example, the structural compression of 1:1 arene-perfluoroarene co-crystals, naphthalene:octafluoronaphthalene (NOFN) and anthracene:octafluoronaphthalene (AOFN), up to 20 and 25 GPa, respectively, as obtained from single-crystal synchrotron X-ray diffraction, and the vibrational modes and reaction kinetics obtained from infrared spectroscopy. We propose structural models for the high-pressure polymers predicted by quantum mechanical computations based on density functional theory, which are in agreement with experimentally determined unit cell parameters (Fig. 1). Based on our results, it is proposed that the polymerization takes place via one-dimensional "zipper" reactions along the π-stacked columns within the co-crystals, preceded by Diels-Alder [4+2] cycloaddition reactions in NOFN.

Financial support from ESRF (and synchrotron beamtime), LASERLAB-EUROPE (grant 654148, EU"s Horizon 2020 program), the Spanish MICINN (grants MAT2016-75586-C4-1-P, PGC2018-097520-A-100, PID2021-125927NA-C22), the Generalitat Valenciana (grant Prometeo/2018/123 (EFIMAT)), and the University of Würzburg is greatly appreciated. Durham"s Hamilton HPC service and the UK Archer supercomputer were used (grant EPSRC EP/P022782/1).

(1) J.C. Collings et al. *New J. Chem.* **2001**, *25*, 141
(2) A. Friedrich et al. *J. Am. Chem. Soc.* **2020**, *142*, 18907

Figure 1: Design of columnar hydrofluorocarbons via pressure-induced polymerization of arene-perfluoroarene co-crystals

Fig. 1

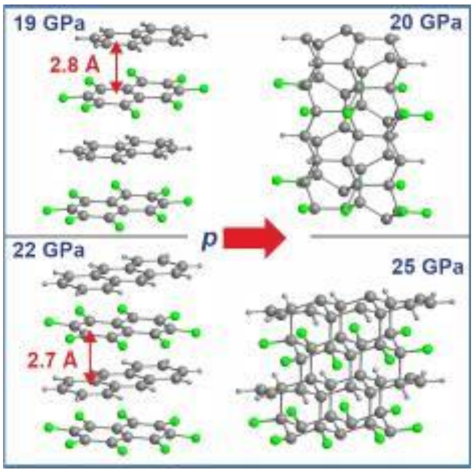

OP-066

Contribution of X-ray crystallography to the full description of molecular switches behavior under pressure at variable temperature

M. Marchivie (Pessac/FR), E. Tailleur (Nancy/FR), P. Rosa (Pessac/FR), J. P. Itié (Gif-sur-Yvette/FR), B. Vignolle (Pessac/FR), P. Guionneau (Pessac/FR)

Since the development of Diamond Anvil Cell[1], the investigations of materials under high pressure (HP) did not stop to increase. Nevertheless, obtaining **HP structural data** is still a challenge especially when combining several thermodynamic variables such as **pressure and temperature**, or when data are recorded on **molecular materials**.

Addressing the additional difficulties due to molecular compounds necessary includes methodology developments in order to access to a reliable characterization, taking account their specificities. Surprisingly, though the scientific community still develops new technics to get accurate data at very high pressure, working with **soft material at pressure bellow 1 GPa is still challenging**. For example, structural data under pressure represent less than 1% of the CSD data base.

Spin CrossOver (SCO) materials are molecular complexes that can switch from a Low Spin (LS) to a High Spin (HS) state upon physical stimuli like pressure, opening potential piezo-switch based applications[2]. The structure-properties relationships of such compounds at ambient conditions are now well established,[3] but their crystallographic investigation under pressure remains very scarcely reported even though new, unexplained or very rare behaviors are observed in numerous examples[4]. Typically, despite the crucial role of polymorphism on such materials, full (P, T) **phase-diagrams of SCO molecular switches are almost unexplored.** In this communication, we show how powerful is crystallography to investigate pressure induced phenomena using**HP single crystal diffraction** as well as **in situ HP Powder X-Ray Diffraction (PXRD).** Thanks to these techniques, we present the full description of SCO compounds along their transitions and explore pressure induced phenomena taking place on **low pressure range** with **extremely small pressure steps**. Beyond the rare determination of the bulk moduli of HS and LS states at different temperatures, such investigations reveal unusual behaviours like negative linear compressibility or unexpected pressure induced phase transitions (fig. 1).

Figure 1: Pressure dependence of PXRD diagram of a SCO compound showing a structural transition around 12 kbar.

References:

(1) J. C. Jamieson, *et al. Rev. Sci. Instrum.* **30**, 1016–1019 (1959)
(2) A. B. Gaspar, *et al. Comptes Rendus Chim. **2018***, 21**,** 1095–1120
(3) P. Guionneau, *Dalt. Trans. **2014***, 43**,** 382–393
(4) H. J. Shepherd *et al*, *Angew. Chemie Int. Ed.*, (51), **2012**, 3910–3914

Fig. 1

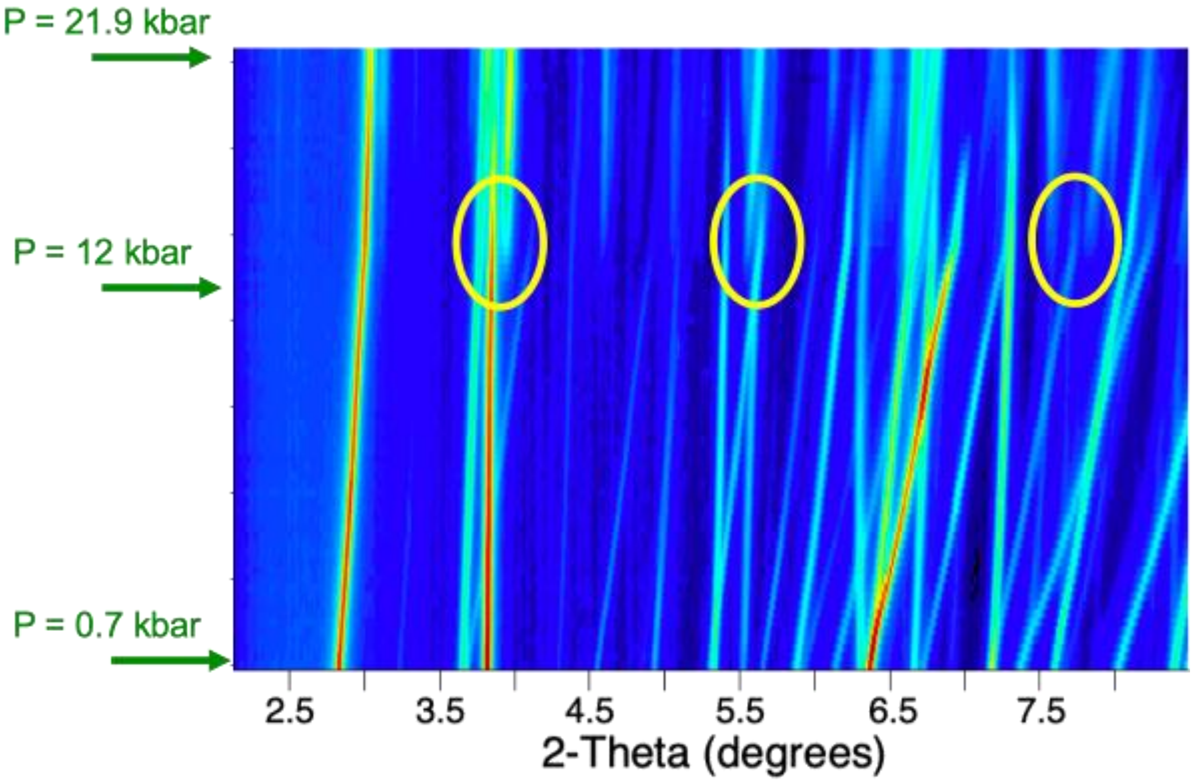

OP-067

The generation of artificial SEM images of nanoparticles by deep neural networks

J. Bals (Essen/DE), M. Epple (Essen/DE)

Deep neural networks have shown great success in the analysis of images of nanoparticles by image segmentation [1], image classification [2], and object detection [3]. A step further is the creation of artificial images of nanoparticles using concepts of artificial intelligence (known as "deep fake" in the cases of pictures and movies of living persons). Artificial intelligence is bringing a faked image so close to a real image that true and simulated images cannot be distinguished, even by an experienced observer. This has considerable implications for the visualization of nanocrystals and nanoparticles.

Recent techniques have shown the potential of artificial data. The program Blender 3 [4] is able to create images of particles that have dropped on a surface (like nanoparticles on an SEM sample holder). We have created images of several thousand objects ("nanoparticles") dropped on a plane-background with Blender. Next, we implemented Generative adversarial networks (GANs) [5] to convert these images into realistic SEM images of agglomerated and deformed nanoparticles. Constraints are the level of the "right" amount of noise to an image created by the GAN to appear realistic and the high amount of computing power which is necessary to create "faked" SEM images.

References:

(1) Ronneberger, O., Fischer, P., & Brox, T. (2015). In: Navab, N. et al. (Eds.): MICCAI 2015, 234-241
(2) He, K., Zhang, X., Ren, S., & Sun, J. (2016). In: Proceedings of the IEEE CVPR 2016, 770-778
(3) Ren, S., He, K., Girshick, R., Sun, J. (2015). In: Proceedings of the NIPS 2015, 91-99
(4) Blender Online Community. (2018). http://www.blender.org, Last visited: 06.05.2022 11:03
(5) Goodfellow, I., Pouget-Abadie, J., Mirza, M., Xu, B., Warde-Farley, D., Ozair, S., Bengio, Y. (2014)., Proceedings of the NIPS 2014, 2672-2680

OP-068

Compression and data reduction in serial crystallography

M. Galchenkova (Hamburg/DE), A. Tolstikova (Hamburg/DE), D. Oberthür (Hamburg/DE), J. Sprenger (Hamburg/DE), W. Brehm (Hamburg/DE), T. White (Hamburg/DE), A. Barty (Hamburg/DE), H. Chapman (Hamburg/DE), O. Yefanov (Hamburg/DE)

Protein crystallography is one of the most successful methods for biological structure determination. This technique requires many diffraction snapshots to get 3D structural information of the studied protein. Even more patterns are needed for studying fast protein dynamics that can be achieved using serial crystallography (SX). Fortunately, new X-ray facilities such as 4th generation synchrotrons and Free Electron Lasers (FELs) combined with newly developed X-ray detectors opened a way to carry out these experiments at a rate of more than 1000 images per second. The drawback of this increase in acquisition rate is the volume of collected data - up to 2 PB of data per experiment could be easily obtained. Therefore, new data reduction strategies have to be developed and deployed. Lossless data reduction methods will not change the data, but usually fail to achieve a high compression ratio. On the other hand, lossy compression methods can significantly reduce the amount of data, but they require careful evaluation of the resulting data quality.

We have tested different approaches for both lossless and lossy compression applied to SX data, proposed some new ways for lossy compression and demonstrated appropriate methods for data quality assessment. By checking the resulting statistics of compressed data (like CC*/Rsplit, Rfree/Rwork) we have demonstrated that the volume of the measured data can be greatly reduced while the quality of the resulting data was kept almost constant. In addition, we tested lossy compression methods on the SAD dataset (thaumatin collected at 4.57 keV, measured at the SwissFEL) and demonstrated that even such very sensitive data can be successfully compressed. It allowed us to determine the limit of application for all considered lossy compressions. Some of the proposed compression strategies, tested on SX and MX datasets, can be used for other types of experiments, even with different sources (for example electron and neutron diffraction).

OP-069

New tools for sequence assignment validation in cryo-EM and crystal structure models of macromolecules

G. Chojnowski (Hamburg/DE)

One of the most elusive errors in macromolecular models are sequence register shifts, where backbone is traced correctly, but residues are systematically assigned an identity of a residue a few amino acids up or down in sequence. The register errors may affect model interpretation and propagate to newly built models from older structures (1). Although register-shifts can be often detected from poor map-model fit or model-geometry outliers, at lower resolutions this becomes increasingly difficult. As a result, detection and correction of sequence assignment issues in macromolecular models usually requires a detailed, residue-by-residue analysis by an experienced crystallographer.

I have shown that register shifts in cryo-EM protein models can be automatically detected using a systematic re-assignment of short model fragments to the target sequence, which was implemented in a *checkMySequence* program (2). This approach revealed register-shift issues in a few percent of cryo-EM protein models deposited in the Protein Data Bank (PDB), which was further confirmed with an orthogonal method based on intramolecular contacts predicted using deep learning-based tools (1).

I will show that the sequence-assignment validation approach implemented in *checkMySequence* can be used for automated identification of register-shift errors in crystal structure models of proteins and nucleic acids, using standard, model-bias corrected maximum likelihood maps. I will also show that, as in the case of cryo-EM, register shift errors in crystal structures deposited in the PDB are relatively common. I will present several examples and show that many, but not all of them could have been avoided if modern Artificial Intelligence-based protein structure prediction methods were used for the structure determination.

(1) Rodríguez, F. S., Chojnowski, G., Keegan, R. M. & Rigden, D. J. (2022) bioRxiv 2022.08.25.505292 (ActaD, 10.1107/S2059798322010415)
(2) Chojnowski, G. (2022). Acta Cryst D78 806-811

OP-070

Treatment of core electrons in quantum crystallography

F. Kleemiss (Regensburg/DE), N. Peyerimhoff (Durham/GB), M. Bodensteiner (Regensburg/DE)

While the greatest advantage of Quantum Crystallography is undoubtedly the correct description of chemical bonding and electron density redistributions in the valence of atoms[1-3] the atomic core has slowly disappeared from the focus of method developers and researchers , while it has for the majority of the periodic table the biggest contribution to scattering of X-rays.

Despite recent advances in automation and the availability of non-spherical scattering factors, the high residual density around heavy scatterers, especially in high-resolution data sets (compare Figure 1a), still cannot be explained. It remains an open discussion what the source of these artifacts is. In the proposed presentation, it will be demonstrated that two effects caused by core electrons could explain the observed patterns: The dipole approximation for forward scattering in resonant scattering treatment (a.k.a. anomalous diffraction)[4] could be a significant overestimation for high angle diffraction data. Additionally, the missing cusp in Gaussian functions which are frequently used to describe the atomic density compared to Slater-type densities, which one would expect for atomic densities, might be a source for similar errors. In combination with the *also* Gaussian description of the atomic displacement, this yields insufficient Fourier behaviour for the description of the structure factors of heavy elements at high resolution. The effects on the calculated electron density around d-block atoms are visualized in Figure 1.

Figure 1: Residual density after HAR of Os-hexa-hydride complex (top), difference density between newly proposed angular dependent treatment of resonant scattering correction and and classical treatment (bottom, left) and non-spherical refinement using Slater-type core density and all-electron treatment (bottom, right).

(1) M. Woińska et al. Chem. Phys. Chem. 18(23) (2017): 3334-3351.
(2) S. Grabowsky et al. Chem. Sci. 8 (2017): 4159-4176.
(3) A. Genoni, P. Macchi, Crystals 10(6) (2020): 473.
(4) D. C. Creagh, International Tables of Crystallography, Volume C (2016), 241-258.

Fig. 1

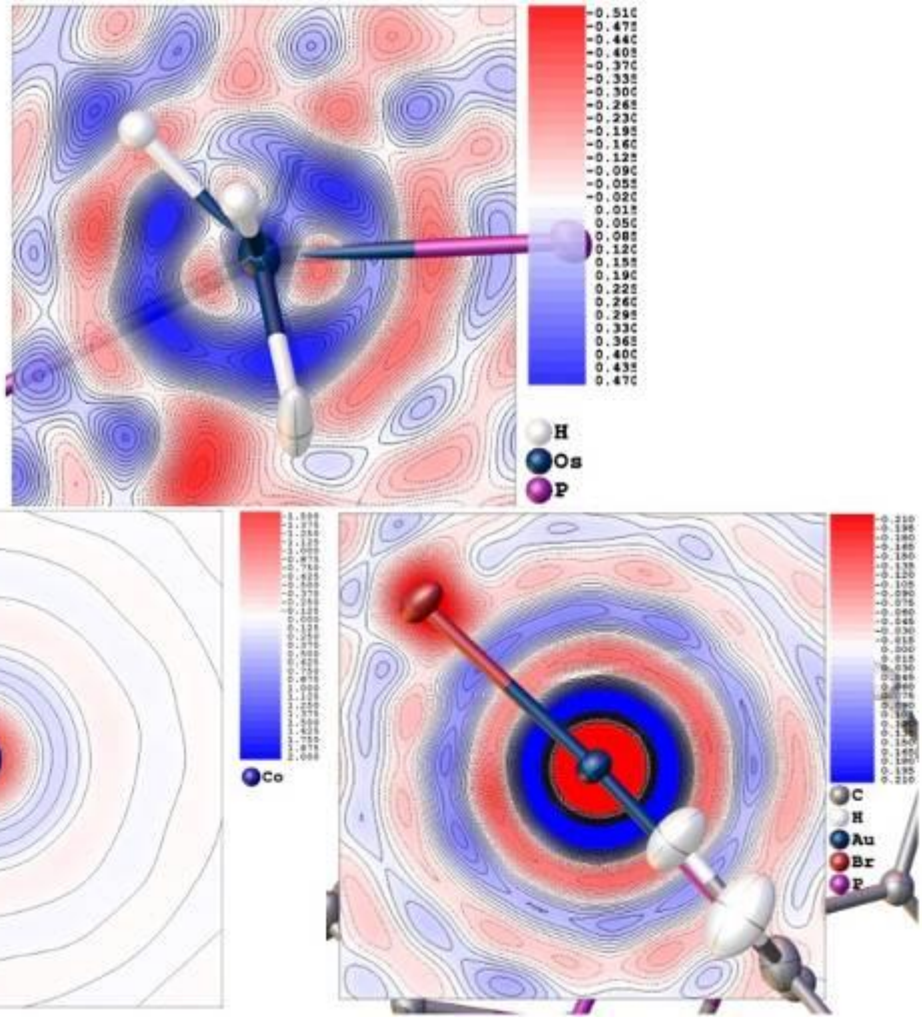
-0.510
-0.475
-0.440
-0.405
-0.370
-0.335
-0.300
-0.265
-0.230
-0.195
-0.160
-0.125
-0.090
-0.055
-0.020
0.015
0.050
0.085
0.120
0.155
0.190
0.225
0.260
0.295
0.330
0.365
0.400
0.435
0.470
H
Os
P
Co
C
H
Au
Br
P

OP-071

Multipole model and topological analysis of chemical bonding in β-boron

C. Eisele (Bayreuth/DE), S. Ramakrishnan (Higashi-Hiroshima/JP), J. K. Bao (Shanghai/CN), S. R. Kotla (Bayreuth/DE), C. Paulmann (Hamburg/DE), L. Noohinejad (Hamburg/DE), M. Tolkiehn (Hamburg/DE), S. van Smaalen (Bayreuth/DE)

Although the structure of β-rhombohedral boron, which crystallizes in the rhombohedral space group *R*-3*m*, has been described already in 1957 [1], there is still an ongoing debate on structural details [2]. *Β*-boron exhibits a three-dimensional framework of interconnected B_{12} icosahedral and $(B_{28})_2B$ clusters. The framework contains 15 unique boron sites. Additionally, interstitial boron (or impurity) atoms can be accommodated in the large cavities within the framework. These interstitial boron atoms are only accommodated in a small fraction of the cavities and therefore called partially occupied sites (POS). In the model by Slack et al. [4], which is the most acknowledged Literature model to date, five POS with occupancies ranging from 0.037 to 0.272 are reported; its hexagonal unit cell has a volume of $V \approx 2465$ Å^3 and contains approximately 320 boron atoms.

We have re-investigated β-boron by means of high-resolution X-ray diffraction data using synchrotron radiation (P24 Beamline, DESY, Hamburg) and samples of high purity. The main features of Slack's model [4] have been confirmed, only slight differences have been found in some of the POS. In addition to a routine structure refinement against the experimental XRD data we have performed a multipolar refinement applying the Hansen and Coppens formalism [5]. The purpose is to give a more accurate description of the total electron density by taking into account deviations from the spherical distribution of the respective atomic electron densities due to chemical bonding.

We will present a characterization of the peculiar chemical bonds in β-boron based on the yielded multipolar parameters applying Bader's theory of quantum theory of atoms in molecules (QTAIM) [6].

(1) Sands D, Hoard J. Rhombohedral elemental boron. *J. Am. Chem. Soc.*, **79**, 5582-5583 (1957)
(2) Ogitsu T, Schwegler E., Galli, G. β-Rhombohedral boron: at the crossroads of the chemistry of boron nd the physics of frustration. *Chem. Rev.*, **113**, 3425-3449 (2013)
(3) Albert B, Hillebrecht H. Boron: Elementary challenge for experimenters and theoreticians. *Angew. Chem. Int. Ed.*, **48**, 8640-8668 (2009)
(4) Slack G, Hejna C, Garbauskas M, Kasper J. The crystal structure and density of β-rhombohedral boron. *J. Solid State Chem.*, **76**, 52-63 (1988)
(5) Coppens, P. X-ray charge densities and chemical bonding, *Oxford University Press, New York* (1997), ISBN 0-19-509823-4
(6) Bader, F. Atoms in molecules: a quantum theory, *Oxford University Press, New York* (1990), ISBN 0 19 855865 1

This research was supported by the DFG under grant number 244734497.

Microsymposium 16 | Bio-Crystallography V: Synchrotrons and new technologies

OP-072

In cellulo crystallography – Overcoming resolution limits by cell fusion

J. Boger (Lübeck/DE), I. Breidbach (Lübeck/DE), R. Schönherr (Lübeck/DE), S. Nachtschatt (Lübeck/DE), L. Redecke (Lübeck/DE)

In cellulo crystallography is an emerging field complementing conventional methods of protein crystallization. It describes the process of recombinant protein crystallization after expression using a baculovirus expression vector system and subsequent crystal diffraction in the living cells. The identification of natively bound ligands in the native cellular environment is unique (Nass et al., 2020) and cannot be replaced by upcoming AI-based structure prediction techniques, like AlphaFold (Jumper et al., 2021, Varadi et al., 2021). We have established an *in cellulo* crystallization workflow, enabling an easy production of homogenous microcrystals highly required for serial and time-resolved experiments at XFELs and synchrotron sources.

However, some protein crystals diffract synchrotron radiation only to low resolution. Signal in higher resolution shells can be intensified either by increasing the brilliance of radiation, e.g., by applying XFEL pulses, or by enlarging the diffractive volume. Since access to XFELs is still difficult for most scientists, optimizing crystal dimensions appears more appealing. In intracellular crystallization the crystal size is controlled by the size of the cell, but not limited to the cell diameter since crystals can also stick out of the cells without affecting the cellular integrity (Schönherr et al., 2015). To overcome this barrier, a protocol for cell fusion using polyethylene glycol was developed and crystal containing syncytia were then introduced into and serially diffracted at a synchrotron beam, finally allowing protein structure elucidation. The diffractive volume of the *in cellulo* grown crystals could be enhanced by a factor of approx. five, resulting in an improvement of resolution by approximately 0.5 Å.

Overcoming this bottleneck of *in cellulo* crystallization will expand the application of this approach in the future by enabling other protein structures to be elucidated by boosting their resolution limits.

OP-073

JINXED: Just in time crystallization for easy structure determination of biological macromolecules

A. Henkel (Hamburg/DE), M. Galchenkova (Hamburg/DE), J. Maracke (Hamburg/DE), O. Yefanov (Hamburg/DE), J. Hakanpää (Hamburg/DE), J. R. Mesters (Lübeck/DE), H. Chapman (Hamburg/DE, Hamburg/DE, Hamburg/DE), D. Oberthür (Hamburg/DE)

Macromolecular crystallography is a well-established method in the field of structure biology and has led to the majority of known protein structures to date. After focusing on static structures, the method is now developing towards the investigation of macromolecular structural dynamics, e.g. by looking at protein-ligand or enzyme-substrate interactions. These experiments often require multiple handling steps of the sensitive protein crystals. These handling steps can cause significant crystal damage, causing a decrease in data quality. These handling steps are avoided in time-resolved experiments based on serial crystallography and room-temperature data collection, where the reaction is triggered within the crystals – either optically or chemically. For the latter, the use of micron-sized crystals is necessary to ensure short diffusion times of ligands and quick saturation within each crystal. Despite crystal size, certain crystal morphologies e.g. small solvent channels can prevent sufficient ligand diffusion. Presented here is a method combining protein crystallization and data collection in a novel one-step-process to overcome the aforementioned challenges. We successfully performed corresponding experiments as a proof-of-principle using hen egg white lysozyme with crystallization times of only a few seconds. This method called JINXED (Just in time crystallization for easy structure determination) promises to result in high-quality data due the avoidance of crystal handling and has the potential to enable time-resolved experiments with crystals containing small solvent channels by adding potential ligands to the crystallization buffer, simulating traditional co-crystallization approaches. Furthermore, JINXED avoids several sample delivery challenges as crystal settling or line clogging. All samples are in liquid form and can therefore be injected by auto-samplers connected to conventional HPLC systems. By adding potential ligands to the crystallizing agent or the protein and with upcoming online and automated data processing, this method may offer the possibility to combine high-throughput ligand screenings and detailed dynamical investigations at atomic resolution with a high level of automation.

Figure 1: Drawings of a) sample environment overview with TapeDrive nozzle, tape, sample line and X-ray beam, b) TapeDrive nozzle with inner (left) and outer mixing (right) channel, c) JINXED principle with TapeDrive nozzle incorporating the protein solution channel (yellow) and crystallizing agent channel (blue). Due to mixing within the sample line on the tape, protein crystallization can be observed.

Figure 2: Schematic drawing of a possible high-throughput setup showing two automated micro-dispensing systems for samples (e.g. protein mixed with compound) and crystallization agents, the sample delivery system CFEL TapeDrive 2.0 including the TapeDrive nozzle (TDN), X-ray beam and detector

(1) JINXED: Just in time crystallization for easy structure determination of biological macromolecules. A. Henkel, M. Galchenkova, J. Maracke, O. Yefanov, J.Hakanpää, J. R. Mesters, H. N. Chapman, D. Oberthür. bioRxiv 2022.10.26.513656; doi: https://doi.org/10.1101/2022.10.26.513656

Fig. 1

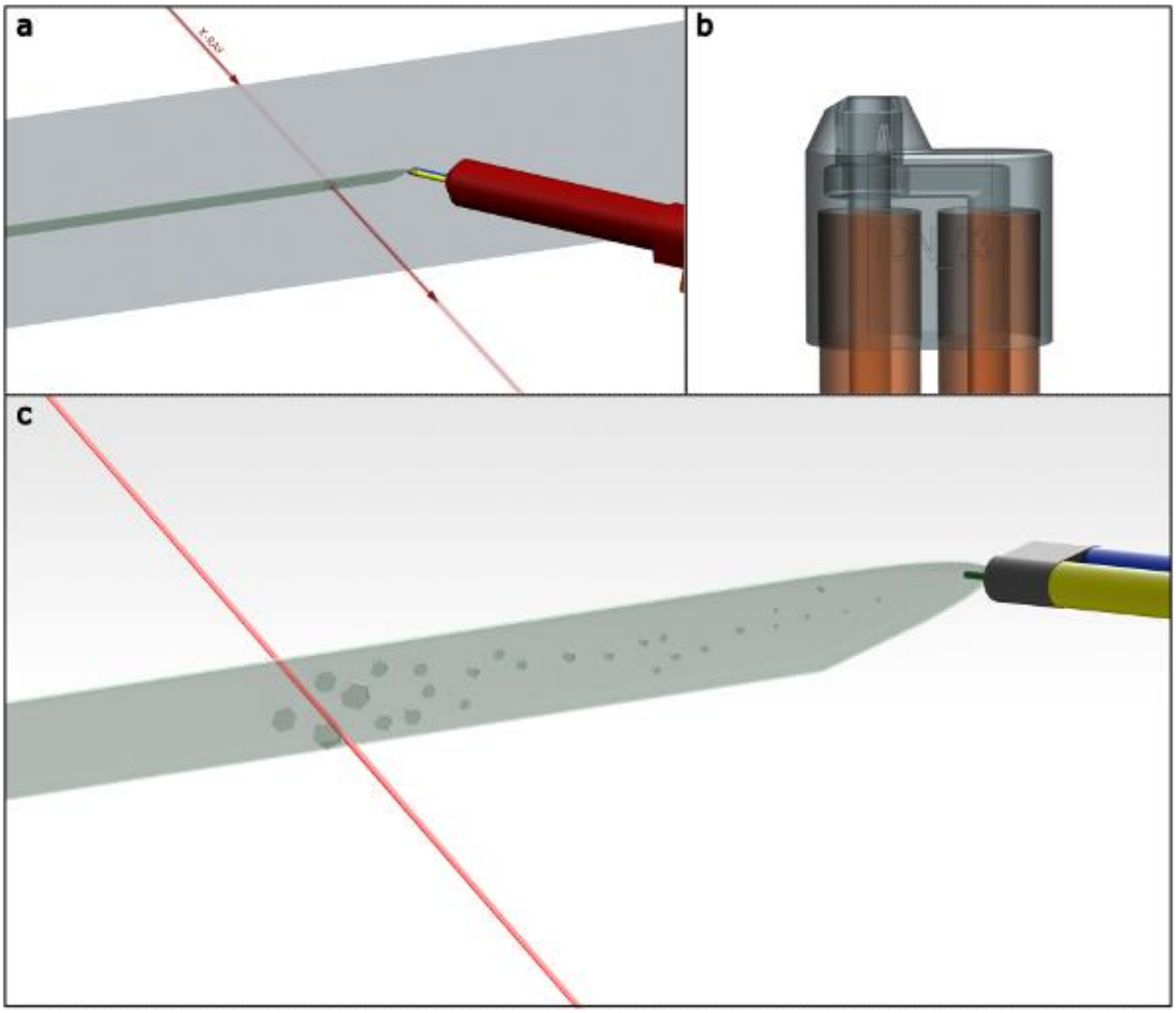

Fig. 2

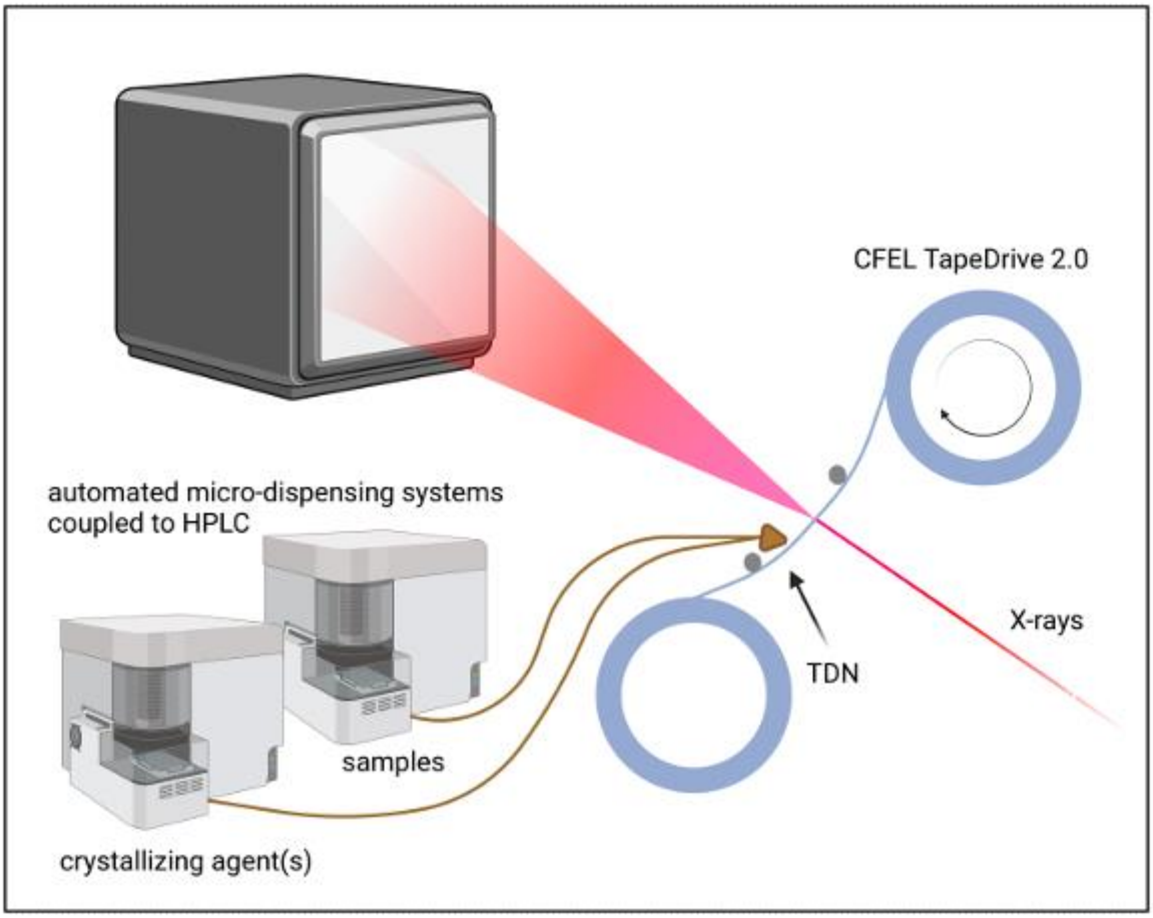
CFEL TapeDrive 2.0
automated micro-dispensing systems coupled to HPLC
X-rays
TDN
samples
crystallizing agent(s)

OP-074

Microsecond time-resolved pink beam serial crystallography

S. Günther (Hamburg/DE), A. Tolstikova (Hamburg/DE), M. Galchenkova (Hamburg/DE), O. Yefanov (Hamburg/DE), P. Reinke (Hamburg/DE), H. Chapman (Hamburg/DE), R. Henning (Chicago, IL/US), M. Levantino (Grenoble/FR), A. Meents (Hamburg/DE)

Protein dynamics are the basis of protein function, whether it is binding to ligands or facilitating chemical reactions. Motions on the femto- to millisecond scale determine protein behavior ranging from bond vibrations to large scale domain movements. Time-resolved X-ray crystallography has begun to discern transient conformations of proteins. Here, the system is removed from its equilibrium by laser light or addition of ligands. While the temporal resolution of ligand binding is generally hampered by the diffusion of ligands into the crystal, mostly to the millisecond range, activation by laser light can resolve femtosecond processes.

While serial crystallography experiments at X-ray free electron lasers can resolve processes in the femtosecond range, experiments at synchrotron sources using monochromatic light are typically limited to the millisecond range and longer due to the lower brilliance. However, pioneering Laue diffraction experiments at synchrotrons demonstrated the feasibility of studies down to the sub-nanosecond regime in single crystal diffraction experiments.

Here we present results from pink beam time-resolved serial crystallography experiments using a fixed-target sample delivery system in combination with a low background setup and an on-axis microscope allowing inline illumination of the sample by a pump laser. Data processing using pinkindexer(1) and CrystFEL(2) allows detection of changes in the central chromophore of photoactive yellow protein on the microsecond scale. In a second set of experiments IR-laser induced temperature jumps were used to induce dynamics in proteins.

With synchrotron sources and beamlines providing 100 ps single X-ray pulses, such as BioCARS beamline 14ID at the Advanced Photon Source, this enables the study of (sub)nanosecond processes at synchrotrons by serial crystallography.

(1) Y. Gevorkov et al., Acta Crystallographica Section A 76, 121 (2020).
(2) T. A. White et al., Journal of Applied Crystallography 45, 335 (2012).

OP-075

Facilities for Macromolecular Crystallography at the HZB

M. S. Weiss (Berlin/DE), L. S. Benz (Berlin/DE), T. Barthel (Berlin/DE), T. Crosskey (Berlin/DE), A. Dillmann (Berlin/DE), R. Förster (Berlin/DE), P. Fröling (Berlin/DE), C. Gless (Berlin/DE), T. Hauss (Berlin/DE), M. Hellmig (Berlin/DE), F. Lennartz (Berlin/DE), J. H. W. Scanlan (Berlin/DE), G. Weber (Berlin/DE), J. Wollenhaupt (Berlin/DE), U. Mueller (Berlin/DE)

The Macromolecular Crystallography (MX) group at the Helmholtz-Zentrum Berlin (HZB) has been in operation since 2003. Since then, three state-of-the-art synchrotron beam lines (BL14.1-3) for MX have been built up on a 7T-wavelength shifter X-ray source [1-3]. Currently, the three beam lines represent the most productive MX-stations in Germany, with about 4000 PDB depositions (Status 11/2022). BLs14.1 and 14.2 are energy tunable in the range 5.5-15.5 keV, while beam line 14.3 is a fixed-energy side station operated at 13.8 keV. All three beam lines are equipped with state-of-the-art detectors: BL14.1 with a PILATUS3S 6M detector, BL14.2 with a PILATUS3S 2M and BL14.3 with a PILATUS 6M detector. BL14.1 and BL14.2 are in regular user operation providing close to 200 beam days per year and about 600 user shifts to approximately 100 research groups across Europe. Recently remote beamline operation has been established successfully at BL14.1 and BL14.2. BL14.3 is been equipped with a MD2 micro-diffractometer, a HC1 crystal dehydration device and a REX nozzle changer making it suitable for room temperature experiments. Additional user facilities include office space adjacent to the beam lines, a sample preparation laboratory, a biology laboratory (safety level 1) and high-end computing resources. Within this presentation/poster a summary on the experimental possibilities of the beam lines and the ancillary equipment provided to the user community will be given.

References:

(1) U. Heinemann, K. Büssow, U. Mueller & P. Umbach (2003). Acc. Chem. Res. 36, 157-163.
(2) U. Mueller, N. Darowski, M. R. Fuchs, R. Förster, M. Hellmig, K. S. Paithankar, S. Pühringer, M. Steffien, G. Zocher & M. S. Weiss (2012). J. Synchr. Rad. 19, 442-449.
(3) U. Mueller, R. Förster, M. Hellmig, F. U. Huschmann, A. Kastner, P. Malecki, S. Pühringer, M. Röwer, K. Sparta, M. Steffien, M. Ühlein & M. S. Weiss (2015). Eur. Phys. J. Plus 130, 141-150.

OP-076

Macromolecular Crystallography at DESY

J. Hakanpää (Hamburg/DE), C. Borges (Hamburg/DE), S. Chatziefthymiou (Hamburg/DE), A. Gruzinov (Hamburg/DE), J. Song (Hamburg/DE), H. Taberman (Hamburg/DE), G. Pompidor (Hamburg/DE), W. Ewert (Hamburg/DE), S. Günther (Hamburg/DE), P. Reinke (Hamburg/DE), P. Fischer (Hamburg/DE), A. Meents (Hamburg/DE), J. Meyer (Hamburg/DE)

DESY"s MX beamline P11 has been operating since 2012 at PETRA III and offers versatile focusing options to match the beam size and desired dose with diverse samples and various kinds of experiments (1). Fast and robust sample changer in combination with Eiger2 X 16M allows data collection as fast as 2 min per sample and fits 23 unipucks simultaneously. Remote operation is realised with simple web-browser based solution and authentication through the user portal, DOOR. P11 user laboratory is equipped with the OLT Shifter for semi-automated crystal harvesting and soaking experiments, ideal for fragment screening projects.

Serial synchrotron crystallography at P11 is enabled mainly with the CFEL tape-drive setup, also capable of time-resolved experiments by the mix-and-diffuse method (2). Real-time autoprocessing of serial data with CrystFEL (3) has been developed within a long-term proposal.

At PETRA IV, we are aiming to form a uniform bio-village at the current location of DESY and EMBL beamlines (P11-P14). P11 has implemented MXCuBE/ISPyB for data acquisition and information management to harmonize the interfaces to the beamlines and is working together with EMBL within a long-term proposal to further develop both software and hardware. Together with EMBL and Hamburg University of Applied Sciences (HAW Hamburg), DESY is currently building up a new logistics chain for MX samples.

Pharmaceutical screening efforts at DESY will be further strengthened with the newly built HiPhaX beamline. The instrument is operating at 16 keV and will be equipped with an Eiger detector, with the goal to perform highly automated data collection with a throughput of more than 1000 samples per 24 hours. Additionally, the instrument will provide unique opportunities for room temperature measurements in combination with multi-crystal sample holders.

(1) Burkhardt A., et al., Status of the crystallography beamlines at PETRA III. Eur. Phys. J. Plus 131, 56 (2016)
(2) Beyerlein K. R., et al., Mix-and-diffuse serial synchrotron crystallography. IUCrJ 4, 769-777 (2017)
(3) White T. A., et al., Recent developments in CrystFEL. J. Appl. Cryst. 49, 680-689 (2016)

OP-077

EMBL@PETRA IV – an Integrated Facility for Structural Biology and Imaging

S. Storm (Hamburg/DE), G. Bourenkov (Hamburg/DE), L. Duke (Hamburg/DE), J. Albers (Hamburg/DE), C. Blanchet (Hamburg/DE), M. Agthe (Hamburg/DE), D. von Stetten (Hamburg/DE), E. Rodriguez Garcia (Hamburg/DE), S. Fiedler (Hamburg/DE), D. Svergun (Hamburg/DE), M. Wilmanns (Hamburg/DE), T. Schneider (Hamburg/DE)

Currently, DESY is planning the fourth generation synchrotron radiation source PETRA IV in Hamburg. As a partner of DESY, EMBL is proposing to contribute an Integrated Facility for Structural Biology and Imaging. Centered on beamlines for macromolecular crystallography (MX), small angle scattering (BioSAXS) and X-ray Imaging, upstream services supporting the preparation of samples, downstream services for the analysis and interpretation of experimental data will be offered in an integrated fashion.

The core of the Integrated Facility is proposed to consist of a set of endstations receiving X-rays from three insertion devices enabling a range of functionalities for structural biology and X-ray imaging:

- static and time-resolved BioSAXS for biological systems,
- static and time-resolved MX,
- medium resolution (better than 1 um) high throughput phase-contrast X-ray tomography (HiTT) for biological systems.

The next generation BioSAXS beamline will benefit from the PETRA IV beam by shorter data collection times, lower sample consumption and unprecedented time resolution for studying biomolecular dynamics. Furthermore, novel SAXS experiments will become possible to bridge the gap between the synchrotron-based and XFEL studies using a second experimental hutch dedicated to advanced experiments.

For MX, the increased brilliance of PETRA IV in combination with advanced optics will enable higher data quality and increased throughput in particular for experiments at higher X-ray energies. The time-scales accessible to time-resolved crystallography will be significantly shortened.

The increased coherence of PETRA IV will revolutionize phase-contrast based X-ray imaging. We plan to provide X-ray imaging in an operational mode ("HiTT" – High-Throughput Tomography) facilitating its use by a wide user community enabling biological questions to be answered. Scale-bridging and correlative imaging will be offered in cooperation with those offering other imaging modalities.

Microsymposium 17 | Inorganic crystal structures I

OP-078

In the search of missing binaries: Ternary approaches of alkali metal thallides

S. Gärtner (Regensburg/DE)

The observed and hitherto reported compounds in the system alkali metal - thallium prove, that there are alkali metal dependent effects on the observed Tl substructures[1]. In order to illuminate the impact of the alkali metals on structure formation and to approximate long missing binaries, we prepare ternary approaches including different alkali metals. Due to severe absorption effects, especially when heavy alkali metals are involved, the characterisation of the formed materials remains challenging. Additionally, we perform theoretical calculations for selected alkali metal thallides in a full relativistic mode (FPLO).

For A:Tl ratio 1:2, missing $K_{15}Tl_{27}$ was approximated in $Cs_{2.27}K_{12.73}Tl_{27}$ [2]. Binary $K_{49}Tl_{108}$ is only possible for potassium while absent $Rb_{49}Tl_{108}$ and $Cs_{49}Tl_{108}$ can only be approached when additional thallium is present [3]. While KTl and CsTl (A:Tl 1:1) include octahedral Tl_6^{6-} anions and are known since a long time [4], RbTl is still missing. We tried different preparation methods including Zintl"s approach in liquid ammonia according to NaTl [5]. Ternary solid state approaches for A:Tl 1:1 including K/Rb showed that a certain amount of rubidium can be realized in the KTl structure. Ternary approaches involving Cs/Rb yielded a new ternary phase [6]. For A:Tl ratio 2:1 Na2Tl including tetrahedral Tl48– is known since the 1960"s. Additional rubidium in ternary approaches allowed for the characterization of the new Zintl phase Na_7RbTl_4 [7].

(1) Gärtner S, Crystals 10(11) 1013 (2020); Corbett JD, Angew. Chem. Int. Ed. 39 670 (2000).
(2) Schwinghammer VF, Tiefenthaler SM, Gärtner S, Materials 14 7512 (2021).
(3) Schwinghammer VF, Janesch M, Kleemiss F, Gärtner S, Z. Anorg. Allg. Chem. 648, e202200117 (2022).
(4) Z Dong Z, Corbett JD, J. Am. Chem. Soc. 115 11299 (1993); Dong ZC, Corbett JD, Inorg. Chem. 35, 2301 (1996).
(5) Zintl E, Goubeau J, Dullenkopf W, Z. phys. Chem. 154 1 (1931); Tiefenthaler S, Korber N, Gärtner S, Materials 12(8) 1356 (2019).
(6) Schwinghammer VF, Gärtner S, in preparation.
(7) Hansen DA, Smith JF, Acta Crystallogr. 22 836 (1967); Schwinghammer VF, Janesch M, Korber N, Gärtner S, Z. Anorg. Allg. Chem. 2022 accpeted.

OP-079

Ammonium and alkali metal selenocyanates

F. Tambornino (Marburg/DE)

Salts of cyanuric acid, cyanates $[OCN]^-$, played a vital role in the development of modern chemistry. The transformation of the "*inorganic*" $[NH_4][OCN]$ into the "*organic*" urea, *i.a.*, led towards the abolishment of the "vitalism" theory.[1] Closely related to cyanate are its group 15 congeners thiocyanate $[SCN]^-$, selenocyanate $[SeCN]^-$, and tellurocyanate $[TeCN]^-$.

The chemistry of the cyanate and thiocyanate anions has been researched extensively and features in introductory and general chemistry textbooks. In contrast, reports on the solid state chemistry of the selenocyanate anion are scarce. Up until recently, only the structures of K[SeCN] and $Hg[SeCN]_2$ were reported.[2] Ammonium selenocyanate, $[NH_4][SeCN]$, has also scarcely been studied. Due to its highly sensitive nature, crystallographic studies are a striking gap in this field.

We show that $[NH_4][SeCN]$ crystallizes isotypically with $[NH_4][SCN]$ in space group $P2_1/c$ To systematically study its stability under various conditions, we employed variable temperature powder X-ray diffraction (VT-PXRD) from r.t. to temperatures close to the melting points. Additionally, the full series of alkali-metal selenocyanates A^I[SeCN] was synthesized either by oxidation of the respective cyanides (*A*=Li–Rb) or by metathesis (*A*=Cs). For Li[SeCN] only ball-milling and subsequent annealing led to its isolation. Their structures were refined from single-crystal and powder X-ray data. Only for Li[SeCN] a possible phase transition was observed that is discussed on the basis of VT-PXRD experiments. It is also the only quasibinary selenocyanate to form a hydrate ($Li[SeCN] \cdot 2H_2O$).[3]

References:

(1) F. Wöhler, *Ann. Phys. Chem.* **1828**, *88*, 253–256. [2] a) D. D. Swank, R. D. Willett, *Inorg. Chem.* **1965**, *4*, 499–501. b) G. A. Bowmaker, A. V Churakov, R. K. Harris, J. A. K. Howard, D. C. Apperley, *Inorg. Chem.* **1998**, *37*, 1734–1743. [3] A. Shlyaykher, M. Ehmann, A. J. Karttunen, F. Tambornino, *Chem. Eur. J.* **2021**, *27*, 13552–13557.

OP-080

Hydrogenation as an instrument for modifying structures and properties of $M\mathrm{Ni}_3$ and $Ln\mathrm{TiGe}$ (M = main-group metal, Ln = lanthanide) intermetallics compounds

M. Sturza (Leipzig/DE), A. Götze (Leipzig/DE), H. Kohlmann (Leipzig/DE)

Investigation of intermetallic and metal-rich compounds that feature direct metal-metal bonds is one of the most dynamic and topical fields of inorganic chemistry, solid-state chemistry, and materials science. Intermetallics and derivative metal-rich compounds, especially those featuring heterometallic bonding are interesting from the structure-property relationships point of view and have further increased interest from the perspective of materials chemistry [1], [2]. In our research, we are particularly interested in investigating the effects that an introduction of a non-metal (chalcogen, pnictogen, or halogen) has upon an intermetallic system, and in developing the ways in which it can be used to control and modify structures and properties of intermetallic-based compounds. When hydrogen is chosen as such an agent to be introduced into a metallic system, the situation becomes much more complicated, since the behavior of hydrogen in a system, the kind of bonds it forms, and the effects it has on the structure varies strongly sometimes even within the same class of compounds. The variety and complexity of the bonding nature of hydrides is complemented by the numerous reactions and conditions used to synthesize them, including metathesis reactions, elimination reactions, solid-gas hydrogenation, and flux reactions.

New results from the hydrogenation of the $M\mathrm{Ni}_3$ (M = Al, Ga, In) and $Ln\mathrm{TiGe}$ (Ln = Ce, La, Nd) systems will be reported. The synthesis by standard high-temperature routes, the investigations of hydrogenation by *in situ* studies (crystal structures by powder diffraction), and by *in situ* thermal analysis (DSC) as a function of T and $p(\mathrm{H}_2)$ will be presented.

(1) R. Pöttgen, D. Johrendt, Intermetallics: Synthesis, Structure, Function, de Gruyter, **2014.**
(2) W. Steurer, J. Dshemuchadse, Intermetallics, IUCr Monographs on Crystallography (Oxford University Press) **2016.**

OP-081

Foreign anion inclusion in $M^{II}_3(Te^{IV}O_3)_2(OH)_2$ (M = Mn, Co, Ni, Mg) phases

F. Eder (Vienna/AT), M. Weil (Vienna/AT)

The rich crystal chemistry of oxidotellurates(IV) is heavily influenced by the stereochemically active $5s^2$ lone pair of Te^{IV}. The resulting one-sided coordination polyhedra of Te^{IV} frequently lead to the formation of modular structures like rod-, layer- or, as for $M_3(TeO_3)_2(OH)_2$ (M = Mn, Co, Ni, Mg) compounds, channel structures. The crystal structures of these $M_3(TeO_3)_2(OH)_2$ phases ($P6_3mc$, $a \approx 13$ Å, $c \approx 5$ Å) consist of a cationic $[M_3(TeO_3)_2(OH)_{1.5}]^{0.5+}$ framework with hexagonal channels extending along [001], which are inhabited by the remaining OH^- anions. (Figure 1a). The lone pairs of the Te atoms are directed towards the centre of these channels.

During our investigations on the Mn^{II}-Te^{IV}-O-(H) system,[1] we obtained the new phase $Mn_3(TeO_3)_2(OH)_2$, isotypic with the corresponding Co- and Ni- compounds.[2] However, significant remaining electronic density was observed in difference-Fourier maps, hinting at the presence of other anions, which were present during the synthesis, inside the channels.

Therefore, we systematically synthesized $M_3(TeO_3)_2(OH)_2$ (M = Mn, Co, Ni, Mg) phases under mild hydrothermal conditions and the presence of different secondary anions besides OH^-.[3] In this regard, CO_3^{2-}, SO_4^{2-}, SeO_4^{2-}, Cl^-, Br^- and NO_3^- were used as counter anions of the employed M^{II}-salts. The hereby obtained products were investigated by powder and single-crystal X-ray diffraction. In order to identify the incorporated secondary anions, energy dispersive X-ray spectrometry (EDS) and Raman-spectroscopy were performed on selected single crystals.

The presence of the various secondary anions can be discerned by a slight increase in lattice parameters, as determined from refinements on basis of powder diffraction data. Additionally, Br^- and Cl^- were detected by high difference electronic density in the centre of the channels, as well as by EDS analyses. SO_4^{2-} was identified from both EDS and Raman spectroscopy, and disordered SO_4^{2-} groups could be modelled in the refinement (Figures 1b, 2). For different framework atoms M, we observed two different orientations of the SO_4^{2-} anions inside the channels. The lighter anions NO_3^- and CO_3^{2-} could neither be detected by EDS nor be modelled reasonably in the refinement, but were clearly visible in the Raman spectra. Occupational disorder of the different types of anions inside the channels and orientational disorder of the larger anions (Figure 1b) complicate the modelling.

Figure 1: The crystal structure of $Mn_3(TeO_3)_2(OH)_{1.5}\{(SO_4)_{0.15}(OH)_{0.20}\}$. a) Projection along [001]. All atoms (Te green, Mn blue, S yellow, O red) drawn as spheres with arbitrary radius. b) One possible arrangement of atoms inside the channels. Occupied sites of channel contents are drawn yellow (S) and dark red (O), unoccupied sites transparent.

Figure 2: Difference contour maps computed with JANA-2020[4] showing planes perpendicular to the channel direction in $Mn_3(TeO_3)_2(OH)_{1.5}\{(SO_4)_{0.15}(OH)_{0.20}\}$. Contour lines are shown at intervals of 0.2 e^- Å^{-3} with cut-offs for minimum and maximum values of −1.5 and 3.0 e^- Å^{-3}, respectively. Left: model with only OH^- inside the channels. Atom names refer to the locations of the corresponding sites in the model containing SO_4^{2-} anions, which is depicted on the right.

(1) Eder, F.; Weil, M. Phase formation studies and crystal structure refinements in the $Mn^{II}/Te^{IV}/O/(H)$ system. *Z. Anorg. Allg. Chem.* 2022. https://doi.org/10.1002/zaac.202200205

(2) Perez, G.; Lasserre, F.; Moret, J.; Maurin, M. Structure cristalline des hydroxytellurites de nickel et de cobalt. *J. Solid State Chem*. 1976, **17**, 143–149.

(3) Eder, F.; Weil, M.; Missen, O.P.; Kolitsch, U.; Libowitzky, E. The Family of $M^{II}_3(Te^{IV}O_3)_2(OH)_2$ (M = Mg, Mn, Co, Ni) Compounds—Prone to Inclusion of Foreign Components into Large Hexagonal Channels. *Crystals* 2022, **12**, 1380.

(4) Petříček V., Dušek M., Palatinus L. Crystallographic computing system JANA2006: general features. *Z. Kristallogr.* 2014, **229**, 345–352.

Fig. 1

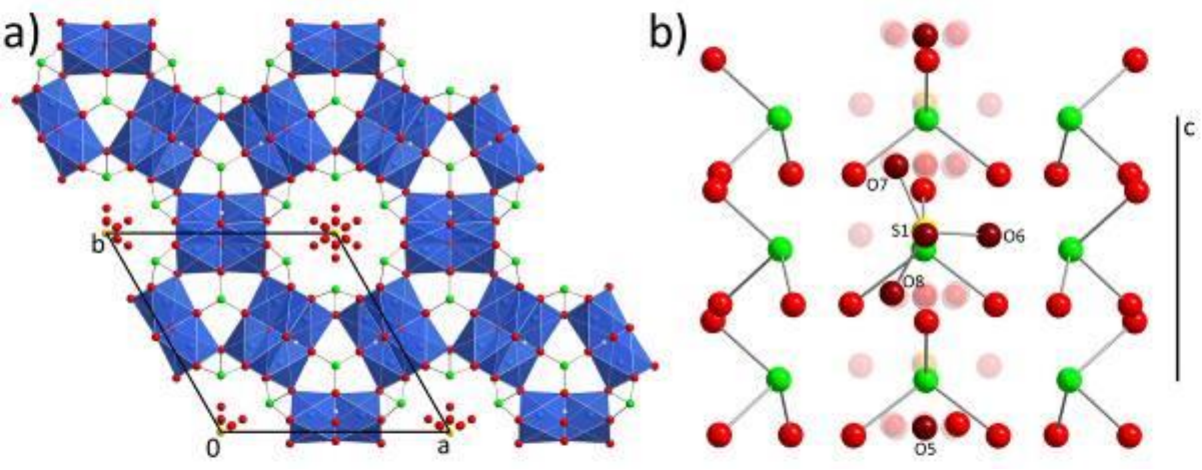
a)
b
0
a
b)
c
O7
S1
O6
O8
O5

Fig. 2

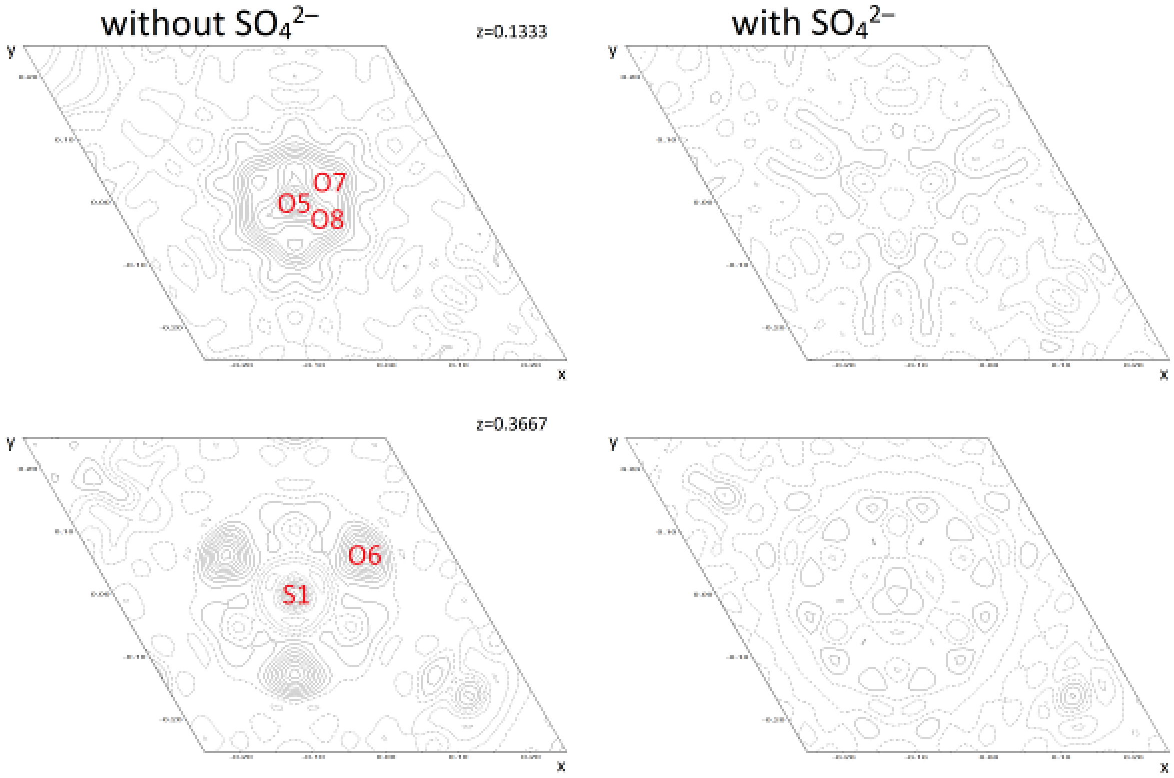
without SO_4^{2-}
with SO_4^{2-}
z=0.1333
z=0.3667
y
x
O7
O5
O8
O6
S1

OP-082

Selenium/Tellurium halides with strong SHG-Effects

M. Bonnin (Karlsruhe/DE), L. Bayarjargal (Karlsruhe/DE), V. Milman (Karlsruhe/DE), B. Winkler (Karlsruhe/DE), C. Feldmann (Karlsruhe/DE)

Second-harmonic generation (SHG) and the underlying frequency doubling probably belong to the most often employed non-linear optical (NLO) processes.[1] NLO materials are essential for numerous optoelectronic applications, including lasers, optical fibers, optical disks, and high-capacity data exchange. Since optical communication becomes more and more relevant for industry and daily life, a further development of NLO materials is urgently required.

We have recently realized several novel materials with strong SHG effects. These include molecular compounds such as $[Mn_2I_4(18\text{-crown-}6)]$[2] or $GaSeCl_5O$[3] as well as $[SeCl_3][GaCl_4]$ and $[TeCl_3][GaCl_4]$ with orientationally ordered tetrahedral building units.[4] All compounds are prepared near room temperature (≤100 °C) with high yield and purity. They all crystallize in polar, chiral Sohncke space groups. $[Mn_2I_4(18\text{-crown-}6)]$ is unique in regard of two aspects as it shows a strong SHG effect as well as intense Mn^{2+}-based emission. Using both features, $[Mn_2I_4(18\text{-crown-}6)]$ efficiently absorbs IR light (1060 nm), which is converted to green light (530 nm) by SHG and further converted to orange light (605 nm) due to luminescence.[2] $GaSeCl_5O$ shows one of the strongest SHG signals known in the visible part of the electromagnetic spectrum (480-700 nm) with an SHG intensity 10-times higher than potassium dihydrogen phosphate (KDP).[3] $[SeCl_3][GaCl_4]$ and $[TeCl_3][GaCl_4]$ exhibit SHG intensities 3-times stronger than KDP.[4] All compounds are characterized by single-crystal structure analysis, spectroscopic methods including the Kurtz-Perry approach, as well as density-functional theory methods. We will present the synthesis, characterization, and the optical properties of the title compounds.

Figure 1: Second-harmonic generation with $[TeCl_3][GaCl_4]$

References:

(1) R. W. Boyd, *Nonlinear Optics*. 4th Ed., Academic Press, New York 2020.
(2) E. Merzlyakova, S. Wolf, S. Lebedkin, L. Bayarjargal, B. L. Neumeier, D. Bartenbach, C. Holzer, W. Klopper, B. Winkler, M. Kappes, C. Feldmann, *J. Am. Chem. Soc.* **2021**, *143*, 798-804.
(3) M. A. Bonnin, L. Bayarjargal, S. Wolf, V. Milman, B. Winkler, C. Feldmann, *Inorg. Chem.* **2021**, *60*, 15653-15658.
(4) M. A. Bonnin, L. Bayarjargal, V. Milman, B. Winkler, C. Feldmann, **2022**, *submitted*.

Fig. 1

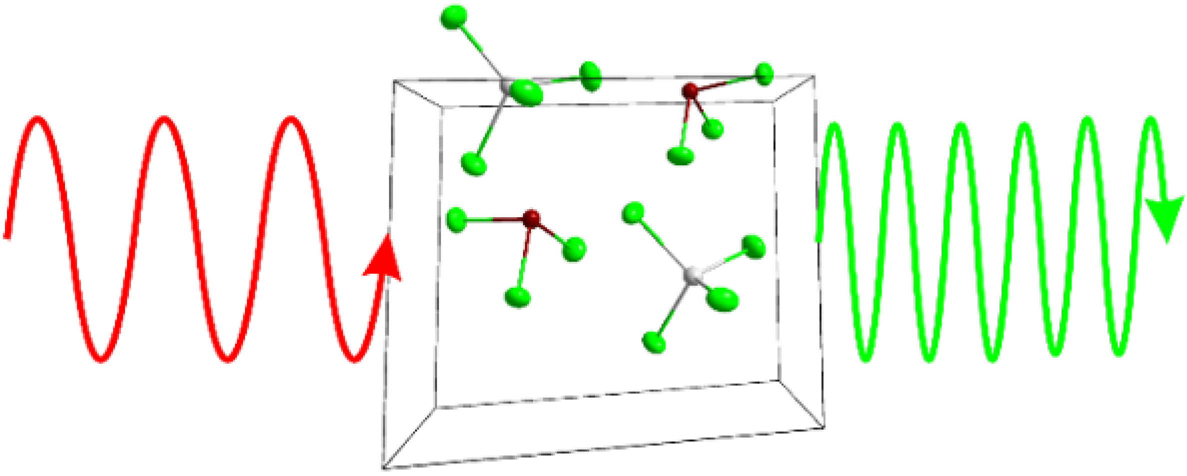

OP-083

Discovery and characterization of a new aluminium phosphate sulfate mineral

T. Witzke (Almelo/NL), G. Nénert (Almelo/NL)

A new mineral with the composition $Al_2(PO_4)(SO_4)(OH,F)(H_2O)\cdot 6H_2O$ was found on the dump of the Lichtenberg open cast, Ronneburg, Thuringia, Germany. In the open cast and surrounding mines uranium-bearing alumn shale was mined from 1950"s to 1990"s. The Ronneburg mining area was one of the largest uranium producers in Europe. The new mineral is an alteration product and was formed on the mine dump. It forms white aggregates of irregular intergrown, tiny acicular crystals of less than 0.1 mm in length and was found only in very small amounts. Lattice parameter and crystal structure were determined from powder diffraction data. This new mineral exhibits P-1 symmetry and lattice parameters a=6.129 Å, b=9.856 Å, c=11.433 Å, α=70.284°, β=85.84°, γ=82.557° and V = 644.36 Å^3. For Z = 2, the calculated density is 2.09 g/cm^3. It is structurally related to sanjuanite, $Al_2(PO_4)(SO_4)(OH)\cdot 9H_2O$, and arangasite, $Al_2(PO_4)(SO_4)F\cdot 9H_2O$. It displays a layered structure of chains of AlO_6 octahedra and PO_4 tetrahedra. These units forming channels parallel to the a axis. The SO_4 tetrahedra are situated close to the chains but probably linked to it only by hydrogen bonds. There are 6 molecules of crystallization water and one water molecule per formula unit is occupying the channels in the structure. Very similar aluminophosphate chains were found in sanjuanite (Colombo *et al.*, 2011).

(1) Colombo, F., Rius, J., Pannunzio-Miner, E.V., Pedregosa, J.C., Camí, G.E., Carbonio, R.E. (2011) The Canadian Mineralogist: 49: 835-847.

Figure 1: a) Rietveld refinement of $Al_2(PO_4)(SO_4)(OH,F)(H_2O)\cdot 6H_2O$ (Rwp = 5.3%) and b) the corresponding crystal structure projected along the a axis.

Fig. 1

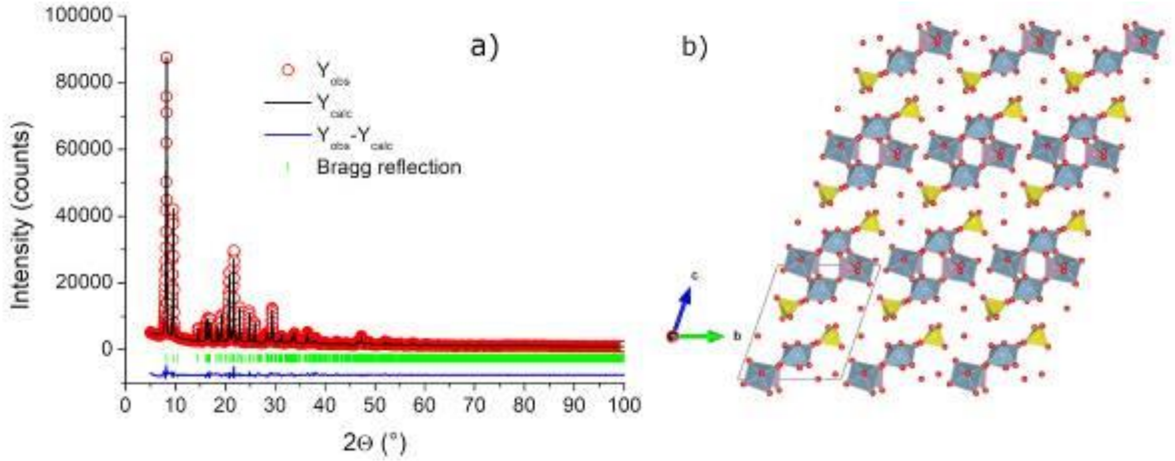

OP-084

Emergent properties under high pressure: Can a finite chain of HCN molecules model a crystal?

C. M. Hsieh (Bremen/DE), T. Neudecker (Bremen/DE)

In computational chemistry, one can simulate a single isolated molecule, a small cluster of molecules or an infinite amount of (crystallized) molecules under periodic boundary condition. Since chemical experiments are usually conducted on a large quantity of molecules, it is intuitive that if a large number of molecules are simulated, the result of a simulation will be comparable to the experimental observation. In terms of the classical philosophical problem of emergence, the question arises: how large is the quantity of molecules that is required to emulate the characteristics of an infinite system of a molecular crystal in quantum chemical simulations?

To answer this question, we study the system of hydrogen cyanide in high-pressure simulations. Previous studies revealed that HCN molecules crystallize in long chains.[1] In addition, the crystal structure of HCN depends on the given external pressure.[2] For simulation of a finite system we applied the *eXtended Hydrostatic Compression Force Field* (X-HCFF)[3] and *Gaussians On Surface Tesserae Simulate HYdrostatic Pressure* (GOSTSHYP)[4] methods, as implemented in Q-Chem,[5] at the PBE/cc-pVDZ level of theory. For comparison, the HCN crystal is simulated using Quantum Espresso,[6,7] in which a planewave basis set in conjunction with pseudopotentials and the PBEsol exchange-correlation functionals are applied.

We conclude that simulating 15-20 HCN molecules is sufficient to reproduce the structural properties of the HCN molecular crystal under pressure. Moreover, Natural Bond Orbital (NBO) [8,9] analysis explains that, for a chain length greater than six HCN molecules in a finite system, the observed elongation of the C-H bond induced by external pressure is caused by the interaction between the lone electron pair of nitrogen and the neighboring C-H σ* orbital.

References:

(1) Dulmage, W. J.; Lipscomb, W. N. The Crystal Structures of Hydrogen Cyanide, HCN. *Acta Cryst.* **1951**, *4*, 330–334

(2) Khazaei, M.; Liang, Y.; Bahramy, M. S.; Pichierri, F.; Esfarjani, K.; Kawazoe, Y. High-Pressure Phases of Hydrogen Cyanide: Formation of Hydrogenated Carbon Nitride Polymers and Layers and Their Electronic Properties. *J. Phys.: Condens. Matter* **2011**, *23*, 405403.

(3) Stauch, T. A Mechanochemical Model for the Simulation of Molecules and Molecular Crystals under Hydrostatic Pressure. *J. Chem. Phys.* **2020**, *153*, 134503.

(4) Scheurer, M.; Dreuw, A.; Epifanovsky, E.; Head-Gordon, M.; Stauch, T. Modeling Molecules under Pressure with Gaussian Potentials. *J. Chem. Theory Comput.* **2021**, *17*, 583–597.

(5) Epifanovsky, E. et al. Software for the Frontiers of Quantum Chemistry: An Overview of Developments in the Q-Chem 5 Package. *J. Chem. Phys.* **2021**, *155*, 084801.

(6) Giannozzi, P. et al. QUANTUM ESPRESSO: A Modular and Open-Source Software Project for Quantum Simulations of Materials. *J. Phys.: Condens. Matter* **2009**, *21*, 395502.

(7) Gianozzi, P. et al. Advanced Capabilities for Materials Modelling with Quantum ESPRESSO. *J. Phys.: Condens. Matter* **2017**, *29*, 465901.

(8) Reed, A. E.; Curtiss, L. A.; Weinhold, F. Intermolecular Interactions from a Natural Bond Orbital, Donor-Acceptor Viewpoint. *Chem. Rev.* **1988**, *88*, 899–926.

(9) Glendening, E. D.; Landis, C. R.; Weinhold, F. In *Complementary Bonding Analysis*; Grabowsky, S., Ed.; De Gruyter, 2021; pp 129–156.

Fig. 1

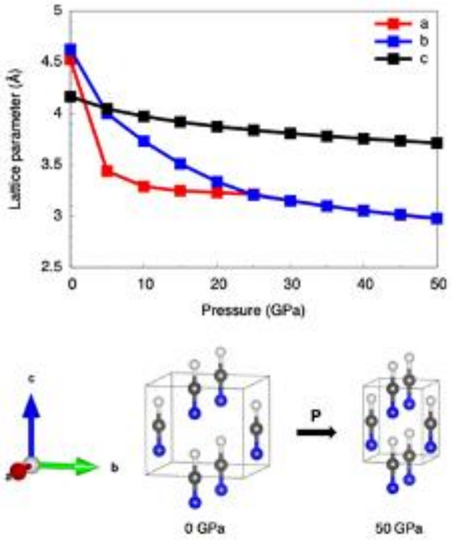

Top: Calculated pressure-dependent changes in the lattice parameters of the HCN crystal.
Bottom: Calculated crystal structures of HCN at 0 GPa and 50 GPa.
Color code: white: hydrogen; grey: carbon; blue: nitrogen.

Fig. 2

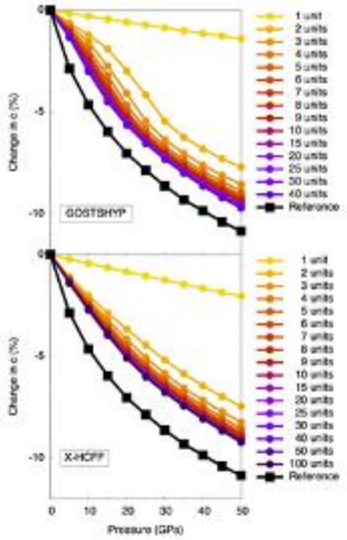

Calculated changes in the lattice parameter c for HCN chains of various lengths, calculated with the GOSTSHYP (top) and X-HCFF (bottom) models (circles). Reference values are provided by calculations on the crystal (black squares).

OP-085

Advances in the parameter space concept for crystal structure determination – Linearization of intensity isosurfaces

M. Vallinayagam (Dresden/DE), M. Nentwich (Hamburg/DE), D. C. Meyer (Dresden/DE), K. Fischer (Saarbrücken/DE), M. Zschornak (Dresden/DE)

As an alternative approach to currently and widely used Fourier transform techniques, a theoretical approach was developed by Fischer, Kirfel, and Zimmermann, namely the *Parameter Space Concept* (PSC), to solve crystal structures by using a minimal number of diffraction intensities*[1-6].* We present recent improvements, which target the implementation of linearized intensity isosurfaces and test the routines on numerous randomly generated structures. In the initial stage progress, pairs of sample atomic coordinates are mapped on two- and three-dimensional parameter spaces (***P2*** and ***P3***). The respective intensity isosurfaces, defined by sign and geometrical structure amplitude, were linearized for given reflection orders and converted into systems of linear inequalities and solved to reobtain the atomic coordinates and evaluate the accuracy of the method. Within this framework, we utilized Equal Point Atom (EPA) and Non-Equal Point Atom (nEPA) models to treat the scattering power of atoms. Results are given for arbitrary centrosymmetric structures with two (see Fig. 1) as well as three degrees of freedom, and specific challenges are highlighted.

Figure 1: PSC solutions and respective errors as well as spatial uncertainties of randomly generated atomic coordinates for synthetic sample structures. The background color represents the average reduction of spatial uncertainty in the atomic coordinates with increasing order *l*. The red circles present the randomly generated atomic coordinate pairs.

(1) K. Fischer *et al.*, Z. Krist. 220 643 (2005)
(2) A. Kirfel *et al.*, Z. Krist. 221 673 (2006)
(3) K. Fischer *et al.*, Croatica Chemica Acta. 81 381 (2008)
(4) A. Kirfel *et al.*, Z. Krist. 224 325 (2009)
(5) H. Zimmermann *et al.*, Acta Cryst. A65 443 (2009)
(6) A. Kirfel *et al.*, Z. Krist. 225 261 (2010)

Fig. 1

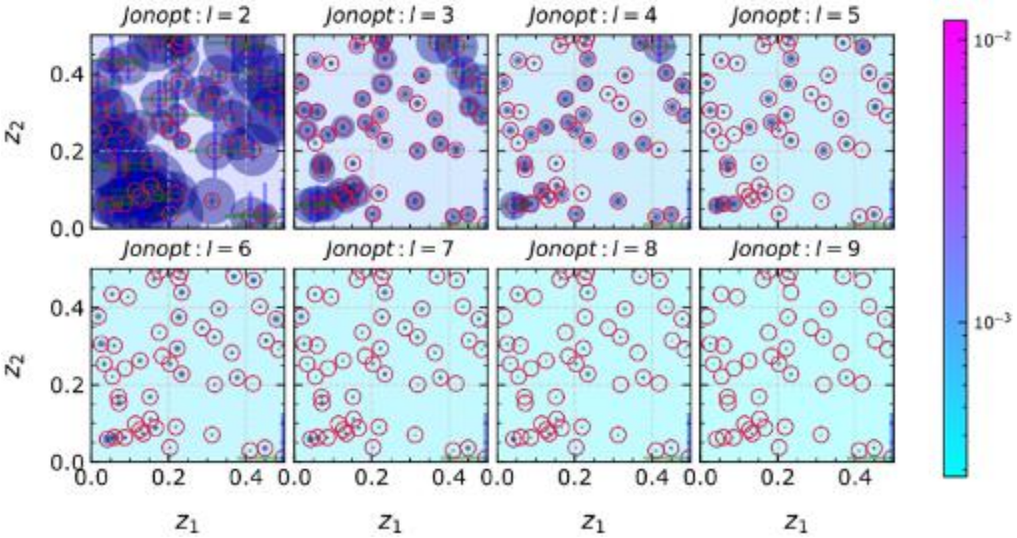

OP-086

Pathway for a martensitic quartz-coesite transition

T. Schaffrinna (Frankfurt am Main/DE), V. Milman (Cambridge/GB), B. Winkler (Frankfurt am Main/DE)

Coesite, a high-pressure polymorph of SiO_2, is a geologically relevant indicator for ultra-high pressure metamorphism and for hypervelocity impacts [1]. Numerous experimental and theoretical studies on the polymorphic transition from quartz to coesite have been carried out. The transition is generally described as a first order reconstructive transition and nucleation and growth models have been established. However, a description of the transition based on thermodynamic equilibrium is inapplicable for impact events, where structures can be substantially strained. There have been no studies in which the transformation from quartz to coesite has been studied by atomistic model calculations with strained unit cells.

Martensitic transformations are diffusionless, solid-to-solid phase transitions, and are often induced by strain. The change of the crystal structure is generally accompanied by the development of a rich microstructure. Here we show that there is a diffusionless, strain-induced pathway for the quartz-coesite transformation based on DFT model calculations.

We identified a martensitic transition path between the two SiO_2 polymorphs by establishing an atom-to-atom relationship between the quartz and coesite structure (Fig. 1) while minimizing the sum of the pairwise atomic distances [2]. This allows to generate intermediate structures, which were investigated by DFT calculations using the CASTEP package [3].

The martensitic transition proceeds via two intermediate transition structures. We investigated the transition from ambient pressure up to 5 GPa and found the maximum reaction enthalpy (~ 0.15 eV/atom) to be pressure invariant (Fig. 2). This value is comparable to those in martensitic phase transformations of other systems [4]. The DFT calculations allowed us to obtain a detailed understanding of the structural changes during this transition.

We are grateful for support by the BIOVIA Science Ambassador program.

(1) Campanale et al. *Geochim. Cosmochim. Acta, 264:105-117 (2019)*
(2) Therrien et al. *J. Chem. Phys., 152:074106 (2020*
(3) Clark et al. *Z. Kristall., 220:567-570 (2005)*
(4) Xiao et al. *Phys. Rev. B Condens. Matter, 88:144102 (2013)*

Figure 1: *Structure of quartz (left) and coesite (right) and intermediate structures along the reaction coordinate.*

Figure 2: *Enthalpy per atom of the quartz-coesite phase transition, relative to the enthalpy of quartz at ambient pressure.*

Fig. 1

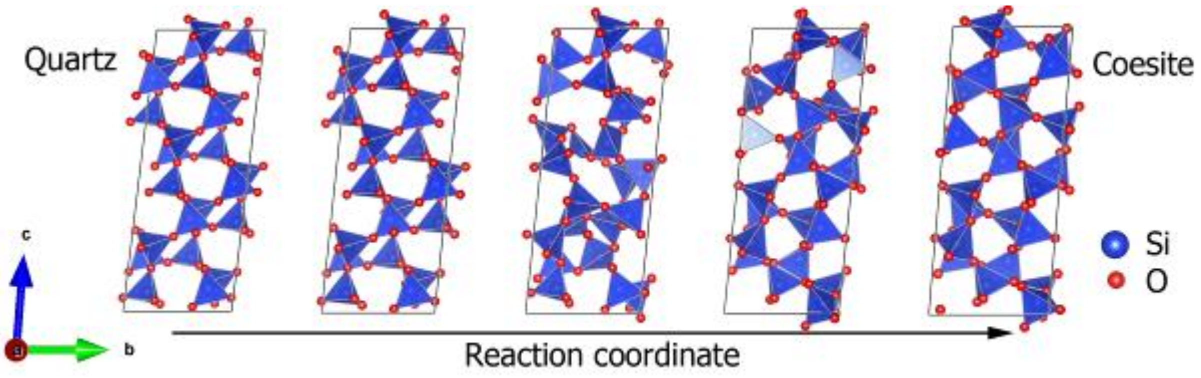

Fig. 2

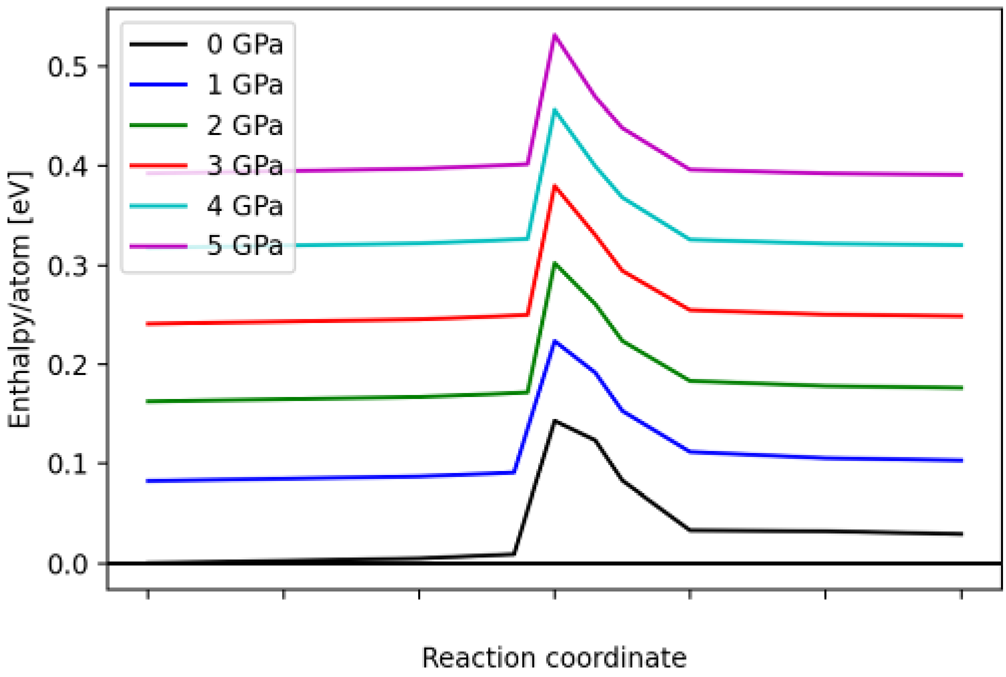
0 GPa
1 GPa
2 GPa
3 GPa
4 GPa
5 GPa
0.5
0.4
0.3
0.2
0.1
0.0
Enthalpy/atom [eV]
Reaction coordinate

OP-087

Beyond sphere packings – *Packings* of sphere packings

M. Petrik (Marburg/DE), W. Hornfeck (Prague/CZ)

Rationalizing crystal structures in terms of sphere packings is an old tradition. While applying it to the structure of beta-manganese (β-Mn) we discovered a new way of using simple sphere packings to build more complex ones [1]. These we call *packings of sphere packings* (PSPs) [2]. The first PSP – isopointal with β-Mn, space group type $P4_132$, no. 213, Wyckoff positions 8c and 12d, x=0.03633 and y=0.17706 – was nearly identical with the iodine substructure of $RbAg_4I_5$, incidentally one of the best solid state ionic conductors known. After this initial discovery an exploratory search yielded dozens of other PSPs. An open online database was, therefore, set up and public contributions of PSPs were solicited [3]. This presentation will, it is hoped, arouse interest and promote further progress.

PSPs make two stringent demands on how the constituent sphere packings are combined: 1. each sphere packing must not lose any of its internal contacts, and 2. all sphere packings must establish contact among each other. The common types of interpenetrating structures, therefore, are ruled out since requirement 2. is not generally met, e. g. in CuO or $MgCu_2$.

PSPs have so far been found of the cubic, hexagonal, tetragonal and orthorhombic type, the number of constituent sphere packings ranging from two to four. The goal is to discover different combinations of sphere packings yielding PSPs. *Different* combinations may, however, yield *the same* resulting structure. Thus not less than fourteen different PSPs all resulting in the fcc structure are listed by now [3].

Ultimately the challenge will be, given a complex structure like fcc or β-Mn, to enumerate all possible ways of splitting it into simpler sphere packings, subject to the two constraints stated above.

(1) M. Petrik, W. Hornfeck and B. Harbrecht, *Z. Anorg. Allg. Chem.* **2014**, *640*, 2328.
(2) M. Petrik and W. Hornfeck, *Z. Anorg. Allg. Chem.* **2016**, *642*, 1023.
(3) *https://spherepacker.github.io/welcome.html*, under "Sphere Packings."

OP-088

Solving the phase problem in crystallography with artificial intelligence

T. Rekis (Copenhagen/DK), A. S. Larsen (Copenhagen/DK), A. Ø. Madsen (Copenhagen/DK)

For a crystal structure to be solved from the diffraction data, it is necessary to obtain the complex structure factors, F_H, of the measured reflections. Their squared moduli, $|F_H|^2$, are proportional to the measured intensities, but the phase angles needed to reconstruct the complete complex numbers are not determined in such experiments. Since the exact solution to this phase problem is not known, several methods to overcome this crucial step in crystal structure determination have been developed over time. For example, direct methods or the charge flipping algorithm can be used for most organic, inorganic, and metal-organic structures. Nevertheless, these methods fail if, for example, the available data resolution is not sufficiently high, the completeness of the data is low, or if the number of atoms in the asymmetric unit is very high, as is the case for macromolecular crystals and some framework structures.

Here we demonstrate how the phase problem can be solved using a neural network. The network has been trained on millions of fictive structures containing metal atoms and/or molecular fragments. At the time of writing the neural network has only been trained on structures in the centrosymmetric space group $P2_{1/c}$ with some limitations on the unit cell size. However, it shows remarkable results.

The trained network was validated with thousands of structures retrieved from several crystallographic databases. Since raw experimental data is not abundantly available, the structure factor amplitudes, $|F_H|$, were generated directly from the structures at several resolution limits. The structure amplitude data were fed into the trained network to output phases. The phases could be retrieved with a striking accuracy leading to very accurate electron density maps and correct structure solutions for over 99% of the validation set entries. Furthermore, the phase accuracy was also high if the resolution limit was chosen to be low, i.e. d_{min} = 2 Å. Several hundreds of experimentally measured diffraction data sets were also used for validation showing the same level of accuracy. Our results indicate that deep learning can be used to obtain electron density maps of structures for which only a limited resolution data can be obtained, and which are problematic to solve using currently available methods.

Microsymposium 19 | Micro- and nano-crystalline materials (Powder diffraction, Disordered material) II

OP-089

Challenging characterization of ultrasmall nanoparticles of coin and platinum metals

O. Prymak (Essen/DE), O. Wetzel (Essen/DE), B. Kruse (Essen/DE), K. Loza (Essen/DE), M. Heggen (Jülich/DE), C. Weidenthaler (Mülheim an der Ruhr/DE), M. Epple (Essen/DE)

Introduction: Ultrasmall nanoparticles (usNPs) with a high specific surface area are promising candidates for catalysis, biomedicine and imaging, photonics and energy storage. For this purpose, a suitable characterization of their chemical composition and potential surface change, e.g. oxidation, is of great importance.

Objectives: This work focuses on the wet-chemical synthesis of usNPs ($d < 2$ nm) of coin (Ag, Au) and platinum (Ru, Rh, Pd, Os, Ir, Pt) metals prepared by reduction with NaBH4 and colloidal stabilization with glutathione (GSH). Since their applicability for catalysis and ligand attachment strongly depends on their surface, a structural characterization of usNPs is very challenging and requires a combination of complex diffraction, spectroscopic and microscopic techniques.

Methods: Different water-dispersed usNPs were synthesized and structurally investigated by a high-resolution transmission electron microscopy (HRTEM), X-ray powder (PXRD) and electron (ED) diffraction, small-angle X-ray scattering (SAXS), X-ray photoelectron spectroscopy (XPS) and disc centrifugal sedimentation (DCS).

Results: HRTEM showed monodisperse usNPs for all metals with a spherical shape and an average size 1.5-2.0 nm, which agreed well with SAXS and DCS data. The chemical composition and single- or polycrystallinity (twinning) of usNPs was verified by PXRD. Although the diffraction peaks were extremely broad due to the very small particle size, a challenging quantitative analysis by Rietveld refinement was possible, so that an important information about the oxidation state and potential unit cell contraction was received. This was also supported by XPS and Fast Fourier transform (FFT) analysis of HRTEM together with ED images.

Conclusion: Ultrasmall nanoparticles of coin and platinum metals can be prepared by a reduction from aqueous precursors partially leading to their oxidation. Despite their very small size, a resulting structural transformation can be identified by combined methods such PXRD, XPS and ED.

OP-090

Synthesis and ultrastructure of ultrasmall monometallic and bimetallic silver-platinum nanoparticles (2 nm)

N. Wolff (Essen/DE), K. Loza (Essen/DE), O. Prymak (Essen/DE), M. Heggen (Jülich/DE), T. Schaller (Essen/DE), F. Niemeyer (Essen/DE), C. Weidenthaler (Mülheim an der Ruhr/DE), M. Epple (Essen/DE)

Introduction (background, relevance and research question): Nanoparticles of noble metals are of high importance in materials science and biomedicine. It is not known whether alloyed nanoparticles of silver and platinum have similar structures to the bulk materials in terms of mixing gaps or the formation of intermetallic phases. Core-shell structures are possible as well. Ultrasmall particles (2 nm) present a particular challenge due to their small size, close to metallic clusters.

Objectives: We present a water-based synthesis of ultrasmall mono- and bimetallic glutathione coated silver-platinum nanoparticles. An extensive physical and chemical characterisation was performed to elucidate the composition and the ultrastructure of these nanoparticles.

Materials & methods (patient collective, method, statistical procedures): A comprehensive colloid-chemical and spectroscopic characterisation of the nanoparticles was carried out by NMR spectroscopy, elemental analysis and disc centrifugal sedimentation (DCS). To visualize the nanoparticle core, high-resolution transmission electron microscopy (HRTEM) was used. X-ray powder diffraction (XRD) gave the crystallinity of the nanoparticles, despite their ultrasmall size. Their electronic structure (especially the oxidation states of silver and platinum) was accessed by X-ray photoelectron spectroscopy (XPS).

Results (results with data and statistics): The diameter of the nanoparticles was about 2 nm. Crystalline domains were detected for pure monometallic nanoparticles (Ag; Pt) whereas bimetallic nanoparticles (AgPt) remained amorphous. However, no clear phase identification was possible by XRD due to the small particle size. Different oxidation states of silver and platinum were detected by XPS.

Conclusion (significance of the work presented and conclusion): The synthesis of ultrasmall mono- and bimetallic silver-platinum nanoparticles was achieved. However, the characterisation of ultrasmall bimetallic nanoparticles remains a challenge due to their small size.

OP-091

A perfect liaison: Combining crystal mapping with PXRD

J. Merkelbach (Villigen/CH), C. Jandl (Villigen/CH), G. Steinfeld (Villigen/CH), D. Stam (Villigen/CH), P. Simoncic (Villigen/CH)

Electron diffraction as a tool for single crystal structure analysis of nanocrystals is well known in the crystallographic community.[1] In recent months we assisted in a range of projects discovering the opportunities of a dedicated electron diffractometer with crystal mapping[2] capabilities outside of that restricted purpose of structure elucidation. And most projects start with X-ray powder diffraction (PXRD) profiles not fully understood.

PXRD is the preferred technique of chemists to screen different batches for phase purity and crystallisation quality. It is good practice to fully assign every signal in the profile. But this can be a challenge with mixtures of three or more components or phases and/or broadened peaks due to nanosized crystallinity. By combining the imaging feature (STEM mode) with the diffraction mode of an electron diffractometer, crystal mapping of dozens to hundreds of nanosized crystals can provide the missing information needed to fully understand the PXRD profiles. This has shown to be especially useful in areas where the powder is the final product and further purification or crystallisation is not intended, like for liquid assisted grinding (LAG) experiments.[3] For a quantitative analysis of the crystal mapping results one has to come back to the PXRD pattern and therefore close the circle of this perfect liaison.

Figure 1: Asymmetric unit of tyramine hydrochloride. Crystals were found as a side product of a sample from a liquid assisted grinding experiment to synthesise tyramine cocrystals. The structure was solved from one ED dataset routinely recorded during a crystal mapping experiment.[3]

(1) Gemmi, M., Mugnaioli, E., Gorelik, T. E., Kolb, U., Palatinus, L., Boullay, P., Hovmöller, S. & Abrahams, J. P. (2019). *ACS Cent. Sci.*, **5**, 1315.
(2) Rauch, E. F., & Véron, M. J. M. C. (2014). *Mater. Charact.*, **98**, 1.
(3) Days, L. C., Mahler, J., Pagola, S., Holder, A. A. & Merkelbach, J., in preparation.

Fig. 1

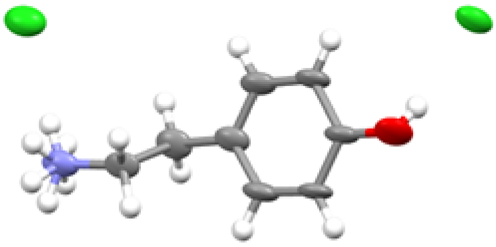

OP-092

Synthesis and characterization of new high-entropy cuprates

A. Kirsch (Copenhagen/DK), M. Tegtmeier (Copenhagen/DK), X. Bredahl Gjelsten (Copenhagen/DK), K. M. Jensen (Copenhagen/DK)

High-entropy oxides (HEO) are a new class of complex solid solutions with 5 or more metal cations in *ca.* equal amounts. Since the first report of a HEO in 2015 [1], these materials have been studied extensively and shown to exhibit attractive properties, e.g. high thermoelectric performances [2]. The structural and chemical flexibility of HEOs offer a tremendous potential to tune the material properties. Although the field is growing rapidly, it is still in its infancy and the accessible compound space is rather unexplored.

With this work, we aimed to study the synthesizability of high-entropy cuprates in a Ruddlesden-Popper type structure $(RE)_2CuO_4$ (RE = rare earth elements) crystallizing in space group *I*4/*mmm.* The compounds were synthesized using a sol-gel strategy and characterized by synchrotron X-ray diffraction with subsequent Rietveld analysis. We report on 5 previously unknown compositions of $(RE)_2CuO_4$ HEOs including RE of different sizes from La to Er. We also systematically investigated the synthesizability of $(La_{0.2}Nd_{0.2}Pr_{0.2}Sm_{0.2}Er_{0.2})_2CuO_4$ from bi-, tri, and tetrametallic precursors, e.g. 2/5 $(La_{0.5}Nd_{0.5})_2CuO_4$ and 3/5 $(La_{0.33}Pr_{0.33}Er_{0.33})_2CuO_4$. During these studies, we discovered a new structure-type in space group $Pna2_1$ that can form as a HEO with a $(RE)_2Cu_2O_5$ composition.

In total, we have synthesized 7 previously unknown compounds and introduced a new structure-type for the design of HEOs. Furthermore, the systematic investigation of the solid solution forming ability within the $(La_{0.2}Nd_{0.2}Pr_{0.2}Sm_{0.2}Er_{0.2})_2CuO_4$ system provides knowledge on the synthetic accessibility of other Ruddlesden-Popper type HEOs. These compounds might show exciting properties, as doping of aliovalent ions in the $(RE)_2CuO_4$ parent structures is known to introduce high Tc-superconductivity [3].

(1) Rost, C. et al. *Nat. Commun.* 6, 8485 (2015)
(2) Jiang, B. et al. *Science* 371, 830-834 (2021)
(3) Anderson, P. W. et al. *Science* 235, 1196-1198 (1987)

OP-093

Sublimation of silver and silver-gold core-shell nanocubes studied by *in-situ* powder diffraction and electron microscopy (SEM, TEM)

A. Karatzia (Essen/DE), K. Loza (Essen/DE), O. Prymak (Essen/DE), M. Heggen (Jülich/DE), M. Epple (Essen/DE)

Introduction: Nanoparticles of noble metals are of great importance as they possess different properties compared to their corresponding bulk material. They present diverse applications in biomedicine, catalysis, optics and electronics. However, bimetallic nanoparticles of noble metals have advantages over monometallic ones, not only because they can combine properties of each component, but also due to synergetic effects that can be developed between two different components. Due to the high specific area, the thermal behavior of nanoparticles is different from the corresponding bulk. Little is known about temperature-induced effects of bimetallic nanoparticles so far.

Objectives: Here, *in-situ* X-ray powder diffraction (PXRD), *in-situ* scanning (SEM) and *in-situ* transmission electron microscopy (TEM), were conducted to assess the behavior, stability, and crystallinity of Ag and Ag-Au core-shell nanocubes up to 1000 °C.

Materials and Methods: The synthesized mono- and bimetallic nanocubes were extensively characterized by ultraviolet and visible spectroscopy, dynamic light scattering, energy dispersive

X-ray spectroscopy, and atomic absorption spectroscopy. They were examined *in-situ* in both SEM and TEM as well as by PXRD. Thermogravimetric analysis was also performed.

Results: The *in-situ* microscopy experiments have shown that Ag nanocubes tend to lose their morphology as the temperature increases. Above about 600 °C, they start to sublime due to the enhanced vapor pressure. Core-shell Ag-Au nanocubes exhibit the same behavior but maintained their morphology longer at higher temperature. *In-situ* PXRD confirmed that silver-containing nanostructures sublime, whereas silver microparticles do not.

Conclusions: Due to the high vapor pressure of Ag (the highest of all other metals of all noble metals), Ag first lost their shape and then sublimated above 600 °C.

OP-094

XtaLAB Synergy-ED: To cryo, or not to cryo, that is the ED question

K. N. Truong (Neu-Isenburg/DE), R. Bücker (Neu-Isenburg/DE), F. White (Neu-Isenburg/DE), T. Stolar (Zagreb/HR), K. Užarević (Zagreb/HR), L. Grisanti (Zagreb/HR), E. Meštrović (Zagreb/HR), M. Meyer (Wrocław/PL), M. Jasnowski (Wrocław/PL), A. Yamano (Tokyo/JP), S. Ito (Tokyo/JP), E. Okunishi (Tokyo/JP), Y. Aoyama (Tokyo/JP), J. Ferrara (The Woodlands, TX/US)

The Rigaku XtaLAB Synergy-ED is a fully integrated electron diffractometer with a seamless workflow from data collection to 3D structure determination. The XtaLAB Synergy-ED is the result of Rigaku's collaboration with JEOL, synergistically combining each partner's core technologies: Rigaku's hybrid-pixel electron detector (HyPix-ED) and CrysAlisPro software, and JEOL's long-standing excellence in electron beam generation and control.

Using 3-dimensional electron diffraction (3DED), a.k.a. microED, single crystals of all classes below one-micron in size can be studied. The XtaLAB Synergy-ED offers a wide range of experiments, including low temperature, which confers benefits such as: reduced beam damage; improved resolution; reduced disorder; and in the case of electron diffraction, stabilization of samples *in vacuo*. As electron diffraction requires samples to be studied under high vacuum, cryo-transfer - freezing of samples prior to introduction to vacuum - is essential for sensitive compounds, e.g. proteins or MOFs. Combining cryo-transfer with variable detector distance further allows the study of solvated crystals, including proteins, in the XtaLAB Synergy-ED.

Here, we report two small molecule examples. Both are supramolecular solids featuring thymine (T) and 2,6-diaminopurine (D) in different stoichiometries (2:1 and 3:2). Thermal analyses (TGA-DSC) show that both samples are hydrated co-crystals. 3DED experiments at room temperature and high vacuum resulted in their anhydrous species (see Figure, left). Cryo-transfer of flash-cooled crystals of the same batch measured at 100 K under high vacuum gave the 2:1 T-D monohydrate co-crystal and 3:2 T-D trihydrate co-crystal, respectively (see Figure, right). Calculated powder patterns from 3DED data match the experimental PXRD data, confirming phase purity. Our work unambiguously demonstrates that cryo-transfer techniques used with the XtaLAB Synergy-ED enabled the determination of hydrated structures, despite high vacuum conditions.

Figure 1: Two examples illustrating cryo-transfer is important: (left) structures measured at ambient temperature and vacuum, and (right) using a cryo-transfer station at 100 K.

Fig. 1

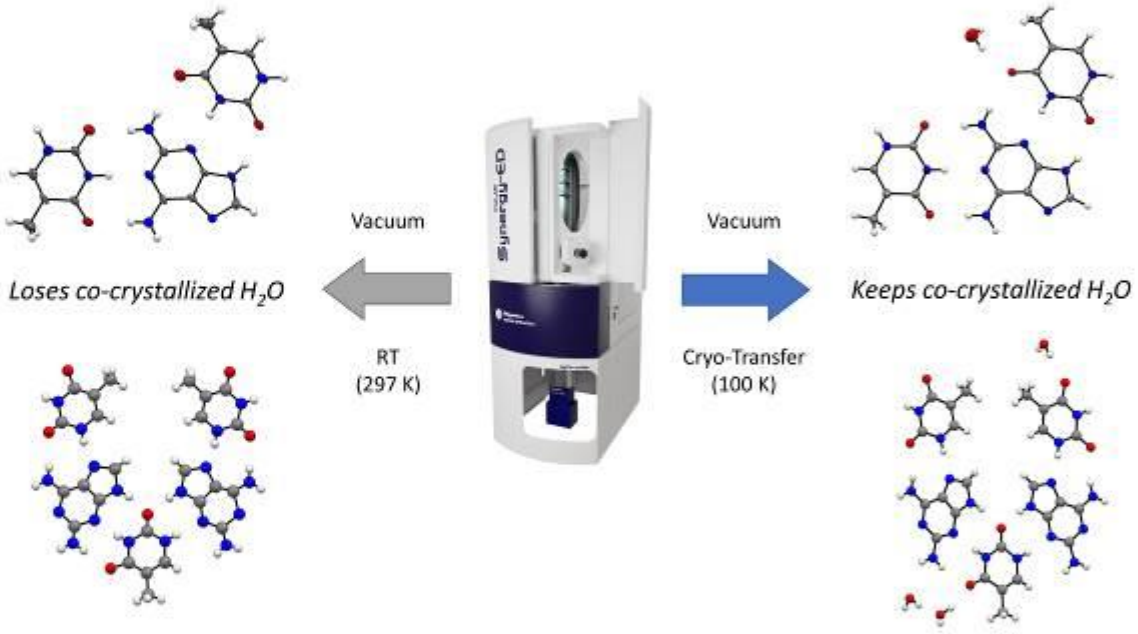
Vacuum
Loses co-crystallized H_2O
RT
(297 K)
Synergy-ED
Vacuum
Keeps co-crystallized H_2O
Cryo-Transfer
(100 K)

OP-095

Structure determination of Nanocrystalline Metal-Organic frameworks by 3D electron diffraction

C. Jandl (Villigen/CH), J. Merkelbach (Villigen/CH), G. Steinfeld (Villigen/CH), E. Hovestreydt (Villigen/CH)

3D Electron diffraction (3D ED, MicroED) is emerging as a powerful technique for the structural elucidation of challenging compounds as it bypasses the main limitation of growing crystals of suitable size for single-crystal X-ray diffraction. Applications range from natural products and pharmacology to geological sciences, advanced materials, nanotechnology, and many more.

Metal-Organic Frameworks (MOFs) are porous materials, which are commonly obtained from solvothermal synthesis and therefore cannot be recrystallised. Structure elucidation is thus limited to the as synthesised material. Being able to work with nanocrystalline powders makes 3D ED the ideal tool to tackle this problem and determine structures from crystals that are too small even for synchrotron facilities.

We show a range of examples including both nanocrystalline samples of known MOFs and new materials, all measured in continuous rotation mode on a dedicated electron diffractometer. High quality data also allow the study of molecular motion in the crystals and the identification of changes of the structures by solvent removal from the pores. The results illustrate the potential of this technique in the field of porous coordination networks and the benefits of dedicated instrumentation that has become available in recent years.

Figure 1: Packing diagrams of selected MOF structures determined by 3D ED: ZIF-8 (top left), UiO-66 (bottom left), Zn-tartrate (top right), CuDPC (bottom right).

Fig. 1

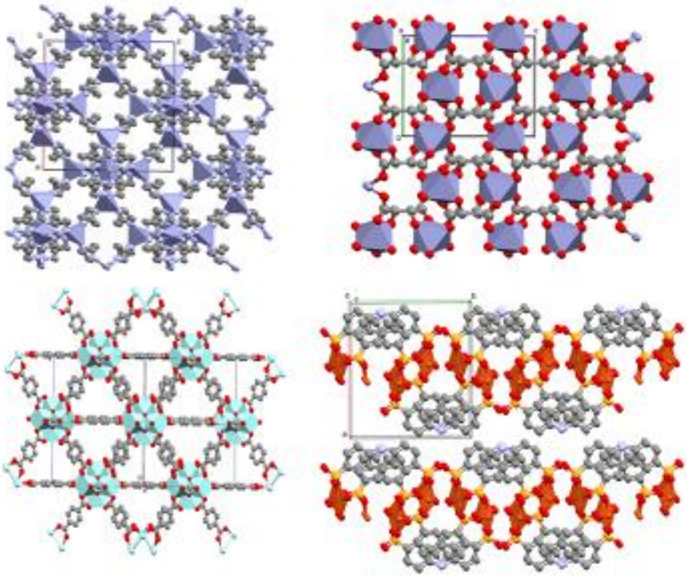

OP-096

3D structure determination with 3 MeV relativistic electrons

A. C. Rodrigues (Hamburg/DE), V. Hennicke (Hamburg/DE), M. Hachmann (Hamburg/DE), W. Brehm (Hamburg/DE), J. Meyer (Hamburg/DE), L. de Melo Costa (Hamburg/DE), K. Bustos (Hamburg/DE), P. Reinke (Hamburg/DE), T. Pakendorf (Hamburg/DE), H. Delsim-Hashemi (Hamburg/DE), M. Barthelmess (Hamburg/DE), K. Fllöttmann (Hamburg/DE), A. Meents (Hamburg/DE)

DESY's Relativistic Electron Gun for Atomic Exploration (REGAE) is an linear accelerator generating electron pulses with energies between 2.5 and 6 MeV, a bunch charge of up to 100 fC and a pulse duration of down 20 fs. It is there ideally suited for time resolved electron diffraction experiments. The advantage of performing diffraction experiments with MeV electrons instead at the typically used 100 - 300 keV, is the gain in sample thickness due to the higher penetration depth of electrons. Compared to x-rays, electrons offer 3 orders of magnitude reduced radiation damage effects.

In this work, we demonstrate a 3D electron diffraction experiment of a mica sample with 3 MeV relatistic electrons. For the experiments a very thing mica crystal was mounted on a silicon frame. We collected a 125° rotation dataset, with a stepsize of 0.01°, using a Jungfrau 1M detector for direct electron collection at 50 Hz frame rate. We were able to improve the signal-to-noise ratio by increasing the number of frames per step to 10.

Geometrical distortions and beam jittering due to residual magnetic fields impose challenges for currently available crystallographic indexing porgrams (XDS, MOSFLM, CrystFEL). In order to overcome these, image correction and centering routines are currently being developed and tested.

A major machine upgrade of REGAE will enable to deliver a micrometer sized electron beam that is well-suited for micro- and nano crystals also inlcuding protein crystals. In particular to the later ones, electron diffraction is a very promising approach due to the lower radiation damage effects compared to X-rays. Microsecond time resolution in this operating mode enable time-resolved diffraction experiments of proteins and viruses in a similar fashion to current experiments at XFELs.

OP-097

3D electron diffraction of perfect crystals is perfect for dynamical refinement

P. Brazda (Prague/CZ), P. Klar (Bremen/DE), L. Palatinus (Prague/CZ)

3D electron diffraction has become popular tools for structure analysis of all kinds of materials, including minerals, zeolites, metal-organic frameworks and pharmaceutical compounds [1]. At first glance, refinements against electron diffraction data are considered less reliable because of the quite high residual factors (*R* factors) of typically 15% to 20%. Although valuable structural information are routinely obtained from the resulting models, the *R* factors are a clear indication that the diffracted intensities are not properly modelled [1]. We discuss shortcomings and ideal conditions of the current 3D ED pipelines, and report how under close to ideal conditions *R* factors better than 3% were obtained [2].

The strong interaction of electrons with matter leads to a high probability of electrons being scattered more than once. This is taken into account in the dynamical theory of diffraction. Current implementations by default assume a perfect crystal with a regular shape, especially with a uniform thickness. Furthermore, effects of inelastic scattering are also ignored. Because of instabilities of the transmission electron microscope, including the electromagnetic lenses or the sample stage rotation, certain parameters like the beam intensity or orientation matrix are not constant throughout the experiment. Hence, the typical 3D ED experiment has a rather long list of experimental features to consider if the goal is an accurate modelling of diffracted intensities.

We measured samples of as-grown nanocrystals of α-quartz at temperatures close to 100 K with an FEI Tecnai G2 and a hybrid-pixel detector (ASI Cheetah). These crystals are idiomorphic and considered perfect in the sense that the shape is as regular as possible with a negligible mosaicity. Data reduction was performed with PETS2. Nominal frame orientation angles and distortions were corrected. In the dynamical refinement with Jana2020 in combination with Dyngo [3], the thickness distribution of the trigonal crystals was taken into account. Furthermore, the Kappa formalism was used to describe atomic form factors of Si and O. Structural parameters, the refined twin fraction and *R* factors are compared for the different refinement steps. For several measurements, the final R_{obs} was around 2.5% with a *wR*all around 3% if all above mentioned parameters were taken into account.

These results indicate that in principle diffracted intensities from 3D electron diffraction can be modelled with an accuracy similar to the modelling of intensities from X-ray diffraction experiments, with the potential to ultimately close the current *R*-factor gap between X-ray diffraction and electron diffraction. However, in general there are clear differences between the experimental conditions and the assumptions. This work forms the basis to analyse and understand the effect of these differences on the resulting model, paving the way for better crystal structure models based on 3D ED.

(1) Gemmi, M., Mugnaioli, E., Gorelik, T., Kolb, U., *et al*. (2019). *ACS Cent. Sci*. **5**, 1315.
(2) Brazda, P., Klar, P.B., Palatinus, L. (2023). *In preparation*.
(3) Palatinus, L., Petricek, V., and Correa, C.A. (2015). *Acta Cryst.* **A71**, 235.

OP-098

Crystal structure determination from low-resolution electron diffraction data – molecular replacement?

T. Gorelik (Braunschweig/DE, Saarbrücken/DE), P. Lukat (Braunschweig/DE), W. Blankenfeldt (Braunschweig/DE)

Within the last decades electron diffraction has developed into a reliable method of structure analysis (Gemmi et al., 2019), featuring the determination of hydrogen positions (Palatinus et al., 2017) and absolute configuration (Brázda et al., 2019). Typically, structure solution is performed with *direct methods*, which rely on the atomicity condition: the resolution of the experimental data has to be at least 1.2 Å. Certain nanocrystalline materials do not provide high-resolution diffraction data – whether due to poor crystallinity, or radiation damage during data collection. In these situations, *global optimisation methods*, typically simulated annealing, are used (Andrusenko et al., 2021; Lightowler et al., 2022). Global optimization algorithms do not require high-resolution data, making use of additional constraints and restrains provided by the molecular connectivity. If the connectivity, or the content of the unit cell (e. g. additional solvent molecules) is not known exactly, global optimization methods can hardly be applied.

In a search for a structure analysis method of molecular crystals with (i) partially unknown unit cell content, delivering (ii) low resolution diffraction data, we were inspired by the success of *molecular replacement* methods for structure determination of proteins. We decided to apply molecular replacement to electron diffraction data of small molecules. Using the rigid part of the molecule as a search fragment, we explored whether the molecular replacement phasing would be able to place the fragment correctly, and whether the rest of the unit cell contend would be evident from the Fourier difference map. We evaluated the feasibility of the approach for X-ray and electron diffraction data of different resolution for a molecule containing rigid and flexible parts.

(1) Andrusenko et al. (2021). Int. J. of Pharm., 608, 121067.
(2) Brázda et al. (2019). Science, 364, 667–669.
(3) Gemmi et al. (2019). Am. Chem. Soc. Cent. Sci., 5, 1315–1329.
(4) Lightowler et al (2022). Angew. Chem. Int. Ed., 61, e202114985.
(5) Palatinus et al. (2017). Science, 355, 166–169.

OP-099

Enhancing the photocatalytic performance of carbon nitrides through controlled local structure modification

D. Piankova (Potsdam/DE), H. Zschiesche (Potsdam/DE), I. Teixeira (São Carlos/BR), E. Svensson (Stockholm/SE), C. W. Tai (Stockholm/SE), N. Tarakina (Potsdam/DE)

Poly(heptazine imides) (PHIs) have become benchmark carbon nitride materials in photocatalysis. The idealized structure of M-PHIs is described as an AAA stacking of heptazine layers forming continuous channels occupied by metals. The photocatalytic activity, however, is strongly dependent on the local-structure arrangement and the concentration of defects. In this work we realized the controlled modification of the local structure by varying the sizes and charges of metals and introducing a rotation between heptazine layers. The combination of X-ray powder diffraction (XRD), low-dose HRTEM imaging, electron radial distribution function (eRDF) analysis obtained from rotational electron diffraction data in cryo conditions and valence electron energy loss spectroscopy enabled to control structural modifications. The general structure models obtained based on low-dose HRTEM images and refinement of XRD data failed to uniquely locate metals to their positions in Na- and Mg-PHI. The analysis of eRDFs of Mg and Na salts revealed that metal cations are equally distributed between interlayer positions and bridging nitrogen atom positions in the channels. The coherence lengths increase in the series H-, Na-, Mg-, K-PHI (reaching ~40 Å), indicating an increase in crystallinity. The eRDF curves of Na- and Mg-PHI display additional broadening of the peaks beyond 8 Å, which is related to twists of layers and the formation of Moiré lattices. DFT calculations showed that these defects modify the band structure of M-PHIs. During photocatalytic tests for the hydrogen evolution reaction, Mg-PHI showed the best photocatalytic performance reaching an unprecedented quantum efficiency of 7.14%. The higher charge of Mg^{2+} compared to all other cations (Na^+, K^+, H^+) leads to a more efficient polarization of the heptazine backbone and a considerably faster interlayer charge transfer in the presence of rotational defects.

We gratefully acknowledge financial support by the Max Planck Society.

Microsymposium 21 | Crystallography in Materials Sciences II

OP-100

Pitfalls in cation and anion mutation of quaternary chalcogenide semiconductors

G. Gurieva (Berlin/DE), D. Matzdorff (Berlin/DE, Berlin/DE), D. M. Többens (Berlin/DE), S. Schorr (Berlin/DE, Berlin/DE)

Most of the current commercial photovoltaic devices are exclusively formed by a single junction solar cells, independently on the used technology. This device configuration permit only achieve maximum theoretical efficiencies in the range of 30-33% depending using an absorber material with an optimal band gap energy of 1.3 – 1.4 eV [1,2]. To achieve further cost reductions in thin film solar cell technologies, devise efficiencies must be increased beyond the single-junction limit. Therefore, there is an increasing interest in semiconductor materials which are potentially suitable for an application as absorber layer in the top cell of a tandem device with a silicon-based solar cell as bottom cell. This requires from the top cell absorber a wider band gap in the range of 1.7 eV. Furthermore, these absorber materials should have a high absorption coefficient for solar light and should contain only earth abundant and non-toxic elements.

Quaternary chalcogenide semiconductors, like Cu2ZnSnS4, Cu2ZnGeS4, Cu2ZnGeSe4 or Cu2ZnSiSe4 show high absorption coefficients, contain only earth abundant, non-toxic elements and have band gap energies between 1.4 eV and 2.2 eV. In order to achieve absorber materials with the required band gap energy of 1.7 eV, cation and anion mutation is an established method for flexible band gap energy tuning.

The formation of solid solution series of chalcogenide compound semiconductors (*B*=Mn, Zn *C*=Si, Ge, Sn and *X*=S, Se) achieved by alloying (mutation) of cations and anions, poses some difficulties in case the end members of the series crystallize in different crystal structure types [3]. There are four different structure types possible: the stannite structure, the kesterite structure, the wurtz-stannite structure and the wurtz-kesterite structure. The basic building block of these structure types are corner sharing tetrahedra. Each cation is tetrahedrally coordinated by the anions as well as each anion is tetrahedrally coordinated the cations. Comparing the four possible crystal structure types the network of corner sharing tetrahedra is preserved but the symmetry decreases by tilting of the coordination polyhedra as well as shifting the cations and anions to more general positions.

We performed a comprehensive study of solid solution series based on compounds to tune the band gap energy of the material to an optimal value. We have synthesized powder samples by solid state reaction and investigated the crystal structure of the mixed crystals by a combination of X-ray and neutron diffraction as well as Multiple Edge Anomalous Diffraction (MEAD) [4] of synchrotron radiation.

We can show that the transformation from the stannite to the kesterite type structure within a solid solution series is characterized by a cation re-distribution process. Thus, by tuning the band gap energy to the optimal value by alloying, the structural disorder in the material increases which might have negative influences on the solar cell efficiency. In case the end members crystallize in the kesterite and the wurtz-kesterite type structure a 2-phase region exists where two chemical identical mixed crystals but with different crystal structures coexist. Such compositional regions should be avoided in the application as absorber material, because these two phases will have different band gap energies which is detrimental for the solar cell efficiency.

Cation and anion mutation in quaternary chalcogenides allows flexible band gap energy tuning. Carefull investigations of the crystal structure of the mixed crystals of a solid solutions series can avoid pitfalls of having a compound semiconductor with the optimal band gap energy value but exhibit properties detrimental for a solar cell application.

(1) W. Shockley, H. J. Queisser, Journal of Applied Physics 32 (1961) 510–519.
(2) S. Rühle, *Solar Energy* 130 (2016) 139-147.
(3) S. Schorr, *Solar Energy Materials and Solar Cells* 249 (2022) 112044.
(4) D. M. Többens et al., *Acta Crystallographica B* 76 (2020) 1027-1035.

Figure caption: Flexible band gap energy tuning by cation and anion alloying in quaternary chalcogenide compound semiconductors (X = S, Se). SQ limit stand for the

Shockley-Queisser limit, describing the maximum possible efficiency of a single junction solar cell

(1) CZTS-Cu2ZnSnS4, AgZTSe-Ag2ZnSnSe4, CZGeS-Cu2ZnGeS4, CZSiSe-Cu2ZnSiSe4.

Fig. 1

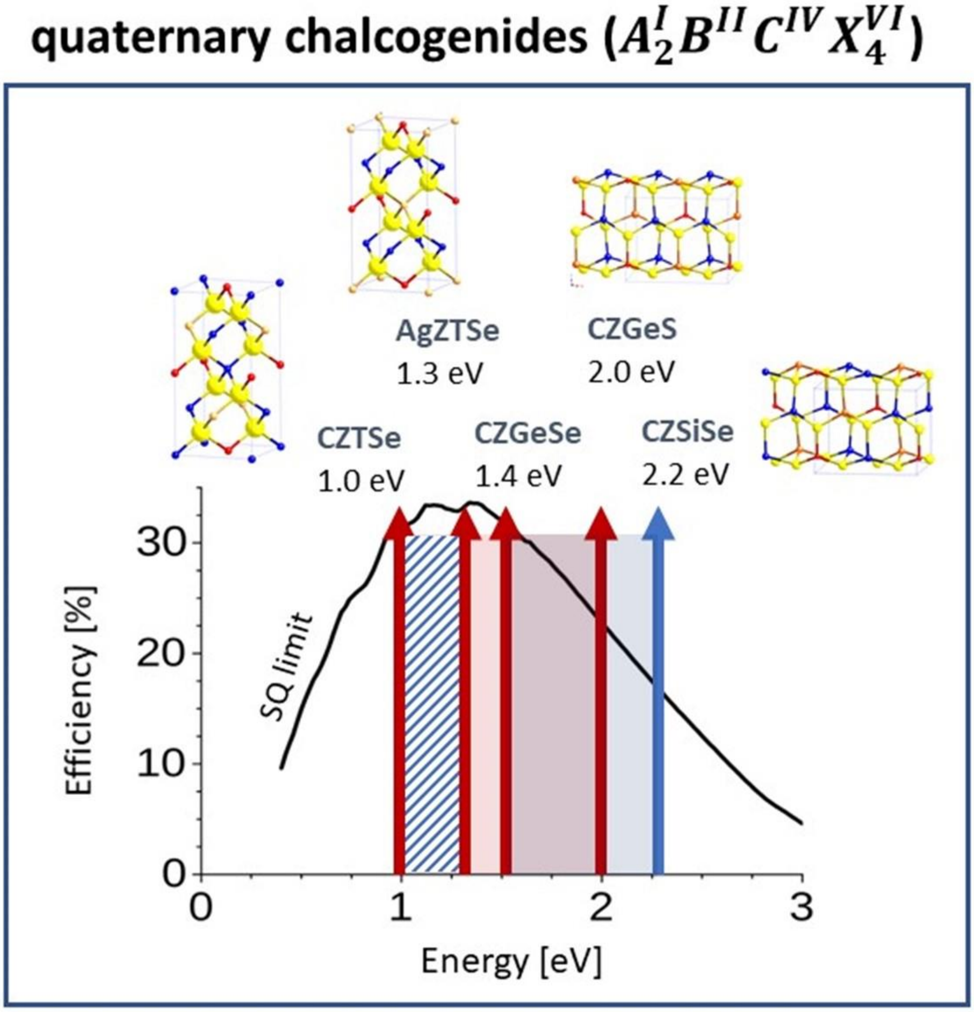

OP-101

Immediate structural response of halide perovskites under lighting revealed trough in-situ X-ray diffraction

J. Breternitz (Berlin/DE), I. Zizak (Berlin/DE), S. Schorr (Berlin/DE, Berlin/DE)

Halide perovskites as materials for solar cells have made a spectacular appearance in the last 10 years. With solar cell efficiencies maxing at 25.7 %, they are close to conventional solar cell materials,[1] while having the advantage of low temperature processing and thin absorber layers. Many different compositions deriving from $MAPbI_3$, the signature material, have been employed to push the solar cell efficiencies higher, spanning a wide variety of perovskite-type crystal structures.[2]

The structural response to external stimuli – such as light – is , however, surprisingly different from conventional semiconductor materials, which can often be thought as highly ordered, very rigid structures. Using in-situ studies conducted at the mySpot beamline at the BESSY II synchrotron light source (HZB),[3] we uncover that light affects the atomic structure of hybrid halide perovskites notably (figure 1), within the experimental resolution of 1 Hz. We show that these changes have a reversible and an irreversible contribution and we elucidate some effects of halide composition on the structural response to light. The understanding of the underlying aspects of these light-induced effects is highly relevant for their use as solar cell materials, since lighting cannot be safely precluded in the use of solar cells. Besides the scientific finding, we will highlight the instrumental developments and data treatment strategy that allowed the collection and interpretation of the results.

Figure 1: Development of the unit cell volume of $MAPbI_{2.95}Cl_{0.05}$ relative to the initial value in an illumination cycling experiment.

(1) https://www.nrel.gov/pv/cell-efficiency.html, accessed 14/11/22
(2) J. Breternitz, *in* Crystallography in Materials Science, Ed. S. Schorr. C. Weidenthaler, de Gruyter, 2020.
(3) I. Zizak, JLSRF, 2016, 2, 101.

Fig. 1

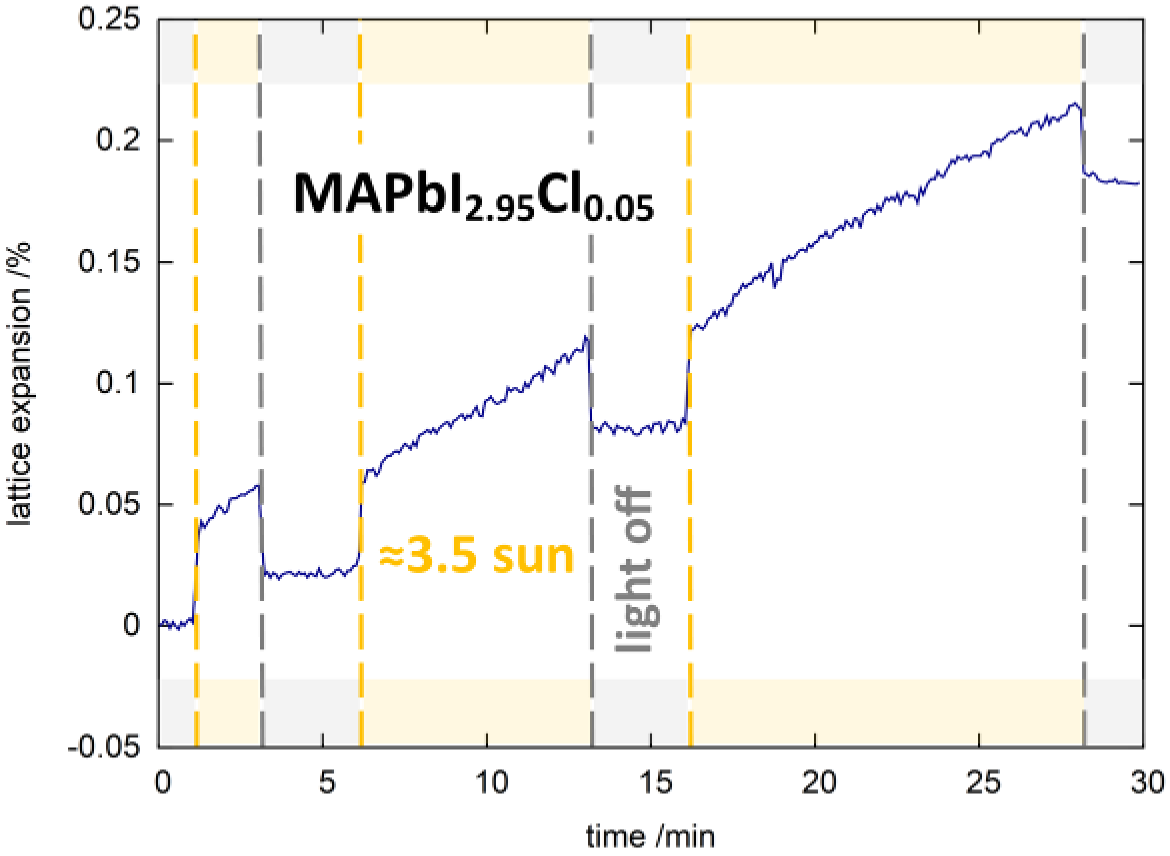

OP-102

Pressure-induced depolarization and phase transitions in $BaTiO_3$-based ferroelectric solid solutions

T. H. Reuter (Frankfurt am Main/DE), L. Bayarjargal (Frankfurt am Main/DE), B. Winkler (Frankfurt am Main/DE)

The symmetry of certain $BaTiO_3$-based solid solutions depends on their composition. Near such "morphotropic" phase boundaries in the composition phase diagram, some of these perovskite-structured materials show interesting properties such as an increase in piezoelectricity or in their remnant polarization[1, 2]. Phase transitions (PT), especially ferroelectric-to-paraelectric PTs, in $BaTiO_3$-based systems can also be induced by applying moderate pressures, in the order of ~ 5 GPa [3]. PTs of this type are accompanied by depolarization and, when using shock compression, a pulsed release of electrical energy, which makes these materials interesting for use as materials with high power output densities[3, 4]. Solid solutions $Ba(Zr,Ti)O_3x$-$(Ba,Ca)TiO_3$ (BZT-xBCT) and $Ba(Sn,Ti)O_3$-$x(Ba,Ca)TiO_3$ (BTS-xBCT) are also promising for the replacement of Pb-containing ferroelectrics. [1, 2].

BZT-xBCT and BTS-xBCT solid solutions were synthesized from the corresponding carbonates and oxides. The composition-dependent changes of their structures were determined by powder x-ray diffraction. Pressure-induced PTs were studied using diamond anvil cells by measuring the change of the second harmonic generation (SHG) signal up to ~ 5 GPa, which results from the pressure-induced depolarization. As an example, for BZT-60BCT and BZT-50BCT, the SHG signal disappeared above 2GPa, indicating the occurrence of a pressure-induced PT (Fig. 1).

Financial support by the DFG (project BA4020/4-1) is gratefully acknowledged.

(1) Xue et al. *Appl. Phys. Lett.* **2011** 99, 12, 122901.
(2) Le Zhang et al. *Appl. Phys. Lett.* **2014** 105, 16, 162908.
(3) Luo et al. *J. Appl. Phys.* **2021** 130, 24, 245102.
(4) Gao et al. *Phys. Rev. Materials*. **2019** 3, 3, 35401.

Fig. 1

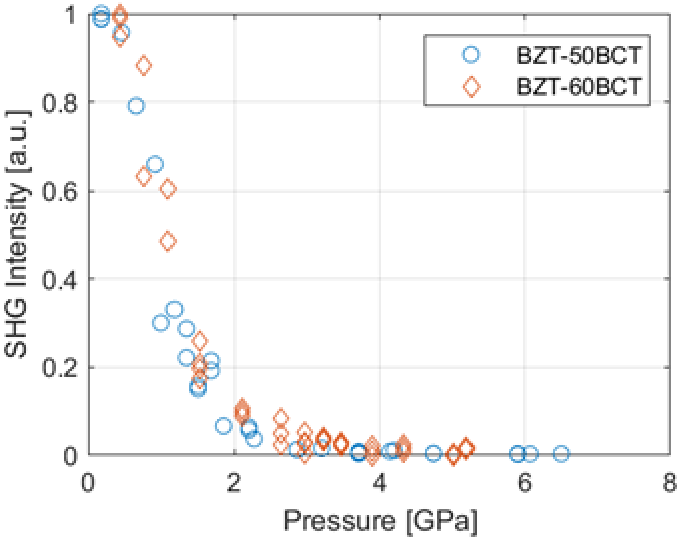

OP-103

Crystallography in hydrogen technology: ammonia as hydrogen carrier

C. Weidenthaler (Mülheim an der Ruhr/DE), S. Gallus (Mülheim an der Ruhr/DE)

Introduction: The energy transition requires the implementation of sustainable energy carriers. Hydrogen is one of these options, but storage is still a challenge. Ammonia, NH_3, is currently being investigated as a suitable candidate as an H2 storage medium and is already used for heavy-duty transportation systems. The efficient splitting of NH_3 into H_2 and N_2 for fuel cell applications requires the development of catalysts where supported transition metals are one amongst others.

Objectives, materials & methods: To understand the function of a catalyst, it is inevitable to use in situ/operando techniques in addition to ex-situ analytics. In this paper, we present a combination of different in situ techniques that were used to investigate structure-property relationships of two different types of Co- and Ni-based catalysts supported on the basic oxides La_2O_3 and Al_2O_3. In addition to in situ diffraction studies, reduction behaviour, surface chemistry, and catalytic activity are also used for the overall discussion.

Results: For Co-based catalysts supported on Al_2O_3, we could show that a significant fraction of the Co catalysts react with Al_2O_3 and forms catalytically inactive $CoAl_2O_4$[1]. This "missing" Co can not be compensated by higher loadings. Alumina is known to prevent sintering and a redispersion of free Co after the reaction was observed. However, the disadvantage of its tendency to form inactive cobalt aluminates predominates.

As a second system, we studied Co on basic La_2O_3 support, which forms in situ from a $LaCoO_3$ precatalyst during NH_3 cracking. Here, the Co crystallites have a mean column length of 5-10 nm and neither react with La_2O_3 nor redisperse after the reaction. The conversion for Co on La_2O_3 is comparable to the most active Co on Al_2O_3 catalyst, despite having multiple higher Co-loading.

(1) Weidenthaler, C.; Schmidt, W.; Leiting, S.; Ternieden, J.; Kostis, A.; Ulucan, T. H.; Budiyanto, E. Chem.Cat.Chem (2022) https://doi.org/10.1002/cctc.202200688

OP-104

Crystallographic structure and point defects vs. efficiency and stability in $Cu_2ZnSn(S,Se)_4$ monograin solar cells

G. Gurieva (Berlin/DE), K. Ernits (Tallin/EE), N. Siminel (Chisinau/MD), A. Manjon Sanz (Oak Ridge, TN/US), D. Sheptyakov (Villigen/CH), M. Avdeev (Sydney/AU), M. Kirkham (Oak Ridge, TN/US), D. Meissner (Tallin/EE, Tallinn/EE), S. Schorr (Berlin/DE, Berlin/DE)

In recent years quaternary chalcogenides have gained a lot of attention, especially the kesterite-type semiconductor compounds $Cu_2ZnSn(S,Se)_4$ (CZTSSe) which consist mostly of earth abundant and non-toxic elements. These compounds are a promising low-cost alternative absorber material for thin film solar cells due to their suitable criteria for photovoltaic applications: *p*-type semiconductor behavior, direct band-gap between 1.0-1.5 eV and absorption coefficient>10^4 cm^{-1}[1]. The record conversion efficiency of 13.5% reported for a CZTSSe based thin film solar cell was reached when the polycrystalline absorber layer exhibits an off-stoichiometric composition [2]. Deviations from stoichiometry cause intrinsic point defects (vacancies, anti-sites, interstitials), which determine the electronic properties of the semiconductor significantly [3]. It is agreed in literature that large band tailing observed in Cu-based kesterite-type semiconductors causes voltage losses limiting the efficiency of kesterite-based devices. The Cu/Zn disorder (Cu_{Zn} and Zn_{Cu} anti-sites in Cu-Zn planes at z=¼ and ¾), which is always present in these compounds [4,5], is discussed as a possible reason for band tailing. Conventional structural characterization is done with X-ray, but in the case of isoelectronic cations, like Cu^+ and Zn^{2+}, they are difficult to distinguish diffraction due to their very similar X-ray form factors. Nevertheless, using neutron diffraction we can distinguish between Cu^+ and Zn^{2+} site occupation in the crystal structure because the neutron scattering length of Cu and Zn is very different [4,5]. Kesterite-type based thin film solar cell technologies are mainly based on polycrystalline absorber layers, which makes it quite hard to correlate the crystallographic structure (determined via neutron diffraction) to the photovoltaic performance of these materials. A promising low-cost alternative technology uses CZTSSe monograins (single crystals of 50-100 µm size) which are fixed in a polymer matrix to form a flexible solar cell [6]. An in-depth analysis of neutron diffraction data provides information on the cation distribution in the crystal structure allowing the determination of the type and concentration of intrinsic point defects including a distinction between Cu^+ and Zn^{2+} [5]. On the other hand, neutron diffraction requires large sample volumes, thus kesterite monograins offer the unique possibility to correlate structural disorder in kesterite-type absorbers with device performance parameters.

We will present a detailed structural investigation of CZTSSe monograins with S/(S+Se)=0.8 based on neutron powder diffraction experiments, examining the influence of small changes in the chemical composition on the Cu/Zn disorder. We will show a correlation between all the obtained knowledge on the chemical composition, the presence and types of secondary phases, the Cu/Zn disorder, the intrinsic point defects, the optical bandgap obtained from diffuse reflectance with the stability and efficiency of the respective devices. We will compare the "optimal" composition area of monograins with S/(S+Se)=0.8 to previously studied S/(S+Se)=0.6.

(1) S. Delbos, EPJ Photovoltaics 2012; 3: 35004.
(2) J. Zhou et al., Nano Energy 89 (2021) 106405.
(3) S. Schorr et al., in: Crystallography in Materials Science, ed. by S. Schorr and C. Weidenthaler, De Gruyter, 2021.
(4) S. Schorr, Solar Energy Materials & Solar Cells 2011; 95: 1482-1488
(5) G. Gurieva et. al., J Appl Phys 2018; 123: 161519/1-12
(6) www.crystalsol.com

Plenary lectures

PT-1

Photosynthesis and Cellular Respiration – Structures and Conclusions

H. Michel (Hannover/DE)

Photosynthesis and cellular respiration are opposite processes through which living organisms gain their energy. Photosynthesis starts with light absorption by light-harvesting antennae, followed by energy transfer to the so-called photosynthetic reaction center where a separation of charges occurs, and electrons are transferred across the photosynthetic membranes. The electrons have to be replenished. The photosystem II reaction centers from chloroplasts and cyanobacteria use electrons from water for this purpose, they able to extract electrons from water causing the release of oxygen to the atmosphere. The related photosynthetic reaction center from the purple bacterium Rhodopseudomonas viridis was the first membrane protein or membrane protein complex to be crystallized so that its structure could be determined.

The aerobic organisms, from bacteria up to humans, use the energy inherent in the reduction of molecular oxygen (dioxygen) to water The final step is catalyzed by the terminal oxidases of the repiratory chain with the cytochrome c oxidases as the most prominent examples. These enzymes use electrons form one side of the membrane and protons from the other side, thereby creating an electric voltage and a pH gradient across the membrane. We had determined the first structure by X-ray crystallography. The catalytic cycle of the cytochrome c oxidases has been considered to start with the oxidized form (O-state). Subsequent electron transfers lead to the E-state, the R-state (which binds oxygen), the P-state (with an already split dioxygen bond), the F-state and the O-state again. We have determined structures of up to 1.9 Å resolution of these intermediates by single particle electron cryomicroscopy . Our results suggest that in the O-state the active site already contains a peroxide dianion and in the P-state an intact dioxygen molecule, the F-state may contain a superoxide anion. Thus the enzyme’s catalytic cycle may have to be turned by 180 degrees.

PT-2

Electron Crystallography in the Spotlight of Materials Science

Y. Krysiak (Hannover/DE)

The relationship between structure and properties is elementary for the applications of crystalline solids. Because of the increasing complexity in materials on different length scales, the development of advanced methods for structure analysis are needed.

In the shadow of X-ray crystallography, nearly 100 years after the discovery of the wave character of electrons, electron crystallography has evolved to encompass both imaging and diffraction techniques, enabling crystallographic analysis of micro- and nanostructures with atomic resolution.

Thanks to the development of the tomographic data acquisition 15 years ago [1], electron diffraction has been rediscovered and continuously developed since then, making it possible to analyse tiny single crystals analogous to single crystal X-ray diffraction. This allows nowadays, on the one hand, determining the structure of small particles, and on the other, to even investigate crystal structures of beam sensitive small molecule structures [2].

The extensive structural exploration of current material classes such as organic [3] and layered materials [4], switchable semiconductors [5], porous catalysts [6], and battery materials [7] is in numerous cases only successful with three-dimensional electron diffraction (3D ED). Therefore, the method has become highly attractive in the field of materials science.

References

(1) Kolb, U., Gorelik, T., Kübel, C., Otten, M.T., Hubert, D.: Towards automated diffraction tomography: part I - data acquisition. Ultramicroscopy. 107, 507 (2007).

(2) Gemmi, M., Mugnaioli, E., Gorelik, T.E., Kolb, U., Palatinus, L., Boullay, P., Hovmöller, S., Abrahams, J.P.: 3D Electron Diffraction: The Nanocrystallography Revolution. ACS Cent. Sci. 5, 1315 (2019).

(3) Plana-Ruiz, S., Krysiak, Y., Portillo, J., Alig, E., Estradé, S., Peiró, F., Kolb, U.: Fast-ADT: A fast and automated electron diffraction tomography setup for structure determination and refinement. Ultramicroscopy. 211, 112951 (2020).

(4) Krysiak, Y., Marler, B., Barton, B., Plana-Ruiz, S., Gies, H., Neder, R.B., Kolb, U.: New zeolite-like RUB-5 and its related hydrous layer silicate RUB-6 structurally characterized by electron microscopy. IUCrJ. 7, 522 (2020).

(5) Fillafer, N., Kuper, H., Schaate, A., Locmelis, S., Becker, J.A., Krysiak, Y., Polarz, S.: Design of Active Defects in Semiconductors: 3D Electron Diffraction Revealed Novel Organometallic Lead Bromide Phases Containing Ferrocene as Redox Switches. Advanced Functional Materials. n/a, 2201126 (2022).

(6) Krysiak, Y., Barton, B., Marler, B., Neder, R.B., Kolb, U.: Ab initio structure determination and quantitative disorder analysis on nanoparticles by electron diffraction tomography. Acta Crystallographica Section A Foundations and Advances. 74, 93 (2018).

(7) Karakulina, O.M., Demortière, A., Dachraoui, W., Abakumov, A.M., Hadermann, J.: In Situ Electron Diffraction Tomography Using a Liquid-Electrochemical Transmission Electron Microscopy Cell for Crystal Structure Determination of Cathode Materials for Li-Ion batteries. Nano Lett. 18, 6286 (2018).

PT-3

Electron Crystallography in the Spotlight of Materials Science

E. Bykova (Cologne/DE)

Development of the scientific instrumentation in the last years (high-brilliance synchrotron beamlines, specialized high-pressure equipment, nano-focusing of the X-ray beam, pulsed laser-heating setups *etc.*) enabled collection of the high-quality X-ray diffraction (XRD) data at the enormous pressures up to 1 TPa and temperatures up to 5000 K. At extreme pressures the chemistry and crystal chemistry of the compounds can change drastically. Laser heating, as a rule, results in multi-phase mixtures composed of unknown phases with unknown compositions. Application of single-crystal XRD opens the way to determine crystal structure of a compound at truly extreme conditions, and thus refine its chemical composition even in complex multi-phase and/or multigrain samples. We will discuss how methods of single-crystal XRD can be applied to study chemical and structural transformations of the earth-related and technology-relevant materials at extreme conditions.

PT-4

Exploring the interface of crystals with life, art and mind: a tale of interdisciplinarity

J. M. García-Ruiz (Armilla/ES)

Along with the invaluable contribution of crystallography to the advancement of science and technology, the very idea of crystal has been highly influential in the world of art and culture. This influence has changed throughout history in correlation with increasing scientific knowledge about crystals. Since the emergence of consciousness hundreds of thousands of years ago, human fascination for crystals has been so deeply rooted in our brains as to shape our perception of patterns. During prehistory, crystals had teleological and theological connotations derived from the hidden power of their singularity among natural objects. Later, from the classical world to the emergence of positive science in the eighteenth century, scholars and experts endorsed mineral crystals with healing powers. The sheer beauty of the external forms of crystals and all they evoke fascinated educated people at that time. But the more significant impact of crystals on the mind and culture started in the XIX century. At that time, the extraordinary connection between the external harmony, redundantly beautiful symmetry of crystals, and their internal order, periodic and iterative, was demonstrated. Since then, the word crystal has been full of evocations such as purity, transparency, beauty, equilibrium, rationality, intelligence, energy, power . . . The notion of crystal transcended scientific thinking to inspire the arts, from literature to painting, architecture to dance, and music to filmmaking. This lecture is a walk through the history of that influence and the aesthetic and scientific debates it has provoked.

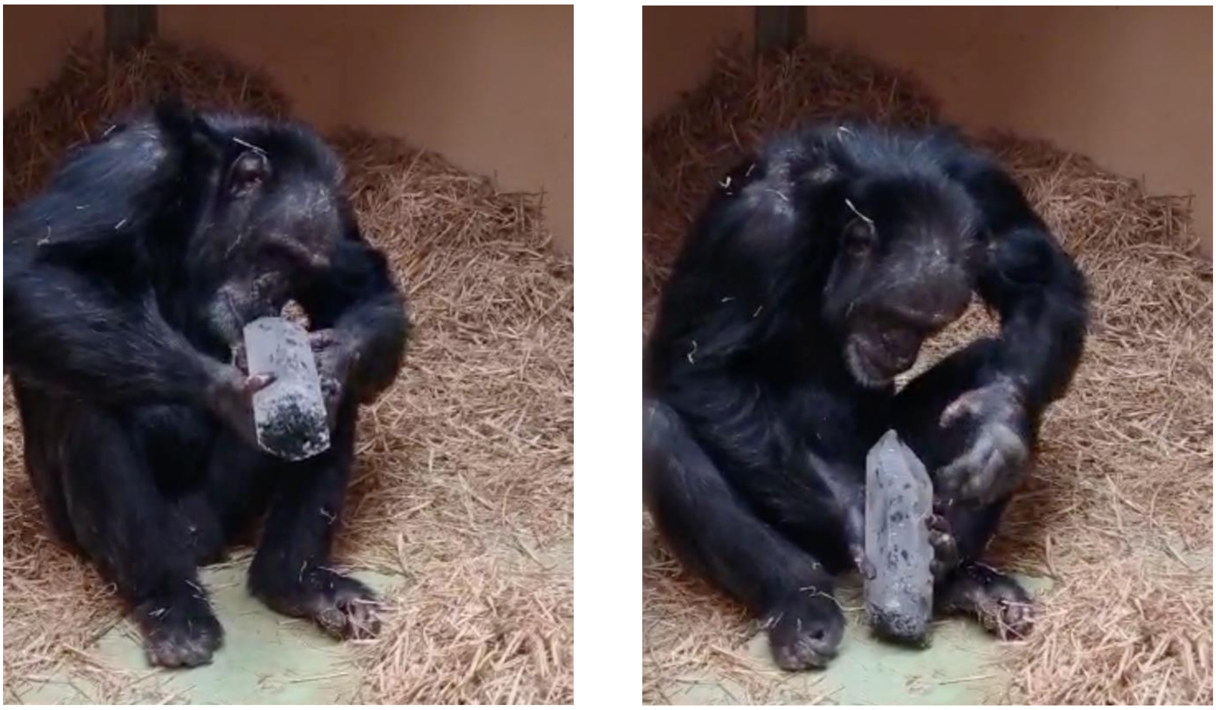

Figure 1: A chimpanzee examines a rock crystal in our experiments to reveal the origin of crystal allure for hominids.

PT-5

3D Electron Diffraction in Pharmaceutical Compounds: Can we measure everything?

J. Benet-Buchholz, M. Martínez-Belmonte, E. C. Escudero-Adán, J. Ceron-Bertran, J. Ramirez, A. Capape (Tarragona/ES), C. Göb, R. Bücker (Neu-Isenburg/DE), S. Ito, A. Yamano (Tokyo/JPN)

Structure determination of nanocrystals using 3D Electron Diffraction (3D ED) has undergone in the last decade a revolution based on the introduction of protocols for 3D acquisition and analysis of electron diffraction data1. Experiments were performed in adapted transmission electron microscopes using customized data collection protocols. The most up-to-date method involves continuous data collection utilizing a highly sensitive shutterless detector and goniometer rotation2. The Rigaku Corporation / JEOL Ltd. launched the XtaLAB Synergy-ED in 2021, which was the first commercial 3D ED Integrated Platform. The system was acquired by ICIQ thanks to public funding in 2022/20233.

The present study employed the Synergy-ED Platform to investigate the solid state of pharmaceutical compounds. The study included characterization of:

- Hydrogen bonds in co-crystals/salts.
- New samples formed during a co-crystal screening.
- Co-crystals highly sensitive to radiation damage.
- Labile hydrates.
- The absolute configuration of chiral compounds.

The tests aim to address questions concerning vacuum degradation, radiation damage and dynamic diffraction effects.

The measurements performed showed excellent results in all analysed samples pointing to a promising future in the use 3D-ED. Especially noteworthy is the use of low temperature for the conservation/protection of vacuum-sensitive molecules and the use of dynamical refinements for the determination of the absolute configuration of pharmaceutical compounds.

[1) M. Gemmi; E. Mugnaioli; T.E. Gorelik; U. Kolb; L. Palatinus; P. Boullay; S. Hovmöller; J.P. Abrahams; *ACS Central Science* (2019), **5** (8), 1315–1329.

[2] I. Nederlof; E. van Genderen; Y.W. Li; J.P.A. Abrahams; *Acta Crystallogr.*, Sect. D: Biol. Crystallogr. (2013), 69, 1223−1230.

[3] Agencia Estatal de Investigación and NextGenerationEU, project EQC2021-006956-P.

PT-6

From crystallographic fragment screen to preclinical candidates: Open science discovery of SARS-CoV-2 antivirals

D. Fearon (Ditcot/UK)

Fragment-based drug discovery is a well-established method for the identification of chemical starting points which can be developed into drugs for use in clinic. Historically, X-ray fragment screening using traditional crystal soaking methods was tedious, low-throughput and time consuming. However, thanks to advances in synchrotron capabilities and the introduction of streamlined crystal soaking facilities, such as the XChem platform at Diamond Light Source, there has been substantial improvements in throughput and integration between sample preparation, data collection and hit identification.

Figure 1: Overview of the XChem fragment screening platform at Diamond Light Source.

To identify starting points for the development of novel antiviral therapeutics, the XChem team and collaborators, performed large crystallographic fragment screens against 8 key SARS-CoV-2 protein targets including the Main protease1. This work identified numerous starting points for the development of potent antiviral therapeutics as exemplified by the COVID Moonshot - a fully open science, structure-enabled, drug discovery campaign targeting the SARS-CoV-2 main protease.2 By leveraging crowdsourced medicinal chemistry design, high throughput structural biology, machine learning and molecular simulations, we developed a novel, orally bioavailable, pre-clinical candidate within 2 years.

Following on from the success of the COVID Moonshot, we have now established the AI-driven Structure-enabled Antiviral Platform (ASAP)3 which aims to deliver oral antivirals for potential future pandemics threats including coronaviruses, flaviviruses and picornaviruses, with the goal of providing global, equitable, and affordable access.

Figure 2: Summary of the progression of fragment hits to lead compounds for SARS-CoV-2 Mpro.

(1) Douangamath, A. et al., Nat Commun., 11, 5047 (2020).
(2) The COVID Moonshot Consortium, bioRxiv, 10.1101/2020.10.29.339317 (2023)
(3) https://asapdiscovery.org/

Fig. 1

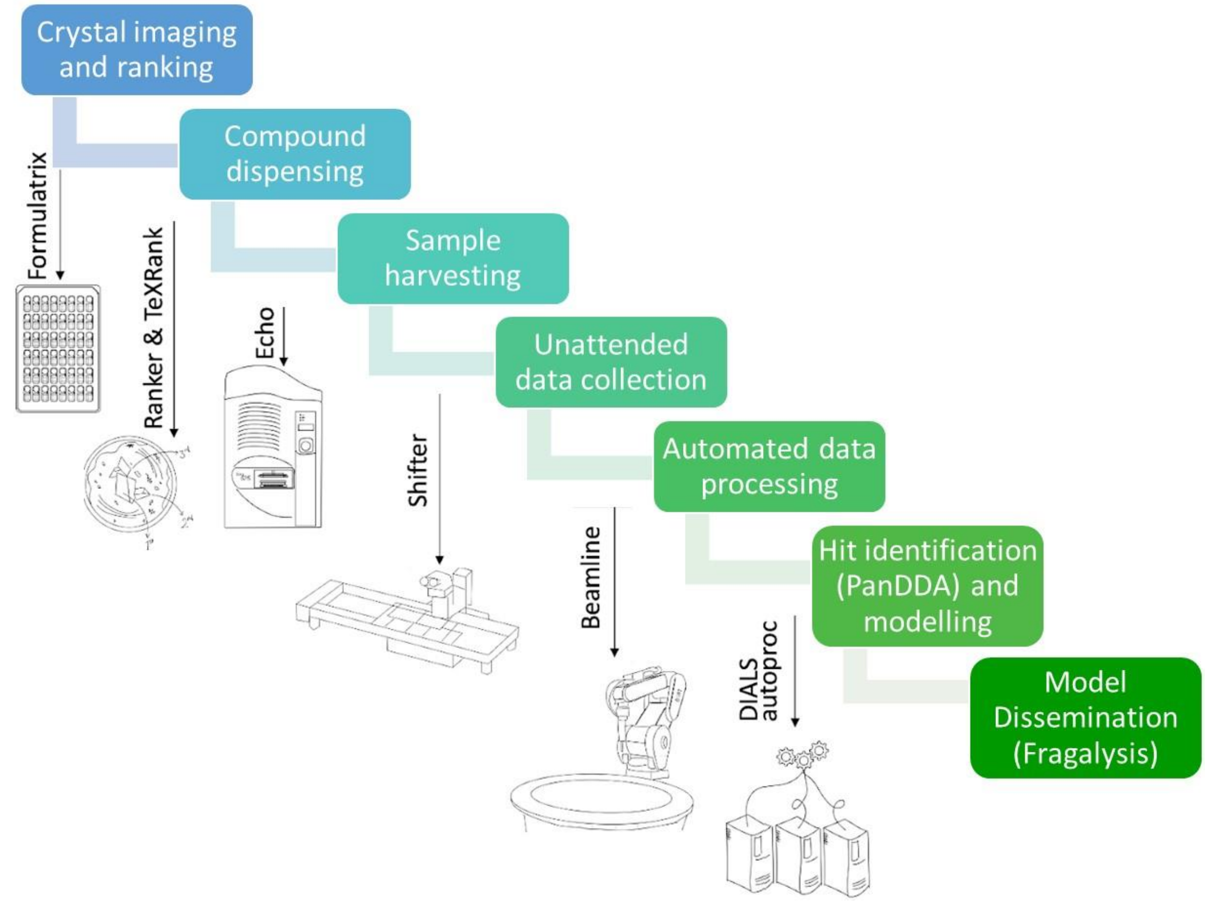
Crystal imaging and ranking
Compound dispensing
Sample harvesting
Unattended data collection
Automated data processing
Hit identification (PanDDA) and modelling
Model Dissemination (Fragalysis)
Formulatrix
Ranker & TeXRank
Echo
Shifter
Beamline
DIALS autoproc

Fig. 2

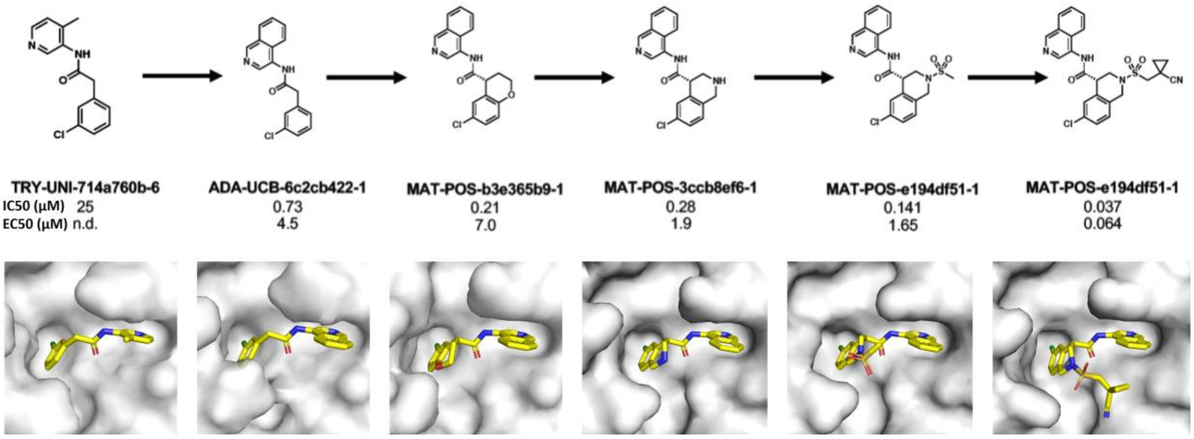
NH
N
O
Cl
O
NH
N
S
O
CN
TRY-UNI-714a760b-6
IC50 (μM) 25
EC50 (μM) n.d.
ADA-UCB-6c2cb422-1
0.73
4.5
MAT-POS-b3e365b9-1
0.21
7.0
MAT-POS-3ccb8ef6-1
0.28
1.9
MAT-POS-e194df51-1
0.141
1.65
MAT-POS-e194df51-1
0.037
0.064

PT-7

Simulating complex crystal structures and their assembly in hard and soft condensed materials

J. Dshemuchadse (Ithaca, NY/US)

Intermetallic compounds and ordered mesoscopic systems (i.e., "hard" and "soft" condensed matter) share structural properties on both ends of the complexity spectrum: while their simplest representatives are trivial sphere packings, their structural diversity has proven to be immense and extends all the way to aperiodic structures. We study the assembly and structural features of complex crystals via numerical simulations, in order to elucidate the emergence of long-range order from short-range interactions. By employing simple coarse-grained models, we gain systematic insights into the phenomena that lead to the crystallization and stabilization of the same intricate crystal structure types across length scales and materials systems. Aiming to deduce general principles of structure formation that will allow for the design of tailored materials in the future, we investigate the connection between building block properties, system properties, and environmental parameters with the crystal structure that a material adopts.

Poster session I | Minerals

PP-001

Miscibility of AFm-phases and the formation of solid solutions containing sulfate, chloride, carbonate and carboxylate anions

S. Gerhardt (Halle (Saale)/DE), T. K. Cortinhas Alves (Halle (Saale)/DE), T. Beirau (Halle (Saale)/DE), S. Stöber (Halle (Saale)/DE)

Lamellar Calcium Aluminate Hydrates (AFm-phases), similar to some naturally existing minerals like Hydrocalumite and Kuzelite, form a double-layered crystal structure with positive charged mainlayers and negative charged interlayers.The general structural formula is $[Me_{2/3}^{2+}\ Me_{1/3}^{3+}\ (OH)_2]^{1/3+}\ [A_{1/3y}^{y-} \cdot mH_2O]^{1/3-}$. These AFm-phases play an important role in the hydration of cementitious materials or in other fields of application like catalysis, medicine and restoration of brownfields. Solid solutions of inorganic and organic AFm-phases have been synthesized in aqueous environment using calciumsulfate, -chloride and -carbonate and various calciumcarboxylate anions forming the interlayers and calcium and aluminum forming the main layers. The synthesis have been varied according to $CaAl_2O_4 + n CaX + 2\ CaO + (1-n) CaY + H_2O_{excess}$ with X containing sulfate, chloride or carbonate and Y being the carboxylate anion of oxalic, malonic, succinic, acetic and benzoic acid used for synthesis. n is increased stepwise by 0.1 mole. Deionised water was added in with a W/S-ratio of 10. Since the system only contains aluminum and calcium besides the anions and water, the cation positions are fixed. Every synthesis-step with the sample containing water has to be done using nitrogen protective atmosphere to decrease the probability of carbon dioxide contamination to prevent carbonation. Most of the endmembers crystallize without building solid solutions with other AFm-phases. Results of the ion chromatography yield that some of the synthesized AFm-phases do not contain all of the offered carboxylate anions but incorporate hydroxide anions for charge balancing instead. Differential scanning calorimetry, thermogravimetry with coupled mass spectrometry and RAMAN spectroscopy were used to evaluate the results of the IC measurements.

PP-002

Comprehensive mineralogical analysis of technogenic soils using spectroscopic methods

S. Ivashevskaya (Petrozavodsk/RU), G. V. Akhmetova (Petrozavodsk/RU)

Today there is an accelerated destruction of forest ecosystems under the influence of anthropogenic activities. Therefore, studies of their recovery in the affected areas are becoming especially relevant. The study of soil and vegetation cover regeneration of technogenic lands is an urgent problem both in theoretical and applied aspects. Soil formation studies have been carried out with various options for forest reclamation of the sand and gravel pit Elk Quarry in Karelia (Russia, 62.101917° N, 33.969944° E).

The following soil properties were evaluated:

- physical and chemical (acidity, nutrient content, general chemical composition);
- biological (microbial biomass, basal respiration);
- mineralogical composition of regenerating soils of reclaimed sand and gravel pits.

Soil analysis relies mainly on time-consuming laboratory methods. Spectroscopic measurement techniques can provide a suitable alternative. X-ray powder diffraction (XRPD) is a powerful tool in the identification of minerals in soils (Thermo Scientific ARL X"TRA Powder X-ray Diffraction System, λcu=1.54056 Å). Raman spectroscopy (RS) is able to provide a molecular fingerprint of individual soil components (Thermo Scientific Almega XR Nicolet Raman spectrometer, laser λ=532 nm). X-ray fluorescence analysis (XRF) is used for multi-element qualitative and quantitative analysis (Thermo Scientific ARL ADVANT'X).

XRPD identified the main minerals in the samples: quartz, microcline, albite, kaolinite and amphibole. The Rietveld method was applied for an approximate quantification of components. A combination of RS and XRF data made it possible to find trace mineral components which are not visible on the X-ray patterns:

- amphibole has been identified as actinolite;
- titanium occurs as rutile, anatase and titanite;
- 5 samples contain traces of epidote, 3 samples - hematite;
- carbon of varying degrees of crystallinity is present in the composition of all samples.

Fig. 1

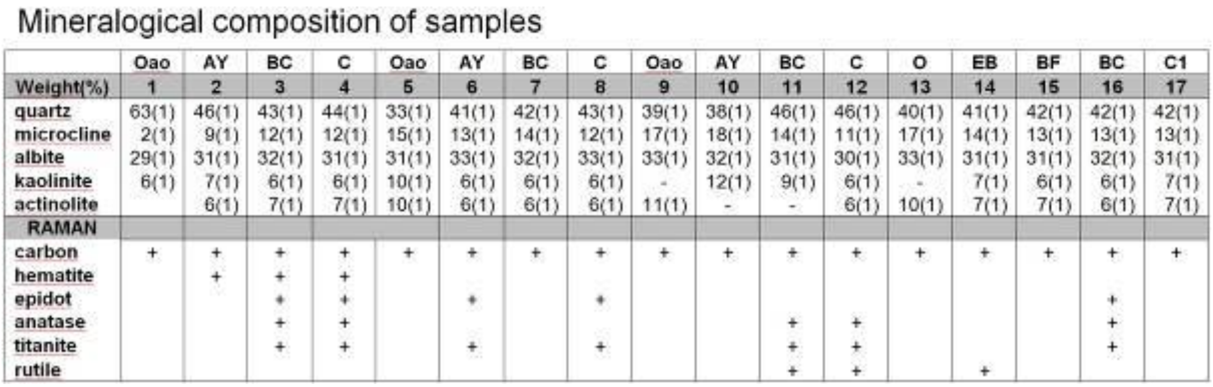

Mineralogical composition of samples

	Oao	AY	BC	C	Oao	AY	BC	C	Oao	AY	BC	C	O	EB	BF	BC	C1
Weight(%)	1	2	3	4	5	6	7	8	9	10	11	12	13	14	15	16	17
quartz	63(1)	46(1)	43(1)	44(1)	33(1)	41(1)	42(1)	43(1)	39(1)	38(1)	46(1)	46(1)	40(1)	41(1)	42(1)	42(1)	42(1)
microcline	2(1)	9(1)	12(1)	12(1)	15(1)	13(1)	14(1)	12(1)	17(1)	18(1)	14(1)	11(1)	17(1)	14(1)	13(1)	13(1)	13(1)
albite	29(1)	31(1)	32(1)	31(1)	31(1)	33(1)	32(1)	33(1)	33(1)	32(1)	31(1)	30(1)	33(1)	31(1)	31(1)	32(1)	31(1)
kaolinite	6(1)	7(1)	6(1)	6(1)	10(1)	6(1)	6(1)	6(1)	-	12(1)	9(1)	6(1)	-	7(1)	6(1)	6(1)	7(1)
actinolite		6(1)	7(1)	7(1)	10(1)	6(1)	6(1)	6(1)	11(1)	-	-	6(1)	10(1)	7(1)	7(1)	6(1)	7(1)
RAMAN																	
carbon	+	+	+	+	+	+	+	+	+	+	+	+	+	+	+	+	+
hematite		+	+	+													
epidot			+	+		+		+								+	
anatase			+	+							+	+				+	
titanite			+	+		+		+			+	+				+	
rutile											+	+		+			

PP-003

Cation and anion ordering in synthetic lepidolites and lithian muscovites: Influence of the OH/F and Li/Al ratio on the mica formation studied by NMR spectroscopy and X-ray diffraction

M. Fechtelkord (Bochum/DE), L. Sulcek (Bochum/DE), B. Marler (Bochum/DE)

A large number of lepidolites $K(Li_xAl_{3-x})[Si_{2x}Al_{4-2x}O_{10}](OH)_yF_{2-y}$ and Li-muscovites $K(Li_xAl_{2-x/3}\square_{1-2x/3})[Si_3AlO_{10}](OH)_yF_{2-y}$ were synthesised using sol-gel mixed oxides in combination with hydrothermal experiments at a pressure of 2 kbar and a temperature of 873 K. The nominal composition ranged between $0.0 \leq x \leq 2.0$ and $0.0 \leq y \leq 2.0$, i.e., from polylithionite $K[Li_{2.0}Al][Si_{4.0}O_{10}](OH)_yF_{2-y}$ over trilithionite $K[Li_{1.5}Al_{1.5}][AlSi_{3.0}O_{10}](OH)_yF_{2-y}$ to muscovite $K[Al_{2.0}\square][AlSi_{3.0}O_{10}](OH)_yF_{2-y}$. ^{1}H, ^{19}F, ^{29}Si, ^{27}Al Magic-Angle Spinning Nuclear Magnetic resonance (MAS NMR) and ^{27}Al Multiple-Quantum Magic-Angle Spinning (MQMAS) NMR spectroscopy has been performed to investigate the order/disorder state of Si and Al in the tetrahedral layers and of Li, Al, OH and F in the octahedral layer. The samples exhibit very small sizes of the mica crystals ranging from 0.1 µm up to 5 µm. With increasing Al content and increasing Si/Al disorder, the crystal sizes decrease. Rietveld structure analyses on 12 samples showed that nearly all samples consist of two mica polytypes (1M and $2M_1$) of varying proportions. In the case of lepidolites, the $1M/2M_1$-ratio depends on the Li/Al ratio of the reaction mixture. The refinement of the occupancy factors of octahedral sites shows that lepidolites ($1.5 \leq x \leq 2.0$) represent a solid solution series with polylithionite and trilithionite as the endmembers. In the case of the Li-muscovites ($0.0 \leq x \leq 1.5$) the $1M/2M_1$-ratio depends on the amount of impurity phases like eucryptite or sanidine depleting the reaction mixture of Li or Al. There is no solid solution between trilithionite and muscovite, instead, the Li-muscovite crystals consist of domains of muscovite and trilithionite of different ratios.

The overall composition of the synthesized micas which consist of two polytypes could be mainly determined by ^{29}Si, ^{1}H and ^{19}F MAS NMR spectroscopy. The Si/Al ratio in the tetrahedral layers and thus the content of $^{[4]}Al$ was calculated by analysing the signal intensities of the ^{29}Si MAS NMR experiments. The Li content x_{est} was calculated from the determined tetrahedral Si:Al ratio of the 29Si MAS NMR signals. The calculated Li-contents xest of samples between polylithionite and trilithionite agree with the expected values. F-rich samples show slightly increased values and the OH-samples lower values. Fluorine containing lepidolites ($x = 1.5 – 2.0$, $y = 0.0$), but no hydroxyl containing lepidolites ($x = 1.5 - 2.0$ and $y = 2.0$) were observed after synthesis. With decreasing Li-content, $x \leq 1.2$, hydroxyl containing Li-muscovites are formed. It was possible to synthesise even fluorine containing Li-muscovites with a Li-content as low as 0.3. The ^{19}F and ^{1}H MAS NMR experiments that F and OH are not distributed statistically but local structural preferences exist. F is attracted by Li-rich and OH by Al-rich environments. The quadrupolar coupling constant which represents the anisotropy of the Al coordination is low for polylithionite with $C_Q = 1.5$ MHz and increases to $C_Q = 3.8$ MHz for trilithionite. For tetrahedral Al a lower increase of C_Q from 1.7 MHz to 2.8 MHz is observed. Advancing from trilithionite to muscovite both quadrupolar coupling constants decrease to 2.5 MHz for octahedral and 1.5 MHz for tetrahedral Al. In polylithionite there is the most isotropic environment for octahedral Al, there are only Li_2Al sites coordinated by F in the octahedral sheets and O from the tetrahedral sheets which are regular containing only Si. The distortion and anisotropy for both Al in tetrahedral and octahedral sheets increases with rising Al content. The most anisotropic environment can be found in trilithionite, especially for octahedral Al.

PP-004

Investigation of structural requirements for distinct cyclization mechanisms in type III PKS

M. Kruse (Braunschweig/DE), W. Blankenfeldt (Braunschweig/DE), L. Beerhues (Braunschweig/DE)

Introduction: Polyketides are a large group of natural products comprising many metabolites of pharmaceutical importance. Plant type III polyketide synthases (PKS) utilize simple starter and extender units to form a wide range of structurally and functionally diverse compounds. Detailed understanding of the enzymatic mechanism could be crucial for the development of novel polyketide-related drugs.

Objectives: Benzophenone synthase (BPS) and biphenyl synthase (BIS) are two highly similar PKS, which use both benzoyl CoA and malonyl CoA as the respective starter and extender substrates, while relying on distinct modes of cyclization to form different products. Despite previous research efforts, the exact cyclization mechanism has not been elucidated yet. The study of a novel, bifunctional PKS from *Hypericum polyphyllum* could provide valuable information on this topic.

Materials & Methods: Surface and active site mutants were generated by site directed mutagenesis. Heterologous expression was followed by purification and crystallization. Crystal structures were solved by molecular replacement. Mutant functionality was monitored by *in vitro* assays.

Results: The truncated protein crystallized more easily, formed more stable crystals and was therefore used for further experiments. Activity assays showed no significant differences between the wild type and the truncated version. In contrast, the K191T active site mutant exhibited reduced activity, but yielded only crystals diffracting to a usable resolution of 3.9 Å.

Conclusion: The low-resolution data was unsuitable for determining the stereochemistry of the reaction. Required co-crystallizations are complicated by the oxidation sensitivity of the enzyme's active site. Use of the closely related *Ha*BPS - for which a high-resolution structure exists - could help, provided that corresponding modifications in the active site result in bifunctionality and that the crystallization experiments can be reproduced.

PP-005

Towards a structural investigation of MamP, a key player in redox control during magnetosome maturation

T. Crosskey (Berlin/DE), F. Lennartz (Berlin/DE), U. Müller (Berlin/DE), M. S. Weiss (Berlin/DE)

Magnetotactic bacteria (MTB) are a group of bacterial species appearing in many diverse phyla. Uniquely, they are distinguished by their ability to biomineralise crystals of magnetite (Fe_3O_4) and greigite (Fe_3S_4) up to the range of 40-100 nm. These membrane-bound crystals are known as magnetosomes, and allow MTB to orient themselves along the axis of the Earth"s magnetic field. This constrains their freedom of movement to allow more precise positioning in their optimal micro-environment at the oxic-anoxic interface of aquatic habitats.

The redox management of Fe^{2+} and Fe^{3+} ions present during nucleation and growth of magnetosomes is crucial, as magnetite and greigite require a precise 1:2 ratio of these ions. There are multiple proteins involved in this control, including MamE, MamT, MamX, and MamP. These proteins all contain at least one magnetochrome domain, which is a class of c-type cytochrome, which each contain a covalently bound haem group with an associated Fe ion. MamP contains two magnetochrome domains, and is known to oxidise Fe^{2+}, although the precise mechanism of this reaction in unknown[1].

The technique of spatially-resolved anomalous dispersion (SpReAD) uses synchrotron radiation to measure the oxidation state of metal ions inside protein crystal by carefully selecting the energy of the incoming X-ray beam[2]. Metal ions with different oxidation states exhibit subtly altered absorption edges. This allows precise measurements at a tunable synchrotron beamline, for example at BESSY II[3], to give information about the redox chemistry of these ions. By using this technique, I hope to gain information about the oxidation state of Fe ions at each position of MamP in conditions both relevant to its physiological functioning, and after some chemical and mutational pertubations. I also hope to experimentally demonstrate interactions with cellular electron donors and acceptors made by MamP. This will allow both a clearer picture of the mechanism of action of MamP and of the nucleation and growth of magnetosomes to emerge.

(1) Siponen, M. I. et al. (2013). *Nature 2013 502:7473*, *502*(7473), 681–684.
(2) Lennartz, F. et al (2022). *Acta Crystallographica Section D: Structural Biology*, *78*(2), 238–247.
(3) Gerlach, M. et al. (2016). JLSRF, 2, A47–A47.

PP-006

Crystal structure of 3-Methylguanine

R. Cameli Manzo (Hamburg/DE, Stuttgart/DE), M. Etter (Hamburg/DE)

Recent studies are exploring the DNA-specific selective pairing of nucleobases in the solid-state. In this context, only pairing of methylated nucleobases has been observed upon heating [1]. In order to understand the underlying pairing mechanisms, also knowledge about the crystal structures of the individual methylated bases is required.

In this study we have solved the crystal structure of (anhydrous) 3-Methylguanine and we show a comparison with the already solved crystal structure of 9-Methylguanine. X-ray powder diffraction (XRPD) data for 3-Methylguanine has been collected at a Stoe laboratory diffractometer with a copper radiation source. Indexing, profile and structure analysis were done using the software TOPAS6. For the crystal structure solution, a Monte Carlo/Simulated annealing (SA) search algorithm was used in order to maximize the agreement between the calculated and the measured diffraction data, and a final Rietveld refinement was carried out. Our results show that 3-Methylguanine crystallizes in the monoclinic crystal system, space group *P*21/*c*, and the lattice parameters and unit cell volume after the final Rietveld refinement are: a = 6.64629(9) Å, b = 10.5269(7) Å, c = 12.2610(7) Å, β = 123.358(3) °, V = 716.51(7). The molecules are arranged into layers formed by N-H-N and N-H-O hydrogen bonds and connected by van der Waals interactions along the stacking axis (Figure 1). A comparison with 9-Methylguanine reveals that the position of methyl group determines some differences in its crystal structure motif; the layers bend becoming sinusoidal and the main interaction within layers is made by N-H-N hydrogen bonds (Figure 2).

(1) Stolar, T., Lukin, S., Etter, M.*, Rajić Linarić, M., Uzarevic, K., Meštrović, E., Halasz, I., DNA-specific selectivity in pairing of model nucleobases in the solid state, *Chem. Commun.*, 2020,56, 13524-13527. https://doi.org/10.1039/D0CC03491F

Figure 1: Crystal structure of 3-Methylguanine.

Figure 2: Crystal structure of 9-Methylguanine, after Stolar et al.

Fig. 1

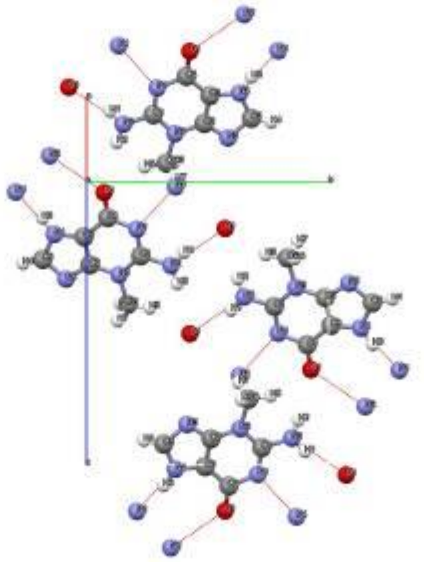

Fig. 2

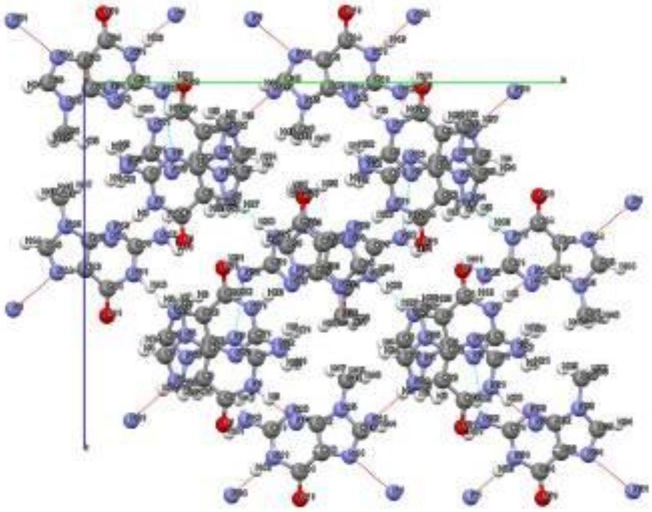

PP-007

High-resolution structure of human nucleoside diphosphate kinase C in complex with different nucleotides

R. Amjadi (Innsbruck/AT), T. Dunzendorfer-Matt (Innsbruck/AT), S. Lomada (Mannheim/DE), T. Wieland (Mannheim/DE), S. Werten (Innsbruck/AT), K. Scheffzek (Innsbruck/AT)

Nucleoside diphosphate kinases (NDPK-C) belong to the NM23 protein family comprises of several members including NDPK-A, -B, and -C. It has been shown that this class I subfamily is particularly enriched at the plasma membrane of patients suffering from end-stage chronic heart failure (HF). In a magnesium-dependent manner, NDPKs catalyze the reversible phosphorylation of nucleoside diphosphates to nucleoside triphosphates.. The enzymes exist as homo- or heteromeric hexamers, the latter are formed with other isoforms. We described a 1.4 resolution structure of human homo-hexameric NDPK-C bound to ADP. We also analyzed the structure of NDPK-C in the presence of GDP, UDP, and cAMP and described the high-resolution structures of the as-yet unidentified complexes. Both of the partial reactions of the NDPK phosphotransferase activity require Mg^{2+} ions. We provided the structural basis by comparing NDPK-C nucleotide complexes in the presence and absence of Mg^{+2} ion. To investigate the nucleotide impact on the NDPK-C conformation, we analyzed a nucleotide-depleted NDPK-C structure and compared it with the nucleotide bound form. The analysis revealed a conformational change upon substrate binding and allowed us to identify flexible regions in the substrate binding site.

Fig. 1

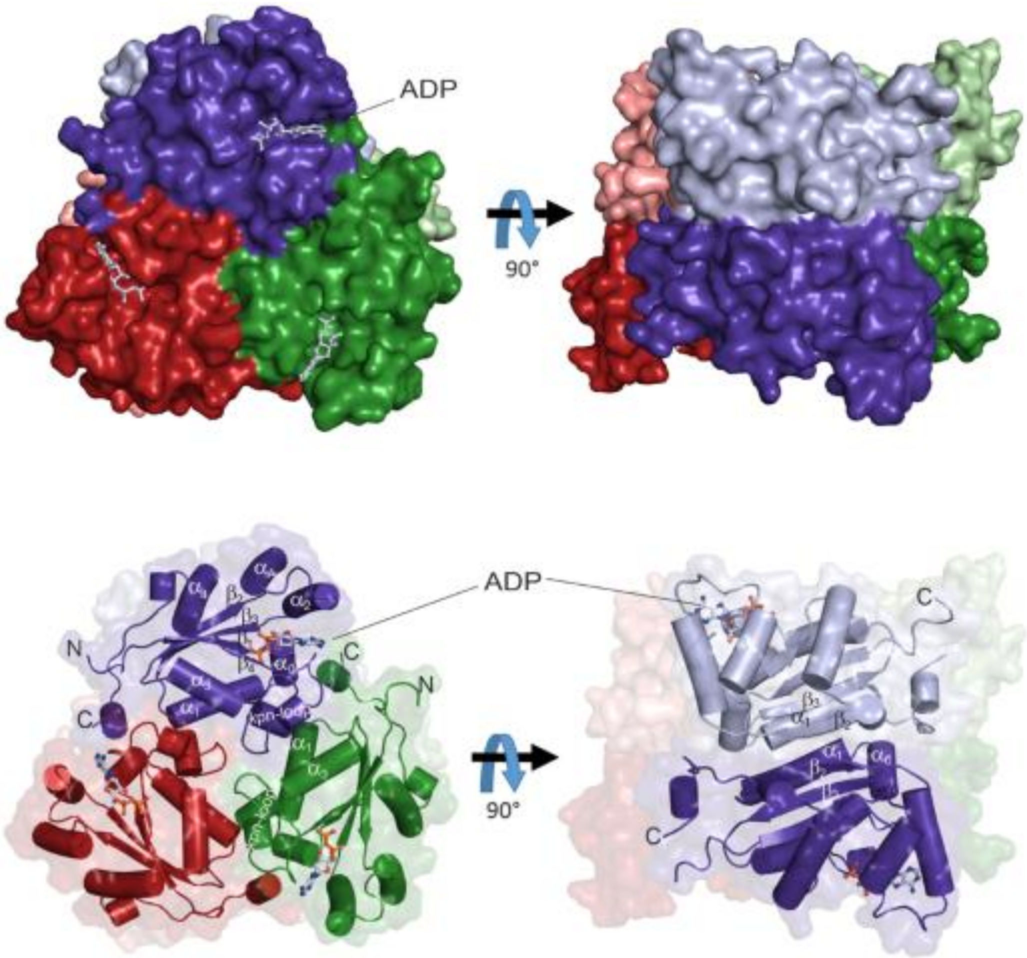

PP-008

Comparative structural analyses of the NHL domains from the human E3 ligase TRIM-NHL family

A. Chaikuad (Frankfurt am Main/DE, Frankfurt am Main/DE), R. Zhubi (Frankfurt am Main/DE, Frankfurt am Main/DE), C. Tredup (Frankfurt am Main/DE, Frankfurt am Main/DE), S. Knapp (Frankfurt am Main/DE, Frankfurt am Main/DE, Frankfurt am Main/DE)

Tripartite motif (TRIM) proteins form one of the largest subfamilies of the RING-type E3 ubiquitin ligases that play a role in diverse processes from homeostasis and immune response to viral restriction1–3. While TRIM proteins typically harbour an N-terminal RING finger, a B-box and a coiled-coil domain, a high degree of diversity lies in their C termini that contain diverse protein interaction modules, most of which, both structures and their roles in intermolecular interactions, remain unknown4,5. Here, crystal structures of the NHL domains of three of the four human TRIM–NHL proteins, namely TRIM2, TRIM3 and TRIM71, are presented. Comparative structural analyses revealed that, despite sharing an evolutionarily conserved six-bladed-propeller architecture, the low sequence identities resulted in distinct properties of these interaction domains at their putative binding sites for macromolecules. Interestingly, residues lining the binding cavities represent a hotspot for genetic mutations linked to several diseases6. Thus, high sequence diversity within the conserved NHL domains might be essential for differentiating binding partners among TRIM–NHL proteins.

(1) Caddy, S. L. *et al.* Viral nucleoprotein antibodies activate TRIM21 and induce T cell immunity. *EMBO J.* **40**, (2021).
(2) Kato, K. *et al.* Structural analysis of RIG-I-like receptors reveals ancient rules of engagement between diverse RNA helicases and TRIM ubiquitin ligases. *Mol. Cell* **81**, 599-613.e8 (2021).
(3) Stremlau, M. *et al.* The cytoplasmic body component TRIM5α restricts HIV-1 infection in Old World monkeys. *Nature* **427**, 848–853 (2004).
(4) D"Amico, F., Mukhopadhyay, R., Ovaa, H. & Mulder, M. P. C. Targeting TRIM Proteins: A Quest towards Drugging an Emerging Protein Class. *ChemBioChem* **22**, 2011–2031 (2021).
(5) Hatakeyama, S. TRIM Family Proteins: Roles in Autophagy, Immunity, and Carcinogenesis. *Trends Biochem. Sci.* **42**, 297–311 (2017).
(6) Hatakeyama, S. TRIM proteins and cancer. *Nat. Rev. Cancer* **11**, 792–804 (2011).

Fig. 1

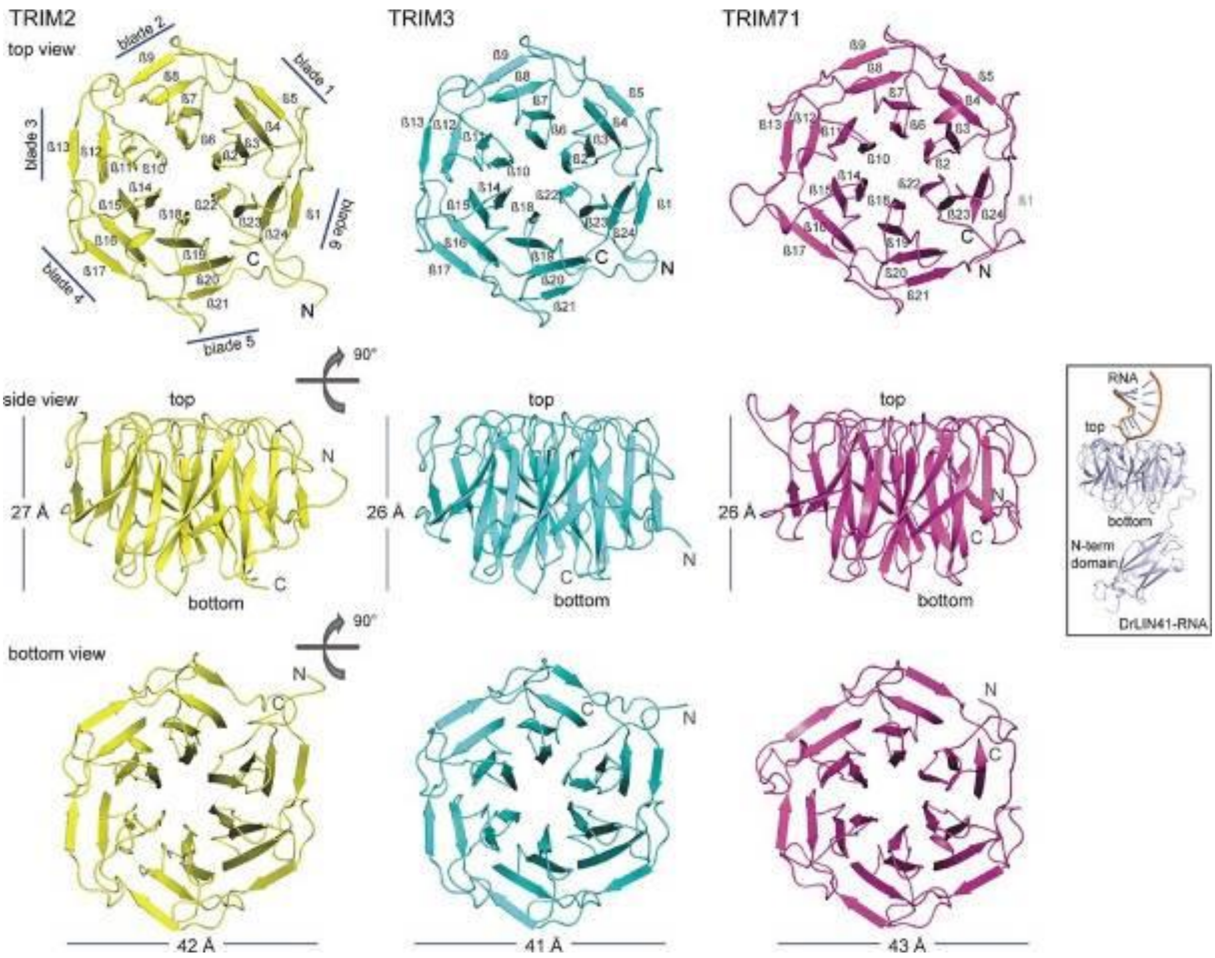

Fig. 2

(a)

Proteins	Mutations	Diseases	References
TRIM2	D640A	CMT; BVCP	Pehlivan et al., 2015
	K567Rfs7X (ter)	axonal neuropathy	Ylikallio et al., 2013
	R741X (ter)	CMT	Magri et al., 2020; Diepen et al., 2005
	N594del	CMT	Magri et al., 2020; Diepen et al., 2005
TRIM71	R608H	congenital hydrocephalus	Welte et al., 2019; Furey et al., 2018
	R751A	congenital hydrocephalus	Welte et al., 2019; Furey et al., 2018
	R796H	congenital hydrocephalus	Welte et al., 2019; Furey et al., 2018

Proteins	Mutations	Diseases	References
TRIM32	D487N	LGMD2H; STM	Schoser et al., 2005; Frosk et al., 2002; Frosk et al., 2005; Kudryashova et al., 2011
	P374L	LGMD2H	Yu et al., 2017
	R394H	LGMD2H	Saccone et al., 2008
	D588del	LGMD2H	Saccone et al., 2008
	T520TfsX13 (ter)	LGMD2H	Saccone et al., 2008
	S594N	STM	Panicucci et al., 2019
	R613X (ter)	LGMD2H	Neri et al., 2013

(b)

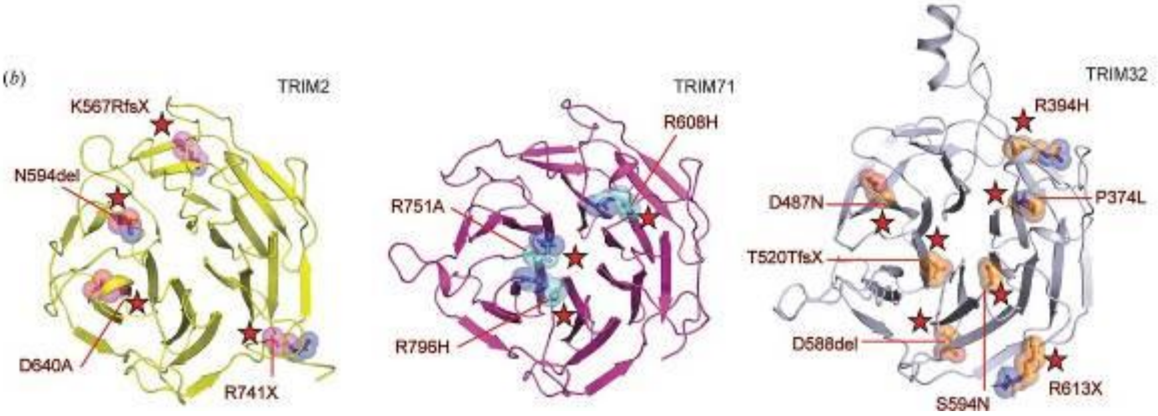

PP-009

Structural characterization of the pyruvate dehydrogenase complex E1 decarboxylation reaction

A. Mehr (Göttingen/DE)

The pyruvate dehydrogenase complex (PDHc) serves a universally important metabolic function in most organisms connecting glycolysis and the citric acid cycle. PDHc converts pyruvate into the vital cellular cofactor acetyl-CoA. *Bacillus subtilis* PDHc is a large protein assembly, 10 MDa in size, consisting of multiple copies of E1, E2, and E3 subunits. The E1 is a thiamine diphosphate (TPP)- dependent enzyme which catalyzes the decarboxylation of pyruvate as a first step. While TPP-dependent decarboxylation mechanisms have been studied in other enzymes, intermediates of the E1 reaction at high resolution and dynamic aspects of TPP-dependent enzyme function remain elusive. To gain comprehensive insights into E1 TPP-dependent decarboxylation of pyruvate, we have used a combination of cryo-trapping and room temperature serial X-ray crystallography to visualize reaction intermediates at high resolution.

PP-010

Structural and functional studies of legumain-mycocypin complexes

T. Elamin (Salzburg/AT), N. Santos (Salzburg/AT), P. Briza (Salzburg/AT), H. Brandstetter (Salzburg/AT), E. Dall (Salzburg/AT)

Under pathophysiologic conditions such as Alzheimer"s disease and cancer, the endo-lysosomal cysteine protease legumain was found to translocate to the cytosol, the nucleus, and the extracellular space. These non-canonical localizations demand for a tight regulation of legumain activity, which is in part conferred by protein inhibitors. While there is a significant body of knowledge on the interaction of human legumain with endogenous cystatins, only little is known on its regulation by fungal mycocypins. Mycocypins are characterized by (i) versatile, plastic surface loops allowing them to inhibit different classes of enzymes and (ii) a high resistance towards extremes of pH and temperature. These properties make mycocypins attractive starting points for biotechnological and medical applications. In this study we show that mycocypins utilize an adaptable reactive center loop to target the active site of legumain in a substrate-like manner. We determined the interaction was further stabilized by variable, isoform-specific exosites, converting the substrate recognition into inhibition. Additionally, we found that selected mycocypins were capable of covalent complex formation with legumain by forming a disulfide bond to the active site cysteine. Furthermore, our inhibition studies with other clan CD proteases suggested that mycocypins may serve as broad-spectrum inhibitors of clan CD proteases. Our studies uncovered the potential of mycocypins as a new scaffold for drug development, providing the basis for the design of specific legumain inhibitors.

PP-011

SARS-CoV-2 Methyltransferase ligand screening and peptide inhibitors

V. Kremling (Hamburg/DE), J. Sprenger (Hamburg/DE), D. Oberthür (Hamburg/DE), H. Chapman (Hamburg/DE), O. Yefanov (Hamburg/DE), M. Galchenkova (Hamburg/DE), P. Middendorf (Hamburg/DE), B. Klopprogge (Hamburg/DE), A. Kiene (Hamburg/DE), J. Carnis (Hamburg/DE), I. de Gennaro Aquino (Hamburg/DE), S. Falke (Hamburg/DE), C. Ehrt (Hamburg/DE), Y. Fernandez Garcia (Hamburg/DE)

Non-structural protein 10 (nsp10) and nsp16 are part of the RNA synthesis complex which is crucial for viral replication in SARS-CoV-2. Nsp16 exhibits methyltransferase activity needed for mRNA capping and is active in heterodimeric complexes with the enzymatic inert nsp10. It has been shown that inactivation of this protein complex interferes severely with viral replication, making it a promising drug target against COVID-19. As only limited information on ligands binding to nsp10-nsp16 is available, we use X-ray crystallography to test small compound libraries (~ 200 compounds) containing potential methyltransferase-binders that were soaked into protein crystals prior to diffraction. We obtained ~30 data sets of the nsp10-16 complex with purine derivatives bound to the substrate binding sites. Promising compounds are being tested in binding and activity assays. In parallel, we are testing small peptides by small-angle-X-ray scattering (SAXS) and virus inhibition assays that potentially disrupt the complex formation with nsp10. Our results can be used for structure-based drug design to fight COVID-19 and may contain potent inhibitors of SARS-CoV-2 methyltransferases.

PP-012

Experimental steps on the way to biotec nacre

D. Blohm (Bremen/DE)

Nacre, mother of pearl, is a bio-ceramic composite with excellent material characteristics (1), but using it is extremely limited as it is available only from animals like mussels, snails and others. Its beneficial properties are based on crystal layers of aragonite in the form of tablets, 0,5 µm thin and about 15 µm in size, glued together by a matrix composed of chitin and proteins.

The biogenesis of native nacre is still an enigma, but nacre-like material can be produced chemically (2). Learning how nacre can be made biotechnically would make this material available for medical and technical applications and can probably help to understand an important step in biological evolution.

The CO2 and NH3 diffusion method was modified to be able to observe and to quantify the crystallization process. Micro-Raman-Spectroscopy was used to determine the crystal polymorphs, nanoparticles were characterized by dynamic light scattering and the surfaces of chitosan films were examined using white light interferometry.

Pure aragonite can be produced under bio-compatible conditions either by using chitosan films as nucleation surface or by inducing aragonite aggregates to release myriads of polymorph-stabile nanoparticles. These nanoparticles, when seeded on chitosan surfaces, grow as thin film crystals like aragonite tablets in nacre. Acetate treated chitosan surfaces form bursting bubbles, in which nanoparticles grow up and seemingly start the formation of growth cones.

The experimental results suggest that nacre-like structures can be obtained under biological conditions in two steps: Producing aragonite nanoparticles and seeding them on aragonite film surfaces in repeated cycles. Whether this layer by layer principle corresponds to any step in the biogenesis of nacre in organisms is not known.

Literature

1. Nudelmann, F., Sem. Cell & Develop. Biol. 46 (2015), 2-10
2. Gao, H.L. et al., Nature Communications 8 (2017): 287

PP-013

The macromolecular neutron single crystal diffractometer BIODIFF for proteins at the Heinz Maier-Leibnitz Zentrum MLZ

A. Ostermann (Garching/DE), T. E. Schrader (Garching/DE)

Neutron single crystal diffraction provides an experimental method for the direct location of hydrogen and deuterium atoms in biological macromolecules. At the FRM II neutron source the neutron single crystal diffractometer BIODIFF, a joint project of the Forschungszentrum Jülich and the FRM II, is mainly dedicated to the structure determination of enzymes. Typical scientific questions address the determination of protonation states of amino acid side chains in the active center, the orientation of individual water molecules essential for the catalytic mechanism and the characterization of the hydrogen bonding network between the enzyme active center and an inhibitor or substrate. This knowledge is often crucial towards understanding the specific function and behavior of an enzyme. BIODIFF is designed as a monochromatic diffractometer and is able to operate in the wavelength range of 2.4 Å to about 5.6 Å. This allows to adapt the wavelength to the size of the unit cell of the sample crystal. Data collection at cryogenic temperatures is possible, allowing studies of cryo-trapped enzymatic intermediates. Recently a hexapod has been installed at BIODIFF which allows an easy online collimator alignment. Some recent examples will be presented to illustrate the potential of neutron macromolecular crystallography. In addition, a potential detector upgrade for BIODIFF will be presented, which will expand the maximum unit cell limits.

PP-014

Scientific techniques for the identification of mineral pigments of North Russian icons

S. Ivashevskaya (Petrozavodsk/RU), I. Nabokova (Petrozavodsk/RU)

The pigments of Abramov's icon-painting workshop from the funds of the Kizhi Museum have been studied. Natural-scientific approaches to art objects expand the possibilities of studying the traditional technique of folk icon painting and attributing museum collections.

X-ray fluorescence (XRF) provides elemental composition information. Whereas X-ray diffraction (XRD) techniques offer information about the arrangement of atoms in a given sample. For example, rutile and anatase are chemically the same (TiO_2), but atoms are arranged differently. It is impossible to distinguish them using elemental analysis. Sometimes such information can be important for dating and authenticating a work of art, as well as for studying the origin of historical materials. The Rietveld method was applied for an approximate quantification of components. The main problem of powder XRD is peak overlapping. Too many components whose spectra overlap can give a picture similar to our patterns. Raman spectroscopy (RS) and XRF can be a kind of filters for separating unsuitable variants. Moreover, the combination of RS and XRF data allows finding individual trace components which are not visible on the X-ray patterns.

Moreover, RS has revealed additional information about our samples. It is known from the literature [1] that icon painters added black paint to the pigments to make the shade darker and more intense. Black could be of two types - lamp and bone. The Raman spectra of four pigments showed peaks corresponding to the D (1580 cm^{-1}) and G (1325 cm^{-1}) carbon lines. If it were a black bone, another line should have been present in the Raman spectrum (961 cm^{-1}). In this way, the use of lamp black was identified.

The rapidly developing technical art history combines scientific analytical applications and traditional stylistic analysis.

(1) A.I. Kosolapov Natural Science Methods in the Examination of Works of Art//St. Petersburg: State Hermitage; Edition 2 (2015), ISBN: 978-5-93572-636-2

Fig. 1

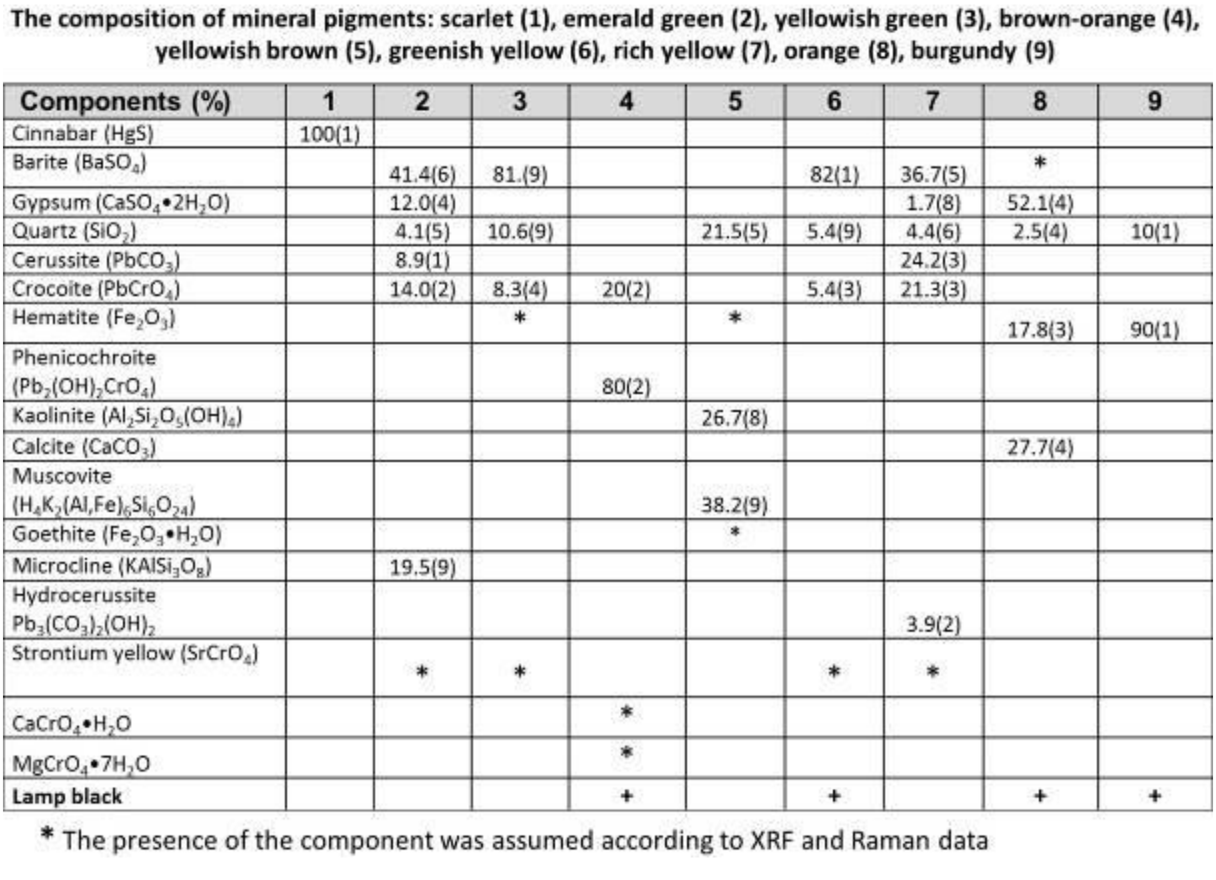

The composition of mineral pigments: scarlet (1), emerald green (2), yellowish green (3), brown-orange (4), yellowish brown (5), greenish yellow (6), rich yellow (7), orange (8), burgundy (9)

Components (%)	1	2	3	4	5	6	7	8	9
Cinnabar (HgS)	100(1)								
Barite ($BaSO_4$)		41.4(6)	81.(9)			82(1)	36.7(5)	*	
Gypsum ($CaSO_4 \bullet 2H_2O$)		12.0(4)					1.7(8)	52.1(4)	
Quartz (SiO_2)		4.1(5)	10.6(9)		21.5(5)	5.4(9)	4.4(6)	2.5(4)	10(1)
Cerussite ($PbCO_3$)		8.9(1)					24.2(3)		
Crocoite ($PbCrO_4$)		14.0(2)	8.3(4)	20(2)		5.4(3)	21.3(3)		
Hematite (Fe_2O_3)			*		*			17.8(3)	90(1)
Phenicochroite ($Pb_2(OH)_2CrO_4$)				80(2)					
Kaolinite ($Al_2Si_2O_5(OH)_4$)					26.7(8)				
Calcite ($CaCO_3$)								27.7(4)	
Muscovite ($H_4K_2(Al,Fe)_6Si_6O_{24}$)					38.2(9)				
Goethite ($Fe_2O_3 \bullet H_2O$)					*				
Microcline ($KAlSi_3O_8$)		19.5(9)							
Hydrocerussite $Pb_3(CO_3)_2(OH)_2$							3.9(2)		
Strontium yellow ($SrCrO_4$)		*	*			*	*		
$CaCrO_4 \bullet H_2O$				*					
$MgCrO_4 \bullet 7H_2O$				*					
Lamp black				+		+		+	+

* The presence of the component was assumed according to XRF and Raman data

PP-015

XRD and DFT studies of new ionic lead compounds Pb[*Ch*CN]$_2$ (*Ch* = O, Se)

A. Shlyaykher (Marburg/DE), A. L. Barba (Marburg/DE), A. Zivkovic (Utrecht/NL), F. Tambornino (Marburg/DE)

The synthesis of the well-known compound lead thiocyanate, Pb[SCN]$_2$, by the action of potassium thiocyanate on lead acetate was described by Liebig about 200 years ago.[1] However, later it was revealed that instead of Pb[SCN]$_2$ they had synthesized Pb[SCN][OH][1], and its crystal structure was subsequently determined by Adovasio and Nardelli.[2] Pure Pb[SCN]$_2$ in contrast is obtained using acid during synthesis, its crystal structure was determined by Mokuolu and Speakman in 1975.[3]

In our studies, we report on syntheses of Pb[*Ch*CN]$_2$ (*Ch* = O, Se)[4] and on their hitherto unknown crystal structures. Pb[OCN]$_2$ and Pb[SeCN]$_2$ crystallize in space group *Pnma* (Pb[OCN]$_2$: a=8.569(2), b=3.9410(9), c=11.659(3) Å; Pb[SeCN]$_2$: a=12.499(2), b=4.2229(7), c=10.6532(14) Å). Surprisingly, both compounds are neither isotypical with their sulfur analogue Pb[SCN]$_2$ (*C*2/*c*, a=9.661, b=6.554, c=8.253 Å, β=92.37°) nor with one another.[3] Quantum chemical calculations allowed to verify determined structures and interpret the recorded solid-state Raman spectra.

(1) D. R. Hall, *J. Am. Chem. Soc.* **1902**, *24*, 570–573.
(2) V. Adovasio, M. Nardelli, *Acta Crystallogr. C* **1995**, *51*, 380–382.
(3) J. A. A. Mokuolu, J. C. Speakman, *Acta Crystallogr. B* **1975**, *31*, 172–176.
(4) H. E. Williams, *Cyanogen Compounds Their Chemistry, Detection and Estimation*, Edward Arnold & Co., London, **1948**.

PP-016

Ba(BO2OH) — A monoprotonated monoborate from hydroflux showing intense second harmonic generation

Y. Li (Dresden/DE), P. A. Hegarty (Dresden/DE), M. Rüsing (Dresden/DE), L. M. Eng (Dresden/DE), M. Ruck (Dresden/DE)

The significance of borates especially in optical applications has been emphasized in many papers and reviews.[1] In most cases, borates are obtained either by high-temperature processes or under hydrothermal conditions for a long reaction time. The hydroflux method [2], which we employed here, is based on a highly concentrated mixture of alkali metal hydroxide and water as reaction medium. Hydroflux syntheses proceed within a few hours and require only a PTFE-lined autoclave that is inert to the alkaline medium and ensures that no water is lost during the reaction. We obtained pure samples of colorless, air-stable Ba(BO2OH) crystals from Ba(NO3)2 and H3BO3 under the ultra-alkaline conditions of a KOH hydroflux at about 250 °C.[3] Product formation depends on the molar water-base ratio *q*(K) = *n*(H2O) : *n*(KOH) = 1.85 and the molar ratio of the starting materials *q*(B) = *n*(H3BO3) : *n*(Ba(NO3)2) = 7. H3BO3 acts as a proton donor (Brønsted acid) rather than a hydroxide acceptor (Lewis acid). Ba(BO2OH) crystallizes in the non-centrosymmetric orthorhombic space group *P*212121. Hydrogen bonds connect the almost planar (BO2OH)2– anions, which are isostructural to HCO3–, into a syndiotactic chain (Figure 1). Upon heating in air to about 450 °C, Ba(BO2OH) dehydrates to Ba2B2O5. Moreover, the non-centrosymmetric structure of Ba(BO2OH) crystals was verified with power-dependent confocal Second Harmonic Generation (SHG) microscopy indicating large conversion efficiencies in ambient atmosphere (Figure 2). Thus, it was demonstrated for the first time that hydroflux is also suitable as an efficient synthetic route for borates. We believe that the hydroflux approach has great potential for the synthesis of (new) functional materials.

Figure 1: Second harmonic images of a selection of Ba(BO2OH) crystallites examined at a fundamental wavelength of 900 nm and an average fundamental power of 130 mW in (a) cross-polarization and (b) parallel polarization of pump and detected light, respectively. Parallel polarization reveals a slightly enhanced response for some selected crystallites, however, due to their unknown orientation within the powder, it is difficult to infer the participating tensor elements. (c) Power dependent response at 900 nm fundamental wavelength recorded in parallel polarization for the two Ba(BO2OH) crystallites marked in (b). Both show the expected quadratic behavior, though with a slightly different strength. (d) Coordination of the barium cation in Ba(BO2OH), (e) Crystal structure of Ba(BO2OH) with pseudo mirror planes perpendicular to the *a*-axis. Ellipsoids shown for the non-hydrogen atoms comprise 90 % of the probability density.

(1) M. Mutailipu, K. R. Poeppelmeier, S. Pan, *Chem. Rev.* **2021**, *121*, 1130–1202.
(2) W. M. Chance, D. E. Bugaris, A. S. Sefat, H.-C. zur Loye, *Inorg. Chem.* **2013**, *52*, 11723–11733.
(3) Y. Li, P. A. Hegarty, M. Rüsing, L. M. Eng, M. Ruck, *Z. Anorg. Allg. Chem*. **2022**, *648*, e202200193.

Fig. 1

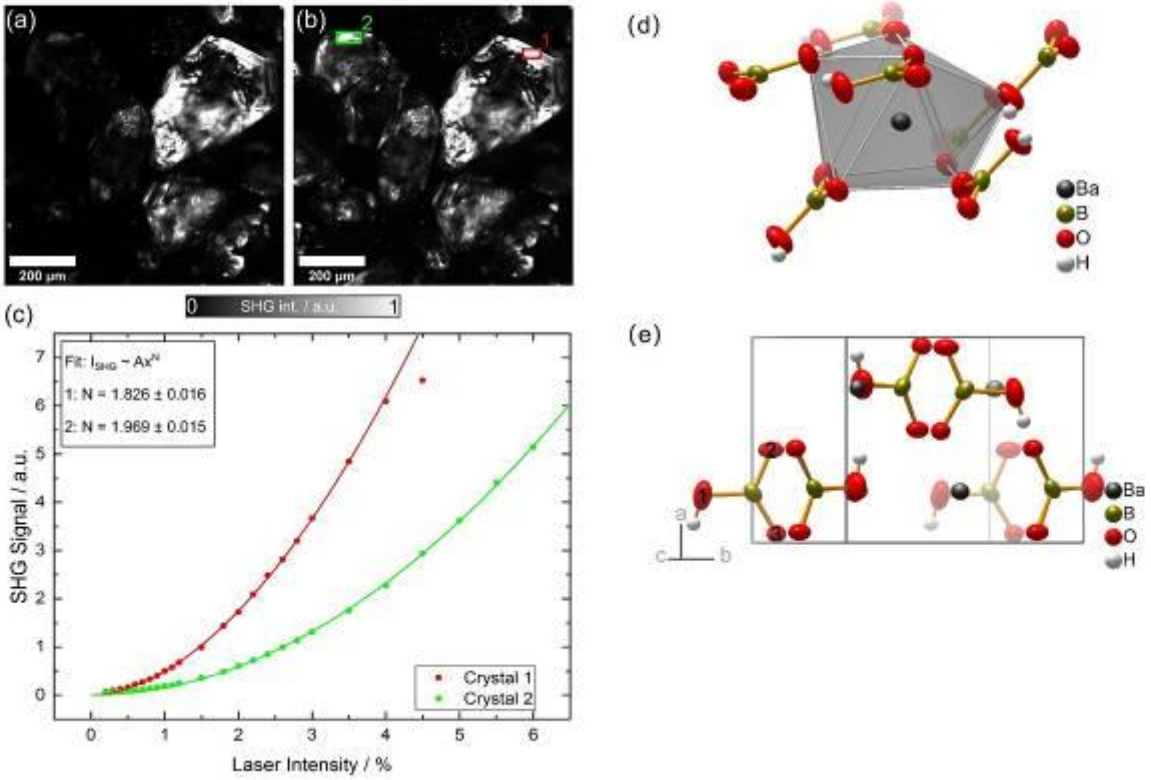
(a)
(b)
2
1
200 µm
200 µm
0
SHG int. / a.u.
1
(c)
Fit: $I_{SHG} \sim Ax^N$
1: N = 1.826 ± 0.016
2: N = 1.969 ± 0.015
SHG Signal / a.u.
Laser Intensity / %
0
1
2
3
4
5
6
7
Crystal 1
Crystal 2
(d)
Ba
B
O
H
(e)
1
2
3
a
c
b
Ba
B
O
H

PP-017

Crystal structures of carbonyl (pseudo)halides

J. Pfeiffer (Marburg/DE), C. Trost (Marburg/DE), F. Tambornino (Marburg/DE)

Scientific research on small molecules is a current topic in chemical research. Understanding their crystal structures is an important stepping stone towards understanding basic principles. Especially interesting are small molecules comprising solely highly reactive functional groups, e.g. carbonyl pseudohalides. Until today only four congeners are reported: $CO(N_3)_2$[1], $CO(NCO)_2$[2], $CO(NCS)_2$[3] and $CO(CN)_2$[4]. Only the former two were crystallographic analysed.[5,6]

In this project we aim to broaden the variety of carbonyl pseudohalides and related compounds for X-ray diffraction analyses. Difficult syntheses as well as air, moisture and temperature sensitive, and at times liquid products, make this a challenging topic. We were able to determine the molecular structures of $CO(NCS)_2$ and $(CONCS)_2$.[7] $CO(NCS)_2$ crystallizes in space group $P2_1/c$ (a = 20.5118(13) Å, b = 3.84410(10) Å, c = 15.9661(11) Å, β = 112.464(5)°) and $(CONCS)_2$ in $Pbca$ (a = 5.4245(2) Å, b = 20.2875(12) Å, c = 6.1642(4) Å). In further studies we were able to synthesize and characterize $CS(SCN)_2$, which crystallizes in space group $P2_1/n$ (a = 5.9384(2) Å, b = 5.7917(2) Å, c = 17.6562(6) Å, β = 97.103(3)°).

In addition, we are interested in the crystal structures of their reaction products with nucleophiles. All of them show extended hydrogen bonding networks in the molecular structure. These molecules could be model compounds for understanding natural interactions.

(1) T. Curtius, K. Heidenreich, *Ber. Dtsch. Chem. Ges.* **1894**, *27*, 2684–2685.
(2) E. Nachbaur, *Monatsh. Chem.* **1966**, *97*, 361–367.
(3) A. E. Dixon, *Proc. Chem. Soc.* **1902**, *18*, 240.
(4) R. Malachowski, L. Jurkiewicz, J. Wojtowicz, *Ber. Dtsch. Chem. Ges.* **1937**, *70*, 1012–1016.
(5) T. M. Klapötke, B. Krumm, S. Rest, R. Scharf, J. Schwabedissen, H.-G. Stammler, N. W. Mitzel, *J. Phys. Chem. A* **2016**, *120*, 4534–4541.
(6) X. Zeng, M. Gerken, H. Beckers, H. Willner, *Inorg. Chem.* **2010**, *49*, 9694–9699.
(7) J. Pfeiffer, C. Trost, A. Pachkovska, F. Tambornino, *Inorg. Chem.* **2021**, *60*, 10722–10728.

PP-018

Crystal structure of $GdSrCa_3O[BO_3]_3$ and $GdSr_2Ca_2O[BO_3]_3$

T. Weigel (Freiberg/DE), E. Mehner (Freiberg/DE), H. Stöcker (Freiberg/DE), D. C. Meyer (Freiberg/DE), J. Götze (Freiberg/DE), J. Hanzig (Freiberg/DE, Freiberg/DE)

The structure family of the rare earth calcium oxoborates $RX_2Z_2O[BO_3]_3$ (RCOB) has been investigated in recent years, mainly with regard to their optical characteristics. Due to their monoclinic-domatic structure (space group *Cm*), they also exhibit pyro- and piezoelectric properties up to the melting point. The structure is stable against the numerous possible substitutions of the rare earth cation site *R*, but all rare-earth cations *R* are known to show partial disorder with the earth alkaline cation positions *X* and *Z*. To study whether a completely ordered stabilization of the cation occupation is possible, the calcium oxoborates were chemically modified using Ca substitution by Sr, Na, Y, Gd on the *X* and *Z* positions. No oxoborate phases could be synthesized by coupled substitution of Ca with Sr, Na, and a rare earth element. Only the single substitution with Sr turned out to be feasible. We found that up to 50 at.-% Sr can be incorporated into the structure, essentially replacing Ca on the *X* position. Samples of $Gd(Ca_{4-x}Sr_x)O[BO_3]_3$ with x = 1, 2 have been recrystallized and selected for single crystal X-ray diffraction. The resulting refinement of the structure and the cation disorder will be presented in this work.

PP-019

Two Hg-rich rubidium Ga/In-mercurides with new structure types: $Rb(Hg_{1-x}Ga_x)_7$ and $Rb_7(Hg_{1-x}In_x)_{23}$ (x=0.1 each)

C. Röhr (Freiburg im Breisgau/DE), M. Wendorff (Freiburg im Breisgau/DE)

Our recent reinvestigation of the Hg-rich parts of the binary phase diagrams K-Hg [1-3] and Rb-Hg [2,4] yielded a series of new alkali mercurides like KHg_4, KHg_5 and KHg_8 (in addition to KHg_6 [5] and KHg_{11} [6]) in the potassium and Rb_7Hg_{36} (in addition to Rb_3Hg_{20} [7]) in the rubidium system. These new binary mercurides all form new singular and mostly very complex structure types. The variation of the valence electron concentration (v.e.c.) by substituting small amount of mercury by equally sized indium with an increased number of v.e. shows a distinct phase width of KHg_4 (up to 25 % In [8]), KHg_5 (up to 10 % In) and Rb_3Hg_{20} (up to 10.3 % In [4]). In addition, the ternary samples prepared in this context yielded the new Hg-rich title compounds $Rb(Hg_{1-x}Ga_x)_7$ and $Rb_7(Hg_{1-x}In_x)_{23}$, both stabilizied by 10 % of the triel elements Ga and In respectively.

The Ga-containing phase $Rb(Hg_{1-x}Ga_x)_7$ ($RbHg_{6.3}Ga_{0.7}$) forms a surprisingly simple, nevertheless new, highly symmetric hexagonal structure [space group $P6_3/mmc$, $hP8$, a=698.0(2), c=999.5(2) pm, $R1$=0.0605], which contains only one rubidium, one pure mercury and one mixed M (Hg:Ga=68:32 %) crystallographic site. The mercury polyanion consists of trigonal prisms (Fig. 1: green polyhedra) formed by Hg only, which are arranged in hexagonal layers of stacking sequence |:AB:| along [001]. These $[Hg_6]$ prisms are connected via corners with empty $[Hg_6M_2]$ cubes (Fig. 1: blue), which among themselves share M vertices to form chains running along the hexagonal c axis. Therewith, the cubes are localized within the octahedral voids of the prism's hexagonal close packing (hcp) and a NiAs-type arrangement of the Hg/Ga polyhedra is formed overall. The trigonal bipyramids (two face sharing tetrahedra) within the hcp of $[Hg_6]$ prisms are occupied by the Rb cations, which are therewith centering large $[RbM_{21}]$ cation coordination polyhedra (ccp; Fig. 1: orange polyhedra). These Rb ccps, the cubes and the trigonal prisms tile the space.

In contrast to this simple structure, the second, In-containing title compound $Rb_7(Hg_{1-x}In_x)_{23}$ ($Rb_7Hg_{20.6}In_{2.4}$) features a quite complex new monoclinic structure [space group $P2_1/c$, $mP120$, a=1244.0(2), b=2319.6(3), c=1239.1(2) pm, β=105.465(2)°, $R1$=0.0403], which contains seven Rb and 23 Hg/M crystallographically different positions. The atoms of the four mixed sites $M(20)$ to $M(23)$ (with 56 to 66 % In) form only slightly distorted cubes (Fig. 2: blue). All faces of these cubes are shared with the square faces of trigonal prisms, which are formed by overall six pure Hg sites in addition (green polyhedra). The resulting $[M_{20}]$ clusters with 'internal' cubes exhibit inversion symmetry and are located at the unit cell origin. Seven further Hg atom types form defect tetrahedra stars (TS) with one missing tip (red clusters $[M_7]$, formed by four $[Hg_4]$ tetrahedra, cf. Fig. 2). The six remaining Hg sites show a slightly reduced Hg-Hg connectivity (CN=5-6) and form the triangluar faces of the Rb ccps only (yellow planes in Fig. 2). The $[M_{20}]$ clusters and $[M_7]$ TS are connected by Hg-Hg bonds and via those additional Hg atoms. The Rb ccp are almost all formed by 15 Hg neighbours [only Rb(5) exhibits a decreased CN of 12]. Two to three further Rb cations are located above the six-membered rings of these ccp. Only Rb(5) shows an ideal Frank-Kasper FK16 polyhedron (12 Hg + 4 Rb). Again, the Rb ccps, the cubes with fused prisms $[M_{20}]$ and the defect $[M_7]$ TS tile the space.

The crystal structures of the two title compounds are compared with other Hg-rich alkali and alkaline-earth mercurides [9,10]. The electronic structure is discussed based on the results of APW+lo DFT band structure calculations and is similarly compared with the bonding situtation in related polar intermetallics.

References:

(1) T. Hohl, C. Hoch, M. Wendorff, C. Röhr, *Acta Cryst. Suppl.* **A78** (2022).
(2) M. Wendorff, C. Röhr, *Z. Kristallogr. Suppl.*, **41**, 79-80 (2021).
(3) T. Hohl, C. Hoch, M. Wendorff, C. Röhr, *Inorg. Chem.* (in preparation).
(4) M. Wendorff, C. Röhr, *Z. Naturforsch.* (in preparation).
(5) Tambornino, C. Hoch, *J. Alloys Compd.* **618**, 299-304 (2015).
(6) E. Biehl, H. J. Deiseroth, *Z. Anorg. Allg. Chem.* **625**, 1073-1080 (1999).
(7) E. Todorov, S. C. Sevov, *J. Solid State Chem.* **149**, 419-427 (2000).
(8) M. Wendorff, C. Röhr, *Z. Kristallogr. Suppl.*, **38**, 86 (2018).
(9) H. J. Deiseroth, Discrete and Extended Metal Clusters in alloys with mercury and other group 12 elements, in Molecular Clusters of the Main Group Elements, Wiley-VCH, Weinheim, Chapter 2.4. 169-187 (2005).
(10) M. Wendorff, C. Röhr, *Z. Kristallogr.* **233**, 515-529 (2018).

Figure 1: Unit cell of the hexagonal crystal structure of $RbHg_{6.3}Ga_{0.7}$ (red/blue/yellow balls: Hg/*M*/Rb). **Figure 2:** Small cutout (*y*= -0.1 to 0.2) of the complex monoclinic crystal structure of $Rb_7Hg_{20.6}In_{2.4}$ (red/blue/yellow balls: Hg/*M*/Rb).

Fig. 1

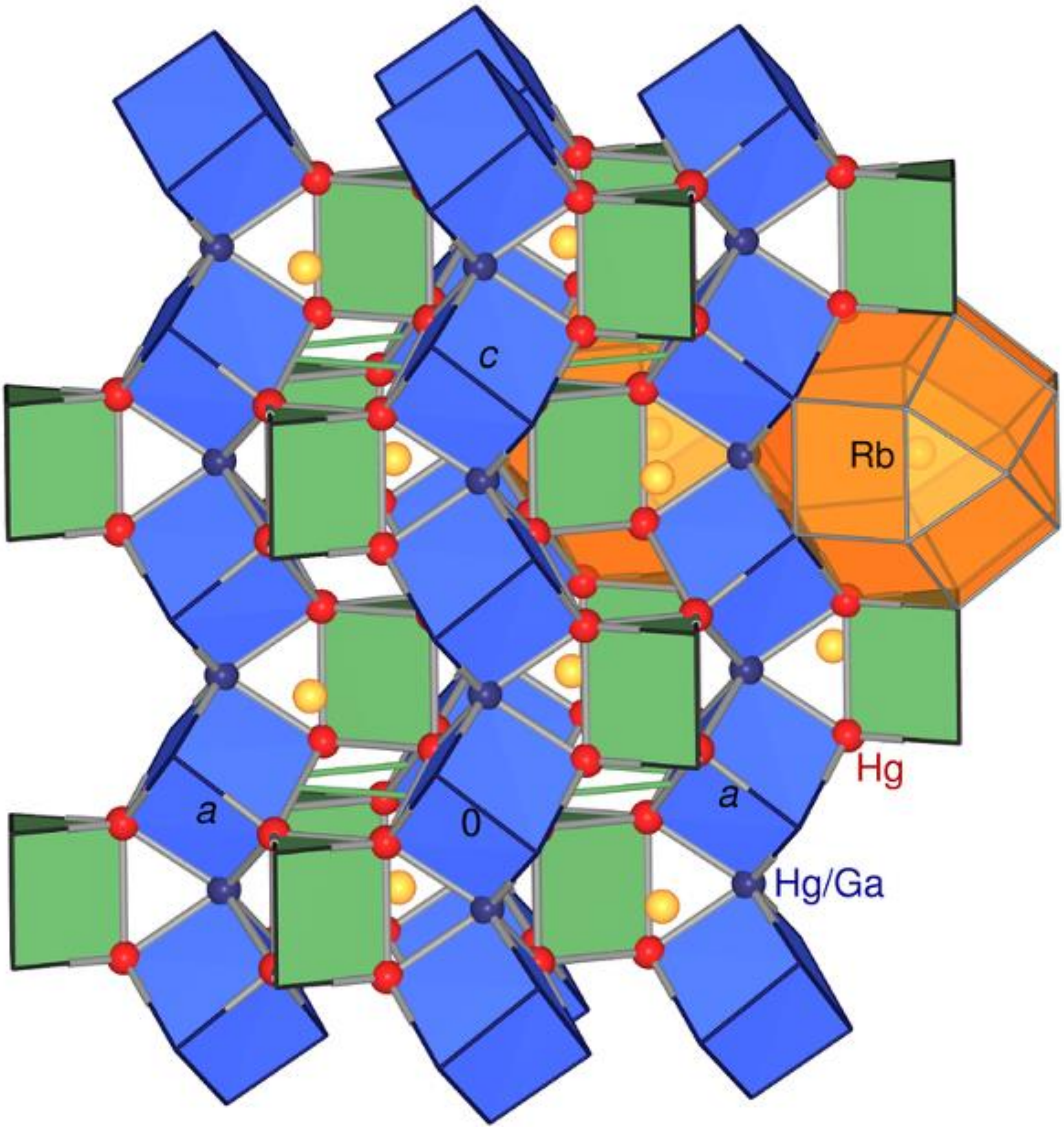

Fig. 2

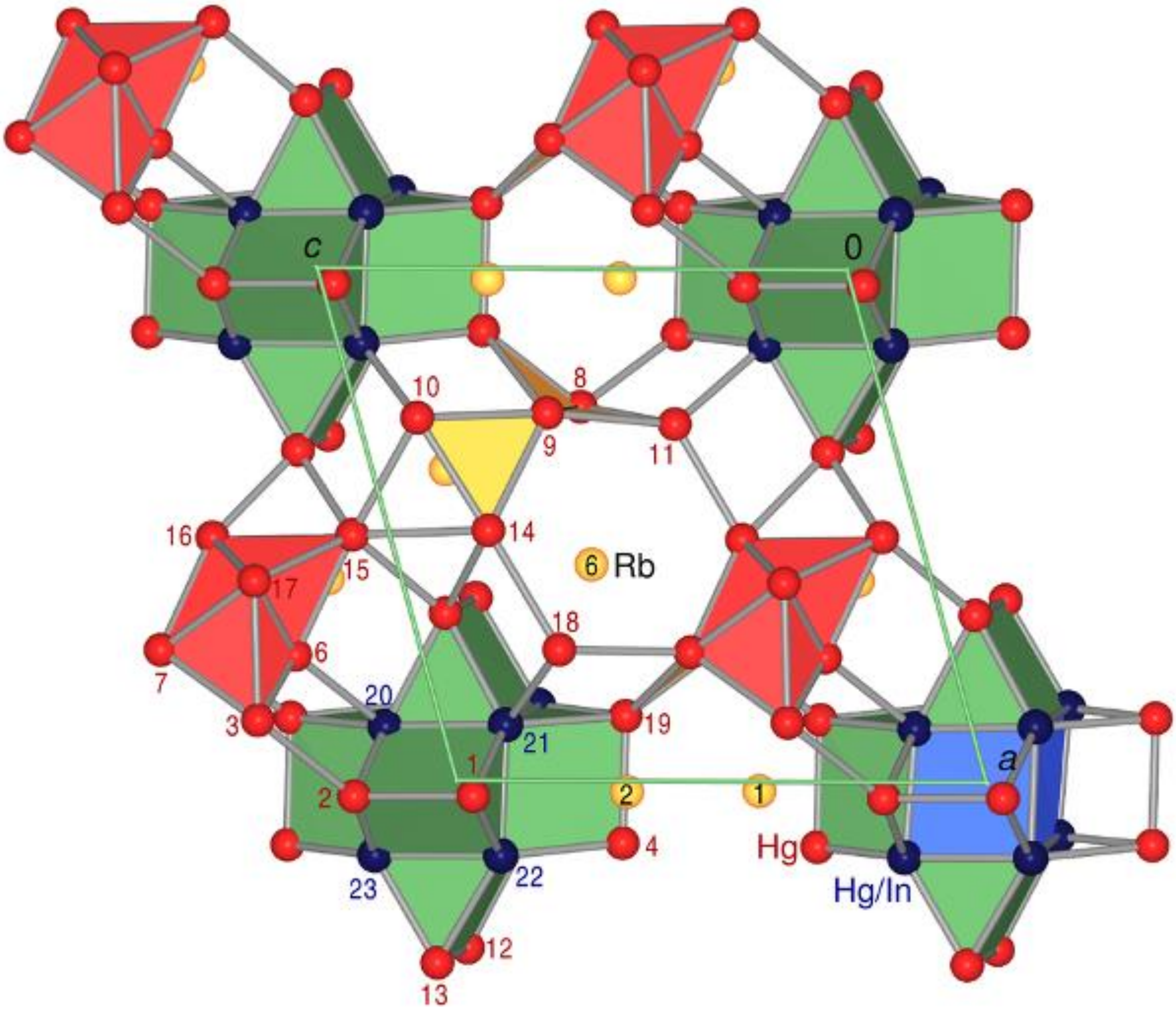
c
0
10
8
9
11
14
6
Rb
16
15
17
7
6
18
3
20
19
21
1
2
2
1
a
4
Hg
Hg/In
23
22
12
13

PP-020

Investigating the Role of the Different Alkali Metals in the Structure Type $K_{14}Cd_9Tl_{21}$

M. Janesch (Regensburg/DE), S. Gärtner (Regensburg/DE, Regensburg/DE)

Corbett et al. discovered a lot of different alkali metal thallides with interesting Tl substructures e.g. the phase $A_{15}Tl_{27}$ (A=Rb, Cs), which crystalizes in the hexagonal space group P-62m.[1] It combines isolated $[Tl_{11}]^{7-}$ clusters, that can be described by the *Wade-Mingos* rules, and two-dimensional $[Tl_{16}]^{8-}$ layers, which do not follow these counting rules. Further studies on this phase yielded the compound $Cs_{14.52}Tl_{28.4}$, where the Cs atom on Wyckoff position 1*b* is partially substituted by a triangle of Tl atoms on Wyckoff position 3*g*.[2] This leads to a partial formal oxidation of the two-dimensional layer from $[Tl_{16}]^{8-}$ to $[Tl_{19}]^{7-}$.

A related structural motif was reported for $K_{14}Cd_9Tl_{21}$ by *Tillard-Charbonnel et al*.[3] where a Cd triangle on Wyckoff position 3*g* is present. We examined this structure type regarding the role of the different alkali metals. Therefore, ternary and quaternary compounds of this structure type were prepared (e.g. $Rb_{14}Cd_9Tl_{21}$ a=10.0131(4) Å, c=17.7296(7) Å). While for the lighter homologues K and Rb a solid solution of the ternary approaches can be expected (e.g. $Rb_{1.78}K_{12.22}Cd_9Tl_{21}$ a=9.8793(2) Å, c=17.1230(2) Å), single crystals of approaches aiming $Cs_{14}Cd_9Tl_{21}$ suggest the involvement of the binary $Cs_{14.52}Tl_{28.4}$ ($Cs_{14.15}Cd_{6.22}Tl_{23.31}$ (a=10.2145(3) Å, c=18.3007(6) Å)). This also holds true for small amounts of Cs in quaternary approaches (e.g. $Cs_{1.34}K_{12.73}Cd_{8.42}Tl_{21.39}$ a=9.9334(4) Å, c=17.0628(7). All presented ternary and quaternary approaches of the composition $A_{14}Cd_9Tl_{21}$ (A=Na, K, Rb, Cs) were prepared by solid state techniques starting with the elements and subsequently fully characterization by single crystal x-ray structure analysis. Additionally, relativistic band structures were calculated by the use of FPLO.

(1) Z. C. Dong, J. D. Corbett, *Inorg. Chem.* **1996**, *35*, 1444–1450.
(2) V. F. Schwinghammer, S.M. Tiefenthaler, S. Gärtner *Materials (Basel).* **2021**, *14*, 7512.
(3) M. Tillard-Charbonnel et al., *Chem. A Eur. J.* **1997**, *3*, 799–806.

Figure 1: Unit cell of the $A_{15}Tl_{27}$ phase (left) and the $K_{14}Cd_9Tl_{21}$ structure type (right) in direction of the crystallographic *a*-axis and the two-dimensional layer in direction of the crystallographic *c*-axis.

Fig. 1

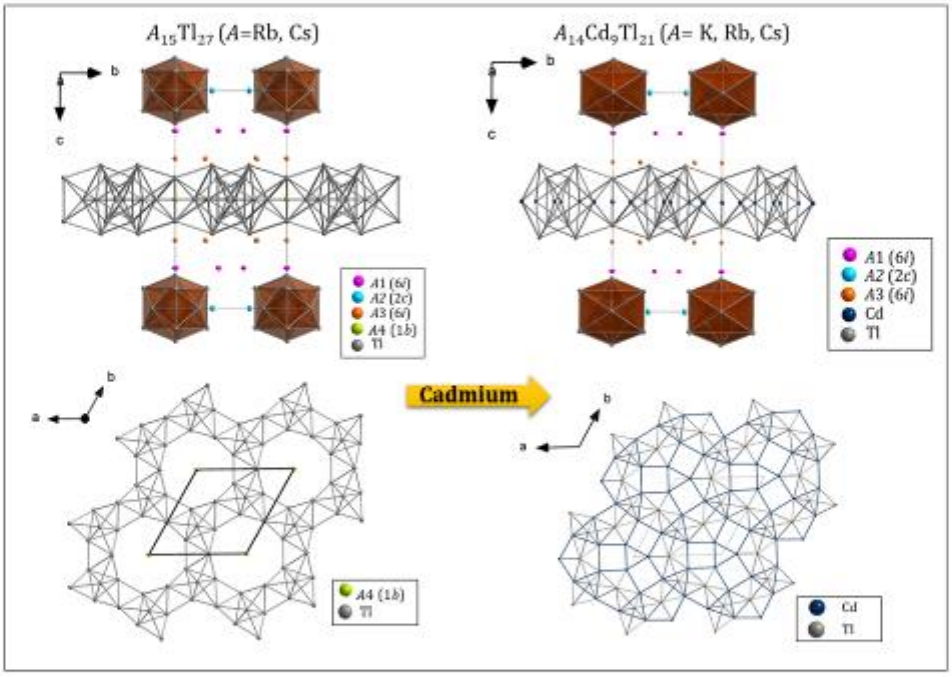

PP-021

A New Structure of $Pt(Bi_xTe_{1-x})_2$

Y. Wang (Dresden/DE), F. Pabst (Dresden/DE), A. Isaeva (Amsterdam/NL), T. Doert (Dresden/DE), M. Ruck (Dresden/DE)

PtBiTe was found by Hulliger to crystalize in the Ullmanite (NiSbS) structure type with the cubic space group *P*$2_1$3. We have discovered another structure of $Pt(Bi_xTe_{1-x})_2$ adopting a trigonal layered structure, resembling the CdI_2 type. Two different synthesis routes were applied: bismuth flux synthesis and microwave-assisted polyol process. In a bismuth flux between 750 °C and 550 °C, the Bi-rich compound $Pt(Bi_{5/8}Te_{3/8})_2$ was obtained. Single crystal X-ray diffraction revealed the space group to be trigonal *P*3*m*1 with lattice parameters of *a* = 4.053(3) Å and *c* = 5.4040(5) Å. At the Wyckoff 1*b* position, Bi and Te are represented in approximately equal proportions, while the 1*c* position is occupied by 77% Bi and 23% Te. This site preference leads to the absence of inversion symmetry and a polar layered structure. The microwave-assisted polyol process proved to be a rapid and mild approach to the synthesis of nanoparticles of Bi-poor $Pt(Bi_{3/8}Te_{5/8})_2$. Trigonal $Ni(Bi_xTe_{1-x})_2$, $Ni(Sb_xTe_{1-x})_2$, and $Pt(Pb_xTe_{1-x})_2$, as well as cubic $Pd(Bi_xTe_{1-x})_2$ were also obtained with this approach.

Figure 1 The layered crystal structure of $Pt(Bi_{5/8}Te_{3/8})_2$.

References:

(1) HULLIGER, F. New Compounds with Cobaltite Structure. Nature 198, 382–383 (1963).
(2) PABST, F. Synthese und Charakterisierung von ternären Verbindungen im Pt-Bi-Te-Phasensystem. Masterarbeit (2017).

Fig. 1

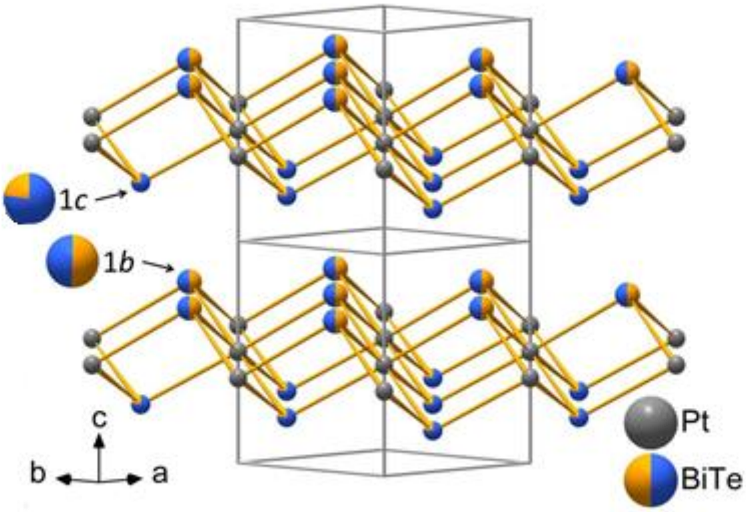

PP-022

Structural, optical and vibrational investigations of dolomite-type structures $MSn(BO_3)_2$ for M = Mn, Fe, Co and Ni

S. Wittmann (Bremen/DE), M. M. Murshed (Bremen/DE, Bremen/DE), V. Bilovol (Buenos Aires/AR, Krakow/PL), T. M. Gesing (Bremen/DE, Bremen/DE)

Dolomites and dolomite-type compounds have drawn diverse attention due to their thermal stability [1] and crystal-chemical properties [2]. New compounds of dolomite-type $MSn(BO_3)_2$ phases (M = Mn, Fe, Co and Ni) have been synthesized using a solid-state method. Rietveld refinements of the X-ray powder diffraction (XRPD) data confirm the rhombohedral space group $R\bar{3}$ for all compositions. The change in metric parameters follows the increasing nature of the M-cation radii. ^{119}Sn Mössbauer spectroscopy demonstrates as well the almost undistorted coordination as the four-fold charge of tin in the SnO_6 octahedra, supported by the insignificant bond-angle variance. Slightly higher but still a very small bond-angle variance suggests that the MO_6 octahedra also keep almost a regular geometry. Considering the high-spin configuration of the two-fold transition M cations each metric parameter shows a linear trend against the cationic radius. As such, the vibrational frequencies of some selective Raman and infrared bands also exhibit linearity with respect to the radii of the M cations. All investigated compounds can be categorized as wide band-gap semiconductors (3 to 4 eV) as suggested by the RATD analysis [3] of the UV/Vis diffuse reflectance spectra. Moreover, the indirect band gap energy increases with increasing size of the M cations.

Figure 1: Crystal structure of MnSn(BO3)2 with MnO_6 an SnO_6 octahedra, and planar BO_3 groups.

(1) Bayer G., Thermal expansion anisotropy of dolomite-type borates Me2+Me4+B2O6, Zeitschrift für Kristallographie 133 (1971) 85-90.
(2) Suknev et al., The infrared spectra of nordenskiöldine and its analogs, Zhurnal Prikladnoi Spektroskopii 10 (1969) 326-328.
(3) Gesing et al., Nano-crystalline precursor formation, stability, and transformation to mullite-type visible-light photocatalysts, J. Mater. Sci. (2022). Doi:10.1007/s10853-022-07854-w

We acknowledge support by DFG under grant number GE1981/14-1.

Fig. 1

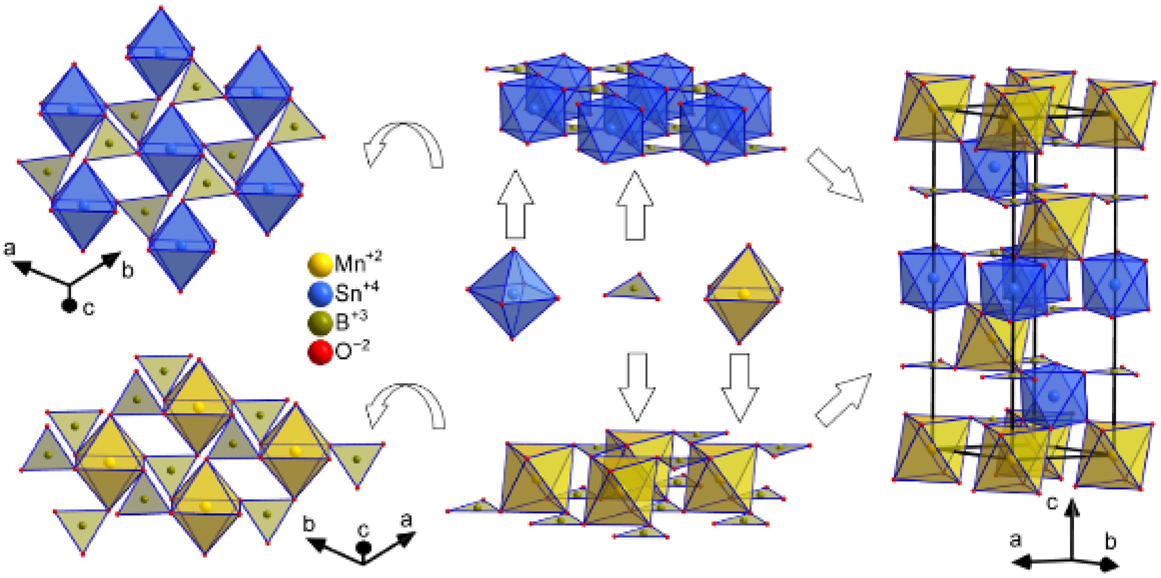

PP-023

Structural characterization of Cu-tpy-2"nucleotide ternary complexes

S. Dilipkumar (Bengaluru/IN), N. Munirathinam (Bengaluru/IN)

Nucleotide molecules contain many electron donor groups to link metal ions. The interaction between these sites and metal ions can produce a variety of deep changes in nucleic acid structure. To elucidate these interactions in biological processes, a number of binary and ternary transition-metal complexes involving nucleotides have been reported; however, most of the investigations covered so far include 5" nucleotides, while study into 2" nucleotides is scarce. In this regard, we have undertaken a crystallographic study on 2"nucleotide-metal ion interactions in ternary complex systems. We have synthesised a series of Cu-tpy-2"nucleotide ternary complexes and are presenting a preliminary account of its X-ray structural characterisation. The complexes include Cu-tpy-2"GMP(A), Cu-tpy-2"CMP(B), Cu-tpy-2"AMP(C) and Cu-tpy-2"UMP(D) [tpy - 2, 2":6", 2" terpyridine, 2"GMP – Guanosine 2"-monophosphate, 2"CMP – Cytidine 2"-monophosphate, 2"AMP – Adenosine 2"-monophosphate, 2"UMP – Uridine 2"-monophosphate]. Here, A is mononuclear, B and C are tetranuclear with different modes of nucleotide binding and D is 1D (linear) Coordination polymer. From the different binding patterns of the nucleotides, we have observed a different binding mode for the nucleotide 2"AMP, where all the 3 free oxygen atoms of the Phosphate group are involved in metal binding rather than two at pH 7.

PP-024

Rim-Brominated Pillarplexes

J. Zuber (Garching/DE), A. Pöthig (Garching/DE)

Complex biological mechanism are prerequisites for the life on earth and could not propagate with the absence of supramolecular (non-covalent) interactions. Mimicking these crucial processes is the scientific discipline of the chemistry beyond the molecule.[1] A subclass of such supramolecular organometallic complexes (SOCs)[2] is depicted by pillarplexes **$M_8L_2(X)_4$** (M = Ag, Au), which are octanuclear NHC complexes forming metallocavitand structures. Apart from the properties of pillarplexes, such as hosting linear molecules in their tubular cavity, intrinsic luminescence or tunable solubilty,[3] rim-modification by introduction of triazolate instead of pyrazolate moieties in the macrocyclic NHC ligand entails structural flexibility and self-recognition properties.[4] To expand the structure and the properties of pillarplexes, here, the introduction of a bromide functionality in the pyrazole unit of the macrocyclic ligand is presented.

Figure 1: Ortep representation of the solid-state structure of $Au_8(LBr_2)_2(PF_6)_4$ shown with 50 % probability displacement ellipsoids. Solvent molecules and anions are omitted for clarity (right).

The successful bromination of the macrocyclic ligand using NBS as well as subsequent metalation and transmetalation to form **$Ag_8(LBr_2)_2(PF_6)_4$** and **$Au_8(LBr_2)_2(PF_6)_4$**, respectively, was validated by NMR spectroscopy, elemental analysis and HRESI-MS. The solid-state structures were solved by single crystal X-Ray diffraction. The tuned reactivity sets a starting point for further functionalization and expanding the structure by cross-coupling reactions of donating functional groups towards network materials.

(1) J. M. Lehn, *Science* **1993**, 1762.
(2) A. Pöthig, A. Casini, *Theranostics,* 2019, **9**, 3150.
(3) P. J. Altmann, A. Pöthig, *J. Am. Chem, Soc.,* 2016, **138**, 13171.
(4) S. Guan, T. Pickl, C. Jandl, L. Schuchmann, X. Zhou, P. J. Altmann, A. Pöthig, *Org. Chem. Front.,* 2021, **8**, 4061

Fig. 1

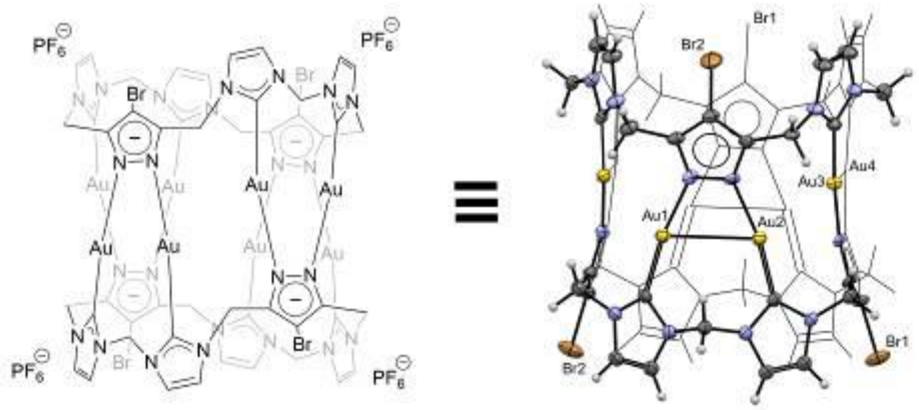

P-025

How to carve out the crystal structure of the polyoxometalate $[Ni(en)_3)]_2[V_{12}As_8O_{40}(H_2O)]*4H_2O$ from synchrotron X-ray powder diffraction data

S. Mangelsen (Kiel/DE), M. Rasmussen (Kiel/DE), N. Pienack (Kiel/DE), C. Näther (Kiel/DE), W. Bensch (Kiel/DE)

Polyoxometallates form numerous structural frameworks (clusters) that are sensitive on the synthesis conditions under kinetic control. [1] Many of these compounds contain V, Nb, Ta, Mo or W as metals, but further heteroatoms can be incorporated, which further increases the chemical variability. [2] Using water soluble salts of such clusters as precursors is a viable route for accessing novel compounds. We found that ageing of a saturated aqueous solution of the novel arsenato polyoxovanadate $[Ni(en)_3]_2[V_6As_8O_{26}]$ yielded another not-identifiable compound. No single crystal could be obtained, but indexing of the powder diffraction data yielded a monoclinic cell with a high figure of merit, indicating the product could be single phased. The ratio of the metals could be estimated from EDX spectroscopy, IR spectroscopy yielded further hints about preservation of the complex cation and reconstruction of the cluster. Thus reciprocal space methods had to be used for structure solution, this case was particularly demanding given the fairly large unit cell and limited information. A first structure model could be obtained from data collected on a lab diffractometer via charge flipping as implemented in TOPAS Academic, but no satisfying refinement could be achieved. Synchrotron diffraction data were employed allowing to determine the rough positions of numerous metal centres. Further refinement using the available chemical knowledge finally yielded the crystal structure of $[Ni(en)_3)]_2[V_{12}As_8O_{40}(H_2O)]*4H_2O$. [3] The formation of this high nuclearity cluster from the smaller cluster $[V_6As_8O_{26}]^{4-}$ is puzzling and contradicts the frequent observation that clusters rather tend to fragment in solution.

(1) D.-L. Long, R. Tsunashima, and L. Cronin, Angew. Chem. Int. Ed. **49**, 1736 (2010).
(2) K. Yu. Monakhov, W. Bensch, and P. Kögerler, Chem. Soc. Rev. **44**, 8443 (2015).
(3) Kondinski, M. Rasmussen, S. Mangelsen, N. Pienack, V. Simjanoski, C. Näther, D. L. Stares, C. A. Schalley, and W. Bensch, Chem. Sci. **13**, 6397 (2022).

PP-026

Synthesis and characterization of AFm-Phases containing selenite and organic molecules

T. K. Cortinhas Alves (Halle (Saale)/DE), S. Gehardt (Halle (Saale)/DE), T. Beirau (Halle (Saale)/DE), S. Stöber (Halle (Saale)/DE)

Cementation is a consolidated practice used to immobilize low and intermediate level radioactive wastes and to improve the performance of these cement-matrix many organic cement-admixtures are been deployed. After hydration and curing, Portland-, calcium aluminate-, and calcium sulphoaluminate cements presents different hydrate phases. Among these hydrated products are calcium aluminate/ferrate hydrate phases (AFm-phases). They belong to a family of lamellar calcium aluminum hydroxy salts and can host different organic, and inorganic anions in the interlayer. The aim of this study is the investigation possible solid solution formation between small organic molecules (from non-corrosive accelerators of cement) and inorganic toxic oxyanions like SeO_3^{2-}. Stoichiometric amounts of CaO, $CaAl_2O_4$, $CaSeO_3 \cdot H_2O$ were mixed with $Ca(HCOO)_2$ at 25°C to investigate the possible formation of different AFm-Phases at different relative humidities. The experiments were conducted in a glove box under an Ar atmosphere to avoid carbonation. In order to characterize the resulted hydrated mixture $C_3A \cdot CaSeO_3 \cdot mH_2O\text{-}C_3A \cdot Ca(HCOO)_2 \cdot nH_2O$ were used X-ray powder diffraction, SEM-EDS, thermal analysis, Raman, IR-spectroscopy and Ion chromatography. The X-ray diffraction patterns of $SeO_3^{2-}/(HCOO)_2^{2-}$-containing mixtures show well crystalline AFm-phases with trigonal/hexagonal or monoclinic structure varying with increasing formate concentration. A Pawley fit was performed to determine the lattice parameters of the compounds. Our Spectroscopic measurements confirm the intercalation of $SeO_3^{2-}/(HCOO)_2^{2-}$ into the interlayer of the synthesized compounds. Scanning electron microscopic analysis shows that the morphology of the synthesized samples varies from well-developed pseudo hexagonal shape like crystal to fibrous aggregates with increasing formate concentration. These results may be helpful to understand possible interactions of organic cement-admixtures and harmful compounds in the hydration products of different types of cements.

PP-027

Synthesis of dimorphic LaFSe and crystal-structure prediction of several more polymorphs of lanthanum fluoride selenide

C. Buyer (Stuttgart/DE), H. Grossholz (Stuttgart/DE), D. Zagorac (Belgrade/RS), J. Zagorac (Belgrade/RS), J. C. Schön (Stuttgart/DE), T. Schleid (Stuttgart/DE)

Lanthanum fluoride selenide LaFSe has been investigated for the first time in the 1970s [1]. By experimenting under different conditions, we were able to reproduce the old and add some new results. A-LaFSe crystallizes in the tetragonal PbFCl-type structure [2] (space group: *P*4/*nmm*, *a* = 413.79(3) pm, *c* = 715.24(5) pm, *Z* = 2) such as its light congener LaFS [3] and emerges by using an NaCl flux at 850 °C or 400 °C in a fluxing LiCl/KCl mixture, when LaF_3 and the elements La and Se are reacted in a 1:2:3-molar ratio. The use of a CsI flux at 800 °C leads to B-LaFSe, which crystallizes isotypically with CeHSe [4] in the hexagonal space group $P6_3/mmc$ (*a* = 421.602(2) pm, *c* = 818.163(7) pm, *Z* = 2). Also much higher temperatures in an induction furnance without any fluxing agent lead to this polymorph. The molar volumes of 36.86 versus 37.92 cm^3/mol turn the less denser B-type modification into the high-temperature form.

Some new structure candidates were generate via global optimizations on the energy landscape of LaFSe, when a combination of the well-known simulated annealing algorithm was employed. About 5000 structures were obtained as local minima on the energy landscape. Finally, all the promising candidates were optimized on the *ab-initio* level to predict the C- and D-type polymorphs in the CeHTe- and LaPtSi-type structure (space groups: *P*-6*m*2 and $I4_1md$, respectively) [5]. Additionally, three more possible, but not favourable structures were found without a known prototypic crystal structure [5].

In the A- to D-type polymorphs of LaFSe, the La^{3+} cations are surrounded by nine anions each. While the La^{3+} is coordinated as a capped square antiprism $[LaF_4Se_5]^{11-}$ in A-LaFSe, its environment can be described as trigonal prism of selenide with three caps of fluoride anions in B-, C- and D-LaFSe. These polymorphs just differ by the connections of the $[LaF_3Se_6]^{12-}$ polyhedra [5] (see Figure 1). Surprisingly there is no accordance to the polymorphs of YFSe, HoFSe or ErFSe [6], which were experimentally found in previous works, since they exhibit coordination numbers lower than nine for the smaller RE^{3+} cations (*RE* = Y, Ho and Er).

Diffuse reflectance spectra of A- and B-LaFSe were measured on polycrystalline samples to obain the optical band gap by using the Kubelka-Munk function. With 2.03 eV for A-LaFSe and 2.80 eV for B-LaFSe, the measured values show a good agreement with the calculated ones from HSE06 functionals [7].

(1) a) Ng.-H Dung, *Bull. Soc. Franç. Mineral. Cristallogr.* **1973**, *96*, 41. b) C. Dagron, *Compt. Rend. Acad. Sci. Paris* **1971**, *273*, 352.
(2) W. Nieuwenkamp, J. M. Bijvoet, *Z. Kristallogr.* **1932**, *81*, 469.
(3) a) Th. Schleid, *Z. Anorg. Allg. Chem.* **1999**, *625*, 1700. b) Th. Schleid, H. Grossholz, *Z. Anorg. Allg. Chem.* **2001**, *627*, 2693.
(4) Th. Schleid, M. Folchnandt, *Z. Anorg. Allg. Chem.* **1996**, *622*, 455.
(5) C. Buyer, H. Grossholz, S. Wolf, D. Zagorac, J. Zagorac, J. C. Schön, Th. Schleid, *Cryst. Growth Des.* **2022**, *in print*. DOI: 10.1021/acs.cgd.2c00810
(6) a) Ng.-H. Dung, *Bull. Soc. Fr. Minéral. Crystallogr.* **1973**, *96*, 44. b) Ng.-H. Dung, *Acta Crystallogr.* **1973**, *B 29*, 2095. c) Ng.-H. Dung, C. Dagron, P. Laruelle, *Acta Crystallogr.* **1975**, *B 31*, 519. d) Ng.-H. Dung, C. Dagron, P. Laruelle, *Acta Crystallogr.* **1975**, *B 31*, 514. e) Ng.-H. Dung, P. Laruelle, *Acta Crystallogr.* **1977**, *B 33*, 3360. f) Ng.-H. Dung, P. Laruelle, *Acta Crystallogr.* **1977**, *B 33*, 1444. g) Ng.-H. Dung, P. Laruelle, *Acta Crystallogr.* **1980**, *B 36*, 1048. h) D. V. Dyck, J. V. Landuyt, S. Amelinckx, Ng.-H. Dung, C. Dagron, *J. Solid State Chem.* **1976**, *19*, 179. i) D. D. Zimmermann, Th. Schleid, *Z. Kristallogr.* **2014**, *S 34*, 139.
(7) J. Heyd, G. E. Scuseria, M. Ernzerhof, *J. Chem. Phys.* **2003**, *118*, 8207.

Figure 1: Interconnection of the coordination polyhedra around La^{3+} in A-, B-, C- and D-type LaFSe.

Fig. 1

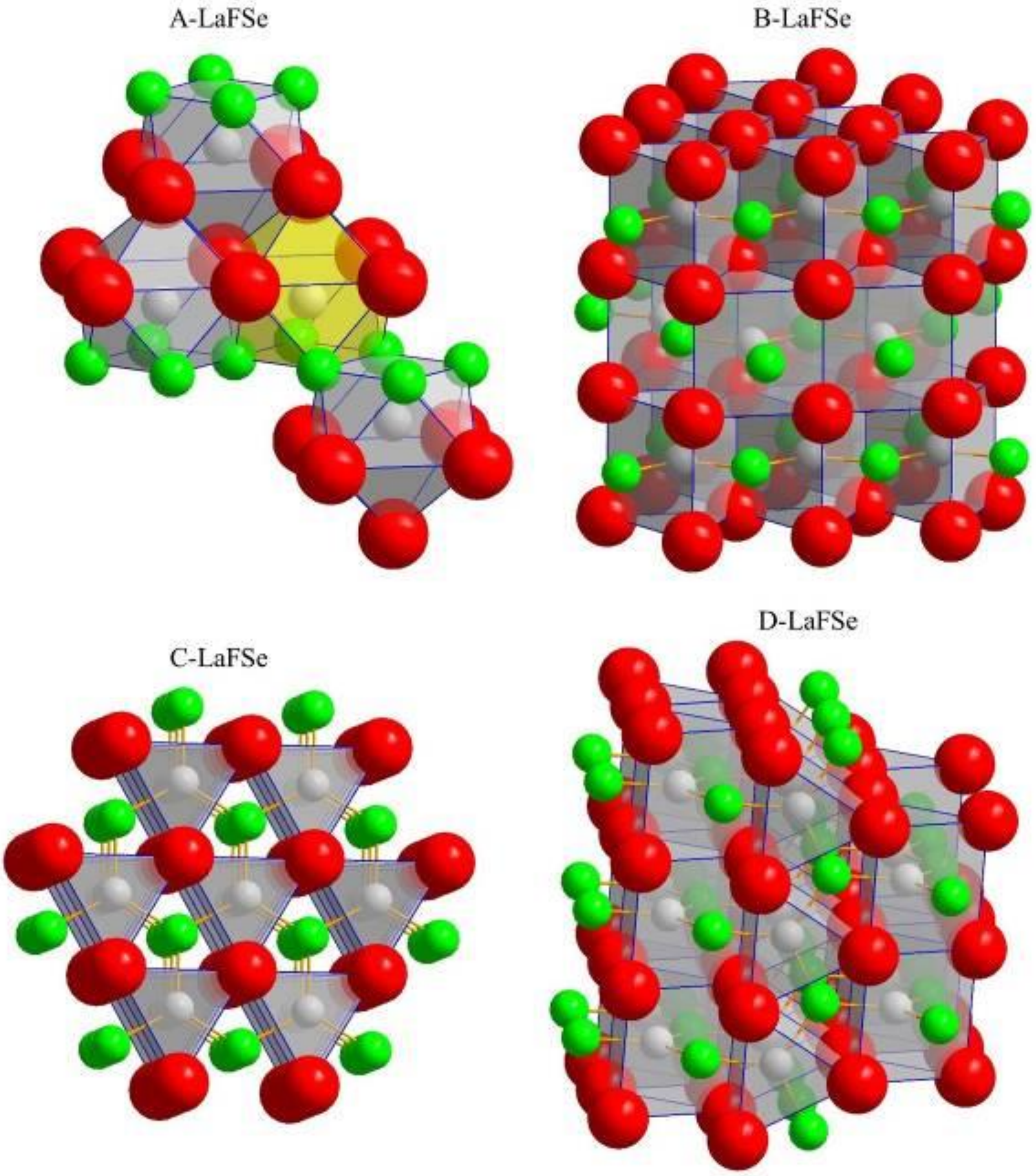

PP-028

Structural and spectroscopic investigation of mechanically induced defective forsterite (Mg_2SiO_4) to describe martian regolith

M. I. Jundullah Hanafi (Bremen/DE, Bremen/DE), M. M. Murshed (Bremen/DE, Bremen/DE), L. Robben (Bremen/DE, Bremen/DE), W. Dononelli (Bremen/DE), A. Kirsch (Copenhagen/DK), T. M. Gesing (Bremen/DE, Bremen/DE)

Forsterite (Mg_2SiO_4) is one of the phases identified in Martian regolith [1], wherein defect-rich structures are expected due to long-lasting space weathering effects [2]. For future use of forsterite as basis to fabricate metals in Mars exploration, precise analysis of defect-rich forsterite (DRF) is of crucial importance. Comparative crystal structure investigations of defect-poor to defect-rich phases were performed by X-ray diffraction (XRD) powder data Rietveld and pair distribution function (PDF) analysis, as well as Raman spectroscopy. Defect-poor forsterite (DPF) was synthesized by high-energy ball milling (BM) with subsequent heating, whereas mechanically induced DRF was obtained by BM of DPF. Rietveld refinements confirm all samples to be pure forsterite. The degree of crystallinity of DRF decreases by approximately 40 %, while its average crystallite size (ACS) is reduced to 25(1) nm compared to 77(1) nm of DPF. The Si-O bonds in DRF were found to be contracted with bond valence sum of 4.19(2) v.u., which can be explained in terms of either distorted SiO_4 or smaller $SiO_{4-\delta}$ coordination where oxygen atoms are partially replaced by voids. PDF-Rietveld with ideal crystal structure suggests that DRF possesses local distortion. Raman spectra of DRF exhibit peak broadening along with global red-shifts, which can be attributed to ACS difference and disorder structure. The findings of defective forsterite structure shed light on the relevant studies for human mission on Mars [3].

(1) D.L. Bish *et al*. Science 341(6153) (2013) 1238932. Doi:10.1126/science.1238932
(2) G. Certini *et al*. Planetary Space Science 186 (2020). Doi:10.1016/j.pss.2020.104922
(3) D. Karl *et al*. Open Ceramics 9 (2022) 100216. Doi:10.1016/j.oceram.2021.100216

We acknowledge support by the state of Bremen within the "Humans on Mars" initiative for APF "Materials on demand" S1P3.

Fig. 1

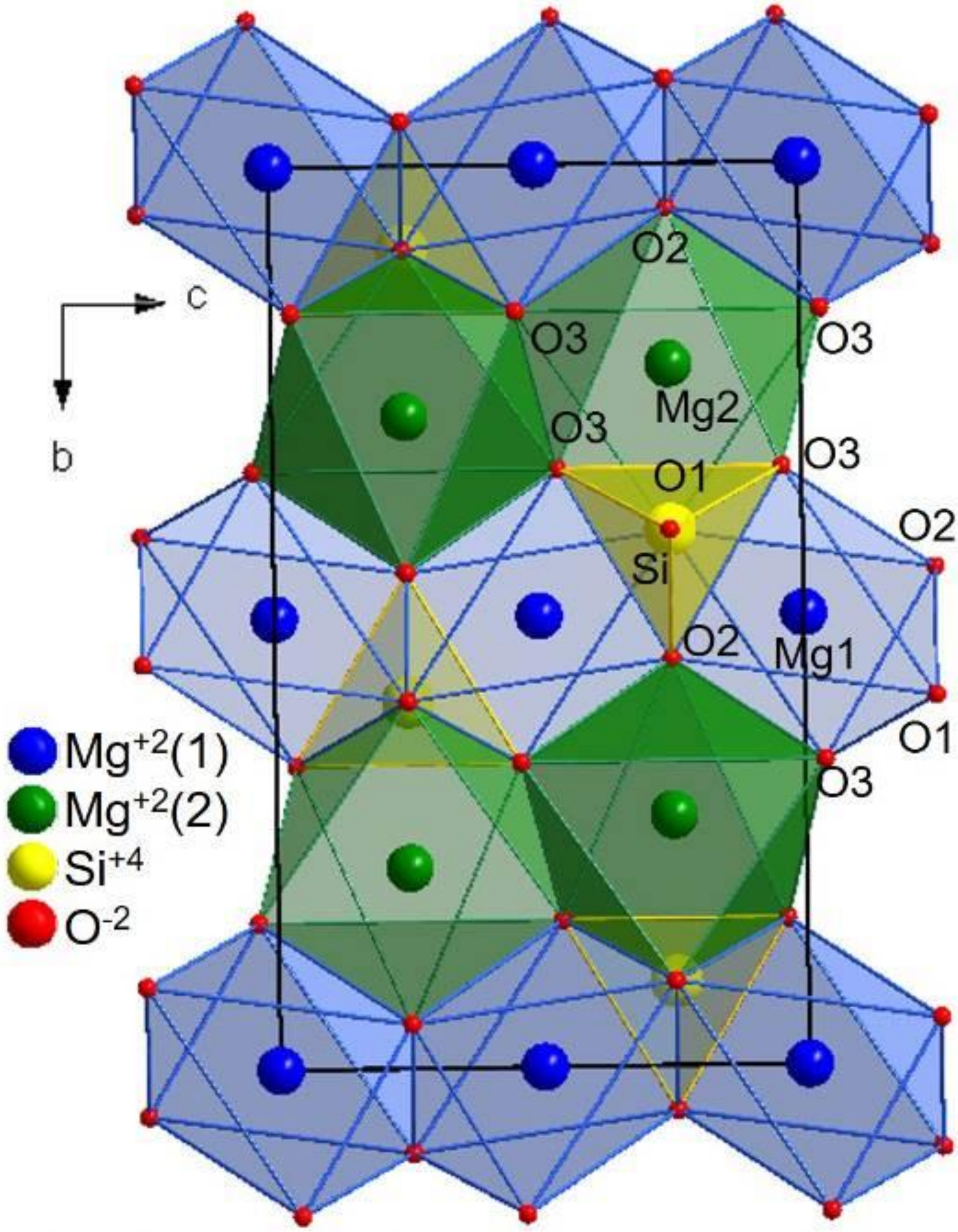

Fig.1: Representative crystal structure of forsterite

PP-029

Structural characterization of the lone electron pair effect on the $(Pb_{1-x}Sr_x)MnBO_4$ mullite-type phases

C. M. Uribe Rincón (Bremen/DE, Bremen/DE), M. M. Murshed (Bremen/DE, Bremen/DE), T. M. Gesing (Bremen/DE, Bremen/DE)

The presence of stereo-chemical active lone electron pairs (LEPs) causes an asymmetric environment on a given cation of the p-block [1]. To what extend the $6s^2$ LEPs of Pb^{2+} cations affect the crystal chemistry, a series of mullite-type $(Pb_{1-x}Sr_x)MnBO_4$ compounds for x = 0 – 1 are synthesized followed by their structural, spectroscopic, and thermogravimetric characterizations. X-ray powder diffraction data Rietveld refinements confirm that each phase crystallizes in the *Pnam* space group (Figure 1). The average crystallite size and micro strain exhibit usual solid-solution mid-range reduction and increase, respectively. Although the cationic radii differ only one picometer between Pb^{2+} ($r^{[6]} = 119$ pm) and Sr2+ ($r^{[6]} = 118$ pm)[2], substitution of Pb^{2+} with Sr^{2+} leads to contraction of the ***a*** lattice parameter along with slight expansion of the ***b*** and ***c*** lattice parameters (Figure 1). Of notes, for a cationic size difference of only 0.8 % the cell volume contracts about 4 % between $PbMnBO_4$ and $SrMnBO_4$. The Wang-Liebau eccentricity (WLE) parameter [3, 4], which is a measure of the distortion of a cation coordination including the associated deformation of the LEP electron density [5], decreases with subsequent dilution of the Pb^{2+} cation in the solid solution. The degree of stereo-chemical activity can be understood in terms of the spatial requirements of the $6s^2$ LEPs in the $MnBO_4^{2-}$ channel, keeping a difference of ~40 pm between the shortest and the longest Pb-O distances for the $PbMnBO_4$, which reduces to ~20 pm for the Sr-O distances in $SrMnBO_4$. As such, the bond-length distortion linearly decreases with increasing strontium concentration due to the change from a PbO_{4+3} to a SrO_7 coordination within cut-off value of 305 pm and 265 pm, respectively. The low-frequency region of the Raman spectra is seen to be distinctive between the Pb- and Sr-containing lattice modes. The gradual higher thermal stability of the $(Pb_{1-x}Sr_x)MnBO_4$ compounds is explained from the higher Sr-O bond strength than that of the Pb-O bonds.

(1) Hamani, O. Masson, P. Thomas, *J. Appl. Crystallogr.* 53 (**2020**) 1243.
(2) R. D. Shannon, *Acta. Crystallogr. A*32 (**1976**) 751.
(3) M. Curti, T. M. Gesing, M. M. Murshed, T. Bredow, C. B. Mendive, *Z. Kristallogr.* 228 (**2013**).
(4) X. Wang, F. Liebau, *Mater. Res. Soc. Symp. Proc.* (**2005**) FF7.4.1-FF7.4.6.
(5) X. Wang, F. Liebau, *Acta Crystallogr.* B63 (**2006**) 216.

Figure 1: Depiction of the $PbMnBO_4$ and $SrMnBO_4$ structures, comparing the difference of the **a** cell parameter between the end members of the series.

Fig. 1

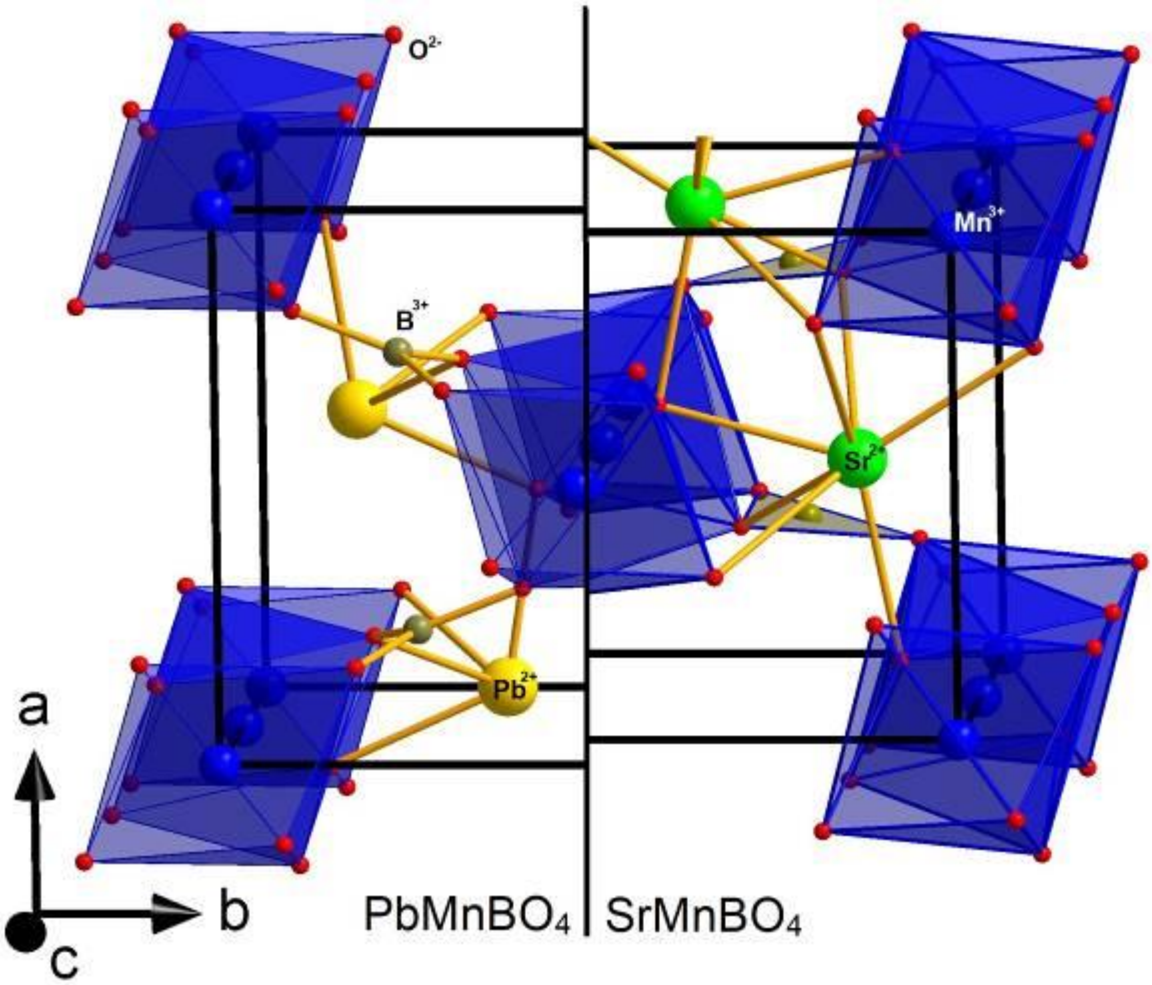

PP-030

$RbEr_2S[S_2][AsS_2(S_2)]$: A Rubidium-Containing Erbium Thioarsenate(III) with a new type of complex anion

K. Engel (Stuttgart/DE), P. L. Lange (Stuttgart/DE), T. Schleid (Stuttgart/DE)

Experimental methods: During an attempt to synthesize $Rb_3Er[AsS_4]_2$ in analogy to $Cs_3La[AsS_4]_2$ [1] from elemental erbium (Er), arsenic sesquisulfide (As_2S_3), rubidium sesquisulfide (Rb_2S_3) and elemental sulfur (S) in a molar ratio of 1:1:1:6 single crystals of rubidium erbium sulfide disulfide thiodisulfidoarsenate(III) with the structured formula $RbEr_2S[S_2][AsS_2(S_2)]$ were obtained instead. Rb_2S_3 was prepared from the elements in a molar ratio of 2:3 in liquid ammonia over a period of three days until full conversion of the alkali metal. The reaction mixture was filled into a fused glassy silica ampoule inside an argon-filled glove box and sealed under dynamic vacuum. The sample was placed in a computer-controlled muffle furnace and heated to 773 K with 25 K/h and kept at this temperature for 20 h. Afterwards it was cooled to 373 K with –2 K/h before the furnace was turned off. The reaction product contained transparent, orange, needle-shaped single crystals, which were stable with regard to air and water. The crystal structure was successfully determined using single-crystal X-ray diffraction (CSD number: 2219896).

Results and discussion: Even if the synthesis route seems familiar regarding the synthesis of compounds like $K_3RE[AsS_4]_2$ for *RE* = Nd, Sm, Gd, Dy previously presented by Wu et al. [2,3] and $Cs_3La[AsS_4]_2$ [1], $RbEr_2S[S_2][AsS_2(S_2)]$ is neither similar in its formula nor in its structure in comparison to well-known alkali-metal-containing rare-earth metal thioarsenates [1–6]. $RbEr_2S[S_2][AsS_2(S_2)]$ crystallizes monoclinically in the space group *C*2/*c* with $a = 2339.86(8)$ pm, $b = 541.78(1)$ pm, $c = 1686.71(5)$ pm and $\beta = 93.108(2)°$ for $Z = 8$. As illustrated in the structural formula this compound includes a new type of complex $[AsS_2(S_2)]^{3-}$ anion, more specifically an isolated ψ^1-tetrahedrally coordinated As^{3+} cation in a thioarsenate(III) anion with two S^{2-} anions ($d(As^{3+}–S^{2-}) = 321 – 230$ pm, $\angle(S^{2-}–As^{3+}–S^{2-}) = 102°$) and a disulfide dumbbell ($d(S^-–S^-) = 207$ pm, $\angle(S^{2-}–As^{3+}–S^-) = 95 – 98°$) end-on coordinated ($d(As^{3+}–S^-) = 232$ pm) as ligands. This disulfide group is also side-on coordinated to the crystallographically unique Rb^+ cation, which is surrounded by two more end-on coordinated disulfide anions $[S_2]^{2-}$ and five S^{2-} anions ($d(Rb^+–S^{-/2-}) = 335 – 394$ pm). These $[RbS_9]^{11-}$ polyhedra form corrugated chains developing along [010] by edge sharing, getting bridged via end-on coordinated disulfide dumbbells. Linked by the $[AsS_2(S_2)]^{3-}$ anions, these chains are building infinite layers parallel to the (100) plane. It should be emphasized that the stereochemically active lone pairs of the $[AsS_2(S_2)]^{3-}$ anions are oriented towards the chains center. Connected with the coordination polyhedra of the two crystallographically different Er^{3+} cations, a three-dimensional network of Rb^+- and Er^{3+}-centered sulfur coordination polyhedra with empty channels along [010] is erected.

Conclusion: The title compound $RbEr_2S[S_2][AsS_2(S_2)]$ (sum formula: $RbEr_2AsS_7$) was successfully synthesized from Er, Rb_2S_3, As_2S_3 and S in a molar ratio of 1:1:1:6. Its structure was solved from single-crystal X-ray diffraction data. The crystal structure shows a new type of complex thioarsenate(III) anion, namely a ψ^1-tetrahedral thioarsenate anion with two sulfide ligands and an end-on coordinating disulfide dumbbell $[S_2As(S_2)]^{3-}$, which has never been reported in a solid previously.

References:

(1) K. Engel, Master Thesis, University of Stuttgart, **2022**.
(2) Y. Wu, C. Näther, W. Bensch, *Inorg. Chem.* **2006**, *45*, 8835–8837.
(3) Y. Wu, W. Bensch, *Solid State Sci.* **2009**, *11*, 1542–1548.
(4) T. K. Bera, M. G. Kanatzidis, *Inorg. Chem.* **2008**, *47,* 7068–7070.
(5) T. K. Bera, M. G. Kanatzidis, *Inorg. Chem.* **2012**, *51,* 4293–4299.
(6) T. K. Bera, R. G. Iyer, C. D. Malliakas, M. G. Kanatzidis, *Inorg. Chem.* **2007**, *46,* 8466–8468.

Figure 1: Complex $[AsS_2(S_2)]^{3-}$ anion (left) and corrugated $[RbS_9]^{11-}$ polyhedra chain along [010] (right).

Figure 2: Three-dimensional network with empty channels along [010].

Fig. 1

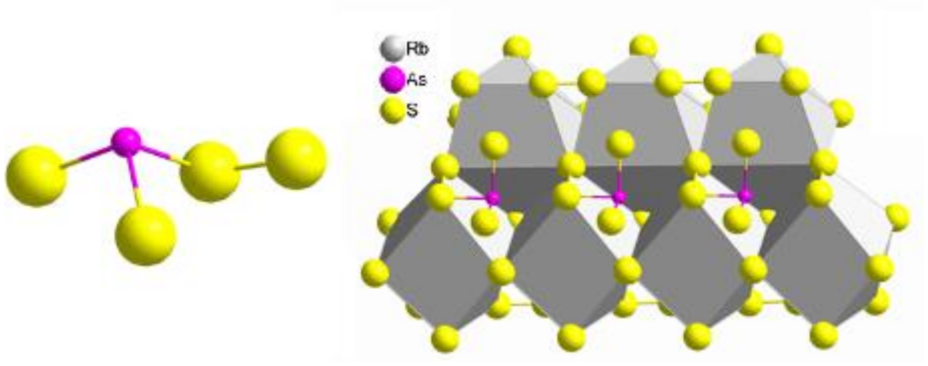

Fig. 2

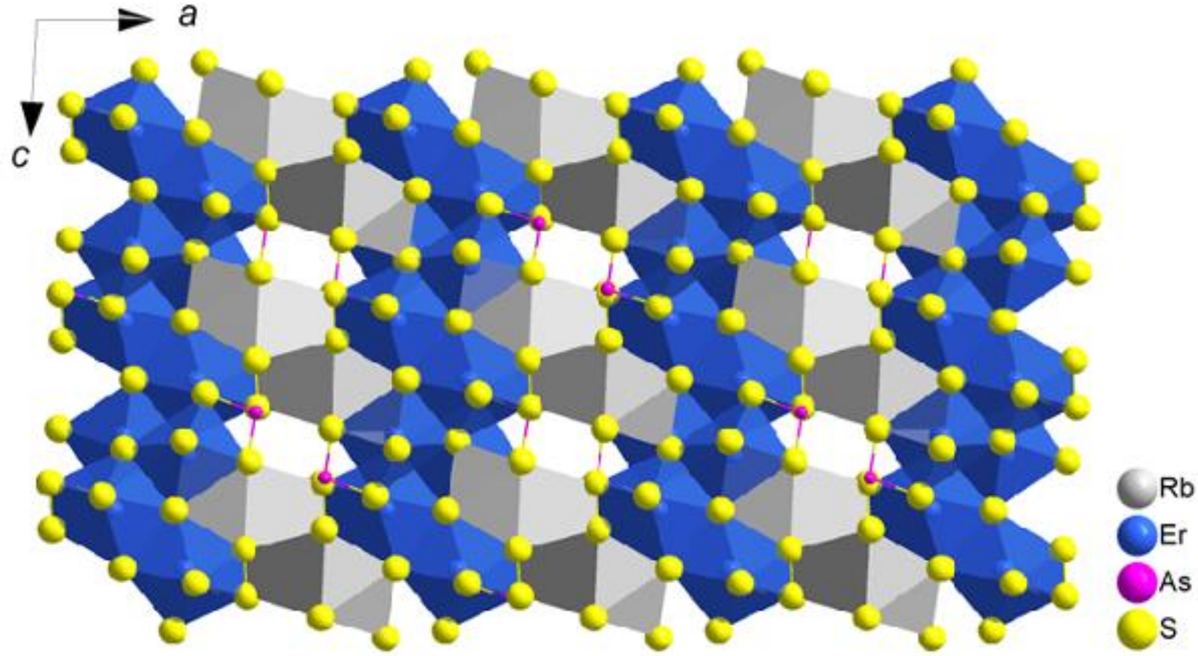

PP-031

Complete structural and magnetic phase diagram of orthorhombic mixed spinel series $Ni_{1-x}Cu_xCr_2O_4$

M. Tovar (Berlin/DE), M. Reehuis (Berlin/DE), N. Stüßer (Berlin/DE), B. Klemke (Berlin/DE), D. M. Többens (Berlin/DE), S. Schorr (Berlin/DE, Berlin/DE)

Members of the mixed crystal series $Ni_{1-x}Cu_xCr_2O_4$ crystallize in a distorted spinel structure [1]. For the end members $NiCr_2O_4$ and $CuCr_2O_4$ strong Jahn-Teller activities on the Ni^{2+} and Cu^{2+} ions at the A site lead to an elongation and a flattening of the NiO_4 and CuO_4 tetrahedra, respectively. Two structural phase transitions where caused by the local distortion, where the crystal structure first undergoes a change from cubic (*Fd3m*) to tetragonal symmetry (*I4₁/amd*) followed by a change to orthorhombic space group *Fddd* at or below room temperature, depending on the Cu-Ni substitution [2,3]. Low-temperature X-ray diffraction by means of a Guinier diffractometer, equipped with a He cryostat and hosted at the HZB X-ray Corelab, was applied in combination with synchrotron and neutron powder diffraction data to elucidate the interplay between structural and magnetic distortion in the complex spinel system.

(1) Dollase, W.A.; O'Neill, H.S.C., Acta Crystallographica C (1997) 53, 657
(2) Reehuis et al., Phys. Rev. B 91 (2015) 024407
(3) Suchomel et al., Phys. Rev. B 86 (2012) 054406

We are thankful to Dr. Ralf Feyerherm for his excellent instrumental support.

Fig. 1

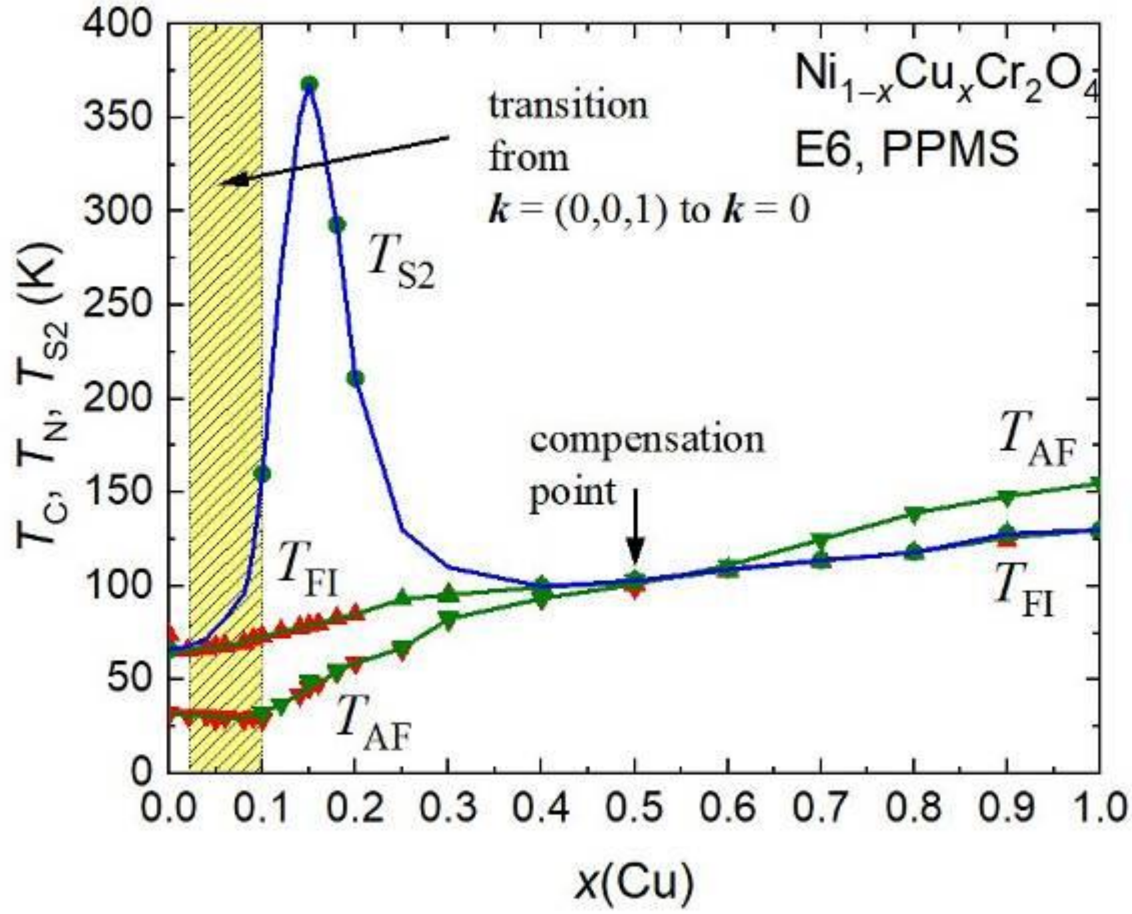

PP-032

A nitridiosilicatephosphate with amphibole structure

M. Pointner (Munich/DE), W. Schnick (Munich/DE), O. Oeckler (Leipzig/DE)

Although nitridosilicates and nitridophosphates show a rich structural chemistry and mixed nitridic networks tend to have a broad range of intriguing properties, mixed nitridosilicatephosphates have only recently become accessible from binary nitrides using a high-pressure high-temperature approach with added mineralizer NH_4F. For instance, this led to $AESiP_3N_7{:}Eu^{2+}$ (AE = Sr, Ba), a tetrahedra-based luminescent material with interesting Si/P occupational disorder.[1]

Starting from the binary nitrides Cr_2N, Si_3N_4 and P_3N_5, the chromium nitridosilicatephosphate $Cr_{5.7}Si_{2.3}P_8N_{24-x}O_x$ ($x \approx 5.6$) was synthesized in a multi-anvil press (T = 1400 °C, p = 10 – 12 GPa). The atomic ratio of cations was confirmed by TEM-EDX spectroscopy; powder X-ray diffraction reveals a minor side phase (CrN). However, EDX measurements show varying ratios of N and O, which could originate from surface hydrolysis. Magnetization measurements and electron paramagnetic resonance should bring clarity about a possible Cr^{+III} ($Cr_{5.7}Si_{2.3}P_8N_{18.4}O_{5.6}$) or Cr^{+IV} ($Cr_{5.7}Si_{2.3}P_8N_{24}$). Electron diffraction revealed the monoclinic metrics of the amphibole structure $AB_2C_5T_8O_{22}(OH)_2$. STEM-HAADF (high angle annular dark field) images display stacking faults in fiber-like crystals. The microfocused beam at ID11 beamline (ESRF) enabled the collection of single crystal data. The structure was solved and refined in $C2/m$. The A position in the amphibole structure $AB_2C_5T_8O_{22}(OH)_2$, which is often not or only partially occupied, is completely occupied by Cr. Octahedral sites are occupied with either Cr or Si but there is one mixed Cr/Si position (also shown in Figure 1). This is supported by Z-contrast imaging and the comparison of octahedral volumes. Tetrahedral double chains do not contain Si common in natural amphiboles but exclusively P, confirmed by STEM-EDX mapping. This material thus constitutes the first (oxo)nitridic amphibole.

(1) L. Eisenburger, V. Weippert, O. Oeckler, W. Schnick, *Chem. Eur. J.* **2021**, *27*, 4461.

Fig. 1

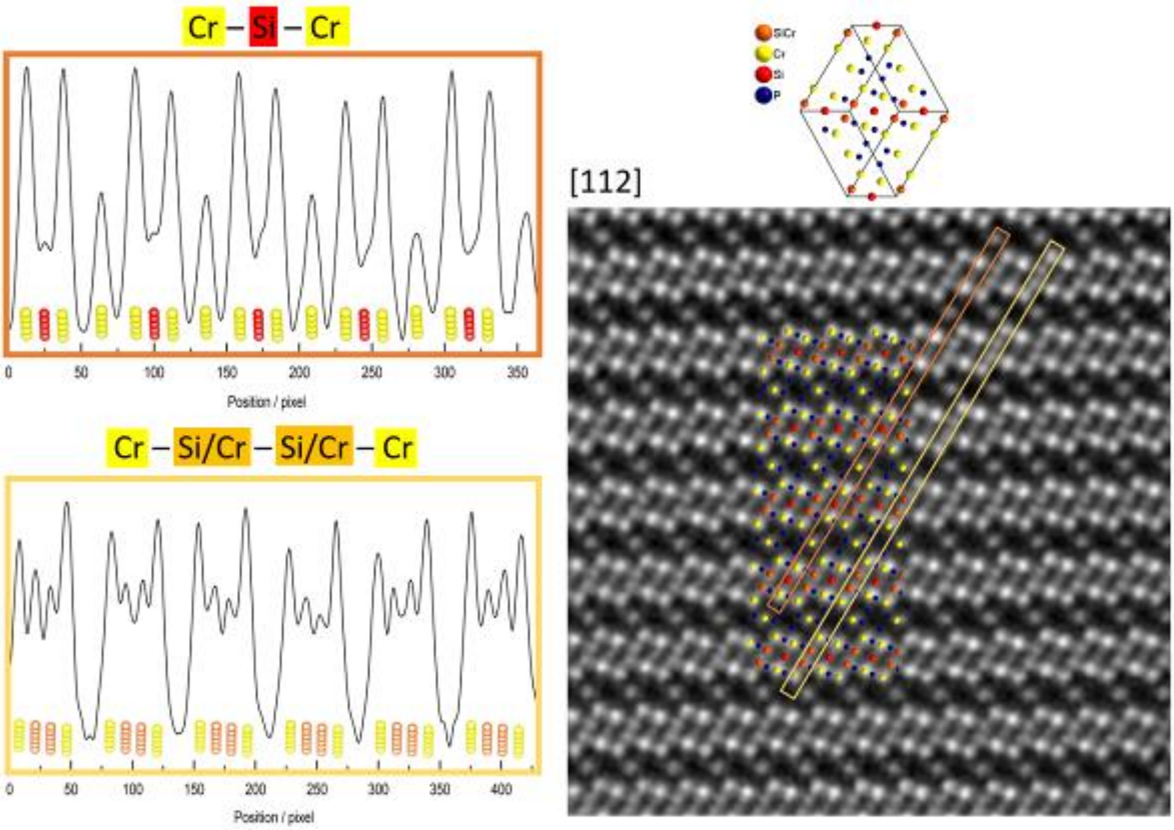

PP-033

Ternary Alkali Metal Thallides *A*Tl (*A*=Rb and K or Cs)

V. Schwinghammer (Regensburg/DE), S. Gärtner (Regensburg/DE, Regensburg/DE)

The Zintl phase NaTl is known since the 1930s.[1] While KTl and CsTl have been reported in the 1990s by Corbett et al. RbTl is still missing.[2,3] Binary approaches did not result in the desired product, therefor several ternary compositions of K/Rb and Cs/Rb have been prepared and analyzed by single crystal X-ray structure analysis in order to approximate RbTl.

Those approaches resulted in the first mixed alkali metal thallides in the *A*:Tl 1:1 ratio. Mixed K/Rb thallides $K_{0.72}Rb_{0.28}Tl$ and $K_{0.54}Rb_{0.46}Tl$ crystallize in the orthorhombic KTl type structure (*Cmce*, a=15.3508(4)/15.4681(11) Å, b=15.0226(5)/15.1269(9) Å, c=8.1483(3)/8.2196(5) Å, V=1879.07(11)/1923.3(2) Å^3, Z=24). Here, differently occupied alkali metal positions are present beside distorted Tl_6^{6-} octahedra as Tl moiety. The largest Rb content can be found at alkali metal position *A*2 (8*e*) (see Figure 1, up left), which is the exo-coordinating position to the Tl_6^{6-} cluster. Contrary to the ternary compounds in the KTl type structure, mixtures of Cs and Rb did not crystallize in the CsTl type structure (space group *Fddd*). Instead, the new Zintl phase $Cs_{0.58}Rb_{0.42}Tl$ crystallizes in the monoclinic space group *C*2/*c* (a=14.2465(2) Å, b=11.1014(2) Å, c=27.5403(5) Å, α=γ=90 °, β=104.063(2) °, V=4225.12(13) Å^3, Z=48). Here, also distorted Tl_6^{6-} octahedra form the Tl substructure with six instead of only 3 symmetrically inequivalent alkali metal positions.

Figure 1: Coordination sphere of the Tl_6^{6-} octahedra of the two already known compounds KTl and CsTl and also for the new ternary compounds (K,Rb)Tl and $Cs_{0.58}Rb_{0.42}Tl$.

(1) E. Zintl, W. Dullenkopf, *Z. phys. Chem.* **1932**, *B16*, 195-205.; S. Tiefenthaler, N. Korber, S. Gaertner, *Materials* **2019**, *12*, 1356-1366.
(2) Z. C. Dong, J. D. Corbett, *J. Am. Chem. Soc.* **1993**, *115*, 11299-11303.
(3) Z. C. Dong, J. D. Corbett, *Inorg. Chem.* **1996**, *35*, 2301-2306.

Fig. 1

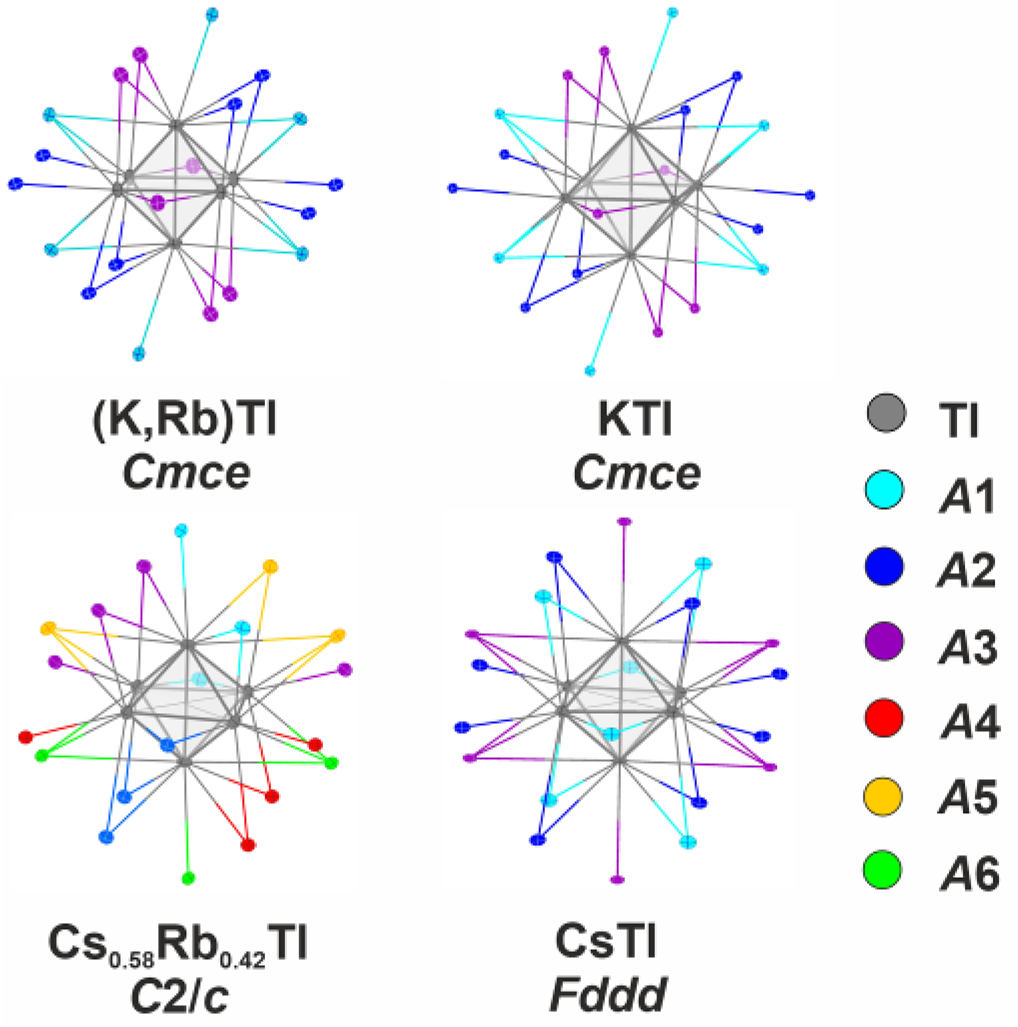

(K,Rb)Tl *Cmce*

KTl *Cmce*

$Cs_{0.58}Rb_{0.42}Tl$ *C2/c*

CsTl *Fddd*

PP-034

Synthesis, characterization and structure-property relations in $Pb_2(Pb_{1-x}Sn_x)O_4$

C. S. Reuter (Bremen/DE), M. M. Murshed (Bremen/DE, Bremen/DE), T. M. Gesing (Bremen/DE, Bremen/DE)

Both Pb_2PbO_4 (Pb_3O_4) and Pb_2SnO_4 are members of the mullite-type family. At ambient condition Pb_2PbO_4 and Pb_2SnO_4 crystallize in space group *P4₂/mbc* and *Pbam*, respectively. At what extend the crystal structure prefers either of the space groups would be an excellent playground for a respective $Pb_2(Pb_{1-x}Sn_x)O_4$ solid solution. Several members of this series have been prepared by solid-state reactions in sealed quartz tubes. X-ray powder diffraction data Rietveld refinements confirm the structures of the red-orange Pb_2PbO_4 and yellow-beige Pb_2SnO_4 phases. Since the Pb^{4+} cation is about 10 pm larger than Sn^{4+}, the MO_6 polyhedral volume decreases linearly with increasing Sn content in the compounds. Therefore, each metric parameter follows Vegard's rule. Moreover, the MO_6 contraction needs more space for the stereo-chemical activity of the $6s^2$ lone electron pairs (LEPs) of the Pb^{2+} cations resulting in symmetry reduction. As such, the Wang-Liebau eccentricity (WLE) [1] parameter, which is a measure of the distortion of a cation coordination including the associated deformation of the LEP electron density [2], increases with increasing tin in the solid solution. DFT calculation suggests the instability of the tetragonal Pb_2PbO_4 phase at low-temperatures while Pb_2SnO_4 keeps orthorhombic symmetry, which is in agreement with the experimental findings. The gradual global blue shift of the Raman mode frequencies can be explained from the contraction of the metric parameters, which is as well supported by the lattice dynamical calculations. The indirect band-gap energy calculated by the RATD method [3] linearly increases from 2.1(1) eV ($x = 0$) to a maximum value of 2.5(1) eV ($x = 0.8$) followed by a sharp drop for $x > 0.8$. Thermogravimetric analysis demonstrates an increasing thermal stability with increasing x, which leads to a stepwise adjustment of the synthesis temperatures within the solid solution.

(1) X. Wang, F. Liebau, Z Kristallogr. 211 (1996) 437
(2) M. Curti et al., Z. Kristallogr. 228 (2013) 629
(3) Th.M. Gesing et al., J. Mater. Sci. 57 (2022) 19280.

Figure 1: Crystal structure of Pb_2SnO_4

Fig. 1

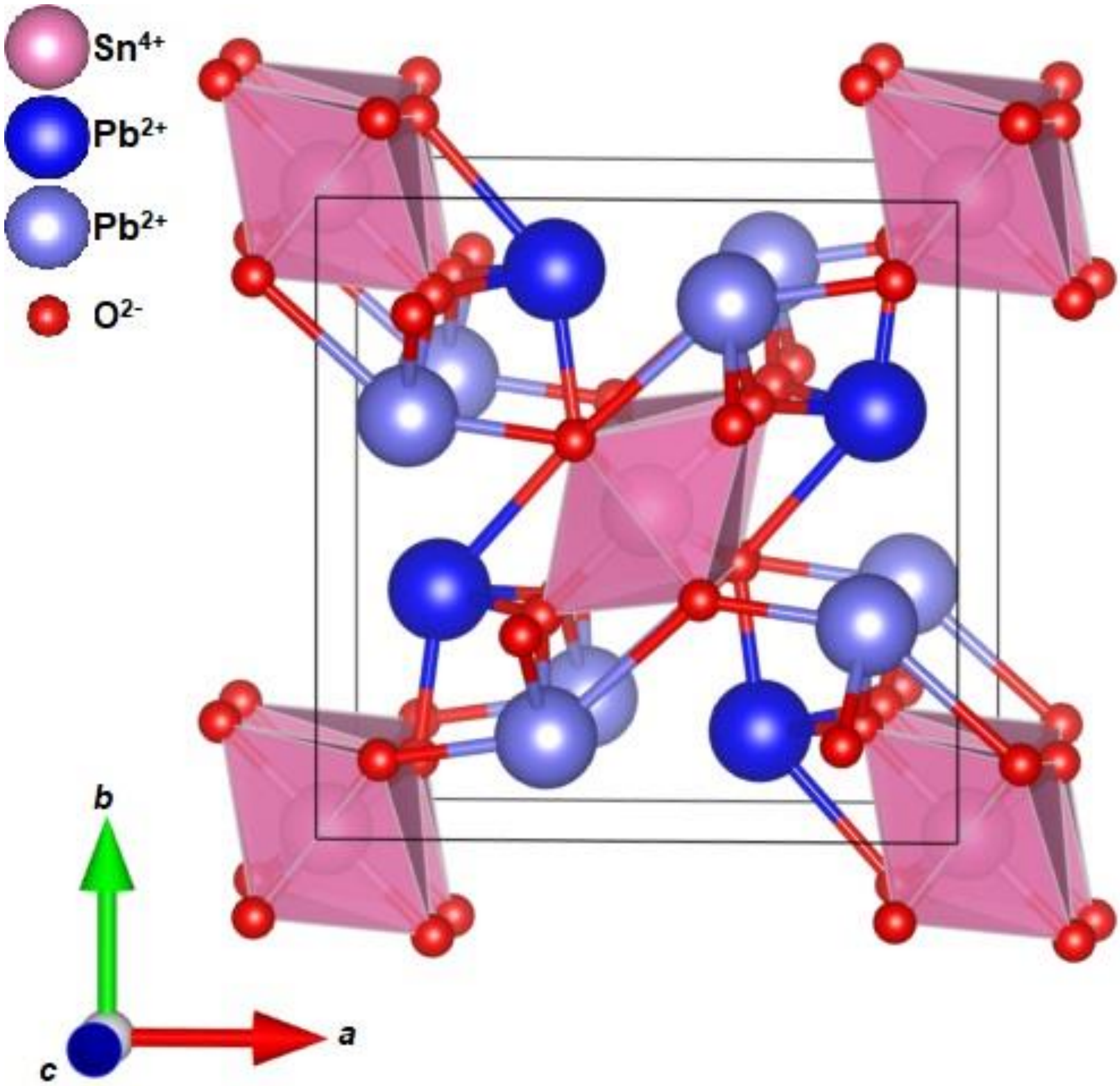

PP-035

Status of the Powder Diffraction and Total Scattering Beamline P02.1 at PETRA III, DESY

M. Etter (Hamburg/DE), V. Baran (Hamburg/DE), H. Jeppesen (Hamburg/DE), A. San José Méndez (Hamburg/DE), A. Schökel (Hamburg/DE), T. Schoof (Hamburg/DE), M. Wendt (Hamburg/DE), S. Wenz (Hamburg/DE)

Powder Diffraction is a well-established method which allows to investigate long-range order structural properties of crystalline materials. On the other hand, Total Scattering measurements in combination with the Pair Distribution Function method is an expanding and powerful technique which allows to investigate the short-range and/or long-range order at the same time, making it possible not only to investigate crystalline materials, but also amorphous solids or liquids. Therefore, the combination of both methods provides a detailed insight into the structure of a wide range of material systems, including organic materials such as pharmaceuticals, co-crystals, covalent-organic frameworks, polymers and fibers, metal-organics such as metal-organic frameworks and inorganic materials such as nanoparticles, ceramics, cements, battery materials, metals and steels, metallic glasses, minerals and mineral glasses, superconductors, strongly (electron-)correlated materials, corrosion products, melts, liquids and so forth. For this huge range of crystalline and non-crystalline materials, structural properties, phase transitions or phase mixtures can be investigated at synchrotron facilities in *ex situ*, *in situ* or *in operando* experiments utilizing either beamline-offered or user-developed sample environments.

The Powder Diffraction and Total Scattering Beamline P02.1 at the PETRA III synchrotron at the DESY facility in Hamburg, Germany, is a specialized station, where researchers from science and industry have the possibility to collect Powder Diffraction and Total Scattering data simultaneously with a fixed energy of 60 keV [1, 2]. In recent years, the station has undergone major upgrades. For example, instead of using a single area detector, a custom-made tandem detector setup was installed, allowing users to measure simultaneously high-resolution Powder Diffraction data and Total Scattering / Pair Distribution Function data on the same sample or the same *in situ* process. Moreover, the old collimator tube was replaced by a flexible telescopic collimator tube allowing the last pin hole to get close to the sample or experiment. This suppresses the undesirable air scattering in front of the sample and therefore leads to a better data quality especially when Total Scattering data is collected. On the sample environment side, a new cryostat with a wide-opening angle was purchased, which will allow also to measure Total Scattering data down to temperature of 4 K. Currently this device is commissioned and will be available latest for the second run period in 2023 (for regular proposals, mail-in options are currently discussed).

Besides regular on-site synchrotron experiments, users can also apply for mail-in / rapid access services for Powder Diffraction and/or Total Scattering / Pair Distribution Function measurements of samples packed in capillaries.

In this presentation, we will inform the scientific community as well as industrial customers about the latest developments at beamline P02.1.

(1) Dippel A.-C. et al., Z. Anorg. Allg. Chem. 2014, 640, 3094.
(2) Dippel A.-C. et al., J. Synchrotron Radiat. 2015, 22, 675.

PP-036

Higher harmonics in X-rays: Effects, evaluation, 'extinction'

M. Nentwich (Hamburg/DE), D. Novikov (Hamburg/DE)

In a conventional X-ray experiment, the beam is misleadingly described as monochrome, although not only the fundamental wavelength λ is reflected at the monochromator, but also the integer multiples m of the as described by Bragg's Law ($m\ \lambda = 2d \sin \theta_B$). Therefore, the beam interacting with the sample also includes undesired higher harmonics, which can falsify the experimental data. Often, the extent of noise caused by the higher harmonics is unclear and its presence is neglected as "small". However, for very sensitive measurements the exact characterization of higher harmonics is crucial, *e.g.* for measuring absolute intensities or when comparing data sets measured at different energies and attenuators.

As the different harmonics are always interfering with each other, a direct determination of their proportions to the total intensity is not possible. Therefore, only an indirect method can estimate their share. We can use the fact that the higher harmonics are less affected by the attenuators. Thus, the (measured, attenuated) intensity I_{atten} is the sum of intensities I_{harmonic} of the different harmonics weighted by the attenuation factor *A*harmonicatten with respect to the energy (of the harmonic) and the attenuator setup

$I_{\mathrm{atten}} = \Sigma_{\mathrm{harmonic}}\ A_{\mathrm{harmonic}}{}^{\mathrm{atten}}\ I_{\mathrm{harmonic}}$.

By using different attenuator settings, we can now construct a linear system of equations to solve for the unknown I_{harmonic}. This approach will deliver a unique solution, without requiring fits or approximations.

The influence of the higher harmonics can be strongly suppressed with some tricks, which are better understood when analyzing their creation in more detail. As early as 1914, Darwin discovered that X-rays are also subject to the laws of refraction, which generally means that the peaks of different harmonics are not at the same θ value. Additionally, the higher the order of a harmonic, the sharper is the shape of the peak. The underlying reflectivity curves can be described by its most important characteristics: *Darwin width* and shift relative to the expected Bragg angle. The acentric position and sharpness of the higher harmonics facilitates to detune the second monochromator crystal in order to completely suppress the higher harmonics while hardly affecting the fundamental.

PP-037

New challenges in non-ambient XRD – New solutions from Anton Paar

B. Puhr (Graz/AT), M. Kremer (Graz/AT), A. O. F. Jones (Graz/AT), T. Müller (Graz/AT), B. Schrode (Graz/AT), P. Vir (Graz/AT)

The investigation of powder or bulk materials using non-ambient X-ray diffraction (XRD) is an indispensable technique for material characterization. The number of different non-ambient parameters that can be changed, and experiments that can be performed are quite diverse. With the current portfolio of non-ambient XRD attachments on the market, a wide range of parameters and experimental requirements can be covered. However, new challenges open the demand for new hardware solutions in non-ambient XRD.

With a brand-new combined non-ambient XRD-Raman attachment, we are now able to study different sample materials (such as catalysts) which change their crystal structures and consequently their properties under elevated temperatures with two different methods simultaneously. A dedicated autoclave chamber allows you to perform in-situ monitoring of hydrothermal reactions with conventional laboratory X-ray diffractometers. The autoclave chamber is a unique attachment for XRD studies under steam atmospheres at temperatures up to 210 °C and 20 bar absolute pressure. With the TTK 600 Low-Temperature Chamber (Figure 1) we can now offer smart innovations for battery research. For studying battery materials – that are often air and moisture sensitive – under high and low temperatures, an antechamber lid allows you to load samples directly in a glove box and transport them in a sealed environment to TTK 600, which is already mounted on the diffractometer. On the other hand, using a special battery sample holder (for reflection and transmission geometry) you can now perform in-operando measurements of coin cells under varying temperatures (between -180 °C and 130 °C).

In this presentation, we will introduce latest developments from Anton Paar and will highlight their feasibility for solving new experimental demands.

Figure 1: TTK 600 Low-Temperature Chamber with mounted antechamber lid

Fig. 1

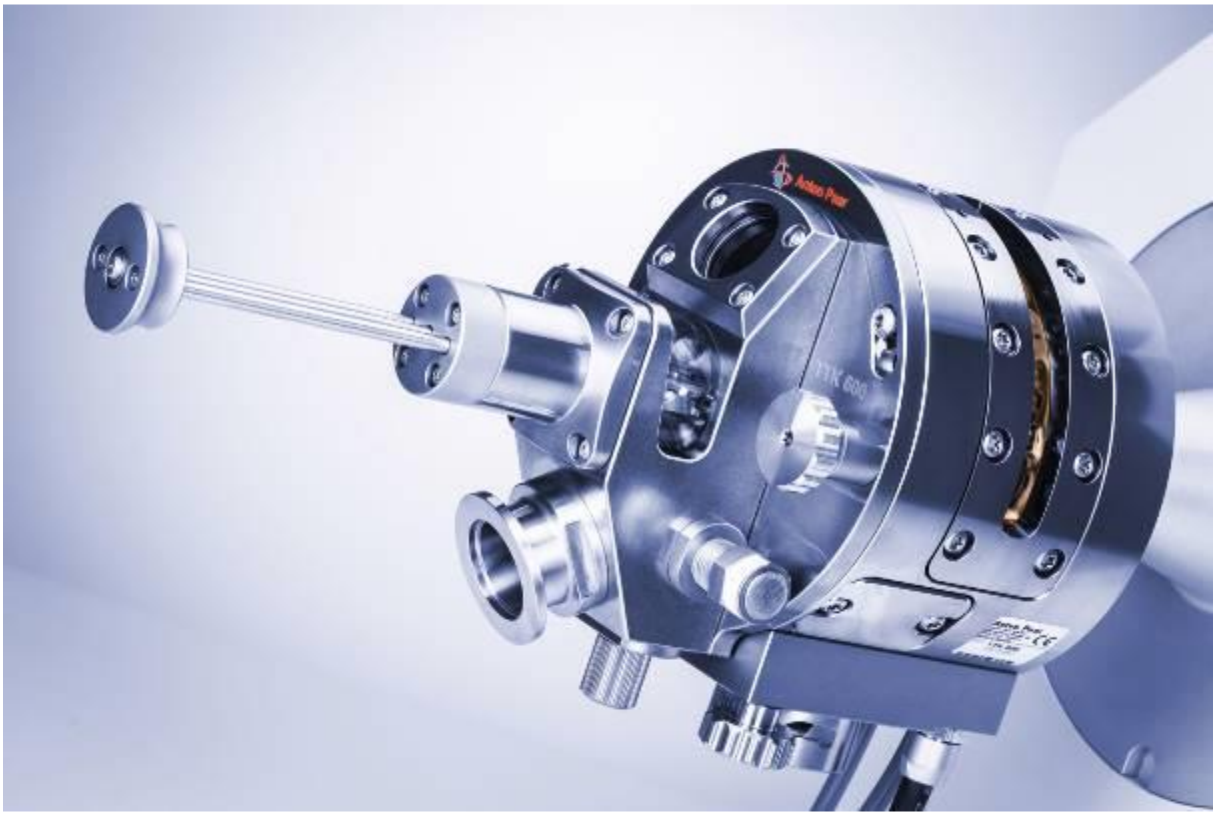

PP-038

The multipurpose powder X-ray diffractometer from Anton Paar

A. O. F. Jones (Graz/AT), M. Kremer (Graz/AT), T. Müller (Graz/AT), B. Puhr (Graz/AT), B. Schrode (Graz/AT), K. Turke (Ostfildern/DE)

With the XRDynamic 500, a multipurpose powder X-ray diffractometer, Anton Paar has recently expanded its portfolio of high-performance X-ray analysis solutions which includes laboratory SAXS instruments, non-ambient XRD attachments, X-ray sources and optics.

XRD is a crucial tool to study the atomic structure of materials such as energy storage materials, pharmaceuticals and catalysts in industrial research as well as in quality control departments. Powder XRD can specifically reveal information about the crystal structure, phase purity, crystallite size, and more, which are fundamental in understanding the physical and chemical properties of these kind of materials.

This contribution will showcase the instruments capabilities in the field of powder XRD, including several application examples and the complementary features with SAXS for both the atomic and nanostructure characterization of state of the art materials.

Fig. 1

PP-039

Area detector prototype for the hot dingle crystal diffractometer HEiDi

M. Meven (Garching/DE, Jülich/DE), R. Engels (Jülich/DE), M. Poli (Garching/DE, Jülich/DE), K. Friese (Jülich/DE), A. Grzechnik (Jülich/DE)

The HEiDi Single crystal diffractometer at the hot source of the neutron source FRM II of the Heinz Maier-Leibnitz Zentrum MLZ in Garching offers high neutron flux down to short wavelengths and large Q range respectively, making it an excellent tool for studies on crystalline and magnetic structural details.

Great efforts have been made to expand the capabilities of the instrument towards new applications, e.g. concerning small samples << 1 mm³ or high pressure experiments [e.g. A. Grzechnik et al, J. Appl. Cryst. 53(1), 1-6 2020, BMBF grant 05K19PA2). These activities are accompanied by developments on new optical components.

A major part of our recent activities focuses on a new position-sensitive 2D detector (PSD) which is under development in collaboration with the Jülich Centre for Neutron Sciences (JCNS) of the Forschungszentrum Jülich. The PSD ^{6}Li glass scintillator prototype covers a sensitive area of 23° x 13° and profits from the high neutron flux in the wavelength range below 1 Angstrom to allow for detection of weak signals up to high Q. In addition, the PSD will allow to establish more efficient sample characterization and data collection in order to tie in with the modern possibilities at X-ray sources.

PP-040

The new PHOTON III HE detector – Unbeatable sensitivity for short wavelength crystallography

T. Stürzer (Karlsruhe/DE), C. Lenczyk (Karlsruhe/DE), A. Abboud (Karlsruhe/DE), M. Adam (Karlsruhe/DE), R. Durst (Karlsruhe/DE)

Several fields in crystallography that greatly benefit from data collected using shorter wavelength X-rays have seen an impressive growth in recent years. This holds for segments such as the development of new heavy-element functional materials, charge-density studies in quantum crystallography and high-pressure studies ranging from geosciences to pharmaceutical research.

All require high precision data from advanced diffraction experiments. However, these hard-radiation experiments can severely suffer from the very low quantum efficiency of many direct photon-counting detectors often making it difficult to obtain sufficiently precise data within reasonable time.

Along a number of selected examples, we will demonstrate how, using the new PHOTON III HE, this problem can be addressed and how the data quality combining a hard radiation source with a modern indirect detector can be improved. The new PHOTON III HE detector benefits from the advanced indirect detection and achieves a very high quantum efficiency for the X-ray energies emitted from Mo-, Ag-, or In-sources.

PP-041

Structural changes of ZrS_2 and HfS_2 during sodium uptake

L. Liers (Kiel/DE), S. Mangelsen (Kiel/DE), M. Behrens (Kiel/DE)

Sodium ion batteries have been investigated intensively for several years now with possible applications in mind such as stationary energy storage of renewable energy sources.[1–3] In order to optimize cell performance and battery aging in those materials, the (de)intercalation processes must be investigated closely. As layered compounds, transition metal dichalcogenides (TMDCs) are suitable host structures for intercalation of alkali metal ions.[4–6] While research of TMDCs has been extensive to date, especially compounds such as ZrS_2 and HfS_2 are underexplored regarding sodium intercalation. Therefore, the influence of different electrolyte salts and solvents on the intercalation mechanism of these TMDCs was studied by combining electrochemical cycling, *ex-situ* X-ray powder diffraction (XRPD) and Rietveld analysis in order to consider the whole picture. We found that the intercalation of sodium into the host structure of ZrS_2 and HfS_2 is indicated by a two-step potential curve using NaOTf in diglyme or $NaPF_6$ in propylene carbonate as electrolytes. Therefore, the intercalation reaction was terminated at different sodiation degrees and characterized by XRPD. Intermediates with unknown structures were assigned to a cointercalation of the electrolyte solvent (diglyme) for all intercalation grades, except for the fully intercalated TMDCs. After a full cycle of discharging and charging the cell one would expect the sodium to be deintercalated completely, but a cointercalated phase could be observed again. During cyclization, a turbostratically disordered structure is formed, resulting in quick fading of the cell capacity. However, it was possible to prevent cointercalation by using other electrolyte solvents (i.e. ethylene carbonate and diethyl carbonate). In conclusion, the choice of electrolyte solvent is crucial with regard to the structural change and the reaction mechanism during electrochemical intercalation, and hence, a critical factor for detrimental structural change. Further investigations of the influence of current rates, electrolyte concentrations and sodiation degrees are planned for the future.

(1) J.-Y. Hwang, S.-T. Myung, Y.-K. Sun, *Chem. Soc. Rev.* **2017**, *46*, 3529–3614.
(2) J. Deng, W.-B. Luo, S.-L. Chou, H.-K. Liu, S.-X. Dou, *Adv. Energy Mater.* **2018**, *8*, 1701428.
(3) P. K. Nayak, L. Yang, W. Brehm, P. Adelhelm, *Angew. Chem. Int. Ed.* **2018**, *57*, 102–120.
(4) J. Rouxel, in *Intercalated Layer. Mater.* (Ed.: F. Lévy), Springer Netherlands, Dordrecht, **1979**, pp. 201–250.
(5) E. A. Marseglia, *Int. Rev. Phys. Chem.* **1983**, *3*, 177–216.
(6) A. Lerf, *Dalton Trans.* **2014**, *43*, 10276–10291.

PP-042

In-house pair distribution function analysis: Sample dependent data collection strategies

K. Krämer (Bremen/DE), T. M. Gesing (Bremen/DE, Bremen/DE), L. Robben (Bremen/DE, Bremen/DE)

Question: Fourier transformed X-ray diffraction data yield the distribution of atomic pair correlation distances in a sample. Opposed to traditional Rietveld refinements of reflections which fulfill Bragg"s equation, the PDF approach additionally utilizes the diffuse scattering between them. The diffuse scattering signal is typically magnitudes lower in intensity than the sharp Bragg reflections and thus has larger statistical uncertainties. Since the error of G(r) contains contributions from every datapoint of the diffraction experiment, it is crucial to minimize the error of each of them.

Methods: We compare different types of samples, from amorphous to highly crystalline and show how the error of their pair distribution functions, as calculated from laboratory diffraction data, behaves over prolonged data collection time. To do this, total scattering data of every sample were collected 168 times for one hour each, resulting in a total of 168 h on a Stoe StadiMP diffractometer, using borosilicate capillaries in Debye-Scherrer geometry (Mo-Kα, $|Q_{max}| = 1340\ pm^{-1}$, Dectris Mythen 1K detector). Data of n-hour measurements were gained by adding intensity of n measurements from $1 \leq n \leq 168$. Calculations of the reduced pair distribution function G(r) were performed using pdfgetx3 [1] .

Results and Conclusion: Each diffractogram was split along the angular axis into several "partial" diffractograms, each extending over 25 °2θ. By only adding intensity data in selected partial diffractograms a variable counting time strategy could be simulated. Through identification of the areas, which contribute the most to the final error, the optimal measurement strategy can be found by minimizing error (Fig. 1) and time. G(r) as calculated from the optimum stitched datasets showed good agreement to those from the optimum unaltered diffractograms.

Funding by the DFG within the project RO5995/2-1 is gratefully acknowledged.

References:

(1) P. Juhas et al., J. Appl. Crystallogr. 46 (2013) 560-566.

Figure 1: Changes of the error of G(r) in various samples

Fig. 1

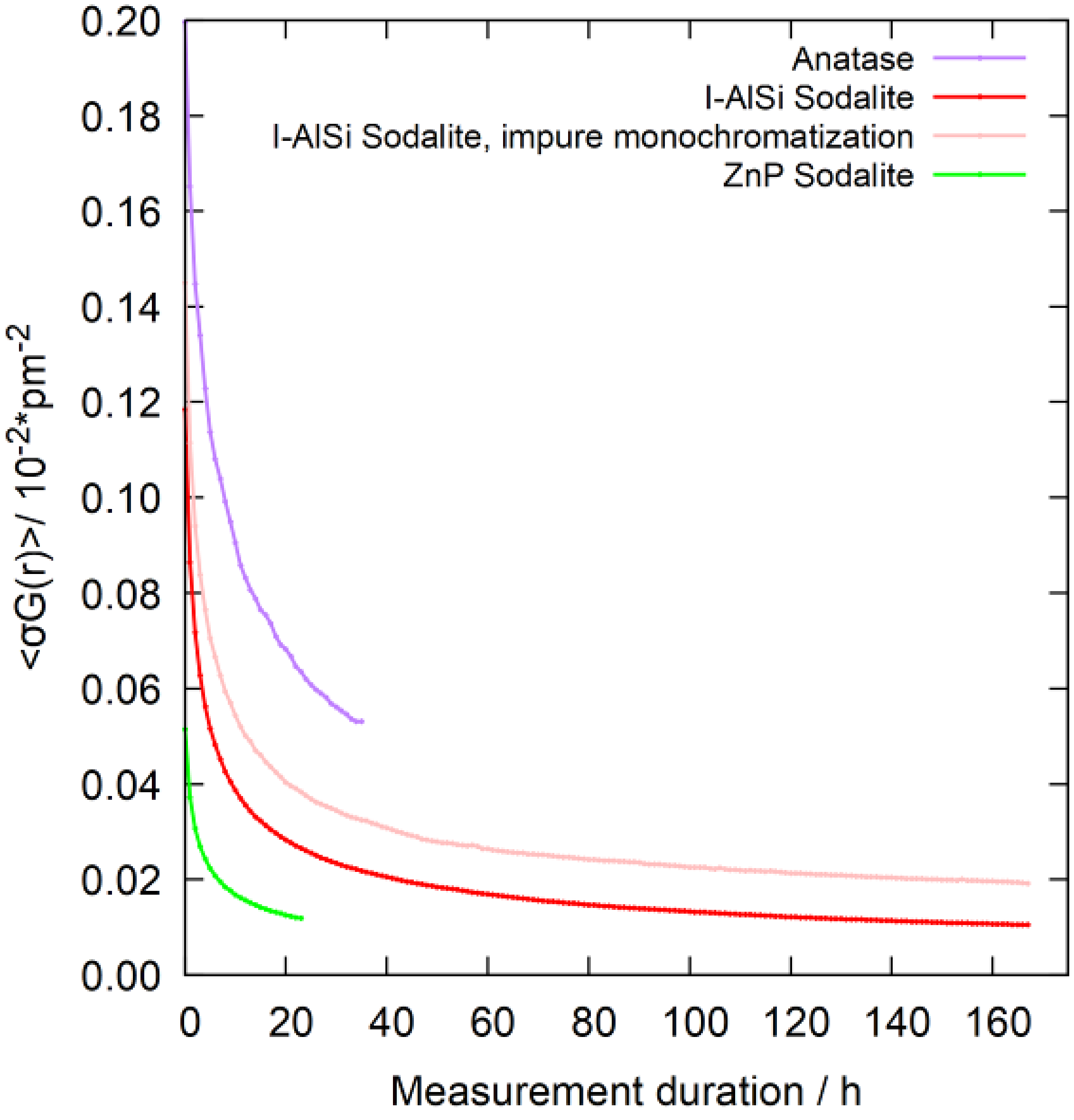
0.20
0.18
0.16
0.14
0.12
0.10
0.08
0.06
0.04
0.02
0.00
<σG(r)>/ 10-2*pm-2
0
20
40
60
80
100
120
140
160
Measurement duration / h
Anatase
I-AlSi Sodalite
I-AlSi Sodalite, impure monochromatization
ZnP Sodalite

PP-043

Using the plate screener XtalCheck-S for high-throughput screening of powder samples

C. J. Schürmann (Neu-Isenburg/DE), P. Le Magueres (The Woodlands, TX/US), M. Del Campo (The Woodlands, TX/US), J. Ferrara (The Woodlands, TX/US), J. Wojciechowski (Neu-Isenburg/DE)

The Rigaku XtaLAB Synergy X-ray diffractometers are versatile instruments. Designed for single-crystal crystallography, they also prove very efficient for powder measurements. Indeed, the powerful and small microfocus X-ray beam, featuring a FWHM between 100 and 150 microns across the Synergy systems family, allows for very small amounts of powder sample (a few micrograms) to be used and leads to the generation of thinner Debye-Scherrer powder rings. Additionally, a beam divergence slit may be used to reduce the divergence of the x-ray beam and decrease the width of the powder rings, improving peak resolution. Lastly, the high sensitivity, very low electronic noise and large dynamic range of the HyPix direct photon counting detectors configured on the XtaLAB Synergy diffractometers enable the use of long exposure times to collect weak reflections at high resolution while preventing pixel overloads for the strong reflections at low resolution.

Various tools for advanced crystallography experiments can also be mounted on the 4-circle Universal Goniometer, such as the XtalCheck-S. The XtalCheck-S is a plate screener originally designed for in-plate screening of protein crystals, but it is also suitable for high-throughput screening of powders, whereby small amounts of sample are put in the wells, instead of protein crystals.

In this presentation, we show how:

- Powder samples are secured in the wells of a crystallization plate.
- The XtalCheck-S and the Rigaku data collection program CrysAlisPro can be used to easily screen powder samples sequentially without user intervention by putting them in queue.
- CrysAlisPro merges images together and reduces the data to intensity vs. 2Θ. The resulting data file is then ready to be imported into your favorite powder processing program for further analysis.

Fig. 1

Fig. 2

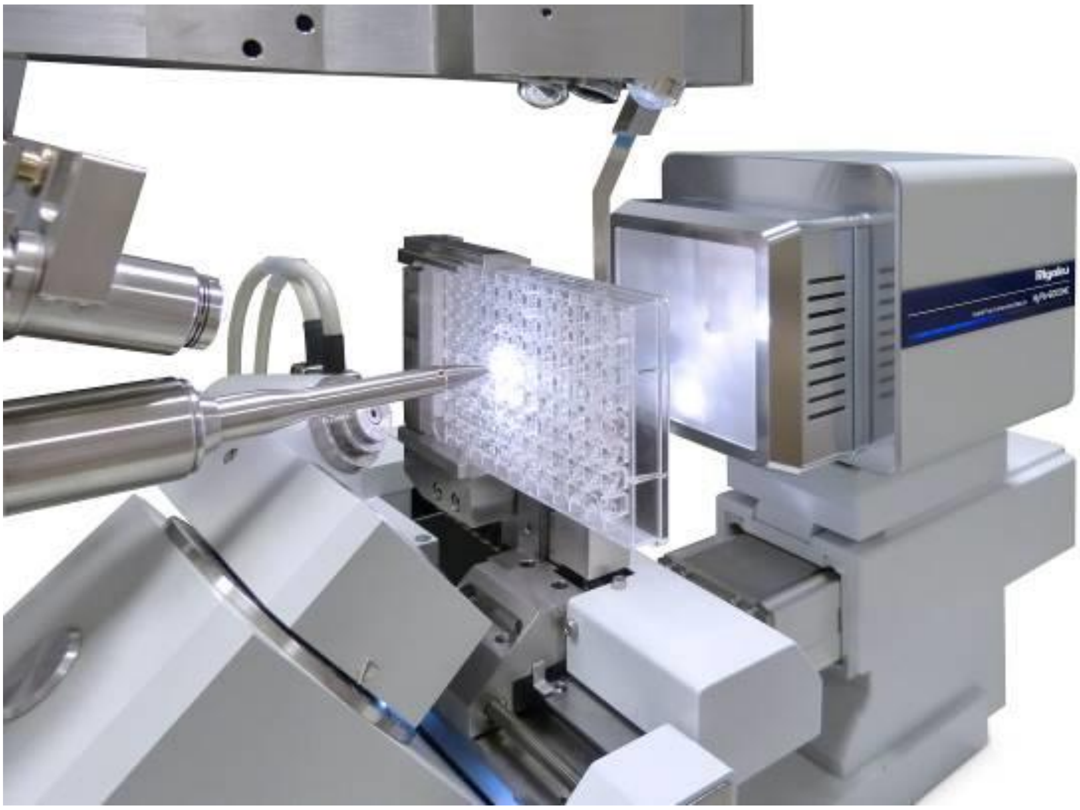

PP-044

Combined Rietveld refinement on X-ray and neutron powder diffraction data: Half or full occupancy of Mg in complex rare-earth perovskite $La_2(Al_{1/2}MgTa_{1/2})O_6$

Y. J. Sohn (Jülich/DE), V. Baran (Garching/DE, Hamburg/DE), R. Gilles (Garching/DE), G. Roth (Aachen/DE), R. Vaßen (Jülich/DE)

New thermal barrier coating (TBC) materials are widely searched to further improve the gas turbine engine efficiency by increasing the hot gas inlet temperature. Suspension plasma-sprayed complex rare-earth perovskite $La_2(Al_{1/2}MgTa_{1/2})O_6$ (LAMT) belongs to one of the promising candidates, and showed a significantly prolonged thermal cycling lifetime [1]. An extensive crystal structure analysis of LAMT has been so far carried out by Rietveld refinements only on X-ray powder diffraction data [2]. However, due to little contrast between the neighbouring Mg and Al elements in the periodic table, the *B*-site cation ordering could not be resolved precisely through X-rays. Therefore, we collected neutron powder diffraction data at the high-resolution powder diffractometer SPODI (FRMII, Garching, Germany) [3]. A combined Rietveld refinement with the software TOPAS [4] using both the X-ray and the neutron powder diffraction data, simultaneously, was then performed. Whereas the heavy element Ta could well be localized through X-rays, substantially different neutron scattering lengths of Mg and Al were beneficial to resolve the *B*-site cation ordering more in detail. Two different structure models in the monoclinic unit cell $P2_1/n$ were refined: 1) full occupancy of Mg on the 2*c*-position, and half occupancy of Al and Ta on the 2*d*-position 2) half occupancy of Mg and Al on the 2*c*-position, and half occupancy of Mg and Ta on the 2*d*-position. A notable discrepancy between the observed and the calculated Bragg peak intensity was detected for the half occupancy of Mg in the unit cell (Fig.1). Hence, a full occupancy of Mg could be successfully pinned down for the rock-salt type ordering of the *B*-site cations in LAMT.

(1) Schlegel N., Sebold D., Sohn Y.J., Mauer G. and Vaßen R. *J. Therm. Spray Technol.* (2015) **24** 1205-1212.
(2) Sohn Y.J., Mauer G., Roth G., Guillon O. and Vaßen R. *J. Am. Ceram. Soc.* (2020) **103** 1404-1413.
(3) Heinz Maier-Leibnitz Zentrum (2015) SPODI: High resolution powder diffractometer. *Journal of large-scale research facilities*, 1, A5.
(4) TOPAS: General profile and structure analysis software for powder diffraction data. (2008) Bruker AXS, Karlsruhe, Germany

Figure 1: Observed (black) and calculated (red) Bragg peak intensity of (011) reflection for a) full Mg occupancy model and b) half Mg occupancy model.

Fig. 1

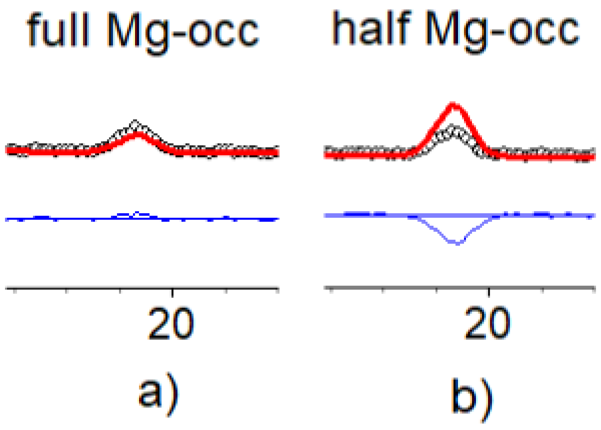

PP-045

Structure and Composition of Size-Tunable Ni–Cu Core–Shell Nanoparticles as analyzed by ASAXS

A. Hoell (Berlin/DE), M. Heilmann (Berlin/DE), R. Wendt (Berlin/DE), C. Prinz (Berlin/DE), R. Bienert (Berlin/DE), J. Radnik (Berlin/DE), A. Guilherme Buzanich (Berlin/DE), F. Emmerling (Berlin/DE)

A facile and efficient methodology is developed for the thermal synthesis of size-tunable, stable, and uniform NiCu core–shell nanoparticles (NPs) for various application in catalysis [1]. Their diameter can be tuned in a range from 6 nm to 30 nm and the Ni:Cu ratio is adjustable in a wide range from 1:1 to 30:1. The NPs are structurally characterized by a method combination of transmission electron microscopy, anomalous small-angle X-ray scattering (ASAXS), X-ray absorption fine structure, and X-ray photoelectron spectroscopy. Here, we focus on the ASAXS method and its ability to analyse nanostructure parts and their compositions at once.

The X-ray absorption edges of Ni and Cu are nearby. Consequently, the strong variation of the anomalous scattering behavior in the energy range from 8 keV to 9 keV is used for this special ASAXS investigation.

ASAXS excluded the hypothesis of a bimetallic core-shell structure and evidenced a core-shell-shell nanostructure. The outer shell is NiO while the inner core is Cu and Ni alloyed. That was proved to be valid for all particle sizes and Ni:Cu ratios. The inner shell is pure Ni dominated.

(1) Heilmann, M. et al, Adv. Eng. Mater. **2022**, 2101308 (1-13).

PP-046

Magnesian Malachite – How much magnesium can we fit in malachite?

S. Mangelsen (Kiel/DE), N. Prinz (Aachen/DE), G. Behrendt (Berlin/DE), M. Zobel (Aachen/DE), M. Behrens (Kiel/DE)

The synthesis of value products like methanol from syngas (CO, CO_2, H_2) is both an established process and a promising route for future energy conversion and storage. [1] The established catalyst system is based on Cu/ZnO, but difficult to the partial reducibility of ZnO under operating conditions. [2] The system Cu/MgO is easier to understand in this respect [3] and a promising single source precursor for these materials could be Mg substituted malachite ($Cu_2CO_3(OH)_2$). Coprecipitation is an established synthetic route for such materials and was employed to explore the synthesis of such magnesian malachites, here subsequent hydrothermal aging was used to foster crystallisation. Herein we focus on the analysis of structural changes with chemical composition, which was analysed by combined refinement of X-ray powder diffraction and pair distribution function data. These precursors are obtained as nanoparticles with mean coherently scattering domain sizes of 20 nm or less, rendering structure analysis more challenging. A maximum of 18 at. % Mg could be incorporated into malachite under retention of phase purity, while up to 37 at. % could be achieved when accepting a phase mixture with a mcguinnessite-like ($MgCuCO_3(OH)_2$) phase. The magnesian malachites show a Vegard-like response to the chemical composition and Mg preferably occupies one of the two available crystallographic sites. A complementary time resolved study of the aging process reveals a progressive incorporation of Mg with time while the crystallinity of the samples increases in the course of 5 – 10 h. [4]

Summarizing, we could prepare promising precursors for Cu/MgO catalysts and yield insight into their structural chemistry. This opens up the way for future studies on the structure chemistry of its activation and behaviour under operating conditions.

(1) G. A. Olah, Angewandte Chemie International Edition **44**, 2636 (2005).
(2) T. Lunkenbein, J. Schumann, M. Behrens, R. Schlögl, and M. G. Willinger, Angewandte Chemie International Edition **54**, 4544 (2015).
(3) L. Pandit, A. Boubnov, G. Behrendt, B. Mockenhaupt, C. Chowdhury, J. Jelic, A.-L. Hansen, E. Saraçi, E.-J. Ras, M. Behrens, F. Studt, and J.-D. Grunwaldt, ChemCatChem **13**, 4120 (2021).
(4) G. Behrendt, N. Prinz, A. Wolf, L. Baumgarten, A. Gaur, J.-D. Grunwaldt, M. Zobel, M. Behrens, S. Mangelsen, Inorganic Chemistry, *Accepted*.

PP-047

Exchange interactions in the iron subsystem in rare-earth orthoferites $RFeO_3$ (R=Ho, Tb)

A. K. Ovsianikov (Aachen/DE), P. Fabrykiewicz (Aachen/DE, Garching/DE), I. A. Zobkalo (Gatchina/RU), W. Schmidt (Grenoble/FR), A. Maity (Garching/DE), K. A. Shaykhutdinov (Krasnoyarsk/RU, Krasnoyarsk/RU), M. Meven (Aachen/DE, Garching/DE), G. Roth (Aachen/DE)

The rare earth orthoferrite family $RFeO_3$ [1-4] (R - a rare earth element) demonstrates a remarkable variety of magnetic properties. Its compounds crystallize in an orthorhombic perovskite structure with the space group *Pnma*. Below the Néel temperature (typically T_N = 600 ÷ 700 K) the iron magnetic moments form a canted antiferromagnetic phase, where the Dzyaloshinsky-Moriya interaction (DMI) is responsible for the canting of the Fe-sublattice. With temperature decrease, increasing exchange interaction between Fe^{3+} and R^{3+} ions leads to a rebalance of energies of the magnetic interactions, which causes spin reorientation transitions. Canted antiferromagnetism and continuous spin reorientation phenomena can be connected with a crystal structure symmetry lowering [5]. Different combinations of DMI and rare-earth ions with different ionic radii and filling of outer shells lead to a variety of magnetic effects.

Thus, it is of significant interest to calculate the values of exchange interactions within the iron subsystem $J_{ij}^{Fe\text{-}Fe}$. The calculation of the values of exchange interaction parameters were performed based on inelastic neutron scattering experiments on spectrometers PUMA@MLZ and IN20@ILL for $TbFeO_3$ [1] and $HoFeO_3$ [3]. The obtained values of exchange interaction parameters are presented in table below together with the literature data. Model with divided interaction along the *b* direction J_b^{Fe} and within the *ac* plane J_{ac}^{Fe} was used. Interaction between next nearest neighbors is denoted as J_{nnn}^{Fe}. Two antisymmetric exchange constants D1 and D2 responsible for the canting along the *b* and *a* directions from the full DM tensor are also given.

Compound/ Magnetic phase	J_b^{Fe}	J_{ac}^{Fe}	J_{nnn}^{Fe}	D1	D2
$TbFeO_3$[1]	4.77(1)	4.55(2)	0.10(2)	0.13(3)	0.10(3)
$YbFeO_3$ [2]	4.675	4.675	0.15	0.086	0.027
$HoFeO_3$ [3]	4.90(5)	4.76(5)	0.150(7)	0.12(2)	0.08(2)
$YFeO_3$ [4]	5.02	4.62	0.22	0.14	0.12

References:

(1) A.K. Ovsianikov, *et al.*, *J. Magn. Magn. Mater.* **563** (2022) 170025
(2) S.E. Nikitin, et al., *Phys. Rev. B***98** (2018) 064424
(3) A.K. Ovsianikov, *et al.*, *J. Magn. Magn. Mater.* **507** (2020) 16 6855
(4) K. Park, *et al.*, *J. Phys. Condens. Matter* (2018) **507** 235802
(5) P. Fabrykiewicz, *et al.*, *Acta Cryst. A***77** (2021) 327

PP-048

Coordination polymers obtained from Berghof reactor

A. Kochel (Wrocław/PL), M. Hołyńska (Wrocław/PL, Marburg/DE)

Coordination polymers may find application as luminescence materials (sensors, diodes), conductors, magnetic materials (magnets, sensors), as well as ion exchagers or for gas storage.

In this study coordination polymers are obtained solvothermally in pressure reactor Berghof. Polydentate ligands are used, mainly aminocarboxylic acids with multiple N/O donor atoms. The starting salts are of d block metals such as Cu or Mn. The synthesis is one-pot and advantegously leads to crystalline products. The sort of obtained products is affected by the sort of reagents, reaction time, reagents" amounts and volumes, pH and temperature values. Thus proper selection of the synthesis parameters allows to predict what type of compound will be obtained and to tune its properties. The figure below shows an example of a luminescent Cu(I,II) coordination polymer with luminescent properties.

Figure 1: 3D coordination polymer with aminocarboxylate ligand and Cu(I,II).

Fig. 1

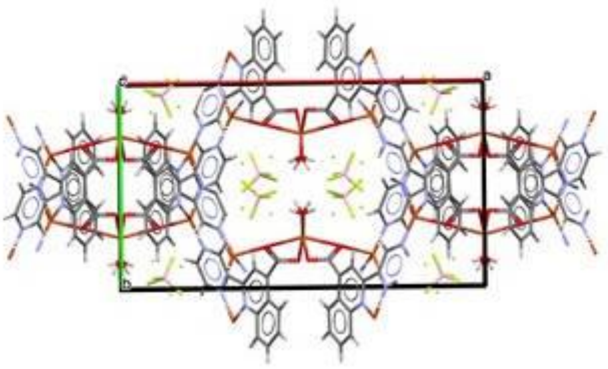

PP-049

Absolute structure determination of a chiral silyl ether by the crystalline sponge method

N. Nöthling (Mülheim an der Ruhr/DE), M. M. Lindner (Mülheim an der Ruhr/DE)

While molecules containing stereogenic carbon atoms are ubiquitous, those with an asymmetrically substituted silicon atom are nonexistent in nature.[1] Molecules that contain chiral silicon atoms are promising for applications in material science, polymer synthesis, as chiral ligands, and in fragrance and medicinal chemistry. The List group has recently reported the first organocatalytic asymmetric approach for the synthesis of enantiopure silanes.[2] Establishing the stereochemistry of the silicon atom was crucial for understanding the reaction mechanism. Here we report our contribution to the first structural investigation of a chiral silyl ether by the crystalline sponge method. The Compound **1** forms an oily liquid at ambient conditions. Various crystallization experiments, e.g. *in situ* crystallization in a glass capillary, the formation of inclusion compounds with as cyclodextrins or tetraaryladamantanes, as well as derivatization to furnish solids were unsuccessful.[3-5] We resorted to the crystalline sponge (CS) method using a metal-organic framework (MOF) as a flexible host structure for the chiral guest molecule.[6-7] After some minor soaking optimization, we were able to include **1** in the crystal sponge. Data collection was performed at the synchrotron beam line P11@PETRAIII, DESY, Hamburg. The results, especially of the absolute configuration determination were verified by seven additional soaking experiments and structure determinations. Moreover, the presence of **1** in the CS was later confirmed by dissolving the investigated crystal and examining it by HPLC analysis. The determined absolute configuration was consistent with computational and experimental CD spectroscopy.

Figure 1: Molecular structure of **1** (left), structure of **1** (colour by elements) included in the MOF (green, middle) and thermal ellipsoids of **1** at 50% probability level (right).

(1) K. Igawa, K. Tomooka, in *Organosilicon Chemistry* (Eds.: T. Hiyama, M. Oestreich), Wiley-VCH Verlag GmbH & Co. KGaA., Weinheim, **2019**, pp. 495-532.
(2) H. Zhou, J. Tae Han, N. Nöthling, M. M. Lindner, J. Jenniches, C. Kühn, N. Tsuji, L. Zhang, B. List, *J. Am. Chem. Soc.* **2022**, 144, 23, 10156–10161.
(3) R. W. Seidel, R. Goddard, N. Nöthling, C. W. Lehmann, *Cryst. Eng. Comm.* **2019**, 21, 3295–3303.
(4) E. Christoforides, A. Papaioannou, K. Bethanis, *Beilstein J. Org. Chem.* **2018**, 14, 838–848.
(5) F. Krupp, W. Frey, C. Richert, *Angew. Chem. Int. Ed.* **2020**, 59, 15875–15879.
(6) Y. Inokuma, S. Yoshioka, J. Ariyoshi, T. Arai, Y. Hitora, K. Takada, S. Matsunaga, K. Rissanen, M. Fujita, *Nature* **2013**, 495, 461–466.
(7) L. Rosenberger, C. von Essen, A. Khutia, C. Kühn, K. Georgi, A. K. Hirsch, R. W. Hartmann, L. Badolo, *Eur. J. Pharm. Sci.* **2021**, 164, 105884.

Fig. 1

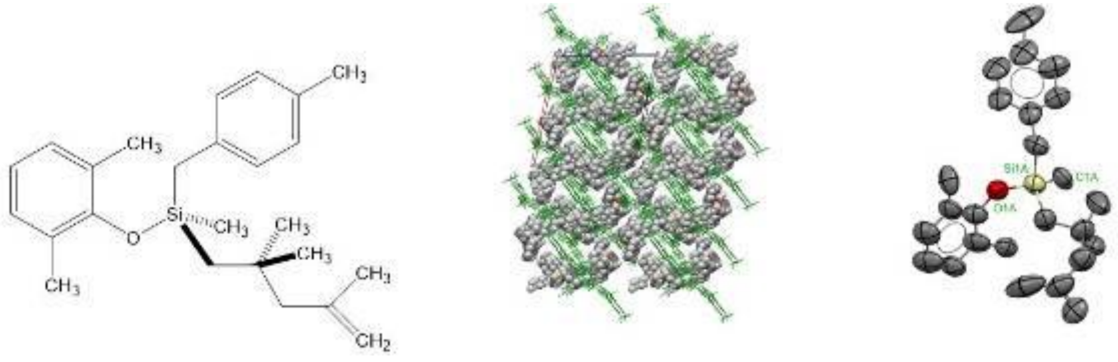

PP-050

Structural systematics of benzamides and carboxamides

J. Gallagher (Dublin/IE), I. Osman (Dublin/IE)

Series of halogenated benzamides and ferrocenylcarboxamides will be presented by highlighting relationshipsin several isomer grids using a variety of physicochemical techniques [1]. The crystal structures of severalstructures will be highlighted including *N*-(ferrocenylmethyl)-pentafluorobenzene-carboxamide **4f**.

Figure legend: ORTEP diagram of **4f** with displacement ellipsoids at the 30% probability level.

Three CPK packing diagrams of the $(Fc...C_6F_5...)_n$ 1D stacking (*a*) as a chain with amides (ball and stick) and the space where the Fc (ferrocenyl) moieties occupy, (*b*) an expanded view with C_6F_5 (in **green**) and (c) with some C_6F_5 groups as ball and stick.

Probing the Electronic Properties and Interaction Landscapes in a Series of N-(Chlorophenyl)pyridinecarboxamides

(1) John F. Gallagher*, Niall Hehir, Pavle Mocilac, Chloé Violin, Brendan F. O"Connor, Emmanuel Aubert, Enrique Espinosa, Benoît Guillot, and Christian Jelsch
(2) *Crystal Growth & Design* 2022, 22, 5, 3343-3358 (Article)

Fig. 1

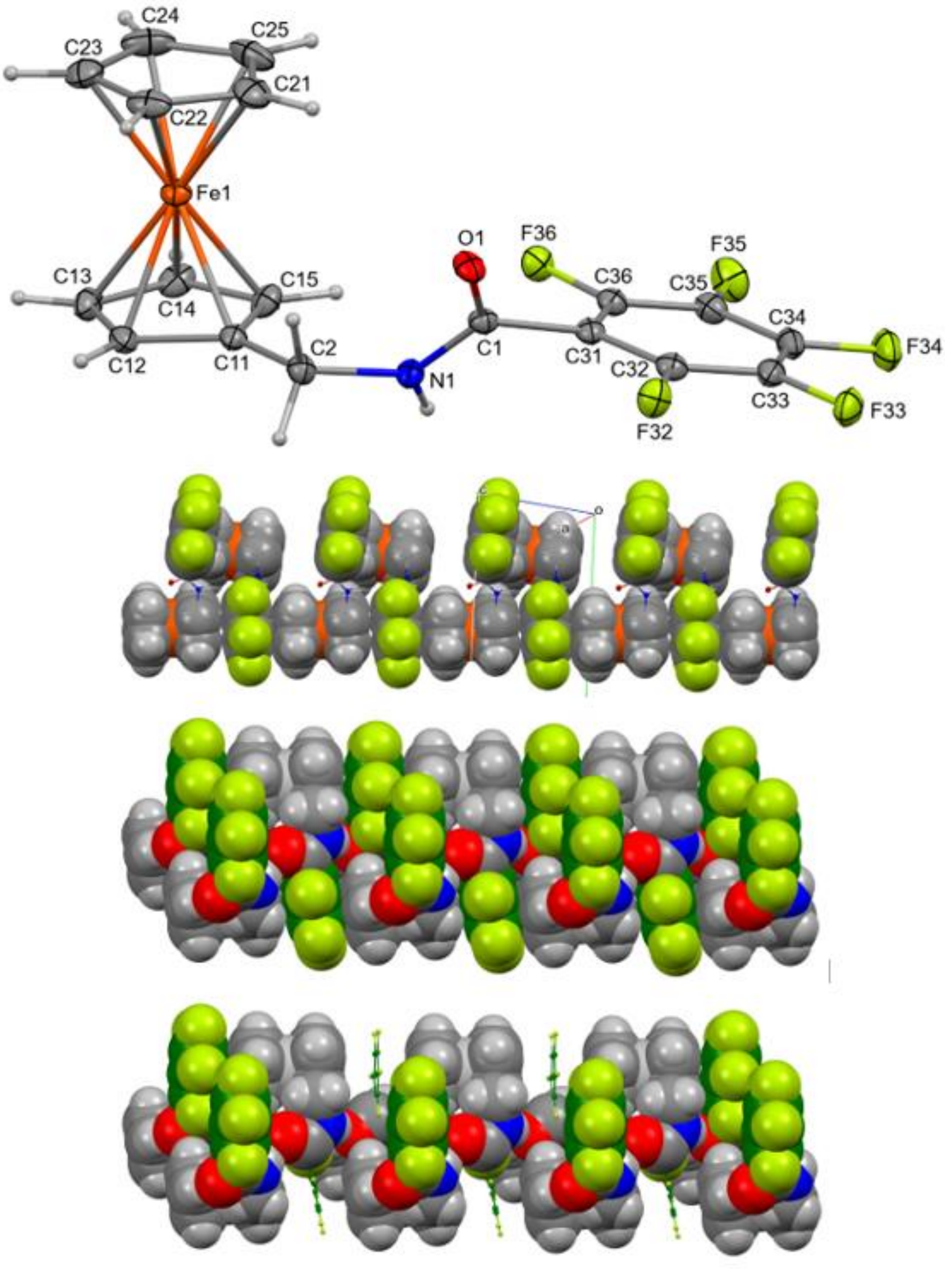
C24
C25
C23
C21
C22
Fe1
O1
F36
F35
C36
C35
C13
C14
C15
C34
F34
C2
C1
C31
C32
C12
C11
N1
C33
F33
F32

PP-051

Leucopterin, the white pigment in the wings of butterflies: crystal structure analysis by combination of powder and single-crystal diffraction with solid-state NMR and DFT-D optimisations

F. Bravetti (Turin/IT, Frankfurt am Main/DE), L. Tapmeyer (Mannheim/DE), K. Skorodumov (Frankfurt am Main/DE), E. Alig (Frankfurt am Main/DE), S. Habermehl (Frankfurt am Main/DE), R. Hühn (Frankfurt am Main/DE), S. Bordignon (Turin/IT), A. Gallo (Turin/IT), C. Nervi (Turin/IT), M. R. Chierotti (Turin/IT), M. U. Schmidt (Frankfurt am Main/DE)

Leucopterin (LCPT), $C_6H_5N_5O_3$, member of the class of pteridines, is the white pigment in the wings of *Pieris brassicae* butterflies. LCPT crystallises in two phases: room- and high-temperature, which differ for the content of water, *i.e.* hemihydrate and anhydrate, respectively. The crystal structures of LCPT were investigated combining powder and single-crystal diffraction data with solid-state NMR (SSNMR) and DFT-D calculations.

The crystal structure of the hemihydrate was solved by single-crystal XRD, but hydrogen atoms positions were still uncertain. Furthermore, LCPT is characterised by tautomerism: indeed, at least 17 possible tautomers can exist. The tautomeric state was elucidated by multinuclear high-resolution SSNMR experiments and DFT-D optimisations. ^{15}N CPMAS spectra showed the presence of one NH_2 and three NH groups, and one unprotonated N atom, which agreed with the ^1H MAS and ^{13}C CPMAS spectra. This information reduced the number of possible tautomers to only 2. The final tautomeric state was assessed analysing ^1H-^1H atom proximities in the ^1H DQ-MAS 2D spectrum. The results of lattice energy minimisations with DFT-D, performed independently of SSNMR on the 17 most chemically reasonable tautomeric forms, were in agreement.

Concerning LCPT anhydrate, its crystal structure could be solved from powder data, after heating the sample to 250 °C. Temperature-dependent X-ray powder diffraction showed an irreversible continuous shift of the reflections upon heating, which reveals that LCPT is a variable hydrate with a continuous transition from the hemihydrate to the anhydrate. The crystal structure of the anhydrate was solved by FIDEL (Acta Cryst., 2022, B78, 195–213), performing a local fit starting from the structure of the hemihydrate. ^1H DQ-MAS 2D spectrum of the anhydrate confirmed that the crystal structure and the hydrogen bond network of the hemihydrate are maintained also in the anydrate.

PP-052

Crystal structure of a propyl 4-((1-(2-methyl-4-nitrophenyl)-1H-1,2,3-triazol-4-yl) methoxy) benzoate-copper-di-chloro complex

M. Hakimov (Namangan/UZ), A. Tojiboev (Tashkent/UZ), I. Ortikov (Tashkent/UZ)

1,2,3-Triazole derivatives are ligands with the applications for example: in anticorrosive agents, agrochemicals and triazole-based coordination compounds have been extensively investigated [1]. The complex of propyl 4-((1-(2-methyl-4-nitrophenyl)-1H-1,2,3-triazol-4-yl) methoxy) benzoate ligand with copper was synthesized and its structural characteristics were determined.

In this work, we succeeded in synthesizing the corresponding 1,2,3-triazole derivative by coupling m-oxybenzoic acid propargyl ether with some 2-substituted-4-nitrophenylazide [2]. As a result, consecutive nitrogen chains in the central ring of that"s molecule are active in forming a complex bond both in terms of the electrons of the element atom and in terms of the outer shell of the molecule.

In contrast to others complex, two molecules of organic ligand of 1H-1,2,3-triazole type are connected trans to copper metal through a coordination bond (figure).

The crystal structure of title compound displays monomeric units and a ligand-metal ratio of 2 : 1, with a square planar geometry around the metal center.

(1) X.-H. Zhou et al., CrystEngComm 11 (2009), p.1964.
(2) Ortikov I.S. et al., 10th -Republic to the scientific conference of young chemists, Namangan, Uzbekistan, November 2022, p.40.

Fig. 1

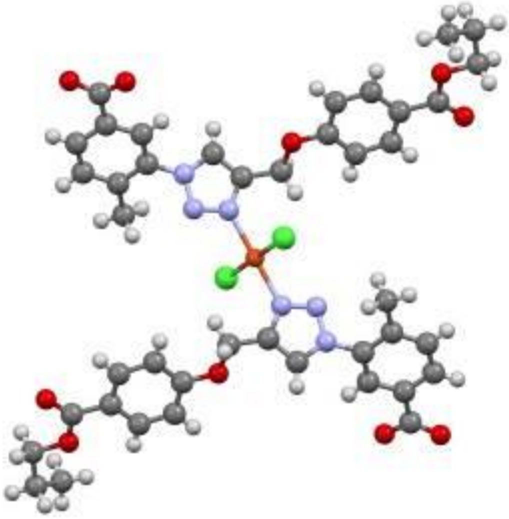

PP-053

Tracking the annealing-induced segregation and ordering of thermoplastic polymer chains by total scattering

M. Terban (Stuttgart/DE), E. Pöselt (Lemförde/DE), M. Malfois (Barcelona/ES), B. Hinrichsen (Ludwigshafen/DE), R. E. Dinnebier (Stuttgart/DE)

The structuring of polymer segments within polyurethanes elastomers has been a longstanding point of interest in the development of industrial thermoplastics for many decades. Different components in the product phase segregate to form a heterogeneous distribution of so-called hard and soft phases. The resulting materials have been most typically studied using small-angle scattering to detect phase segregation and measure the relative distribution of hard regions. The wide-angle region, however, has been less effectively utilized, due primarily to the small size and relatively poor ordering of molecules within the domains, often on the scale of only several nanometers. Here, we seek to investigate the structuring of polymer segments within these small domains using a total scattering approach.

This study considered a set of polyurethane samples with varying concentrations of hard and soft segment components and subjected to a range of annealing conditions to promote segregation and ordering. We utilized both small-angle and wide-angle scattering regimes to investigate the nature of phase segregation and intra-domain structuring. The results are then contextualized in comparison to the resulting changes in physical, thermal and mechanical properties of the products.

Using pair distribution function analysis, we are able to distinctly observe changes in the local molecular ordering coupled to the phase segregation as a function of temperature. By further extracting the changing signal, we could begin to probe the nature of the structural ordering using distinct structure models. While the idea of a unique structure to describe such localized ordering is not likely well-defined, this process helps us to more directly test qualitative ideas about the nature of the para-crystalline state of the material.

PP-054

Obtaining and analysing organic crystals and co-crystals

M. Nicolov (Timisoara/RO)

Question: A new type of crystals of betulinic acid + vitamin C and fisetin + vitamin C in isopropyl alcohol/ methanol / ethanol monosolvate was obtained in a hydrothermal experiment, with superior antitumoral activity on various cell lines.

Materials: All reagents used in the assay procedures were of analytical standard and were purchased from Sigma-Aldrich, Germany and Chemical Company SA, Iasi, Romania.

Methods:

- ***Synthesis of*** *(BA_VC or FISETIN-VC in IPA/EtOH/MeOH)* ***cocrystals from isopropyl alcohol / methanol/ ethanol*** was done by using BA, FISETIN ,vit.C and the solvents. The mixture was heated closed to the boiling temperature of the solvents, then cool slowly to room temperature protected from light. The formation of the first crystals was after 10 days
- ***Physico chemical properties***: The morphology of the samples were determined by **Scanning electron microscopy (SEM)** and the thermal response of each product was performed via **differential scanning calorimetry (DSC)**. Each sample was measured in the temperature interval of 25-350 °C at a heating rate of 10 °C/min under constant argon flow. ***X-ray powder diffraction and FT-IR*** spectra were realized in order to determine the structure of the new synthesized crystals.
- ***Antioxidant activity*** of the compound was evaluated by **DPPH** radical scavenging assay. A solution of radical DPPH was used as a standard antioxidant stock solution and a solution of ascorbic acid (0.167 mmol·L-1) in ethanol 96% (v/v) was used as etalon. Samples were analyzed by using a Uvi Line 9400 Spectrophotometer from SI Analytics at 516 nm for 20 minutes.
- ***Determination of cell viability*** was performed on several cancerous cell lines (MCF7, MDA-MB-231, HeLa, A375, B164A5 and B16F0) and non-tumorigenic human cells (HaCat) in order to verify the cytotoxic effects of the BA-VC IPA / EtOH / MeOH. The cells were stimulated with different concentrations (3, 10 and 30 µM) and incubated at three intervals of time. The antiproliferative activities of the tested samples were determined by **MTT** and **Alamar blue** assay and the absorbance measured using a xMark™ Microplate Spectrophotometer (Biorad) at 570 nm and 600 nm (reference) wavelengths.

Results: SEM images show morphological changes between the pure ingredients and their co-crystallization product and we can indicate the formation of a new phase. Different solvent molecules BA: VC and FISETIN:VC obtained in MeOH / EtOH// IPA result in the dissimilarities among patterns were needle-shaped or plate-shaped.

XRPD spectra of cocrystals differ significantly from the ones recorded for pure ingredients, that suggest the formation of cocrystals instead of physical mixtures.

Differential scanning calorimetry shows a single broad peak corresponding to the water loss below 100 C for all types of cocrystals, in EtOH, MeOH and IPA. In all casses we can notice the disappearance of the pure substances" characteristic peaks .

Conclusions: Physico chemical analysis (optical, SEM, DSC, XRPD, FTIR) antioxidant and in vitro activity of the new compounds obtained gave us the information that were formed new compounds with improved characteristics and superior antitumoral activity when compared with the components.

References:

(1) W.Tang, N.H.Chen, G.Q. Li, G.C.Wang and Y.L.Li, 2014, Crystal structure of betulinic acid methanol monosolvate ,*Acta Cryst.,* E70, 01242-01243.

(2) R. Dovesi, V. R. Saunders, C. Roetti, R. Orlando, C. M. Zicovich-Wilson, F. Pascale, B. Civalleri, K. Doll, N. M. Harrison, I. J. Bush, P. D'Arco, M. Llunell, M. Causa and Y. Noel CRYSTAL14, (2014*) CRYSTAL14 User's Manual*. University of Torino, Torino.

(3) C. Jelsch, B. Guillot, A. Lagoutte, C. Lecomte, 2005,Advances in protein and small charge-density refinement methods using MoPro, J. Appl. Crystallogr., 38, 38-54.

PP-055

Polymorphism in toxic medications: exploring the crystal chemistry of lead and cadmium naproxen

G. Nénert (Almelo/NL)

Sodium naproxen is widely used as a non-steroidal anti-inflammatory active pharmaceutical ingredient (API). The crystal structure of this API has been reported back in 1990 [1]. Despite 3 decades of research on this API, only one single polymorph has been reported. On the other hand, physicochemical stability may become a serious problem during new drug development and thus pseudo-polymorphism have been widely investigated for sodium naproxen. So far, 4 hydrates have been reported and characterized [2]. So, while the pseudo-polymorphism is rather rich, polymorphism is unusually simple with only one known representative. This is a rather unusual case as polymorphism for APIs tends to be rather rich [3]. With that in mind, we have started exploring other salts of naproxen, which could have been within Severus Snape"s potion class: lead and cadmium salts.

While cadmium exhibits only one hydrated form, lead naproxen exhibits a very rich polymorphism with one hydrate as illustrated in Fig. 1. All polymorphic structures have been determined using high resolution powder diffraction and are discussed in light of the already exhibiting sodium naproxen.

Figure 1: Temperature dependence of Pb[C14H13O3]2.xH2O illustrating the temperature stability range of the 4 polymorphs and of its dihydrate

(1) Kim, Y. B.; Park, I Y; Lah, W R *Arch. Pharm. Res.*, **1990**, *13(2)*, 166 – 173.
(2) Bond, A. D.; Cornett, C.; Larsen, F. H.; Qu, H.; Raijada, D.; Rantanen, J. *IUCrJ*, **2014**, *1*, 328 – 337.
(3) Lee, E. H. *Asian Journal of Pharmaceutical Sciences*, **2014**, *9*, 163 – 175.

Fig. 1

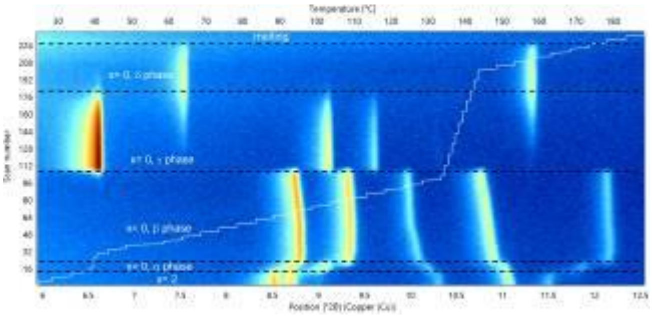

PP-056

Pillarplex rotaxanes with α,ω-Dicarboxylic acids

A. Heidecker (Garching/DE), A. Pöthig (Garching/DE)

The class of supramolecular organometallic complexes (SOCs)[1] are discrete organometallic assemblies with structure-dictating metal-carbon bonds. One example are the Pillarplexes $[M_8L_2](X)4$ bearing macrocyclic ligands (L), which are connected linear by eight metal ions (M = Au, Ag)[2]. The pillarplexes exhibit tuneable solubility, intrinsic luminescence and the possibility for rim-functionalization.[3-4] Furthermore, their tubular cavity allows the shape-selective encapsulation of linear guest molecules and enables the pillarplexes to form pseudorotaxanes or rotaxanes either achieved by capping the guest with bulky stopper motifs or introducing sterically demanding guests.[4-5] The dicarboxylic acids – exceeding the static pillarplex pore opening (4.3 Å) with a diameter of 5.4 Å – were chosen as potential guest molecules to form rotaxanes upon conformational change of the pillarplex (e.g. breathing). Here, a series of pillarplex rotaxanes with encapsulated α,ω-diacids is presented.

Figure 1: Structural and general composition of pillarplex rotaxanes formed by encapsulation of linear α,ω-dicarboxylic acids.

The successful uptakeStructural and general composition of pillarplex rotaxanes formed by encapsulation of linear α,ω-dicarboxylic acids. of dicarboxylic acids was validated by NMR, IR spectroscopy, elemental analysis and their host-guest complex formation was studied by ^{1}H NMR titration. The solid-state structures were solved by single crystal X-Ray diffraction and evaluated towards the guest encapsulation and their non-covalent interactions including the influence on the crystal packing. Indeed, intermolecular interactions which are highly depending on the length of the encapsulated diacids.

(1) A. Pöthig, A. Casini, *Theranostics,* 2019, **9**, 3150.
(2) P. J. Altmann, A. Pöthig, *J. Am. Chem, Soc.,* 2016, **138**, 13171.
(3) S. Guan, T. Pickl, C. Jandl, L. Schuchmann, X. Zhou, P. J. Altmann, A. Pöthig, *Org. Chem. Front.,* 2021, **8**, 4061.
(4) P. J. Altmann, A. Pöthig, *Angew. Chem. Int. Ed.,* 2017, **56**, 15733.
(5) A. A. Heidecker, M. Bohn, A. Pöthig, *Z. Kristallogr. - Cryst.,* 2022, **237**, 167.

Fig. 1

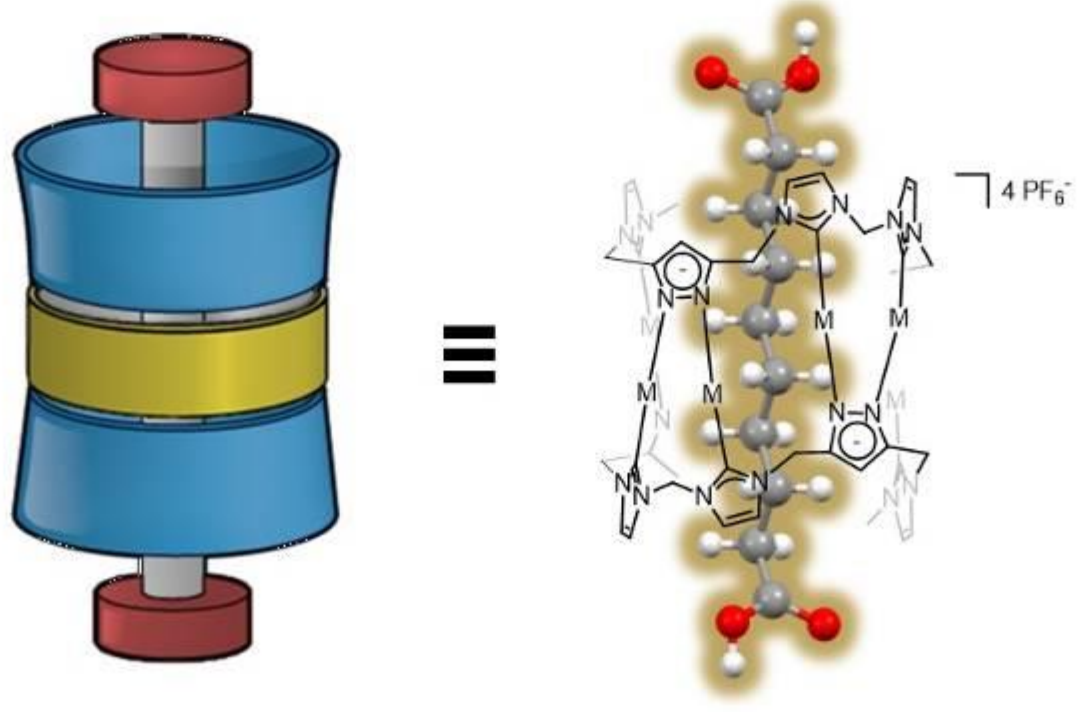

PP-057

A series of four isostructural copper halogenido pentelates with interesting optical properties

J. Möbs (Marburg/DE), R. James (Tempe, AZ/US), P. Epure (Marburg/DE), J. Heine (Marburg/DE)

Heavy group 15 halogenido metalates are an emergent class of materials for semiconductor applications as they show similar properties as the famous lead halide perovskites, which are intensely discussed for photovoltaic and LED applications[1,2] while being generally non-toxic.[3] They can be roughly divided into two groups: Compounds with heavy halides, especially iodido bismuthates, that feature small bands gaps suitable for solar absorption but rarely show photoluminescent behavior[4] and compounds with lighter halides, like bromido antimonates or chlorido antimonates and bismuthates, that show larger band gaps but strong photoluminescence.[5] The optoelectronic properties of these compounds can be tuned by the incorporation of transition metals and especially the addition of copper into iodido bismuthates has been shown to further narrow their band gaps improving their absorption properties.[6] Although halogenido cuprates are renowned for their luminescent properties[7], these copper iodido bismuthates rarely show them as well.

Here, we present a series of four isostructural metalates, [pizim][ECuX$_6$] (pizim = 1,4-di(propan-2-ylidene)piperazine-1,4-diium; E = Sb, Bi; X = Br, I), which are stabilized by the unusual pizim-di-cation, formed *in situ* from piperazinium and acetone. All compounds show strong absorption in the visible range with optical band gaps from 1.77 eV for the Bi/I-compound to 2.70 eV for the Sb/Br-variant. Additionally, they feature complex photoluminescence patterns of multiple overlapping peaks at room temperature and all but the Bi/I-compound also at 85 K upon excitation at 405 nm. The shape of the absorption as well photoluminescence spectra point towards a combination of classical band gap transitions and excitons.

Figure 1: Tauc-plots of diffuse reflectance uv-vis data of all four substances as well as an excerpt of the crystal structure.

References:

(1) Jena, A. K.; Kulkarni, A.; Miyasaka, T. Halide Perovskite Photovoltaics: Background, Status, and Future Prospects. *Chem. Rev.* **2019**, *119* (5), 3036–3103. DOI: 10.1021/acs.chemrev.8b00539.
(2) Quan, L. N.; Rand, B. P.; Friend, R. H.; Mhaisalkar, S. G.; Lee, T.-W.; Sargent, E. H. Perovskites for Next-Generation Optical Sources. *Chem. Rev.* **2019**, *119* (12), 7444–7477. DOI: 10.1021/acs.chemrev.9b00107.
(3) Mohan, R. Green bismuth. *Nat. Chem.* **2010**, *2* (4), 336. DOI: 10.1038/nchem.609.
(4) Jain, S. M.; Phuyal, D.; Davies, M. L.; Li, M.; Philippe, B.; Castro, C. de; Qiu, Z.; Kim, J.; Watson, T.; Tsoi, W. C.; Karis, O.; Rensmo, H.; Boschloo, G.; Edvinsson, T.; Durrant, J. R. An effective approach of vapour assisted morphological tailoring for reducing metal defect sites in lead-free, $(CH_3NH_3)_3Bi_2I_9$ bismuth-based perovskite solar cells for improved performance and long-term stability. *Nano Energy* **2018**, *49*, 614–624. DOI: 10.1016/j.nanoen.2018.05.003.
(5) Li, Z.; Li, Y.; Liang, P.; Zhou, T.; Le Wang; Xie, R.-J. Dual-Band Luminescent Lead-Free Antimony Chloride Halides with Near-Unity Photoluminescence Quantum Efficiency. *Chem. Mater.* **2019.** DOI: 10.1021/acs.chemmater.9b02935.
(6) Möbs, J.; Gerhard, M.; Heine, J. $(HPy)_2(Py)CuBi_3I_{12}$, a low bandgap metal halide photoconductor. *Dalton Trans.* **2020**, *49* (41), 14397–14400. DOI: 10.1039/D0DT03427D.
(7) Artem"ev, A. V.; Davydova, M. P.; Hei, X.; Rakhmanova, M. I.; Samsonenko, D. G.; Bagryanskaya, I. Y.; Brylev, K. A.; Fedin, V. P.; Chen, J.-S.; Cotlet, M.; Li, J. Family of Robust and Strongly Luminescent CuI-Based Hybrid Networks Made of Ionic and Dative Bonds. *Chem. Mater.* **2020**, *32* (24), 10708–10718. DOI: 10.1021/acs.chemmater.0c03984.

Fig. 1

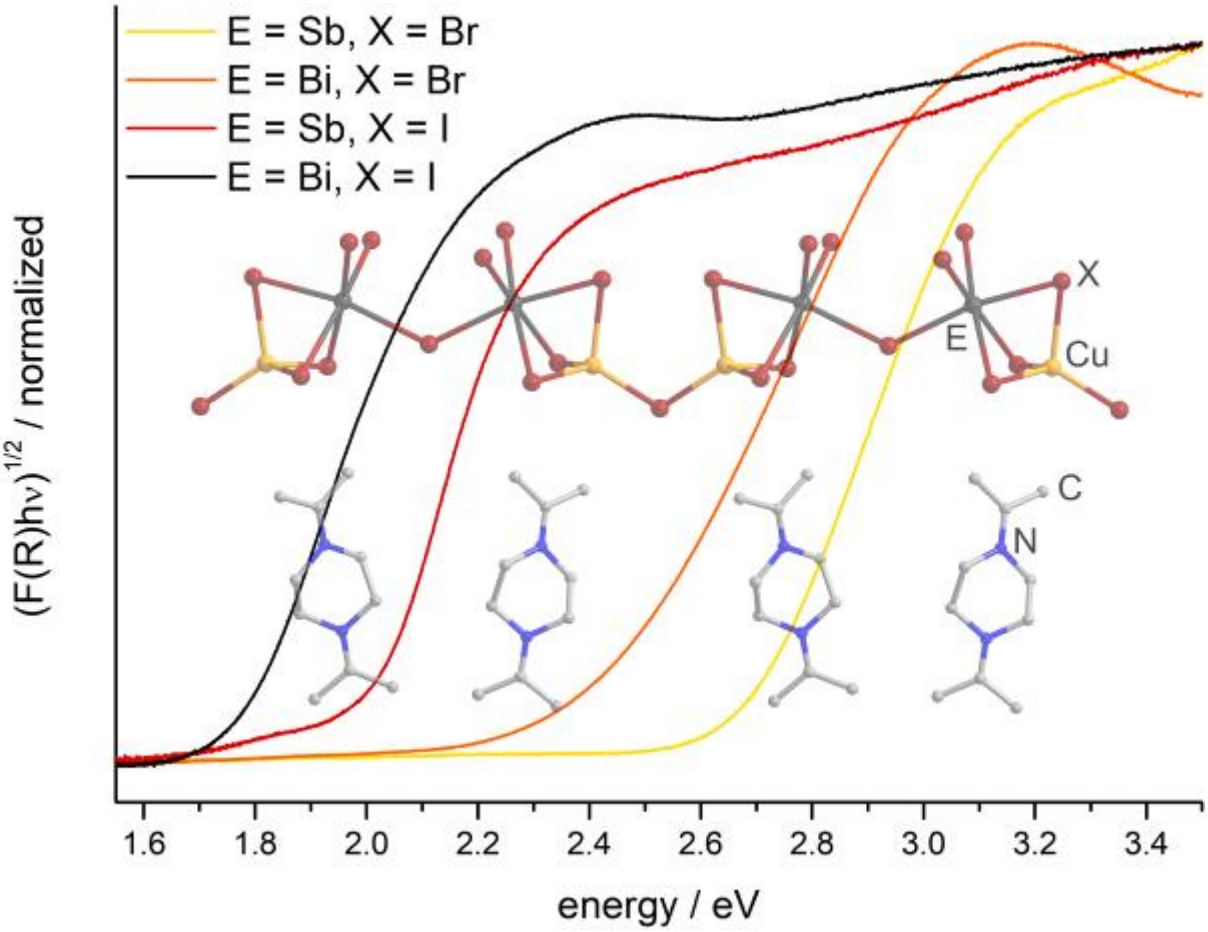
E = Sb, X = Br
E = Bi, X = Br
E = Sb, X = I
E = Bi, X = I
X
E
Cu
C
N
(F(R)hν)^1/2 / normalized
1.6
1.8
2.0
2.2
2.4
2.6
2.8
3.0
3.2
3.4
energy / eV

PP-058

Experimental and theoretical study of solid solutions in the system $Nd_3Ga_5O_{12}$ – $Gd_3Ga_5O_{12}$

S. Tovstopyat (Moscow/RU), N. Eremin (Moscow/RU), M. Nickolsky (Moscow/RU)

Compounds with a garnet structure are promising crystalline matrices for the disposal of long-lived radioactive waste. The concentration of U and Th in natural garnets is very low and does not exceed fractions of a percent; therefore, special theoretical and experimental studies of artificial phases are required to select the compositions of actinide matrices with a garnet structure.

Rare earth elements are analogs of actinides in many respects. The aim of this work was the synthesis of rare-earth gallate ceramics with a garnet structure and preliminary modeling of the structural characteristics of compounds of given compositions.

Among rare-earth garnets, phases of aluminate, gallate, and ferrite compositions are of particular interest, where Al^{3+}, Ga^{3+}, Fe^{3+} occupy tetrahedral and octahedral positions. The data on rare earth Nd-Gd gallates solid solution with a garnet structure is absent. Hence, the task was to obtain ceramics of the equimolar composition of neodymium-gadolinium gallate $Nd_{1.5}Gd_{1.5}Ga_5O_{12}$.

Structure characteristic of $(Nd,Gd)_3Ga_5O_{12}$ garnet have been calculated by means on GULP software (Gale and Rohl, 2003). In addition, various thermodynamic parameters were obtained. The unit cell parameter was also obtained using the multiple linear regression equation.

Ceramics was obtained by solid-phase sintering of Nd2O3, Gd2O3 and Ga2O3. The reagents were ground for two hours, pressed into tablets, and sintered for 5 hours at a temperature of 1400°C. After receiving, the samples were studied by means of a powder diffraction and a scanning electron microscopy.

Bibliography:

(1) Gale J. D., Rohl A. L. The general utility lattice program (GULP) //Molecular Simulation. - 2003. - T. 29. - No. 5. - S. 291-341.

PP-059

Preparation and characterization of apremilast multicomponent solid systems

Y. Naumkina (Prague/CZ, Tomsk/RU), J. Čejka (Prague/CZ), E. Korotkova (Tomsk/RU)

Introduction Apremilast belongs to Class IV of the Biopharmaceutical Classification System with low water solubility (7 mg/ml). It is one of the water-insoluble drugs that face poor solubility leading to low permeability. The cocrystallisation method is believed to modify the chemical and physical properties while retaining the biological function of the chemical properties. According to the literature data, up to 20 multicomponent structures of Apremilast with different aromatic coformers were produced by the method of slow evaporation from solution and investigated.[1,2]

Objectives: In this work, we applied cocrystallization methods (the slow evaporation from solution, sublimation and mechanochemical cocrystallization techniques) for the preparation of Apremilast new solid forms and structure characterization.

Materials & methods: Multicomponent solid systems were prepared with various coformers (selected from the GRAS list) which have high water solubility by the different cocrystallization techniques. The obtained cocrystals were characterized by Single-Crystal X-ray Diffraction (SCXRD). Pharmaceutical significant properties such as solubility, stability and dissolution rate were evaluated.

Results: The important physical and chemical properties of the new forms of Apremilast were evaluated to acknowledge whether the new solid system provides the necessary improvements.

Conclusion: The molecules of Apremilast and the guest molecule are preferentially retained by aromatic-aromatic interactions in the obtained solid forms.

(1) Dudek, M. K., Kostrzewa, M., Paluch, P., & Potrzebowski, M. J. π-Philic Molecular Recognition in the Solid State as a Driving Force for Mechanochemical Formation of Apremilast Solvates and Cocrystals. Crystal Growth & Design, 2019 18(7), 3959–3970.

(2) Dudek, M. K., Wielgus, E., Paluch, P., Śniechowska, J., Kostrzewa, M., Day, G. M., Bujacz, G. D., & Potrzebowski, M. J. Understanding the formation of apremilast cocrystals. Acta Crystallographica Section B Structural Science, Crystal Engineering and Materials, 2019, 75(5), 803–814.

PP-060 - PP-069

Abstracts siehe Seite 65 ff.

PP-070

Crystallographic studies of MST3 kinase inhibitor complexes reveal unique ligand-induced structural variations

D. I. Balourdas (Frankfurt am Main/DE, Frankfurt am Main/DE), M. Rak (Frankfurt am Main/DE, Frankfurt am Main/DE), J. Amrhein (Frankfurt am Main/DE, Frankfurt am Main/DE), J. Gerninghaus (Frankfurt am Main/DE, Frankfurt am Main/DE), T. Hanke (Frankfurt am Main/DE, Frankfurt am Main/DE), A. C. Joerger (Frankfurt am Main/DE, Frankfurt am Main/DE), S. Knapp (Frankfurt am Main/DE, Frankfurt am Main/DE, Frankfurt am Main/DE, Frankfurt am Main/DE)

The MST (mammalian sterile20-like) subfamily of serine/threonine kinases can be subdivided into structurally related MST1/2 and MST3/4/STK25 kinases. MST1 and MST2 kinases are key modules of the Hippo signaling, while MST3, MST4, and STK25 are involved in the regulation of the cytoskeleton and Golgi apparatus.1 Recent data suggest that MST3 participates in multi-protein heterocomplexes involved in various biological processes including, cell proliferation, cell migration, and apoptosis.2,3 However, despite the clinical significance of MST family proteins, drug discovery efforts on this protein family have been scarce due to the lack of selective and well-characterized chemical tools.4

In this work, we aimed to develop highly target selective chemical probes and narrow selectivity chemogenomic compounds against the MST-protein family, and specifically against MST3, as tools for further elucidating their biological roles in cellular systems and to facilitate future translational efforts. We have determined several high-resolution crystal structures of MST3 in complex with a diverse set of small-molecule inhibitors, including macrocycles with atypical hinge-binding motifs. Some of those inhibitors induced unique binding modes covering both DFG-in and DFG-out conformation. In one instance, for example, binding of a macrocyclic ligand resulted in a large shift in the relative orientation of the N-and C-terminal subdomain. Our data provide intriguing insights into the structural plasticity of MST3 family kinases and, importantly, also offer starting points for the development of selective MST3-targeting drugs.

References:

(1) Thompson, B. J. & Sahai, E. MST kinases in development and disease. *J. Cell Biol.* **210**, 871–882 (2015).
(2) Mehellou, Y. *et al.* Structural insights into the activation of MST3 by MO25. *Biochem. Biophys. Res. Commun.* **431**, 604–609 (2013).
(3) Sugden, P. H., McGuffin, L. J. & Clerk, A. SOcK, MiSTs, MASK and STicKs: The GCKIII (germinal centre kinase III) kinases and their heterologous protein-protein interactions. *Biochem. J.* **454**, 13–30 (2013).
(4) Olesen, S. H., Zhu, J. Y., Martin, M. P. & Schönbrunn, E. Discovery of Diverse Small-Molecule Inhibitors of Mammalian Sterile20-like Kinase 3 (MST3). *ChemMedChem* **3**, 1137–1144 (2016).

Fig. 1

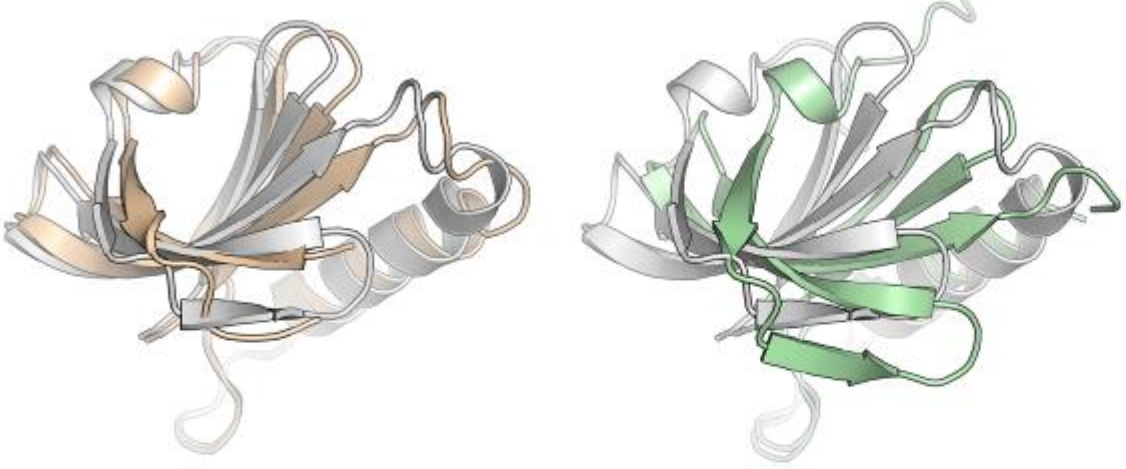

Fig. 2

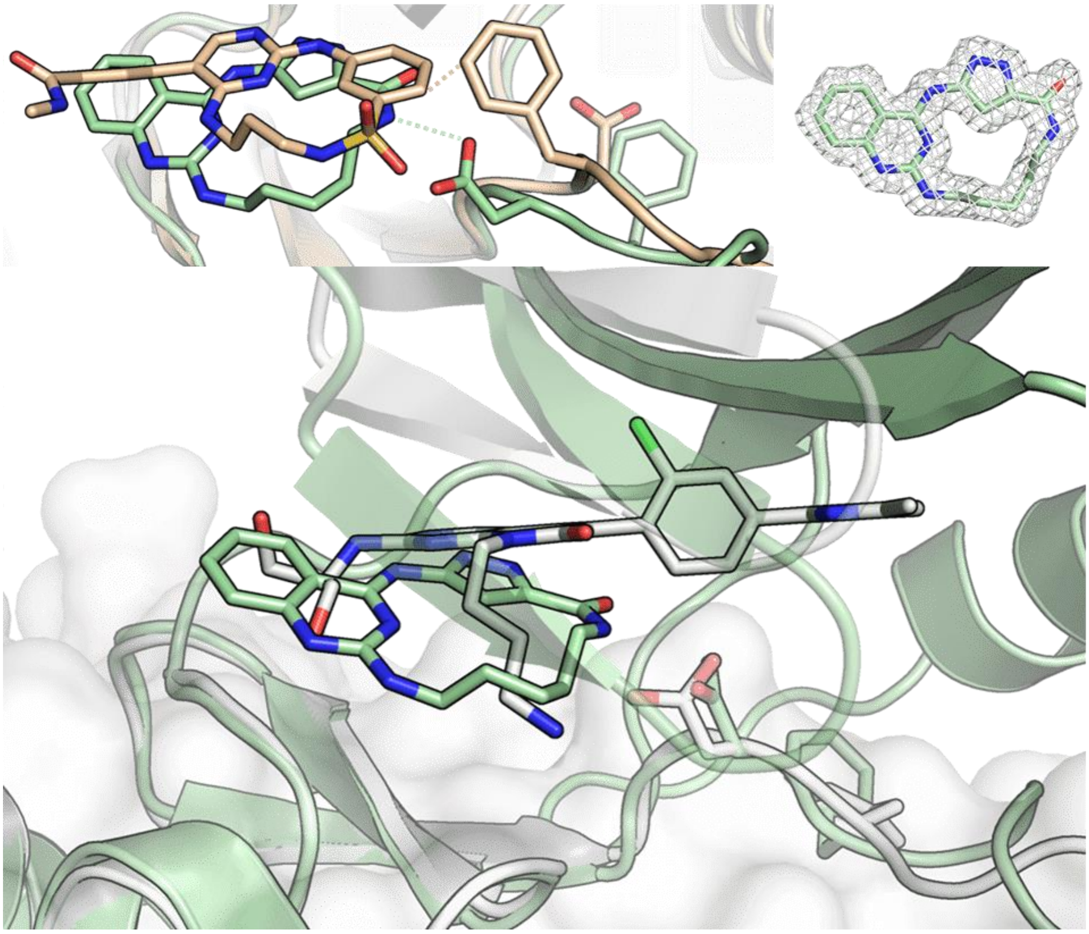

PP-071

Structural basis of p53 inactivation by cavity-creating cancer mutations and its implications for the development of mutant p53 reactivators

A. C. Joerger (Frankfurt am Main/DE)

The tumor suppressor p53 is inactivated by mutation in about half of all human cancer cases. Reactivation of mutant p53 is therefore a prime target in the development of novel cancer therapies [1]. Most p53 cancer mutations are missense mutations located in the DNA-binding domain, and many of those mutations reduce the thermodynamic stability of the protein, resulting in unfolding, followed by rapid aggregation at physiological conditions. In a proof-of-concept study, we have previously shown that the cavity-creating p53 cancer mutation Y220C is an ideal paradigm for developing small-molecule drugs based on protein stabilization, and we have developed a series of Y220C-specific binders that act as potent chemical chaperones, restoring p53 signaling in tumor cells with homozygous Y220C mutation [2, 3]. In our ongoing efforts to expand the druggable p53 mutome [4], we have now systematically analyzed the energetic and structural effects of other potentially cavity-creating cancer mutations in the p53 DNA-binding domain. The tested cancer mutations were all highly destabilizing, drastically lowering the melting temperature of the protein by up to 17 °C. Crystallographic studies complemented by molecular dynamics simulations showed that some of those cancer mutations create internal cavities of varying size and shape, whereas others induce unique surface lesions. Intriguingly, for one of the cancer hotspot mutants, our structural studies revealed a pronounced plasticity of the mutation-induced surface crevice, which may be exploited for the development of small-molecule stabilizers. I will also point out general principles for reactivating thermolabile cancer mutants and highlight special cases where mutant-specific drugs are needed for pharmacological rescue of p53 function in tumors.

References:

(1) Joerger AC, Fersht AR. The p53 Pathway: Origins, Inactivation in Cancer, and Emerging Therapeutic Approaches. Annu Rev Biochem. 2016;85:375-404.
(2) Bauer MR, Jones RN, Tareque RK, Springett B, Dingler FA, Verduci L, Patel KJ, Fersht AR, Joerger AC, Spencer J. A structure-guided molecular chaperone approach for restoring the transcriptional activity of the p53 cancer mutant Y220C. Future Med Chem. 2019;11:2491-504.
(3) Baud MGJ, Bauer MR, Verduci L, Dingler FA, Patel KJ, Horil Roy D, Joerger AC, Fersht AR. Aminobenzothiazole derivatives stabilize the thermolabile p53 cancer mutant Y220C and show anticancer activity in p53-Y220C cell lines. Eur J Med Chem. 2018;152:101-14.
(4) Bauer MR, Kramer A, Settanni G, Jones RN, Ni X, Khan Tareque R, Fersht AR, Spencer J, Joerger AC. Targeting Cavity-Creating p53 Cancer Mutations with Small-Molecule Stabilizers: the Y220X Paradigm. ACS Chem Biol. 2020;15:657-68.

PP-072

Structural and biophysical studies on drug-resistant mutations of the SARS-CoV-2 main protease

R. Hilgenfeld (Lübeck/DE, Lübeck/DE), J. Röske (Lübeck/DE, Lübeck/DE), K. Zhang (Lübeck/DE, Lübeck/DE), U. Curth (Hannover/DE), X. Sun (Lübeck/DE), H. El Kilani (Lübeck/DE, Lübeck/DE)

The SARS-CoV-2 main protease (Mpro) is a well-established target for the development of antiviral inhibitors [1]. One such inhibitor, Paxlovid, which is a combination of nirmatrelvir [2] and ritonavir, has already been introduced into the market. However, as SARS-CoV-2 is an RNA virus, the emergence of resistance mutations has to be expected. A number of such mutations have already been characterized [3-5], although they do not play a role yet in clinical settings; these include S144A, E166V/A, H172Y, Q189K, and the triple mutant L50F+E166A+L167F. We have recombinantly produced these mutants and studied the corresponding proteins by X-ray crystallography, enzymology, and biophysical approaches. The potential of each mutant to lead to a wide-spread nirmatrelvir-resistance scenario will be discussed. We will also demonstrate that one of our own inhibitors [6], while showing some degree of cross-resistance with nirmatrelvir, exhibits much higher inhibitory activity against the Mpro carrying the E166V mutation, compared to nirmatrelvir.

(1) Zhang L, Lin D, Sun X, Curth U, Drosten C, Sauerhering L, Becker S, Rox K, Hilgenfeld, R.: *Science* **368**, 409-412 (2020).
(2) Owen DR, et al.: *Science* **374**, 1586-1593 (2021).
(3) Hu Y, Lewandowski EM, Tan H, Zhang X, Morgan RT, Zhang X, Jacobs LMC, Butler SG, Gongora MV, Choy J, Deng X, Chen Y, Wang J.: bioRxiv. 2022 Sep 6:2022.06.28.497978. doi: 10.1101/2022.06.28.497978.
(4) Jochmans D., et al.: BioRxiv preprint doi: https://doi.org/10.1101/2022.06.07.495116 (2022).
(5) Moghadasi SA et al.: BioRxiv preprint, doi: 10.1101/2022.08.07.503099 (2022)
(6) Cooper MS, Zhang L, Ibrahim M, Zhang K, Sun X, Röske J, Göhl M, Brönstrup M,
(7) Cowell JK, Sauerhering L, Becker S, Vangeel L, Jochmans D, Neyts J, Rox K, Marsh GP, Maple HJ, Hilgenfeld R.: *J. Med. Chem*. **65**, 13328-13342 (2022).

Poster session I | Bio-Crystallography IV: Synchrotrons and high throughput methods

PP-073

High energy, high resolution large unit cell X-ray crystallography on the P14@PetraIII Beamline

U. Dakshinamoorthy (Göttingen/DE)

The undulator beamline P14 is a part of the Integrated Facility for Structural Biology operated by the European Molecular Biology Laboratory at the PETRA III storage ring at DESY (Hamburg, Germany). At high energies, a white beam compound refractive lens transfocator in 2:1 geometry is used to deliver a top-hat beam that can be shaped to any size between 20 and 300 µm at the sample position. A Dectris CdTe 16M EIGER2 was installed in 2021 which in combination with high-energy (26.7 keV) top-hat beams geometrically allows ultra-high resolution studies of protein crystals. To further improve data quality, the Global Phasing Ltd (GPhL) workflow has been deployed through the P14 MXCuBE2 interface that calculates crystal symmetry and orientation based data acquisition strategies. This helped us collect complete and uniformly redundant data within a defined dose budget, leading to ultra-high resolution datasets for small to large unit cell crystals. Automated data processing and refinement procedures have been developed in collaboration with GPhL. Together the established procedures empower efficient and high-throughput interrogation of even the most complex crystal systems with high accuracy and precision.

PP-074

Structural and functional insight into a secreted, N-glycosylated Protein—Human zonulin in celiac disease towards drug discovery

J. Song (Hamburg/DE), S. Chatziefthymiou (Hamburg/DE), A. Gruzinov (Hamburg/DE), G. Pompidor (Hamburg/DE), H. Taberman (Hamburg/DE), R. Maitschke-Rajasekharan (Hamburg/DE), P. Lewe (Hamburg/DE), S. Witt (Hamburg/DE), T. Jin (Hamburg/DE), J. Hakanpää (Hamburg/DE)

Celiac disease (CeD) is defined as an autoimmune disease triggered by undigested gluten. Currently, the treatment of a lifelong gluten-free diet (GFD) is insufficient to control the disease. Wherefore, the drug development is underway [1]. The zonulin-mediated modulation of paracellular transport for undigested gluten is considered to pivotal step in pathogenesis of CeD [2]. Zonulin, a secreted protein, is shown to be the single chain of pre-haptoglobin-2 (Hp2) with four N-glycosylation sites on β chain [3]. *Recently, a synthetic small peptide inhibitor, Larazotide (AT1001) has been exploited to block the zonulin-induced increasing intestinal permeability (IP) [4].* To shed light on the function of zonulin, we aim to study its three-dimensional (3D) structure using X-ray crystallography. This information will be a very useful tool for the research focusing on the treatment of celiac disease.

For the purpose to get insight into the native structure with N-glycosylation, the mammalian HEK 293T cells are used to produce zonulin. To date we have expressed and purified the glycosylated protein in HEK 293T cells and we are ready to proceed with the trials towards the structural characterization of the protein.

To successfully yield diffraction-quality crystals for X-ray crystallography, we will use mass spectrometry (MS), dymamic light scattering (DLS), small-angle-X-ray scattering (SAXS) to characterize the structural properties for optimization of crystallization conditions. To investigate the 3D structure without ligands, the diffraction data will be collected and the phase problem will be addressed by the molecular placement (MR) method. To determine its binding affinity to the ligands, the soaking experiment will be focused characterizing the binding sites of small molecular inhibitors.

References

(1) Zingone, F., *et al*, *World J. Castrointest. Pharmacol. Ther.*, 1, 36 (2010).
(2) Fasano, A., *Physical Rew.,* 91, 151 (2011).
(3) Tripathi, A., *et al*, *Proc. Natl. Acad. Sci. USA*, 106, 16799 (2009).
(4) Hoilat, G.J., *et al*, *Clin. Res. Hepatol. Gastroenterol.*, 46, 101782 (2022).

PP-075

With a pinch of zinc: Solving the disorder problem in 'NaCd$_2$': Syntheses and crystal structures of Na$_{47}$(Cd$_{1-x}$Zn$_x$)$_{102}$ (x=0.088) and Na$_8$(Cd$_{1-x}$Zn$_x$)$_{17}$ (x=0.124)

I. Junker (Freiburg im Breisgau/DE), K. Köhler (Freiburg im Breisgau/DE), C. Röhr (Freiburg im Breisgau/DE)

The first report on the complex cubic binary compound 'NaCd$_2$' reaches no more than sixty years back, when Samson [1] published the first structure determination based on 960 reflections measured using Weissenberg film methods (space group Fd3m, a=3056 pm, R=17 %). He was able to localise 17 atomic positions, but among them one [Cd(9)] was only half occupied due to too short distances, and seven sites were assigned a Na/Cd mixed occupation. Twenty-five year later, Yang, Anderson and Stenberg published an alternative description of the ordered part of the structure [2]. Even though they collected new four-circle diffractometer data (892 reflections), they only validate the model derived by Samson and did not comment on problems like the Na/Cd mixed positions, ADP parameters and difference electron densities etc. [3]. Ten years later, Bergman [4] presented a new stochastic derivation of this 'trial structure' and already disputed the statistic Na/Cd site occupation. Although an extensive paper on the chemical bonding in 'NaCd$_2$' (based on Yang's equivocal model of 1987) appeared in 2007 [4], the crystal structure and exact composition of 'NaCd$_2$' are ambiguous until now.

In the course of our systematic studies on the 'coloring' of alkali and alkaline earth metallides of the late p-block elements, we studied the phase formation in the ternary system Na-Cd-Zn. Besides 'NaCd$_2$', both binary section Na-Zn and Na-Cd contain only one intermetallic compound in the Na-pure section (NaZn$_{13}$ [6,7] and Na$_2$Cd$_{11}$ [8]). For both these two phases we determined a very small substitution of Zn↔Cd only. Close to 'NaCd$_2$', the new ternary Zn-poor title compounds Na$_{47}$Cd$_{93}$Zn$_9$ ('NaCd$_2$'-type) and Na$_8$Cd$_{14.9}$Zn$_{2.1}$ (new structure type) were identified and characterized.

The structure of Na$_{47}$Cd$_{93}$Zn$_9$ (cubic, Fd-3m, a=3034.2(8) pm, R1=0.0482) and 'NaCd$_2$' is best described using two interpenetrating diamond network **A** and **B**. The network **A** consists of MgZn$_2$-type [Cd$_4$] tetrahedra columns [Cd(1) to Cd(7)] with [Cd(10)$_4$] tetrahedra in a MgCu$_2$-type connection at the -43m symmetric nodes (Fig. 1 a, green tetrahedra network). These [Cd$_4$] tetrahedra are enclosed by the sodium centered truncated tetrahedra (tt; overall FK^{16} polyhedra) around Na(2) (red polyhedra in Fig. 1 a), Na(3) (orange) and Na(4) (yellow). The -43m nodes of the second network **B** are FK$^{16}_{28}$ clusters [Na(1)M(8,10)$_{16}$]. 24 of the 28 triangles of this polyhedron are shared with FK^{16} ccps around Na(5) and Na(6). The remaining four faces M(10)$_3$ are capped by Zn(9) atoms [or the Zn(9)$_2$ dumbbells], which solve all the disorder problems within the cluster around Na(1) as well as in the intersection region of two adjacent Cd$_{76}$ balls (cluster shells/polyhedra in Fig. 1 b and c after [9]: Na(1)@FK$^{16}_{28}$[Cd(8,10), 320-340 pm, darkblue]@F$^{28}_{16}$[Na(5,6)/Zn(9), 520-590 pm, yellow] @F$^{76}_{40}$[Cd(5,6,7,9,11,12), 780-820 pm, transparent blue]). This ordered Zn-substituted derivative of 'NaCd$_2$' allowed for a reliable analysis of the electronic structure, based on a FP-APW+lo band structure calculation, which shows - in contrast to the results reported in [5] - no general difference of the chemical bonding within the two 3D networks.

The second new orthorhombic compound Na$_8$Cd$_{14.9}$Zn$_{2.1}$ (space group $Pnma$, a = 972.34(3), b = 1534.39(5), c = 1572.74(5) pm, Z = 4, R1 = 0.0569) contains only slighty more sodium (Na:M = 47.06 %) and zinc (Zn:Cd = 14.1 %) than the cubic 'NaCd$_2$'-type phase Na$_{47}$Cd$_{93}$Zn$_9$ (Na:M = 46.08 %; Zn:Cd = 9.7 %). Herein, Na(1), Na(3) and Na(5) exhibit the expected FK^{16} (12+4) polyhedra found in the pure Laves phases. For Na(2), two of the hexagons of the tt are capped by M(11) atoms instead of Na. Na(4), which is surrounded mainly by pure Cd positions, shows - consistent with the thus somewhat larger neighbours - a slightly reduced FK^{15} polyhedron only. As expected from the compounds composition and the sodium coordination polyhedra, all pure Cd and mixed Cd/Zn sites [except M(11)] are icosahedrally surrounded. Most sites show the Laves specific 6M+6A coordination, only Cd(4) and M(10) exhibit 7 Zn/Cd and 5 Na neighbours. The atoms M(11), which form a M(11)-M(11) dumbbell, show a somewhat increased coordination number of 7+7. The [NaM_{12}] and [Na(2)M_{14}] ccps do not fully tile the space. In contrast to the Laves phases, where mainly vertex-sharing [M_4] tetrahedra are formed inbetween the tt, the small space inbetween the ccps in the structure of Na$_8M_{17}$ is quite concentrated and resembles a cutout of a tetrahedra packing with heavily condensed tetrahedra: The unconnected clusters (Fig. 2, green) are built up by six face-sharing tetrahedra, which form a M(4) monocapped pentagonal bipyramid [= icosahedra cap, i.e. five tetraedra with a common edge M(3)-M(5)]. The overall structure thus exhibits only [M_4], [NaM_3] and [Na$_2M_2$] tetrahedra (no octahedra, cubes, prisms etc) and therewith represents, similar to the simple AB$_2$ Laves phases, a pure Frank-Kasper type tetrahedra packing.

References:

(1) St. Samson, *Nature* **4838**, 259-262 (1962).
(2) Q-B. Yang, St. Anderson, L. Stenberg, *Acta Crystallogr.* **B43**, 14-16 (1987).
(3) Q-B. Yang, St. Anderson, *Acta Crystallogr.* **B43**, 1-14 (1987).
(4) G. Bergman, *Acta Crystallogr.* **B52**, 54-58 (1996).
(5) D. C. Fredrickson, St. Lee, R. Hoffmann, *Angew. Chem.* **119**, 2005-2023 (2007).
(6) E. Zintl, W. Haucke, *Naturwissenschaften* **25**, 717 (1937).
(7) M. Wendorff, C. Röhr, *J. Alloys Compd.* **421**, 24-34 (2006).
(8) C.-H. Wong, Ch. Chieh, T.-Y. Lee, *Acta Crystallogr.* **19**, 849-852 (1965).
(9) W. Steurer, J. Dshemuchadse, *Intermetallics. Structure, Properties and Statistics*, Oxford University Press, 2016.

Figure 1: Crystal structure of $Na_{47}Cd_{93}Zn_9$: a. Two interpenetrating diamond-like networks **A** (green $[Cd_4]$ tetrahedra in a mixed $MgCu_2$/$MgZn_2$ Laves-type connection surrounded by yellow $NaCd_{12}$ tt) and network **B** with blue $[NaCd_{16}]$ FK^{16} polyhedra at the nodes (red/blue/yellow balls: Cd/Zn/Na); b-d. Details of network **B**, showing the shells around the tetrahedral nodes and the sligtly overlapping $F^{76}{}_{40}$ polyhedra with the $Zn(9)_2$ dumbbell; e. Difference electron density distribution (at 10 e^{-} 10^{-6} pm^{-3} level) in pure '$NaCd_2$' calculated omitting the positions *M*(8) to *M*(11). (red/blue/yellow balls: Cd/Zn/Na; yellow/orange/red polyhedra: Na ccps).

Figure 2: Crystal structure of $Na_8Cd_{14.9}Zn_{2.1}$: a. Perspective view of the unit cell; b. Projection along [010]; c. View along [100] (red/blue/yellow balls: Cd/Zn/Na; yellow/orange/red polyhedra: Na ccps).

Fig. 1

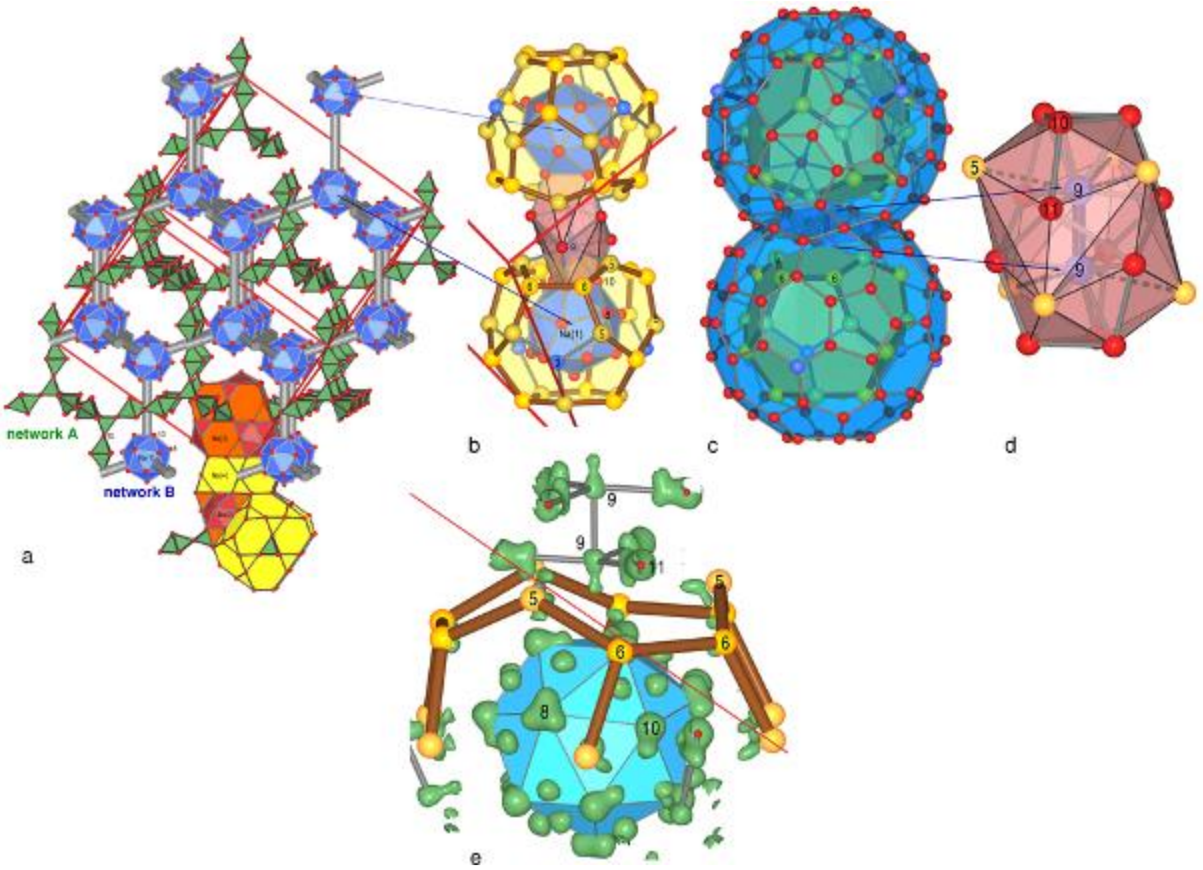

Fig. 2

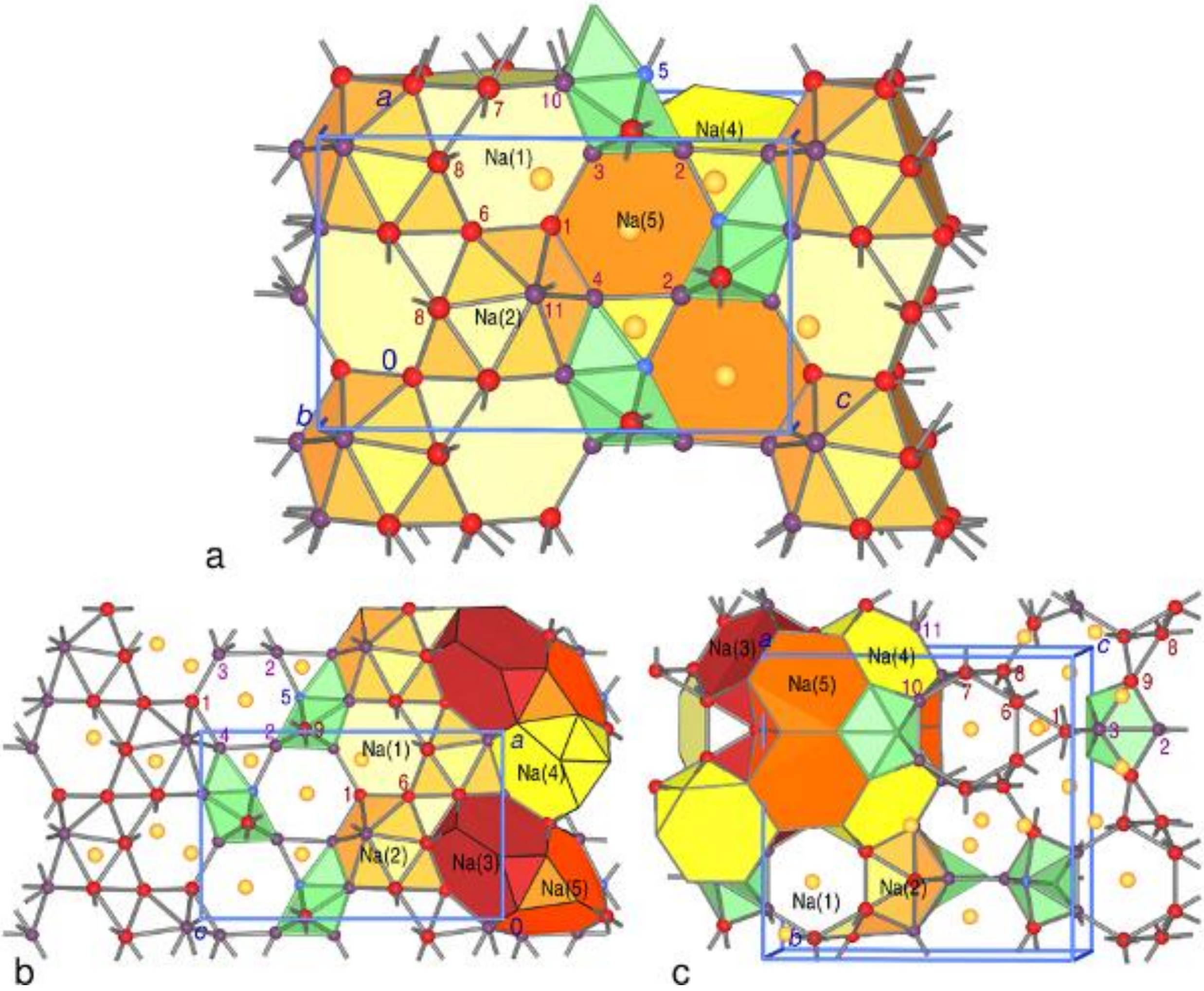

PP-076

Incommensurate structures and radiation damage in $Rb_2V_3O_8$ and $K_2V_3O_8$ fresnoites

A. Grzechnik (Jülich/DE, Aachen/DE), V. Petricek (Prague/CZ), D. Chernyshov (Grenoble/FR), C. McMonagle (Grenoble/FR), T. Geise (Aachen/DE), H. Shahed (Jülich/DE), K. Friese (Aachen/DE, Jülich/DE)

Structures and phase transitions in $K_2V_3O_8$ and $Rb_2V_3O_8$ mixed-valence vanadate fresnoites are studied with synchrotron single-crystal diffraction at low temperatures and ambient pressure. $K_2V_3O_8$ exhibits a phase transition to an incommensurately modulated structure at about 115 K. At 100 K, the satellite reflections can be indexed with two **q** vectors, $\mathbf{q}_1 = (\alpha, \alpha, 0.5)$ and $\mathbf{q}_2$ $(-\alpha, \alpha, 0.5)$, where $\alpha \approx 0.3$. Although no mixed satellite reflection are observed, the modulated structure is better described in (3+2) than in (3+1) dimensional space. The geometries of the VO_4 and VO_5 building units are rigid and it is mainly slight rotations of these polyhedra and small variation of the intermediate K-O distances that are modulated. The prolonged exposure to the high-brilliance synchrotron beam suppresses the incommensurate phase. The previously postulated phase transition to the incommensurate phase in $Rb_2V_3O_8$ at 270 K is not observed in our data. One of the reasons could be that the intense radiation also affects the modulation in this material. Strategies to collect and analyse single-crystal diffraction data measured with very intense synchrotron radiation using modern low-noise pixel area detectors will be discussed.

PP-077

$Sr_{13}Cd_{59}$: The corrected composition and crystal structure of a complex binary cadmide (and most likely many other isotypic intermetallics)

M. Otteny (Freiburg im Breisgau/DE), M. Wendorff (Freiburg im Breisgau/DE), C. Röhr (Freiburg im Breisgau/DE)

By means of powder data, the two long-known title compounds '$Sr_{13}M_{58}$' (M=Cd, Hg) [1,2] have been assigned to form the complex hexagonal $Gd_{13}Cd_{58}$-type structure ($hP142$, $P6_3/mmc$, $a\approx1500$, $c\approx1500$ pm; 4 Sr and 12 Cd sites [3]). In this $A_{13}M_{58}$ aristotype (magenta 'unit cell' in Fig. 1 a), Cd centered cubes [Cd(4)@Cd(9,10,12)$_8$] (**C**, blue) are arranged in kagomé nets, which are stacked in identical orientation |:AA':| along the hexagonal c axis. Along the resulting triangular channels (1/3,2/3,z, Fig. 1 c) the remaining Cd atoms [except Cd(1), Cd(6) and Cd(8)] form vertex-sharing tetrahedra stars (**TS**, build up by 5 tetrahedra; green) and hexa-capped double tetrahedra stars (μ-**DTS**, formed by 17 tetrahedra; red). These Cd building blocks are thus cutout of a tetrahedra packing (t.p.) and clearly show the crystal-chemical relation to structures types like e.g. the Th_6Mn_{23}-Eu_3Mg_{16} family [4] or complex cubic intermetallics like e.g. the YCd_6-, Eu_4Cd_{25}- or $Ba_{20}Hg_{103}$-type [5]. The hexagonal 0,0,z channels (Fig. 1 b) are occupied by [Sr(1)@Cd(1,6,8)$_{14}$] cation coordination polyhedra (ccps; yellow), which show an unusual shape and small coordination number (CN) of 14 only. Indeed, single crystal structure refinements of several isotypic phases (mainly rare-earth zincides [6-8]) of this 'hexagonal' structure type lack from crystallographic problems like e.g. strange/large ADPs and split positions and the correct orthorhombic symmetry of almost all members of this structure type is hidden by the formation of trills; the presence of additional superstructure reflections was observed for the Pu zincide by Larson and Cromer as early as 1967 [3]. In 2002, Gomez and Lidin [6] partly resolved the twinning for the dysprosium zincide, which they reported to crystallize in the orthorhombic subgroup $Pnma$ with $a_{\mathrm{ortho}}=c_{\mathrm{hex}}$, $b_{\mathrm{ortho}}=a_{\mathrm{hex}}$ and $c_{\mathrm{ortho}}=\sqrt{3}a_{\mathrm{hex}}$ (group subgroup relation: $P6_3/mmc \rightarrow$ t3 $\rightarrow Cmcm \rightarrow$ k2 $\rightarrow Pnma$, cf. [9]). Due to 1/3 unoccupied cubes, the compound's formula was corrected to '$Dy_{13}Zn_{57}$'. This structure refinement is nevertheless not too convincing (very high residual electron density of 17 $e^-/10^6$ pm^3, anisotropic refinement impossible, some large isotropic displacement parameters). In 2006, the same group reported the structure refinement of an - again twinned – data set of the terbium zincide in the further reduced subgroup $P2_12_12_1$ [7]. Herein, the authors detected two additional Zn atoms/f.u. and the composition was thus corrected to $Tb_{13}Zn_{59}$. For a series of ternary Zn-containing strontium cadmides/mercurides the very same composition and structure model was also achieved in the centrosymmetric space group $Pnma$ [9]. Indeed, this structure model was then refined using the data of one singluar untwinned crystal of the mixed Zn/Cd phase $Sr_{13}Cd_{56.8}Zn_{2.5}$ only, which exhibits Cd/Zn statistically occupied positions and an extra Cd↔Zn_2 substitution. [Fortunatly, additional extra problems resulting from a partial RE↔Zn_2 substitution like in the rare-earth zincides [7,8] are lacking for Sr cadmides, mercurides and their Zn-substituted derivatives].

The corrected orthorhombic crystal structure of the binary cadmide, which is an index 6 hettotype of the original hexagonal structure ($oP288$, $Pnma$, a=1586.8, b= 1587.5, c=2775.4 pm, $R1$=2.2%), could now be realiably determined from an untwinned single crystal, which was obtained from stoichiometric melts of the two elements.
Therewith, the composition of the phase (and similarly its derivatives) is corrected to $Sr_{13}Cd_{59}$. In the orthorhombic structure 1/3 of the cubes (light blue in Fig. 1) are no longer centered (→$Sr_{13}Cd_{57}$, cf. '$Dy_{13}Zn_{57}$' above) but squeezed, leaving space for two further Cd atoms/f.u. (red arrows, →Sr13Cd59, cf. $Tb_{13}Zn_{59}$ above). The rearrangement of the atoms mainly concerns the hexagonal channels and fixes all crystallographic and crystal-chemical issues of the original hexagonal structure(s): The ccps of Sr(1) and Sr(2a,b) are extended to 16 Cd, no unusual cavities are left over and finally this part of the structure is also completely realized by the space filling of the Sr ccps and additional vertex-sharing tetrahedra (gray polyhedra).

The new crystal data of $Sr_{13}Cd_{59}$ are the basis for the refinement of all twinned data sets of the whole structure family $Sr_{13}(Cd/Hg)_{59}$ and their partly Zn (up to 25 % [9]) and Mg (up to 18 %, this work) substituted derivatives. They finally enabled quantum-chemical calculations of the chemical bonding within a family of complex intermetallics closely related to iQCs. The results thereof clearly show the ionic [Sr charges: q_{Sr}=+1.20(2)] as well as covalent Cd-Cd bonding contributions [q_{Cd}=-0.06 to -0.44] and thus justify the structure description via space-tiling of alkaline-earth ccps and polyanionic building blocks like TS, extended DTS, C etc. representing cutouts of tetrahedra packings.

(1) G. Bruzzone, *Gazzetta Chimica Italiana* **102**, 234-242 (1972).
(2) G. Bruzzone, F. Merlo, *J. Less-Common Met.* **35**, 153-157 (1974).
(3) A. C. Larson, D. T. Cromer, *Acta Cryst.* **23**, 70 (1967).
(4) K. Köhler, C. Röhr, *Acta Cryst.* **A75**, e425 (2019)
(5) M. Schwarz, M. Wendorff, C. Röhr, *Z. Kristallogr.* **232**, 515 (2017).
(6) C. P. Gomez, S. Lidin, *Solid State Sci.* **4**, 901-906 (2002).
(7) Sh. Piao, C. P. Gomez, S. Lidin, *Z. Kristallogr.* **221,** 391-401 (2006).
(8) Sh. Piao, S. Lidin, *Inorg. Chem.* **46**, 6452-6463 (2007).
(9) C. Röhr, M. Wendorff, *Z. Kristallogr. Suppl.* **36**, 143-144 (2016).

Figure 1: Crystal structure of $Sr_{13}Cd_{59}$. a: Projection of the unit cell along the pseudo-hexagonal *a* axis. b: Filling of the pseudo-hexagonal channels with extended Sr(1) ccps (yellow polyhedra). c: Filling of the pseudo-trigonal channels with tetrahedra stars (**TS**, light green), and extended double tetrahedra stars (extended **DTS**, red). (red/yellow balls: Cd/Sr).

Fig. 1

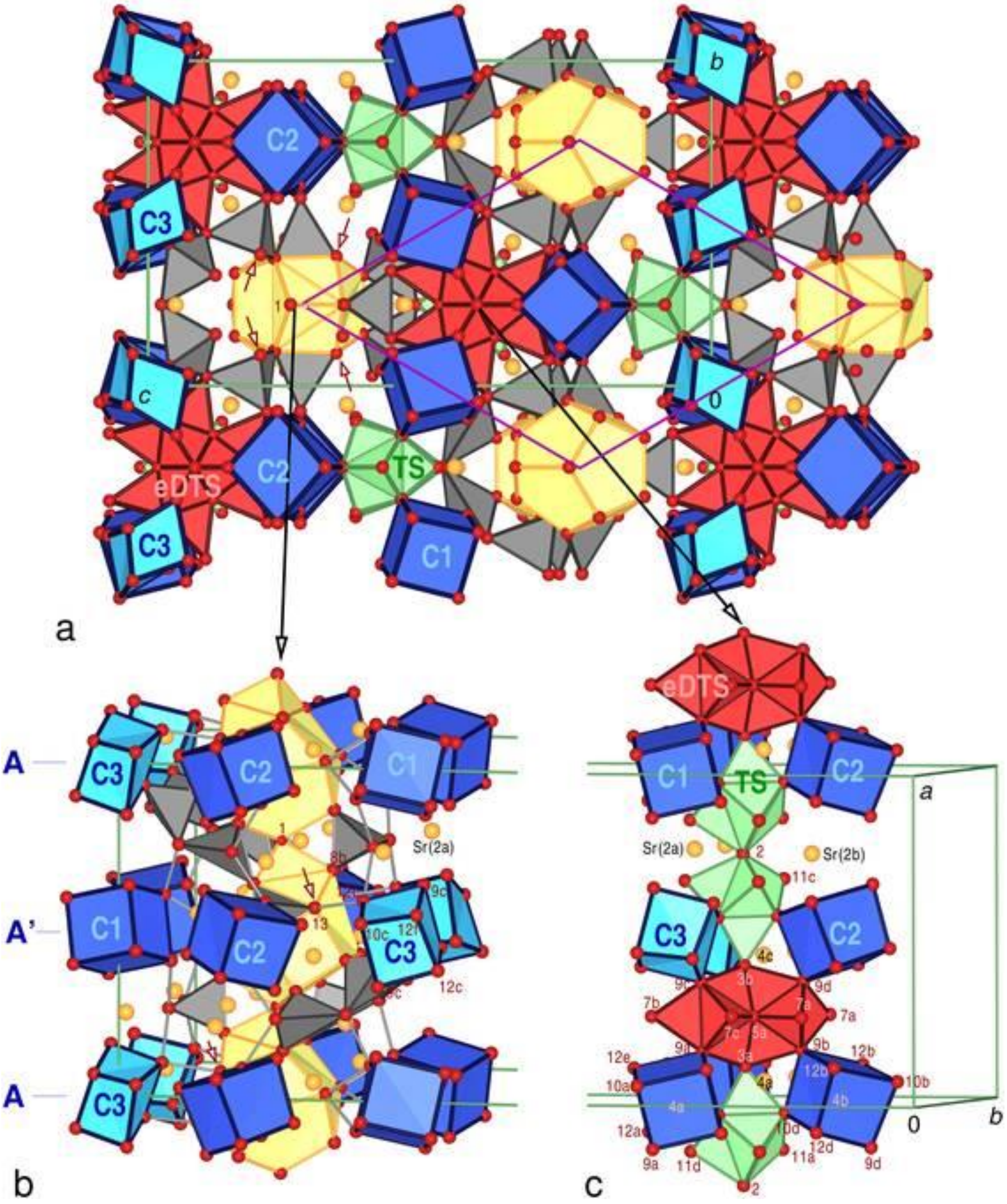

b
C2
C3
c
0
eDTS
TS
C1
1
a
A
A'
8b
13
10c
12f
9c
12c
Sr(2a)
Sr(2b)
2
11c
4c
3b
7b
7a
7c
5a
9d
9b
12e
12b
10a
10b
4a
4b
12a
10d
12d
9a
11d
11a
b
c

PP-078

Elucidating host-guest interactions in UV filter-zeolite composites by combining IR spectroscopy and DFT calculations

M. Fischer (Bremen/DE), R. Fantini (Modena/IT), M. Sisti (Modena/IT), L. Mino (Turin/IT)

Introduction and objectives: The encapsulation of organic UV filters into zeolite hosts could help to enhance their stability while at the same time limiting their potential ecotoxicity. In prior work, the UV filters octinoxate (OMC) and avobenzone (AVO) were successfully incorporated into different zeolites (Fantini *et al.*, 2021). Among the obtained ZEOfilter materials, the zeolites 13X and K-LTL emerged as the most promising hosts due to their favorable UV absorption properties. More recently, a combination of diffraction and spectroscopic methods was used for an in-depth characterization of these ZEOfilters. Ongoing work aims to enhance the interpretation of experimental data through a combination with dispersion-corrected density functional theory (DFT) calculations, with emphasis on host-guest interactions and their impact on the structure of the adsorbed UV filters.

Results: DFT structure optimizations of adsorption complexes of OMC and AVO in zeolite 13X were carried out, considering *cis* and *trans* isomers of OMC and keto and enol tautomers of AVO. While the results for AVO pointed to a preference for the enol form, which has better UV absorption properties, the calculations for OMC delivered more negative adsorption energies for the less efficient *cis* isomer. However, adsorption energies alone do not necessarily allow for meaningful conclusions, as an isomerization in the pores might be prevented by steric constraints. DFT-computed IR spectra of *cis*- and *trans*-OMC showed notable differences between the isomers in the frequency range of 1300 $\mathrm{cm^{-1}}$ to 1800 $\mathrm{cm^{-1}}$. Upon adsorption, a more prominent red-shift of the C=O stretching band was predicted for *cis*-OMC as compared to *trans*-OMC, which was attributed to a stronger interaction of the *cis* isomer with the Na^+ cations of 13X. In the ongoing analysis, a critical comparison to experimental IR spectra is used to determine the dominant isomer in the adsorbed form.

References:

(1) Fantini, R., Vezzalini, G., Zambon, A., Ferrari, E., Di Renzo, F., Fabbiani, M. & Arletti, R. (2021). *Microporous Mesoporous Mater.* **328**, 111478.

PP-079

Ferroelectric phase transition in barium titanate: An ab-initio- molecular dynamics approach

C. Ludt (Freiberg/DE), M. Zschornak (Freiberg/DE)

Ferroelectric materials as well as their phase transitions are important phenomena for technical applications. The occurring spontaneous polarization can be controlled by external perturbation like temperature or pressure, as well as be reoriented by electric fields.

Barium titanate ($BaTiO_3$) is the prototype representative of ferroelectric perovskites. With properties like piezoelectricity, dielectric susceptibility, good optical and transport attributes, multiferroism etc., it is an interesting functional material due to its variety of possible applications e.g., nonvolatile memory, high-κ dielectrics, and piezoelectric sensors.

Here, ab-initio-molecular-dynamics (AIMD) is used to approach this phase transition, driven by temperature as well as external pressure. Therefore, density functional theory (DFT) determines the forces, which are utilized in the molecular dynamics (MD) to simulate the trajectory of the given system. The isothermal – isobaric (NpT) ensemble is chosen, which allows dynamic volume, and so additional degrees of freedom, i.e., the lattice parameters. The velocity of the system"s particles is controlled by a thermostat, which governs the average kinetic energy in the system, i.e., the temperature, as well as a barostat, which implies an external pressure on the system.

With the chosen method, the nature of the phase transition in barium titanate can be revealed. The Curie Temperature could be reproduced for a given supercell and the phase diagram can be confirmed.

Poster session II | Electron crystallography and microscopy

PP-080

Structures of Vitamin D derivatives by electron diffraction

K. Woźniak (Warsaw/PL), K. K. Jha (Warsaw/PL), M. Chodkiewicz (Warsaw/PL), M. Wanat (Warsaw/PL), B. Gruza (Warsaw/PL), A. Kutner (Warsaw/PL), T. Góral (Warsaw/PL, Warsaw/PL), P. Dominiak (Warsaw/PL)

Vitamins D are a group of fat-soluble secosteroids. Ergocalciferol (vitamin D2) and cholecalciferol (vitamin D3) are major forms of vitamins D which occur in fungi and animal organisms.[1] 1α,25-Dixydroxyvitamin D2 (ercalcitriol, 1,25(OH)2D2) and 1α,25-dihydroxyvitamin D3 (calcitriol, 1,25(OH)2D3) are the most active forms of vitamin D2 and D3, respectively. The biological activity of vitamins D (Fig. 1) is expressed mostly through the interactions with the nuclear vitamin D receptor (VDR). VDR, after binding natural agonists, calcitriol or ercalcitriol, forms the heterodimer with nuclear retinoid X receptor (RXR). This complex binds with DNA and regulate the vitamin D-dependent gene expression. Autoimmune diseases such as type 1 diabetes, multiple sclerosis, rheumatoid arthritis, and others such as influenza or tuberculosis occur more often in countries with limited access to sunlight and thus the lowered vitamin D endogenous production.

Figure 1: Upper row from left: Structures and the numbering system of vitamins D: 1,25(OH)2D2 (ercalcitiol) and 1,25(OH)2D3 (calcitriol) and structures of the vitamin D analogs studied: PRI-2204, PRI-1901 (Solverol); bottom row: 1a-hydroxyvitamin D2 and PRI-2191 (Tacalcitol). H-atoms omitted for clarity.

Only a small number of the vitamin D analogues crystalize well enough for structural X-ray studies [2-4]. We have previously solved the X-ray structure of the synthetic precursor of 1,25(OH)2D2, i.e. 1a-hydroxyvitamin D2 (1a-OH-D2) and showed that the molecule adopts exclusively an A-ring chair b-conformation [5]. Most vitamin D compounds form nanocrystals which can be structurally characterized only by more advanced techniques, including electron diffraction (ED). In this communication, we will also present ED structures of 1,25(OH)2D3 analogs, the side-chain, and A-ring modified VDR agonists coded PRI-2204 and PRI-1901, respectively.

We will present details of series of structures of the studied derivatives of the vitamin D resulting from kinematic refinement of the electron diffraction data collected in our Lab., comparison of the ED structures with known X-ray structures of the corresponding vitamin D derivatives, results of HAR and TAAM refinements [6] based on aspherical atomic electrostatic potentials and utilizing results of kinematic refinement, and, hopefully, also results of dynamical refinement [7] for the best ED data sets.

References:

(1) A. Norman, Vitamin D; Elsevier, 2012; ISBN 978-0-323-14143-7; S. Kato, *J. Biochem. (Tokyo)* 127 (**2000**) 717

(2) M. Wanat, M. Malinska, A. Kutner, K. Woźniak, *Molecules,* 27(6) (2022) 1757

(3) M. Wanat, M. Malińska, A. Kutner, K. Woźniak, *Molecules,* 25(8) (2020) 802

(4) M. Wanat, M. Malińska, A. Kutner, K. Wozniak, *Cryst. Growth Des*. 18(6) (2018) 3385

(5) W. Kołodziejski, K. Woźniak, P., J. Herold, M. Dominiak, A. Kutner*, J. Mol. Structure,*734, (2005) 149

(6) B. Gruza, M. L. Chodkiewicz, J. Krzeszczakowska, P. M. Dominiak, Acta Cryst.. A76 (2020) 92.

(7) L. Palatinus, V. Petricek, C. A. Correa, Acta Cryst., A71 (2015) 235

Acknowledgments: This research was funded by the University of Warsaw IDUB grants BOB-IDUB-622-20/2021, IUDUB PSP: 501-D112-20-0006100 and by Polish NCN grant 2020/39/I/ST4/02904

Fig. 1

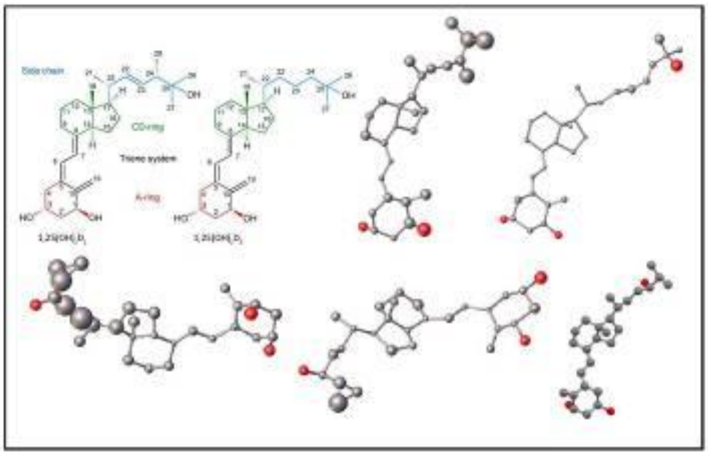
Side chain
CD-ring
Triene system
A-ring
HO
OH
1,25(OH)$_2$D$_2$
1,25(OH)$_2$D$_3$

PP-081

On the cutting edge of electron diffraction quality

E. Hovestreydt (Villigen/CH), J. Merkelbach (Villigen/CH), C. Jandl (Villigen/CH), G. Steinfeld (Villigen/CH), D. Stam (Villigen/CH)

Introduction: So far, **Electron Diffraction** has been done in TEMs, resulting in *challenging experiments* and *limited datasets*, yet ED allowed structures to be obtained from powders, that were unsolvable with either conventional or even synchrotron PXRD. Until recently, no ***dedicated*** **Electron Diffractometer** that would focus on the *diffraction* capability over imaging has been commercially available. *Quality* would greatly benefit relative to TEM data, allowing for *faster* and *more complete* datasets as well.

Methods: Here we present data from **the Electron Diffractometer**, a smart combination of a 5-axis, 140° rotation, nanometer-precise *goniometer* and a radically simplified *electron beam*, designed for *electron-crystallography* by X-ray diffractionists.

Results: The data quality obtained is clearly superior to previously reported, indicating the general higher performance of a dedicated electron-diffractometer compared to equipment commonly used until today.

Conclusion:

- even at ambient temperature, good data from organic samples can be obtained

- reliable performances in continuous rotation enables rapid data collection

Fig. 1

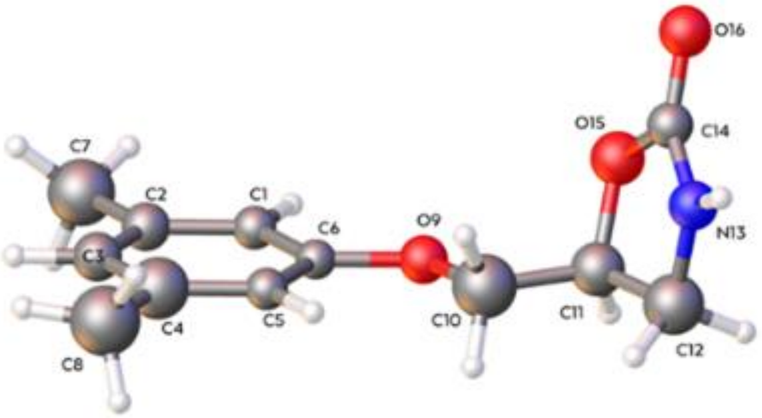

PP-082

Thermal conversion of platinum-group metals by in situ transmission electron microscopy

K. Loza (Essen/DE), A. Karatzia (Essen/DE), M. Heggen (Jülich/DE), M. Epple (Essen/DE)

Nanoparticles of platinum-group metals are valuable materials for numerous applications, for example, homogeneous and heterogeneous catalysis, nanomedicine, and bioimaging. Porous and faceted nanostructures are of particularly high interest in heterogeneous catalysis. Most metal-based heterogeneous catalytic reactions occur at elevated temperature. Gaseous environment and heat treatment may alter the surface properties of the nanoparticles. Here, we report on the dynamic morphological evolution of dispersed iridium/iridium dioxide, silver and core-shell silver-gold nanoparticles, prepared by a colloid-chemical route. Prior to electron microscopy, the synthesized materials were extensively characterized by physicochemical methods as uv/vis-spectroscopy, dynamic light scattering, energy-dispersive X-ray spectroscopy, and thermogravimetry. A nanoreactor setup permitted the observation of the particle transformation in real-time under precise temperature and gas control at high resolution. We followed the morphological and crystallographic changes in dynamic chemical environments (vacuum, oxygen, nitrogen, argon/4 % hydrogen, all at 1 bar) up to 1000 °C. We observed morphology changes and faceting of dispersed iridium/iridium dioxide as well as surface sublimation and shape transformation of silver nanocubes. Further thermal treatment of the sample resulted in a temperature-dependent crystallite growth due to the migration of atoms. Neither disintegration nor generation of smaller particles were observed.

PP-083

ANTEMA: An Automated Nanoparticle Transmission Electron Micrograph Analysis based on machine learning procedures

N. Gumbiowski (Essen/DE), K. Loza (Essen/DE), M. Heggen (Jülich/DE), M. Epple (Essen/DE)

High-resolution transmission electron microscopy (HRTEM) is an important tool for analysing nanoparticles. The micrographs show information about the size and shape of the particles as well as their inner structure. These parameters all influence the physical and chemical properties of the particle and therefore how they can be used for different applications. Consequently, it is essential to get detailed data on particle shape and size and the synthetic parameters that dictate them. With high frame rates and increasing capabilities of transmission electron microscopes a lot of data can be generated. However, analysing these micrographs is often done manually which is a tedious and time-consuming process. This becomes even more obvious for *in-situ* TEM experiments where hundreds of frames must be analysed.

To facilitate faster and more in-depth analysis of HRTEM images we have developed an automated image processing module using machine learning techniques. First, the particles need to be separated from the noisy amorphous background. This is realized by a neural network which was trained on labelled HRTEM images. The obtained segmentation maps are then further processed such as splitting overlapping particles. After obtaining binary maps for all particles in the image, shape and size related parameters like circularity, equivalent diameter, and Feret diameter are extracted. All these steps are implemented in a fully contained automated routine which is able to analyse an HRTEM image within a few seconds. The detected particles can also be further analysed in regards to their inner structure (e.g. crystallinity). This permits the automated analysis of large quantities of data and gives more insight into nanoparticle structures compared to a manual analysis. It also avoids an operator-induced bias during manual image analysis.

PP-084

In-situ investigation of solid phase evolution during lyophilization of mannitol-based antibody formulations using an XRPD climate chamber

S. Weber (Ludwigshafen/DE), M. Börner (Ludwigshafen/DE), V. Seiler (Ludwigshafen/DE), M. Witting (Ludwigshafen/DE), N. Nagel (Ludwigshafen/DE)

1. Introduction: Crystalline mannitol is commonly used as bulking agent in antibody formulations to provide structure to the lyophilized cake and prevent collapse. The quality of the lyophilized cake hereby substantially depends on the solid state of the incorporated mannitol. While crystalline anhydrous mannitol helps to create a firmer cake structure this is not true for amorphous mannitol. The hemihydrate is also an undesired physical form as it may reduce the drug product stability by releasing bound water molecules into the cake.

2. Objectives: Our aim was to identify the freeze drying process parameters with the most impact on the final mannitol composition and to use them afterwards for optimization of the final lyophilizate.

3. Materials & Methods: X-ray powder diffractometer Empyrean Series II from Malvern Panalytical; Climate chamber CHC+ from Anton Paar; SEM from JEOL; mannitol-based antibody formulations and the corresponding placebos

4. Conclusion: An X-ray powder diffraction (XRPD) climate chamber was used to provide in situ an insight into each step of the whole freeze drying cycle with respect to the evolution of crystalline mannitol phases. This enabled us to efficiently optimize the conditions for the lyophilization process of mannitol-based antibody formulations of compositions representative for marketed biologics and the corresponding placebos. A characterization of the final lyophilized cakes by SEM and XRPD, gained from the XRPD climate chamber and from a freeze dryer, demonstrated the comparability of both techniques and proved the transferability of optimized process parameters.

PP-085

New insights in the mechanical phase transition of anatase to rutile (TiO_2) from in situ synchrotron investigations

H. Petersen (Mülheim an der Ruhr/DE), C. Weidenthaler (Mülheim an der Ruhr/DE)

Mechanochemistry is a fast-growing research field. One reason is its potential to develop cost-and energy-efficient as well as environmentally friendly processes.[1] Also, the possibility to stabilize alternative reaction pathways and products through a local energy-transfer raises interest. However, mechanochemistry was long-time considered a black box, until recently the first in situ investigations were published, leading to new insights into mechanochemical processes.[2,3] We report on the phase transition from anatase to rutile. Ex-situ investigations showed, that anatase can be transformed mechanically to brookite and further to rutile via mechanical activation.[4,5] The ex-situ experiments revealed that the first reaction step to the intermediate phase (brookite) is followed by a slower transformation to rutile.[5] However, to study the reaction mechanism and the resulting kinetics of the phase transition, in situ investigations, especially with a good time resolution are mandatory. In particular, since the chance of sample environment and the duration before the actual measurement may lead to changes in metastable reaction steps. In our in situ synchrotron powder diffraction experiments we observed an altered reaction mechanism (Figure 1). Instead of a transformation of anatase first to brookite, anatase directly transforms to the thermodynamic stable rutile modification.

Figure 1: Time-dependent synchrotron powder diffraction data of milling anatase with 25 Hz from (a) ex-situ data and (b) in situ experiments. The small letters mark the main reflection of the respective phases (a: anatase, r: rutile, b: brookite).

(1) P. Baláž et al., Hydrometallurgy, 77 (2005) 9-17.
(2) T. Friščić et al., Nat. Chem., 5 (2013) 66-73.
(3) L. Batzdorf et al., Angew. Chem., 54 (2015) 1799-1802.
(4) G. Mi et al., Materials Science Forum, 675–677 (2011) 283–286.
(5) F. Delogu et al., J. Mater. Sci., 53 (2018) 13331–13342.

Fig. 1

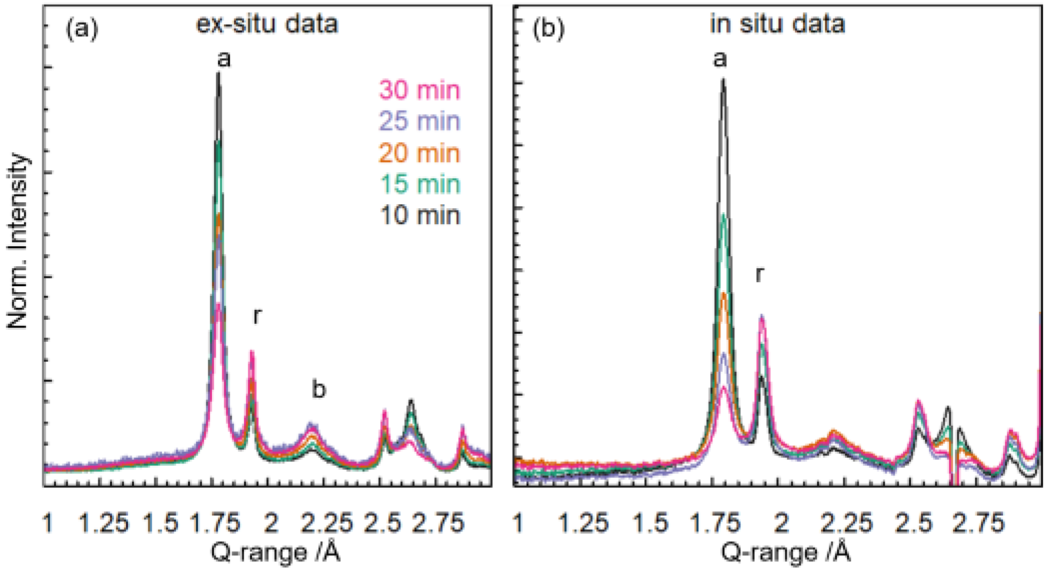

PP-086

Influence of CO_2 on the stability of siderite ($FeCO_3$) at high pressures and temperatures

L. Bayarjargal (Frankfurt am Main/DE), D. Spahr (Frankfurt am Main/DE), J. König (Frankfurt am Main/DE), B. Winkler (Frankfurt am Main/DE)

Carbonates are the dominant carbon host in the Earth"s crust and in subduction zones. Hence, the knowledge of their phase stabilities is necessary to understand the deep carbon cycle. Especially, Fe-bearing carbonates are of great interest as iron-incorporation affects the phase stabilities of Ca- and Mg-carbonates. The stabilities of Fe-bearing carbonates and $FeCO_3$ have been investigated at several *p,T*-conditions.

According to previous studies, siderite is stable up to its melting curve between 7 GPa and 20 GPa [1]. Below 7 GPa and at pressures between 20-50 GPa, $FeCO_3$ decomposes to various forms of iron oxide, carbon and CO_2 when heated to high-temperatures [1,2]. Above 50 GPa, a decomposition to iron oxides and different sp^3-hybridized Fe-carbonates can be observed. These sp^3-carbonates are at least stable up to 110 GPa [2]. It is most likely that phase stabilities depend on further parameters i.e. oxygen fugacity or the chemical environment. However, no experiments with $FeCO_3$ in different environments such as CO_2 have been carried out so far.

In this study we have investigated the influence of different environments (CO_2 and Ne) on the phase stability of $FeCO_3$ at high *p,T*-conditions using a custom-built laser heated mini diamond anvil cell (Fig.1 a). Samples and decomposition products were characterized by SEM, X-ray diffraction and Raman spectroscopy. We confirmed the decomposition of $FeCO_3$ in Ne in agreement with earlier studies (Fig.1 b,c)[1,2]. In contrast, we found no decomposition and no reaction between 20-50 GPa and up to 2500 K (Fig.1 d), when CO_2 was present. These results differ from Ca- and Sr-carbonates, where novel carbonates are formed by reaction with CO_2 [3,4].

Financial support by the DFG (FOR2125/CarboPaT, BA4020, WI1232) is gratefully acknowledged.

(1) Kang, et al., Chem. Geol. 400, 34 (2015)
(2) Cerantola, et al., Nat. Commun., 8, 15960 (2017)
(3) Spahr et al., J. Am. Chem. Soc. 144, 2899 (2022)
(4) König et al., ACS Earth Space Chem. 6,73 (2022)

Fig. 1

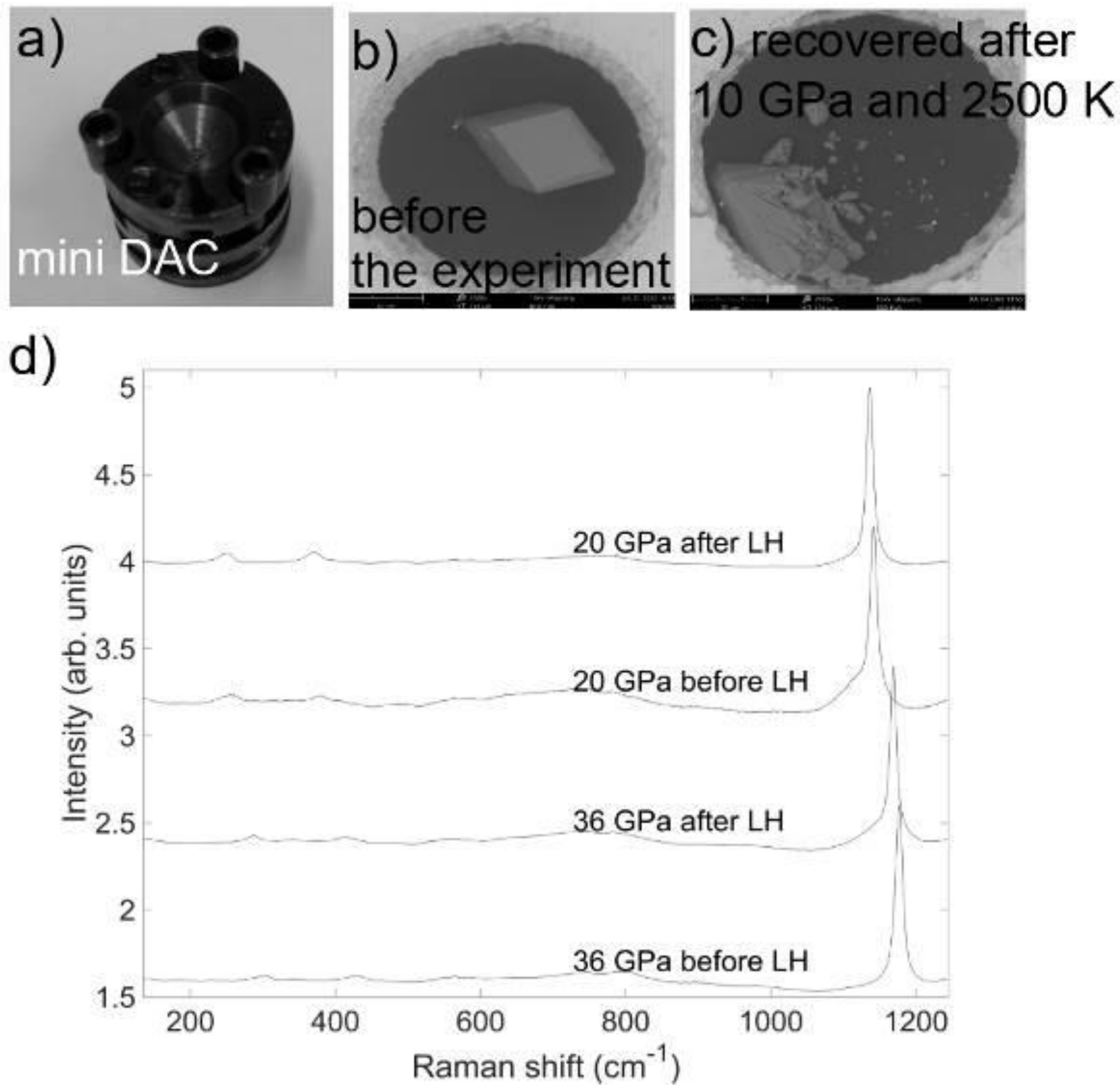
a)
mini DAC
b)
before
the experiment
c) recovered after
10 GPa and 2500 K
d)
Intensity (arb. units)
Raman shift (cm^{-1})
1.5
2
2.5
3
3.5
4
4.5
5
200
400
600
800
1000
1200
20 GPa after LH
20 GPa before LH
36 GPa after LH
36 GPa before LH

PP-087

NanoExtrem: Nano-focus end-station with double-sided CO_2 laser heating for X-ray diffraction, fluorescence and imaging experiments at ID27@ESRF

W. Morgenroth (Potsdam/DE), M. Mezouar (Grenoble/FR), G. Garbarino (Grenoble/FR), A. Pakhomova (Grenoble/FR), B. Wehinger (Grenoble/FR), M. Herrmann (Cologne/DE), M. Schulze (Cologne/DE), S. Jahn (Cologne/DE), L. Libon (Potsdam/DE), M. Wilke (Potsdam/DE)

The ESRF has built a new high-pressure beamline ID27 for nano-focused X-ray diffraction, fluorescence and imaging (XRD, XRF, XRI) at the extremely brilliant source EBS which is in operation since end of 2021.

In the framework of a first joint BMBF-funded project 'NanoExtrem', research groups from the Universities of Potsdam and Cologne have been contributing to the construction of this end-station by providing personnel and instrumentation. We are continuing this collaboration supported by a second BMBF-funded project 'NanoExtrem2'. Here, it is planned to add high-resolution X-ray emission spectroscopy (XES) and pulsed laser heating to the capabilities of the beamline.

This 'high-flux nano-XRD' beamline is optimized for the needs of the geo- and materials-science community for in-situ XRD, XRF and XRI studies at extreme conditions. It is possible to study materials relevant to processes of the deep Earth or other planetary bodies in an unprecedented manner.

Two already characterized highlights: The nano-beam has been focused to 300 × 300 nm and is available in the energy range 15 to 25 keV. The gain in flux when using the pink beam is by a factor of 70 compared to the monochromatized microbeam 2 × 2 µm. We will present performance parameters and results from experiments.

We acknowledge many divisions within the ESRF for construction and the German BMBF for financial support. BMBF project 'NanoExtrem' 05K19IP2 (Potsdam) and 05K19PK2 (Köln), 2019–2022 and 'NanoExtrem2' 05K22IP2 (Potsdam), 2023–2025.

PP-088

Mineralogy of large ocean worlds: I*n situ* high-pressure studies of hydrates

A. Pakhomova (Grenoble/FR), B. Journaux (Seattle, WA/US), I. E. Collings (Villigen/CH), S. Petitgirard (Zurich/CH), T. Boffa Ballaran (Bayreuth/DE)

Icy satellites of Jupiter and Saturn are the only celestial bodies beyond Earth where the presence of liquid water has been discovered in the form of subsurface oceans underlying the ice crusts [1]. Volatiles, salts and organic compounds are expected to be dissolved in the subsurface oceans and to form crystalline hydrates at the relevant thermodynamic conditions (pressures up to 1.7 GPa and temperatures ~100-350 K) [2]. Herein we report on usage of *in situ* single-crystal X-ray diffraction in a cryostat-cooled diamond anvil cell for the investigation of stability, polymorphism, and mineral physics of hydrates at conditions relevant for icy moons. The case studies on NaCl-H2O and $(CH_3)_2CO$ (acetone)–H_2O systems are presented. In the NaCl-H_2O system, we have discovered three novel NaCl hydrates, and determined two of their crystal structures (2NaCl·17H2O and NaCl·13H_2O) [3]. These unique structures are "hyper-hydrated" as pressure forces Na^+ and Cl^- ions dissociation within the crystal lattices. In the acetone-H_2O system, we have observed formation of clathrate hydrates - crystalline compounds consisting of hydrogen-bonded water molecules configured as cages that enclose small molecules of guest substances. Four clathrate hydrates of acetone have been synthesized. Three of them possess already known trigonal (sTr), orthorhombic (sO), and tetragonal (sT) structures while one is of previously unknown orthorhombic structure, so-called sO-II [4]. Structural analysis suggests that oxygens of acetone are hydrogen-bonded to the closest water oxygens of the host frameworks. The results and their application to the chemistry and evolution of the large ocean worlds will be discussed.

(1) Nimmo, F. & Pappalardo, R. T. (2016). Ocean worlds in the outer solar system. *J. Geophysical Res: Planets* **121**, 1378.
(2) Journaux, B., Kalousová, K., Sotin, C. *et al*. (2020) Large ocean worlds with high-pressure ices. *Space Sci. Rev.* **216**, 7.
(3) Journaux B., Pakhomova A., Collings I. E., Petitgirard S., Boffa Balaran T., *et al*. On the discovery of hyper-hydrated sodium chloride hydrates, stable at icy moon conditions. *Under revision in PNAS.*
(4) Pakhomova A., Collings I. E., Journaux B., Petitgirard S., Boffa Balaran T. *et al*. (2022) Host–guest hydrogen bonding in high-pressure acetone clathrate hydrates: *in situ* single-crystal X-ray diffraction study *J. Phys. Chem. Lett*. **13**, 1833.

PP-089

Liquid sulfur density and viscosity measurements by proton radiography

R. Belikov (Frankfurt am Main/DE), D. Merges (Frankfurt am Main/DE), D. Varentsov (Darmstadt/DE), K. Weyrich (Darmstadt/DE), M. Schanz (Los Alamos, NM/US), F. Mariam (Los Alamos, NM/US), R. Gavrilin (Moscow/RU), A. Skobliakov (Moscow/RU), A. Khurchiev (Moscow/RU), D. Nikolaev (Chernogolovka/RU), A. Müller-Münster (Frankfurt am Main/DE), G. Schmidt (Frankfurt am Main/DE), B. Winkler (Frankfurt am Main/DE)

An experimental set-up for density and viscosity measurements at pressure up to 100 bar and temperature up to 500 °C was built. Measurements of the liquid sulfur properties at the pressure and temperature conditions similar to the Venus surface were done with proton radiography at GSI. Data on sulfur density at 400—440 °C and viscosity in the temperature range of 200—400 °C at the constant pressure of 90 bar was acquired. Figure 1 shows a drawing and photos of the experimental set-up.

Time-resolved radiographic imaging of falling sphere experiments at moderate pressures (up to 200 bar) and variable temperatures (150 < T < 900 K) allows to determine viscosities and densities of liquids and melts and to characterise pressure-induced liquid-to-liquid phase transitions in molecular liquids thus providing an insight into the pressure-dependence of the fragility of liquids and melts.

Authors acknowledge support by BMBF under grant number 05P21RFFA2.

Fig. 1

PP-090

Next generation MetalJet sources enabling 10µm high brightness high energy beams for high pressure diffraction application

J. Hållstedt (Kista/SE), S. Hu (Kista/SE), G. Gopakumar (Kista/SE), E. Espes (Kista/SE)

The interest of exploring new materials at more extreme conditions is becoming increasingly important both for fundamental research as well as for application in e.g. superconductors and hydrogen storage. An important tool to characterize and understand these materials is by applying High pressure Xray diffraction HPXRD. This application rely on high energy Xrays to achieve good transmission through the Diamond anvil cell (DAC) and in order to capture large part of the reciprocal space. In addition, with smaller crystals higher pressures can be achieved at the expense of diffraction intensity. For this reason more advanced application of this technology has so far been limited to a rather limited number of synchrotron beam lines. To aid the scientists and to accelerate research we have demonstrated unprecedented high energy beams suitable for high pressure application utilizing the latest high power MetalJet microfocus Xray source. In this case the E1+ using I2 Indium alloy. The Xray source was coupled to a special high grade Montel optic with slits. The main beam characteristics were as follows:

- Monochromatic 24keV (Indium kalfa)
- Down to 10µm beam size (at sample position)
- 2-15 mRad divergence (slit controlled)
- Flux approximately 1e7 photons /sec. for 10 µm beam.

In this communication we demonstrate the setup and provide first glimpse of HPXRD results possible from this unique setup.

PP-091

How reliable are energies of phonon DOS determined from thermal expansion data?

R. J. Angel (Padova/IT), G. Novelli (Edinburgh/GB), S. Parsons (Edinburgh/GB), M. Alvaro (Pavia/IT)

The volume thermal expansion of solids at ambient pressure is often fitted with a function:

$V = V_0 + \gamma U(T)/K$ ....(1)

derived by integrating the Grüneisen relationship over temperature and assuming that γ and the bulk modulus *K* are independent of temperature. U(T) is the internal energy which can be expressed as a sum of several appropriate functions such as Einstein or Debye oscillators (e.g. [1]) as appropriate. While *K* of inorganic crystals typically decreases by <3% from 0 to 300 K, a decrease of 30-40% is normal for molecular solids. We have therefore investigated whether (1) can be used to provide reliable estimates of the characteristic temperatures and energies of the phonon density of states of molecular crystals by comparing the results to those obtained by fitting Mie-Grueneisen-Debye EoS (in which *K* and γ vary with temperature).

The low-temperature volume data [2] of deuterated methanol monohydrate can be fitted equally well with (1) or a MGD EoS, with both requiring two Debye functions to obtain a good fit. The assumption of constant bulk modulus in (1) results in higher Debye temperatures than those obtained from the MGD EoS. This is a general result, and thus Debye temperatures from fitting (1) should be interpreted with caution.

In contrast, fits to the volume expansion of d-HMT requires two Debye functions using (1), but only one in the MGD Eos, indicating that the properties of the second Debye oscillator obtained by fitting (1) are spurious and do not represent features of the phonon density of states of the crystal.

We conclude that the oscillator energies obtained by fitting the Grueneisen EoS (1) to volume data of molecular solids should be interpreted with caution, and that thermal-pressure EoS with multiple oscillators should be used when data to constrain the compressional behaviour are available.

(1) Murshed & Gesing (2013) Mat. Res. Bull. 48: 3284
(2) Fortes et al. (2011) Science, 331: 742

PP-092

Investigation of structural modifications under extreme conditions

I. Tzifas (Darmstadt/DE), K. O. Voss (Darmstadt/DE), M. Lang (Knoxville, TN/US), M. E. Toimil-Molares (Darmstadt/DE), C. Schroeck (Darmstadt/DE, Frankfurt am Main/DE), C. Trautmann (Darmstadt/DE)

We present the newly-built high-pressure irradiation platform at the heavy ion accelerator facility at GSI, where materials are simultaneously exposed to high static pressures and to heavy ion beams of several tens of GeV energy. The irradiation can induce unique defect configurations and chemical changes in materials yielding structural modifications, including point and cluster defects, amorphization or crystalline-to-crystalline phase transformations. Pioneering experiments at the SIS-18 accelerator at GSI revealed that the combination of pressure and ion irradiation can lead to the synthesis of new phases far from the thermodynamic equilibrium and to the possibility to recover a high-pressure phase upon pressure release [1,2]. The compression is achieved by using Diamond Anvil Cells (DACs), while a metallic gasket with a drilled hole in its center keeps the sample anchored. To prevent possible damage to the diamonds, the samples are irradiated through the gasket by using a remote-controlled adjustable collimating system. Monitoring of beam-induced structural changes is provided by online analysis of the sample in the DAC by means of Raman spectroscopy through the two diamond anvils. To understand further the fundamental mechanisms of radiation-induced structural modifications under pressure, ex-situ synchrotron-XRD measurements are employed to characterize the radiation responses of various materials. The aim of this development is to provide a user platform in Cave A with SIS-18 beams and at a later stage in the APPA Cave of the new FAIR facility.

(1) Lang, M., Zhang, F., Zhang, J., Wang, J., Schuster, B., Trautmann, C., Neumann, R., Becker, U., Ewing, R.C. *Nanoscale manipulation of the properties of solids at high pressure with relativistic heavy ions. Nat. Mater* 2009, 8(10): p. 793-797 https://doi.org/10.1038/nmat2528

(2) Glasmacher UA, Lang M, Keppler H, Langenhorst F, Neumann R, Schardt D, Trautmann C, Wagner GA (2006) Phase transitions in solids stimulated by simultaneous exposure to high pressure and relativistic heavy ions. Phys Rev Lett 96:195701-1–195071-4, https://doi.org/10.1103/PhysRevLett.96.195701

PP-093

High temperature behavior of Mn-bearing, Bi-rich hingganite-(Y) from the Jaguaraçu Pegmatite, Brasil

A. Shagova (St Petersburg/RU), L. Gorelova (St Petersburg/RU), O. Vereshchagin (St Petersburg/RU), A. Kasatkin (Moscow/RU)

Minasgeraisite-(Y) ($Y_2CaBe_2Si_2O_{10}$) is a rare mineral from gadolinite group. Due to its rareness, crystallographic and chemical data were obtained separately [1][2]. The aims of this work were to comprehensively study gadolinite group mineral from minasgeraisite-(Y) type locality (the Jaguaraçu Pegmatite, Brasil) and obtain data on its high temperature behaviour (27-1000 ˚C). Both elemental analysis and single crystal structure refinement revealed that studied sample should be considered as Mn-bearing, Bi-rich hingganite-(Y). Room temperature data showed good similarity to previously obtained data by Cooper & Hawthorne [2], except space group (*P*21/*c* instead of *P*1). All unit cell parameters continuously expand below 900 °C, whereas above this temperature decomposition begins (Fig. 1). Expansion of the unit cell parameters is connected to increase in the volume of $YO_6(OH)_2$ antiprism, while SiO_4 and BeO_4 tetrahedra remains stable. Studied mineral showed anisotropic thermal behavior (α_{max} / α_{min} = 3.4), the maximum and minimum expansion occur within the layer plane along *b* and *c* directions. The volume thermal expansion is low ($\alpha_V = 20 \times 10^{-6}$ °C^{-1}) in comparison with gadolinite-(Y) ($\alpha_V = 28 \times 10^{-6}$ °C^{-1} [3]). Mn-bearing, Bi-rich hingganite-(Y) appeared to be more stable than borosilicate analogues (< 720 °C [4]), but less stable than another beryllosilicate analogue (~1050 °C [3]).

The studies were done at the RC SPSU "Geomodel" and "X-Ray diffraction methods of research" and funded by the Russian Science Foundation, grant 22-27-0043.

Figure 1: The unit cell parameters of studied sample.

(1) Foord E.E., Gaines R.V., Crock J.G et al. (1986) *Am. Min.*, 71, 603–607.
(2) Cooper M.A., Hawthorne F.C. (2018) *Min. Mag.*, 82, 301–312.
(3) Gorelova L.A., Panikorovskii T.L., Pautov L.A. et al. (2021) *J. Solid State Chem.*, 299, 1–12.
(4) Krzhizhanovskaya M.G., Gorelova L.A., Bubnova R.S. et al. (2018) *Phys. Chem. Miner*, 45, 463–473.

Fig. 1

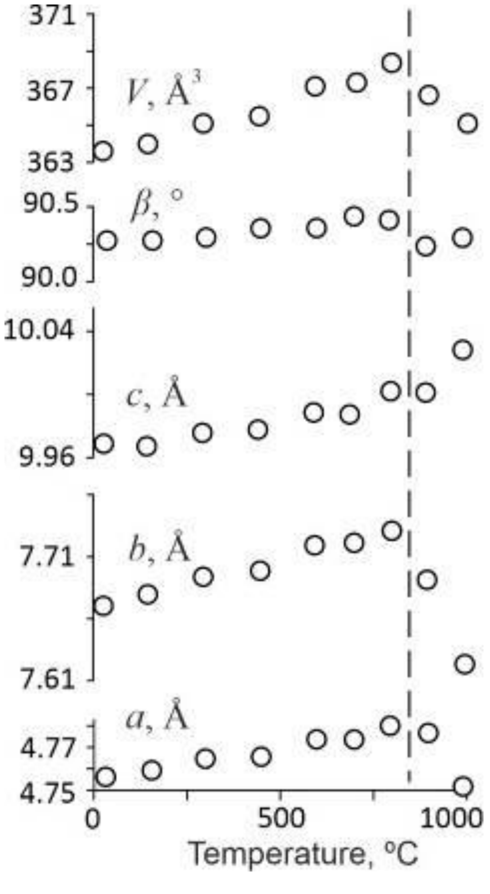

PP-094

Synthesis, structure and properties of of BaCO3(*hR*5)-type PbCO3

W. Crichton (Grenoble/FR), L. Bayarjargal (Frankfurt am Main/DE), V. Milman (Cambridge/GB), B. Winkler (Frankfurt am Main/DE)

A new recoverable form of PbCO$_3$ has been synthesized at a pressure of 10.8 GPa and at temperatures higher than 735 K with a trigonal rhombohedral lattice of a = 5.20727(14)Å and c = 8.4326(3)Å, at standard conditions. This new structure of PbCO$_3$, Figure 1, which has been derived from in situ diffraction data and then was confirmed and refined using DFT calculations, is of BaCO$_3$(*hR*5)-type, also known for BaCO$_3$ at 1 bar and high temperatures. Data collected during its coexisitence with aragonite-type PbCO$_3$ indicates an increase of density of 4.8% at the transition. Our observations of the transformation are compatible with the transformation in the 6-10 GPa range to the field labelled PbCO3-III in previous studies of the phase diagram. DFT calculations have been employed to understand the Raman signature of this phase and predict properties such as its non-linear optical activity.

Figure 1: Relaxed DFT structure for PbCO$_3$ at 10 GPa.

Fig. 1

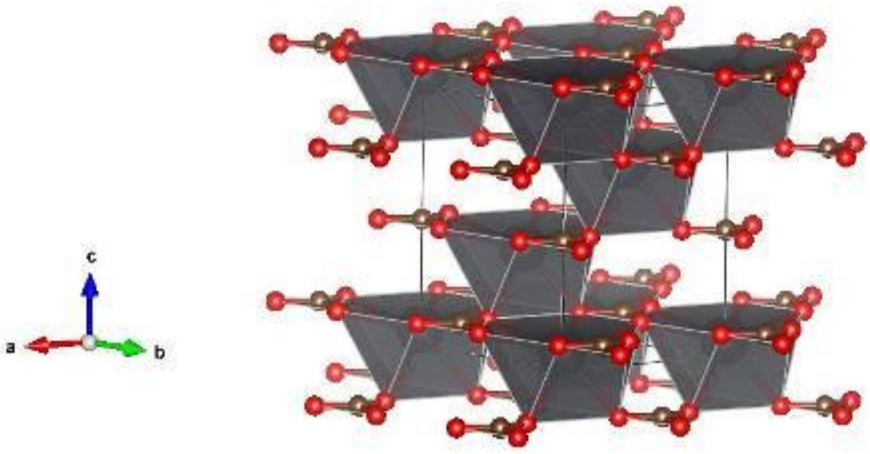

PP-095

Negative thermal expansion, thermodynamic properties, temperature-dependent Raman scattering and crystal growth of large single crystals of metal-organic framework structures

E. Haussühl (Frankfurt am Main/DE), L. Bayarjargal (Frankfurt am Main/DE), D. Spahr (Frankfurt am Main/DE), J. Büscher (Frankfurt am Main/DE), R. Luchitskaia (Frankfurt am Main/DE), B. Winkler (Frankfurt am Main/DE)

Metal-organic framework structures (MOFs) consist of transition metals that are connected via organic ligands. Together they form frameworks with cavities, which can contain guest molecules. The incorporation of guest molecules allows to build MOFs with tailored properties by exchanging the transition metals, organic ligands or guest molecules. Metal-guanidinium formates (***M*GuFo**), $[C(NH_2)_3][M^{2+}(HCOO)_3]$, belong to the perovskite-type MOFs with the general formula ABX_3, where $B = M^{2+}$ is a metal cation (here $M^{2+} = Cu^{2+}$, Zn^{2+}, Mn^{2+}, Co^{2+}) which is octahedrally coordinated by formate ions ($X = HCOO^-$, abbreviated as Fo^-) [1]. The metal and formate ions form *M*−Fo−*M* chains and build up a three-dimensional framework with cuboid cavities, which are occupied by the small organic guanidinium cations ($A = [C(NH_2)_3]^+$). **Mn**-, **Zn**- and **Co-GuFo** crystallize in the orthorhombic space group *Pnna*, while the **Cu**-member crystallizes in $Pna2_1$ [1].

In this study, large single crystals having optical quality and dimensions up to about 20 × 20 × 30 mm^3 were grown from aqueous solution. The thermal expansion, temperature-dependent Raman scattering and heat capacity of ***M*GuFo** with $M^{2+} = Cu^{2+}$, Zn^{2+}, Mn^{2+}, Co^{2+}, were determined.

The main part of these orthorhombic compounds with $M^{2+} = Zn^{2+}$, Mn^{2+}, Co^{2+} exhibit negative thermal expansion along one direction, which was also found in trigonal **CdGuFo** and **CaGuFo** [2-3]. To understand the driving force of the negative thermal expansion, the crystal structure of **ZnGuFo** was solved at several temperatures between 100 K and 350 K.

(1) Hu K-L et al. Chem. Eur. J. 15, 12050 (2009)
(2) Collings I E et al. Dalton Trans. 45, 4169 (2016)
(3) Haussühl E et al. J. Phys. Chem. C 126, 6427−6435 (2022)

E.H. and J.B. acknowledge support by DFG under grant number HA 5137/5.

PP-096

Mineral-like copper oxyvanadates with different dimensions of OCu_4 complexes

V. Ginga (Leipzig/DE, St Petersburg/RU), O. Siidra (St Petersburg/RU), A. Tsirlin (Leipzig/DE)

Related to the development and research of functional materials, the most popular and relevant area of scientific research in recent years is the study of the behavior of magnetic materials at different temperatures [1]. Particular attention has been paid to the area of low-dimensional magnet systems [2]. Of particular interest to researchers are compounds containing the cations Cu^{2+} and V^{4+}. This is due to the observed magnetic phenomena arising from the complex spin-1/2 network of these ions. Some minerals Cu^{2+} and V^{4+} have such a structure. However, due to the presence of impurities, investigation of the magnetic properties of natural samples is not possible. Nevertheless, minerals are actively used as prototypes for obtaining new synthetic compounds and studying their unique functional properties [3].

A large number of copper and vanadium oxysalt minerals with interesting structural architectures are found in natural conditions on fumaroles with a highly oxidizing environment. A significant variety of such minerals characterizes the fumaroles of scoria cones of the Northern Breakthrough of the Great Tolbachik Fissure Eruption of 1975-1976 (GTFE) [4]. A characteristic feature of the exhalative minerals of Cu^{2+} oxysalts is the presence of additional oxygen atoms forming oxocentered tetrahedra $[OCu_4]^{6+}$ [5]. The $[OCu_4]^{6+}$ tetrahedron is the simplest frustrated block, since it contains four spin triangles with potentially competing magnetic interactions. To date, many of the analogues of exhalative copper minerals with additional oxygens have been characterized as frustrated antiferromagnets [6].

The authors of this work obtained synthetic compounds based on rare exhalative minerals of the copper oxyvanadate chloride group: α-$Cu_4O_2(VO_4)Cl$ (*Pbcm*) (**1**), β-$Cu_4O_2(VO_4)Cl$ (*P*2/*n*) (**2**), $Cu_5O_2(VO_4)_2 \cdot (KCl)_{0.5}$ (**3**), $Cu_5O_2(VO_4)_2 \cdot (CuCl)$ (**4**) and $Cu_9O_2(VO_4)_4Cl_2$ (**5**). The synthesis was mineralogically inspired, and within the framework of the method of CVT reactions, approximate conditions were selected to the fumaroles of the Second Scoria Cone of the GTFE 1975-1976 [7].

The results of a detailed consideration of the features of crystal chemistry, thermal and magnetic properties of the studied compounds will be presented. The report will also contain the magnetic configurations of magnetic moments of copper in crystal structures of 1-5 with different dimensions of oxocentered complexes.

Figure 1: Comparison of complexes of $[OCu_4]^{6+}$ oxocentered tetrahedra in compounds **1**-**5** obtained in the framework of this work in the CuO-V_2O_5-$CuCl_2$ system. The crystal structures of the presented compounds **1**-**5** are based on complexes of different dimensions formed from oxocentered tetrahedra $[OCu_4]^{6+}$ with the participation of different types of linkages (corner, edge and their alternation). The oxocentered complexes of compounds **1**, **2** and **3** are based on $[O_2Cu_4]^{4+}$ dimers. In compound **1** they form 1D chains, in compound **2** dimers participate in the formation of 2D $[O_2Cu_4]^{4+}$ layers, and in compound **3** dimers form 2D $[O_2Cu_5]^{6+}$ ribbons. In the lowest symmetry compound **5**, one-dimensional 1D $[O_2Cu_6]^{8+}$ chains are observed, which are exact fragments of 2D $[O_2Cu_5]^{6+}$ layers in compound **4**.

(1) Zhang, S., Zhang, C., Ma, L., Ma, T., Wang, T., Gao, M. & Li, F. (2022). Phys. Condens. Matt. 638B, 413846.
(2) Chamorro, J. R., McQueen, T. M., & Tran, T. T. (2021). Chem. Rev. 121 (5), 2898-2934.
(3) Krivovichev, S. V. (Ed.). (2008). Minerals as Advanced Materials I. 236 p. Berlin: Springer.
(4) Fedotov, S.A., Flerov, G.B., Chirkov, A.M. (1984). The Great Tolbachik Fissure Eruption (1975-1976, Kamchatka). 637 p. Moscow: «Science» Publishing.
(5) Krivovichev, S.V., Filatov, S.K. (1999). Am. Miner. 84, 1099–1106.
(6) Inosov, D. S. (2018). Quantum magnetism in minerals. Adv. Phys. 67, 149−252.
(7) Vergasova, L.P., Filatov, S.K. (2016). J. Volcanol. Seismol. 10, 71–85.

Fig. 1

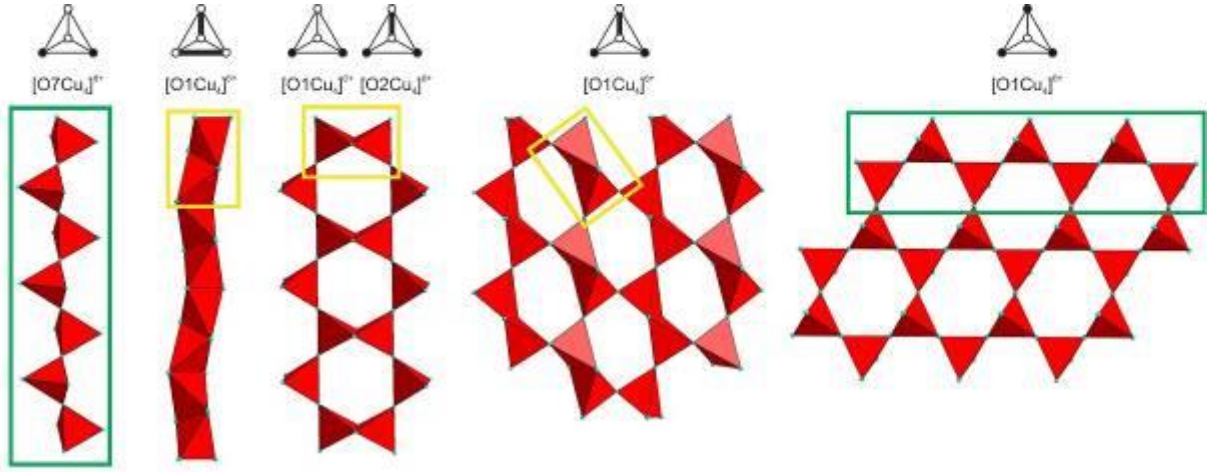

1D chain
$[O_2Cu_6]^{8+}$
$Cu_9O_2(VO_4)_4Cl_2$

1D chain
$[O_2Cu_4]^{4+}$
α-$Cu_4O_2(VO_4)Cl$

2D ribbon
$[O_2Cu_5]^{6+}$
$Cu_5O_2(VO_4)_2\cdot(KCl)_{0.5}$

2D layer
$[O_2Cu_4]^{4+}$
β-$Cu_4O_2(VO_4)Cl$

2D layer
$[O_2Cu_5]^{6+}$
$Cu_5O_2(VO_4)_2\cdot(CuCl)$

PP-097

Investigation of by-products of processed spodumene mineral concentrates to lithium hydroxide

J. Woskowski (Halle (Saale)/DE, Halle (Saale)/DE), S. Stöber (Halle (Saale)/DE), A. Neumann (Halle (Saale)/DE, Halle (Saale)/DE), H. Roggendorf (Halle (Saale)/DE), R. Wehrspohn (Halle (Saale)/DE, Halle (Saale)/DE)

Large quantities of aluminosilicates/ leached spodumen (LS) are produced during the processing of spodumene concentrate into lithium hydroxide. To avoid deposition, the potential reuse of these materials in the cement industry will be investigated. Initial XRD and XRF analyses show that the LS can be represented by the SiO_2-CaO-Al_2O_3 system and have a similar chemical composition as fly ash. Mineralogically, LS consists primarily of leached and residual spodumene and quartz. Trace elements, among them possible lithium remnants, will be determined by ICP-MS. Quantitative phase determination will be done by the Rietveld Method. Additional structure information will be gained by NMR, IR and/or Raman spectroscopy. To clarify the use of LS as supplementary cementitious materials, the hydration properties of different cement mixtures of LS powders and ordinary portland cement (OPC) will be investigated. The reaction behaviour of the LS in connection with OPC will be determined by calorimetry and the phase formations by X-ray methods. Especially, phases influencing the chemical reactivity of LS will be in the focus of structural investigations.

PP-098

Advancements in anomalous diffraction for cation order determination at beamline KMC-2

D. M. Többens (Berlin/DE), D. Matzdorff (Berlin/DE), Y. Tomm (Berlin/DE), G. Gurieva (Berlin/DE), S. Schorr (Berlin/DE, Berlin/DE)

Isoelectric cations are hard to distinguish by routine laboratory X-ray diffraction, as their scatting power is very similar. Besides neutron radiation, anomalous X-ray diffraction is commonly used to overcome this problem, utilizing the strong energy dependency of scattering factors close to the element-specific X-ray absorption edges. A variant of this, Multiple Edge Anomalous Diffraction (MEAD) [1] was found by us to work particularly well for the purpose of determination of cation arrangement within a known parent structure. This method calls for measuring the energy dependency of the intensity of individual Bragg peaks around the X-ray absorption edge of chemical elements (Figure 1).

The energy range of 5 – 14 keV of beamline KMC-2 at BESSY II, HZB, Berlin [2] allows to do measurements at the absorption edges of technically relevant elements, in particular the transition metals of the 4th period. Mn, Fe, Cu, Zn, Ga, Ge form a wide range of chalcogenides semiconductors, many of which have drawn wide attention for their potential applications in many fields [3]. Depending on their band gaps these materials are interesting for thin film solar cells, high-temperature thermoelectric materials, and nonlinear optics. Solid solutions of both cations and anions allow fine tuning of physical properties. It is well established that the cation arrangement in the respective structure is crucial for the electronic properties.

The compounds listed above crystallize in structure types derived by cation ordering from the cubic sphalerite type or the hexagonal wurtzite type crystal structure. The particular cation arrangement results either in kesterite or wurtz-kesterite structures, stannite or wurtz-stannite structures, or defect chalcopyrite types. These can be distinguished by MEAD and / or Joint Rietveld refinement at multiple energies.

(1) Többens, D.M., et al., *Acta Crystallographica B*, 2020. 76, 1027-1035.
(2) HZB, *Journal of large-scale research facilities*, 2016. 2, A49.
(3) Schorr, S. and G. Gurieva, Energy band gap variations in chalcogenide compound semiconductors: influence of crystal structure, structural disorder, and compositional variations, in Crystallography in Materials Science: From Structure-Property Relationships to Engineering, S. Schorr and C. Weidenthaler, Editors. 2021, 123 - 138.

Fig. 1

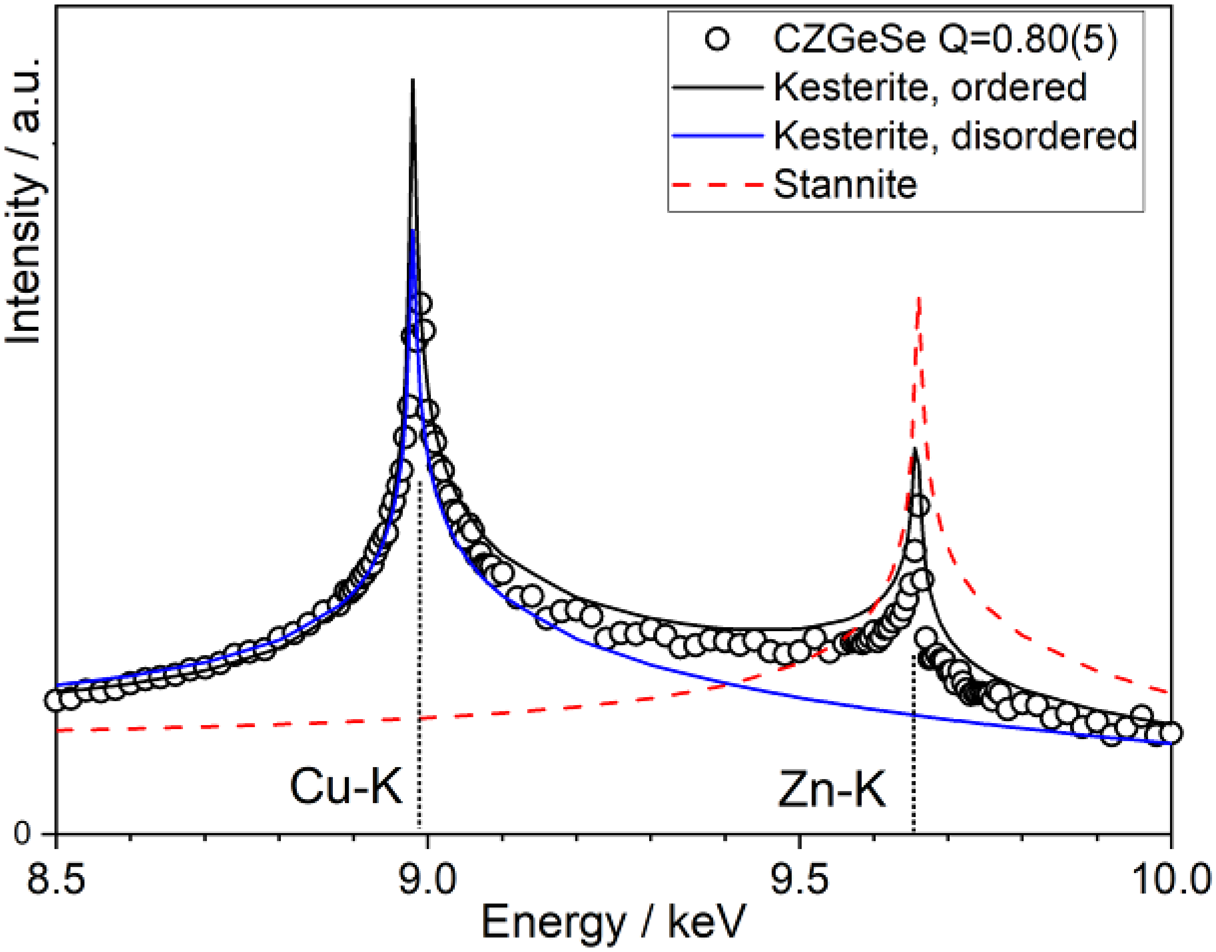

Fig. 1 Observed and simulated MEAD spectra of $Cu_2ZnGeSe_4$ for Bragg peak 011. Order parameter Q of cation disorder estimated from simulations.

PP-99

The polar guanidinium tartrates $[C(NH_2)_3]_2(L\text{-}C_4H_4O_6)\cdot H_2O$ and $[C(NH_2)_3]_2(L\text{-}C_4H_4O_6)$: Crystal growth, crystal structures and phase relations

I. Cisarová (Prague/CZ), I. Matulková (Prague/CZ), I. Nemec (Prague/CZ), C. Grams (Cologne/DE), J. Hemberger (Cologne/DE), P. Becker (Cologne/DE), L. Bohatý (Cologne/DE)

In an earlier publication [1] polar monoclinic (space group *P*2$_1$) guanidinium tartrate monohydrate, $[C(NH_2)_3]_2(L\text{-}C_4H_4O_6)\cdot H_2O$ (abbreviated as $Gu_2tart\cdot H_2O$), had been investigated concerning its piezoelectric and pyroelectric tensors [d_{ijk}] and [p_i]. The observed variability of the determined tensor components d_{222} and p_2 at 293 K with time and external electric field had given rise to the assumption that $Gu_2tart\cdot H_2O$ might be a ferroelectric, however, without further substantiation.

This motivated our investigation of the temperature-dependent phase stability of $Gu_2tart\cdot H_2O$ and our search for a possible paraelectric parent phase by means of thermal analysis, temperature-dependent powder-XRD and Raman spectroscopy as well as thermo-optical and temperature-dependent dielectric measurements. All measurements were performed using samples prepared from large single crystals grown at 311 K by controlled evaporation of the solvent over ca. 3 months.

According to these investigations $Gu_2tart\cdot H_2O$ decomposes by a peritectic reaction at 362 K with formation of crystals of the anhydrous phase Gu_2tart and a corresponding solution. The possibility of growth of Gu_2tart allowed us to determine the crystal structures of both compounds, which show a very close relationship of their atomic arrangements, but different symmetry (*P*2$_1$ vs. *C*2). The discovery of the peritectic nature of the decomposition of $Gu_2tart\cdot H_2O$ paved the way towards growth of large single crystals of anhydrous Gu_2tart, which was performed successfully at 371 K.

None of our temperature-dependent investigations of $Gu_2tart\cdot H_2O$ gave an indication of a structural phase transition to a paraphase below the peritectic reaction, etching of a (010) surface, however, revealed that the crystals show a domain structure. Based on detailed (temperature-dependent) dielectric investigations the possibility of ferroelectricity of $Gu_2tart\cdot H_2O$ will be discussed.

(1) W. Krumbe, S. Haussühl, R. Fröhlich, Z. Kristallogr. **187** (1989) 309.

PP-100

Multi-polymorphic tailormade thin-film titania phases as reference system for photocatalytic persistent organic pollutant degradation

O. Thueringer (Bremen/DE), A. Wollbrink (Bremen/DE), T. M. Gesing (Bremen/DE, Bremen/DE)

Titania (TiO_2) is known as highly efficient photocatalyst with an active band-gap transition in the UV region [1]. Because of its high activity, it is often used as a standard compound for photocatalytic (pc) degradation [1]. As the TiO_2 polymorphs, anatase, rutile and brookite play a major role in photocatalysis, it is important to be precise in synthesis of each phase due to the high difference in band-gap energy and pc efficiency. Additionally, the kind of inter-junctions between different polymorphs of TiO2 results in noticeable changes in their pc activity. For these reasons a systematic study of the synthesis process in hand with the respective absorption behavior is still of importance. As starting material, a solgel process containing a titano-organic-precursor (TTIP) is used [2]. Two different temperature treatments in the range of 373 K to 1023 K, were performed in terms of a thermodynamic and kinetic approach. The powder samples are characterized by several methods, e.g., XRPD, SEM, UV/Vis. For selected samples the pc activity is evaluated on a new concept of an in-situ flow cell (fig. 1) using thin films deposited on glass slides. Results indicate that the two different temperature treatments show slight differences in their phase composition with same average crystallite sizes, but still finally equilibrate in a short transformation or formation time. Pc degradation of dyes (e.g., methyl orange) designates inter-junctions between different phases as most active compounds, related to a modification of the band-gap energy. This work delivers a precise overview of different, pc active phases, including the synthesis and characterization of various thin-film systems and makes it to a very powerful tool for constructing efficient pc systems for application.

We acknowledge support by DFG (grant nr. GE1981/13-1).

Figure 1: Flow cell for photocatalysis

(1) Q. Guo et al. *Adv. Mater. 31 (*2019) e1901997
(2) A. Cenovar et al. *Adv. Nat. Sci.1 (*2012) 133-142

Fig. 1

PP-101

Expanding the family of mineral-like anhydrous alkali copper sulfate framework structures: new phases, topological analysis and evaluation of ion migration potentialities

A. Borisov (Kiel/DE), O. Siidra (St Petersburg/RU), V. Kovrugin (Bordeaux/FR), A. Golov (Vitoria-Gasteiz/ES), A. Holzheid (Kiel/DE), W. Depmeier (Kiel/DE)

To date, the most wide-spread method of energy storage is the use of Li-ion batteries [1]. However, an urgent problem is the limitation of lithium resources. In this connection, the search for new materials for electrochemical applications has become one of the important issues of materials science in recent years. K- and Na-ionic anhydrous sulfates and phosphates have received the greatest attention as possible alternatives. In order to avoid expensive methods of explorative chemistry for the search of new materials, it seems perspective to use the approach «from minerals to materials» [2,3]. We will present the results of the study of synthetic analogs of fumarolic sulfate minerals [4,5,6], as well as an evaluation of the migration properties of alkaline cations in their crystal structures. These compounds are both structural or stoichiometric analogs of saranchinaite Na2Cu(SO4)2 (with Na, K and Rb cations) and itelmenite Na2CuMg2(SO4)4 – two sulfate minerals recently discovered in the fumaroles of Tolbachik volcano (Kamchatka Peninsula). The synthesis of analogs of these minerals was carried out by methods of solid-state and gas transport reactions. The migration of alkaline cations in the crystal structures of the new compounds was evaluated using the BVEL and procrystal methods, as well as the porosity and density parameters of the frameworks were analyzed. Based on the results of this analysis, compounds of the cryptochalcite-cesiodimite structural type showed threshold energy values for the migration of alkaline cations of 2.14 eV, which allows us to consider them as prototypes of materials for electrochemical applications. 1. Goodenough J.B. & Park K.-S. J. Am. Chem. Soc. 2013, 135, 1167–1176. 2. Yakubovich O. et al. Minerals. 2020, 10, 524. 3. Kovrugin V.M. et al. Cryst. Growth Des. 2019, 19, 1233–1244. 4. Borisov A.S. et al. J. Appl. Cryst. 2021, 54, 237–250. 5. Siidra O.I. et al. Mineral. Mag. 2021, 85, 831–845. 6. Siidra O.I. et al. Acta Crystallogr. 2021, B77, 1003–1011.

Fig. 1

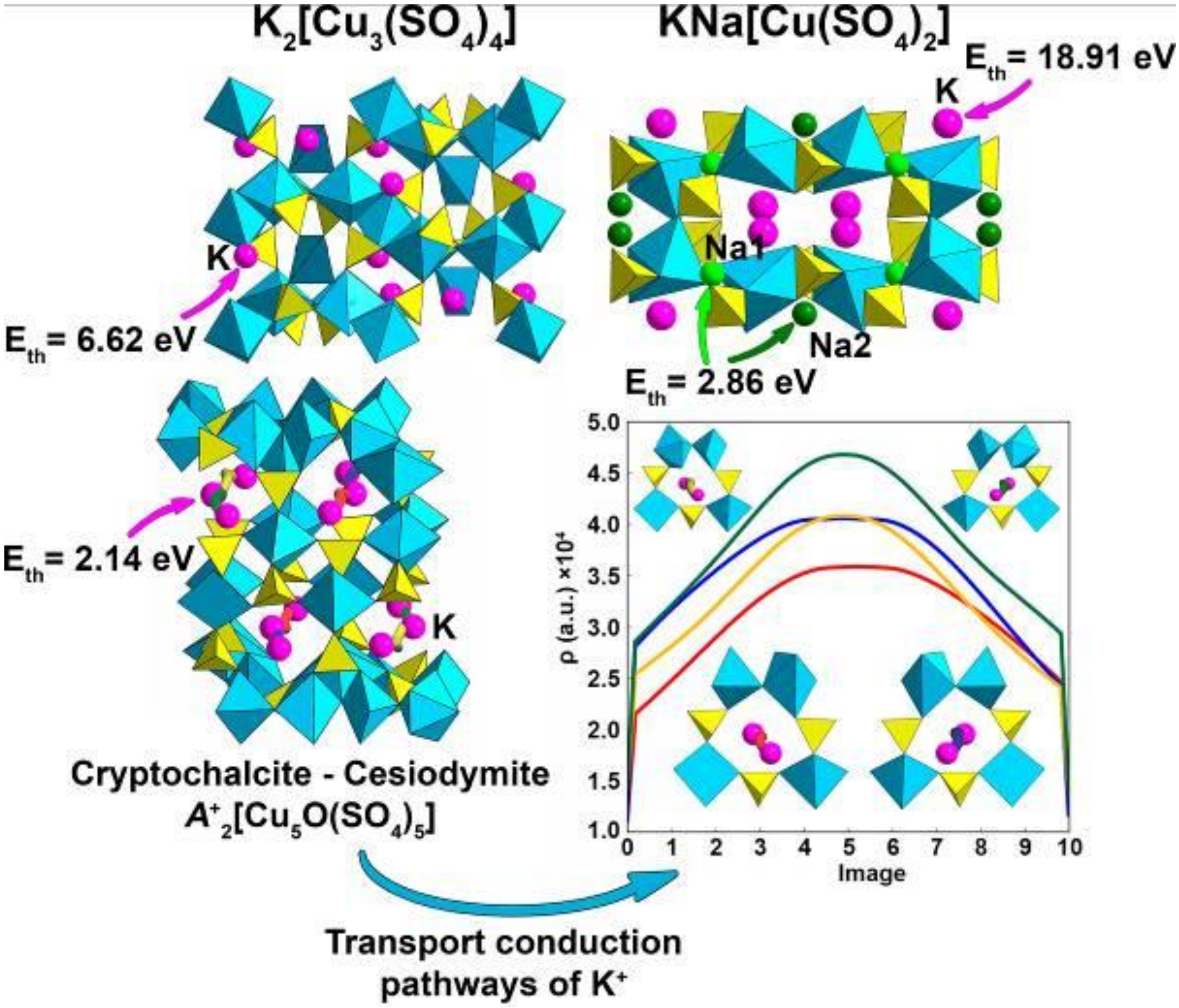
K$_2$[Cu$_3$(SO$_4$)$_4$]
KNa[Cu(SO$_4$)$_2$]
E$_{th}$= 18.91 eV
K
K
E$_{th}$= 6.62 eV
Na1
Na2
E$_{th}$= 2.86 eV
E$_{th}$= 2.14 eV
K
Cryptochalcite - Cesiodymite
A^+_2[Cu$_5$O(SO$_4$)$_5$]
ρ (a.u.) ×10^4
5.0
4.5
4.0
3.5
3.0
2.5
2.0
1.5
1.0
0
1
2
3
4
5
6
7
8
9
10
Image
Transport conduction pathways of K$^+$

PP-102

On the ordered structure of mechanochemically prepared $MAPbCl_3$

G. Schuck (Berlin/DE), D. M. Többens (Berlin/DE), S. Schorr (Berlin/DE, Berlin/DE)

Research interest has increasingly focused on hybrid perovskites $MAPbX_3$ like $[CH_3NH_3]+$ (MA), X = I or Cl as future photovoltaic material. In our recent investigation on wet-chemically produced $MAPbCl_3$ powders [1] we could show by Rietveld analysis of temperature-dependent synchrotron XRD data that two orthorhombic structures ("o1" and "o2") can be observed at low temperatures. At the lowest measured temperatures (below 140 K), "o1" and "o2" occur simultaneously, whereby the ratio of "o1" and "o2" depends on the Temperature (Fig. 1) and the degree of grinding with which the powder was prepared [1]. It has been observed that the more intensely the powder was ground (i.e. the more the sample was exposed to mechanical stress), the more phase "o2" is present. Furthermore, it was observed that the cubic room-temperature structure of $MAPbCl_3$ transforms directly into the two orthorhombic low-temperature structures without an intermediate tetragonal structure. Although the space group of the two $MAPbCl_3$ crystal structures, "o1" and "o2" is *Pnma*, as in the low-temperature phase of $MAPbI_3$, the cell of the "o1" crystal structure of $MAPbCl_3$ is with *a* = 2*ap*; *b* = 2*ap*; *c* = 2*ap* larger than the analogous cell of the orthorhombic low-temperature structure of $MAPbI_3$ with *a* = √2*ap*; *b* = 2*ap*; *c* = √2*ap* (where *ap* is the primitive cubic perovskite lattice parameter). Whereas in the "o2" structure of $MAPbCl_3$ the smaller cell (*a* = √2*ap*; *b* = 2*ap*; *c* = √2*ap*) could be observed. The results described in [1] partially correspond to the investigations by Alvarez-Galván et al. however, even three orthorhombic phases were observed by these authors at low temperatures [2]. Preliminary analysis from temperature-dependent synchrotron XRD measurements on mechanochemically prepared $MAPbCl_3$ ($mcMAPbCl_3$) powders indicate the absence of the low-temperature orthorhombic phase "o1" observed in wet-chemically prepared $MAPbCl_3$. However, at the lowest measured temperatures in $mcMAPbCl_3$, more complex ordering phenomena occur which have not yet been finally analyzed.

(1) G. Schuck, et. al., J. Phys. Chem. C, 2022, 126, 5388
(2) C. Alvarez-Galván et al., Cryst. Growth Des. 2019, 19, 2, 918–924

Fig. 1

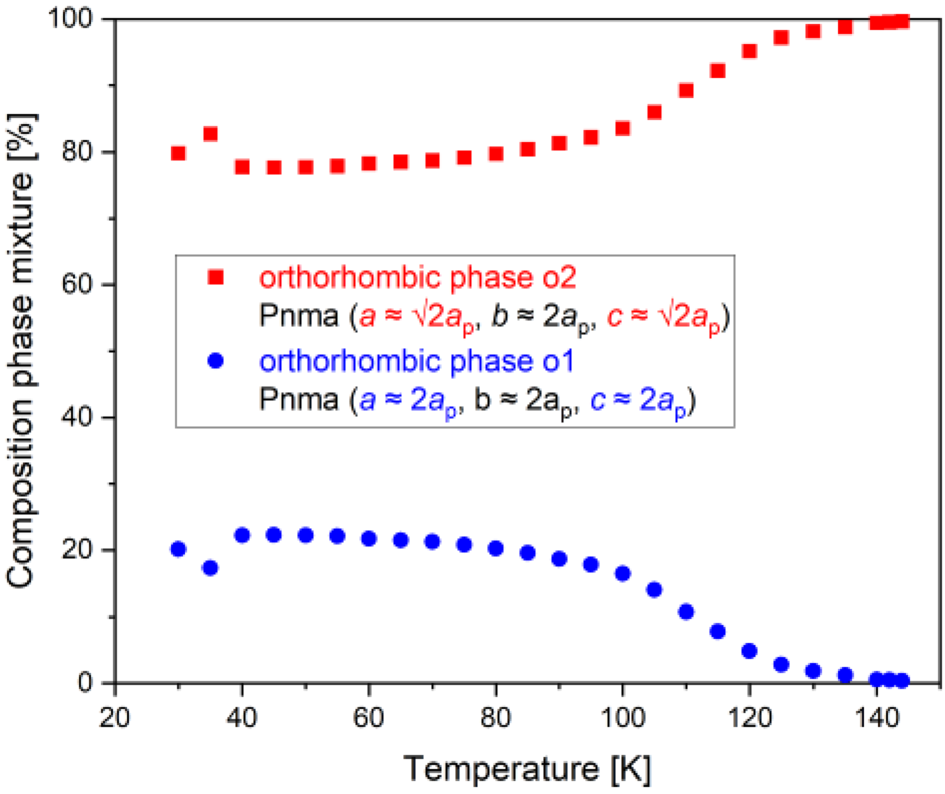

PP-103

The effect of a magnetic field on the precipitation of calcium carbonate polymorphs

S. Ouhenia (Bejaia/DZ), L. Amer (Bejaia/DZ), D. Chateigner (Bejaia/DZ, Caen/FR), I. Belabbas (Bejaia/DZ)

Introduction: Scale deposit issues frequently affect industrial systems, altering their operation and having negative energy and financial effects [1]. The primary component of these scales is frequently calcium carbonate (CaCO3) [2]. CaCO3 has a low solubility in water and tends to adhere onto the surfaces. The shape of the three anhydrous polymorphs of CaCO3, calcite, aragonite, and vaterite, is typically linked to the difficulty of removing them using water or other liquid flow [3]. Because of its rhombohedral crystal structure, the calcite phase creates deposits that are the most stable and dense. Vaterite and aragonite, in contrast, have spherical and needle-like shapes, respectively, which make them less adherent to surfaces and easier to remove. Chemical treatments using acidic substances are typically employed to remove calcium carbonate in order to prevent the scaling phenomena in industrial devices. Such a method has a number of disadvantages, including (i) its high cost, (ii) its detrimental effects on both humans and the environment, and (iii) its potential to cause corrosion issues in metal installations [5].

Objectives: An alternative method to chemical treatments is a physical techniques to treat the scale deposit problem [6]. One of these methods, which makes use of a magnetic field, has come to be recognized as both effective and promising [6]. In the current work, we investigated the impact of the applied magnetic field, on the precipitation of CaCO3.

Materials and Methods: Two solutions of CaCl2 and K2CO3 are mixed at different temperatures: 20°, 50°, and 80° C (with the presence or not of magnetic field (MF), which varied from 50 to 175 mT). The solid precipitates were collected, rinsed and dried under vacuum. The samples were examined using X-ray diffraction, and SEM analysis. Rietveld method and Popa anisotropic model are used to study the mechanism of action of the MF on the growth of different polymorphs of calcium carbonate.

Results: It was shown that the polymorphs' selectivity and proportions, as well as the shape and sizes of the CaCO3 particles, were all affected by the magnetic field. It was also shown that the MF reduced the overall precipitation rate of CaCO3 minerals in the solution. SEM images (Fig. 1) showed that the magnetic field modifies the shape of the rhombs of calcite as reflected by the destruction of the particles at 25 and 50 °C with a considerable decrease in their size at 80 °C. These results demonstrate that a magnetic field can effectively reduce the adhesion of calcite to surfaces, suggesting a potential use for it in preventing the growth of scale in industrial installations.

Conclusion: In this study, the effect of a magnetic feld, on the crystallisation and morphology of CaCO3 was investigated using a quantitative phase analysis based on the Rietveld method. The results showed that the presence of a MF alters the growth of the calcite phase. This was clearly observed through the decrease in its volume fraction at ambient temperature and in the destruction of the rhombs of its particles at 25 and 50 °C as it has been revealed by SEM images (figure 1). The presence of a MF also reduces the overall precipitation rate of CaCO3 and infuences the formation of the vaterite phase.

Figure 1: SEM images of CaCO3 particles synthesised at 25°C and and MF of 175 mT. Destruction of rhombs of calcite and cauliflowers shape of vaterite with a nucleation of small crystallites of vaterite on calcite particles .

References:

(1) A. Fathi et al., Effect of a magnetic water treatment on homogeneous and heterogeneous precipitation of calcium carbonate. Water Res. 40(10), 1941–1950 (2006).
(2) E. Chibowski, A. Szczes, L. Holysz, Influence of sodium dodecyl sulfate and static magnetic field on the properties of freshly precipitated calcium carbonate. Langmuir 21(18), 8114–8122 (2005).
(3) S. Kobe et al., The influence of the magnetic field on the crystallisation form of calcium carbonate and the testing of a magnetic water-treatment device. J. Magn. Magn. Mater. 236(1–2), 71–76 (2001).
(4) M. Gryta, The influence of magnetic water treatment on CaCO3 scale formation in membrane distillation process. Sep. Purif. Technol. 80(2), 293–299 (2011).
(5) C.Y. Tai et al., Magnetic effects on crystal growth rate of calcite in a constant-composition environment. J. Cryst. Growth 310(15), 3690–3697 (2008).

(6) A. Szkatula, M. Balanda, M. Kopeć, Magnetic treatment of industrial water. Silica activation. Eur. Phys. J.-Appl. Phys. 18(1), 41–49 (2002).

Fig. 1

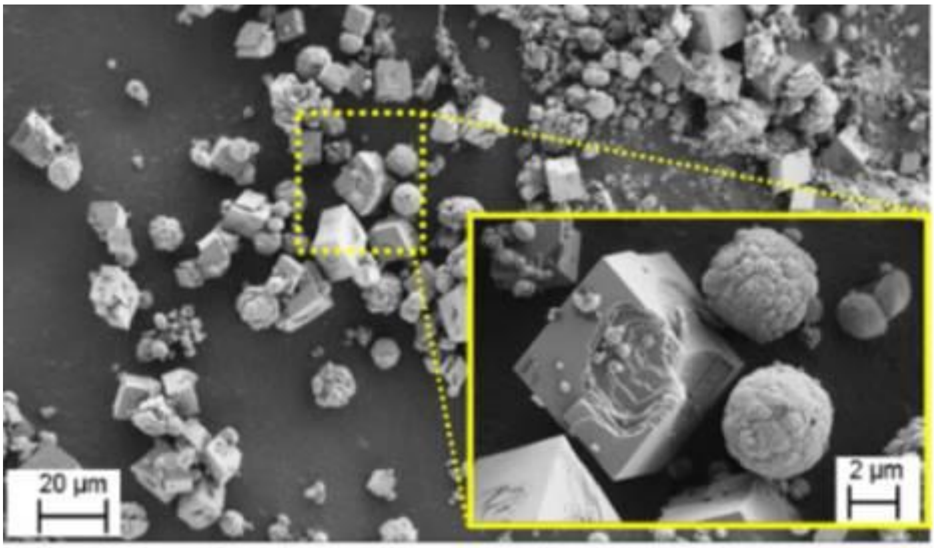

PP-104

Crystal growth and characterization of the 12L-Perovskite $Ba_4MIr_3O_{12}$ with $M = Eu^{III}$, Ce^{IV} and Nb^{V}

H. Schilling (Cologne/DE), P. Becker (Cologne/DE)

Highly frustrated magnetic systems are of great interest due to their exceptional properties and are topic of active research in solid state sciences. Within these systems, there are promising structures to investigate, such as iridium-based perovskites with a 12L stacking sequence. The iridium-based 12L-perovskites are characterized by isolated $[Ir_3O_{12}]$ triples of face-sharing $[IrO_6]$ octahedra ("trimers") [1]. In order to study the magnetic properties of the 12L perovskites, attempts were made to synthesize $Ba_4MIr_3O_{12}$ type single crystals with $M = Eu^{III}$, Ce^{IV} and Nb^{V}. For $M = Ce^{IV}$ and Nb^{V} it is expected that each trimer will result in a total magnetic moment $S \neq 0$, which can lead to competing intra- and inter-trimer magnetic interactions at low temperatures [2, 3]. For $M = Eu^{III}$ it is expected that each trimer will result in a total magnetic moment $S = 0$ [2]. The crystals were grown from melt solution using a $BaCl_2$ flux at cooling rates of 1.8 and 3 K/h. X-ray diffraction and simultaneous thermal analysis (STA) were used to determine the crystal structures and to investigate the temperature-dependent phase stabilities. $Ba_4MIr_3O_{12}$ with $M = Eu^{III}$ or Ce^{IV} is unstable at high temperature and melts incongruently. $Ba_4MIr_3O_{12}$ with $M = Nb^{V}$ melts congruently and forms single crystals with a size up to 500 µm.

(1) Y. Shimoda, Y. Doi, M. Wakeshima, Y. Hinatsu, *Inorg. Chem.* **48** (2009) 9952-9957

(2) Y. Shimoda, Y. Doi, M. Wakeshima, Y. Hinatsu, *Journal of Solid State Chemistry* **183** (2010) 1962–1969

(3) G. S. Thakur, S. Chattopadhyay, T. Doert, T. Herrmannsdorfer, C. Felser, *Crystal Growth & Design* **20**(5) (2020), 2871-2876

PP-105

Crystal structure of Pigment Yellow 75 from laboratory X-ray powder diffraction data

S. Ivashevskaya (Petrozavodsk/RU), M. U. Schmidt (Frankfurt am Main/DE)

For the colouration of plastics, lacquers, coatings and printings inks, hydrazone pigments are widely used nowadays. In contrast to soluble azo dyes, hydrazone pigments are generally insoluble in their application medium. In their final applications, the pigments are not dissolved, but finely dispersed, with particle sizes typically between 50 and 500 nm. The crystal structures are maintained, and the final properties of the material strongly depend on the crystal structure.

P.Y. 75 offers a reddish hue, good weather fastness and easy dispersing characteristics. It is commonly used for the formulation of yellow highway marking paints. The low solubility of the pigment in all solvents impedes the growth of single crystals suitable for X-ray analyses.

An X-ray powder pattern of P.Y. 75 was measured at room temperature in a capillary (0.7 mm) in transmission mode on a laboratory STOE-Stadi-P diffractometer using Cu$Ka1$-radiation.

After indexing, the crystal structure was successfully solved from laboratory powder diffraction data using simulated annealing in direct space with the program *DASH* [1]. The starting molecular model was built in Cartesian coordinates using the data of similar molecules [2] from Cambridge Structural Database. The molecule has 9 flexible torsion angles, which combined with 3 translational and 3 orientational degrees of freedom corresponds to a total of 15 degrees of freedom. The structure was Rietveld refined using restraints (bond lengths and angles, planarity of aromatic ring systems) with *TOPAS* [3]. In the crystal structure the molecules are planar with intramolecular hydrogen bonding.

Crystallographic data for P.Y. 75: a = 8.255(1) Å, b = 8.459(1) Å, c = 15.139(2) Å, a = 102.12(1)°, b = 90.42(1)°, g = 116.72(1)°, V = 916.91(16) Å^3, $P\bar{1}$, Z = 2.

(1) W.I.F. David, K. Shankland, J. van de Streek, E. Pidcock, W. D.S. Motherwell & J.C. Cole, J. Appl. Cryst. **39** (2006), 910
(2) A.Whitaker, Acta Crystallogr. **42**(1986), 1566
(3) A.A. Coelho, TOPAS-Academic 5; Coelho Software: Brisbane, 2012

Fig. 1

The nine flexible torsion angles in the molecule used in the structure solution step

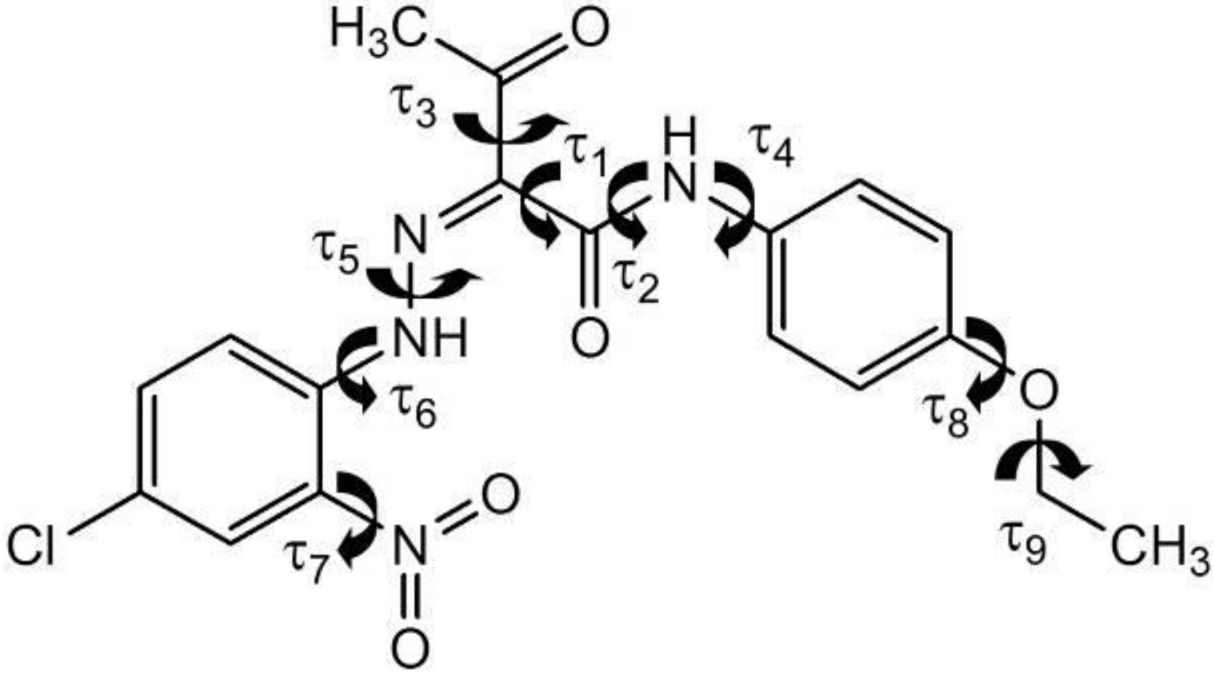

PP-106

High-pressure polymorph of pyrene

W. Zhou (Bayreuth/DE), Y. Yin (Bayreuth/DE), A. Aslandukov (Bayreuth/DE, Bayreuth/DE), L. Dubrovinsky (Bayreuth/DE), N. Dubrovinskaia (Bayreuth/DE)

Polycyclic aromatic hydrocarbons have long attracted interest as potential materials for various optical, optoelectronic, and electronic applications. In addition to application-oriented research, much work has been done for understanding the fundamental processes associated with their structure-property relationships. For example, the electronic and excitonic processes in aromatic crystals have been strongly linked to both the number of aromatic rings in the molecular structure and the arrangement of molecules in the crystal. External pressure is an effective way to affect packing of molecular units, and high-pressure single-crystal X-ray diffraction (SCXRD) is the best method to study it.

In order to analyze the crystal structure of pyrene ($C_{16}H_{10}$) at high pressure, we loaded single crystals of pyrene into a BX90-type DAC equipped with diamonds with the culets size of 250 μm and a rhenium gasket with a hole of ~120 μm in diameter. The samples were characterized using Raman spectroscopy in house and synchrotron SCXRD at the European Synchrotron Radiation Facility (ESRF). SCXRD analysis shows that at 2.5 GPa we got a new monoclinic phase that we call pyrene-IV (space group #14, P21/c, a = 7.6733(13) Å, b = 6.9186(3) Å, c = 16.4075(9) Å, β = 100.776(9)°), as other tree pyrene polymorphs have been previously known. The structure of pyrene-IV was solved and refined to R1 = 10.9 % and closely reproduced by ab initio calculations, which also confirmed its dynamical stability.

In the crystal structure of pyrene-IV, the molecules are arranged in a herringbone pattern. Contrary to pyrene structure known at ambient conditions, in which molecules of four fused benzene rings are flat, in pyrene-IV four-ring molecules are curved.

To explore the intermolecular interactions in pyrene crystals, we use Hirshfeld surfaces and fingerprint plots. They are unique for a given molecule in a particular polymorphic form. Hirshfeld surface show that two sides of the molecule are involved in quite different contacts with neighboring molecules. The fingerprint plot indicates that the bonds length of C — H- π hydrogen are ~ 3.0 Å and the distance of π - π stacking is ~ 3.4 Å.

PP-107

Synthesis and spectroscopic characterization of $(Bi_{1-x}M_x)_2O_3$ (M = Y, Gd, Er, Tb, Yb)

M. I. Hossain (Bremen/DE), M. M. Murshed (Bremen/DE, Bremen/DE), T. M. Gesing (Bremen/DE, Bremen/DE)

Many studies are known describing the different polymorphic forms of bismuth oxides (α-, β-, γ-, δ-Bi_2O_3) e.g., [1]. Of them, the high-temperature stable δ-phase has drawn particular attention for its O^{2-} ion conductivity at high temperatures [2], which possesses CaF_2-type structure with 25 % oxygen vacancies. Due to the dynamic nature of the oxygen atoms, leading to a time-averaged structure of the δ-phase, even ingenious quenching could not stabilize the phase at ambient condition. As such, stabilizing of the δ-phase to room temperature is commonly realized by substituting additional cations into α-Bi_2O_3. To further verify these findings, yttrium and selected transition-metal cations were used to stabilize δ-$(Bi_{1-x}M_x)_2O_3$ (M = Y, Gd, Er, Tb and Yb). Each composition is characterized by X-ray powder diffraction data Rietveld refinements. Whereas Raman spectroscopy studies on pure Bi_2O_3 cannot distinguish between the high-temperature δ- and its room-temperature α-analogue [3], the vibrational features of the metal oxide substituted δ-phases are well characterized using selective laser excitation. Due to characteristic f−f and f−d electronic transitions, the phononic information cannot not be separated. As such, it is of critical importance to find a transparent region with neither f-f nor f-d transitions using UV/Vis diffuse reflectance spectroscopy prior to the Raman investigations. The symmetric oscillation between O–M–O and its respective band width refers to the intrinsic disorder within the structure. Their convoluted peak maxima at 618 cm^{-1} Raman shift can be assigned to the Bi/M-O stretching modes of the time-averaged edge-truncated cube $(Bi/M)(O_{3/4})_8$ polyhedra. Analysis of the UV/Vis diffuse reflectance spectrum using the RATD method [4] results in e.g., band gaps of 2.22(2) eV and 2.05(2) eV for the Gd- and Y-containing δ-phase, respectively.

(1) H.A. Harwig, On the structure of bismuthsesquioxide: the α, β, γ, and δ-phase, Z. Anorg. Allg. Chem. 444 (1978) 151-166. Doi:10.1002/zaac.19784440118

(2) S. Hui, J. Roller, S. Yick, X. Zhang, C. Decès-Petit, Y. Xie, R. Maric, D. Ghosh, A brief review of the ionic conductivity enhancement for selected oxide electrolytes, J. Power Sources 172(2) (2007) 493-502. Doi:10.1016/j.jpowsour.2007.07.071

(3) R. Sharma, N. Benshalom, M. Asher, T.M. Brenner, A. Kossi, O. Yaffe, R. Korobko, Dynamic disorder in Bi sub-lattice of δ-Bi2O3, Cond-mat.mtrl-sci (2022) 1-6. Doi:10.48550/arXiv.2205.13289

(4) T.M. Gesing, M.M. Murshed, S. Schuh, O. Thüringer, K. Krämer, T. Neudecker, C.B. Mendive, L. Robben, Nano-crystalline precursor formation, stability, and transformation to mullite-type visible-light photocatalysts, J. Mater. Sci. (2022) 1-20. Doi:10.1007/s10853-022-07854-w

PP-108

Magnetic, electric and toroidal polarisation modes describing the physical properties of crystals - $NdFeO_3$ case

P. Fabrykiewicz (Aachen/DE, Garching/DE), R. Przeniosło (Warsaw/PL), I. Sosnowska (Warsaw/PL)

We present a general classifications [1, 2] to answer the question: *which groups allow to describe a given magnetic, electric and toroidal polarisation mode?* These three classifications are based on magnetic point groups used in two contexts: (i) the magnetic point group of the magnetic crystal class and (ii) the magnetic site symmetry point group of the Wyckoff position of interest. The following statements are true for magnetic, electric and toroidal modes: (i) there are 64 unique modes: 3 pure ferro-(magnetic/electric/toroidal), 13 mixed ferro-(magnetic/electric/toroidal) with antiferro-(magnetic/electric/toroidal) and 48 pure antiferro-(magnetic/electric/toroidal), (ii) a continuous reorientation of magnetic/electric/toroidal moment is possible only in triclinic or monoclinic symmetry [3], (iii) canted antiferro-(magnetic/electric/toroidal) ordering is possible only in monoclinic or orthorhombic symmetry.

To visualise the similarities of magnetic, electric and toroidal modes, we propose a new Rotation-Inversion (RI) notation [1] of magnetic point groups which does not prioritise or distinguish any of three generalised inversions: space inversion -1, time inversion 1' and the space-and-time inversion -1'. In RI notation each operation is presented as a product of one proper rotation and one generalised inversion. The general classifications of modes are presented for the case of $NdFeO_3$.

References

(1) P. Fabrykiewicz, R. Przeniosło and I. Sosnowska, *Acta Cryst. A* (in press)
(2) P. Fabrykiewicz, R. Przeniosło and I. Sosnowska, *Acta Cryst. A*77 (2021) 327-338
(3) R. Przeniosło, P. Fabrykiewicz and I. Sosnowska, *Acta Cryst. A*74 (2018) 705-708

PP-109

$Na_2Ca_3Si_2O_8$ or γ-$Na_2Ca_6Si_4O_{15}$? A hybrid approach combining 3D single-crystal electron and powder X-ray diffraction for solving a 50-year-old problem

V. Kahlenberg (Innsbruck/AT), H. Krüger (Innsbruck/AT), J. Vinke (Innsbruck/AT), S. Ito (Tokyo/JP), C. J. Schürmann (Neu-Isenburg/DE)

Phase assemblages of mixtures containing Na_2CO_3, $CaCO_3$ and SiO_2 in the molar ratio 1:3:2 have been studied at elevated temperatures. Synthesis experiments have been performed at 1000, 1100 and 1200 °C within a DTA-TG apparatus. Mass losses during heating and annealing periods of the high-temperature treatment have been studied *in-situ* using thermogravimetry. For the run at 1200 °C, the solid-state reactions resulted in almost phase pure polycrystalline material of a previously unknown high-temperature polymorph of $Na_2Ca_6Si_4O_{15}$, whose formation was triggered by significant Na_2O-losses at the reaction temperature. The new so-called γ-phase has been structurally characterized by a combination of 3D single-crystal electron and powder X-ray diffraction. Basic crystallographic data at ambient conditions are as follows: monoclinic symmetry, space group $C\,2$, a = 17.2066(1) Å, b = 5.47863(3) Å, c = 7.32583(4) Å, β = 91.435(4)°, V = 690.38(1) Å^3, Z = 2. Structure solution was accomplished by electron diffraction, whereas the subsequent refinement calculations were based on the Rietveld method using high-resolution data from a laboratory powder diffractometer. Similar to the other two already known $Na_2Ca_6Si_4O_{15}$ modifications, the crystal structure of the γ-phase contains both [Si_2O_7]-dimers and insular [SiO_4]-moieties. Tetrahedra and [CaO_6]-octahedra form a three-dimensional framework whose topological characteristics have been studied. The remaining Ca and Na cations are located on five symmetrically independent positions located in cavities of the network. There are sufficiently strong arguments that previously described "triclinic $Na_2Ca_3Si_2O_8$" is actually misinterpreted γ-$Na_2Ca_6Si_4O_{15}$ and that a sodium calcium silicate with a molar ratio of Na_2O:CaO:SiO_2 = 1:3:2 does probably not exist. Our investigation is an excellent example that 3D electron diffraction has transformed from an exotic technique for crystal-structure determination into an indispensable method for problems where small sizes of the crystallites is an issue.

PP-110

Electron Diffraction – The Swiss knife among the analytical equipment for solid state characterization for pharmaceuticals

D. Stam (Villigen/CH), G. Santiso-Quinones (Villigen/CH, Basel/CH), C. Schauerte (Bochum/DE), M. Pop (Cluj-Napoca/RO), J. Merkelbach (Villigen/CH), C. Jandl (Villigen/CH), G. Steinfeld (Villigen/CH)

In 1928, a milestone experiment by Devisson and Germer [1] showed that diffraction of electrons acts like waves, corroborating the theories of quantum mechanics. Almost one hundred years later, this very phenomenon can be exploited to get unprecedented answers to nanoscopic questions using a dedicated Electron Diffractometer. Electron Diffraction is now taking up momentum for crystal structure elucidation on materials which cannot be crystallized in large particles, as required for single crystal X-ray diffraction.

In 2018 Smeets et al.[2] introduced serial electron crystallography for structure and phase analysis of nanocrystalline materials. The downside of using a TEM device is that you cannot fully analyze all particles on the sample grid due to the design of the sample stage or goniometer. Recently a dedicated electron diffractometer came on the market which is not based on a TEM device but principally developed for electron diffraction. With the ease of use of these devices in combination with the unique goniometer design you are now able to automatically characterize nanocrystalline materials on the full sample grid.

This opens new innovative applications for people working in the industry and academic world for applications like impurity profiling, detecting micro crystallinity in amorphous materials, assisted solid state screening, which no other technology can do at this moment as swift and accurate. It shows that electron diffraction on a dedicated device is the Swiss knife see Fig 1 for solid state characterization, with respect to broadest range of applications.

This contribution aims to offer different case studies to show these new applications using electron diffraction for people working in the pharmaceutical and related industry or academia.

Figure 1: Electron Diffraction – The Swiss knife among the analytical equipment for solid state characterization useful for many applications in the pharmaceutical and related industry or academia

(2) Davisson, C. J.; Germer, L. H. (1928). *Reflection of Electrons by a Crystal of Nickel* Proceedings of the National Academy of Sciences of the United States of America, **14 (4),** 317–322.
(3) Smeets S, Zou X, Wan W. (2018) *Serial electron crystallography for structure determination and phase analysis of nanocrystalline materials.* J Appl Crystallogr.;**51(Pt 5),** 1262-1273

Fig. 1

PP-111

On the development of MagStREXS: A software to study magnetic structures

P. Bereciartua (Hamburg/DE), J. Rodríguez-Carvajal (Grenoble/FR), S. Francoual (Hamburg/DE)

Resonant Elastic X-ray Scattering (REXS) is a unique technique that combines features of X-ray diffraction and X-ray spectroscopy. It is an element, site, and valence specific probe that makes possible to study different types of charge, spin, and orbital orderings, both in solids and thin films [1,2]. This technique is also used to study magnetic phases, and, in this context, REXS and neutron techniques can be considered complementary. In some cases, REXS technique is particularly relevant: to study compounds including atoms with a large neutron absorption cross-section, like Gd, Eu, Dy… [3], in the case of magnetic structures that cannot be determined unambiguously by neutron techniques [4], or with magnetic phases involving more than one magnetic species. However, the analysis of the different types of data that can be collected in a REXS experiment is highly complex.

MagStREXS is a crystallographic software dedicated to the determination of **Mag**netic **St**ructures through **R**esonant **E**lastic **X**-ray **S**cattering and it is aimed to facilitate the analysis of REXS diffraction data to study magnetic structures. This software is under development since mid-2017 at beamline P09 [5] at PETRA III (DESY) and it is based on CrysFML, a library that includes some functionalities especially oriented to deal with magnetic structures.

Hereby, we will present an overview of MagStREXS, the main features implemented until now and some examples of the magnetic structures that have been studied with this software in the field of highly correlated systems.

(1) J. P. Hill and D. F. McMorrow (1996) *Acta Cryst.* A**52**, 236-244
(2) Y. Murakami and S. Ishihara (2017) "Resonant X-Ray Scattering in Correlated Systems", Springer Tracts in Modern Physics **269**
(3) T. Kurumaji, T. Nakajima, *et al.* (2019) *Science* **365**, 914-918
(4) J. Sears, L. E. Chern, *et al.* (2020) *Nature Physics* **16**, 837-840[5] J. Strempfer, S. Francoual, *et al.* (2013) *J. Synchrotron Rad.* **20**, 541-549

PP-112

Methylxanthine/Halogen System: An energetic point of view study

I. S. Konovalova (Düsseldorf/DE, Kharkiv/UA), M. Wyshusek (Düsseldorf/DE), G. J. Reiss (Düsseldorf/DE)

There is a general interest concerning halogen inclusion compounds, as these substances are used for several applications[1]. Furthermore, the bonding situation between a dihalogen molecule and various organic molecules is of theoretical interest[2]. We have a longstanding interest in the crystal structures and phase relations of methylxanthine based compounds[3]. As it is known that for theophylline (*theo*) at least four polymorphs and also some cocrystals are already reported, we decided to search for new compounds in the theophylline/halogen system. Dissolving elemental iodine and theophylline (*theo*) in diluted hydroiodic acid and cooling to 5 °C leads to purple/black crystals of $\mathit{theo}_2 \cdot \mathrm{I}_2$ ($P2_1/c$, a = 6.0794(1) Å, b = 16.9054(3) Å, c = 9.2013(2) Å, β = 99.973(3)°; $R_{\mathrm{gt}}(F)$ = 0.0208 {3185 refl.}; $wR_{\mathit{ref}}(F^2)$ = 0.0477 {3514 refl.}). Neighboring *theo* molecules are pairwise connected to dimers by two N–H-O hydrogen bonds (2.7664(2) Å; 170.2°). Each dimer is connected to two iodine molecules *via* N-I bonds (2.8880(1) Å; 177.0°) to form a chain structure.

In the case of this theophylline and iodine cocrystal the presence of only three types of weak intermolecular interactions (C–H-O, C–H-π and I-N) and strong N–H-O hydrogen bonds complicates the description of the crystal structure. The existence of the intermolecular interactions is confirmed by topological analysis of the electron density distribution within the Bader's theory (Atoms in Molecules). It is difficult to determine the main structural motif in the solid state only on the basis of geometric considerations. It is not known which interaction has the energetically dominant role in the crystal structure. Analysis of packing from the energetic viewpoint provides more information about the supramolecular organization of the cocrystal.

(1) W.T. Pennington, T.W. Hanks, H.D. Arman, H.D. Halogen Bonding with Dihalogens and Interhalogens. In: P. Metrangolo, G. Resnati, (eds.) Halogen Bonding. Structure and Bonding, Vol. 126, Springer, Berlin, **2007**.
(2) C. Laurence, J. Graton, M. Berthelot, M. J. El Ghomari, *Chem. Eur. J.* **2011**, *17* 10431-10444.
(3) G. Cavallo, P. Metrangolo, R. Milani, T. Pilati, A. Priimagi, G. Resnati, G. Terraneo, Chem. Rev.2016 116, 2478-2601

Fig. 1

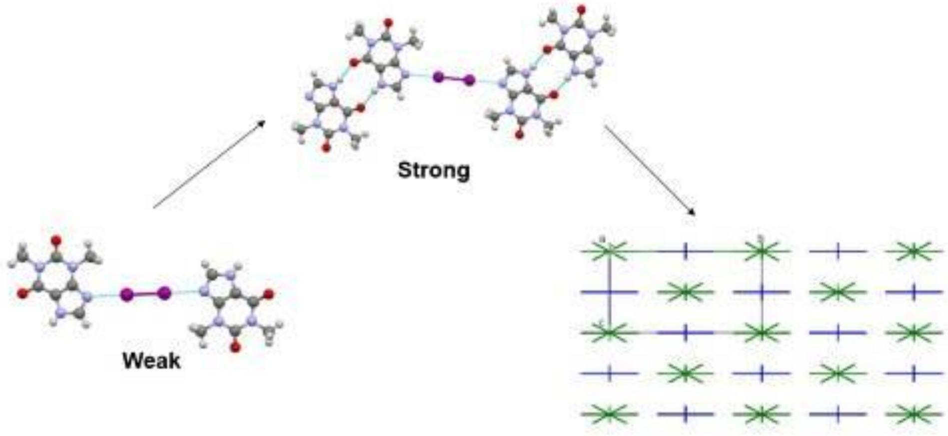

PP-113

Oxoscandates with scandium in tetrahedral coordination

I. Zaytseva (Munich/DE), C. Hoch (Munich/DE)

A number of crystal structures of oxoscandates has been reported, and in all known crystal structures the trivalent Sc cation is coordinated by oxide anions in an octahedral way. In this situation, typical Sc—O distances range from 2.07 to 2.24 Å [1,2] The Shannon radius for Sc^{3+} (CN = 6) r_{Sh} = 74.5 pm is close to the one of Zn^{2+} (r_{Sh} = 74 pm for CN = 6). In contrast to the variable coordination behaviour of Zn^{2+}, Sc^{3+} shows an unequivocal preference for octahedral coordination towards oxygen. The only example for a tetrahedral coordination of Sc^{3+} has been reported for a nitridoscandate. [3] The first tetrahedral oxoscandate anion was found in the suboxometalate Cs_9ScO_4 [4], and we report here on three further crystal structures in which [ScO_4] anionic units occur. They can be found as isolated neso-scandate anions $[ScO_4]^{5-}$ in the new hydroxide scandate $Cs_6[ScO_4][OH]$ (own structure type, monoclinic, space group $C2/m$, a = 17.2879(11), b = 11.9489(9), c = 6.9708(5) Å, β = 93.506(3)°, V = 1437,3(2) Å^3, Z = 4) or in the new suboxometalate Cs_7ScO_4 (own structure type, monoclinic, space group $P2_1/c$) and also in a tetracatena arrangement in the new oxoscandate $Cs_{14}Sc_4O_{13}$ ($K_{14}Fe_4O_{13}$ structure type [5], monoclinic, space group $P2_1/c$, a = 7.4801(2), b = 32.3193(7), c = 7.3795(2) Å, β = 119.4092(6)°, V = 1554.11(3) Å^3, Z = 2). In all cases, the oxoscandate anions show only minor distortions from ideal tetrahedral geometry despite low point symmetry. Typical Sc—O distances in the tetrahedral anionic entities range from 1.955 to 2.092 Å.

(1) R. Hoppe, B. Schepers, H. J. Röhrborn, E. Vielhaber, Über Oxoscandate: $LiScO_2$ und $NaScO_2$, Z. Anorg. Allg. Chem., 339, 130-143 (1965).

(2) H. Müller-Buschbaum, H. G. von Schnering, Zur Kenntnis des $CaSc_2O_4$, Z. Anorg. Allg. Chem., 336, 295-305 (1965).

(3) R. Niewa, D. A. Zherebtsov, S. Leoni, Li_3ScN_2: the first nitridoscandate(III) – tetrahedral Sc coordination and unusual MX_2 framework, Chem. Eur. J., 9, 4255-4259 (2003).

(4) C. Hoch, J. Bender, A. Wohlfarth, A. Simon, The suboxometallates A_9MO_4 (A = Rb, Cs; M = Al, Ga, In, Fe, Sc), Z. Anorg. Allg. Chem., 635, 1777-1782 (2009).

(5) H. P. Müller, R. Hoppe, Das erste oligomere Oxoferrat(III): $K_{14}(Fe_4O_{13})$, Z. Anorg. Allg. Chem., 580, 57-70 (1990).

IZ acknowledges support by DFG under grant number 444769550.

PP-114

$TmSb_2O_4Br$: The first Tetragonal Lanthanoid Oxoantimonate Bromide without mixed-cation occupation

R. J. C. Locke (Stuttgart/DE), T. Schleid (Stuttgart/DE)

In the system of rare-earth metal oxoantimonate halides with the composition $RESb_2O_4X$ there is a great structural diversity, although all these structures share some common features. For X = Br, compounds with the rare-earth metals RE = Y, Eu – Dy[1–3] are known so far, which crystallize in the monoclinic space group $P2_1/c$ and exhibit antimony-oxygen chains with vertex-connected ψ¹-tetrahedral $[SbO_3]^{3-}$ anions. The lattice parameters a and b become more and more similar with the heavier lanthanoids and furthermore the monoclinic angle β successfully approaches 90°. Two different structure types are known for X = Cl with an own one for RE = Sm and Eu[4] in the centrosymmetric tetragonal space group $P4/ncc$ showing a doubled lattice parameter c as compared to the other tetragonal oxoantimonate(III) chlorides. These occur with a slightly different structure for RE = Y, Gd – Lu[1,5] in the non-centrosymmetric space group $P42_12$. Both tetragonal structures contain rings of antimony and oxygen instead of the antimony-oxygen chains. Furthermore, with $Sm_{1+x}Sb_{2-x}O_4X$ (X = Cl and Br)[6] cation-disordered examples exist, which crystallize isotypically to $SmBi_2O_4Cl$[7] in the tetragonal space group $P4/mmm$, but exhibit a mixed occupation of samarium and antimony in the original bismuth layer. Almost colorless, platelet-shaped crystals of $TmSb_2O_4Br$ were obtained by reacting thulium sesquioxide with antimony sesquioxide and thulium tribromide and a flux of rubidium bromide in evacuated glassy silica ampoules at 750 °C via solid-state synthesis within three days. $TmSb_2O_4Br$ crystallizes isotypically to the chloride series $RESb_2O_4Cl$ (RE = Y, Gd – Lu) in the tetragonal non-centrosymmetric space group $P42_12$ with a = 772.89(2) pm and c = 901.34(3) pm for Z = 4 (CSD-2219078). The crystal structure contains two positions for the Tm^{3+} cations (Tm1 (2*a*): 0, 0, 0 and Tm2 (2*c*) 0, 1/2, 0.01376(13)), only one Sb^{3+} site (Sb (8*g*): 0.23979(11), 0.20363(11), 0.27620(12)) and two O^{2-} (O1 (8*g*): 0.0601(12), 0.2451(12), 0.1305(13) and O2 (8*g*): 0.4648(12), 0.2491(12), 0.1637(13)) as well as two Br^- (Br1 (2*b*): 0, 0, 1/2 and Br2 (2*c*): 0, 1/2, 0.4863(4)) anion positions each. Around each Tm^{3+} cation eight oxygen atoms form hemiprisms $[TmO_8]^{13-}$, which are linked by four edges to form layers 2D-$\{[TmO_{8/2}]^{5-}\}$ parallel to the (001) plane (Figure 1, *left*). The Sb^{3+} cations together with three oxygen atoms each build ψ¹-tetrahedra $[SbO_3]^{3-}$. Out of the three oxygen atoms, two are connected to another Sb^{3+} cation, while the third one maintains contact to only one of them. Four of these $[SbO_3]^{3-}$ units form 0D-$\{[Sb_4O_8]^{4-}\}$ rings (Figure 1, *mid*), which also reside within the (001) plane. Between the layers with Sb^{3+} cations nearly planar layers of Br^- anions are intercalated almost free of bonds (d(Sb–Br) = 333 – 350 pm). Therefore there is no real close connectivity to another differently charged layer, because two layers of Sb^{3+} cations flank the layers with Tm^{3+} cations via the oxygen atoms according to 2D-$\{[Sb(TmO_{8/2})Sb]^+\}$. Figure 1 (*right*) shows the complete unit cell of $TmSb_2O_4Br$ as viewed along [010].

(1) Locke, R. J. C., Goerigk, F. C., Schäfer, M. J., Höppe, H. A., Schleid, Th. (2022). *Roy. Soc. Chem. Adv.* **12**, 640.
(2) Goerigk, F. C., Paterlini, V., Dorn, K. V., Mudring, A.-V., Schleid, Th. (2020). *Crystals* **10**, 1089.
(3) Locke, R. J. C., Goerigk, F. C., Schleid, Th. (2021). *Z. Kristallogr.* **S41**, 78.
(4) Locke, R. J. C., Schleid, Th. (2022). *Z. Anorg. Allg. Chem.* **648**, e202200118.
(5) Locke, R. J. C., Goerigk, F. C., Schleid, Th. (2022). *Z. Naturforsch.* **77b**, 495.
(6) Goerigk, F. C., Schleid, Th. (2019). *Z. Anorg. Allg. Chem.* **645**, 1079.
(7) Kurz, M. V., Locke, R. J. C., Erden, A., Schleid, Th. (2022). *Acta Crystallogr.* **A78**, e574.

Figure 1: Infinite layers of edge-linked square hemiprisms $[TmO_8]^{13-}$ (*left*), an isolated ring $[Sb_4O_8]^{4-}$ of four vertex-linked ψ¹-tetrahedra $[SbO_3]^{3-}$ (*mid*) and the extended tetragonal unit cell of $TmSb_2O_4Br$ as viewed along [010] (*right*).

Fig. 1

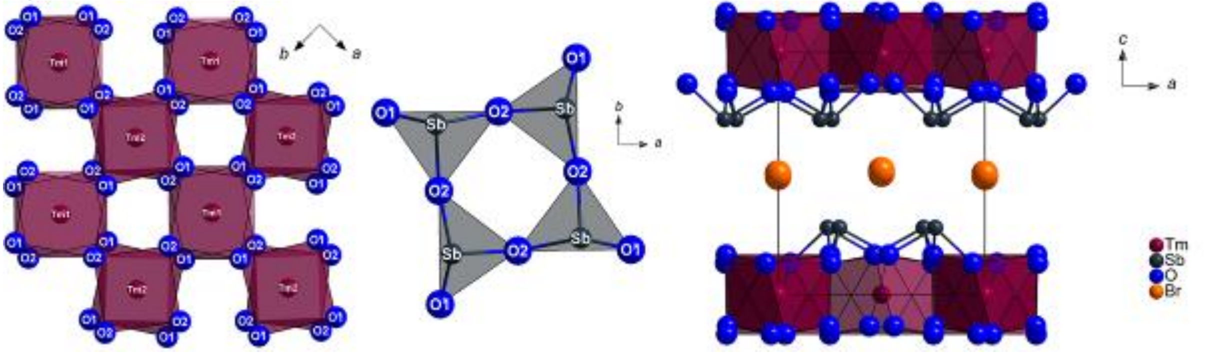

PP-115

$(NH_4)_4(SO_4)[CB_{11}H_{12}]_2$: A New Double Salt with Carbaborate Anions Crystallizing in a Monoclinic Variety of the *anti*-K_2NiF_4-Type Structure

A. Friedly (Stuttgart/DE), T. Schleid (Stuttgart/DE)

The general trend of the $[B_{12}H_{12}]^{2-}$ anions to build double salts has already been demonstrated by many examples, such as the *anti*-perovskite series $A_3I[B_{12}H_{12}]$ (A = K – Cs) [1]. The fact that an ammonium sulfate carbaborate crystallizes instead of a more simple ammonium carbaborate itself exhibits the strong tendency of carborate anions $[CB_{11}H_{12}]^-$ to form double salts similar to the related $[B_{12}H_{12}]^{2-}$ dianions. The synthesis of a new mixed anionic salt was realized by the reaction of ammonia with the free acid $(H_3O)[CB_{11}H_{12}]$ in aqueous brine. To produce this free carbaborate acid, an acidic cation exchanger was used. Due to its regeneration with sulfuric acid, sulfate anions were introduced into the crystalline sample. So an ammonium sulfate carborate with the composition $(NH_4)_4(SO_4)[CB_{11}H_{12}]_2$ was obtained, serendipitously. $(NH_4)_4(SO_4)[CB_{11}H_{12}]_2$ occurs as colorless, prismatic single crystals and crystallizes monoclinically in the space group $C2/c$ with the lattice parameters a = 2715.32(9) pm, b = 713.91(2) pm, c = 1391.24(5) pm and β = 109.203(2)° for Z = 4 (CSD number: 2219651). The extended unit cell of $(NH_4)_4(SO_4)[CB_{11}H_{12}]_2$ is shown in Figure 1. Its crystal structure consists of 2D-$\{[[(N1)H_4]_{2/2}[(N2)H_4]_{2/2}[(N3)H_4]_{2/1}(SO_4)]^{2+}\}$ layers made of corner-sharing $[(SO_4)(NH_4)_6]^{4+}$ octahedra. The linking ammonium cations $[(N1)H_4]^+$ and $[(N2)H_4]^+$ connect the $[(SO_4)(NH_4)_6]^{4+}$ octahedra in the b and c directions. The N1-site has the site symmetry -1, but this site symmetry contrasts to the symmetry of a tetrahedral ammonium cation. Additionally the ammonium cation $[(N1)H_4]^+$ is located between two sulfate anions with parallel edges (Figure 2). That is the reason, why it is not possible for the ammonium cation to coordinate with an edge to the edges of both sulfate anions. So disordering of the hydrogen atoms can be observed. In the case of the ammonium cation $[(N2)H_4]^+$ the edges of the both adjacent sulfates are orthogonal to each other and the ammonium cation $[(N2)H_4]^+$ coordinates to both $[SO_4]^{2-}$ edges with an own edge and no disorder is observed. The carbaborate anions are placed between the layers located in the middle of four unlinked corners of the $[(SO_4)(NH_4)_6]^{4+}$ octahedra. This structural motif corresponds to that one of an *anti*-K_2NiF_4-type structure [2], since a monocapped square antiprismatic overall coordination sphere $\{[CB_{11}H_{12}](NH_4)_9\}^{8+}$ of $(NH_4)^+$ cations is achieved.

References:

(1) I. Tiritiris, Th. Schleid, *Z. Anorg. Allg. Chem.* **2003**, *629*, 1390–1402.
(2) D. Balz, K. Plieth, *Z. Elektrochem.* **1955**, *59*, 545–551.

Figure 1: Extended unit cell of $(NH_4)_4(SO_4)[CB_{11}H_{12}]_2$ as viewed along the b-axis.

Figure 2: Orientation of the sulfate anions nearby the disordered $[(N1)H_4]^+$ cations in the crystal structure of $(NH_4)_4(SO_4)[CB_{11}H_{12}]_2$.

Fig. 1

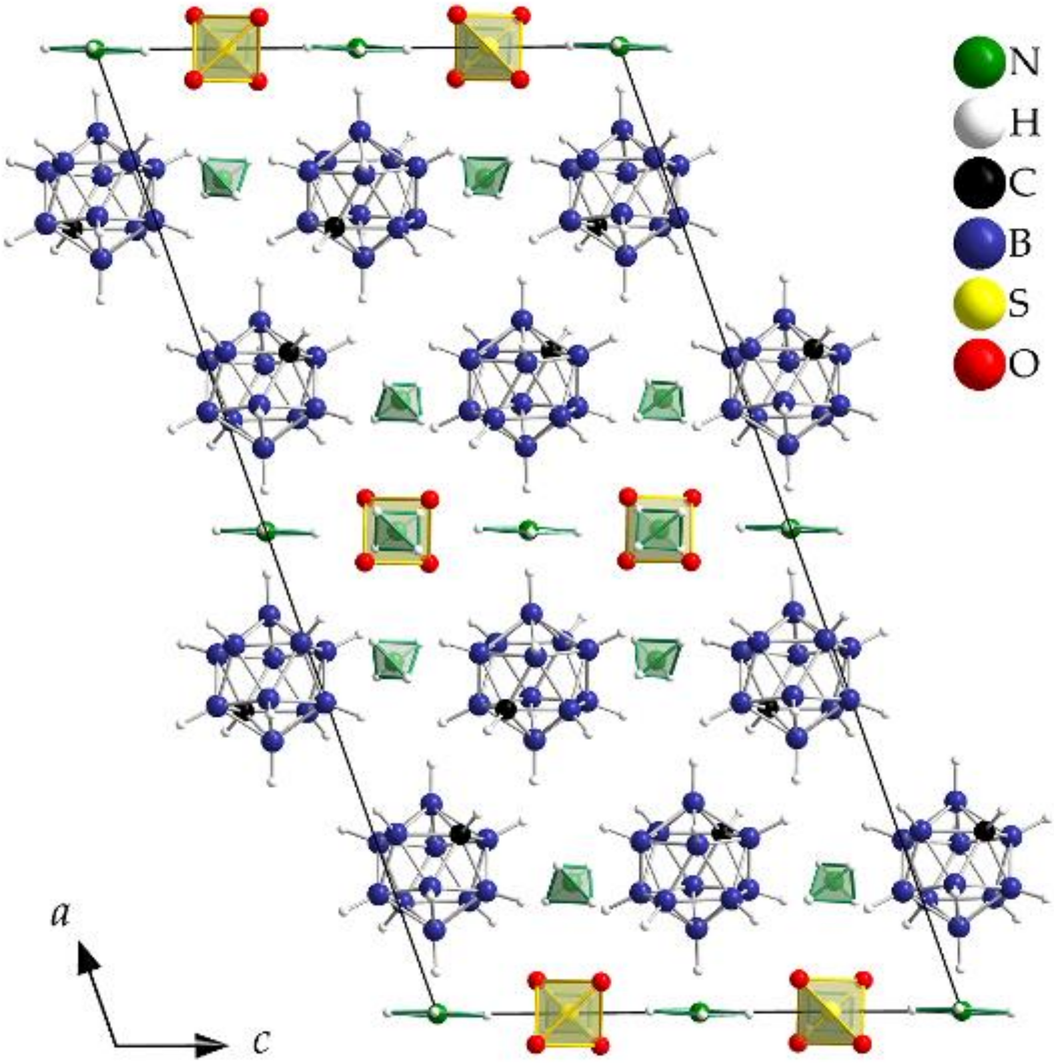

Fig. 2

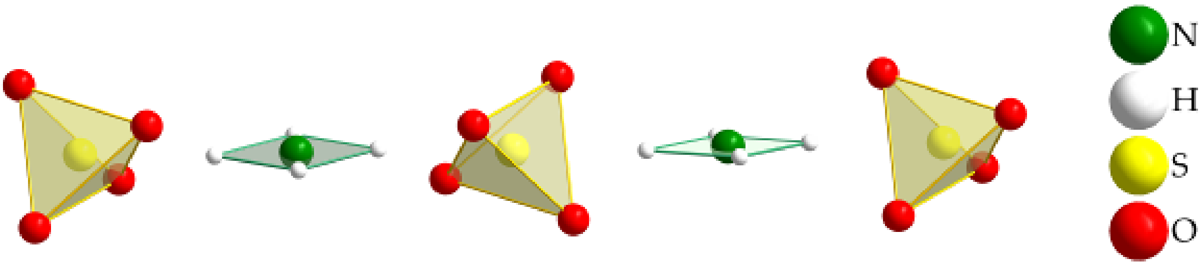

PP-116

The new alkaline metal mercuride oxides Cs_8Hg_8O and Rb_8Hg_8O

L. Nusser (Munich/DE), C. Hoch (Munich/DE)

While its neighbouring elements Pt, Au and Tl reportedly form anions in combination with electropositive metals, Hg does not form anions that easily. When reacted with electropositive metals, mercury tends to form amalgams, which feature negatively polarised Hg atoms or atom groups $[Hg_n]^{\delta-}$, but no "true" mercuride anions due to a considerable but in all cases incomplete electron transfer. Recently, we presented the caesium mercuride oxide double salt $Cs_{18}Hg_8O_6$ ($I23$, a = 13.3920(10) Å, V = 2401.8(5) Å^3, Z = 2) featuring the first "true" mercuride anion $[Hg_8]^{6-}$ next to isolated oxide anions [1].

In analogous reactions of caesium or rubidium with mercury and oxygen, the new compounds Cs_8Hg_8O and Rb_8Hg_8O have been synthesised. Both compounds contain cubic $[Hg_8]^{6-}$ anions alongside isolated oxide anions coordinated by the respective alkaline metal cations.

Cs_8Hg_8O is dimorphic: α-Cs_8Hg_8O (trigonal, space group $R3$, a = 10.0844(11), c = 46.475(6) Å, V = 4093.1(8) Å^3, Z = 6) transforms at ~220 °C into the β modification (trigonal, space group $R3$, a = 10.080(6), c = 116.71(7) Å, V = 10270(11) Å^3, Z = 12). Both Cs_8Hg_8O modifications represent new structure types. Due to the very similar trigonal a axes, α and β modifications tend to form epitaxially intergrown crystals, resulting in interesting diffraction patterns and raising a challenge in terms of structural determination of either modification.

Rb_8Hg_8O (trigonal, space group $R3$, a = 9.6454(10), c = 68.12(3) Å, V = 5488(3) Å^3, Z = 8)crystallises in its own structure type, showing four split positions for rubidium statistically occupied by two cations in total. It has striking structural analogies to the caesium compounds.Another close structural relation can be seen with the thallium compound Cs_8Tl_8O [2].

All of these three new structures can be derived from closest packings of $[Hg_8]$ cluster anions, in which the oxide-centered rubidium coordination polyhedra occupy octahedral voids, resulting in topological NaCl (α-Cs_8Hg_8O) and NiAs (β-Cs_8Hg_8O and Rb_8Hg_8O) type structures in different stacking variants in direction of the extraordinarily long hexagonal c axes.

(1) L. Nusser, T. Hohl, F. Tambornino, C. Hoch, *Z. Anorg. Allg. Chem.* 2022, *648*, e202100389.
(2) A. Karpov, M. Jansen, *Angew. Chem. Int. Ed.* 2005, 44, 7639–7643.

L. N. acknowledges support by DFG under grant number 513247541.

PP-117

Dialuminate $A_6[\mathrm{Al}_2Q_6]$(A=K, Rb, Cs; Q=S, Se, Te) mit $[\mathrm{Al}_2Q_6]^{6-}$ -Tetraederdimeren

M. Schwarz (Freiburg im Breisgau/DE), V. Daiber (Freiburg im Breisgau/DE), C. Röhr (Freiburg im Breisgau/DE)

In der Verbindungsklasse der Chalkogenido-Di-Aluminate mit den komplexen Anionen $[\mathrm{Al}_2Q_6]^{6-}$ waren bereits einige wenige Verbindungen bekannt ($\mathrm{K_6Al_2Se_6}$, $\mathrm{K_6Al_2Te_6}$, $\mathrm{Cs_6Al_2Te_6}$ [1-3]). Aus Schmelzen der Elemente unter Schutzgasatmosphäre bei Maximaltemperaturen von 700 °C wurden die bislang unbekannten Verbindungen der Reihe $\mathrm{A_6}[\mathrm{Al}_2Q_6]$ (A=K, Rb, Cs; Q=S, Se, Te) [1-3] dargestellt. Sie kristallisieren in drei verschiedenen Strukturtypen: $\mathrm{K_6[Al_2S_6]}$ kristallisiert im $\mathrm{K_6[Al_2O_6]}$-Strukturtyp (monoklin, Raumgruppe $C2/m$, a=791.33(5), b=1282.27(8), c=1029.85(6)pm, β=127.193(1) °); die Struktur von $\mathrm{Cs_6[Al_2S_6]}$ ist ein Hettotyp des $\mathrm{Ba_6[Al_2Sb_6]}$-Typs (monoklin, $C2/c$, a=1935.69(13), b=724.10(5), c=1339.49(9)pm, β=90.134(2)°) - ableitbar durch einen translationengleichen Symmetrieabstieg mit Index 2, wohingegen die übrigen Verbindungen den $\mathrm{Cs_6[Ga_2Se_6]}$-Typ bilden (monoklin, Raumgruppe $P2_1/c$; z.B. $\mathrm{K_6[Al_2Se_6]}$: a=802.1(1), b=1287.7(2), c=1043.4(2)pm, β=127.598(3)°). Mit der Synthese und Charakterisierung wird die Reihe der Chalkogenido-Di-Aluminate der schweren Alkalimetalle vervollständigt. Zum Verständnis der Strukturchemie dient eine Einordnung der Verbindungen und ihrer Strukturen in ein Strukturfeld mit Di-Metallaten der ebenfalls dreiwertigen Zentralatome Indium, Gallium und Eisen [4,5], worin insgesamt 10 verschiedene Strukturtypen gefunden werden. Die Bindungssituation in den komplexen Salzen wurde mittels Bandstrukturrechnungen auf DFT-LAPW-Niveau untersucht und mit den Ergebnissen von DFT-MO-Rechnungen des Anions verglichen. Mittels UV/Vis-Spektroskopie konnte außerdem die Größe der Bandlücke der Verbindung $\mathrm{Cs_6[Al_2Se_6]}$ experimentell ermittelt werden.

(1) B. Eisenmann, A. Hofmann. Crystal structure of hexapotassium di-µ-selenido-bis(diselenidoaluminate), $\mathrm{K_6Al_2Se_6}$ *Z. Kristallogr. NCS* **197** (1991) 173-174.
(2) ibid. 157-158
(3) ibid. 253-254.
(4) M. Langenmaier, S. Wissinger, C. Röhr. $\mathrm{K_6In_2}Q_6$ (Q=S, Se, Te): Missing Links in the Series of Alkali Chalcogenido Ditrielates(III) *Z. Anorg. Allg. Chem.* **646** (2020) 138-148.
(5) M. Schwarz, P. Stüble, C. Röhr. Rubidium chalcogenido diferrates(III) containing dimers $[\mathrm{Fe}_2Q_6]^{6-}$ of edge-sharing tetrahedra (Q= O, S, Se) *Z. Naturforsch.* **75(8)b** (2017) 529-547.

Fig. 1

1 $Na_6In_2S_6$
2 $Na_6Fe_2S_6$
3 h.t.-$Na_6Al_2S_6$
4 $Rb_6In_2S_6$/$K_6Fe_2O_6$
k2
5 $K_6Mn_2O_6$
6 $Ba_6Al_2Sb_6$
7 $Cs_6Ga_2Se_6$/$K_6Al_2Se_6$
8 $K_6In_2Te_6$
9 $Cs_6In_2O_6$/$Rb_6Tl_2O_6$
10 $Cs_6Al_2O_6$

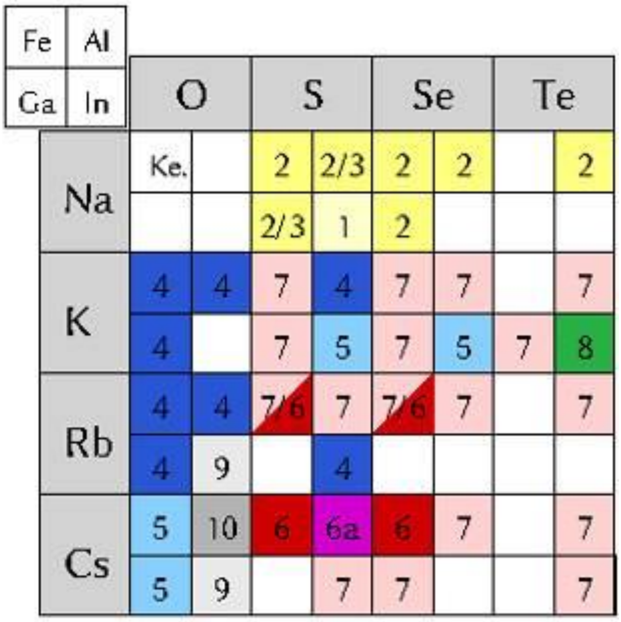

Fe	Al
Ga	In

	O		S		Se		Te	
Na	Ke.		2	2/3	2	2		2
			2/3	1	2			
K	4	4	7	4	7	7		7
	4		7	5	7	5	7	8
Rb	4	4	7/6	7	7/6	7		7
	4	9		4				
Cs	5	10	6	6a	6	7		7
	5	9		7	7			7

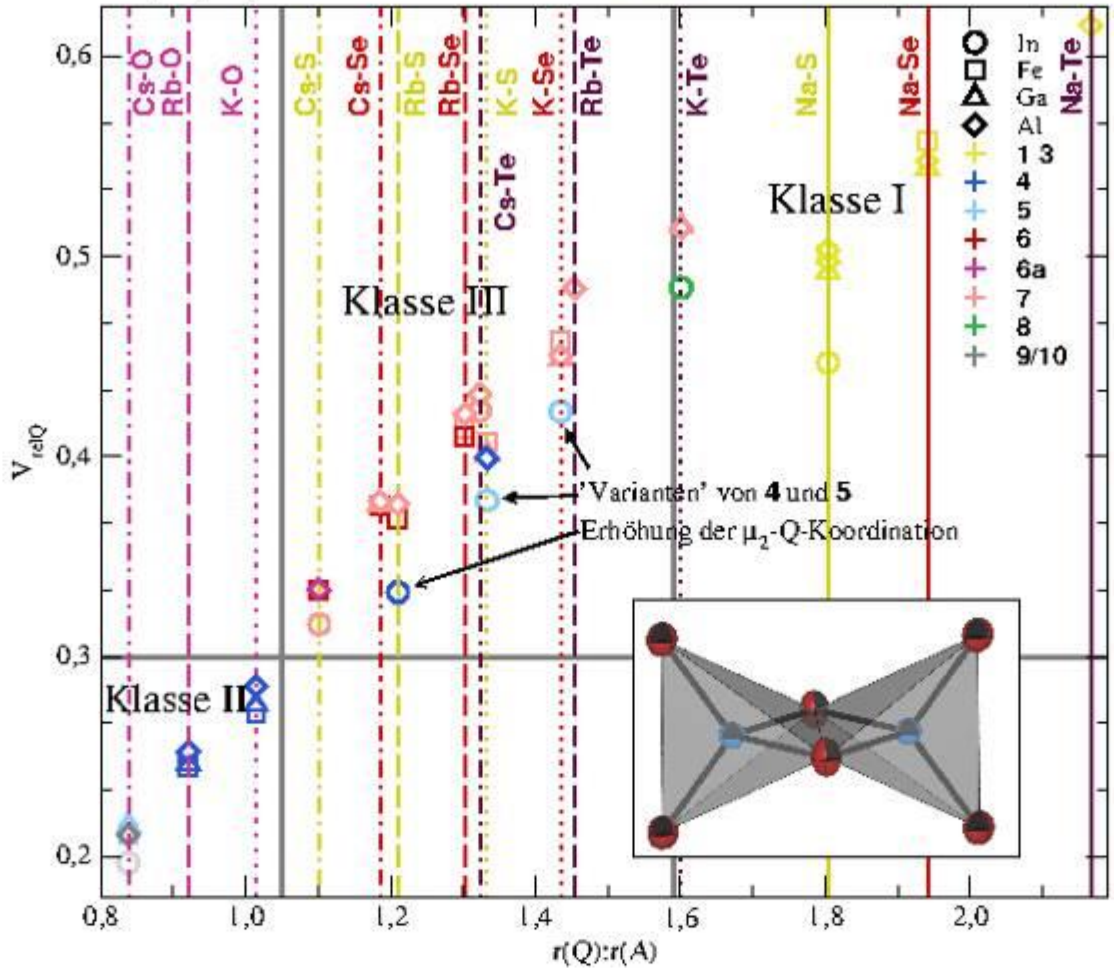

PP-118

Synthesis and characterization of zinc/zirconium co-substituted ferrites

Y. M. Dreer (Stuttgart/DE), R. Niewa (Stuttgart/DE)

The synthesis of new hexaferrites is an ongoing field of interest due to their tunable magnetic properties. Their applications range from data storage, microwave devices and optical devices to permanent magnets and waste water treatment [1]. The aim of this work was the synthesis and crystal growth of the M-type ferrite $BaFe_{12-2x}Zn_xZr_xO_{19}$ ($0.1 \leq x \leq 2.0$), in order to investigate the influence of the substitution on the structure and the magnetic properties. Via flux growth, single crystals with diameters up to 0.5 mm were obtained.

Both structure refinements based on powder and single crystal XRD show that the lattice parameters of $BaFe_{12-2x}Zn_xZr_xO_{19}$ increase with increasing degree of substitution. Furthermore, the Fe(4)-atoms (Wyckoff site 4*f*) in the center of face-sharing octahedra doubles from oxide anions were determined as the preferred position of Zr^{4+}-cations for mixed site occupation, whereas the tetrahedrally coordinated Fe(3) sites are assumed to be the preferred position for zinc [2]. Due to substitution with both a divalent and a tetravalent ion, charge neutrality should be maintained. Microprobe analyses indicate that the maximum degree of substitution is around $x = 1.2$ at a synthesis temperature of $T = 1300$ °C. However, the possibility of a higher substitution with Zr than Zn is also suggested.

Although the elements within a single crystal are distributed homogeneously, various crystals from the same synthesis experiment display different degrees of substitution. Moreover, with increasing amount of zinc and zirconium, the formation of additional ferrite phases was observed, such as the W-type ferrite.

Literature:

(1) R. C. Pullar, *Prog. Mater. Sci.* **2012**, *57*, 1191. [2] Z. Yang, C. S. Wang, X. H. Li, H. X. Zeng, *Mater. Sci. Eng. B* **2002**, *90*, 142–145.

PP-119

News from the detector front – Ag(I)/Bi(III)-based bromides as alternatives

C. F. Schweinle (Freiburg im Breisgau/DE), S. Sahsuvar (Freiburg im Breisgau/DE), H. Hillebrecht (Freiburg im Breisgau/DE, Freiburg im Breisgau/DE), M. Fiederle (Freiburg im Breisgau/DE, Freiburg im Breisgau/DE)

X-ray is a very common diagnostic tool, not only in human medicine, but also in science and industry.[1] Common x-ray detector materials include silicon, cadmium zinc telluride and other compounds that have a high atomic number. [2] The new generation of detectors being developed by researchers have a very low detection limit and high sensitivity, allowing the necessary dose of X-rays to be decreased.

Having a closer look at this new generation, halide perovskites are emerging. First research has been done on lead containing materials, such as (MA)PbX$_3$ (X=Br,I).[3,4] Lead, however, is a toxic metal, not only for humans, but also for the environment. In 2018, Cs$_2$AgBiBr$_6$ was introduced as a promising candidate for x-ray detection.[5]

One figure of merit for an x-ray detector is the density of traps. Corn boundaries can behave as such traps,[6] so researchers are developing large single crystals.

Halide perovskites are not the only materials used for x-ray detection, however. Low-dimensional perovskite-like phases, such as Ruddlesden-Popper or Dion-Jacobson phases, can also be used.[7]

To the best of our knowledge, the only known single crystal structure of a Dion-Jacobsen phase found in literature uses 1,4-butanediammonium (BDA).[8]

Using a controlled cooling method which was adopted by *Yin* et al.[9], testing different additives and seed crystals, we are now able to grow single crystals of Cs$_2$AgBiBr6 with a minimum size of 10 mm. All the new DJ-phases have been crystallized from a hot hydrobromic acid solution, with a stoichiometric amount of AgBr, Bi$_2$O$_3$, and the corresponding amine.

During our research, we"ve found that using toluene or sodium acetate are good additives for the crystal growth. It is also recommended to use a temperature program which begins to cool down from higher temperatures. Cooling down from 80 °C to room temperature leads to small crystals less than 1 mm in size.

Using the pyridinium cations 2-Picolylamine (2-PCA), 3-Picolylamine (3-PCA) and 4-Picolylamine (4-PCA), (2-PCA)$_2$AgBiBr8 (*P*21 a = 8.283(6 Å, b = 17.389(14) Å, c = 9.172(7) Å, ß = 102.704(10)°), (3-PCA)$_2$AgBiBr8 (*P*21/*c* a = 8.195(3) Å, b = 17.370(7)(4) Å, c = 18,469(8) Å, ß = 102,090(19)°), (4-PCA)$_2$AgBiBr8 (*P*21/*c* a = 8.149(5) Å, b = 17.649(12) Å, c = 18.292(11) Å, ß = 101.775(11)°) results in yellow plates. All AgBr$_6$ octahedra can be described with a 2+4 coordination (compressed octahedra). The degree of compression differs in the different compounds. The structure of all these new compounds can be described as alternating layers, constructed from corner-sharing AgBr$_6$ and BiBr6 octahedra, separated by organic spacer cations. All of the amine groups are protonated, which allows hydrogen bonds to form with the bromide ions. No pi-stacking can be observed in any of the structures with the pyridinium cations, since the distance between the rings is higher than five Ångstroms.

(1) R. J. Parmee et al., *Nano Converg.* **2015**, *2*. [2] L. Basiricò, A. Ciavatti, B. Fraboni, *Adv. Mater. Technol.* **2021**, *6*, 2000475. [3] H. Wei et al., *Nature Photon* **2016**, *10*, 333. [4] S. Yakunin et al., *Nature Photon* **2015**, *9*, 444. [5] J. A. Steele et al., *Adv Mater* **2018**, *30*, e1804450. [6] J. Ghosh, P. J. Sellin, P. K. Giri, *Nanotechnology* **2022**, *33*. [7] Z. Li et al., *Mater. Today Commun.* **2021**, *48*, 155. [8] L. Mao et al., *JACS* **2019**, *141*, 19099. [8] L. Yin, et al., *Adv. Optical Mater.* **2019**, *7*, 1900491.

PP-120

Low valent copper clusters as decomposition products of Copper(I) Boryl complexes

C. Kleeberg (Braunschweig/DE), W. Drescher (Braunschweig/DE), C. Borner (Braunschweig/DE)

Introduction: Copper(I) borly complexes are widely recognised as central intermediates in copper catalysed borylation reactions with diboranes(4) as boron sources.[1] In the course of our studies on the isolation of this class of complexes and their reactivity we observed repeatedly the formation of low valent copper clusters of different nature as decomposition products or intermediates.[2,3]

Methods: During our investigation on the complex [(IDipp)Cu–Bneop] (IDipp = 1,3-bis(2,6-diisopropyl-phenyl)imidazole-2-ylidene, neop = $(OCH_2)_2CMe2$) we obtained repeatedly – though in only miniscule amounts – very small single crystals of the copper clusters $[(IDipp)_{12}Cu_{179}]$ and $[(IDipp)_6Cu_{55}]$. Both compounds were characterised by single-crystal X-ray diffraction.[3]

Results & Conclusions: *include Figure here*

Figure 1: Ball-and-Stick representations of the clusters $[(IDipp)_6Cu_{55}]$ and $[(IDipp)_{12}Cu_{179}]$ (only Cu (red to yellow) and carbene Carbon atoms (grey)).

The copper atoms in the cluster $[(IDipp)_6Cu_{55}]$ adopt – approximately – icosahedral symmetry (Figure). It may be dissected in an inner shell comprising of a, slightly distorted, centred icosahedron of copper atoms (Cu_{13}) and an outer shell comprising an icosahedron of copper atoms (Cu_{12}) with additional copper atoms in the middle of all edges (Cu_{30}). Crystallographically the cluster does not exhibit icosahedral symmetry but is situated only on a centre of inversion in a spacegroup of the type P-1 (Z = 1, Z'' = ½).

$[(IDipp)_{12}Cu_{179}]$ crystallises in the monoclinic spacegroup type $P2_1/n$ and is situated on an inversion centre, however, the cluster itself does not possess inversion symmetry, resulting in extensive disorder of the copper atoms within $[(IDipp)_{12}Cu_{179}]$. As $[(IDipp)_6Cu_{55}]$, this bigger cluster may be dissected into different shells, again showing icosahedral motifs. The structures of both clusters as well a as the details of the single-crystal X-ray diffraction structure determination will be discussed in detail.

References:

(1) D. Hemming, R. Fritzemeier, S. A. Westcott, W. Santos, P. G. Steel, *Chem. Soc. Rev.* **2018**, *47*, 7477.
(2) C. Borner, L. Anders, K. Brandhorst, C. Kleeberg, *Organometallics,* **2017**, *36*, 4687; C. Kleeberg, C. Borner, *Organometallics* **2018**, *37*, 4136.
(3) W. Drescher, C. Borner, C. Kleeberg, *N. J. Chem.* **2020***, 45,* 14957.

Fig. 1

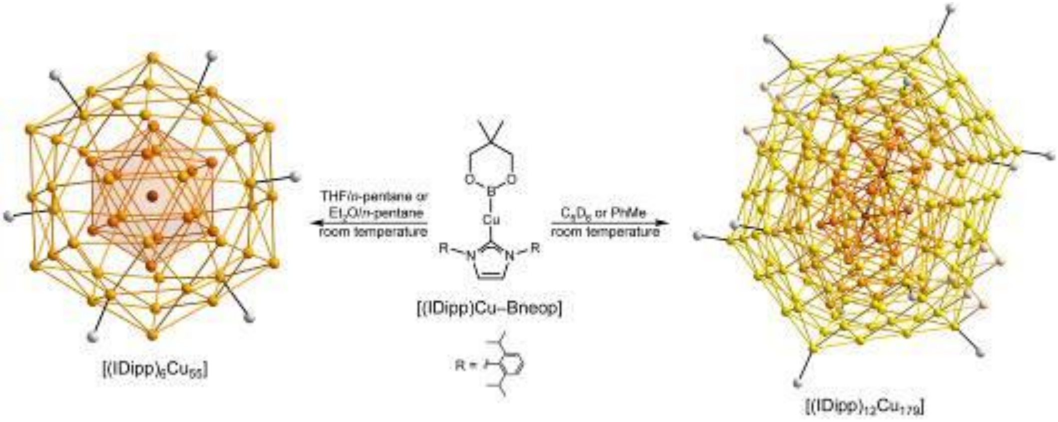

PP-121

Formation and properties of mullite-type photocatalysts for the degradation of persistent organic pollutions

S. Schuh (Bremen/DE), A. Wollbrink (Bremen/DE), T. M. Gesing (Bremen/DE, Bremen/DE)

Water pollution with persistent organic pollutants (POPs) is one of the bigger environmental problems. Semiconductor based photocatalysis seems to be a promising process for the decomposition of these hazardous substances [1]. Optimization of narrow band-gap Bi2*M*4O9 (*M* = Al, Fe) photocatalysts for enhanced photocatalytic activity in the visible light region [2] could be a tool of choice. To reveal the correlation between phase composition, average crystallite size, band-gap energy and photocatalytic activity the formation of solid-solution single phase using respective bismuth-metalate-DNG precursors [3] is performed. Of this, various mullite-type Bi2*M*4O9 (*M* = Al, Fe) samples are synthesized with nano- to micro-crystalline average crystallite sizes between 25 nm and 270 nm. Characterization is carried out by X-ray powder diffraction (XRPD), Raman- and UV/Vis spectroscopy. Photocatalytic activity is determined by modified ex-situ liquid-UV/Vis measurements.

Noticeable changes in the nature of the band-gap (direct or indirect) and its energy are observed related to the composition and average crystallite size for the solid-solutions of Bi2(Al1-xFex)4O9 and its endmembers (x= 0 or 1). For x = 0.1 to 0.7, the band-gap energy tends to increase with increasing the average crystallite size and vice versa for x = 0.8 to 1.0. Furthermore, the nature of the band-gap transition is shifted from indirect towards direct with the increase in average crystallite size for aluminum-rich samples.

(1) M. R. Hoffmann, S. T. Martin, W. Choi, D. W. Bahnemann, *Chem. Rev. 95* (1995) 69-96.
(2) M.Curti, A.Kirsch, L. Granone, F. Tarasi, G. López-Robledo, D. W. Bahnemann, M. M. Murshed,Th. M. Gesing,C. B. Mendive, *ACS Catalysis 8* (2018) 8844-8855.
(3) Th. M. Gesing, M. M. Murshed, S. Schuh, O. Thüringer, K. Krämer, T. Neudecker, C. B. Mendive, L. Robben,*J. Mater. Sci. 57* (2022) 19280-19299.

We acknowledge support by DFG under grant number GE1981/13-1.

PP-122

Re-investigation of the crystal structure of $CuSn(OH)_6$ by x-ray and neutron powder diffraction

E. Häußler (Dresden/DE), A. A. Kulbakov (Dresden/DE), D. C. Peets (Dresden/DE), D. S. Inosov (Dresden/DE), T. Doert (Dresden/DE)

Recently, the crystal structure of $CuSn(OH)_6$ in space group *P*4₂/*nnm* (No. 134)[1] was questioned by Mitchell et al.[2] due to strongly distorted $A(OH)_6$ octahedra, which do not match the tilt patterns of the octahedra. Additionally, the mirror plane perpendicular to [110] should be absent for double cation hydroxides with an ordered ReO_3 superstructure. In this contribution we will present the re-investigation of the $CuSn(OH)_6$ structure by means of powder x-ray and neutron diffraction experiments.

Samples were prepared by precipitation of the powders from aqueous solutions of $CuCl_2 \cdot 2\,H_2O$ and $Na_2Sn(OH)_6$. Indexing and refining the x-ray powder patterns with a Le-Bail fit yielded good agreement with the tetragonal metrics similar to the ones described by Morgenstern-Badarau ($a = b = 7.586(1)$, $c = 8.103(1)$, $\alpha=\beta=\gamma=90$ °)[1] in 1976. Subsequent Rietveld refinements confirmed that the choice of the space group $P4_2/nnm$ (No. 134) is indeed incorrect and thus a translationsgleiche descent to space group $P4_2/n$ (No. 86) was carried out. This symmetry reduction removes the mirror plane bisecting Cu or Sn octahedra and thus allows all oxygen positions to be located on the general position 8*g* in this space group. Afterwards the structure model was fitted to the powder x-ray and neutron patterns by Rietveld refinements using the Fullprof suite[3,4]. The obtained structure can be described as a 3D network of alternating corner-sharing $Cu(OH)_6$ and $Sn(OH)_6$ octahedra with more reasonable distortions (see figure 1).

(1) I. Morgenstern-Badarau, *J. Solid State Chem.* **1976**, *17*, 399–406.
(2) R. H. Mitchell, M. D. Welch, A. R. Chakhmouradian, *Mineral. Mag.* **2017**, *81*, 411–461.
(3) T. Roisnel, J. Rodríquez-Carvajal, *Mater. Sci. Forum* **2001**, *378–381*, 118–123.
(4) J. Rodríguez-Carvajal, *Phys. B Condens. Matter* **1993**, *192*, 55–69.

We acknowledge support by the CRC 1143 from the DFG under project-id 247310070.

Figure 1: The structure of $CuSn(OH)_6$ in $P4_2/n$ (space group no. 86).

Fig. 1

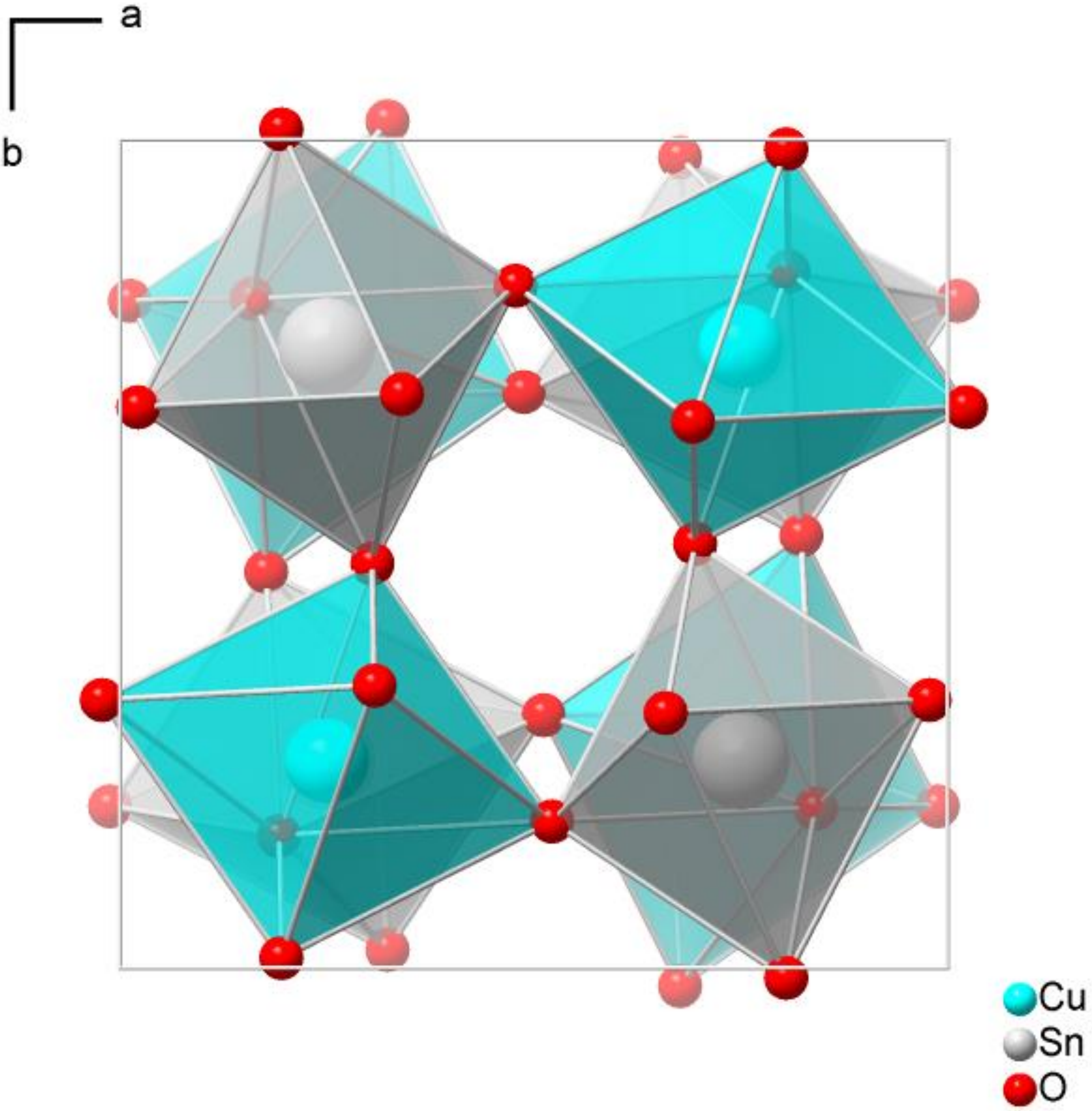

PP-123

New rare iodate selenites with potential for non-linear optical properties

K. Eble (Freiburg im Breisgau/DE), H. Hillebrecht (Freiburg im Breisgau/DE)

Non-linear optics play a large role in the development and improvement of lasers, one of the most important technologies of today and the future. Currently, much research is being done in the field of non-linear optical materials, with a primary focus on finding and developing new materials which can be used with lasers to produce non-linear optical effects, such as second harmonic generation (SHG). This is due to limitations found in many available materials, such as poor physical or chemical stability, low SHG response, or a low laser damage threshold. Finding suitable candidates for use as non-linear optical materials proves to be a large challenge, however, as such materials must fulfill certain criteria in order to show effects such as SHG, the most important of which is lacking an inversion center in the unit cell.

One group of materials which shows much promise is that of iodate selenites. To date, only one such compound has been found, namely $Th(IO_3)2(SeO_3)$. [1] Herein, new members of the rare iodate selenite substance group are reported, though primary focus is given to a candidate for SHG effects, namely $Bi(IO_3)(SeO_3)$.

$Bi(IO_3)(SeO_3)$ was found using a similar strategy as illustrated by Wang et al., namely orientating around a known compound, replacing an anion with the desired one and balancing the created difference in charge with a cation of now fitting charge and similar size to the original cation. [1] In this case, orthorhombic ($Pna2_1$) $Th(SeO_3)_2$ served as the inspiration, whereby one $(SeO_3)^{2-}$ unit was replaced by $(IO_3)^-$, and Th^{4+} by the appropriately charged Bi^{3+}, which also happens to be similar in size to it"s role model. This lead to orthorhombic ($Pna2_1$) $Bi(IO_3)(SeO_3)$, which shares the same space group and very similar cell parameters with $Th(SeO_3)_2$. Interestingly, the two anionic sites are not ordered, but rather are occupied in a 7:3 ratio by the respective anions, leading to the sum compound $Bi(IO_3)(SeO_3)$. This material shows promise as a worthwile SHG, since aside from being acentric and transparent, it contains many components found in other strong SHG materials (Bi_{3+}, Se(IV), $(IO_3)^-$). [2,3,4]

(1) Y. Wang, Y. Wang, L. Zhang, L. Chen, Z. Liu, X. Yin, D. Sheng, J. Diwu, J. Wang, N. Liu, Z. Chai, S. Wang, *Inorg. Chem.* **56**(6), *2017,* 3702
(2) H. Hellwig, J. Liebertz, L. Bohatý, *Solid State Commun.* **109**(4), *1998*, 249
(3) M. Liang, C. Hu, F. Kong, J. Mao, *J. Am. Chem. Soc.* **138**(30), *2016*, 9433
(4) H. Büsener, A. Renn, A. Hese, *Laser and Optoelektronik* **3**, *1982*, 11

PP-124

Investigation on the crystal structure and phase transition of $K_{9.6}Ca_{1.2}Si_{12}O_{30}$ at elevated temperatures

H. Liu (Innsbruck/AT), V. Kahlenberg (Innsbruck/AT), H. Krüger (Innsbruck/AT), E. Dachs (Salzburg/AT)

Due to the fact that potassium calcium silicates can be involved in a wide range of residual materials, such as steelmaking slags, biomass combustion ashes, and fertilizers generated from oil-shale industrial by-products, the oxide system K_2O-CaO-SiO_2 (KCS) has been in the focus of interest. A more accurate and complete understanding of the structure and thermodynamic properties of all phases in the phase diagram is still needed to enhance the quality of thermodynamic modeling and the ultimate accurate prediction of the behavior of potassium calcium silicates at high temperatures.

Despite being one of the eight ternary phases already proposed by Morey et al. in 1930 [1], no detailed single-crystal diffraction data for $K_{9.6}Ca_{1.2}Si_{12}O_{30}$ (or $K_8CaSi_{10}O_{25}$) are available to date. Two previous studies based on laboratory powder X-ray diffraction data pointed to the presence of two different structures at room temperature. Gunawardane et al. 1975 [2] suggested that this phase is isostructural with $K_8SrSi_{10}O_{25}$ and $K_8BaSi_{10}O_{25}$, each of which has similar hexagonal R-centered unit cells. The cell parameters of $K_8CaSi_{10}O_{25}$ obtained by powder diffraction were a = 11.125 Å and c = 10.987 Å. In another more recent study (Kahlenberg et al. 2006 [3]), the crystal structure was solved from powder diffraction data using direct methods aided by distance least-squares optimization. It represents an interrupted framework structure and adapts the non-centrosymmetric space group $R3c$ with a doubled c-lattice parameter when compared with the data from Gunawardane et al.

In the present study, $K_{9.6}Ca_{1.2}Si_{12}O_{30}$ (or $K_8CaSi_{10}O_{25}$) in form of pure polycrystalline powders as well as single crystals were prepared from (i) solid-state reactions between stoichiometric mixtures of the corresponding oxides/carbonates and (ii) annealing a previously prepared glass for longer periods of time. Heat capacity data indicated the presence of two weak thermal effects at higher temperatures. The synthesized compound was characterized by single-crystal X-ray diffraction. A first single-crystal X-ray diffraction experiment on a freshly synthesized sample (quenching in the air) at room conditions revealed a hexagonal R-centered cell with a = 11.16 Å and c = 22.03 Å. A subsequent HT-data collection at 600°C implied, that at least one structural transition occurred, resulting in a change to half of the c-lattice parameter at ambient temperature. For the phase stable at 600°C, basic crystallographic data are as follows: The trigonal compound belongs to the centrosymmetric space group $R\text{–}3m$. Unit-cell parameters are a = 11.2359(11) Å, c = 11.1803(13) Å, V = 1222.4(2) $Å^3$, Z = 3. Further diffraction studies performed at different temperatures during cooling showed that satellite reflections occur in the range between 466 and 433°C, which then exist down to room conditions. The satellite reflections, however, are not compatible with trigonal symmetry.

(1) Morey GW, Kracek FC, Bowen NL. The ternary system K_2O-CaO-SiO_2. J Glass Technol. 1930;14:149–187.
(2) Gunawardane RP, Glasser FP. Crystal chemistry and synthesis of ternary silicates and germanates containing alkali (Na^+, K^+) and alkaline earth (Ca^{2+}, Sr^{2+}, Ba^{2+}) cations. Zeitschrift für anorganische und allgemeine Chemie. 1975;411(2):163–172.
(3) Kahlenberg V, Kaindl R, Többens DM. The crystal structure of the interrupted framework silicate $K_{9.6}Ca_{1.2}Si_{12}O_{30}$ determined from laboratory X-ray diffraction data. Journal of Solid State Chemistry. 2006;179(7):1948–1956.

PP-125

Vacancy-ordered perovskite variants: $A_3As_2X_9$ (A = Rb, Cs, CH_3NH_3; X = Cl-I) and $Cs_4As_2CuCl_{12}$

M. Daub (Freiburg im Breisgau/DE), H. Hillebrecht (Freiburg im Breisgau/DE)

The introduction of $CH_3NH_3PbI_3$ as a semiconductor material for optoelectronic applications [1] resulted in an enormous boost in research on metal halide perovskites and related compounds. Such perovskites related compounds include divalent halides ABX_3, double perovskites $A2BB"X6$ with mono and trivalent cations. Also, defect representatives with tetravalent ($A_2B\square X_6$), trivalent ($A_3B_2\square X_9$), or tri and divalent ($A_4BB_2"\square X_{12}$) cations. While compounds of the type $A_3B_2X_9$ are well known and characterized for the heavier penteles Bi and Sb, [2] for *B* = As there is not much to be found in the literature. [3] To fill this gap, we conducted investigations with As_2O_3 and the corresponding alkali or methylammonium halide in concentrated aqueous hydrohalic acid. This allowed us to prepare $A_3As_2X_9$ (*A* = Rb, Cs; *X* = Cl-I and *A* = CH_3NH_3; *X* = Br, I) and to characterize their crystal structural and optical properties. $A_3As_2X_9$ (*A* = Rb, Cs; *X* = Cl, Br) can be described in the space group *P*-3*m*1 ($Cs_3Bi_2Br_9$ type). The structure can be derived from the cubic stacking mode (***c***)$_3$ and comprises corner-sharing octahedra forming double layers. All iodides can be derived from the stacking mode (***hcc***)$_2$, two AsI_6 octahedra are connected face-sharing to form isolated dimers. While $Cs_3As_2I_9$ and $(CH_3NH_3)_3As_2I_9$ can be described in the space group *P*6$_3$/*mmc* ($Cs_3Cr_2Cl_9$ type), $Rb_3As_2I_9$ shows a lower symmetry (*C*2/*c*, LT-$Cs_3Bi_2Cl_9$ type). $(CH_3NH_3)_3As_2Br_9$ (*Pnma*, $Cs_3Bi_2Cl_9$ type) can also be derived from the stacking mode (***hcc***)$_2$, however now four-membered rings of corner-sharing AsBr6 octahedra form zigzag chains .

The 2D structures were of particular interest to us. From the heavier homologues it is known that the addition of divalent cations such as Cu^{2+}, Mn^{2+}, Cd^{2+} lead to the vacancy-ordered quadruple perovskites of the typ $A_4BB_2"\square X_{12}$. [4-6] In a first experiment, when $Cs_3As_2Cl_9$ was dissolved in conc. aqueous HCl and CuO was added, red transparent platelets were obtained beside black polyhedral crystals. The red crystals turned out to be the vacancy-ordered quadruple perovskite $Cs_4As_2CuCl_{12}$ (*C*2/*m*, *a* = 12.921(6), *b* = 7.242(3), *c* = 12.922(5) Å and β = 111.961(6)°), while the black crystals can be interpreted as a disordered variant $CsCu_{0.25}As_{0.5}Cl_3$ (*Pm*-3*m*, *a* = 5.2048(10) Å).

Literature:

(1) A. Kojima, K. Teshima, Y. Shirai, T. Miyasaka *J. Am. Chem. Soc.* **2009**, *131*, 6050.
(2) J.-H. Chang, T. Doert, M. Ruck Z. *anorg. allg. Chem*. **2016**, *642,* 736-748.
(3) J. L. Hoard, L. Goldstein J. Chem. Phys. **1935**, *3*, 117.
(4) M. B. Gray, J. D. Majher, N. P. Holzapfel, P. M. Woodward *Chem. Mater.* **2021**, *33*, 6, 2165–2172.
(5) B. Vargas, R. Torres-Cadena, D. T. Reyes-Castillo, J. Rodríguez-Hernández, M. Gembicky, E. Menéndez- Proupin, D. Solis-Ibarra *Chem. Mater.* **2020**, *32*, 1, 424–429.
(6) B. Vargas, E. Ramos, E. Pérez-Gutiérrez, J. C. Alonso, D. Solis-Ibarra *J. Am. Chem. Soc.* **2017**, *139*, 27, 9116–9119.

PP-126

Structural and magnetic properties of $Sr_3Fe_{2+x}Mo_{1-x}O_{9-3x/2}$ (x = 0.45, 0.60, and 1)

A. El Hachmi (Settat/MA), S. El Ouahbi (Settat/MA), B. Manoun (Settat/MA), H. Lassri (Settat/MA)

Perovskite oxides Sr3$Fe_{2+x}Mo_{1-x}O_{9-3x/2}$ (x = 0.45, 0.60, and 1) were synthesized in polycrystalline form using solid–state reaction route, in the air [1]. The crystal structure of these compositions was resolved and refined using the Rietveld method, and revealed that (x = 0.45 and 0.60) adopt a tetragonal space group *I4/mcm*; while (x = 1.00) adopts another tetragonal space group *P4/mmm*.

The magnetic measurements were carried out using superconducting quantum interference device (SQUID) sensor (MPMS-XL-7AC, Quantum Design). Magnetization as a function of the applied magnetic field was made for temperatures $4.2 \leq T \leq 156$ K, with a maximum applied field up to 5 T.

We investigate in detail the magnetic, magnetocaloric properties and phenomenological model of perovskite type: $Sr_3Fe_{2+x}Mo_{1-x}O_{9-3x/2}$ (x = 0.45, 0.60, and 1) [2]. With a Curie temperature from 132 to 144 K, the magnetic transition nature undergoes a secondorder magnetic phase transition from ferromagnetic to paramagnetic states. We have used the thermodynamic Maxwell relation to determine the magnetic entropy change ($-\Delta SM$) in the studied compositions. Moreover, we report a theoretical investigation of the magnetocaloric effect using a phenomenological model. The model parameters and their variation with temperature and the magnetic field were obtained. The theoretical predictions (adopted model) were found to be consistent with the experimental results.

Keywords: Perovskites $Sr_3Fe_{2+x}Mo_{1-x}O_{9-3x/2}$, Phase transition, Magnetocaloric effect, Magnetic transition

References:

(1) El Hachmi, A., Manoun, B., Sajieddine, M., Tamraoui, Y., El Ouahbi, S. *Polyhedron* 200 (2021) 115133
(2) El Hachmi, A., El Ouahbi, S., Manoun, B., Lassri, H. *Journal of Superconductivity and Novel Magnetism* 35, 1299–1306 (2022)

PP-127

Richardsite Zn_2CuGaS_4 – a mixed crystal of Sphalerite and Gallite

Y. Tomm (Berlin/DE), D. Abou-Ras (Berlin/DE), G. Gurieva (Berlin/DE), S. Schorr (Berlin/DE, Berlin/DE)

The new mineral Richardsite reported by Bindi and Jaszczak [1] belongs to the adamantine family. With the composition Zn_2CuGaS_4 it can be regarded as a mixed crystal in the solid solution series ZnS and $CuGaS_2$.

According to [2], solid solutions exist between sphalerite ZnS and chalcopyrite $CuFeS_2$. [3-10] studied the systems chalcopyrite-type $CuB^{III}C^{VI}_2$ – ZnC with B^{III}= Al, Ga, In and C^{VI}= S, Se, Te. Due to the similarities in the crystal structure, unit cell dimensions and bonding type, $CuGaS_2$ may form a solid solution with ZnS [10]. However, since both compounds are not isotypic, there should be a composition-dependent structural transition from the tetragonal chalcopyrite to the cubic sphalerite type structure. On the other hand, detailed structural investigations by X-ray and neutron diffraction as well as transmission electron microscopy on the systems $2(ZnX)_x(CuInX_2)_{1-x}$ with X=S, Se, Te indicated the existence of a miscibility gap (two-phase field), where both a tetragonal and a cubic phase coexist [6-10]. Thus a similar behavior in the system $2(ZnS)_x(CuGaS_2)_{1-x}$ can be expected.

Here we report on the crystal growth of Zn_2CuGaS_4 using chemical vapor transport. The evolved material and the crystals grown were characterized with respect to their chemical composition, crystal structure and bandgap energy.

The CVT grown single crystals show different chemical compositions. We found a crystal with the composition $Zn_{0.49}Cu_{0.26}Ga_{0.25}S$ which corresponds to a $2(ZnS)_x(CuGaS_2)_{1-x}$ mixed crystal with x~0.5 (equivalent to Zn_2CuGaS_4). The refinement of XRD data has shown that this material adopts the sphalerite type structure assuming a statistic distribution of the cations on one Wyckoff position. For another crystal we found the composition $Zn_{0.37}Cu_{0.32}Ga_{0.31}S$ which corresponds to a $2(ZnS)_x(CuGaS_2)_{1-x}$ mixed crystal with x~0.37. This crystal consists of a tetragonal chalcopyrite-type as well as a cubic sphalerite-type phase, Bragg peaks of both phases can be found in the XRD pattern. The phase distribution obtained by electron backscatter diffraction (figures below) depict tetragonal domains (blue) in various orientations within a cubic matrix (red). Thus this crystal is placed within the two-phase field of the $2(ZnS)_x(CuGaS_2)_{1-x}$ solid solution.

References:

(1) L. Bindi, J.A. Jaszczak, Minerals **2020**, 10, 467
(2) P.B. Barton, P.M. Bethke, Am. Miner. **1987**, 72 (5-6), 451-467
(3) E. F. Apple, J. Electrochem. Soc. **1958** 105, 251.
(4) M. Robbins, M. A. Miksovsky, J. Solid State Chem. **1972**, 5, 462.
(5) P. G. Gallardo, Phys. Stat. Sol. a **1992**, 134, 119.
(6) S. Schorr, G. Wagner, J. Alloys Comp. **2005**, 396, 202
(7) G. Wagner, F. Fleischer, S. Schorr, J. Cryst. Growth **2005**, 283, 356
(8) G. Wagner, S. Lehmann, S. Schorr, J. Solid State Chem. 178 **2005**, 3631-3638
(9) L. Roussak, G. Wagner, S. Schorr, K. Bente, J. Solid State Chem. 178 **2005**, 3476-3484
(10) S. Schorr, Thin Sol. Films 515 **2007**, 5985 – 5991

Figure 1: Single crystal $2(ZnS)_x(CuGaS_2)_{1-x}$ with x=0.37 a) SEM image, b) EBSD map

Fig. 1

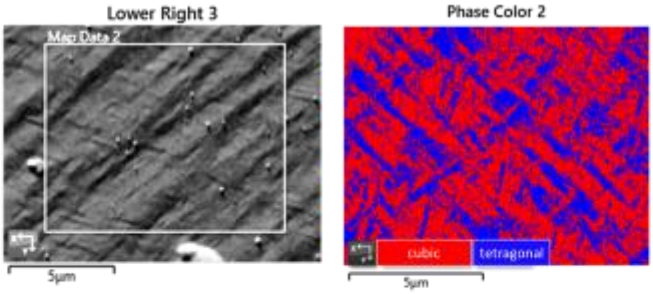

PP-128

Accurate crystal structures of ices from X-ray and electron diffractions with Hirshfeld atom refinement

K. Woźniak (Warsaw/PL), M. Chodkiewicz (Warsaw/PL), R. Gajda (Warsaw/PL)

Background: Water is an essential chemical compound for living organisms, and twenty of its different crystal solid forms (ices) are known. Still, there are many fundamental problems with these structures such as establishing the correct positions and thermal motions of hydrogen atoms. The list of ice structures is not yet complete as DFT calculations and spectroscopic measurements have suggested existence for additional as of yet unknown phases. In many ice structures, neither neutron diffraction nor DFT calculations nor X-ray diffraction methods can easily solve the problem of hydrogen atom disorder or accurately determine their atomic displacement parameters.

Methods: We applied a new way of refinement of single crystal high pressure X-ray synchrotron and laboratory X-ray and electron diffraction data called Hirshfeld Atom Refinement. This method utilizes aspherical atomic scattering factors (X-rays), and aspherical atomic electrostatic potentials (ED), based on so called stockholder (Hirshfeld) partition and is especially effective in the case of refinement of crystals of H-rich compounds.

Results: Here we present accurate crystal structures of H_2O, D_2O and mixed (50%H_2O/50%D_2O) ice VI and ice VII obtained by Hirshfeld Atom Refinement (HAR) against high pressure single crystal synchrotron and laboratory X-ray diffraction data as well as results of refinement hexagonal ice obtained by HAR against electron diffraction data. It was possible to obtain O-H bond lengths and anisotropic atomic displacement parameters for disordered hydrogen atoms which are in good agreement with the corresponding results of single crystal neutron diffraction data.

Conclusions: Our results show that Hirshfeld atom refinement against X-ray diffraction and electron diffraction data is a tool which can compete with neutron diffraction in detailed studies of polymorphic forms of ice and crystals of other hydrogen rich compounds. As neutron diffraction is relatively expensive, requires larger crystals which might be difficult to obtain, and access to neutron facilities is restricted, cheaper and more accessible X-ray measurements combined with HAR can facilitate the verification of the existing ice polymorphs and the quest for the new ones.

Figure 1: Examples of water clusters (259 in total) considered.

References:

(1) M. L. Chodkiewicz, R. Gajda, B. Lavina, S. Tkachev, V. B. Prakapenka, P. Dera, K. Woźniak, Accurate crystal structure of ice VI from X-ray diffraction with Hirshfeld Atom Refinement, *IUCRJ*, 9 (**2022) 573-579.**

Acknowledgements: Financial support of this work by the National Science Centre, Poland, through OPUS 21 grant number DEC-2021/41/B/ST4/03010 is gratefully acknowledged. The work was accomplished at the TEAM TECH Core Facility for crystallographic and biophysical research to support the development of medicinal products sponsored by the Foundation for Polish Science (FNP) and at the Cryoelectron Microscopy and Electron DIffraction Core Facility at CENT (Univercity of Warsaw, Poland). The synchrotron radiation experiments were performed at the APS (Proposal No. GUP-71134) and DESY (Proposal I-20200083 EC).

Fig. 1

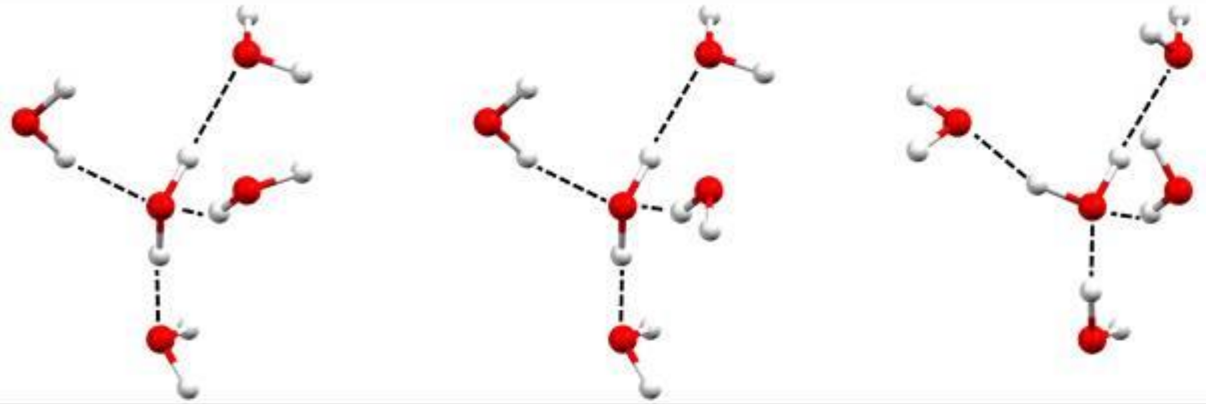

PP-129

Structural features of interaction 4-aminopyridine with layered semiconductors

A. Rahimli (Baku/AZ), I. Amiraslanov (Baku/AZ)

It is known that layered hexagonal and orthorhombic phases of the InGaS3 compound and FePS3 crystals intercalated by 4-aminopyridine (4-AP) molecules have been synthesized and studied. Numerous experiments have shown that when interacting with layered sulfides, 4-aminopyridine molecules are more effective in the formation of intercalate than other analogs close to it in size and active groups. This report will present the results of the interaction of the single crystals of layered selenite of α-In2Se3 with 4-aminopyridine molecules.

The α-In2Se3 crystals are promising material, which characterized layered structure with sp.gr. R3m. At 200 °C this structure transformed into a new layered structure with sp.gr. R-3m. This phase transition is reversible and belongs to "single crystal to single crystal" type. The α-In2Se3 crystals are well investigated by different authors. Particularly was found that these crystals exhibited huge anisotropic properties with regard to both their electrical resistivity and Seebeck coefficient. At 20 K the in-plane vs. out-of-plane electrical resistivity anisotropic-ratio was approximately 490,000. The optical energy gap of the single crystal was found to be 1.367 eV at 5 K. Using a vertical metal/α-In2Se3/ITO junction is reported showing a clear band edge characteristic in spectral sensitivity at 680 nm, which corresponds to an ultra-high sensitivity of 1000 A/W. In addition, the asymmetric barrier height arising from the ITO and Au contacts to the α-In2Se3 vertical junction resulted in a photovoltaic effect with VOC ~ 0.1 V and ISC ~ 0.4 μA under an illumination of 520 nm.

Single crystals of α-In2Se3 were grown by using the Bridgman method. The structural characteristics of the obtained material were refined by the XRD method and the unit cell parameters are as follows: sp.gr. R3m, V = 402.2(2) A3, a(A) = 4.0214(5); c(Å) = 28.793(7). Further, these crystals and crystalline 4-AP were placed in an evacuated quartz ampoule and heated to 250 °C. In doing so, we hoped to obtain a new intercalated compound. However, as a result, a new yellow polycrystalline compound (YPC) was formed. It was determined that the obtained new compound belongs to the orthorhombic phase and is characterized by the following parameters: Sp.gr. C2221, V=1032.76 A3, a = 24.95 (Å), b = 3.972 (Å), c = 10.420 (Å).Below are X-ray diffraction patterns of α-In2Se3 and YPC crystals. (Fig. 1). The report will provide detailed information about the research of a new substance synthesized as a result of Solid-Liquid interaction.

Literature:

(1) Chi, Yang; Sun, Zong-Dong; Xu, Qian-Ting; Xue, Huai-Guo; Guo, Sheng-Ping Hexagonal In2Se3: A Defect Wurtzite-Type Infrared Nonlinear Optical Material with Moderate Birefringence Contributed by Unique InSe5t. ACS Appl. Mater. Interfaces 2020, 12, 15, 17699-17705. https://pubs.acs.org/doi/10.1021/acsami.9b23085
(2) Guilherme Almeida, Sedat Dogan, Giovanni Bertoni, Cinzia Giannini, Roberto Gaspari, Stefano Perissinotto, Roman Krahne, Sandeep Ghosh, Liberato Manna. Colloidal Monolayer β-In 2 Se 3 Nanosheets with High Photoresponsivity. J. Am. Chem. Soc. 2017, 139, 8, 3005–3011. https://doi.org/10.1021/jacs.6b11255
(3) Xin Tao and Yi Gu. Crystalline−Crystalline Phase Transformation in Two-Dimensional In2Se3 Thin Layers. Nano Lett. 2013, 13, 3501−3505 dx.doi.org/10.1021/nl400888p
(4) L. Debbichi, O. Eriksson, and S. Lebègue, Two Dimensional Indium Selenides Compounds: An ab-initio Study.J. Phys. Chem. Lett. 2015, 6, 15, 3098–3103 https://doi.org/10.1021/acs.jpclett.5b01356
(5) Xin Tao and Yi Gu. Crystalline−Crystalline Phase Transformation in Two-Dimensional
(6) In2Se3 Thin Layers. Nano Lett. 2013, 13, 3501−3505 dx.doi.org/10.1021/nl400888p
(7) Hyung-Gon Kim, In-Soen Min, Wha-Tek Kim. The phase transition temperature of the a-In2Se3 single crystal. Solid State Communications, Vol. 64, No. 5, pp. 819-822, 1987. https://doi.org/10.1016/0038-1098(87)90708-3

Fig. 1

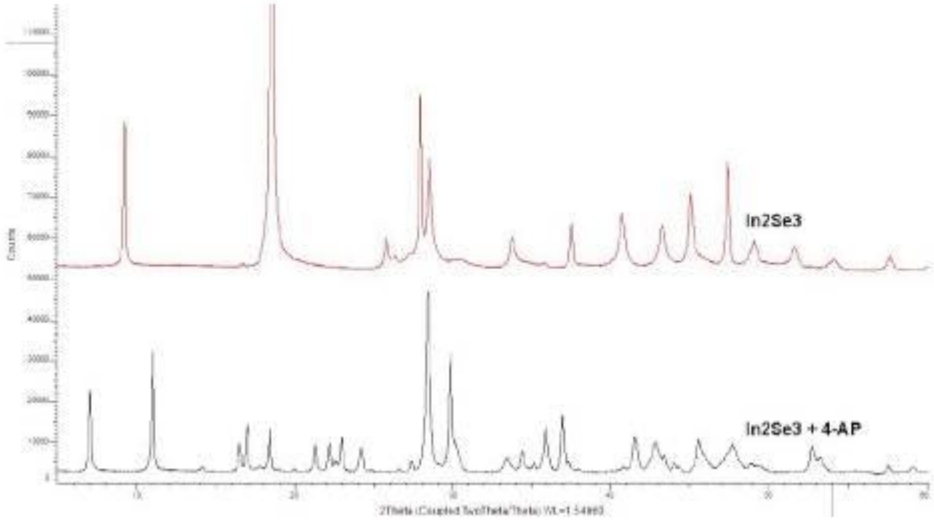
110000
100000
90000
80000
70000
60000
50000
40000
30000
20000
10000
0
Counts
In2Se3
In2Se3 + 4-AP
10
20
30
40
50
60
2Theta (Coupled TwoTheta/Theta) WL=1.54060

Late Poster

PP-130

Sodium-ion solid electrolytes – computational search and experimental validation

T. Leisegang, K. Uhlemann, S. Kachariya, M. Momeni (Freiberg/DE)

Currently, lead-acid and lithium-ion batteries dominate the market, with the latter continuing to grow rapidly in importance. This leads to considerable future supply risks for the necessary raw materials as the quantities required exceed those available on the market today by up to a factor of 10. Therefore, the search for new material systems and battery concepts appears to be purposeful to further diversify battery technologies and thus minimize the raw material supply risks as well as social and environmental impacts of their procurement.

Accordingly, novel material systems must combine readily available raw materials, enable high energy densities of the batteries, and ensure a higher safety during their operation. The Na-ion battery, utilizing liquid electrolyte, is already on the cusp of commercialization. To increase its safety, cyclability, and energy density, solid electrolytes are promising.

Here, we present the results of a material screening to identify Na+ ion conductors for sustainable solid electrolytes for room-temperature Na-ion batteries. We selected the promising candidate Na2Mg3Zn2Si12O30, synthesized it by solid-state reaction, and characterized the crystal structure and the ionic conductivity. We successfully obtained a new Na-ion conductor.